Investigation of new solar cell technology III-V//Si behavior under irradiations for space applications

Karim Medjoubi

INSTITUT POLYTECHNIQUE DE PARIS

NNT : 2021IPPAX004

Thèse de doctorat

Investigation of the emerging III-V//Si tandem solar cell behavior under irradiations for space applications

Thèse de doctorat de l'Institut Polytechnique de Paris
préparée à l'École Polytechnique

École doctorale n°626 Ecole Doctorale de l'Institut Polytechnique de Paris (ED IP Paris) - Spécialité de doctorat : Physique

Thèse présentée et soutenue à Le Bourget-du-Lac, le 03/02/2021, par

Karim Medjoubi

Composition du Jury :

Pr. Pere Roca i Cabarrocas Professeur à l'Ecole Polytechnique, LPICM	Président
Dr. Isabelle Monnet Directrice de recherche, CEA	Rapporteur
Dr. Stéphane Collin Directeur de recherche, CNRS	Rapporteur
Mr. Dominique Vergnet Expert senior, Airbus DS	Examinateur
Dr. Victor Khorenko Directeur de développement R&D, AzurSpace	Examinateur
Dr. Bruno Boizot Directeur de recherche, CEA	Directeur de thèse
Dr. Romain Cariou Ingénieur Chercheur, CEA	Encadrant

à mes Parents

Remerciements

Ce travail de thèse a été réalisé au Commissariat à l'Énergie Atomique et aux Énergies Alternatives - CEA, sur les sites du LITEN-INES et du LSI à l'école Polytechnique.

Je tiens à remercier en premier lieu mon encadrant Romain CARIOU et mon directeur de thèse Bruno BOIZOT. Merci à Bruno de m'avoir choisi et confié cette thèse et pour son soutien continu durant ces trois années. Je le remercie aussi pour son implication & sa disponibilité, pour m'avoir accueilli au sein du LSI et m'avoir guidé dans le monde de l'irradiation. Je tiens également à te remercier Bruno pour tous tes conseils et de m'avoir motivé à combiner la rédaction et la recherche d'emploi. Ensuite, je tiens à remercier Romain de m'avoir transmis son amour de la recherche scientifique et la rigueur. Je te remercie pour ton suivi tout au long de cette thèse, ta disponibilité permanente pour répondre à mes questions et à surmonter toutes les problématiques scientifiques et techniques. Merci aussi à vous pour votre bonne humeur et votre bienveillance, vous êtes comme une famille pour moi.

J'ai eu aussi un excellent jury de thèse : Pere Roca i Cabarrocas, Isabelle Monnet, Stéphane Collin, Dominique Vergnet et Victor Khorenko, avec qui j'ai eu l'honneur d'échanger; je les remercie pour leurs apports à ce manuscrit.

Je souhaite adresser mes remerciements à toute l'équipe du SMPV pour l'excellente ambiance de travail, pour les discussions scientifiques et amicales à la salle de café : Fabien, Yannick, Julien, Thomas, Julien, Anderson, Ichrak, Carla, Tatiana, Nicolas, Nouha, Romain, Bertrand, Clément, Imad, Mosaab, Marion, Aude, Caroline, Arnaud, Sarah et Martine. Un remerciement spécial à Philippe pour m'avoir accueilli dès le premier jour de mon stage et de m'avoir formé à l'utilisation de beaucoup d'équipements. Je te remercie aussi pour ton soutien et tes conseils.

Un grand merci à l'équipe du LETI : Laura Vauche, Elias Veinberg Vidal, Pierre Mur et Christophe Jany pour m'avoir initié au domaine du photovoltaïque.

Une deuxième partie de ma thèse a été réalisée au sein du LSI, Je voudrais remercier tous les membres : Michèle, Marie-Noelle, Elodie, Romain, Valérie, Marie-Claude, Audrey, Uliana, Simone, Valentin, Duy-Quang, Pierfrancesco et Mohamed. Je voudrais remercier spécialement Olivier et Jérémie avec qui j'ai beaucoup travaillé. Merci à vous pour les campagnes d'irradiations, l'installation des différents équipements et tous les défis soulevés pour les manips in-situ.

En dehors du cadre professionnel, je remercie mes amis : Amine, Amine et Amine, grand Abdou, Farid, Yasser, Raid et Imène pour leur soutien aussi bien durant les moments difficiles de cette thèse que dans les moments de joie, merci à vous.

Plus que tout, je remercie ma grande famille et ma belle-famille pour leurs soutien et encouragements à chaque étape de ma vie.

Je remercie beaucoup mes frères et sœurs, d'être toujours présents à mes côtés : Sara, Amine, Hatem, Lyna et Brahim. Vous êtes ma force !

A ma Binôme : Bouchra ma femme, merci pour toutes les nuits blanches que tu as passé à mes côtés en période de rédaction, merci pour tes corrections et le fameux « je prépare le plan pour la n^{ième} fois ». Merci d'avoir toujours cru en moi, de m'avoir toujours épaulé, tu es mon inspiration !

Mes parents ! Papa je te remercie pour ton encouragement continu, tes motivations et d'avoir toujours cru en moi. Je me souviens lorsque tu m'as expliqué l'effet photovoltaïque il y a une quinzaine d'année, tout à commencer à-ce-moment-là, tu as créé en moi l'esprit d'un chercheur. Maman je te serai éternellement reconnaissant pour tout ce que tu as fait pour moi. Merci pour ton acharnement lors de mes études, tu as vu, nous avons réussi. Merci de m'avoir toujours motivé, soutenu dans mes choix et su me recadrer quand j'avais tort. Merci d'être toujours présente à mes côtés. Tu es la lumière de ma vie !

Table of Contents

General Introduction

The exploration and discovery of space has evolved over time, from the use of the first telescope in 1609 to the multiple spacecraft and satellites up and running in space today. These vehicles are designed to fly and operate outside our planet to accomplish a broad range of missions. **Why space?**

The space race began during the Cold War between the USA and the USSR, during which every government wanted to show their technological superiority. In 1957, *Sputnik-1* and *-2* were the first satellites to be launched into space in low earth orbit (*LEO*) to measure the density of atmospheric layers. In 1958, the USA launched its first satellite called Explorer 1, which discovered for the first time the existence of the Earth's Van Allen magnetosphere. Then missions succeeded one another, promoted by several actors in the world. The broad range of missions performed in space fall into three major sectors: military, economic and scientific. Notwithstanding, they all have in common the need for electrical power. **The question is where do these spacecraft get their energy?** Indeed, the energy supply is necessary to send/receive signal to/from the ground, for its positioning and orientation throughout its mission duration (viability).

Multiple types of power generators were used for satellite, namely: batteries, nuclear, radioisotope and solar cells. Each technology has its own advantages and challenges in terms of system cost, mass, limits of use and viability. Historically, c-Si solar cells were developed by *Bell Laboratory* and were rapidly adapted for space applications. Their first use was indeed aboard *Vanguard I* launched in 1958 (see Fig. 1). The solar generator used there was based on Si solar cell technology with 8 - 10% efficiency[1]. Since then, solar cells became the dominant energy source in space because of the low launching cost of this type of system. However, the challenging points for Si solar cells are their relatively low efficiency back in time and their degradation against irradiation; in addition solar power limits of use in terms of distance from the Sun since it is the source of energy. Research

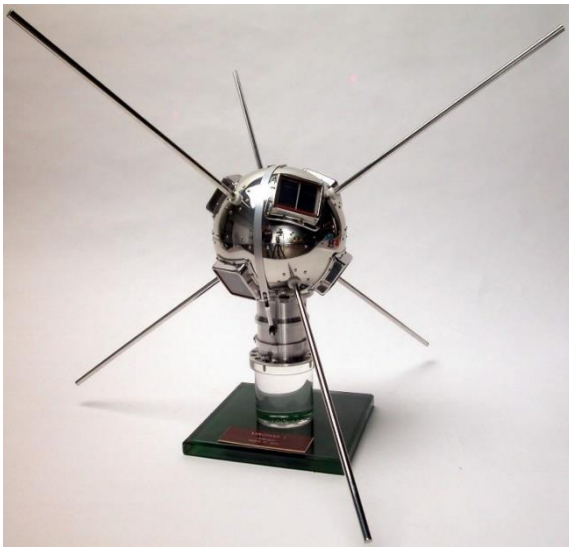

Fig. 1 *Replicas of the Vanguard 1 satellite built by the Naval Research Laboratory. Credit National Air Museum*

[1] R. L. Easton et al., "Vanguard I IGY Satellite (1958 Beta)," *Rev. Sci. Instrum.*, Feb. 1959, doi: 10.1063/1.1716492.

has been carried out on one hand to improve their initial conversion efficiency by optimizing the architecture (e.g. use of back surface fields, etc.), and on the other hand, by increasing their radiation hardness (e.g. switch from n- to p-type bulk solar cells).

Given the significant expansion of space missions as well as the technological advances in spacecraft operations, the need for power has also increased. In the 1980s, Si cell technology was gradually abandoned and replaced by III-V materials (mainly GaAs) offering better performances and higher radiation hardness. However, the performances of these single junction cells was still limited. A new double junction cell technology was proposed and adopted with an improved absorption and conversion of the solar spectrum, and thus offering initial efficiencies reaching 21.5% at that time. This dual-junction technology was launched for the first time in 1990 (see Fig. 2[2]). However, it also became obsolete at some point, and has subsequently been supplanted from 2000 on by triple-junctions cells with efficiency is above 25%, which became the state of the art technology for use in space applications until now. Nowadays the efficiency of this technology is reaching 37.9% (see NREL efficiency chart[3]). The cost of these cells is very high compared to other solar cells technologies due to the scarcity of some III-V materials and the relatively complex manufacturing process. However, up to now, and for this space PV market, cost as well as environmental impacts have not been the mains priorities.

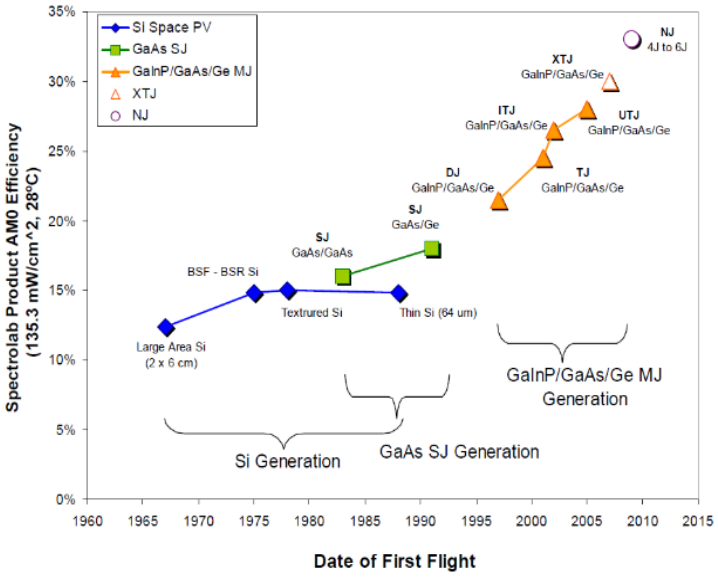

Fig. 2 *Historical evolution of satellites powered by Spectrolab solar cells as a function of the date of first launch*

The behavior of solar cells can differ from one environnement to another, depending on the total fluence of the space mission, the irradiation characteristics, the operating temperature and the irradiance intensity (e.g. 10 years at Geostationary Earth Orbit - *GEO* - where cells are operating under AM0 spectrum at 80°C, corresponds to a 1MeV electron fluence of

[2] C. Fetzer *et al.*, 19th Space Photovoltaic Research and Technology Conference 2007.
[3] https://www.nrel.gov/pv/cell-efficiency.html

10^{15} e.cm^{-2}). For instance, researchs have shown that degradation of III-V/Ge triple-junction solar cells at Normal Irradiance and Room Temperature (*NIRT*) conditions is driven by the GaAs middle cell degradation[4,5], whereas at Low Intensity and Low Temperature (*LILT*) conditions, the germanium subcell becomes the limiting one[6]. In addition, the main drawback of III-V multi-junction cells remains their high cost, which can be 2 to 3 orders of magnitude higher than terrestrial Si photovoltaics today. Indeed, the terrestrial silicon PV industry has now reached a high degree of industrial maturity (>100 GW annual market) and very low prices (2018 module ~ 0.2€/W[7,8]).

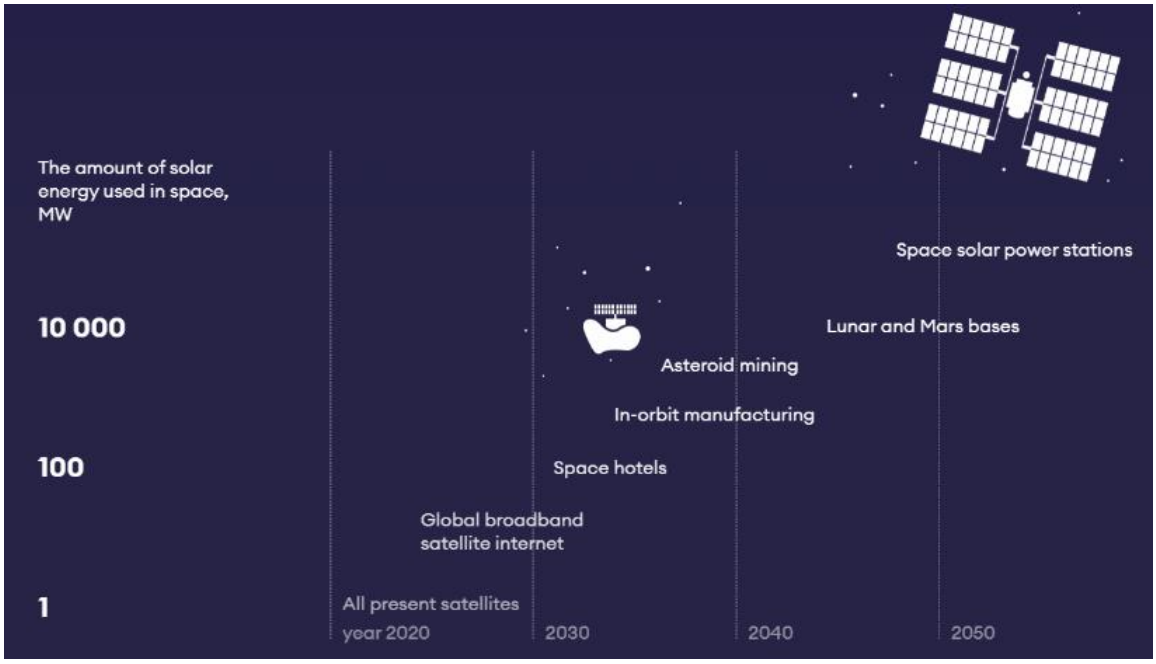

Fig. 3 *Projection of PV market size for future space applications, credit: Regher Solar*[9].

Today, the annual PV market size for space applications is estimated around 1 MW. Taking into account all future applications such as the launch of thousands of satellites for worldwide internet covering (*LEO* constellations), space tourism and the creation of lunar and martial bases, this PV market may grow by two orders of magnitude each coming decade (see Fig. 3). Thus, within this context of market growth, application diversifications, and the cost reduction challenge that space technologies are facing (the "NewSpace" revolution), it is worth investigating the hybrid III-V//Si solar cell technology potential for space. Silicon is an

[4] M. Imaizumi et al., *Prog. Photovolt. Res. Appl.*, doi: 10.1002/pip.2840.
[5] G. Yan et al., *J. Lumin.*, vol. 219, p. 116905, Mar. 2020, doi: 10.1016/j.jlumin.2019.116905
[6] S. Park, et al., *E3S Web of Conferences*, 2017, vol. 16, p. 04004.
[7] M. A. Woodhouse, National Renewable Energy Lab.(NREL), Golden, CO (United States), 2019
[8] https://www.ise.fraunhofer.de/en/publications/studies/photovoltaics-report.html
[9] http://regher.com/

interesting candidate as an alternative bottom cell for III-V multi-junction solar cells for several reasons. Nowadays, the record III-V//Si cells reach similar begin-of-life performances (> 34% AM1.5g) than conventional III-V/Ge solar cells[10,11,12]. Si material has a significantly lower cost than Ge and its density is more than twice smaller compared to Ge (mass saving)[13]. Low cost III-V/Si fabrication process (direct growth) has recently demonstrated efficiencies of 25.9%[14]. While the silicon high diffusion length makes it more sensitive to irradiation compared to Ge, it is possible to mitigate this weak radiation hardness by appropriate choices of thickness, doping, impurities and architecture[15,16,17].

The aim of this work is thus the investigation of the emerging III-V//Si (2- and 3-junctions) multi-junction solar cells technology behavior and limitations for space applications. **The main problematics addressed in this thesis are the following**:

- *How do Si-based tandem cells behave when exposed to electrons/protons irradiations ?*
- *What are the mechasnisms and the amplitudes of the degradations under irradiations ?*
- *What are the temperature dependance of those effects ?*
- *What is the most interesting III-V//Si cell architecture depending on the space environment (near-Earth and deep space)?*
- *What are the advantages and limitations of this technology in comparison with actual space standard ?*

Chapter I is divided into three major parts. In a first section, the fundamental aspects are presented from the properties of the semiconductor to the design of a single-junction solar cell. The limitations that lead to the development of multi-junction solar cells are presented along with the solutions that these technologies offer. Due to the different lattice parameters of III-V and Si materials, several challenges are to be solved for the fabrication of this emerging III-V on Si multi-jonction technology. The solutions proposed in the literature are thus summarized. In a second section, we detail the specificities of the space environment in terms of temperature, spectrum and illumination intensity and their effects on solar cells properties; the space

[10] S. Essig *et al.*, *Nat Energy* **2,** 17144 (2017), doi: 10.1038/nenergy.2017.144.
[11] R. Cariou *et al.*, *Nat Energy* **3,** 326–333 (2018), doi: 10.1038/s41560-018-0125-0.
[12] *D. Lackner et al., Sol. RRL, vol. 4, no. 9, p. 2000210, 2020, doi: 10.1002/solr.202000210.*
[13] E. M. Gaddy, doi: 10.1002/(SICI)1099-159X(199603/04)4:2<155::AID-PIP128>3.0.CO;2-#.
[14] M. Feifel *et al.*, *IEEE J. Photovolt.*, vol. 8, no. 6, pp. 1590–1595, Nov. 2018, doi: 10.1109/JPHOTOV.2018.2868015.
[15] M. Cappelletti, et al., Meas. Sci. Technol. vol. 28. 2013, Doi: 10.1088/1361-6501/ab46e4
[16] A. ur Rehman et al., *J. Korean Phys. Soc.*, vol. 68, no. 4, pp. 593–598, Feb. 2016, doi: 10.3938/jkps.68.593.
[17] M. Yamaguchi et al., *Appl. Phys. Lett.*, vol. 68, no. 22, pp. 3141–3143, May 1996, doi: 10.1063/1.115804

radiative environment is introduced as well. In the last part, the effects of charged particles of a broad spectrum (type of particles, energy and fluence) on the behaviour of solar cells are presented.

In **chapter II**, the architectures of the solar cells used in this work, namely c-Si 1J, AlGaAs//Si 2J and GaInP/AlGaAs//Si 3J, as well as their manufacturing processes based on surface activated wafer bonding are detailed. In order to compare and analyze precisely the behavior of the solar cells, especially the multi-junctions, in various environmental conditions (temperature, intensity and irradiation), reliable and reproducible characterizations are necessary. To ensure this, the calibration and measurement methods of these devices using two types of solar simulator (flash & *LED*) are discussed. In the last section, we present the specifications of the particles accelerators that were used for this study, as well as the chosen irradiation conditions (fluence, energy, flux, temperature). In addition we present the adopted protocols for the irradiation and characterization processes in both near-Earth and deep space conditions.

Chapter III is dedicated to study the behavior of the III-V//Si devices for near-earth space applications, i.e. under 1-sun AM0 irradiance and room temperature conditions; irradiations are thus performed at room temperature. First, simulations of particle-matter interactions are performed in the case of electrons and protons for the various cell architectures studied here. These simulations underline the differences between each cells architectures and irradiation particles. Then, through experimental tests and post-irradiation *I-V* measurements it was possible to identify which cell parameter is the most impacted by the irradiations and the most harmfull for the output power, and compare the degradation rates of each architecture with fluences. By measurements of the quantum efficiency, it was possible to analyze individual subcells degradations. These measurements have also been used in a physical model to extract the Si bottom cell minority carrier lifetime, a critical parameter strongly impacted by irradiations. The case of proton irradiations is more complex, since their lower penetration depth results in a non uniform degradation within the c-Si absorber. An optoelectronic model was applied to reconstruct the *I-V* characteristic curves of the III-V sub-cells based on quantum efficiency and spectral electroluminescence measurements. With this approach, we were able to quantify the degradation on each sub-cells and thus derived their relative contributions to the multi-junction device degradation.

In chapter IV, the behavior of these III-V//Si solar cells is investigated for deep space applications, i.e. for low intensity and low temperature conditions; consequently some cells were irradiated at cryogenic temperatures. As a first step, the behavior of these cells at low temperatures is investigated through thermal cycling. Secondly, the effects of intensity and temperature on the key electrical parameters are studied and shown to be in good agreement with the theory. The degradations after irradiation at 120 K & 300 K are compared: while similarities appear between both conditions, the amplitude of losses is more pronounced at low temperature. The effect of heating up to room temperature for the cells irradiated at 120 K were investigated; the improvement observed suggest some defects annealing. In both the *NIRT* and *LILT* cases, the behavior of Si-based tandem solar cells are compared to conventional space qualified III-V/Ge cells.

CHAPTER I Solar cells and irradiation theoretical background

I.1 Introduction

As explained in the general introduction, the solar cell assemblies on board of satellites face different extreme environments during their mission duration, whether around the Earth for telecommunications, or further away into the solar system for scientific and discovery applications.

The first part of this chapter is dedicated to the fundamental concepts of semiconductors, differentiating direct and indirect bandgap with their interaction with photons. The working principles and architecture of Single-Junction (SJ) solar cells as well as their fundamental limitations will be discussed. The Multi-Junction (MJ) solar cells, offering a solution to overcome the single-junction theoretical efficiency limits (i.e. optical and thermalization losses), will then be introduced. An overview of fabrication processes of two-terminal cells will be presented, with a focus on III-V materials integration on silicon by hetero-epitaxy or direct bonding, with their corresponding challenges.

The second part of this chapter is dedicated to the description of the space environment in terms of illumination intensity and temperature in the solar system: starting from the high temperature and high illumination intensity near the sun, up to the low temperature and low illumination level environment corresponding to the deep space. The variation of the solar cells electrical properties with irradiance intensity and temperature will be presented for single-junctions, while highlighting the complexity for electrical parameters evolution prediction in the case of the multi-junction solar cells.

In a third part, the space radiative environment will be presented in terms of particle types, origin, energy and flux near Earth and for Jupiter (deep space) environments. The different mechanisms of particle-matter interactions will be explained, with a focus on the effects resulting mainly from atomic displacements, which is at the same time, the least present energy loss mechanism, and the one affecting the most the behavior of crystalline solar cells. The irradiation defects will be briefly presented and we will mainly illustrate their effects on the electrical behavior of solar cells.

I.2 Physics of solar cells

In this section, we are interested in a brief description of semiconductors and their behavior under light excitation, in correlation with light absorption processes (for direct & indirect bandgaps). We will then describe the architecture of single-junction solar cells with the corresponding optical and electrical losses defining the theoretical maximum efficiency. Finally, we will present the advantages of tandem solar cells in overcoming limits of SJ conversion efficiency as well as the challenges of manufacturing two-terminal silicon-based solar cells.

I.2.1. Photon-semiconductor interactions

Semiconductor band structure

Semiconductors are materials with electrical conductivity values, σ, between conductive materials (e.g. metal, $\sigma > 10^3$ S.cm) and insulator (e.g. glass, $\sigma < 10^{-10}$ S.cm). The physical reason responsible for electrical conducting, semi-conducting or insulating property is the availability or lack of free charge carriers [1], [2]. Since the conductivity is tunable by voltage, doping, light, temperature & strain, the semiconductor materials can act as an insulator or a conductor. In semiconductors crystal, valence electrons are interacting with nuclei and electrons of the adjacent atoms. The consequence of these interactions and the crystal atomic order is the creation of distinct closely spaced electrons energy states forming electron energy bands corresponding to the different allowed states of energy as presented in Fig. I-1 [1], [3]. At zero Kelvin, all electrons in semiconductors are located in their lowest energy state (i.e. they stay in the valence band E_v), and by gaining enough energy electrons can move from the valence band to the energy states of the conduction band E_c, where they are free to move to other available states by diffusion or driven by electric field (drift). The minimum amount of energy needed for this transition is therefore (E_c - E_v). This energy difference is called the bandgap, E_g, as indicated in Fig. I-1. At temperature higher than zero Kelvin, the electrons are thermally excited and some of them can move to the conduction band. When electrons leave the valence band, a positive charge is left behind that can travel in the crystal: it is called a hole. This process corresponds to the generation of electron-hole pairs.

There are two types of semiconductors, elemental and compound materials. Elemental materials are found in column IV of the periodic table such as silicon (Si) or germanium (Ge). Compound material are composed of different elements from the periodic table, for instance gallium arsenide (GaAs); when composed of elements of the column III and V of the periodic

table, they are called III-V b. Compound semiconductor can also be made from the combination of column II and VI (II-VI semiconductor) such as zinc oxide (ZnO), or cadmium telluride (CdTe).

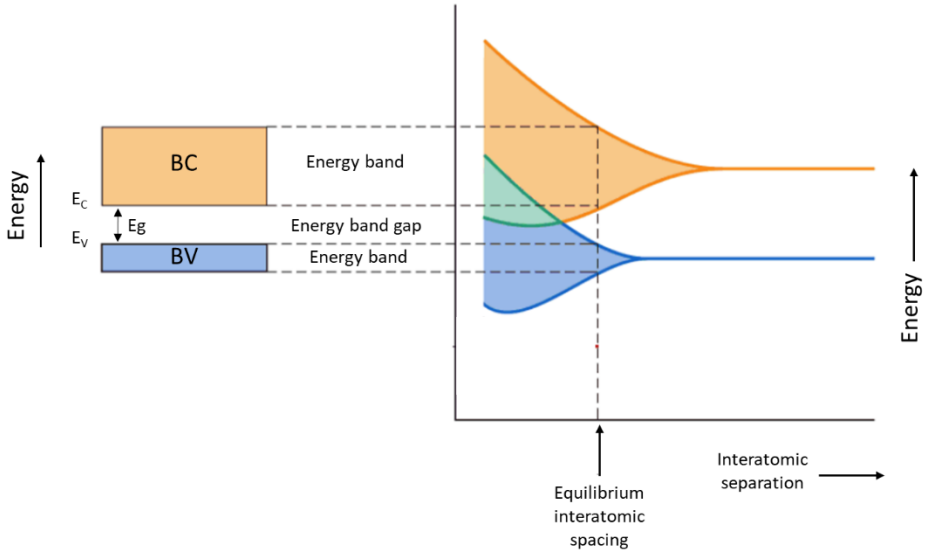

Fig. I-1 *Left: conventional representation of electron band structure in semiconductor, right: Schematic plot of electrons state energy separation of an aggregate of atoms as a function of interatomic distance, taken from [2].*

The Fig. I-2 illustrates a simplified energy band diagram. The allowed electron energies are plotted as a function of wave vector (k, expressed in cm^{-1}) for two main types of bandgap structures. When the maximum of the valence band and the minimum of the conduction band energies occur at the same wave vector, it corresponds to a direct bandgap. In that case, a single photon with energy higher than E_g is sufficient to create an electron-hole pair (see Fig**.** I-2 right) [4]. With increasing photons energy, the kinetic energy of the photo-generated electron-hole pairs also increases. To reach thermal equilibrium the excess energy will be lost as heat as the electrons and holes are scattered by lattice vibrations, down to the conduction and valence band edges. This thermalization process takes places at a time scale of about 10^{-12} s. Many III-V and II-VI compound semiconductors have a direct bandgap, including for example GaAs, InP or CdTe.

The so-called indirect bandgap is shown in Fig. I-2 (left). The maximum of valence band energy and the minimum of conduction band energy are located at different wave vector values. Examples of indirect bandgap are Si, Ge and AlP. In this case, a single photon with energy higher than E_g is not sufficient for the creation of an electron-hole pair. As the momentum of photons is very small, compared to that of crystal (electrons associated momentum), the absorption can only occur through the participation, absorption or emission, of phonons

(representative of atoms vibration) with a certain momentum simultaneously with the absorption of a photons to change the wave vector. Direct absorption without phonons absorption is also possible when photons energy is high enough (as presented in Fig. I-2, it occurs at ~ 3.3 eV for Si). The thermalization process also occurs in this type of bandgap structure [5]–[8].

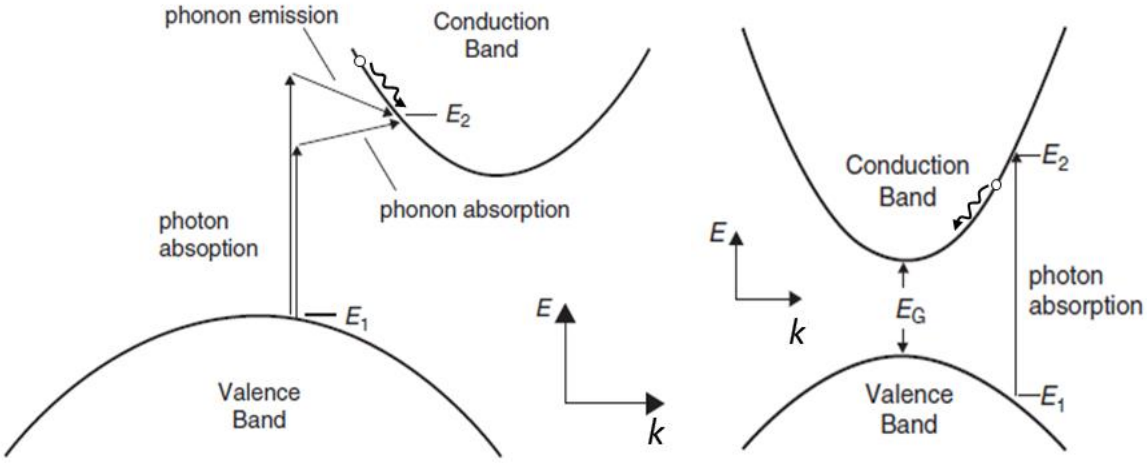

Fig. I-2 *Bandgap structure for semiconductor, left: photon absorption in indirect bandgap, right: photon absorption in direct bandgap [5].*

Photons absorption coefficient

The interaction between photons and semiconductor is characterized by an essential intrinsic material property: the absorption coefficient α(E). It quantifies the probability of absorbed photons per unit of material thickness as a function of their energy. The absorption coefficient of a given photon energy, E, is proportional to the probability, $P_{1\text{-}2}$, of the transition of an electron from initial state E_1 to the final state E_2, the density of electrons in valence band and the density of available states in the conduction band, $g_v(E_1)$ and $g_c(E_2)$ according to Eq. I-1.

$$\alpha(E) \propto \sum P_{1-2}.g_v(E_1).g_c(E_2) \qquad \text{I-1}$$

Due to the strong absorption of photons in direct bandgap semiconductors, the absorption coefficient is high and can range from 10^2 to 10^6 cm^{-1} near the bandgap energy. In other terms, all photons are absorbed in few micrometers: as presented in Fig. I-3, practically all the photons with energy close to GaAs bandgap E_g 1.42 eV are absorbed in 0.8 µm. In the case of direct bandgap, the absorption coefficient for most semiconductors near the band edge can be expressed as a function of a material dependent constant C^* (Eq. I-2) [6]–[8]. Beyond ~ 100 meV above E_g, this approximation is no longer valid; the absorption coefficient begins to stabilize.

$$\alpha(E) = C^*\left(E - E_g\right)^{1/2} \qquad \textit{I-2}$$

Indirect bandgap semiconductor are generally weaker absorber due to the necessity of the contribution of both photons and phonons for the creation of electron-hole pairs. Near the band edge, the absorption coefficient can be approximated as the sum of two processes according to Eq. I-3; absorption α_a (Eq. I-4) and emission α_e (Eq. I-5) of phonons with energy E_{ph}. Typical values of total absorption coefficient near bandgap can reach 10^{-1} to 10^{-2} cm^{-1}. As a result, photons will penetrate deeply in the semiconductor before their absorption.

$$\alpha(E) = \alpha_a + \alpha_e \qquad \textit{I-3}$$

With $$\alpha_a(E) = \frac{C\left(E - E_g + E_{ph}\right)^2}{e^{E_{ph}/kT} - 1} \qquad \textit{I-4}$$

And $$\alpha_e(E) = \frac{C\left(E - E_g + E_{ph}\right)^2}{1 - e^{-E_{ph}/kT}} \qquad \textit{I-5}$$

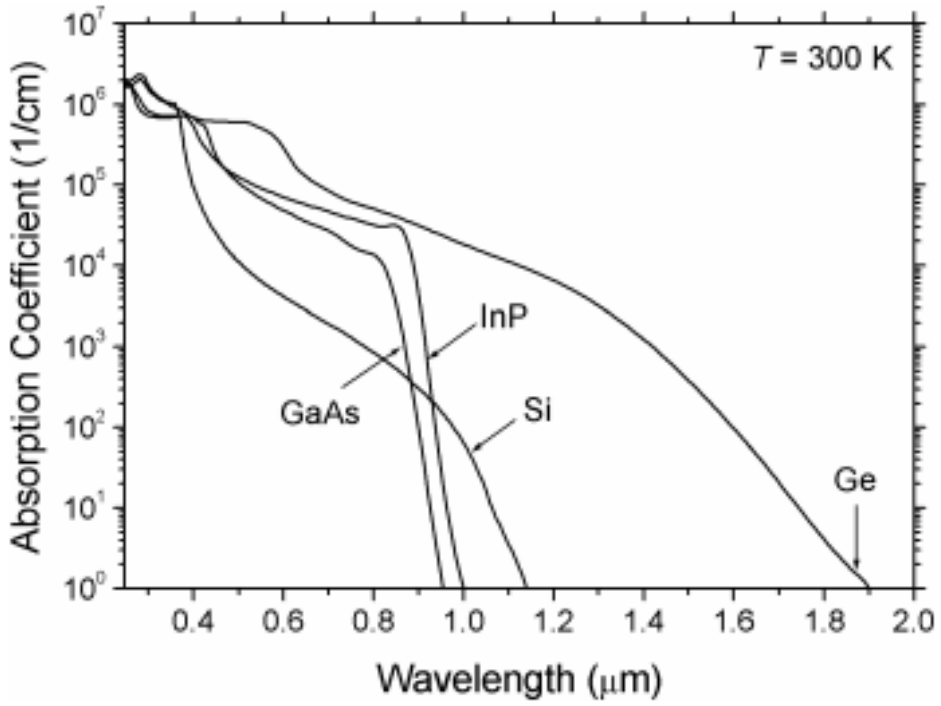

Fig. I-3 *Absorption coefficient as a function of wavelength for different intrinsic semiconductors, direct bandgaps: GaAs and InP, indirect bandgaps: Si and Ge [7].*

The Fig. I-3 presents absorption coefficient of the Si indirect bandgap semiconductor as a function of photons energy. Below 3.3 eV (376 nm), photons are absorbed in approximately 100 Å of material. Near the Si bandgap, the photons should penetrate a thickness of 2700 μm to be absorbed. As seen previously, these direct absorptions are no longer possible for lower energy. This reduces the probability of transition and hence the absorption coefficient.

Semiconductor doping

Adding impurities to the lattice changes the conductivity of semiconductor materials. The controlled process of adding atoms to intrinsic semiconductor is known as doping [9]. The conductivity of extrinsic semiconductor (with doping atoms) may vary by factors of thousands to millions in comparison to intrinsic semiconductor [10]. Two types of atoms are used for doping semiconductor: acceptor and donor, depending on their number of electrons on the valence band [11]–[13].

A p-type semiconductor is produced by introducing an acceptor such as Ga, In or B atoms to an intrinsic column IV semiconductor for example as presented in Fig. I-4. Each acceptor atom has three valence electrons. When it replaces an atom in the crystal lattice, only three valence electrons will be shared with the surrounding atoms having four valence electrons and therefore leading to the production of holes. The number of holes in extrinsic (acceptors doped) semiconductors is much greater than free electrons in intrinsic semiconductor. Thus, the conductivity is higher. Because of the positive charge of majority carriers (i.e. holes), the semiconductor is called p-type.

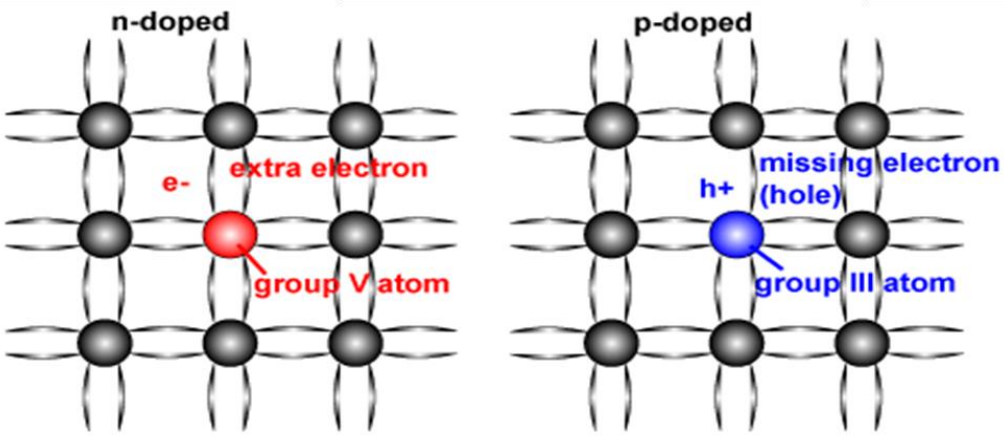

Fig. I-4 *Schematic of a column IV semiconductor crystal lattice doped with elements from column V to produce n-type and from column III to create p-type.*

An n-type semiconductors is formed by the introduction of donor such as Sb, As or P to an intrinsic semiconductor. Each atom has five valence electrons. When it replaces atoms in the crystal lattice, only four electrons are shared with the surrounding atoms. The fifth electron becomes a free electron (see Fig. I-4). The conductivity of extrinsic (donor doped) semiconductors is increased due to the higher number of free electrons. Because of the negative charge of majority carriers (i.e. electrons) these semiconductors are called n-type.

If no charge collecting structures are introduced in the semiconductor materials, the photo-generated electrons will tend to lose energy and re-occupy a low energy state in a valence band in a process called recombination. There is finally no net effect of the absorption besides emission of photons or heating up the material, depending on the recombination mechanism.

I.2.2. Single junction solar cells

The solar cells provide the additional function of electron-hole pairs separation before their recombination and enable charged-carriers collection. The electron-hole pairs separation happens with the influence of the internal electric field produced by the p-n junction where a n-type and a p-type semiconductors are joined together. Fig. I-5 presents a typical p-n junction architecture with a strong concentration difference of electrons and holes between the two types of semiconductor. When p- and n-type semiconductors are brought into contact, the electrons diffuse from the n-type side to the p-type side and, similarly, the holes flow by diffusion from p-type to n-type side. However, this leaves uncompensated ionized donor (N_D^+) in the n-type and acceptor ions (N_A^-) in the p-type, which are fixed to the lattice atoms on both sides and are unable to move. The fixed charges create an electric field (or electrostatic potential difference) across the junction in an opposite direction to carriers diffusion. We can see from Fig. I-5 that the free carriers energy will decrease quickly (electrons tend to lose their energy and inversely holes tend to gain energy) in the neighborhood of the p-n junction. This region is called depletion region or S*pace Charge Region* (*SCR*) since it is depleted of both electrons and holes and only the ionized fixed atoms remain [6], [14], [15]. The electric field is responsible for the movement of holes from the n-type to p-type and inversely for electrons, i.e. from p-type to n-type. This carrier flow is called drift. When diffusion starts, the diffusion current is high and drift current is low. As diffusion continues, the space charge region extends. This intensify the electric field and hence the drift current. The process continues until equilibrium is reach between both current. This is how p-n junction is created [8].

The Si p-n junction is usually formed by taking a p-type (respectively n-type) wafer and by introducing (e.g. by diffusion or implantation), close to its surface, n-type (respectively p-type) dopants. This process is usually performed at high temperature, with additional annealing step for dopant atoms activation. The junction is often formed very close to the front surface from where the light enters the cell [6], [16]. Two regions are distinguishable; the emitter which represents the layer on the top usually very thin (~ 0.5 μm in case of Si) and the base region, called also bulk, where almost all photons are absorbed.

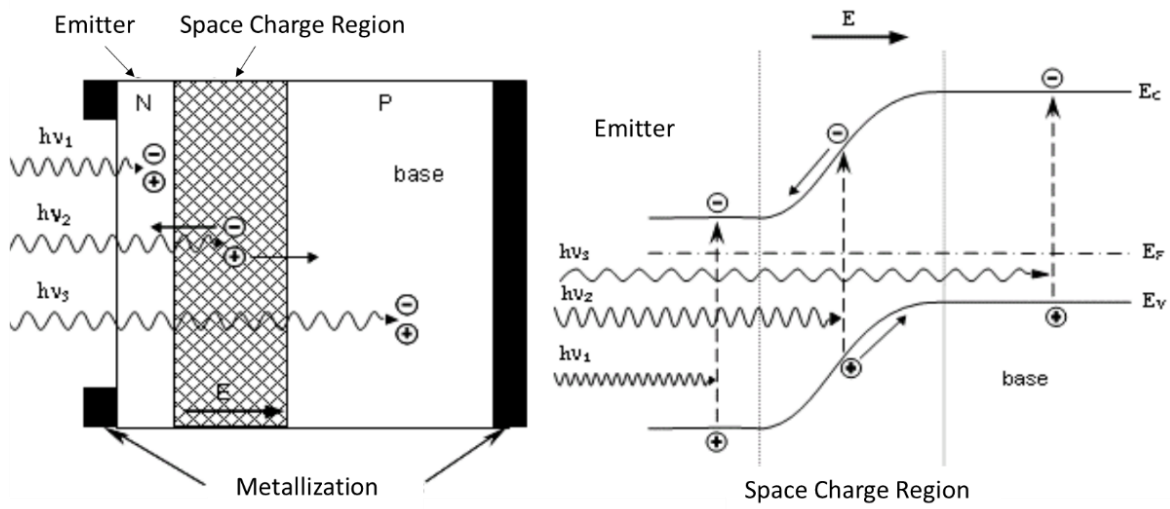

Fig. I-5 *Schematic representation (not at scale) left: structure of solar cell p-n junction, right: corresponding band diagram.*

Charges generation and recombination mechanisms

The photovoltaic effect can be briefly described as follows: when light enters a p-n junction, the semiconductor material absorbs photons with energy above its bandgap. Since the emitter thickness is very small compared to the bulk, the majority of the absorption takes place in the bulk. The photo-generated electron-hole pairs that diffuse long enough in the material to reach the junction will be separated by the electric field where they become majority carriers, i.e. electron (resp. hole) created in p-type (resp. n-type) where are minority carrier becomes majority carrier in n-type (resp. p-type) after being separated (see Fig. I-5). Therefore, electrons are swept to the n-type, which becomes negatively charged and holes are swept to the p-type, which becomes positively charged, creating a voltage. By connecting the front and rear contact by an external circuit, electrons (majority carrier) have high probability to be collected by the metallization, so they flow by creating an electric current that provides power to the connected load. Finally, they are returning to the solar cell through the other contact where they recombine with holes, returning to the valence band with the same energy as at the first.

The average distance traveled by electrons (in p-type bulk region) in the crystal before recombination with holes in the valence band is called minority carrier diffusion length, L (μm); it is expressed as a function of lifetime, τ (μs), through diffusion coefficient, D ($cm^2.s^{-1}$), according to Eq. I-6. It depends on the purity of the material, the doping level and the intrinsic property of the material.

$$L = \sqrt{D.\tau} \qquad \text{I-6}$$

When the thermal equilibrium of a semiconductor is temporary disturbed, for example by a flash light absorption (or other means), the photo-generated excess carrier density (electrons and holes) tends to decrease toward their equilibrium values through recombination. Three bulk recombination mechanisms are important to consider for solar cells operation: radiative, Auger and Shockley Read Hall (*SRH*). The corresponding lifetimes, τ, are related to the excess carrier concentration, Δn (cm^{-3}), through the recombination rate of mechanism i, U_i, according to Eq. I-7.

$$\tau = \frac{\Delta n}{U_i} \qquad \textit{I-7}$$

In radiative recombination, often called band-to-band recombination, electrons in the conduction band directly recombine with holes in the valence band resulting in photon emission with energy equal to the bandgap energy as presented in Fig. I-6. The rate of recombination U_{rad} ($cm^{-3}.s^{-1}$) can be expressed as Eq. I-8:

$$U_{rad} = B_r\,(np - n_i^2) \qquad \textit{I-8}$$

Where B_r ($cm^3.s^{-1}$) is the radiative recombination coefficient intrinsic to the material, *np* term represents the product of non-equilibrium electron-hole concentration and n_i^2 represents the intrinsic concentration at equilibrium. Values of B_r range from 10^{-9}-10^{-11} $cm^3.s^{-1}$ for direct bandgaps and from 10^{-13}-10^{-15} $cm^3.s^{-1}$ for indirect bandgap materials. The radiative recombination mechanism is dominant in direct bandgap materials [6].

In Auger recombination [17], the energy of transition is given to another carrier by increasing its kinetic energy, i.e. electron in conduction band or hole in valence band, as shown in Fig. I-6. The electron (or hole) kinetic energy is dissipated in the semiconductor by thermalization (heat generation) and returns to energy level near the band edge. Since the process occurs with three particles interaction, it is most pronounced at high doping levels or high injection level. The net recombination rate for two electrons in non-equilibrium condition is expressed as Eq. I-9:

$$U_{Auger} = B_{Auger,p}\,(n^2 p - n_0^2 p_0) \qquad \textit{I-9}$$

Values of B_{Auger} in the case of GaAs and Si are for instance in the order of 10^{-30} $cm^6.s^{-1}$ [17]–[19]. In direct bandgap where the radiative recombination is most dominant, Auger recombination is negligible. However, in indirect bandgap semiconductor such as Si or Ge, Auger is the dominant recombination process, which causes the theoretical intrinsic limitation on indirect bandgap semiconductor solar cell efficiency [19].

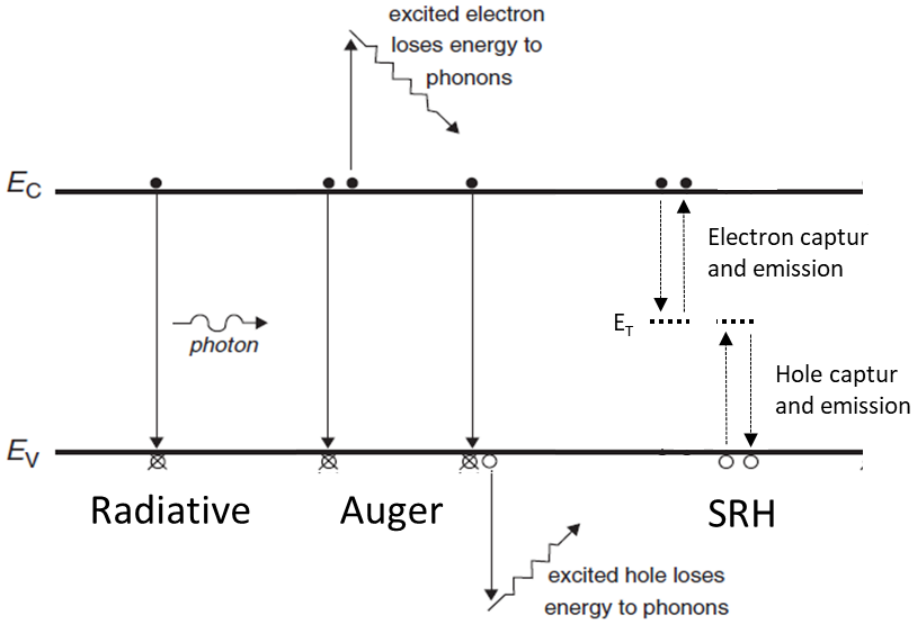

Fig. I-6 *Schematic representation of recombination mechanisms in a semiconductor [6], [8].*

In practice, most semiconductors will have crystallographic defects, impurities or vacancies incorporated in their crystal structure during growth. It is plausible that these atomic impurities produce defect level states deep in the bandgap, which have the ability to capture a free carrier through non-radiative recombination. This assisted trap mechanism is practically limiting loss in most solar cells. Shockley, Read and Hall [20], [21] introduce the theory of this recombination mechanism. Four fundamental processes are possible for recombination in trap states with concentration N_t (cm^{-3}) at an energy level E_t (eV), as schematically presented in Fig. I-6:

- A free electron is captured by an unoccupied energy level;
- An electron is emitted to the conduction band from an occupied energy level;
- A hole is captured by an occupied energy level in the bandgap;
- A hole is emitted into an occupied state in the valence band.

The recombination rate through single level trap is given by:

$$U_{SRH} = \frac{pn - n_i^2}{\frac{p + n_i e^{(E_i - E_t)/kT}}{\sigma_n \nu_{th} N_t} + \frac{n + n_i e^{(E_t - E_i)/kT}}{\sigma_p \nu_{th} N_t}} \qquad \text{I-10}$$

Where $\sigma_{n,p}$ is the capture cross section (cm^2) for electrons or holes, ν_{th} is the thermal velocity of carrier ($cm.s^{-1}$) and E_i (eV) is the Fermi level in intrinsic semiconductor. Since multiple traps

levels can be present in the forbidden band, the total recombination rate is the contribution of each trap (see Eq. I-11).

The bulk minority carrier lifetime, τ_{bulk} (s), which refers to the average time that a minority carrier passes into excited states before its recombination, can be described by the following equation:

$$\frac{1}{\tau_{bulk}} = \frac{1}{\tau_{rad}} + \frac{1}{\tau_{Auger}} + \sum_{trap,i} \frac{1}{\tau_{SRH,i}} \qquad \textit{I-11}$$

The interface between two materials of different natures, like those occurring at the front and the rear surface of solar cell have a high defect concentration due to dangling bonds and impurities. They manifest as an almost continuum of energy states in the bandgap, which act as recombination of free carriers reaching those interfaces (see Fig. I-7). This type of defect can be treated as for bulk SRH recombination, however the associated recombination rate is expressed per unit of surface and per second, as a function of electrons effective surface recombination velocity S_n (cm.s^{-1}) through Eq. I-12 [22].

$$U_S = S_n(n - n_0) \qquad \textit{I-12}$$

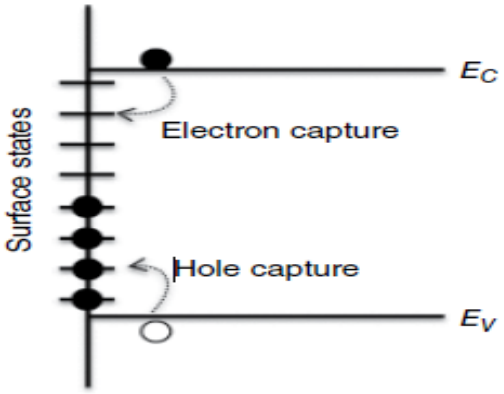

Fig. I-7 *Electrons and holes recombination at the surface.*

Although many solar cell architectures and layer stacks exist, common features or design principles are used in every devices. As an example of typical solar cells design, the structure of a c-Si homojunction solar cell with contact on both sides is shown in Fig. I-8.

Light absorption enhancement:

Crystalline silicon surface reflects 35% - 50% of photons depending on their wavelength. In order to minimize the photons reflection at the interface air/semiconductor, an Anti-Reflective Coating (*ARC*) is used as presented in Fig. I-8. The *ARC* can be either conductive or

a dielectric layer with a defined thickness so that the interference effects in the coating induce a phase shift between both wave reflected from the top of *ARC* and the semiconductor surfaces. These phase-shifted reflected waves destructively interfere with each other, leading in zero net reflected energy. Several layers combination can be used depending on targeted wavelength range and solar cell materials: i) typical one-layer *ARC*: SiO_2, SiN_x, TiO_2, ZnS [23]; ii) typical bi-layers *ARC*: SiN_x/SiO_2, TiO_2/SiO_2 ii) typical tri-layers *ARC*: $TiO_2/HfO_2/MgF_2$ [24]–[26]. The plasma-enhanced chemical vapor deposition technique is suitable for *ARC* deposition, with the advantage being a relatively low temperature (typically < 500°C) [8].

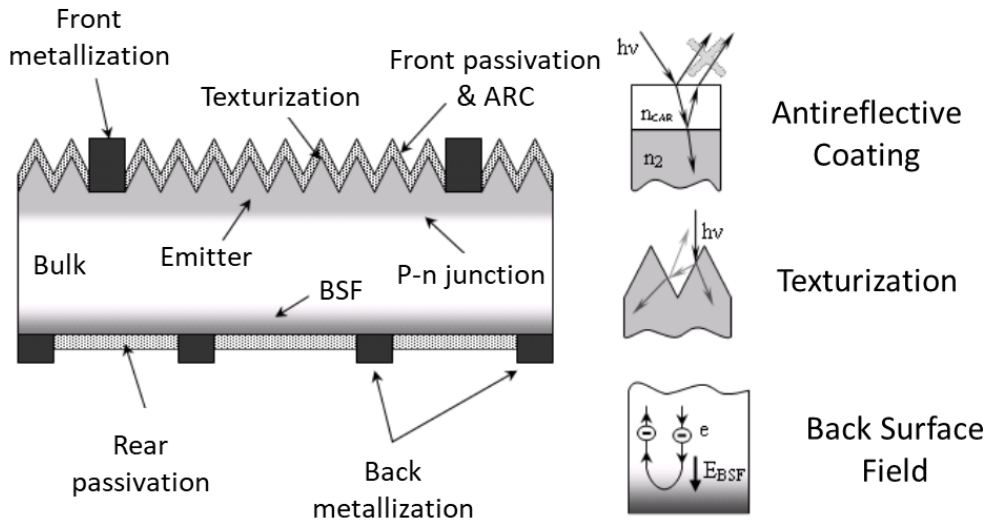

Fig. I-8 *Typical crystalline silicon solar cell architecture.*

The surface texturing is also an effective process to reduce reflections at the solar cell surface as presented in Fig. I-8. It aims at developing a micrometric topography on the surface, generally in the form of upward or downward pyramids for c-Si. As the wavelength of the incident light is shorter than the dimensions of the structure, the incident rays follow the laws of geometric optics. When a perpendicular ray arrives at the surface of the cell it will be reflected by one of the pyramid face towards an adjacent one, this double reflection decreases the total reflection coefficient. Different processes are used to texture the surface: mechanical, physical (e.g. plasma etching) or chemical (e.g. wet etching) [8], [27]–[29].

As seen above, absorption coefficient is dependent on semiconductor material and can reach very low values for indirect bandgap such as Si, especially at high wavelength. In order to counter-balance this effect, rear mirror can be implemented in addition to front texturation. In such configuration, the light path into the solar cell is increased thanks to multiple internal

reflections; therefore, it enhances the absorption and enable full absorption in a moderate thickness. This is commonly called light trapping or light confinement techniques [30].

In order to reduce the thickness of solar cells, which allows process-time and material saving, a technique called photonic or light trapping is used. As explained in section I.2, each material has an intrinsic property that defines the minimum thickness necessary for the absorption of a photon. By reducing the thickness of the cell, significant optical losses (incomplete light absorption) then take place that reduces the photo-generating current. However, light trapping allows decoupling of the solar cell thickness and the thickness traveled by a photon by adding back reflectors and surface texturization, which reflects the photon at the back and increases the number of passes due to total internal reflection. Recent researches have for instance reported 19.9% efficiency under AM1.5G for a 205 nm thick GaAs absorber with Ag back mirror reflector including nano-imprinted TiO_2 structure [31].

Front and rear surface passivation:

Semiconductor surfaces are usually responsible for a high defect density (dangling bonds, impurities, etc.) leading to non-negligible losses due to electron-hole pairs recombination at the surface. Indeed, surface recombination velocity can reach high values such as 10^5 - 10^6 $cm.s^{-1}$. As the recombination rate is directly related to the defects density (see Eq. I-11), the first strategy is to reduce the number of defects at the surface by deposition of dielectric layer, this is called chemical passivation [6]. The main passivation layers used for Si are AlO_x, SiO_2 and SiN_x, deposited at the following high temperatures 1000 °C, and 300 – 450 °C, respectively. Both techniques are sensitive to subsequent treatments with hydrogen to obtain low surface recombination velocity values (typically 10 – 100 $cm.s^{-1}$) [6], [32].

A second strategy consists of the creation of potential barrier at the back of solar cell (Back Surface Field, *BSF*) with highly doped region (e.g. p^+-p junction for p-type bulk) to ensure that the minority carriers remain in the bulk (see Fig. I-8). Therefore, they are kept away from highly recombining surfaces by field effect passivation. The two techniques are often used in combination with each other in high-efficiency cells concept.

Metallization:

The metal contacts at the front and rear side are used to collect the photo-generated carriers. The contacts must be ohmic, i.e. linear *I-V* characteristic of the contact. In addition, the contact

resistance is a critical parameter: a high contact resistance increases the ohmic losses and thus decreases the electrical performances [33].

Different processes are used to realize the contacts. For the majority of the industrial silicon solar cell, Ag pastes are screen-printed, therefore, ~100 µm wide fingers are obtained. However, in laboratory and at R&D level, photolithography and evaporation processes are used to form 10-15 µm wide metal fingers. Ti/Pd/Ag composition offers low contact resistance and high conductivity [6].

I.2.3. Electrical model & electrical operation

From an electrical point of view, a photovoltaic cell behaves like a diode. In obscurity, the Shockley diode equation describes the evolution of current density, J ($mA.cm^{-2}$), as a function of applied voltage, V (V) according to Eq. I-13.

$$J = J_0 \left[\exp\left(\frac{V}{nV_T}\right) - 1\right] \qquad \textit{I-13}$$

Where J_0 is the dark saturation current density that is related to recombination (low J_0 indicates high junction quality) and n the ideality factor. Thermal voltage is defined as $V_T = kT/q$, where q is the absolute value of electron charge, k is Boltzmann constant and T the temperature.

Under illumination, the solar cell produces current, J_{ph}, in opposite direction of dark saturation current. In practice due to non-perfect characteristics, shunt resistance R_{SH} (Ω.cm) and series resistance R_S (Ω.cm) are commonly considered in the diode model as presented schematically in Fig. I-9.

Eq. I-14. presents mathematical description of current evolution as a function of applied voltage of solar cell under illumination.

$$J = J_{ph} - J_0 \left[exp\left(\frac{V + JR_S}{nV_T}\right) - 1\right] - \frac{V + JR_S}{R_{SH}} \qquad \textit{I-14}$$

The current voltage characteristic, also known as *I-V* curve, of solar cell under illumination is presented in Fig. I-9 top-right. This plot illustrates three important factor for solar cell: short-circuit current, open circuit voltage and maximum power point. At small applied voltage, the dark saturation current density J_0 is negligible hence the solar cell is at short-circuit current, J_{SC}, and is approximated to the photo-generated current, J_{ph}, (see Eq. I-14). When increasing applied voltage, p-n junction current (recombination current) becomes important, therefore, the solar cell current drops rapidly.

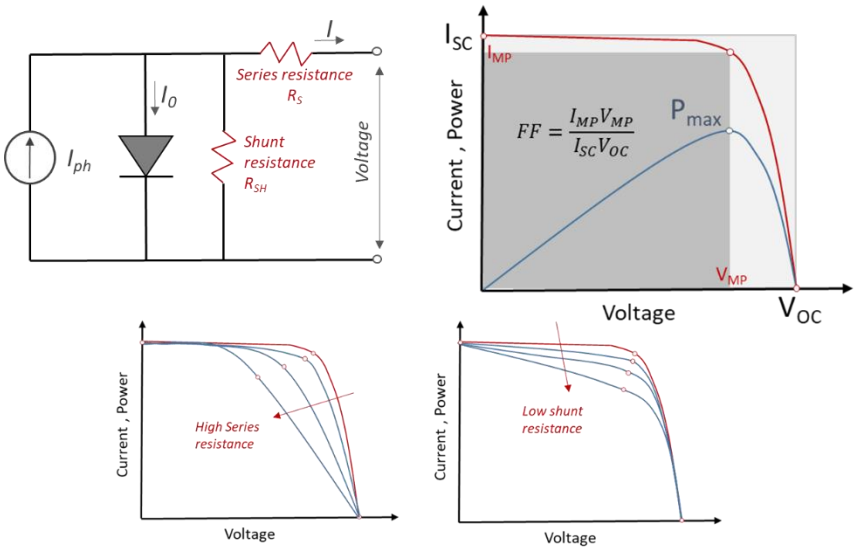

Fig. I-9 *Electrical model of solar cell top-left: Circuit diagram of a solar cell with shunt and series resistances, top-right: Current-voltage characteristic of solar cell under illumination and extraction of electrical parameters (J_{SC}, V_{OC} and FF), bottom-left: effect of series resistance on I-V curve, bottom-right: effect of shunt resistance on IV curve [34].*

The open circuit voltage, V_{OC}, is obtained when all photo-generated current flows through the diode, hence no current is drawn from the solar cell (I = 0). From Eq. I-15, the V_{OC} can be expressed as a function of J_{ph} and J_0 according to Eq. I-15.

$$V_{OC} = \frac{nkT}{q} Ln\left(\frac{J_{SC} + J_0}{J_0}\right) \approx \frac{nkT}{q} Ln\left(\frac{J_{SC}}{J_0}\right) \qquad \text{I-15}$$

The third key parameter is the maximum achievable power output, P_{max}, with corresponding $V = V_{MP}$ and $J = J_{MP}$. As seen in Fig. I-9 at this point of the curve, the rectangle area below defined by V_{MP} & J_{MP} is maximum, i.e. the output power is at its maximum. Equation I-16 defines the fill factor, FF (%), linked to this maximum power point. It can be understood graphically: FF is defined as the ratio of the rectangle area defined by V_{MP} & I_{MP} divided by the rectangle defined by Voc and Jsc (see dark and light grey areas in Fig. I-9).

$$FF = \frac{P_{max}}{J_{SC}V_{OC}} = \frac{J_{MP}V_{MP}}{J_{SC}V_{OC}} \qquad \text{I-16}$$

A key figure of merit for a solar cell is its power conversion efficiency, η(%), which is defined as the ration of P_{max} (W) and the incident power, P_{in} that is related to the spectrum distribution and its intensity.

$$\eta = \frac{P_{max}}{P_{in}} = \frac{FF\, J_{SC}\, V_{OC}}{P_{in}} \qquad \text{I-17}$$

The effect of R_S and R_{SH} on the *I-V* curve is illustrated in Fig. I-9 (bottom). Series resistances are the sum of the contribution from the different solar cell layers & interfaces: emitter, base and metallization (especially metal semiconductor interfaces) in addition to lateral resistances in each layer. The power losses due to R_S are more important for high photo-generated current J_{ph}, according to the first law of Joule; indeed the ohmic losses are proportional to the square of current. On the contrary, the effect of R_{SH} is more pronounced at low photo-generated current. Point defects in p-n junction, presence of impurities during process (diffusion metallization) or solar cell edges imperfections can be at the origin of the R_{SH}. Both resistances have a direct impact on the fill factor of the solar cell, hence on the output maximum power. In some cases, very large R_S (resp. low R_{SH}) can affect the short circuit current (resp. the open circuit voltage).

I.2.4. Limits of single junction

From equation I-17, it is clear that a high short circuit current J_{SC}, a high open circuit voltage V_{OC} and a fill factor FF as close as possible to one are needed for an efficient solar cell. Before introducing the multi-junction solar cells and the solutions they provide compared to single junction cells, first, the different losses that occur on single junction solar cells are presented.

The fundamental efficiency losses in a p-n junction are transmission losses and hot carrier thermal losses. Therefore, the efficiency is intrinsically limited by the bandgap of the materials. Wide bandgap materials can absorb only high energy photons, generating low short-circuit current but a high carrier potential after thermalization. On the other hand, small bandgap materials will absorb more photons, generating high short-circuit current, however low potential energy by charge carrier. These two losses are responsible for more than 40% efficiency losses for silicon single junction solar cells. Radiative recombination losses are, in the ideal case, the only recombination losses in the material.

The maximum theoretical efficiency known as the Shockley and Queisser (SQ) limit can be calculated using detailed balance theory, formulas and theory can easily be found in literature [8], [35]. In these calculations, all photons with energy higher than the bandgap ($E > E_g$) are assumed to be totally absorbed by the material, in other words the material is considered as optically thick enough to absorb all the photons as explained above in I.2.1. This limit corresponds to an ideal case where only radiative recombination of electron-hole pairs is considered. The non-radiative recombination is not considered: surface recombination depends

mainly on the structure of the solar cell and surface conditions, while volume recombination depends mainly on the quality of the material (dislocations, impurities, deep levels). In this case, the lifetime (equivalent to diffusion length) of the minority carrier is the main parameter and it is assumed to be infinite. Electrical losses (resistive) as well as optical (surface reflection) are also not considered, and are primarily dependent on the technological manufacturing processes and architecture of the cell. For the AM1.5G solar spectrum, the theoretical maximum limit of SQ is ~33.7% for an ideal material of 1.34 eV bandgap as presented in Fig. I-10 [36].

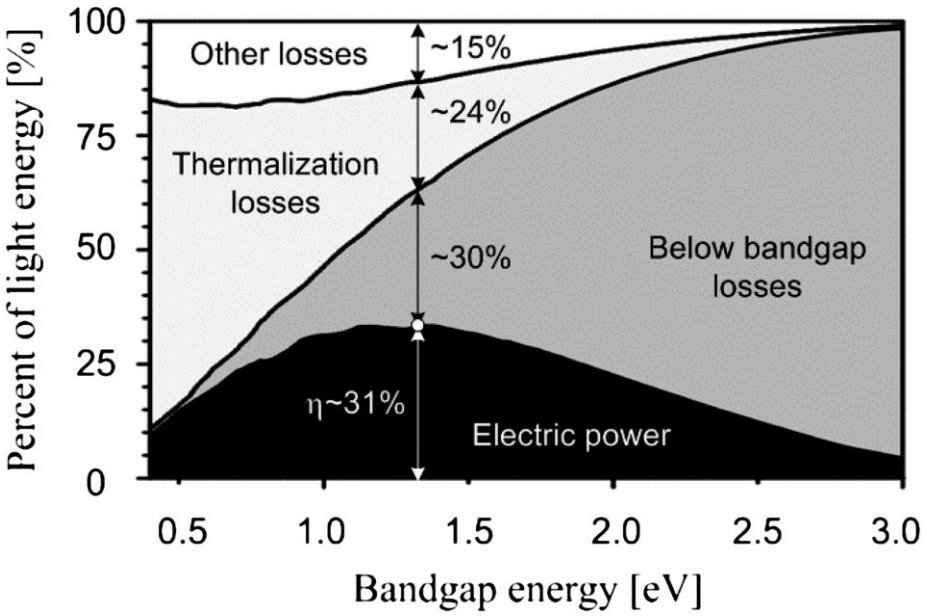

Fig. I-10 *Ideal solar cell efficiency as a function of semiconductor bandgaps with the corresponding thermalization and optical losses[35].*

I.2.5. Multi-junction/Tandem solar cells

The best solution to decrease thermalization and transmission issues, hence increase solar cell efficiency is the multi-junction (MJ) solar cell also called tandem. The principle of a MJ solar cell is based on combining (often in series) several p-n junctions, or sub-cells, of different bandgap energies, so that the junctions are optimized for different wavelengths for converting the broad solar spectrum more efficiently. This is achieved by spatial spectrum splitting or stacked sub-cell with two, three, or four terminals configurations as presented in Fig. I-11. Even the conception simplicity of spatial spectrum splitting, it is undesirable for mechanical and optical complexities [8]. In the case of three- and four-terminal configurations, it requires complicated structures, assembly processing and module configuration that make them less desirable than two-terminal configurations. Only the two-terminal configurations will be discussed in this thesis.

In a monolithical solar cell, the junctions are stacked in order of decreasing gap energy Eg, so that the light passes through the higher gap energy layer first. Photons of higher energies than this gap energy are absorbed, and those of lower energy reach the second junction. The process then repeats itself, depending on the number of junctions assembled. Earlier research works focused on GaInP/GaAs double-junction cells. These cells consist of a stack of two junctions, one made of GaInP, a high-gap material (1.85 eV) that absorbs the higher-energy photons, which are grown on another cell, manufactured with a lower gap material such as GaAs (1.4 eV) and which absorbs photons of lower energy. The second generation of MJ solar cells was the triple-junction GaInP/InGaAs/Ge (1.85eV/1.42eV/0.67eV) presented schematically in Fig. I-12. The sub-cell is named following the light path in the device: so the GaInP is called *top*, the InGaAs is named *middle* and finally, the *bottom* refers to the Ge. Each sub-cell is composed typically of four layers: emitter and base layers, forming the p-n junction, and the window and the *BSF* acting as passivation and minority carrier barrier for front and back side as discussed above. The sub-cells are series-connected by tunnel junctions with low resistivity, so the device has only one front and one back contact. This architecture optimizes the solar spectrum conversion as shown in Fig. I-11 where each sub-cell is optimized to absorb a dedicated portion of it spectrum.

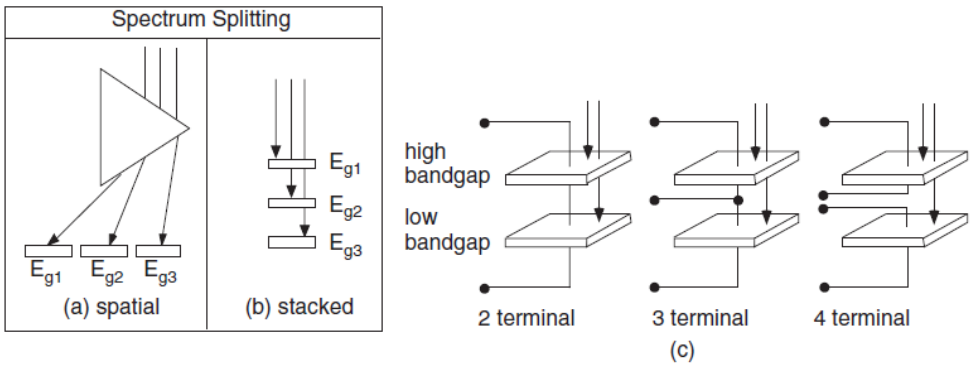

Fig. I-11 *Schematic representation for the different multi-junction approaches: spectrum splitting (a) spatially (b) stacked approach. (c) Double-junction 2-, 3-, and 4-terminal monolithic electrical configuration.*

Detailed balance theory can be applied for a multi-junction solar cell as for single junction. An efficiency of 45% under terrestrial 1 sun is calculated for dual-junction with sub-cell bandgap of 0.94 eV and 1.6 eV and can reach 50% for triple-junction with bandgap of 1.9, 1.4 and 0.9 eV [37]–[40]. The efficiency increases with the number of junctions and reaches, for an infinite number of junction, 68% under 1-sun and 87% under maximum concentration (46300 times the solar spectrum) [38], [41]. However, semiconductors with arbitrary bandgap values and very good quality do not exist in reality; it implies practical limitations. The current

record for a solar cell efficiency with a 6-junction stack is 47.1% and 39.2% under 143 suns and 1 sun, respectively.

Manufacturing Process

In a monolithically MJ solar cell, the complete device, including all sub-cells and interconnecting layers, is usually grown in a single manufacturing process called epitaxy. In large commercial scale, metal organic chemical vapor deposition reactors are used for manufacturing conventional GaInP/GaAs/Ge solar cells, on up to 6-inches III-V or Ge wafers. To obtain an efficient tandem solar cell, high-purity epitaxial growth is necessary. This is achieved by the development of advanced growth technologies, namely, Molecular Beam Epitaxy (*MBE*), Metal Organic Chemical Vapor Deposition (*MOCVD*) and other techniques [42]–[44]. There are however three main scientific challenges for implementing such structures, namely:

1. The semiconductor materials that constitute each sub-cell must have a compatible crystalline structure, so they can be grown in the same epitaxial growth.
2. Reducing electrical and optical losses in the interconnection layers between sub-cells.
3. A good choice of the material bandgap for a better repartition of solar spectrum hence the optimum produced current and voltage by each sub-cell.

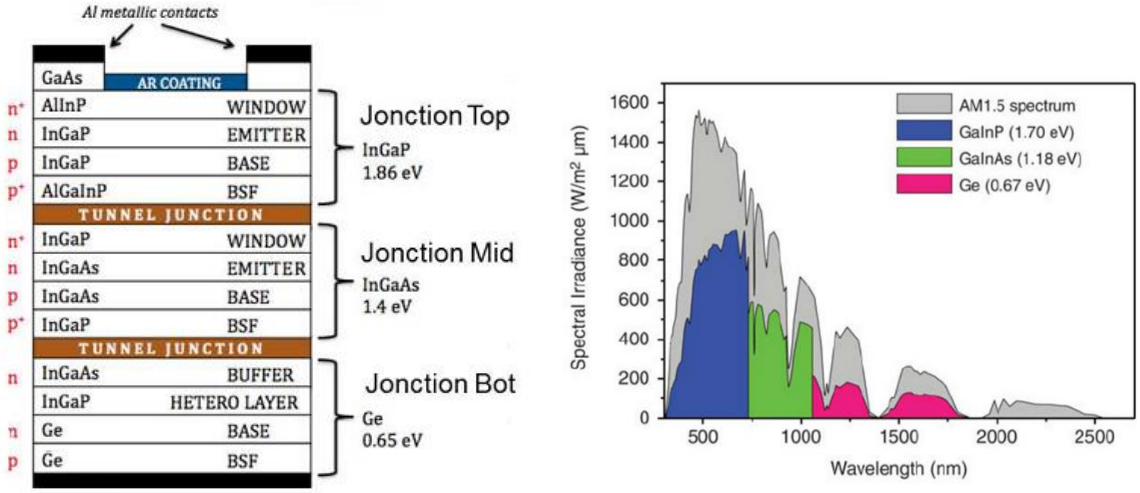

Fig. I-12 *Schematic representation of (left) InGaP/InGaAs/Ge triple-junction solar cell architecture and (right) the corresponding absorbed energy of each sub-cell.*

The crystalline structure compatibility refers to the fact that each semiconductor layer in the device (see Fig. I-13) needs to have very low defect density in both bulk and interfaces; for an efficient MJ solar cell, high minority carrier lifetime and diffusion length are necessary, and

they are linked to the crystal quality. Epitaxial growth limits the use to a certain group of semiconductor materials with the same lattice constant and same crystallographic structure. This type of MJ solar cells are called Lattice-Matched (*LM)* cell. In Fig. I-13, the bandgap energy is plotted as a function of lattice constant for elemental and compound semiconductor materials used in a MJ solar cell. As an example of semiconductor materials that can be used for 3J LM solar cells, we will consider Ge, GaAs, and GaInP. The main disadvantage of this constraint leading to efficiency decrease is the limitation of semiconductor material in terms of bandgap well adapted to cover properly the solar spectrum. One option to increase the accessible semiconductor materials is to use relatively different lattice constant semiconductor materials with a thin buffer layer in-between to manage the crystal mismatch and release the stress; this allows a better choice of bandgaps with respect to the target light spectrum. These multi-junction devices are called Metamorphic (or lattice-Mismatched) (*MM)* cell.

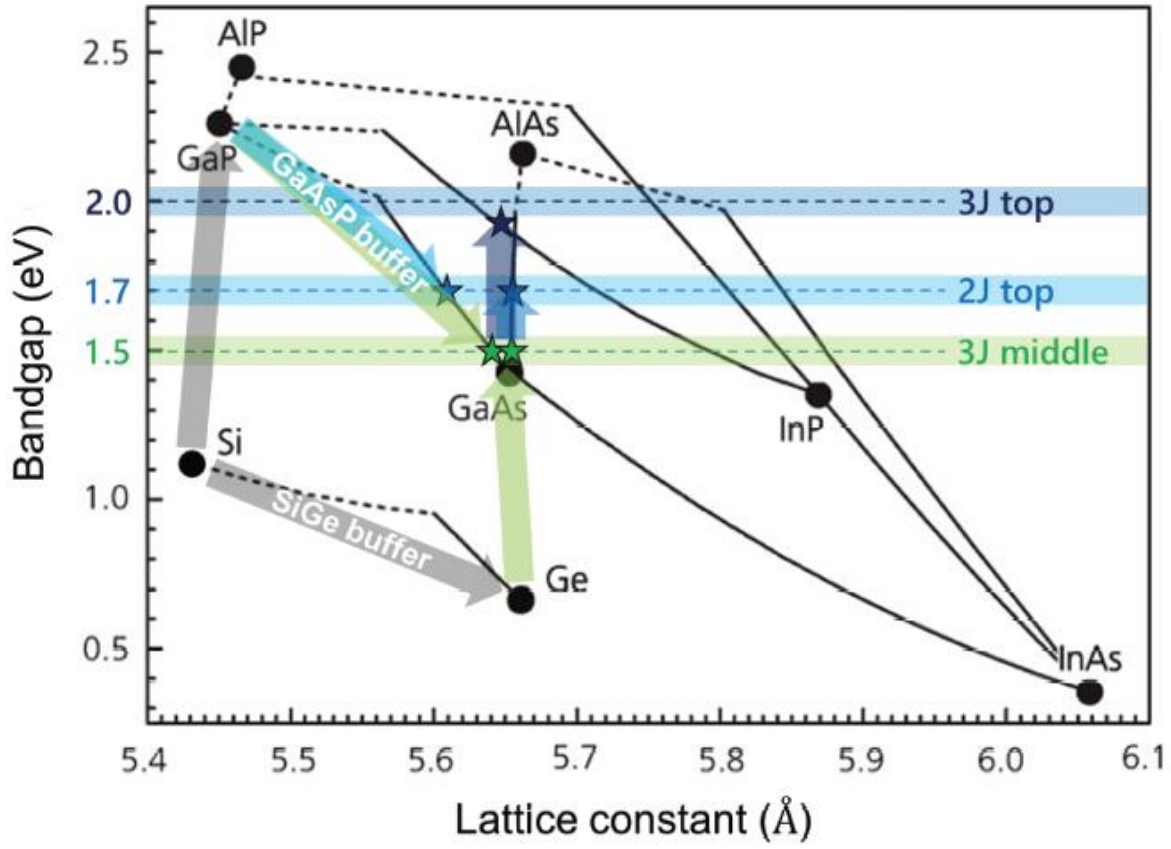

Fig. I-13 *Semiconductors bandgaps energy as a function of lattice parameter, arrows indicate graded buffer layers path; optimum bandgaps for 2J and 3J Si based multi-junctions are highlighted.*

The most appropriate interconnection layer of two sub-cells in a III-V MJ device is the tunnel junction. Their purpose is to ensure direct tunneling current between (thus minimum

ohmic losses) p-type and n-type majority carriers of front and rear adjacent sub-cells. They are heavily doped region p^+-n^+ with very small thicknesses so that electrons can pass through by tunnel effect from one sub-cell to another. They should also be transparent to the light path to the next sub-cell; this can be achieved by high bandgap materials. They should also exhibit a low resistive loss, having low equivalent series resistance and higher peak tunneling current than the operational current of the multi-junction solar cell [45].

Electrical operation on two-terminal MJ solar cells

Since the sub-cells are series-connected, the MJ solar cell overall current I_{MJSC} is limited by the sub-cell that photo-generates the lowest current according to Eq. I-18 (e.g. 3J). On the other part, the multi-junction voltage is the sum of all sub-cells voltages minus the voltage of the tunnel diode because they are in reverse bias (see Eq. I-19). One of the advantages of this configuration, is the low photo-generated current (compared to single junction) hence the reduced series resistance effects especially at high light intensity levels. Therefore, the challenge is to find the optimum sub-cells bandgaps to achieve an equality of photo-generated current under specified solar spectrum in order to limit the current losses and therefore the solar cell heating which degrades in return the MJ solar cell performances. Evolution of solar cell electrical properties as a function of temperature and light intensity will be presented later in section I.3.

$$I_{MJSC} = Min\left(I_{Top}, I_{Middle}, I_{Bottom}\right) \quad \text{I-18}$$

$$V_{MJSC} = \sum_i V_i - \sum V_{Tunnel\ diode} = V_{top} + V_{middle} + V_{Bottom} - (V_{TD1} + V_{TD2}) \quad \text{I-19}$$

In order to explain more properly the behavior of a MJ solar cell, *I-V* characteristic of triple-junction GaInP/GaInAs/Ge solar cell is presented in Fig. I-14 with the corresponding *I-V* characteristic of each sub-cell. We take the example of an arbitrary point, A, in the flat part of curve IV of the triple-junction, where the operating or biasing point of each sub-cell is identified by ($V_{A,TC}$, J_A), ($V_{A,MC}$, J_A), ($V_{A,BC}$, J_A), for top, middle and bottom sub-cell respectively. At this operating point, the top sub-cell limits the current of the 3J while the other two sub-cells (middle and bottom) are in forward bias, since this is the only possible way to deliver the operating current J_A.

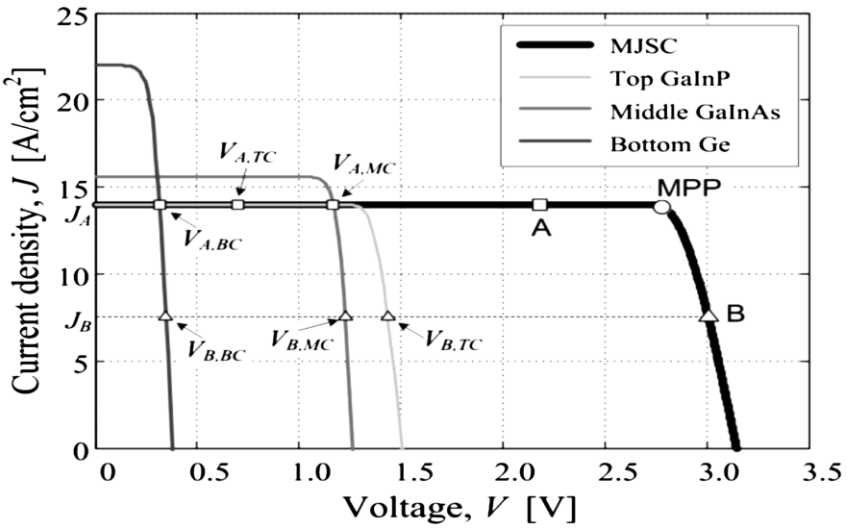

Fig. I-14 *Current-voltage characteristic of GaInP/GaInAs/Ge triple-junction solar cells under illumination with the corresponding sub-cells current-voltage characteristics [35].*

If we increase the voltage of 3J to reach the point of maximum power, the voltage of the limiting sub-cell, i.e. top in this case, increases while the voltage of the other sub-cells remains the same close to the open circuit voltage. However, going beyond the *MPP*, point B for example, the three sub-cells increase their bias point to match with the total current J_B of the 3J. In summary, in all cases where there is a current mismatch, it is the limiting sub-cell that defines the operating coordination of the multi-junction while the other sub-cells operate in conditions close to their open circuit voltage [35]. The excess current photo-generated by the other sub-cells will be lost by recombination and thus heating up the device.

I.2.6. Integration of III-V on Si for multi-junction solar cell

As explained in the introduction, in general, the integration of silicon as a substrate offers a lower cost perspective of the overall device in comparison to the use of germanium or GaAs substrate; in addition, it also offers a higher mechanical strength. Besides the use of Si as a substrate, the integration of silicon as an active region (sub-cell) for the double-, triple- and four-junction architecture enable high efficiency devices by combining high efficiency III-V material with a mature and low cost silicon solar cells (unlike material as III-V or Ge).

Fig. I-15 shows theoretical maximum efficiencies simulation according to multi-junction sub-cell materials bandgap. A theoretical efficiency of 45% is expected for double-junction based on silicon (1.1 eV) bottom sub-cell combined with a 1.7 eV bandgap material for top sub-cell (see Fig. I-15 left). For the triple-junction cell, maximum efficiency is presented as a function of top and middle sub-cells bandgaps considering silicon (1.1 eV) as a bottom sub-cell

in Fig. I-15 (right). An efficiency over 50% is expected when using a 2.0 eV and 1.5 eV bandgap materials for top and middle sub-cells respectively.

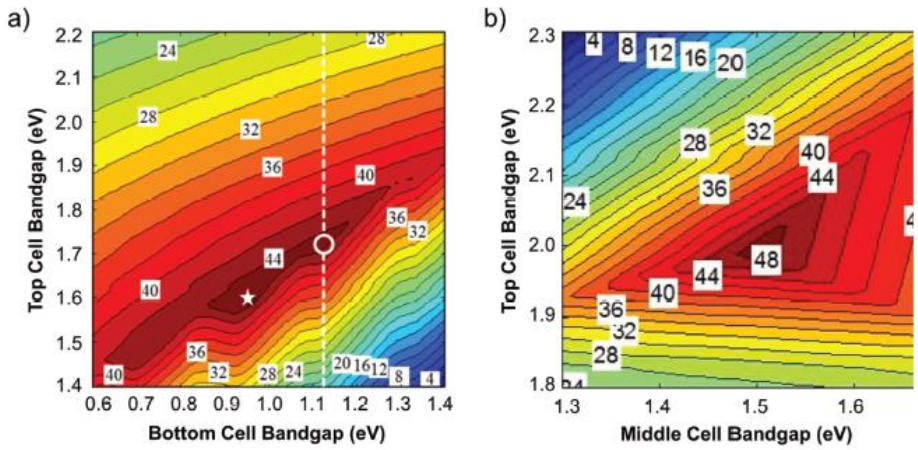

Fig. I-15 *Maximum theoretical efficiency limits under 1 sun AM1.5G spectrum for (left) double-junction efficiency as a function of top and bottom bandgap energies (right) Triple-junction efficiency according to top and, middle bandgaps for Si (1.12 eV) bottom sub-cell [46].*

From Fig. I-13, we can see that there is no material with 1.7 eV (respect. 2.0 eV and 1.5 eV) lattice match to the silicon for the conception of double-junction (respect. triple-junction). Thus, in this case, the challenge is to combine materials with high lattice mismatch (4% compared to GaAs family) for an efficient MJ based silicon solar cell. Other important problem lies at the interface, where polar III-V are in contact with non-polar silicon material. In addition, the high thermal expansion coefficient mismatch can create issues.

In the configuration of the material epitaxy on a substrate with high lattices mismatch, as the case of GaAs and Si, this misfit causes growth in compressive strains (large lattice constant grown on smaller substrate lattice constant). Consequently, the in-plane epitaxial layer lattice parameter is compressed to match with the one of the substrate lattice parameters. The outer-of-plane layer lattice parameter will be larger than the one in the equilibrium as a response to the elastic deformation and to ensure volume conservation as presented in Fig. I-16. However, after a critical thickness (which depends on the temperature of growth and lattice parameter misfit) of the grown layer, it is more favorable to break some bonds, hence create defects in the crystal known as threading dislocation. These defects are at the origin of the p-n junction shunting and reduce the shunt resistance of the solar cell, affecting the fill factor. These defects decrease also the minority carrier lifetime controlling the separation and collection probability of photo-generated charges. Threading dislocation production at the interface finally decreases

the short-circuit current of the MJ Solar cell. The overall effect is the limitation of solar cell conversion efficiency [47], [48].

During III-V materials epitaxy, a first mono-atomic layer of a group III material is deposited followed by a mono-atomic layer of group V. Due to the non-planarity of the Si (100) surface, an antiphase domain is created during growth because of the shift in deposited atoms. An As-As and Ga-Ga bonds are becoming more and more important as the thickness of the deposited layer increases. These double charged bonds are considered as defects and are not suitable for the operation of solar cells. Using an offset orientation of Si surface (4° - 6°) was the best solution found to prevent the formation of antiphase lines. A surface offcut of 2° was also reported by Yamaguchi [49].

Typical temperature during crystal growth of III-V materials is high, of the order of 600 °C for Metal Organic Vapor Phase Epitaxy *MOVPE*. Given a high thermal expansion coefficient misfit between III-V and Si (GaAs thermal expansion coefficient is twice that of Si), after cooling down to room temperature, thermal stresses are formed in the grown crystalline structure. This induces the formation of defects and dislocations that degrade the electrical and optical properties of the solar cells.

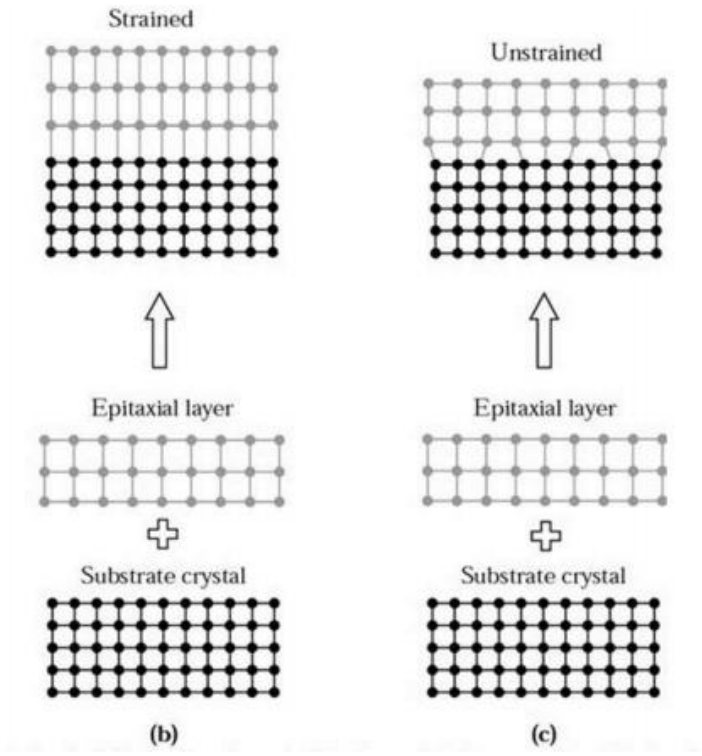

Fig. I-16 *Schematic Illustration of (left) compressive strained and (right) relaxed hetero-epitaxial structures during direct epitaxial growth of GaAs layer on Si.*

Difficulties encountered in the design of silicon based MJ solar cells have been reported. Different approaches have been proposed in the literature to overcome these difficulties like reducing as much as possible the Threading Dislocation Density (*TDD)*, by the epitaxial or non-epitaxial methods. The advantages and inconveniences of these techniques will be presented hereunder.

I.2.6.1 Epitaxial approach

Over the last decades, researchers have considered the direct growth of GaAs on Si by hetero-epitaxy. However, as explained it leads to high *TDD* around 10^8 - 10^9 cm^{-2} at the interface. Cycled thermal annealing is the most efficient method to reduce *TDD*. Thermal annealing decreases at best the *TDD* to 10^7 cm^{-2} [50], [51]. As an example, Soga et al. [52] grew AlGaAs on active Si by MOVPE at 950 °C with five thermal cycling iterations. The solar cells produced in this work have the best efficiency 21.2% reported up to now under AM0 spectrum. However, high *TDD* values still limit the solar cell efficiency.

Another epitaxial approach consists on the insertion of layers between III-V and Si, called buffer layers, in which the composition changes gradually. The role of these layers is to change progressively the lattice constant between Si and III-V in such a way the transition is smooth. In Fig. I-13, we present the pathways, i.e. alloys materials, to accommodate the misfit between Si and GaAs lattice constants. The presence of defects in the buffer layers has no effect on the recombination of the minority carriers because these layers are far from the p-n junction, and they are ideally electrically conductive regions while being optically transparent with respect to the cell below. However, considering the thickness of these buffer layers, the total device series resistance is still increased to some extent, and thus it still have some effect on the device fill factor and thus efficiency.

The well developed and often studied buffer layer is the $Si_{1-x}Ge_x$ alloy. By changing the composition of Ge from 0% to 100%, we can adjust the lattice constant and thermal expansion coefficient at the final layer, i.e. Ge, which fits very well with the GaAs, hence, subsequent direct growth is possible; literature reports low *TDD* around 10^6 cm^{-2} with this approach [53]. However, SiGe alloys have a lower bandgap energy than the next sub-cell, i.e. silicon (see Fig. I-13). Consequently, these buffer layers can absorb photons and thus reduce the photo-generated current of the Si sub-cell. SiGe alloys are suitable as cheap “virtual” substrate for III-V growth, but not well optimized for tandem solar cells based on Si active cells.

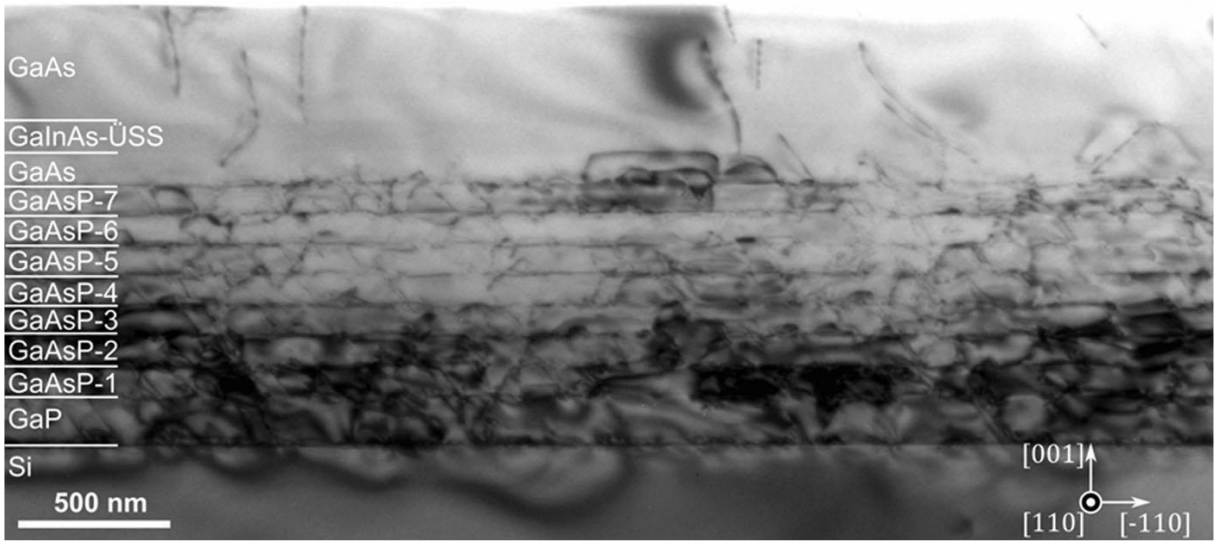

Fig. I-17 *TEM image of high threading dislocation density during direct growth of GaAs on Si by using $GaAs_xP_{1-x}$ graded buffer layer to reduce lattice constant mismatch [54].*

A more appropriate option for III-V/Si tandems is to use alloy with bandgap higher than Si, and therefore optically transparent to Si is $GaAs_xP_{1-x}$ (see Fig. I-13). The lattice constant of GaP is close to that of Si (0.37%) and therefore directly grows upon Si with low *TDD*. By varying the composition of As from 0% (GaP) to 100% (GaAs) it allows a slow increasing of lattice constant to fit with GaAs (see Fig. I-17). Feifel et al. have reported a *TDD* of $2.2x10^6$ cm^{-2} for triple-junction GaInP/GaAs/Si [55]. The device uses GaAsP buffer layer approach with a GaNP layer for decreasing *TDD* at the GaP/Si interface. Their latest reported results show even lower *TDD*, and reach certified efficiency of 25.9% under AM1.5G. Further improvements are expected by simply current matching the structure.

Among the other options studied, the use of III-V-N alloy (dilute nitride) seems to be the best solution for the top sub-cells design. The advantage of these materials is the compatibility of the lattice constant with Si and their high bandgap, thus transparency with respect to Si. However, a short minority carrier diffusion length and the difficult control of the composition of the quaternary materials characterize this approach.

I.2.6.2 Wafer bonding approach

Although the direct epitaxy approach offers a simpler, easier and lower cost perspective for integration in industrial processes, the efficiency of Si-based MJ solar cells is still limited by the high *TDD* and Si degradation at the high temperature growth process of III-V materials. Hence, alternative non-epitaxial approaches are studied in literature. When two wafers of the same or different nature are put together even at room temperature, they spontaneously bond

together at atomic scale by weak Van der Waals or hydrogen bridges [56], [57]. This technique requires a perfect surface: flat & cleaned surfaces, mirror polished and no roughness [58]. Usually thermal treatment is employed to reinforce the interface strength. Hereunder three main wafer bonding techniques are presented: hydrophobic, hydrophilic, and surface activated bonding.

In **hydrophobic** Si-Si bonding, the wafers have bare surfaces that are hydrogen-terminated surfaces with some fluorine-Si bonds leaving electronically passivated surfaces as presented in Fig. I-18. This is due to a commonly effective used process to eliminate silicon dioxide by hydrofluoric acid (HF) etching. First Van der Waals bonds (Si-H-H-Si) bridges are produced during an annealing at 300 - 700 °C, the hydrogen removal for Si surface and Si-Si bonds production follow the reaction I-20 [59], [60]:

$$Si - H \; + \; Si - H \; \rightarrow \; Si - Si \; + \; H_2 \qquad \textit{I-20}$$

The advantage of this technique is no intermediate (oxide or amorphous) layer is needed. However, the first problem with this process is the presence of hydrogen bubbles as a result of the reaction (I-20) trapped at the interface. The second issue is the complex native oxide on GaAs surface such as Ga_2O_3 that are difficult to eliminate by chemical etching. Several researches were performed on GaAs//Si bonding but none of the interfaces shows an Ohmic behavior [61]–[63] requires for tandem solar cell.

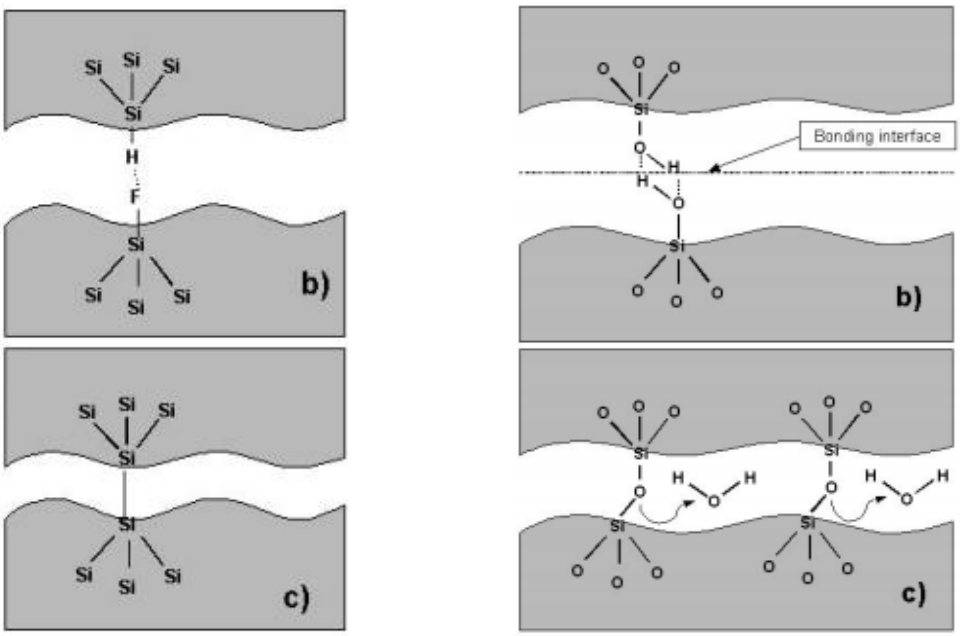

Fig. I-18 *Direct bonding process for (left) Hydrophobic via H- and F- atoms with van der Waals bridge and formation of Si-Si bonds after annealing, (right) Hydrophilic via OH group and the formation of Si-O-Si bonds.*

For **hydrophilic Si-Si** bonding, OH-bonds is at the Si wafer surfaces. At the initial stage, the water forms a bridge between the two surfaces with a Si-O-Si oxide bond and H_2O (see Fig. I-18 right). During annealing treatment, the water diffuses out of the interface or react with surfaces to form more OH bonds [64]. Consequently, Si-O-Si bonds are formed between wafers according to reaction I-21:

$$Si - OH \ + Si - OH \rightarrow Si - O - Si + H_2O \qquad \textit{I-21}$$

Water molecules are produced during this reaction. The water is even trapped at the interface or infiltrate through the oxide to react with Si and form trapped hydrogen (H_2), and increase the oxide thickness according to the following reaction I-22 [60]:

$$Si + 2H_2O \rightarrow SiO_2 + 2H_2 \qquad \textit{I-22}$$

The advantage of this process is the simplicity of having a hydrophilic surface for GaAs and Si wafer since it implies the use of native oxide for bonding. However, the formed oxide layer at the interface and trapped water and hydrogen induce additional series resistance [65], [66]. The trapped water and hydrogen can be avoided by changing the hydrophilicity of the surface and the use of different bonding atmosphere [46], [59].

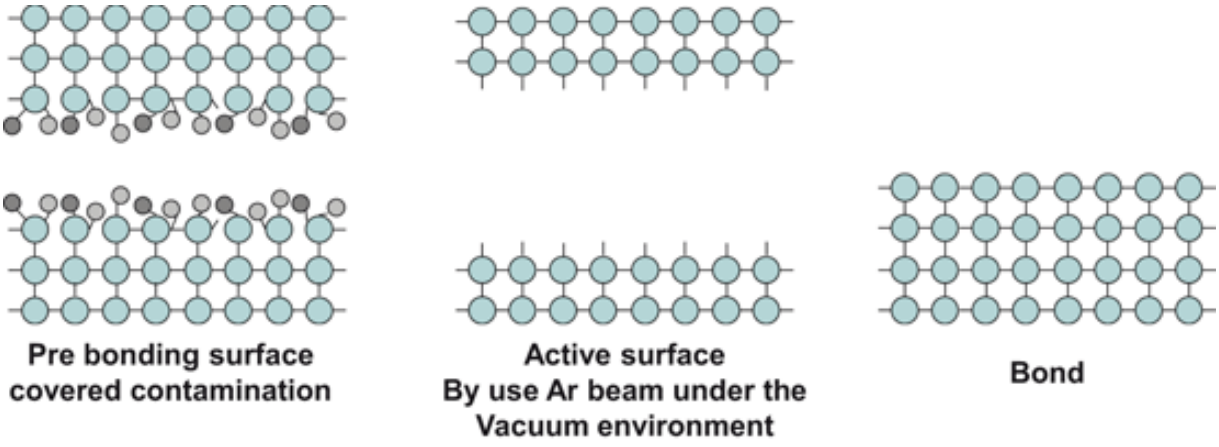

Fig. I-19 *Schematic illustration for the surface activated bonding process at room temperature [71].*

Surface Activated Bonding (*SAB*), was studied by Suga et al. for the integration of III-V on Si for optical devices [67]–[70]. *SAB* provides a combination of low thermal stress and defects with high bonding based on chemical covalent bonds. Consequently, the two wafers surfaces need to be atomically cleaned, activated and with perfect surfaces properties (flatness, smoothness). In order to remove oxides from the surfaces of the wafers, keV irradiations with inert atoms species (e.g. Ar) are performed at low temperature under vaccum, for removing impurities and creating dandling bonds. When the two wafers are pressed together, strong

covalent bonds are formed by the interaction of dangling bonds with other atoms. Fig. I-19 illustrates schematically *SAB* process.

The *SAB* process does not require thermal cycling annealing treatment to obtain a sufficient bond strength, unlike hydrophilic or hydrophobic bonding processes. This low temperature does not induce thermal stress at the interface. In addition, this process offers the possibility to bond two materials regardless of their crystal structure or lattice parameter without intermediate buffer layers or threading dislocations [72]. *SAB* process was extensively studied and applied for the integration of high efficiency III-V on Si for MJ solar cell [54], [73], [74]. However, few nanometers thick amorphous layer is formed at the interface (see Fig. I-20 left) due to atoms sputtering that can partially degrade electrical properties, i.e. result in higher series resistance and potential optical losses.

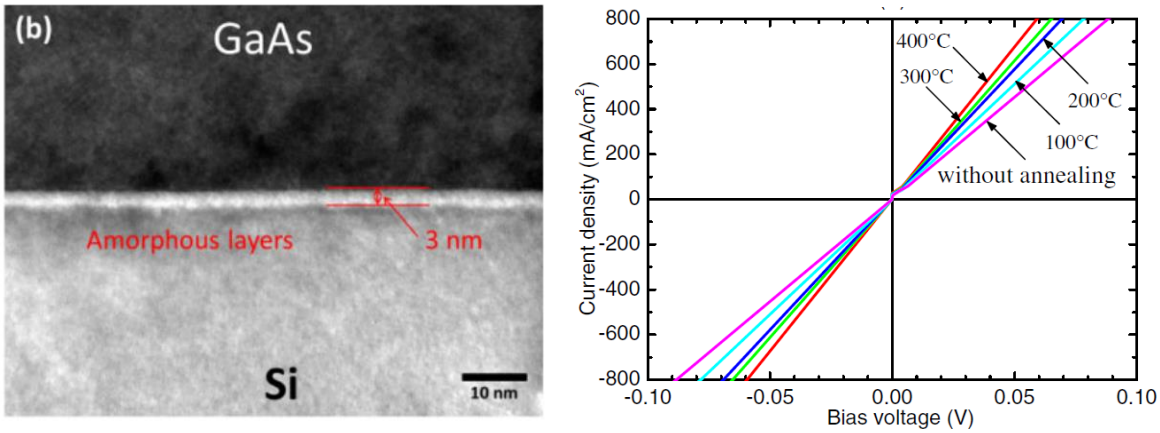

Fig. I-20 *(Left) Transmission Electron Microscopy image for n+-GaAs//n+-Si interface processed by surface activated bonding resulting in 3 nm amorphous layer, (right) I–V characteristic of the n+-GaAs//n+-Si without and with thermal annealing at 100 °C, 200 °C, 300 °C and 400 °C to enhance the junction conductivity [75].*

One way to reduce the amorphous layer and enhance the series resistance is to perform thermal annealing. A group from Osaka university has studied the GaAs//Si interface electrical properties obtained by *SAB* process, by annealing at 400 °C the 3nm amorphous layer recrystallizes offering a 7.10^{-2} Ω.cm [75], [76]. They have reported an efficiency of 3J solar cell GaInP/GaAs//Si of 24.4% under AM1.5G spectrum [77]. Yu et al. have studied the evolution of the amorphous layer during thermal annealing; they reported a significant improvement of *I-V* characteristic after annealing at 400 °C due to the reduction of the amorphous layer thickness from 11.3 nm down to 2 nm. After annealing at 600 °C the amorphous layer has vanished, however a non-perfect crystalline structure was achieved [78]. Essig et al. have reported that series resistance can be reduced to 3.6×10^{-3} Ω.cm by: 1) increasing the doping level at the two surfaces, 2) increasing the temperature during bonding to 120 °C and

3) performing annealing at 400 °C for 1 min [79]. Nowadays, the best-published efficiency for Si based triple-junction solar cell manufactured by SAB process is reported by Cariou et al. of 33.3 % under AM1.5G spectrum [80]; the same group has even announced 34.1% recently.

The advantages and challenges of the above detailed III-V integration processes, epitaxial growth (direct and buffer layers) and non-epitaxial (hydrophobic, hydrophilic, and *SAB*) are summarize in Tab**.** I-1.

Tab. I-1 Overview of the main advantages and challenges of the various approaches for the integration of III-V on Si for high efficiency two-terminal multi-junction solar cell

Path	Advantages	Challenges
Direct growth w/o buffer layer	• No III-V substrate needed • Low cost potential • Standard MOCVD growth	• High lattice constant mismatch • High thermal expansion coefficient misfit • High *TDD* (10^8-10^9 cm^{-2})
Direct growth via buffer layers	• No III-V substrate needed • Low cost potential • Standard MOCVD growth • *TDD* below 10^6 cm^{-2} possible	• Transparency of buffer layer for Si bottom cell • High thermal expansion coefficient misfit
Hydrophobic	• No intermediate layer • III-V and Si sub-cells fabricated separately	• Difficulty to remove GaAs oxide • Annealing needed
Hydrophilic	• Simplicity of surface preparation • III-V and Si sub-cells fabricated separately	• Oxide intermediate layer • Presence of voids and trapped H_2 • Annealing needed
SAB	• Good *I-V* characteristic • No annealing needed • Best reported efficiency of 2T silicon based MJSC	• Costly process (surface preparation, high vacuum, substrate removal etc.)

I.3 Space environments

The space environment is an aggressive environment for satellites and its components during a scientific, commercial, or military mission. Considering satellites powered by solar panels, an overview of their direct operating environments such as temperature and irradiance intensity over the solar system are presented below. The radiation source and their quantification will be also introduced in this section. Many other space constraints have influence on solar arrays, such as high vacuum, debris impact and electrostatic discharge; however, those constraints have not been studied in this PhD thesis.

I.3.1. Solar Intensity and Temperature

Before explaining the evolution of irradiance intensity and its applicability on supplying satellite and scientific exploration mission, we present hereunder a comparison of the solar spectrum on the outer space and at the earth surface.

The spectral distribution or intensity of the sun can be compared to the behavior of a blackbody at a temperature of 5800 K according to Planck's radiator law [81]. This lead to an emission peak at a wavelength of 0.5 µm for a power, at his surface, of about 60 MW/m^2. However, due to the Sun-Earth distance, only a small fraction of these emitted photons are intercepted on Earth; thus resulting in a much lower power density (~1367 W.m^{-2}).

The air mass (AM) defines the length that photons take through atmosphere to reach Earth's surface; it is defined as follow (Eq. I-23):

$$Air\ Mass\ (AM) = \frac{1}{cos\theta} \qquad \textit{I-23}$$

Where θ is the angle from the vertical (zenith angle). AM is always higher or equal to one at Earth's surface.

The atmosphere acts as a filter of the solar spectrum irradiance, which causes a reduction in irradiance intensity and changes in spectral distribution. Ozone gases absorb and attenuate UV radiation below 280 nm. Water vapor (H_2O) and carbon dioxide (CO_2) absorb mainly in the infrared region (close to their binding energy), which leads to "holes" in the solar spectrum [82]. An integrated irradiance (overall solar spectrum range) of 1000 W.m^{-2}, called 1-sun by PV literature, was defined as a standard for comparing solar cells performances for terrestrial applications. The corresponding spectrum can be AM1.5D or AM1.5G, with D to denote direct sunlight and G to denote global sunlight, which includes direct and diffused irradiance. However, above the Earth atmosphere where the sunlight does not pass or interact

with the atmospheric components, the spectrum is unaltered and named AM0 with a total irradiance intensity that varies from 1414 $W.m^{-2}$ (in December) to 1321 $W.m^{-2}$ (in July). Thus for optimizing and comparing the behavior of intended solar cells for space applications, the AM0 reference spectrum used is presented by the American Society for Testing and Materials (ASTM) as ASTME490-10 [83]. Recent research from Gueymard et al. [84] has revised the extraterrestrial composition of the solar spectrum by surface observation, satellites, high altitude balloon, and found a solar constant of 1361.1 $W.m^{-2}$ and recommend revision of ASTM E490. A comparison of the blackbody, AM0 and AM1.5D spectrum is presented in Fig. I-21.

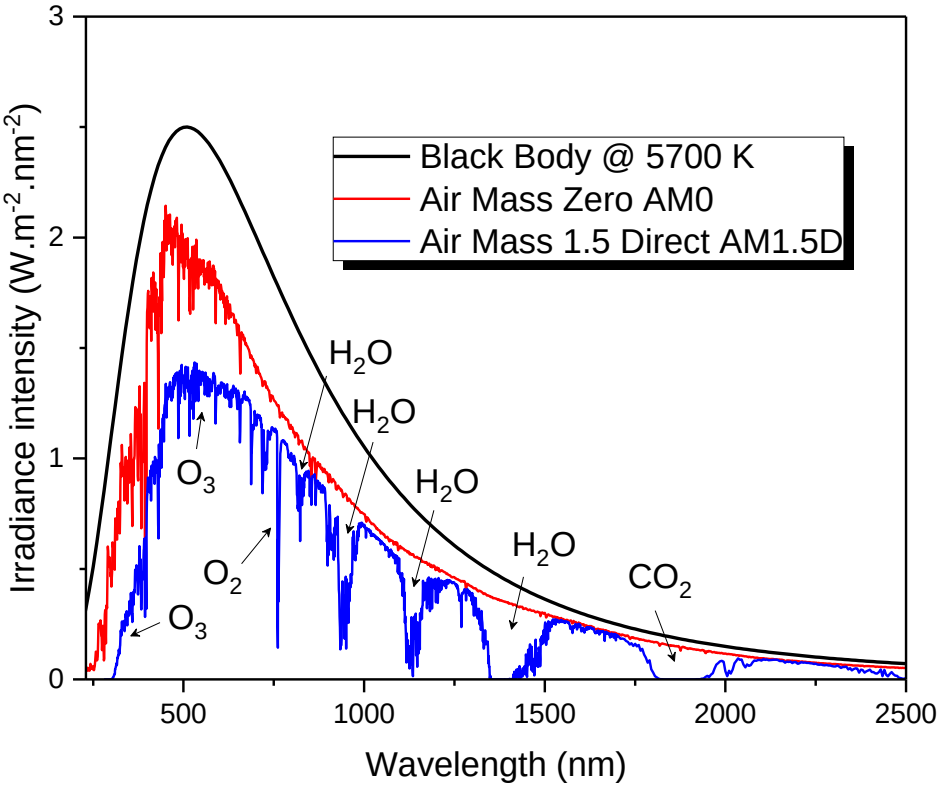

Fig. I-21 *Comparison of the solar spectrum at the earth surface AM1.5D and the spectrum above the atmosphere AM0 used for space application.*

In the space community, the intensity around earth, i.e. 1367 $W.m^{-2}$ is used as a reference to define intensity over the solar system. The irradiance intensity, X, at position, R, on the solar system is calculated by the multiplication of the reference around earth by the inverse square of its distance to the sun, called astronomical unit. The calculated intensity for the solar system planets is presented in Fig. I-22 [85]. As one can see, solar irradiance varies enormously between missions toward the sun where the intensity can reach 9000 $W.m^{-2}$ (6.67 x AM0) and

on the other hand missions to deep space, i.e. outer planets, can reach very low intensities as in the case of 50 $W.m^{-2}$ (0.037 x AM0) at Jupiter [86]. Regarding these low intensities, missions require solar arrays with high power capability (> 30 KW) at 1 A.U. to produce the necessary power (> 500 W) at far distances (> 5 A.U.). The first solar powered spacecraft, Rosetta, reaching distance as far as 5 A.U. was launched by European Space Agency in 2004 and it has proven the applicability of silicon solar cells at low intensity providing a total power of 395 W at 5.25 A.U. [87]–[90]. The Juno mission also solar-powered [91], is using 3J solar cells with a total capability of 14 KW at 1 A.U and 450 W at Jupiter, is actually orbiting around Jupiter and demonstrating the feasibility of such technology for deep space.

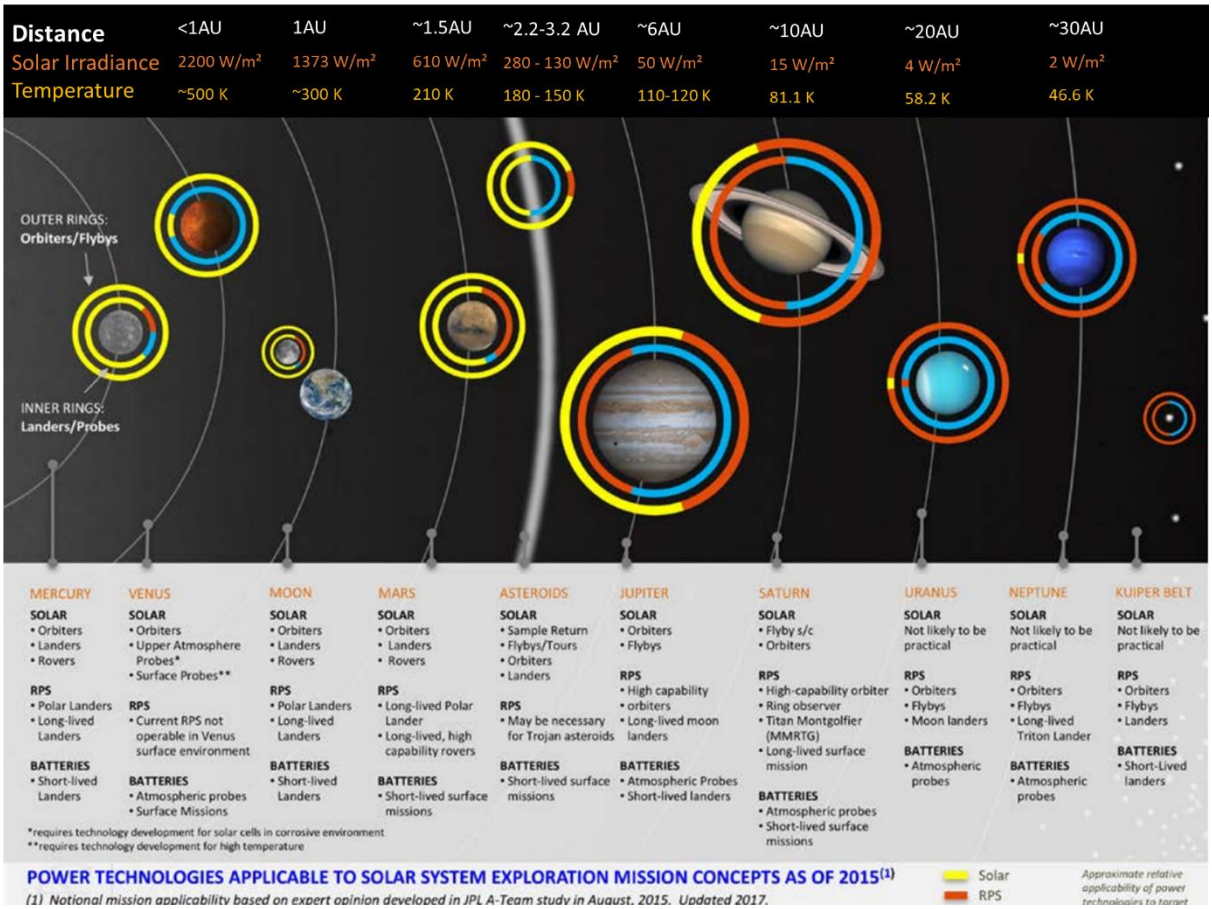

Fig. I-22 *Solar irradiance and temperature for operating environment in the solar system [86], [92]–[94].*

In addition to the solar irradiance constraint, solar cells onboard of spacecraft or satellites face important thermal constraints. Missions approaching the sun can reach temperatures as high as 460 °C at Venus, as we move away from the sun towards the outer planets, the temperature drops and reach -130 °C at Jupiter when facing the sun. The solar cells as subjected to high thermal cycling due to the difference between temperature when facing the sun and at the opposite side of the planet (thus in the shadow), which causes mechanical stress and cracks

due to different material thermal expansion [95], [96]. In terms of electrical properties, solar cells exhibit significant losses of open circuit voltage at high temperature (< 1 A.U.) and short-circuit current at low temperature (> 1 A.U.). The operating temperature at the solar system planets is illustrated in Fig. I-22.

I.3.2. Effect of irradiance intensity

Modeling of electrical parameters under the different operating environment gives a first approximation on the power output and therefore the applicability of a specific solar cell technology for each space mission. As seen above, the irradiance intensity can be increased/decreased by a factor X depending on the distance from the Sun. We can translate the influence of the irradiance intensity on the different electrical quantities of the cells, in particular on the Jsc and on the Voc. As a first approximation, the short-circuit current increases linearly with concentration according to Eq. I-24. Since there is no variation of the solar spectrum shape when increasing/decreasing irradiance intensity, the short-circuit current to consider remains the lowest among all the sub-cells.

$$J_{SC}(X) = X.J_{SC}(1\ sun) \qquad \textit{I-24}$$

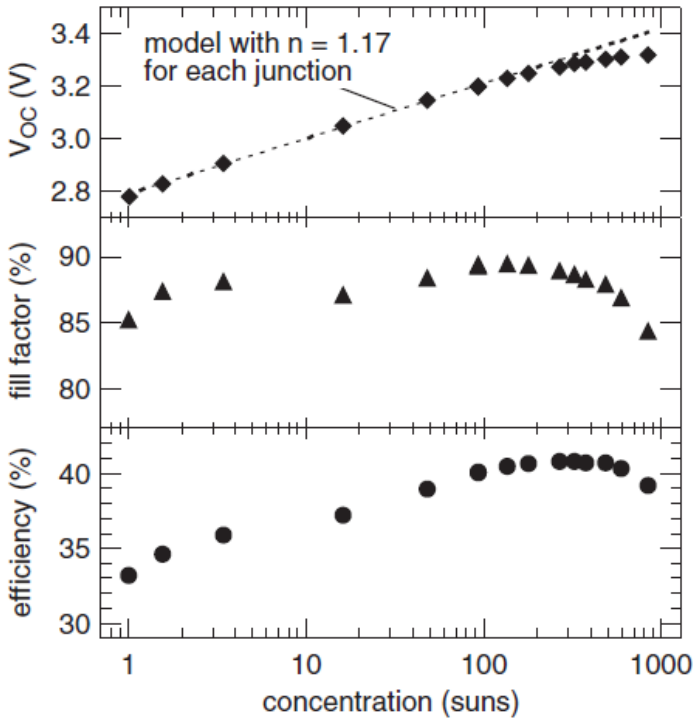

Fig. I-23 *Electrical parameters evolution as a function of irradiance intensity (concentration) for a triple-junction solar cell GaInP/$Ga_{0.96}In_{0.04}As$/$Ga_{0.63}In_{0.37}As$, (top) open circuit voltage, (middle) fill factor, (bottom) efficiency, the short circuit current not shown here is assumed to increase proportionally with irradiance intensity [35].*

The Shockley diode equation gives the open circuit voltage evolution as a function of irradiance intensity factor according to Eq. I-25:

$$V_{OC}(X) = V_{OC}(1\ sun) + \frac{nkT}{q} Ln(X) \qquad \text{I-25}$$

We can see that the open circuit voltage is less sensitive than the short-circuit current, and varies as a logarithmic function with irradiance intensity (see Fig. I-23). Since the sub-cells are series connected in two terminal MJ solar cell, the variation of open circuit voltage of the overall device is the sum of each sub-cell V_{OC} values. As for V_{OC}, the efficiency varies in logarithmic function of irradiance intensity according to Eq. I-26. However, the efficiency is limited by the degradation of fill factor at high concentration due to series resistance related losses as presented in Fig. I-23 where the maximum efficiency is achieved at X = 400 suns in the case of this specific solar cell.

$$\eta(X) = \eta(1\ sun).\left[1 + \frac{nkT}{q}\frac{Ln(X)}{V_{OC}(1\ sun)}\right]\frac{FF(X)}{FF\ (1\ sun)} \qquad \text{I-26}$$

I.3.1. Effect of temperature

The effect of temperature on the solar cell is due mainly to the sensitivity of the bandgap of the active region to temperature variation. In general, the bandgap energy of semiconductor material decreases with increasing temperature, which is due to the increase of interatomic spacing, therefore lower potential is seen by electrons [97], [98]. The evolution of the bandgap due to temperature can be modeled by the Varshni relation according to Eq. I-27 [99]:

$$E_g(T) = E_g(0) - \frac{\alpha\, T^2}{T + \beta} \qquad \text{I-27}$$

Where the E_g (eV) is the bandgap at the absolute temperature, T (K) is the temperature, α (eV.K^{-1}) and β (K) are material related constant, in general, they are used as fitting parameters.

In order to predict the solar cell performances at operating temperature, it is necessary to analyze the temperature performances using basic cell equations. The material properties, diffusion length and minority carrier lifetime are summed in one constant, therefore temperature dependence of J_0 is expressed by Eq. I-28 [100]–[102] where it varies as a function of only E_g and T.

$$J_0 = const\ .T^3\ exp\left(-\frac{E_g(T)}{kT}\right) \qquad \text{I-28}$$

Short circuit current is the result of three main solar cells properties (internal absorbance, spectral reflectance, and electronic properties). Small effect of temperature is assumed for reflectance and electronic properties thus lower effect on short circuit current. However, at very high and low temperature, the effect becomes non-negligible. The high variation of bandgap, i.e. cutoff energy, with temperature is the main cause of this increasing or decreasing short circuit current due to reducing or increasing of the absorbed portion on the irregular shapes of solar spectrum.

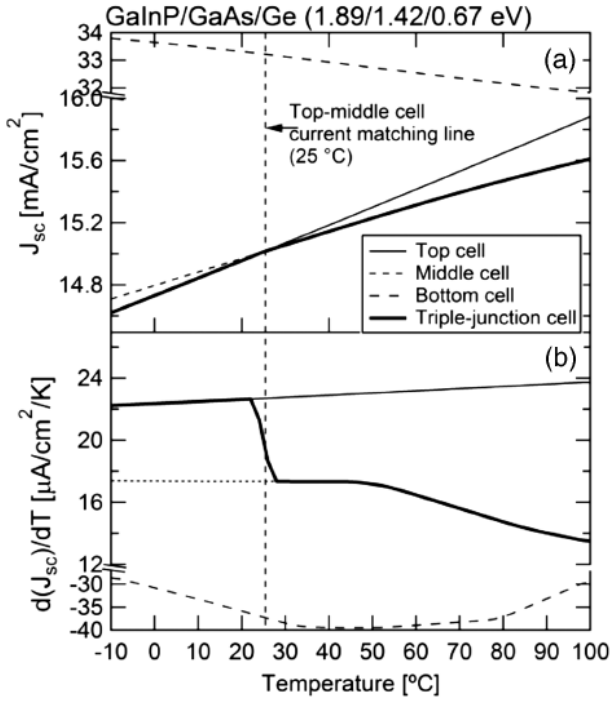

Fig. I-24 *(a) Triple junction GaInP/GaAs/Ge short-circuit current density evolution with temperature defining the crossover temperature at 25 °C for inversion of limiting sub-cell top/middle (b) evolution of short-circuit current density temperature coefficient dJ_{SC}/dT of each sub-cell as a function of temperature [35].*

For multi-junction solar cells the variation of short circuit current density is complex, given the current of the overall device is limited by the smallest sub-cell short-circuit current. In general, the semiconductor material has a different J_{SC} temperature coefficient; hence, there will be a crossover point, with below the multi-junction limited by one sub-cell and above the multi-junction limited by another sub-cell. An example is given in Fig. I-24 (a) for GaInP/GaAs/Ge triple-junction short circuit current density evolution with temperature for each sub-cell. In this architecture, the multi-junction is top-middle current matched at room temperature and the top-middle limit the 3J current. On one hand, when increasing temperature above 25 °C the 3J is limited by the middle sub-cell, on the other hand, when decreasing the temperature below 25 °C the top sub-cell limits the current of 3J. A comparison between J_{SC}

temperature coefficients (dJ_{SC}/dT) of each sub-cell is presented in Fig. I-24 (b). Under 25 °C the 3J dJ_{SC}/dT is governed by the top sub-cell at 22 $\mu A.cm^{-2}.K^{-1}$; above this crossover temperature, the middle sub-cell governs the dJ_{SC}/dT of triple-junction around 17 $\mu A.cm^{-2}.K^{-1}$.

The effect of temperature on **open circuit voltage** is simpler than that of short-circuit current. By combining Eq. I-15, Eq. I-27 and differentiating them with respect to temperature, the analytical expression of open circuit voltage with temperature for a single junction is expressed as Eq. I-29:

$$\frac{\mathrm{d}V_{OC}}{\mathrm{d}T} = \frac{1}{T}\left[V_{OC} - \frac{3kT}{q} + \frac{T}{q}\frac{\mathrm{d}E_g}{\mathrm{d}T} - \frac{E_g}{q}\right] \qquad \textit{I-29}$$

From the above equation, the following statement can be made for the temperature dependence of open circuit voltage:

- Linear variation is assumed to quantify the sensitivity of V_{OC} to temperature;
- V_{OC} is independent of the spectrum variation unlike for J_{SC} variation;
- The effect of J_{SC} variation on V_{OC} is low due to low dJ_{SC}/dT and the logarithmic variation of V_{OC} on $J_{SC;}$
- The V_{OC} coefficient is always negative since bandgap has a negative temperature coefficient and E_g/q is always higher than $V_{OC;}$
- The higher the V_{OC} the lower its temperature coefficient, even for the same semiconductor material

The V_{OC} of two-terminal multi-junction is the sum of all sub-cell V_{OC}. Hence, the temperature coefficient of the overall device is the sum of all sub-cell temperature coefficients. As explained above the effect of J_{SC} on derivative V_{OC} is negligible, therefore, temperature coefficient is assumed to be linear in order to quantify its sensitivity to temperature for both single- and multi-junction solar cells even at low temperature reaching 110 K [103].

A comparison of modeled temperature coefficient (dV_{oc}/dT) at 300 K according to Eq. I-29 of different solar cell material and architectures is presented in Tab. I-2. The negative temperature coefficient of V_{OC} allows a high boost at low temperature and significant losses at high temperature. From this point of view, solar cells are suitable for low temperature rather than a high temperature operating environment. For high operating temperatures, solar cells with low absolute temperature coefficient are more preferable to reduce the V_{OC} losses.

Tab. I-2 *Comparison of modeled V_{OC} temperature coefficient at 300 K for several solar cells materials and architecture [8], [104]*

Cell	V_{OC} at 300 K (mV)	dVoc/dT ($mV.K^{-1}$)	$1/V_{OC}$ dVoc/dT ($\%.K^{-1}$)
PERL Si	711	-1.7	-0.24
Si (AzurSpace)	628	-2.02	-0.32
Ge	200	-1.8	-0.90
GaAs	1050	-2.0	-0.19
GaInP	1350	-2.2	-0.16
GaInP/GaAs	2400	-4.4	-0.17
GaInP/GaAs/Ge	2600	-6.0	-0.23

The **fill factor** parameter as explained has a non-direct physical explanation; it reflects the effect of parasite shunt and series resistances on the *I-V* characteristic under illumination. An empirical expression of a single junction fill factor as a function of open circuit voltage was proposed and is expressed according to Eq. I-30 [101], [105]. From this equation, it appears that the temperature coefficient is negative and higher values of FF are expected for lower bandgap.

$$FF = \frac{q\frac{V_{OC}}{kT} - \ln\left(q\frac{V_{OC}}{kT} + 0.72\right)}{q\frac{V_{OC}}{kT} + 1} \qquad \textit{I-30}$$

In a multi-junction solar cell, fill factor depends mainly on current matching between the different sub-cells. The calculated FF and its temperature coefficient for triple-junction solar cell GaInP/GaAs/Ge with the corresponding sub-cell are presented in Fig. I-25 (left). The main statement from this illustration are:

- The Fill factor temperature coefficient, dFF/dT, follows the behavior of that of dJ_{SC}/dT and fluctuates in the inversion of limiting sub-cell region;
- Low dFF/dT values are expected (from experimental measurements) in the case of multi-junction comparing to dJ_{SC}/dT and dV_{OC}/dT, therefore its effect on the efficiency is relatively low.

The efficiency is proportional to the product $J_{SC}.V_{OC}.FF$ and, therefore, the temperature coefficient of efficiency is determined by the sensitivity of J_{SC}, V_{OC}, and FF to temperature. The

efficiency temperature coefficient is expressed as the sum of all parameters temperature coefficient according to Eq. I-31:

$$\frac{1}{\eta}\frac{\mathrm{d}\eta}{\mathrm{d}T} = \frac{1}{V_{OC}}\frac{\mathrm{d}V_{OC}}{\mathrm{d}T} + \frac{1}{J_{SC}}\frac{\mathrm{d}J_{SC}}{\mathrm{d}T} + \frac{1}{FF}\frac{\mathrm{d}FF}{\mathrm{d}T} \qquad \textit{I-31}$$

In the case of an ideal single-junction cell, the temperature coefficient in general negative to temperature i.e. is not always constant as a function of temperature. This effect is due to the influence of the irregularity of the dJ_{SC}/dT and dFF/dT, however, this non-linear behavior remains relatively small. For multi-junction, as presented in Fig. I-25 (right) the temperature coefficient has the same trend as for single junction and is smother than can be expected due to high irregularity shown in Fig. I-24 and Fig. I-25 (left). In fact, the variation of these two parameters with an opposite sign happens to attenuate the irregularities.

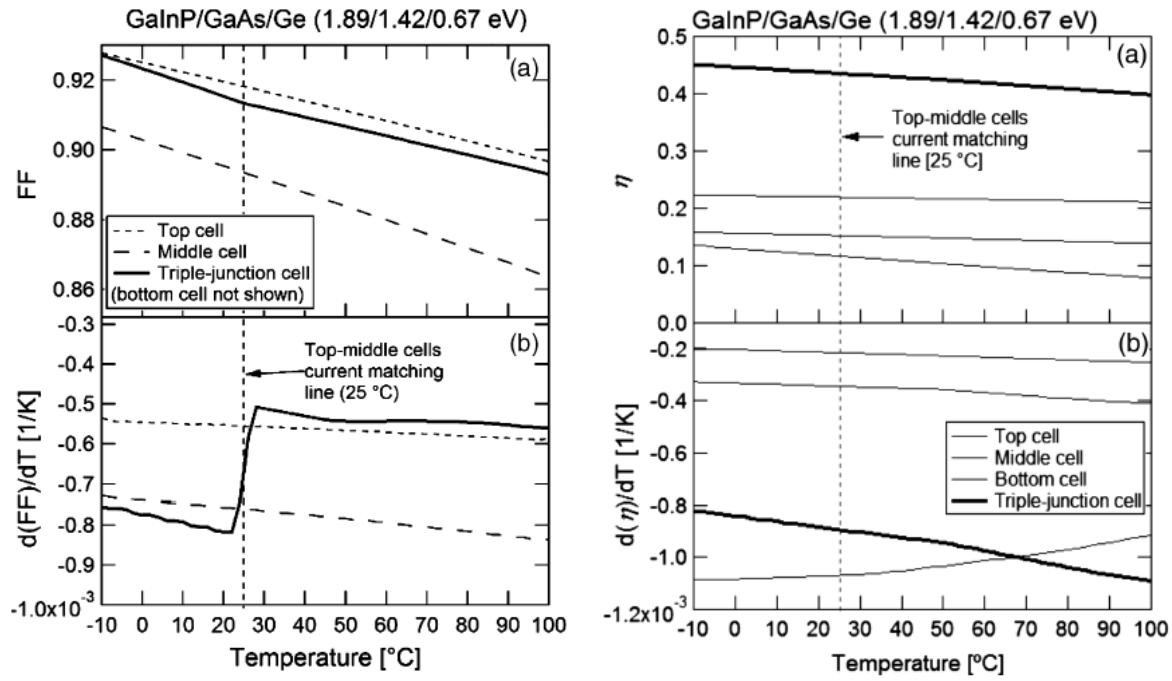

Fig. I-25 *Ideal triple junction GaInP/GaAs/Ge electrical parameters evolution as a function of temperature with the corresponding temperature coefficient of (left) fill factor (right) efficiency [35].*

In the case of temperature variation around 25 °C and at current matching between sub-cells for multi-junction solar cell, an assumption of constant coefficient can be set with an accurate fit in most cases [35], [106]. At very low temperature below 200 K, the efficiency increase tends to have more flatten behavior. At extremely high temperature, the efficiency decreases and tends to zero [106].

As seen above, space mission satellite operates in different environments namely, *High Temperature and High Intensity* (near sun), *Normal Intensity and Room Temperature* (near earth), Low Temperature *and Low Intensity* (outer planets). Fig. I-26 presents the efficiency temperature coefficient as a function of semiconductor bandgap. From this curve, two main statements are set [86], [107]:

- Higher bandgap materials provide a lower efficiency temperature coefficient, therefore, they are clearly more suitable to use for near sun missions. As an example, a solar cell made from GaInP has a temperature coefficient 2 times smaller than GaAs. GaInP solar cell will therefore produce three-times higher power than GaAs cells around 400 °C;
- Inversely lower bandgap materials have a higher efficiency temperature coefficient, thus are preferable to use for outer planets. As the case of Si compared to GaAs or to GaInP solar cells.

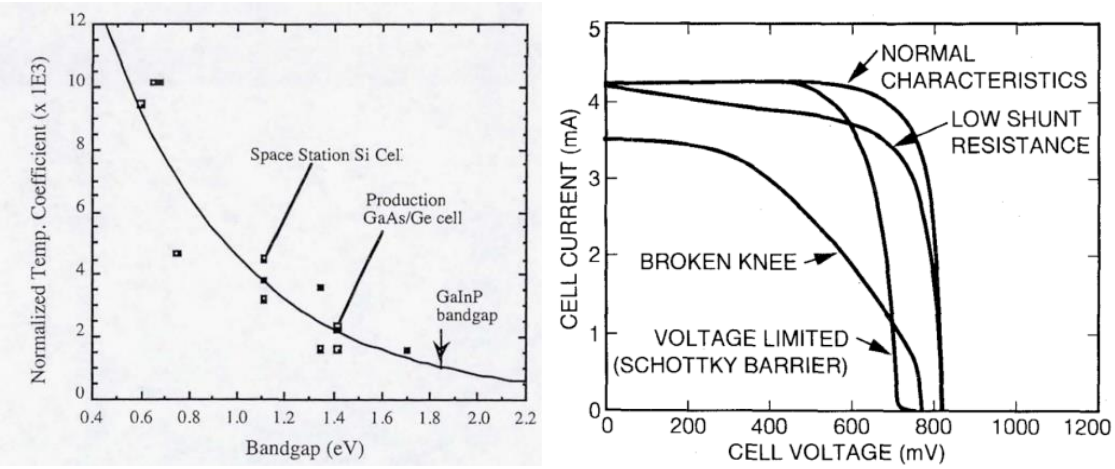

Fig. I-26 *(Left)Efficiency temperature coefficient as a function of semiconductor bandgap energy [86] (right) Low Temperature and Low Intensity LILT operating conditions effects on solar cell I-V characteristics [108], [109].*

The major technical challenge for a solar powered mission at deep space is the Low Intensity and Low Temperature (*LILT)* operating conditions. For a long time, Si solar cells were deeply studied in such conditions thanks to their historical evolution in space application [89], [93], [109]–[112]. As explained above, enhancement of efficiency is expected at low temperature due to the high open circuit voltage thermal coefficient. However, anomalous degradation are also observed at the operating conditions of deep space, namely: Schottky barrier formation, shunting (leakage current) and broken knee or flat spot phenomenon that induce fill factor degradations and hence efficiency. An example of the induced degradation on

the *I-V* curve are shown in Fig. I-26 (right) by comparison to a normal *I-V* behavior. A low shunt resistance detectable even at room temperature can have significant effects on the output parameters of the cell, in particular at low intensity. To overcome this issue, a change in the manufacturing process is required to reduce the defect density, especially around the cell edges. The Schottky barrier also called S-like shape are caused by majority carrier barrier at the hetero-interface with a band offset higher than 20 meV, which affects mostly the fill factor than open circuit voltage. This effect is only visible by measurements at low temperature below 150 K. One of the used methods to suppress this effect is increasing of doping level at the back and the front surface fields that decrease the temperature of Majority Carrier Barrier (*MCB)* appearance [113], [114].

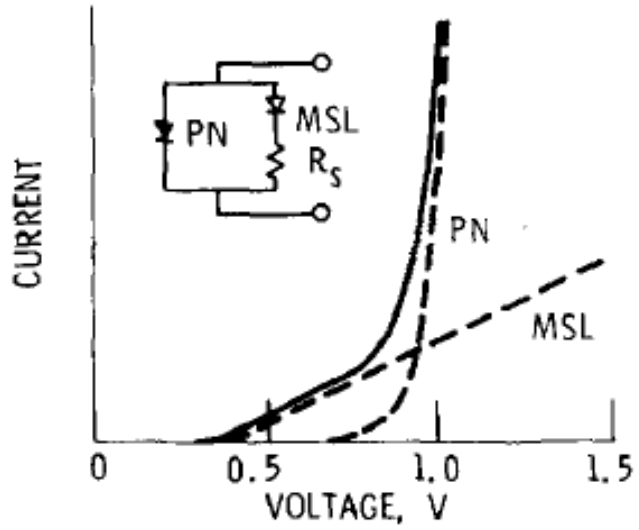

Fig. I-27 *Schematic diagram of flat spot effect on solar cell I-V characteristic [112].*

The flat spot effects manifest itself as a broken knee in the vicinity of the maximal power point. In general, cells give no sign of defectiveness when measured at room temperature. By contrary, it occurs in both illuminated and dark *I-V* characteristics at low temperature. It is suggested that a Metal-Semiconductor Like interface (*MSL),* in parallel to the p-n junction is at the origin of the flat spot effect. The double break on the *I-V* characteristics are due to the difference of series resistance of the *MSL* interfaces. At negligible series resistance, the *I-V* characteristics are totally controlled by *MSL*. However, by increasing the forward bias near the $V_{OC,}$ the *I-V* characteristics follow the p-n junction behavior (see Fig. I-27). To prevent the formation of *MSL* under the metallization, crystallographic orientation, thermal annealing, junction depth, and metallization alloys were studied [112]. TiPdAg contact with TiN layer

acting as a diffusion barrier between the cell and the metallization or deep junction have proven good results for preventing the flat spot effect. Nowadays, both single- and multi-junction solar cells used for deep space applications integrate the above-mentioned optimizations for an efficient behavior at *LILT* conditions [93], [109], [115]–[121].

I.3.1. Radiative space environment

The solar cells onboard satellites and space missions do not face only wide temperature and illumination intensity spectrum in the space environment, but are also continuously exposed to a high-energy radiative environment that affect solar cells output parameters. This environment consists of both charged and neutral particles, i.e. protons, electrons, neutrons and ions with a wide range of atomic numbers originating from solar winds and flares, galactic cosmic rays and radiation belts [104]–[110].

- Trapped particles

The most important radiation sources to the planets-orbiting satellite are the trapped particles by their magnetic fields forming the radiations belts. Around the Earth, the radiation belts are called also Van Allen belts; they consist mainly of electrons with an energy of few MeV and protons up to several hundreds of MeV. The particles are subjected to the Lorentz force and have helicoidally trajectories following the lines of the Earth magnetic field, giving the belts a toroidal shape with respect to the axis of the magnetic dipole as presented in Fig. I-28.

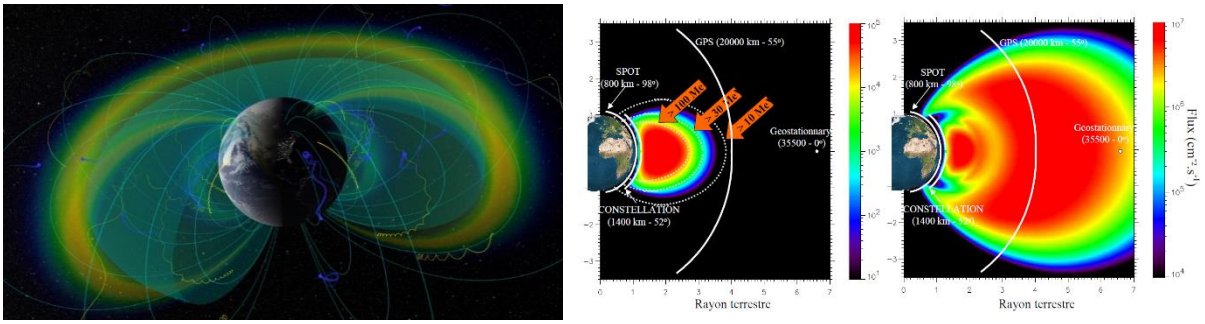

Fig. I-28 *(Left) Aspect of the Van Allen belts, credit: NASA's Scientific Visualization Studio (right) electrons and protons flux in the inner and the outer belts [129].*

There are two Van Allen radiation belts: one trapping protons and the other trapping electrons. The proton belt consists of protons of energies in the range [1 keV - 100 MeV] in a zone from 1 to 6.6 Earth Radii (6378 km), R_E. The trapped electrons had energies in the range [1 keV - 30 MeV] from 1 to 10 R_E. A view of the two radiation belts is shown in Fig. I-28 (right) for protons with energies above 10 MeV and electrons with energies above 1 MeV. A maximum flux is observed at 1.5 R_E for the proton of 10 MeV. The electron belt is composed of two parts,

inner and outer. The inner belt is centered around 1.2 R_e and extends up to 2.8 R_E for electrons of 1 MeV. In this area, electron flows are stable and energies can reach a few tens of MeV. The outer electron belt is centered around 5 R_E and extends to 10 R_E.

- Solar flares and winds

The corona plasma is so hot that the Sun gravity cannot hold it back. The protons, electron and alpha particles in the upper rings move away in all directions in a continuous flow of particles known as the solar wind with a flux of 10^{10}-10^{12} $cm^{-2}.s^{-1}$. Near Earth, or any other planet with a magnetic field, this wind meets a magnetosphere that forms a shield around the planet. This encounter generates a shock wave and compresses the magnetosphere that faces the Sun.

The solar flare occurs on the visible surface of the Sun, it is defined as a jet of material ionized thousands of kilometers away before being diluted in space. A solar flare is related to the sun 11-year cyclic activity, with 4 years of minimum activity where solar flare is rare and 7 years of maximum activity where solar flare are more probable. The ejected particles are mainly protons with high energy (few to hundreds of MeV) and high flux, or heavy ions with energy ranging from 1 to 10 MeV.

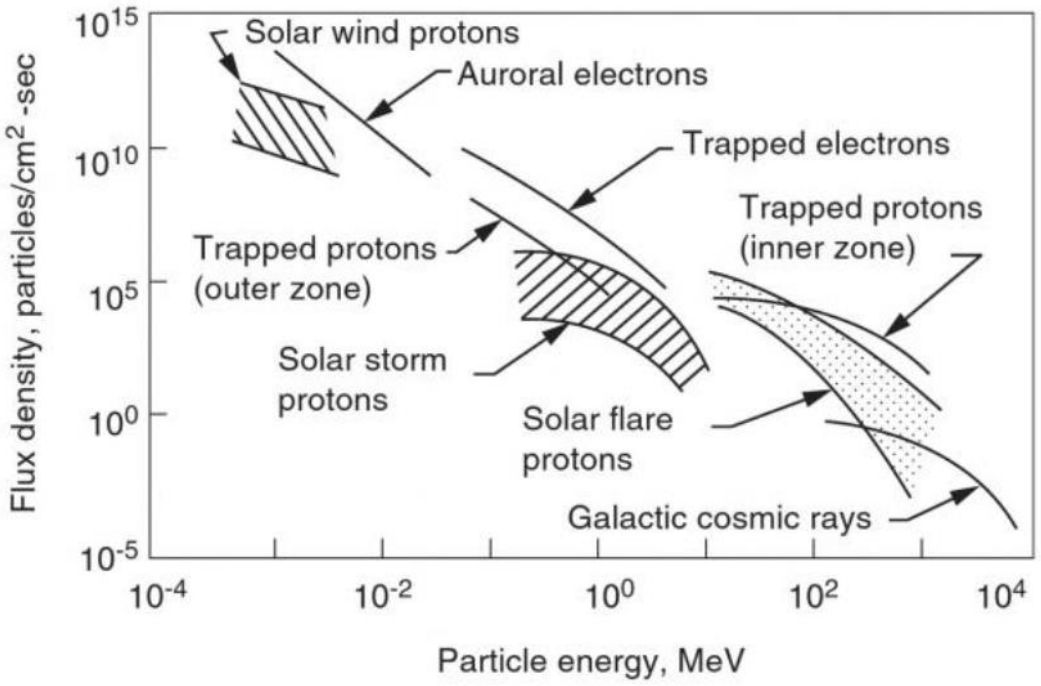

Fig. I-29 *Particles flux density as a function of energy depending on the radiation source for space environment Source: NASA-STD-3000 154* [https://msis.jsc.nasa.gov/sections/section05.htm.](https://msis.jsc.nasa.gov/sections/section05.htm)

- Galactic Cosmic-Rays radiation

Galactic radiation comes from beyond the solar system, and consists mainly of protons (85%), alpha particles (14%), and heavy nuclei (1%) which energy can reach 10 GeV/nucleon. However, the integrated flux of these particles, of the order of 2 - 4 $.cm^{-2}.s^{-1}$, is relatively lower than the above-mentioned sources. The summary of particle fluxes and energies is presented as a function of radiation sources in Fig. I-29.

The spectrum of particles in terms of composition, energy and flux is different from one mission to another and from one planet to another. As an example, we can consider Jupiter the biggest planet in our solar system, which is made of gas and has more than 60 natural satellites. Tab. I-3 illustrates a comparison between Jupiter and Earth environment. Clearly, Jupiter is 11 times larger than the earth and its magnetic moment is 2.10^4 times greater than that of the earth. The difference in rotation rates (Jupiter spin over two times faster than Earth) is also important parameters. This explains the large magnetosphere of Jupiter, which can extend up to 100 R_J. Besides solar wind and the ionosphere, Jupiter magnetosphere is fueled by volcanic activity from the satellite Io [130], [131].

Tab. I-3 *Comparison between Jupiter and Earth characteristics*

Characteristics	Jupiter	Earth
Radius (km)	7.14×10^4	6.38×10^3
Magnetic moment ($G.cm^3$)	1.59×10^{30}	8.10×10^{25}
Rotation period (h)	10	24
Main plasma sources	Io Satellite Ionosphere Solar wind	Solar wind Ionosphere

Fig. I-30 shows the spectra of trapped electrons and protons for a geosynchronous orbit where there are the most telecommunications satellite and Europa moon (9.5 R_J) which is the highest priority for NASA missions or JUICE mission planned on 2022 by ESA [132]. The spectra of trapped electrons and protons were obtained by using the AP8 [133] model for protons and AE8 [134] for electrons. These models give an estimation of omni-directional fluxes for protons in the energy range of [40 keV - 500 MeV] and electrons for the range [40 keV - 7 MeV]. From Fig. I-30, it is clear that the particles trapped at Jupiter are more

energetic and are 1-2 orders of integral flux higher than that at Earth. This implies an additional requirement for the design and radiation hardness of used solar cells in this environment.

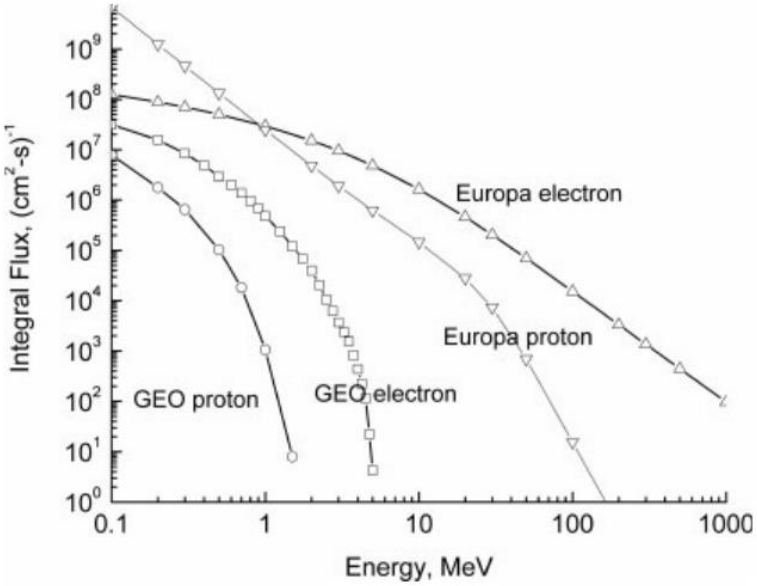

Fig. I-30 *The flux of trapped proton and electrons radiations as a function of energy in Jupiter environment (Europa moon) compare to Earth (GEO orbit) [86], [132], [135].*

I.4 Interaction particles - materials

In the interaction between the radiative environment and matter, different mechanisms come into play. They depend on the target atom, but also on the properties of the incident particle (type, energy). When charged, energetic and massive particle enters a material, it slows down continuously by interaction with electrons and nuclei of the target material. There are two dominant type of interaction: inelastic and elastic collisions.

For **inelastic collision**, the particle losses energy through the interaction with electrons cloud of the target material. The sum of kinetic energy before and after collision is not conserved in this type of interaction, where the energy difference goes to excite electrons of the material, mainly by ionization. Generally, it is the most likely process in the interaction between space radiation and semiconductor and is the main mechanism for energy loss. In **elastic collision**, the charged particles can have columbic interaction with the nucleus of the target material by Rutherford scattering where the kinetic energy before and after collision is conserved. In some cases, if the energy is sufficient the atom can be displaced from its site in the crystal lattice. The energy losses due to the interaction of the incident particle with the electron cloud, the nuclei, and the electric field of the atoms and is defined by Eq. I-32

$$-\frac{dE}{dx}\Big|_{Total} = -\frac{dE}{dx}\Big|_{electronic} - \frac{dE}{dx}\Big|_{nuclear} - \frac{dE}{dx}\Big|_{rays} \quad \text{I-32}$$

The main radiation damage in the field of solar cells can be sorted in two categories: ionization and atomic displacement.

I.4.1. Ionizations

When energetic particles penetrate matter, they loss energy and slow down. The lost energy is transferred to the first contact electrons called "delta rays". In the second step, the delta rays themselves ionize and deposit their energy in different forms: phonons, excitations and the creation of electron-hole pairs (e-h) [122]. The energy loss of the associated particle is called stopping power, dE/dx. It can be expressed in MeV.μm^{-1} but also in MeV/g.cm² if it is normalized to the density of the target material. Another important parameter is the Linear Energy Transfer (*LET)* that represents the amount of energy absorbed by the target material per unit path traveled by the projectile.

$$LET = -\frac{dE}{dx}\Big|_{electronic} \quad \text{I-33}$$

The relationship between the stopping power that refers to the energy lost by the particle and the *LET*, which refers to the amount of energy absorbed by the material is

$$-\frac{dE}{dx} = -\frac{dE}{dx}\Big|_{electronic} - \frac{dE}{dx}\Big|_{rays} \quad \text{I-34}$$

The difference of energy express the energy lost by electromagnetic radiation mainly bremsstrahlung that is emitted by particle deflection when interaction with electric field of the target atoms. This radiation is mainly gamma rays and becomes important for high-energy particles (> 10 MeV for electrons and > 1 GeV for protons). The average energy absorbed per unit mass in the form of ionization is called *TID* (Total Ionizing Dose) [119], and is expressed as a function of *LET* by Eq. I-35:

$$TID = LET.Ø \quad \text{I-35}$$

with Ø is the fluence of the incident particles. This equation is valid under the assumption of quasi-rectilinear trajectories of the particles [120]. The commonly used unity in radiation effect community is rad (1 Gy = 100 rad). It is important to note that the dose is related to the type of particle, its energy and the target material.

Ionization related-defects can be at the origin of solar cells transmission losses and darkening of cover glass. The created electron-hole pairs which interact with impurities atoms

in the material forms charged complex defects (color center) that can be stable at room temperature [138].

I.4.2. Displaced atoms

A particle passing through crystalline material can collide with an atomic nucleus of the crystal lattice by elastic or inelastic collision. However, in the range of charged particle energy for space applications, we only consider elastic collisions, which are classified according to their energy. At high energy, the projectile can penetrate the electrons cloud and knock on the nuclei; this collision is known as Rutherford. At low energy, the collision occur with the surrounding electrons cloud of the target atom and known as hard sphere collision that is more probable.

The first atom to collide is called PKA (Primary Knock-on Atom). If sufficient energy is transferred, the target atom is displaced from its site, thus creation of interstitial-vacancy defect, known as Frenkel pairs as presented in Fig. I-31 [139]. In turn if the displaced atom has sufficient energy, it can undergo similar collisions with other atoms. The secondary displacement will probably be of the hard sphere collision. To displace an atom from its site (e.g. Si), one has to take into account the sublimation energy of the atom (4.9 eV), the vacancy creating energy (2.3 eV) and other energies related to losses (phonons and electronic). In literature, the minimum amount of displacement energy, E_d, is in the range of 11 - 12.9 eV for Si [16], [140]. In GaAs material, E_d values have a crystal orientation dependence thus angular related variation; however, for thick solar cell an average of 10 eV was reported. The relationship between E_d and the threshold energy, E_t, is expressed by Eq. I-36 and Eq. I-37 for electrons and protons respectively.

$$E_{d,\ electron} = 2\frac{m_e E_t}{M\ m_e C^2}(E_t + 2m_e C^2) \qquad \textit{I-36}$$

$$E_{d,\ proton} = \left(\frac{4\ M\ m_p E_t}{M + m_p}\right) E_t \qquad \textit{I-37}$$

With m_e electron mass
m_p proton mass
M atomic weight
$m_e C^2$ electronic mass-energy equivalence

In order to quantify the energy transferred to a material by non-ionizing phenomena, the concept of *NIEL* (Non-Ionizing Energy Loss) is introduced. This concept is based on the assumption that the total concentration of stable electro-active defects created by the atomic

displacements depends only on the total energy deposited under form of displacement and not the type or initial energy of the particle incidental. More details can be found in [123]–[128].

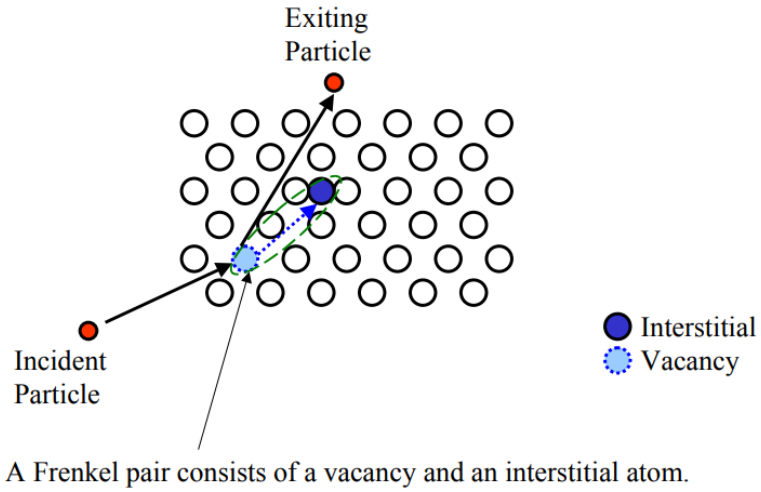

Fig. I-31 *Displacement damage mechanism.*

The *NIEL* consists of the elastic nuclear energy part (coulombic and nuclear interactions) and inelastic nuclear (neglected) radiation. Therefore, it can be calculated for the particles (electrons, protons, etc.) by the sum of the contributions of the elastic and inelastic :

$$NIEL = -\frac{dE}{dx}\Big|_{nuclear} = \frac{N}{\rho}.(\sigma_e T_e + \sigma_i T_i) \qquad I\text{-}38$$

Where, N is the Avogadro number, ρ is the density of the target material, σ_e and σ_i are respectively the effective cross-sections of elastic and inelastic interactions, T_e and T_i are the mean recoil energies associated with these elastic and inelastic interactions. *NIEL* is generally expressed in $MeV.cm^2.g^{-1}$. Example of electron, protons and neutrons *NIEL* plots are presented for Si and GaAs semiconductor material in Fig. I-32. *NIEL* values for different particles, energies and target materials are tabulated in the literature, as for example we refer to *SR-NIEL*[18]. The total displacement dose *DDD* (Displacement Damage Dose) received can be expressed in terms of *NIEL* and fluence Ø according to:

$$DDD = NIEL\,.\,\emptyset \qquad I\text{-}39$$

The non-ionizing energy deposited by the electrons increases as the particle energy increases. In contrast, for heavy ions (e.g. protons) the deposited energy is higher for low incident particle energy, i.e. the deposited energy is higher at end track of the ion where it is implanted.

[18] SR-NIEL : http://www.sr-niel.org/

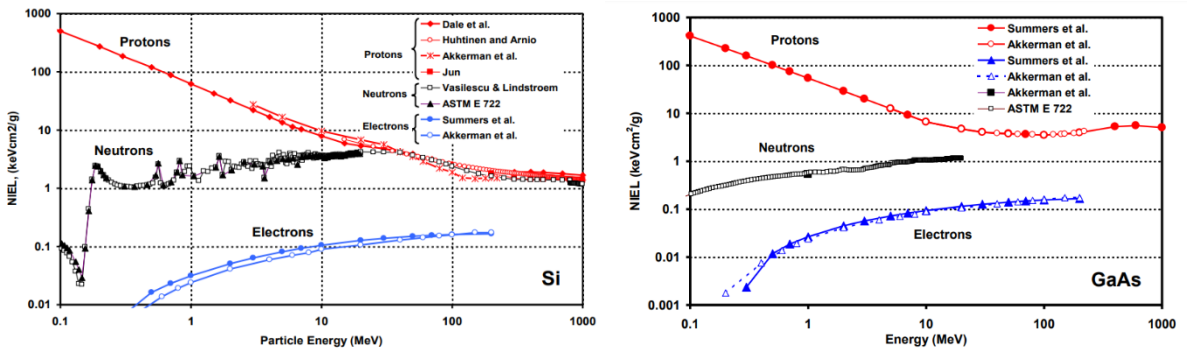

Fig. I-32 *Non Ionizing Energy loss, NIEL, for electron, protons and neutrons penetrating (left) Si and (right) GaAs for energy higher than the threshold[147].*

The probability of atomic displacement by a particle whose energy is greater than the threshold energy can be expressed as a function of displacement cross section, σ_d, with an average secondary displacement number, ν [16], [140]. According to this concept, the number of displaced atoms N_d can be estimated according to Eq. I-40:

$$N_d = n_a \, \sigma_d \, \nu \, \emptyset \qquad \textit{I-40}$$

Where n_a is the number of atoms per unit of volume and $\emptyset$ is the fluence.

In Tab. I-4 and Tab. I-5, examples of the different quantities above explained in the case of Si and GaAs irradiated by electrons and protons at different energy. The calculated N_d in Tab. I-4 are displacement rate (cm^{-1}) by incident particle of energy E. By multiplying this rate by the fluence (cm^{-2}), then the rate will be per unit volume. The total number of atom displacements created by a particle of energy E is the integral of the displacement rates in the range E to E_0, where E_0 is the particle energy at the exit of the material.

Tab. I-4 *Displacement rates for electrons and protons on Si and GaAs, the used displacement energy for Si and GaAs are 12.9 eV and 10 eV respectively [16], [140].*

Electrons Particles				
Energy (MeV)	**Silicon**		**GaAs**	
	$\sigma_d \, 10^{-24}$ (cm^2)	N_d disp/cm	$\sigma_d \, 10^{-24}$ (cm^2)	N_d disp/cm
0.5	58.4	3.4	92.6	4.13
1	67.8	5.16	153.2	8.62
2	73.6	7.35	187.8	14.17

Tab. I-5 *Displacement rates for electrons and protons on Si and GaAs, the used displacement energy for Si and GaAs are 12.9 eV and 10 eV respectively [16], [140].*

Protons Particles				
Energy (MeV)	**Silicon**		**GaAs**	
	$\sigma_d\ 10^{-20}$ (cm^2)	N_d disp/cm	$\sigma_d\ 10^{-20}$ (cm^2)	N_d disp/cm
0.5	7.06	15.634	18	32.788
1	3.53	8.429	9	17.770
2	1.77	4.52°	4.5	9.573

I.4.3. Atomic displacement defects creation

The mechanism of stable fault creation after an atomic displacement collision is shown in Fig. I-33. After the impact of the first atom, the accumulated energy dissipates in the form of atoms vibrations, causing a peak of heat along the trace of the recoil nucleus in the order of a picosecond. As a result, amorphous pockets can be created depending on the melting temperature of the target material. These amorphous pockets recrystallize after a few nanoseconds of the collision [148], [149]. The gaps and interstitial created at room temperature are mobile, and therefore a large part (85% - 90%) of them recombine almost instantaneously at 10^{-9} seconds [139].

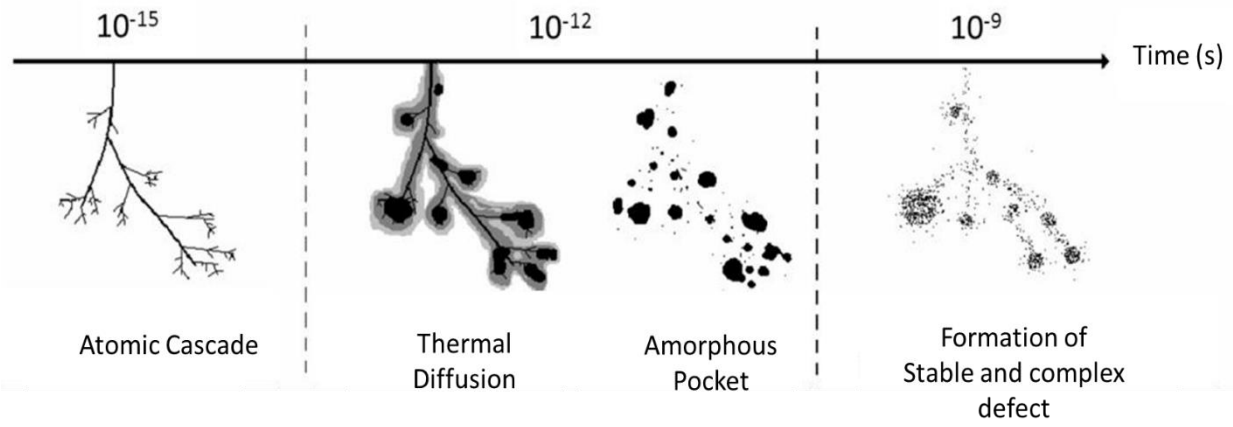

Fig. I-33 *Schematic description of stable defect formation due to particle radiation [150].*

The remaining proportion of the defects in the atomic cascade will form stable defects. These entities can be of the same type, i.e. vacancies or interstitials, or even dopants (P or B in

the case of Si) or impurities introduced during the manufacturing process (carbon, oxygen, etc.). The stabilization of these defects induces the creation of complex defects, either punctual or aggregates. If the defect is composed only of vacancy or interstitial, they are qualified as intrinsic defects as in the case of di-vacancies (V-V) [151]. Whereas if the defect contains at least one impurity (dopant or other), the defect is called extrinsic, as in the case of Vacancy-phosphorus (V-P in p-type Si). It is important to note that these defects are out of thermodynamic equilibrium, are electrically active, and have energy state E_t in the bandgap. In general, E_t is expressed as a function of the bottom of the conduction band E_C (i.e. $E_C - E_t$) and the top of the valence band E_V (i.e. $E_V + E_t$). Radiation induced defects characteristics were deeply studied by Deep Level Transient Spectroscopy, (*DLTS*), and/or Electron Paramagnetic Resonance (EPR) spectroscopy. Example of well-known defects are listed in Tab. I-6 for Si semiconductor. In the case of III-V materials such as GaAs, there are several types of Frenkel pairs since there is two type of atom that constitute the material; Arsenide interstitial or vacancy (As_i, V_{As}) and Gallium interstitial or vacancy (Ga_i, V_{Ga}). In addition, antisite defect are also considered that mean Ga Atom on As site and vice versa; denoted by Ga_{As} and As_{Ga}. Some defect characteristics in irradiated GaAs are presented in Tab. I-7 for GaAs [151]–[160].

Tab. I-6 *Defect characteristic (energy, identification and annealing stage) of irradiated Si [151], [160]–[175].*

Defect	Energy	Identification/ charge states	Remarks
E-Center	E_C - 0.45	V-P (0/-)	Anneal at 150 °C High fluence induces type inversion
A-Center	E_C - 0.17	V-O (V_iO) (VO_i)	Depending on Oxygen concentration and fluence
Di-vacancy	E_C - 0.23 E_C - 0.42 E_V + 0.2	V-V (V2) -/-- 0/- +/0	Anneal at 200 - 300 °C
Defect #1	E_V + 0.36	V-B	Not stable Anneal at 260K Donor like defect
Defect #2	E_V + 0.36	C_i-O_i (+/0)	Anneal at 623 K
Defect #3	E_C - 0.26	B_i-O_i	Anneal at 200 °C

Tab. I-7 *Defect characteristic (energy, identification and annealing stage) of electrons irradiated GaAs*

Label	Energy	Identification/ charge states	Remarks
E1	E_C - 0.045	V_{As} (-/--)	
E2	E_C - 0.14	V_{As} (0/-)	
E3	E_C - 0.30	V_{As}-As_i	
E4	E_C - 0.74	As_{Ga}+V_{As} As_i	Annealing temperature at 220 °C
E5	E_C - 0.96	V_{As}-As_i	
H0	E_V + 0.06	V_{As}-As_i	
H1	E_V + 0.25	V_{As}-As_i	
H2	E_V + 0.41	V_{Ga}-related	Annealing temperature at 280 K

These discrete energy levels change the electrical properties of the semiconductor, thus solar cells in five different ways depending on the position of the discrete energy level in the bandgap, which are shown schematically in Fig. I-34 [176], [177].

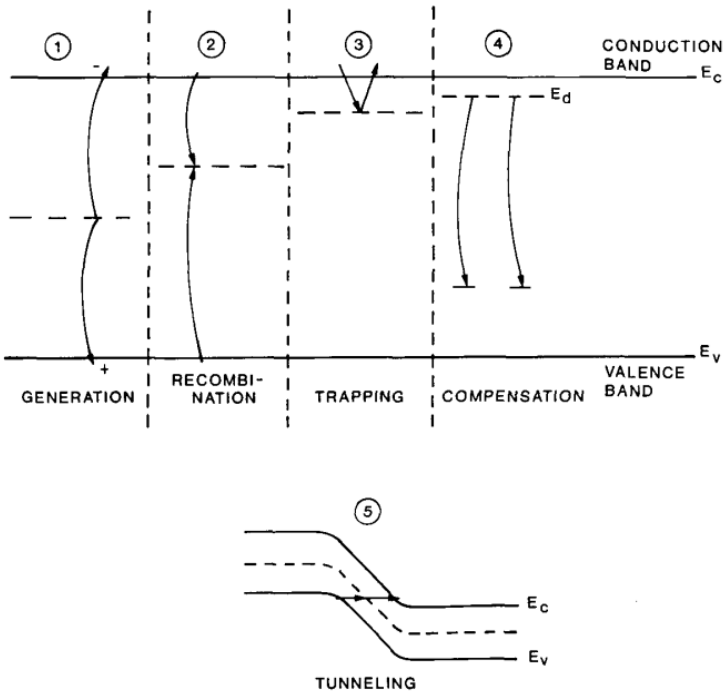

Fig. I-34 *Schematic description of the induced-degradation on irradiated solar cells depending on the traps energy level in the bandgap [176].*

Generation: a defect at an energy E_t captures an electron from the valence band and emits it into the conduction band. This is equivalent to emitting an electron and a hole in the conduction and valence band respectively. As explained in section I.2, this phenomenon constitutes a large part of the dark current. The generation rate of these defects is at its maximum when E_t is in the middle of the bandgap. Therefore, a high defect density induces a high J_0 thus higher degradation is expected on the open circuit voltage of the solar cell according to Eq. I-15.

Recombination: Contrary to generation defects, recombination consists in capturing an electron from the conduction band and re-emitting it to the valence band by defects with energy E_t. This phenomenon induces a strong degradation of minority carriers lifetime and therefore induces a strong degradation of the solar cell short-circuit current.

Trapping: a defect can capture free charge (e.g. electron from E_C) carriers and re-emit them in the same band (electrons in E_C) after a certain period. This can disturb the density of the charge carriers and thus their movement.

Compensation: deep acceptor (resp. donor) defects can compensate free electrons (respect. holes) available from donor (respect. acceptor) dopant. This results in a reduction in the density of the dopants and thus of the majority charge carriers (carriers removal).

Tunneling: free charges can be tunneled from one band to the other. The additional energy levels induced by defects located in this zone increase the phenomenon probability.

I.4.4. Irradiation effects on solar cells electrical properties

The major effect of atom displacement defects due to radiation is their effect on the minority carrier lifetime of the solar cells. Precisely, on the base layer lifetime, which is most sensitive in solar cell operation (almost all carriers photo-generation happen in this layer). Since the lifetime is inversely proportional to the recombination rate, the contribution of the recombination of the different defects can be added together to express the final lifetime as:

$$\frac{1}{\tau} = \frac{1}{\tau_0} + \frac{1}{\tau_e} + \frac{1}{\tau_p} \qquad \textit{I-41}$$

Where τ is the minority carrier lifetime, τ_0, τ_e and τ_p are the minority carrier lifetime before, after electrons and protons irradiation, respectively.

One of the most analytical expression used to estimate the degradation on solar cells depending on type, energy and fluence of the irradiation, and the target material and its quality is expressed in Eq. I-42 for minority carrier lifetime [127]:

$$\frac{1}{\tau} = \frac{1}{\tau} + \sum \sigma_i \nu_{ti} I_{ti}\, \emptyset = \frac{1}{\tau} + K_\tau \emptyset \qquad \textit{I-42}$$

Where τ_0 is the pre-irradiated value of τ, I_{ti} is the introduction rate of the i^{th} recombination center, σ_i is the capture cross section of the i^{th} recombination center, ν_{ti} is the thermal velocity of the minority carriers, and Ø is the fluence. The defect characteristic are regrouped in one single parameters called damage coefficient of minority carrier lifetime, K_τ in $cm^2.s^{-1}$.

However, it is easier and more meaningful to present the damage coefficient as a function of the diffusion length of the minority carriers. Using the relationship between lifetime and diffusion length $L^2 = D.\tau$ of the minority carriers, Eq. I-42 then becomes:

$$\frac{1}{L^2} = \frac{1}{L_0^2} + K_L \emptyset \qquad \textit{I-43}$$

Where L_0, L is the diffusion length before and after irradiation respectively. K_L (dimensionless) is the minority carrier diffusion length related damage coefficient. The lowest is the damage coefficient the lowest is the degradation of the diffusion length by the incident particle, hence lowest is the degradation of electrical properties [178].

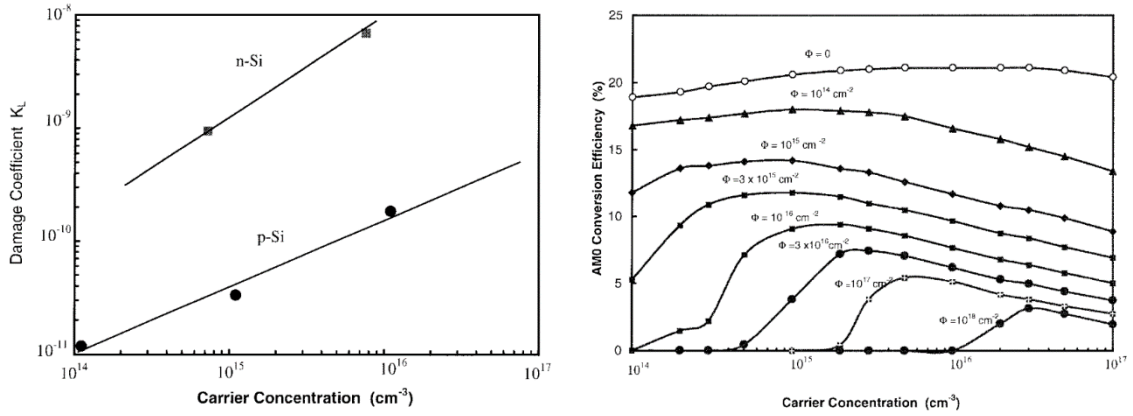

Fig. I-35 *(Left) Diffusion length damage coefficient as a function of base carrier concentration for p-type and n-type FZ silicon solar cells after 1MeV electrons irradiation; (right) p-type Si FZ efficiency under AM0 spectrum as a function of base carrier concentration for different 1 MeV electron irradiation [183].*

It has been shown in the literature that p-type Si solar cells have a better resistance to space radiations. This is due to the created defects characteristics (type, density and capture cross section). For example, carrier removal rate, R_C, in n-type silicon solar cells (0.3 cm^{-1}) is twice as high as in p-type. Yamaguchi team [161] and other research groups [159], [179]–[182] have deeply study the effect of irradiation on solar cells. In Fig. I-35, the damage coefficient is shown as a function of base doping concentration in case of irradiated FZ for both n- and p-type. At first sight, it is notable that p-type has a lower K_L than n-type over wide range of the doping

concentration; hence higher radiation resistance of p-type solar cells. The damage coefficient is proportional to base doping concentration; therefore, low base concentration is suitable for space application in order to reduce the effect of space radiation.

Modelled conversion efficiencies under an AM0 spectrum for a p-type silicon solar cell after 1-MeV electrons irradiations are shown in Fig. I-35. It is shown that a doping concentration in the range 10^{15} cm^{-3} (13 Ω.cm) is preferable for low fluence (< 10^{14} cm^{-2}), however, by increasing the fluence up to 3.10^{15} cm^{-2}, low doping concentration in the range of 4.10^{14} cm^{-3} (33 Ω.cm) offers maximum efficiency. Beyond a fluence of 3.10^{15} cm^{-2} and up to 10^{18} cm^{-2}, the base doping concentration for optimum conversion efficiency increases with increasing the electrons fluence.

The standard approach to quantify the degradation of solar cells is the observation of electrical parameters evolution: short-circuit current J_{SC}, open circuit voltage V_{OC}, fill factor and efficiency η [16], [140]. The following empiric equation I-44 shows the relationship of the above-mentioned parameters, E_p with the fluence.

$$E_p = E_{p,0} - C_{E_p}.\ln\left(1 + \frac{Ø}{Ø_x}\right) \qquad \textit{I-44}$$

Where $E_{p,0}$, E_p design a specified electrical parameters before and after irradiation respectively, Ø is the fluence, $Ø_x$ is the fluence from which the electrical parameters have a linear variation with the fluence and C_{Ep} is a constant that represent the decrease of the electrical parameters per decade in the logarithmic region. In some review, $Ø_x$ and C_{Ep} are used as fitting parameters [184].

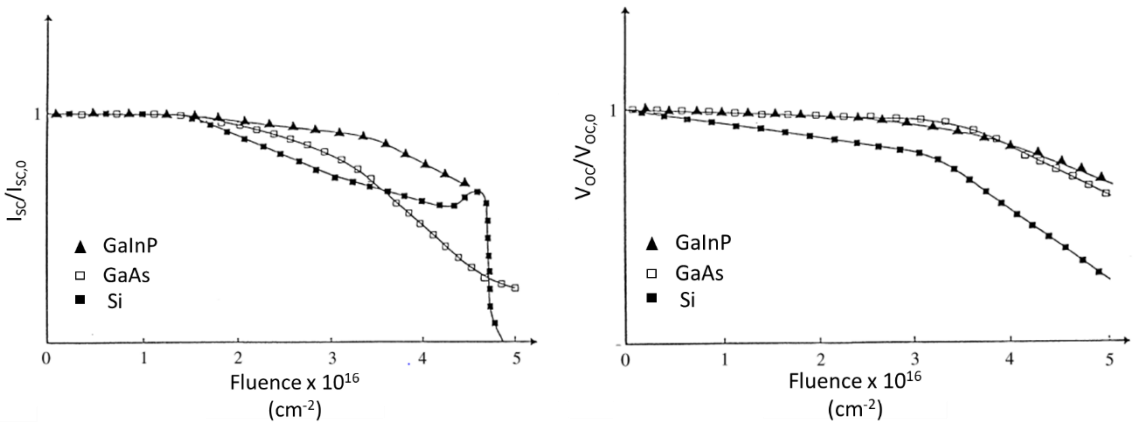

Fig. I-36 *Electrical parameters normalized to pre-irradiated values variation for Si, GaAs and GaInP solar cells as a function of 1-MeV electrons irradiations fluence (left) Short-circuit current (right) Open circuit voltage [185].*

The variation of short circuit current J_{SC} and open circuit voltage V_{OC} normalized to its pre-irradiation value, $J_{SC,0}$, $V_{OC,0}$, is shown as a function of 1-MeV fluence are shown in Fig. I-36. The solar cells, i.e. Si, GaAs and GaInP were measured under 10% AM0 and at room temperature [185].

It is clear that Si is the most sensitive to irradiation where $Ø_x$ is the weakest. The large Si minority carrier lifetime before irradiation induces higher sensitivity to irradiation. In addition, the degradation of Si at low fluence is more important compared to other cells, this is due to high introduction defect rate or higher capture cross section of introduced defects. However, at higher fluence below $4.5x10^{16}$ cm^{-2}, the short circuit current for GaAs and GaInP have more degradation rate than Si.

The anomalous Jsc degradation beyond $4.5x10^{16}$ cm^{-2} has been the subject of several studies in order to identify its origin [172], [186]–[188]. The decrease of short circuit current can be explained by the broadening of the space charge region toward the back surface of the cell, which explain the continuous degradation of open circuit voltage. The abrupt decrease of short circuit current observed by further irradiation was explained by an inversion of base type from p to n, hence a shift of junction from n/p/p+ in the front to n/n/p+ at the back of the cell. The shift of junction is due to high carrier removal due to majority carrier traps and deep donor defects. The anomalous degradation observed for Si solar cell occur at a fluence in the range of 10^{16} cm^{-2} in case of electrons irradiation and in the range of 10^{14} cm^{-2} for protons particles, however it depend strongly on the base concentration [189].

I.5 Summary

- Semiconductor materials differ on the one hand in their band diagram, direct bandgap (GaAs, InP) or indirect bandgap (Si, Ge) which induces a difference in the absorption coefficient (lower in materials with indirect bandgap). On the other hand, their bandgap energy in turn defines the minimum photon energy for the creation of electron-hole pairs, thus absorption range of solar spectrum.
- Solar cells are minority carrier based devices, which are characterized by a lifetime that correspond to the average time an electron (or hole) passes in the conduction band before its recombines.
- Intrinsic recombination mechanisms are present in all semiconductor materials; Auger and radiative recombination in indirect and direct bandgap materials respectively. The minority carrier lifetime is also strongly affected by *SRH* recombination due to the presence of defects in the crystal structure mainly at manufacturing process.
- For decades, research has been devoted to the development of solar cell architectures. The optimization of passivation layers, surfaces texturization antireflective coating, and metallization has made it possible to achieve efficiencies close to the single junction theoretical limit.
- The concept of multi-junction solar cells offers a solution to reduce losses mainly by minimizing thermalization and transmission losses. *MJSC* allow to exceed the theoretical conversion limit of single junction cells (33.7%). Recent NRL research has shown a record efficiency of a 6-junction cell at 39.2% under 1-sun.
- Theoretically, silicon-based multi-junction solar cells present promising conversion estimates of 45% efficiency for a double junction and more than 50% for a triple junction. However, several challenges need to be solved for the integration of III-V materials on Si to difference of lattice constant, thermal expansion coefficient and polarity.
- Different approaches were studied and reported in literature; epitaxial growth: direct growth or by the use of intermediate buffer layer to reduce the threading dislocation density, direct bonding: the use of hydrophobic, hydrophilic or surface activated bonding, *SAB*.
- In *SAB* process no annealing step is necessary and threading dislocation were not reported in literature. Contrary to hydrophilic bonding, no oxide interlayer are required for bonding and a low inclusion or cavities are reported compared to hydrophobic

bonding. However, a few nanometers of amorphous layer results from the Ar bombardment at the interface may create some additional series resistance, and the use of ultra-high vacuum and surface polishing steps impact the overall process cost.

- Depending on the space mission, and comparing to the environment around the earth (Normal irradiance and temperature in the range of 350 K) solar cells can operate at high temperature and high intensity for missions close to the Sun, going down to low temperature 120 K and very low intensity 50 W/m² close to Jupiter.
- The prediction of the performances of multi-junction solar cells is relatively complicated compared to that of single-junction cells especially as a function of temperature, due to the intervention of several materials characteristics and series connected-related issues.
- Generally, the temperature coefficient of the conversion efficiency is negative, i.e. efficiency increase by decreasing temperature and vice versa. However, the combination of low intensity and low temperature can have non-negligible effects on the behavior of solar cells, namely flat spot, s-like shape and low shunt resistance effects, which are not detectable at room temperature.
- A wide particle spectrum is present in the space environment in terms of type (electron, neutrons, and heavy ions), energy ranging from 10^{-3} up to 10^{4} MeV, flux in the range 10^{-5} - 10^{15} #.cm^{-2}.s^{-1}. These particles are the result of solar activity, cosmic radiation and particle trapping by the magnetospheres of the planets. Calculation of the equivalence total fluence received by the solar cells during mission depends on the duration, destination and trajectory.
- Particles can interact by elastic or inelastic collisions, mainly causing ionization, which affects the transmission of cover glass, or by atomic displacement that affects highly solar cells electrical output.
- Atom displacement occurs when an incident particle transfers enough energy to an atom and knock it from its site in the crystal lattice, thus creating vacancy-interstitial pairs called Frenkel pair, which can interact with other pairs or with impurities or dopants to form complex and stable defects.
- Depending on energy, charge state, and capture cross section of the defects that can act as recombination, generation, trapping or compensation centers, which reduce mainly the minority carrier lifetime, hence the electrical output of solar cells.

I.6 References

[1] A. D. Polyanin and A. Chernoutsan, *A Concise Handbook of Mathematics, Physics, and Engineering Sciences*. CRC Press, 2010.

[2] W. D. C. Jr and D. G. Rethwisch, *Fundamentals of Materials Science and Engineering: An Integrated Approach*. John Wiley & Sons, 2012.

[3] W. K. Chen, *The Electrical Engineering Handbook*. Elsevier, 2004.

[4] T. Li, M. Mastro, and A. Dadgar, *III-V Compound Semiconductors: Integration with Silicon-Based Microelectronics*. CRC Press, 2016.

[5] V. Benda, "8 - Photovoltaics: The Basics," in *A Comprehensive Guide to Solar Energy Systems*, T. M. Letcher and V. M. Fthenakis, Eds. Academic Press, 2018, pp. 151–179.

[6] A. Reinders, P. Verlinden, W. van Sark, and A. Freundlich, *Photovoltaic Solar Energy: From Fundamentals to Applications*. John Wiley & Sons, 2017.

[7] J. Piprek, "Chapter 4 - Optical Waves," in *Semiconductor Optoelectronic Devices*, J. Piprek, Ed. Boston: Academic Press, 2003, pp. 83–120.

[8] A. Luque and S. Hegedus, Eds., *Handbook of photovoltaic science and engineering*, 2nd ed. Chichester, West Sussex, U.K: Wiley, 2011.

[9] P. YU and M. Cardona, *Fundamentals of Semiconductors: Physics and Materials Properties*, 4th ed. Berlin Heidelberg: Springer-Verlag, 2010.

[10] S. Zhuiykov, Ed., "1 - Electrons and holes in a semiconductor," in *Nanostructured Semiconductor Oxides for the Next Generation of Electronics and Functional Devices*, Woodhead Publishing, 2014, pp. 1–49.

[11] D. B. Holt and B. G. Yacobi, *Extended Defects in Semiconductors: Electronic Properties, Device Effects and Structures*. Cambridge University Press, 2007.

[12] A. K. SINGH, *Electronic Devices and Integrated Circuits*. PHI Learning Pvt. Ltd., 2011.

[13] B. P. Singh and R. Singh, *Electronic Devices and Integrated Circuits*. Pearson Education India, 2006.

[14] J. M. Fiore and Open Textbook Library, *Semiconductor devices: theory and application*. 2018.

[15] "The Solar Cell," in *Principles of Solar Cells, LEDs and Diodes: The role of the PN junction*, Chichester, UK: John Wiley & Sons, Ltd, 2011, pp. 159–213.

[16] B. E. Anspaugh, R. G. Dowing, H. Y. Tada, and J. R. Carter Jr, *Solar Cell Radiation Handbook*, Third Edition. National Aeronautics and Space Administration, 1982.

[17] M. J. Kerr and A. Cuevas, "General parameterization of Auger recombination in crystalline silicon," *J. Appl. Phys.*, vol. 91, no. 4, pp. 2473–2480, Jan. 2002, doi: 10.1063/1.1432476.

[18] U. Strauss, W. W. Rühle, and K. Köhler, "Auger recombination in intrinsic GaAs," *Appl. Phys. Lett.*, vol. 62, no. 1, pp. 55–57, Jan. 1993, doi: 10.1063/1.108817.

[19] A. Richter, M. Hermle, and S. W. Glunz, "Reassessment of the Limiting Efficiency for Crystalline Silicon Solar Cells," *IEEE J. Photovolt.*, vol. 3, no. 4, pp. 1184–1191, Oct. 2013, doi: 10.1109/JPHOTOV.2013.2270351.

[20] W. Shockley and W. T. Read, "Statistics of the Recombinations of Holes and Electrons," *Phys. Rev.*, vol. 87, no. 5, pp. 835–842, Sep. 1952, doi: 10.1103/PhysRev.87.835.

[21] R. N. Hall, "Electron-Hole Recombination in Germanium," *Phys. Rev.*, vol. 87, no. 2, pp. 387–387, Jul. 1952, doi: 10.1103/PhysRev.87.387.

[22] L. Hughes, *Advanced Semiconductor Fundamentals (Modular Series on Solid State Devices*.

[23] J. Zhao, A. Wang, P. P. Altermatt, S. R. Wenham, and M. A. Green, “24% efficient perl silicon solar cell: Recent improvements in high efficiency silicon cell research,” *Sol. Energy Mater. Sol. Cells*, vol. 41–42, pp. 87–99, Jun. 1996, doi: 10.1016/0927-0248(95)00117-4.
[24] S. Saylan, T. Milakovich, S. A. Hadi, A. Nayfeh, E. A. Fitzgerald, and M. S. Dahlem, “Multilayer antireflection coating design for GaAs0.69P0.31/Si dual-junction solar cells,” *Sol. Energy*, vol. 122, pp. 76–86, Dec. 2015, doi: 10.1016/j.solener.2015.07.049.
[25] S. A. Hadi *et al.*, “Design Optimization of Single-Layer Antireflective Coating for $GaAs_{1-x}P_x$/Si Tandem Cells With x = 0.17, 0.29, and 0.37,” *IEEE J. Photovolt.*, vol. 5, no. 1, pp. 425–431, Jan. 2015, doi: 10.1109/JPHOTOV.2014.2363559.
[26] N. Shigekawa and J. Liang, “Impacts of optical properties of anti-reflection coatings on characteristics of InGaP/GaAs/Si hybrid triple-junction cells,” in *2015 IEEE 42nd Photovoltaic Specialist Conference (PVSC)*, Jun. 2015, pp. 1–4, doi: 10.1109/PVSC.2015.7356076.
[27] Z. Xi, D. Yang, W. Dan, C. Jun, X. Li, and D. Que, “Investigation of texturization for monocrystalline silicon solar cells with different kinds of alkaline,” *Renew. Energy*, vol. 29, no. 13, pp. 2101–2107, Oct. 2004, doi: 10.1016/j.renene.2004.03.003.
[28] M. J. Stocks, A. J. Carr, and A. W. Blakers, “Texturing of polycrystalline silicon,” *Sol. Energy Mater. Sol. Cells*, vol. 40, no. 1, pp. 33–42, Mar. 1996, doi: 10.1016/0927-0248(95)00077-1.
[29] P. Fath, C. Borst, C. Zechner, E. Bucher, G. Willeke, and S. Narayanan, “Progress in a novel high-throughput mechanical texturization technology for highly efficient multicrystalline silicon solar cells,” *Sol. Energy Mater. Sol. Cells*, vol. 48, no. 1, pp. 229–236, Nov. 1997, doi: 10.1016/S0927-0248(97)00105-0.
[30] D. Kray, M. Hermle, and S. W. Glunz, “Theory and experiments on the back side reflectance of silicon wafer solar cells,” *Prog. Photovolt. Res. Appl.*, vol. 16, no. 1, pp. 1–15, 2008, doi: 10.1002/pip.769.
[31] H.-L. Chen *et al.*, “A 19.9%-efficient ultrathin solar cell based on a 205-nm-thick GaAs absorber and a silver nanostructured back mirror,” *Nat. Energy*, vol. 4, no. 9, pp. 761–767, Sep. 2019, doi: 10.1038/s41560-019-0434-y.
[32] A. G. Aberle and R. Hezel, “Progress in Low-temperature Surface Passivation of Silicon Solar Cells using Remote-plasma Silicon Nitride,” *Prog. Photovolt. Res. Appl.*, vol. 5, no. 1, pp. 29–50, Jan. 1997, doi: 10.1002/(SICI)1099-159X(199701/02)5:1<29::AID-PIP149>3.0.CO;2-M.
[33] M. Bashahu and A. Habyarimana, “Review and test of methods for determination of the solar cell series resistance,” *Renew. Energy*, vol. 6, no. 2, pp. 129–138, Mar. 1995, doi: 10.1016/0960-1481(94)E0021-V.
[34] R. Cariou, “Epitaxial growth of Si(Ge) materials on Si and GaAs by low temperature PECVD: towards tandem devices,” thesis, Palaiseau, Ecole polytechnique, 2014.
[35] C. Algora and I. Rey-Stolle, Eds., *Handbook of concentrator photovoltaic technology*. Chichester, West Sussex: Wiley, 2016.
[36] S. Kasap and P. Capper, Eds., *Springer Handbook of Electronic and Photonic Materials*. Springer US, 2007.
[37] S. P. Bremner, M. Y. Levy, and C. B. Honsberg, “Analysis of tandem solar cell efficiencies under AM1.5G spectrum using a rapid flux calculation method,” *Prog. Photovolt. Res. Appl.*, vol. 16, no. 3, pp. 225–233, 2008, doi: 10.1002/pip.799.
[38] A. Martí and G. L. Araújo, “Limiting efficiencies for photovoltaic energy conversion in multigap systems,” *Sol. Energy Mater. Sol. Cells*, vol. 43, no. 2, pp. 203–222, Sep. 1996, doi: 10.1016/0927-0248(96)00015-3.
[39] C. H. Henry, “Limiting efficiencies of ideal single and multiple energy gap terrestrial solar cells,” *J. Appl. Phys.*, vol. 51, no. 8, pp. 4494–4500, Aug. 1980, doi: 10.1063/1.328272.

[40] E. F. Fernández, A. J. García-Loureiro, and G. P. Smestad, “Multijunction Concentrator Solar Cells: Analysis and Fundamentals,” in *High Concentrator Photovoltaics*, P. Pérez-Higueras and E. F. Fernández, Eds. Cham: Springer International Publishing, 2015, pp. 9–37.
[41] A. De Vos and H. Pauwels, “On the thermodynamic limit of photovoltaic energy conversion,” *Appl. Phys.*, vol. 25, no. 2, pp. 119–125, Jun. 1981, doi: 10.1007/BF00901283.
[42] S. P. Tobin *et al.*, “Assessment of MOCVD- and MBE-growth GaAs for high-efficiency solar cell applications,” *IEEE Trans. Electron Devices*, vol. 37, no. 2, pp. 469–477, Feb. 1990, doi: 10.1109/16.46385.
[43] A. J. Ptak, S. W. Johnston, S. Kurtz, D. J. Friedman, and W. K. Metzger, “A comparison of MBE- and MOCVD-grown GaInNAs,” *J. Cryst. Growth*, vol. 251, no. 1, pp. 392–398, Apr. 2003, doi: 10.1016/S0022-0248(02)02201-7.
[44] A. W. Bett, R. Adelhelm, C. Agert, R. Beckert, F. Dimroth, and U. Schubert, “Advanced III–V solar cell structures grown by MOVPE,” *Sol. Energy Mater. Sol. Cells*, vol. 66, no. 1, pp. 541–550, Feb. 2001, doi: 10.1016/S0927-0248(00)00236-1.
[45] K. Louarn, “Etude et réalisation de jonctions tunnel à base d’hétérostructures à semi-conducteurs III-V pour les cellules solaires multi-jonction à très haut rendement,” phd, Université de Toulouse, Université Toulouse III - Paul Sabatier, 2018.
[46] E. V. Vidal, “Fabrication, characterization and simulation of III-V on Si multi-junction solar cells,” PhD thesis, Université Grenoble Alpes, 2018.
[47] T. W. Kim, B. R. Albert, L. C. Kimerling, and J. Michel, “InGaP solar cell on Ge-on-Si virtual substrate for novel solar power conversion,” *J. Appl. Phys.*, vol. 123, no. 8, p. 085111, Feb. 2018, doi: 10.1063/1.5018082.
[48] K. N. Yaung, M. Vaisman, J. Lang, and M. L. Lee, “GaAsP solar cells on GaP/Si with low threading dislocation density,” *Appl. Phys. Lett.*, vol. 109, no. 3, p. 032107, Jul. 2016, doi: 10.1063/1.4959825.
[49] M. Yamaguchi, “Potential and present status of III–V/Si tandem solar cells,” in *2014 IEEE 40th Photovoltaic Specialist Conference (PVSC)*, Jun. 2014, pp. 0821–0826, doi: 10.1109/PVSC.2014.6925041.
[50] V. Terzieva *et al.*, “Benefits and side effects of high temperature anneal used to reduce threading dislocation defects in epitaxial Ge layers on Si substrates,” *Thin Solid Films*, vol. 517, no. 1, pp. 172–177, Nov. 2008, doi: 10.1016/j.tsf.2008.08.144.
[51] D. Jung, P. G. Callahan, B. Shin, K. Mukherjee, A. C. Gossard, and J. E. Bowers, “Low threading dislocation density GaAs growth on on-axis GaP/Si (001),” *J. Appl. Phys.*, vol. 122, no. 22, p. 225703, Dec. 2017, doi: 10.1063/1.5001360.
[52] T. Soga, K. Baskar, T. Kato, T. Jimbo, and M. Umeno, “MOCVD growth of high efficiency current-matched AlGaAsSi tandem solar cell,” *J. Cryst. Growth*, vol. 174, no. 1, pp. 579–584, Apr. 1997, doi: 10.1016/S0022-0248(97)00064-X.
[53] K. H. Lee *et al.*, “Reduction of threading dislocation density in Ge/Si using a heavily As-doped Ge seed layer,” *AIP Adv.*, vol. 6, no. 2, p. 025028, Feb. 2016, doi: 10.1063/1.4943218.
[54] F. Dimroth *et al.*, “Comparison of Direct Growth and Wafer Bonding for the Fabrication of GaInP/GaAs Dual-Junction Solar Cells on Silicon,” *IEEE J. Photovolt.*, vol. 4, no. 2, pp. 620–625, Mar. 2014, doi: 10.1109/JPHOTOV.2014.2299406.
[55] M. Feifel, D. Lackner, J. Ohlmann, J. Benick, M. Hermle, and F. Dimroth, “Direct Growth of a GaInP/GaAs/Si Triple-Junction Solar Cell with 22.3% AM1.5g Efficiency,” *Sol. RRL*, vol. 3, no. 12, p. 1900313, 2019, doi: 10.1002/solr.201900313.
[56] T. Abe, T. Takei, A. Uchiyama, K. Yoshizawa, and Y. Nakazato, “Silicon Wafer Bonding Mechanism for Silicon-on-Insulator Structures,” *Jpn. J. Appl. Phys.*, vol. 29, no. 12A, p. L2311, Dec. 1990, doi: 10.1143/JJAP.29.L2311.

[57] B. Aspar *et al.*, “The generic nature of the Smart-Cut® process for thin film transfer,” *J. Electron. Mater.*, vol. 30, no. 7, pp. 834–840, Jul. 2001, doi: 10.1007/s11664-001-0067-2.
[58] J. Haisma and G. A. C. M. Spierings, “Contact bonding, including direct-bonding in a historical and recent context of materials science and technology, physics and chemistry: Historical review in a broader scope and comparative outlook,” *Mater. Sci. Eng. R Rep.*, vol. 37, no. 1, pp. 1–60, Apr. 2002, doi: 10.1016/S0927-796X(02)00003-7.
[59] T. Suni, *Direct wafer bonding for MEMS and microelectronics*. Espoo: VTT, 2006.
[60] A. Plößl and G. Kräuter, “Wafer direct bonding: tailoring adhesion between brittle materials,” *Mater. Sci. Eng. R Rep.*, vol. 25, no. 1, pp. 1–88, Mar. 1999, doi: 10.1016/S0927-796X(98)00017-5.
[61] Y. C. Zhou, Z. H. Zhu, D. Crouse, and Y. H. Lo, “Electrical properties of wafer-bonded GaAs/Si heterojunctions,” *Appl. Phys. Lett.*, vol. 73, no. 16, pp. 2337–2339, Oct. 1998, doi: 10.1063/1.122454.
[62] F. Shi, K.-L. Chang, J. Epple, C.-F. Xu, K. Y. Cheng, and K. C. Hsieh, “Characterization of GaAs-based n-n and p-n interface junctions prepared by direct wafer bonding,” *J. Appl. Phys.*, vol. 92, no. 12, pp. 7544–7549, Nov. 2002, doi: 10.1063/1.1522484.
[63] P. Kopperschmidt, S. Senz, G. Kästner, D. Hesse, and U. M. Gösele, “Materials integration of gallium arsenide and silicon by wafer bonding,” *Appl. Phys. Lett.*, vol. 72, no. 24, pp. 3181–3183, Jun. 1998, doi: 10.1063/1.121586.
[64] M. Alexe and U. Gösele, Eds., *Wafer Bonding: Applications and Technology*. Berlin Heidelberg: Springer-Verlag, 2004.
[65] E. Veinberg-Vidal *et al.*, “Manufacturing and Characterization of III-V on Silicon Multijunction Solar Cells,” *Energy Procedia*, vol. 92, pp. 242–247, Aug. 2016, doi: 10.1016/j.egypro.2016.07.066.
[66] J. Schone, F. Dimroth, A. W. Bett, A. Tauzin, C. Jaussaud, and J.- Roussin, “III-V solar cell growth on wafer-bonded GaAs/Si-substrates,” in *2006 IEEE 4th World Conference on Photovoltaic Energy Conference*, May 2006, vol. 1, pp. 776–779, doi: 10.1109/WCPEC.2006.279571.
[67] H. Takagi, K. Kikuchi, R. Maeda, T. R. Chung, and T. Suga, “Surface activated bonding of silicon wafers at room temperature,” *Appl. Phys. Lett.*, vol. 68, no. 16, pp. 2222–2224, Apr. 1996, doi: 10.1063/1.115865.
[68] T. Suga and K. Miyazawa, “Metal/Metal- And Metal/Ceramic Interfaces Produced By Means Of A Surface Activation Method At Room Temperature,” in *Metal–Ceramic Interfaces*, M. Rühle, A. G. Evans, M. F. Ashby, and J. P. Hirth, Eds. Oxford: Pergamon, 1990, pp. 189–195.
[69] T. Suga, Y. Takahashi, H. Takagi, B. Gibbesch, and G. Elssner, “Structure of AlAl and $AlSi_3N_4$ interfaces bonded at room temperature by means of the surface activation method,” *Acta Metall. Mater.*, vol. 40, pp. S133–S137, Jan. 1992, doi: 10.1016/0956-7151(92)90272-G.
[70] T. Suga, Y. Takahashi, and H. Takagi, “Surface activated bonding -an approach to joining at room temperature,” *Ceram Trans*, vol. 35, pp. 323–331, 1993.
[71] H. Fusano, Y. Inaba, and T. Nonaka, “Wafer and Die Bonding Processes,” in *Three-Dimensional Integration of Semiconductors: Processing, Materials, and Applications*, K. Kondo, M. Kada, and K. Takahashi, Eds. Cham: Springer International Publishing, 2015, pp. 139–165.
[72] Y. Ohno *et al.*, “Chemical bonding at room temperature via surface activation to fabricate low-resistance GaAs/Si heterointerfaces,” *Appl. Surf. Sci.*, vol. 525, p. 146610, Sep. 2020, doi: 10.1016/j.apsusc.2020.146610.
[73] K. Derendorf *et al.*, “Fabrication of GaInP/GaAs//Si Solar Cells by Surface Activated Direct Wafer Bonding,” *IEEE J. Photovolt.*, vol. 3, no. 4, pp. 1423–1428, Oct. 2013, doi: 10.1109/JPHOTOV.2013.2273097.

[74] N. Shigekawa, J. Liang, R. Onitsuka, T. Agui, H. Juso, and T. Takamoto, "Current–voltage and spectral-response characteristics of surface-activated-bonding-based InGaP/GaAs/Si hybrid triple-junction cells," *Jpn. J. Appl. Phys.*, vol. 54, no. 8S1, p. 08KE03, Jul. 2015, doi: 10.7567/JJAP.54.08KE03.
[75] J. Liang, L. Chai, S. Nishida, M. Morimoto, and N. Shigekawa, "Investigation on the interface resistance of Si/GaAs heterojunctions fabricated by surface-activated bonding," *Jpn. J. Appl. Phys.*, vol. 54, no. 3, p. 030211, Feb. 2015, doi: 10.7567/JJAP.54.030211.
[76] J. Liang, T. Miyazaki, M. Morimoto, S. Nishida, N. Watanabe, and N. Shigekawa, "Electrical Properties of p-Si/n-GaAs Heterojunctions by Using Surface-Activated Bonding," *Appl. Phys. Express*, vol. 6, no. 2, p. 021801, Jan. 2013, doi: 10.7567/APEX.6.021801.
[77] N. Shigekawa *et al.*, "Hybrid triple-junction solar cells by surface activate bonding of III–V double-junction-cell heterostructures to ion-implantation-based Si cells," in *2014 IEEE 40th Photovoltaic Specialist Conference (PVSC)*, Jun. 2014, pp. 0534–0537, doi: 10.1109/PVSC.2014.6924976.
[78] T. Yu, M. R. Howlader, F. Zhang, and M. Bakr, "Nanobonding for Multi-Junction Solar Cells at Room Temperature," *ECS Trans.*, vol. 35, no. 2, p. 3, Apr. 2011, doi: 10.1149/1.3568842.
[79] S. Essig and F. Dimroth, "Fast Atom Beam Activated Wafer Bonds between n-Si and n-GaAs with Low Resistance," *ECS J. Solid State Sci. Technol.*, vol. 2, no. 9, p. Q178, Jul. 2013, doi: 10.1149/2.031309jss.
[80] R. Cariou *et al.*, "III–V-on-silicon solar cells reaching 33% photoconversion efficiency in two-terminal configuration," *Nat. Energy*, vol. 3, no. 4, pp. 326–333, Apr. 2018, doi: 10.1038/s41560-018-0125-0.
[81] D. R. Myers, "The Solar Resource," in *Solar Hydrogen Generation*, Springer, 2008, pp. 19–39.
[82] A. T. Mecherikunnel and J. Richmond, "Spectral distribution of solar radiation," 1980.
[83] E21 Committee, "Standard Solar Constant and Zero Air Mass Solar Spectral Irradiance Tables," ASTM International. doi: 10.1520/E0490-00AR19.
[84] C. A. Gueymard, "Revised composite extraterrestrial spectrum based on recent solar irradiance observations," *Sol. Energy*, vol. 169, pp. 434–440, Jul. 2018, doi: 10.1016/j.solener.2018.04.067.
[85] The American Society for Testing and Materials (ASTM), "2000 ASTM Standard Extraterrestrial Spectrum Reference E-490-00 | Grid Modernization | NREL." https://www.nrel.gov/grid/solar-resource/spectra-astm-e490.html.
[86] S. Bailey, G. Landis, and R. Raffaelle, "The next generation of space cells for diverse environments," 2002.
[87] S. Brambillasca, F. Topputo, A. Ercoli-Finzi, R. Campesato, and C. SpA, "*LILT* Measurement on Silicon Solar Cells of Rosetta Lander Philae," in *XX AIDAA Congress, Milano, Italy, June*, 2009, vol. 29.
[88] K.-H. Glassmeier, H. Boehnhardt, D. Koschny, E. Kührt, and I. Richter, "The Rosetta Mission: Flying Towards the Origin of the Solar System," *Space Sci. Rev.*, vol. 128, no. 1, pp. 1–21, Feb. 2007, doi: 10.1007/s11214-006-9140-8.
[89] C. J. Gelderloos, K. B. Miller, R. J. Walters, G. P. Summers, and S. R. Messenger, "Low intensity low temperature performance of advanced solar cells," in *Photovoltaic Specialists Conference, 2002. Conference Record of the Twenty-Ninth IEEE*, 2002, pp. 804–807.
[90] G. D'Accolti *et al.*, "The Solar Array Photovoltaic Assembly for the ROSETTA Orbiter and Lander Spacecraft's," vol. 502, p. 445, Apr. 2002.
[91] S. Dawson, P. Stella, W. McAlpine, and B. Smith, "JUNO Photovoltaic Power at Jupiter," in *10th International Energy Conversion Engineering Conference*, American Institute of Aeronautics and Astronautics.

[92] A. J. Juhasz, “An analysis and procedure for determining space environmental sink temperatures with selected computational results,” *AIP Conf. Proc.*, vol. 552, no. 1, pp. 805–814, Feb. 2001, doi: 10.1063/1.1358011.
[93] D. A. Scheiman and D. B. Snyder, “Low intensity low temperature (*LILT*) measurements of state-of-the-art triple junction solar cells for space missions,” in *2008 33rd IEEE Photovoltaic Specialists Conference*, May 2008, pp. 1–6, doi: 10.1109/PVSC.2008.4922707.
[94] J. Meseguer, I. Pérez-Grande, and A. Sanz-Andrés, “2 - Space environment,” in *Spacecraft Thermal Control*, J. Meseguer, I. Pérez-Grande, and A. Sanz-Andrés, Eds. Woodhead Publishing, 2012, pp. 15–38.
[95] C. M. Vermillion, “Thermal cycling effects on solar cell interconnection tabs on an OAO-B sample module,” 1971.
[96] X. Wang, H. Geng, S. He, Y. O. Pokhyl, and K. V. Koval, “Effect of thermal expansion coefficient on the stress distribution in solar panel,” *Int. J. Adhes. Adhes.*, vol. 27, no. 4, pp. 288–297, Jun. 2007, doi: 10.1016/j.ijadhadh.2006.01.011.
[97] P. B. Allen and V. Heine, “Theory of the temperature dependence of electronic band structures,” *J. Phys. C Solid State Phys.*, vol. 9, no. 12, pp. 2305–2312, Jun. 1976, doi: 10.1088/0022-3719/9/12/013.
[98] H. Y. Fan, “Temperature Dependence of the Energy Gap in Semiconductors,” *Phys. Rev.*, vol. 82, no. 6, pp. 900–905, Jun. 1951, doi: 10.1103/PhysRev.82.900.
[99] Y. P. Varshni, “Temperature dependence of the energy gap in semiconductors,” *Physica*, vol. 34, no. 1, pp. 149–154, Jan. 1967, doi: 10.1016/0031-8914(67)90062-6.
[100] N. G. Dhere and J. V. Santiago, “Computation of photovoltaic parameters under lunar temperature variation,” *12th Space Photovolt. Res. Technol. Conf. SPRAT 12*, pp. 298–306, May 1993.
[101] M. A. Green, “Solar cells: operating principles, technology, and system applications,” 1982.
[102] P. Singh and N. M. Ravindra, “Temperature dependence of solar cell performance—an analysis,” *Sol. Energy Mater. Sol. Cells*, vol. 101, pp. 36–45, Jun. 2012, doi: 10.1016/j.solmat.2012.02.019.
[103] G. A. Landis, D. J. Belgiovane, and D. A. Scheiman, “Temperature coefficient of multijunction space solar cells as a function of concentration,” in *2011 37th IEEE Photovoltaic Specialists Conference*, Jun. 2011, pp. 001583–001588, doi: 10.1109/PVSC.2011.6186260.
[104] J. Zhao, A. Wang, S. J. Robinson, and M. A. Green, “Reduced temperature coefficients for recent high-performance silicon solar cells,” *Prog. Photovolt. Res. Appl.*, vol. 2, no. 3, pp. 221–225, 1994, doi: 10.1002/pip.4670020305.
[105] D. T. Cotfas, P. A. Cotfas, and O. M. Machidon, “Study of Temperature Coefficients for Parameters of Photovoltaic Cells,” *International Journal of Photoenergy*, Apr. 01, 2018. https://www.hindawi.com/journals/ijp/2018/5945602.
[106] G. A. Landis, “Review of solar cell temperature coefficients for space,” Sep. 1994, Available: https://ntrs.nasa.gov/search.jsp?R=19950014125.
[107] G. Landis, P. Jenkins, D. Scheiman, and R. Rafaelle, “Extended temperature solar cell technology development,” in *2nd International Energy Conversion Engineering Conference*, 2004, p. 5578.
[108] F. T. C. H. Bartels, “Solar cell low temperature, low solar intensity operation,” presented at the 8th photovoltaic specialists conference, August 04, 1970 - August 06, 1970, Jan. 1970. Available: https://ntrs.nasa.gov/search.jsp?R=19710035376.
[109] P. M. Stella, F. S. Pool, M. A. Nicolet, and P. A. Iles, “PV technology for low intensity, low temperature (*LILT*) applications,” in *Photovoltaic Energy Conversion, 1994., Conference*

Record of the Twenty Fourth. IEEE Photovoltaic Specialists Conference-1994, 1994 IEEE First World Conference on, 1994, vol. 2, pp. 2082–2087.
[110] G. A. Landis and J. Fincannon, "Study of power options for Jupiter and outer planet missions," in *Photovoltaic Specialist Conference (PVSC), 2015 IEEE 42nd*, 2015, pp. 1–5.
[111] R. Hoheisel, A. W. Bett, J. H. Warner, R. J. Walters, and P. P. Jenkins, "Low Temperature Low Intensity Effects in III-V Photovoltaic Devices for Deep Space Missions," in *2018 IEEE 7th World Conference on Photovoltaic Energy Conversion (WCPEC) (A Joint Conference of 45th IEEE PVSC, 28th PVSEC 34th EU PVSEC)*, Jun. 2018, pp. 3763–3767, doi: 10.1109/PVSC.2018.8547331.
[112] V. G. Weizer and J. D. Broder, "On the cause of the flat-spot phenomenon observed in silicon solar cells at low temperatures and low intensities," *J. Appl. Phys.*, vol. 53, no. 8, pp. 5926–5930, Aug. 1982, doi: 10.1063/1.331435.
[113] R. Hoheisel and A. W. Bett, "Experimental Analysis of Majority Carrier Transport Processes at Heterointerfaces in Photovoltaic Devices," *IEEE J. Photovolt.*, vol. 2, no. 3, pp. 398–402, Jul. 2012, doi: 10.1109/JPHOTOV.2012.2199080.
[114] R. Hoheisel, R. J. Walters, and A. W. Bett, "Low temperature effects in photovoltaic devices for deep space missions," in *2015 IEEE 42nd Photovoltaic Specialist Conference (PVSC)*, Jun. 2015, pp. 1–5, doi: 10.1109/PVSC.2015.7355666.
[115] C. Signorini *et al.*, "*LILT* Qualification Test Results of Silicon 10LiTHI-ETAP^{R}3 Solar Cells," *ESASP*, vol. 502, p. 581, May 2002.
[116] G. Strobl *et al.*, "Silicon and gallium arsenide solar cells for low intensity, low temperature operation," in *Proceedings of 1994 IEEE 1st World Conference on Photovoltaic Energy Conversion - WCPEC (A Joint Conference of PVSC, PVSEC and PSEC)*, Dec. 1994, vol. 2, pp. 2124–2128 vol.2, doi: 10.1109/WCPEC.1994.521641.
[117] G. Strobl and H. K. Fiebrich, "Production Experience with Hi-ETA®/NR-*LILT* Silicon Solar Cells for ROSETTA Qualification," *ESASP*, vol. 416, p. 519, 1998.
[118] P. M. Stella, G. L. Davis, R. L. Mueller, D. D. Krut, D. J. Brinker, and D. A. Scheiman, "The performance of advanced solar cells for interplanetary missions," in *Conference Record of the Twenty-Eighth IEEE Photovoltaic Specialists Conference - 2000 (Cat. No.00CH37036)*, 2000, pp. 1354–1357, doi: 10.1109/PVSC.2000.916143.
[119] C. Baur *et al.*, "Development status of triple-junction solar cells optimized for low intensity low temperature applications," in *Photovoltaic Specialists Conference (PVSC), 2013 IEEE 39th*, 2013, pp. 3237–3242.
[120] V. Khorenko *et al.*, "BOL and *EOL* Characterization of Azur 3G *LILT* Solar Cells for ESA Juice Mission," 2017, doi: 10.1051/e3sconf/20171603011.
[121] A. Ulloa-Severino *et al.*, "Power subsystem approach for the Europa mission," Oct. 2016. Available: https://trs.jpl.nasa.gov/handle/2014/46212.
[122] L. D. Edmonds, C. E. Barnes, and L. Z. Scheick, *An Introduction to space radiation effects on microelectronics*. Pasadena, California: Jet Propulsion Laboratory, 2000.
[123] R. C. Filz, *Corpuscular Radiation: A Revision of Chapter 17, Handbook of Geophysics and Space Environments*. Office of Aerospace Research, U.S. Air Force, 1968.
[124] J. A. Pellish, "Radiation Engineering for Designers," 2015.
[125] *Read "Testing at the Speed of Light: The State of U.S. Electronic Parts Space Radiation Testing Infrastructure" at NAP.edu.* .
[126] S. Girard *et al.*, "Recent advances in radiation-hardened fiber-based technologies for space applications," *J. Opt.*, vol. 20, no. 9, p. 093001, Aug. 2018, doi: 10.1088/2040-8986/aad271.
[127] W. C. Cooley and R. J. Janda, "Handbook of space-radiation effects on solar-cell power systems," National Aeronautics and Space Administration Washington DC, 1963.

[128] A. E. Nicogossian, R. S. Williams, C. L. Huntoon, C. R. Doarn, J. D. Polk, and V. S. Schneider, *Space Physiology and Medicine: From Evidence to Practice*. Springer, 2016.
[129] A. Luu, "Méthodologie de prédiction des effets destructifs dus à l'environnement radiatif naturel sur les MOSFETs et IGBTs de puissance," Université de Toulouse, Université Toulouse III-Paul Sabatier, 2009.
[130] R. Allioux, "Simulation de l'environnement plasma de Ganymède : contraintes radiatives pour l'orbiteur JGO-JUICE," phd, Université de Toulouse, Université Toulouse III - Paul Sabatier, 2012.
[131] C. Rastoin, "Les electrons de jupiter et de la galaxie dans l'heliosphere d'apres l'experience ket a bord de la sonde spatiale ulysse," thesis, Paris 7, 1995.
[132] I. Jun and H. B. Garrett, "Comparison of high-energy trapped particle environments at the Earth and Jupiter," *Radiat. Prot. Dosimetry*, vol. 116, no. 1–4 Pt 2, pp. 50–54, 2005, doi: 10.1093/rpd/nci074.
[133] D. M. V. Sawyer, "AP-8 trapped proton environment for solar maximum and solar minimum", Dec. 1976. Available: https://ntrs.nasa.gov/search.jsp?R=19770012039.
[134] J. I. Vette, *The AE-8 trapped electron model environment*, vol. 91. National Space Science Data Center (NSSDC), World Data Center A for Rockets …, 1991.
[135] S. Bailey and R. Raffaelle, "Operation of Solar Cells in a Space Environment," in *Practical Handbook of Photovoltaics (Second Edition)*, Elsevier, 2012, pp. 863–880.
[136] T. P. Ma and P. V. Dressendorfer, *Ionizing Radiation Effects in MOS Devices and Circuits*. John Wiley & Sons, 1989.
[137] C. Inguimbert *et al.*, "Radiation-induced degradation of optoelectronic sensors," in *Electro-Optical and Infrared Systems: Technology and Applications XVI*, Oct. 2019, vol. 11159, p. 111590N, doi: 10.1117/12.2532289.
[138] "H. Y. Tada, *Solar Cell Radiation Handbook*. National Aeronautics and Space Administration, Jet Propulsion Laboratory, Institute of Technology, 1982.
[139] C. C. Foster, "Total Ionizing Dose and Displacement-Damage Effects in Microelectronics," *MRS Bull.*, vol. 28, no. 2, pp. 136–140, Feb. 2003, doi: 10.1557/mrs2003.42.
[140] B. E. Anspaugh, "GaAs solar cell radiation handbook," 1996.
[141] J. R. Schwank, "Basic mechanisms of radiation effects in the natural space radiation environment," Sandia National Labs., Albuquerque, NM (United States), SAND-94-1580C; CONF-940726-12, Jun. 1994. Available: https://www.osti.gov/biblio/10158182.
[142] P. V. Dressendorfer, "Basic mechanisms for the new millennium," Sandia National Labs., Albuquerque, NM (United States), SAND-98-1388C; CONF-980705-, Sep. 1998. Available: https://www.osti.gov/biblio/658465.
[143] J. Srour, C. J. Marshall, and P. W. Marshall, "Review of displacement damage effects in silicon devices," 2003, doi: 10.1109/TNS.2003.813197.
[144] G. P. Summers, E. A. Burke, and M. A. Xapsos, "Displacement damage analogs to ionizing radiation effects," *Radiat. Meas.*, vol. 24, no. 1, pp. 1–8, Jan. 1995, doi: 10.1016/1350-4487(94)00093-G.
[145] Z. Xiaofeng, Z. Kaiming, and X. Xi, "Total dose effects in MOS devices under different dose rates," *Nucl. Electron. Detect. Technol.*, vol. 25, no. 3, pp. 322–325, 2005.
[146] S. C. Lee, G. Teowee, R. D. Schrimpf, D. P. Birnie, D. R. Uhlmann, and K. F. Galloway, "Total-dose radiation effects on sol-gel derived PZT thin films," *IEEE Trans. Nucl. Sci.*, vol. 39, no. 6, pp. 2036–2043, Dec. 1992, doi: 10.1109/23.211401.
[147] C. Poivey, "TNID Total Non Ionizing Dose or DD Displacement Damage," CERN, May 09, 2017.
[148] L. F. Makarenko, S. B. Lastovski, F. P. Korshunov, L. I. Murin, and M. Moll, "Primary defect transformations in high-resistivity p-type silicon irradiated with electrons at cryogenic

temperatures," *Phys. B Condens. Matter*, vol. 404, no. 23, pp. 4561–4564, Dec. 2009, doi: 10.1016/j.physb.2009.08.101.
[149] B. R. Gossick, "Disordered Regions in Semiconductors Bombarded by Fast Neutrons," *J. Appl. Phys.*, vol. 30, no. 8, pp. 1214–1218, Aug. 1959, doi: 10.1063/1.1735295.
[150] P. ARNOLDA, "La création de défauts de déplacements atomiques dans le silicium et son impact sur les composants électroniques à applications spatiales," Université Toulouse III-Paul Sabatier, 2011.
[151] G. D. Watkins, "Intrinsic defects in silicon," *Mater. Sci. Semicond. Process.*, vol. 3, no. 4, pp. 227–235, Aug. 2000, doi: 10.1016/S1369-8001(00)00037-8.
[152] D. Pons and J. C. Bourgoin, "Irradiation-induced defects in GaAs," *J. Phys. C Solid State Phys.*, vol. 18, no. 20, pp. 3839–3871, Jul. 1985, doi: 10.1088/0022-3719/18/20/012.
[153] H.-J. Lim, H. J. Von Bardeleben, and J. C. Bourgoin, "Study of defects in GaAs by differential thermal analysis," *J. Appl. Phys.*, vol. 62, no. 7, pp. 2738–2741, 1987, doi: 10.1063/1.339847.
[154] D. Stievenard, X. Boddaert, J. C. Bourgoin, and H. J. Von Bardeleben, "Behavior of electron-irradiation-induced defects in GaAs," *Phys. Rev. B*, vol. 41, no. 8, pp. 5271–5279, 1990, doi: 10.1103/PhysRevB.41.5271.
[155] D. Stievenard, X. Boddaert, and J. C. Bourgoin, "Irradiation-induced defects in p-type GaAs," *Phys. Rev. B*, vol. 34, no. 6, pp. 4048–4058, 1986, doi: 10.1103/PhysRevB.34.4048.
[156] J. C. Bourgoin, K. Khirouni, and M. Stellmacher, "The behavior of As precipitates in low-temperature-grown GaAs," *Appl. Phys. Lett.*, vol. 72, no. 4, pp. 442–444, 1998, doi: 10.1063/1.120781.
[157] J. C. Bourgoin, H. J. Von Bardeleben, and D. Stiévenard, "Native defects in gallium arsenide," *J. Appl. Phys.*, vol. 64, no. 9, pp. R65–R92, 1988, doi: 10.1063/1.341206.
[158] H. J. Von Bardeleben and J. C. Bourgoin, "Formation of AsGa antisite defects in electron-irradiated GaAs," *J. Appl. Phys.*, vol. 58, no. 2, pp. 1041–1043, 1985, doi: 10.1063/1.336284.
[159] R. Y. Loo, G. S. Kamath, and S. S. Li, "Radiation damage and annealing in GaAs solar cells," *IEEE Trans. Electron Devices*, vol. 37, no. 2, pp. 485–497, Feb. 1990, doi: 10.1109/16.46387.
[160] C. Claeys and E. Simoen, *Radiation Effects in Advanced Semiconductor Materials and Devices*, vol. 57. Berlin, Heidelberg: Springer Berlin Heidelberg, 2002.
[161] M. Yamaguchi, "Radiation-resistant solar cells for space use," *Sol. Energy Mater. Sol. Cells*, vol. 68, no. 1, pp. 31–53, 2001.
[162] J. C. Bourgoin and N. de Angelis, "Radiation-induced defects in solar cell materials," *Sol. Energy Mater. Sol. Cells*, vol. 66, no. 1, pp. 467–477, Feb. 2001, doi: 10.1016/S0927-0248(00)00208-7.
[163] J. W. Corbett, G. D. Watkins, R. M. Chrenko, and R. S. McDonald, "Defects in Irradiated Silicon. II. Infrared Absorption of the Si-A Center," *Phys. Rev.*, vol. 121, no. 4, pp. 1015–1022, Feb. 1961, doi: 10.1103/PhysRev.121.1015.
[164] J. W. Corbett and G. D. Watkins, "Production of Divacancies and Vacancies by Electron Irradiation of Silicon," *Phys. Rev.*, vol. 138, no. 2A, pp. A555–A560, Apr. 1965, doi: 10.1103/PhysRev.138.A555.
[165] G. D. Watkins and J. W. Corbett, "Defects in Irradiated Silicon: Electron Paramagnetic Resonance and Electron-Nuclear Double Resonance of the Si-E Center," *Phys. Rev.*, vol. 134, no. 5A, pp. A1359–A1377, Jun. 1964, doi: 10.1103/PhysRev.134.A1359.
[166] G. D. Watkins and J. W. Corbett, "Defects in Irradiated Silicon. I. Electron Spin Resonance of the Si-A Center," *Phys. Rev.*, vol. 121, no. 4, pp. 1001–1014, Feb. 1961, doi: 10.1103/PhysRev.121.1001.

[167] N. Zangenberg, J.-J. Goubet, and A. Nylandsted Larsen, “On-line DLTS investigations of the mono- and di-vacancy in p-type silicon after low temperature electron irradiation,” *Nucl. Instrum. Methods Phys. Res. Sect. B Beam Interact. Mater. At.*, vol. 186, no. 1, pp. 71–77, Jan. 2002, doi: 10.1016/S0168-583X(01)00876-X.
[168] C.-S. Guo, R.-M. Wang, Y.-W. Zhang, G.-X. Pei, S.-W. Feng, and Z.-X. Li, “Identifying defect energy levels using DLTS under different electron irradiation conditions,” *Nucl. Sci. Tech.*, vol. 28, no. 12, Dec. 2017, doi: 10.1007/s41365-017-0331-7.
[169] G. D. Watkins and J. W. Corbett, “Defects in Irradiated Silicon: Electron Paramagnetic Resonance of the Divacancy,” *Phys. Rev.*, vol. 138, no. 2A, pp. A543–A555, Apr. 1965, doi: 10.1103/PhysRev.138.A543.
[170] M. Yamaguchi *et al.*, “Deep level analysis of radiation-induced defects in Si crystals and solar cells,” *J. Appl. Phys.*, vol. 86, no. 1, pp. 217–223, Jun. 1999, doi: 10.1063/1.370698.
[171] H. Matsuura *et al.*, “Si Substrate Suitable for Radiation-Resistant Space Solar Cells,” *Jpn. J. Appl. Phys.*, vol. 45, no. 4R, p. 2648, Apr. 2006, doi: 10.1143/JJAP.45.2648.
[172] S. J. Taylor, M. Yamaguchi, S. Matsuda, T. Hisamatsu, and O. Kawasaki, “Investigation of carrier removal in electron irradiated silicon diodes,” *J. Appl. Phys.*, vol. 82, no. 7, pp. 3239–3249, Oct. 1997, doi: 10.1063/1.365631.
[173] S. J. Taylor *et al.*, “Comparison of the effects of electron and proton irradiation on n+–p–p+ silicon diodes,” *J. Appl. Phys.*, vol. 83, no. 9, pp. 4620–4627, May 1998, doi: 10.1063/1.367246.
[174] A. Khan *et al.*, “Influence of the dopant species on radiation-induced defects in Si single crystals,” *J. Appl. Phys.*, vol. 87, no. 12, pp. 8389–8392, Jun. 2000, doi: 10.1063/1.373552.
[175] F. Hönniger, “Radiation damage in silicon: Defect analysis and detector properties,” 2008.
[176] J. R. Srour and J. M. McGarrity, “Radiation effects on microelectronics in space,” *Proc. IEEE*, vol. 76, no. 11, pp. 1443–1469, Nov. 1988, doi: 10.1109/5.90114.
[177] R. J. Walters, S. Messenger, J. H. Warner, C. D. Cress, M. Gonzalez, and S. Maximenko, “Modeling of radiation induced defects in space solar cells,” in *Physics and Simulation of Optoelectronic Devices XIX*, Feb. 2011, vol. 7933, p. 79330P, doi: 10.1117/12.873902.
[178] H. J. Hovel, Ed., “Chapter 7 Radiation Effects,” in *Semiconductors and Semimetals*, vol. 11, Elsevier, 1975, pp. 149–165.
[179] H. B. Curtis and R. E. Hart, “Performance of GaAs concentrator cells under electron irradiations from 0.4 to 2.3 MeV,” in *Conference Record of the Twentieth IEEE Photovoltaic Specialists Conference*, Sep. 1988, pp. 1020–1023 vol.2, doi: 10.1109/PVSC.1988.105858.
[180] J. R. Woodyard and G. A. Landis, “Radiation resistance of thin-film solar cells for space photovoltaic power,” *Sol. Cells*, vol. 31, no. 4, pp. 297–329, Sep. 1991, doi: 10.1016/0379-6787(91)90103-V.
[181] S. R. Messenger, E. A. Burke, R. J. Walters, J. H. Warner, G. P. Summers, and T. L. Morton, “Effect of Omnidirectional Proton Irradiation On Shielded Solar Cells,” *IEEE Trans. Nucl. Sci.*, vol. 53, no. 6, pp. 3771–3778, Dec. 2006, doi: 10.1109/TNS.2006.886220.
[182] G. P. Summers, S. R. Messenger, E. A. Burke, M. A. Xapsos, and R. J. Walters, “Low energy proton-induced displacement damage in shielded GaAs solar cells in space,” *Appl. Phys. Lett.*, vol. 71, no. 6, pp. 832–834, Aug. 1997, doi: 10.1063/1.119660.
[183] M. Yamaguchi, A. Khan, S. J. Taylor, M. Imaizumi, T. Hisamatsu, and S. Matsuda, “A detailed model to improve the radiation-resistance of Si space solar cells,” *IEEE Trans. Electron Devices*, vol. 46, no. 10, pp. 2133–2138, Oct. 1999, doi: 10.1109/16.792008.
[184] S. R. Messenger, G. P. Summers, E. A. Burke, R. J. Walters, and M. A. Xapsos, “Modeling solar cell degradation in space: A comparison of the NRL displacement damage dose and the JPL equivalent fluence approaches,” *Prog. Photovolt. Res. Appl.*, vol. 9, no. 2, pp. 103–121, 2001.

[185] J. C. Bourgoin and N. de Angelis, “Radiation-induced defects in solar cell materials,” *Sol. Energy Mater. Sol. Cells*, vol. 66, no. 1, pp. 467–477, Feb. 2001, doi: 10.1016/S0927-0248(00)00208-7.
[186] M. Imaizumi, M. Yamaguchi, S. J. Taylor, S. Matsuda, O. Kawasaki, and T. Hisamatsu, “Mechanism for the anomalous degradation of Si solar cells induced by high-energy proton irradiation,” *Sol. Energy Mater. Sol. Cells*, vol. 50, no. 1–4, pp. 339–344, 1998.
[187] M. Yamaguchi, S. J. Taylor, S. Matsuda, and O. Kawasaki, “Mechanism for the anomalous degradation of Si solar cells induced by high fluence 1 MeV electron irradiation,” *Appl. Phys. Lett.*, vol. 68, no. 22, pp. 3141–3143, May 1996, doi: 10.1063/1.115804.
[188] S. Z. Karazhanov, “Mechanism for the anomalous degradation of proton- or electron-irradiated silicon solar cells,” *Sol. Energy Mater. Sol. Cells*, vol. 69, no. 1, pp. 53–60, Aug. 2001, doi: 10.1016/S0927-0248(00)00358-5.
[189] Y. Morita, T. Ohshima, I. Nashiyama, Y. Yamamoto, O. Kawasaki, and S. Matsuda, “Anomalous degradation in silicon solar cells subjected to high-fluence proton and electron irradiations,” *J. Appl. Phys.*, vol. 81, no. 9, pp. 6491–6493, May 1997, doi: 10.1063/1.364437.

CHAPTER II Experimental methods: solar cell devices, characterizations & irradiations

II.1 Introduction

In this chapter, the methodology established to investigate the behavior of solar cells for space environments is presented for both near earth and deep space conditions. At first, we present the different solar cells architectures together with a brief description of the manufacturing process of single-junction and tandem solar cells used in this thesis. In the second part, the set-ups used for electrical and optical characterizations are presented. In order to understand the electrical degradation of complex devices such as multi-junction solar cells, specific set-up and processes are necessary, such as the use of voltage/light bias for reliable spectral measurements, or reference solar cells and accurate solar simulator spectrum for trustworthy current voltage characterizations. Thus, the characterizations and calibrations of the two types of solar simulators (Xe flash and *LED* illumination) used in this thesis will be presented. The last section of this chapter is dedicated to the particle accelerator facilities (electrons and protons), with a focus on their working principle and the in-situ characterization methodology.

II.2 Solar cells Architectures

Two types of tandem solar cells architectures (double and triple junction) were used in this PhD thesis. The first architecture is composed of two junctions (2J): the top sub-cell is ternary semiconductor AlGaAs and the bottom cell is composed of monocrystalline silicon, c-Si (see Fig. II-1 middle). The second architecture is a triple junction (3J) solar cell in which the top and middle sub-cells are ternary semiconductor, GaInP and AlGaAs respectively, and the bottom sub-cell is c-Si (see Fig. II-1 right).

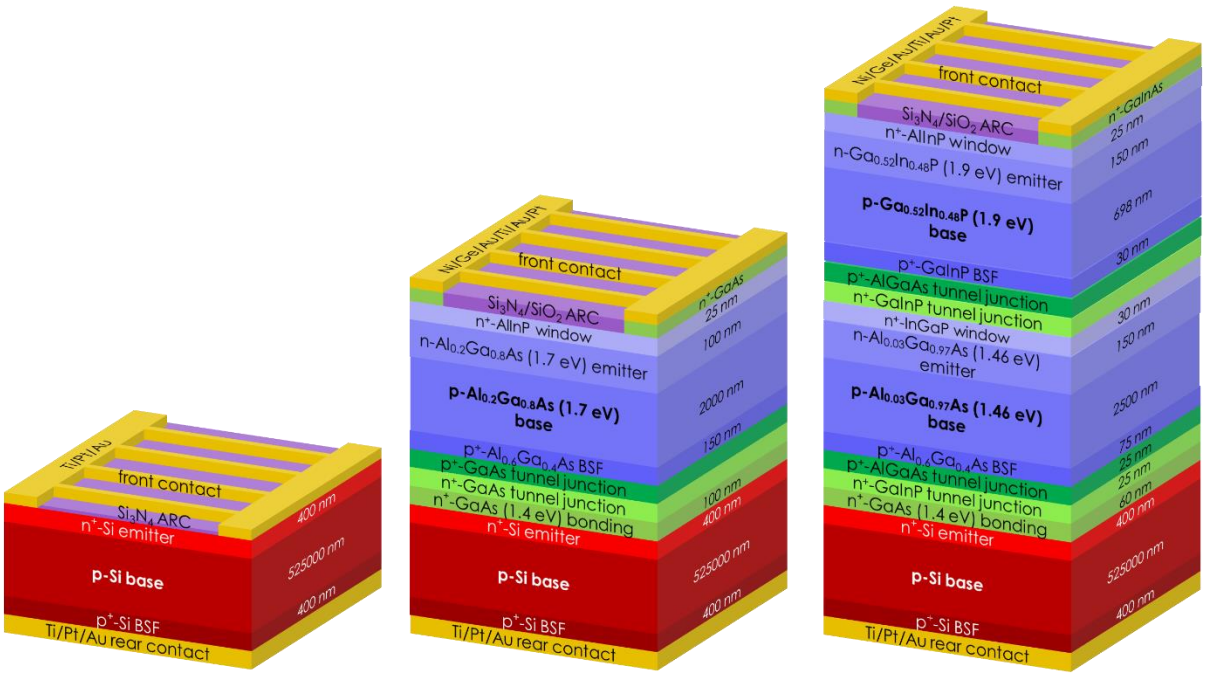

Fig. II-1 *Schematic of selected solar cells architectures for (left) single junction c-Si (1J), (middle) 2J AlGaAs//Si and (right) 3J GaInP/AlGaAs//Si used in this PhD thesis.*

In order to compare the behavior of these two tandem solar cells architectures under different operating environments (details in the following section), a single junction (1J) crystalline silicon c-Si was also used as a reference device (see Fig. II-1 left). Among the set of Si cell/sub-cell available for this PhD thesis, we have selected devices with identical characteristics (thicknesses, doping level, material type, etc.) for all the three architectures.

These solar cells were developed, prior to this PhD thesis work, in the context of *CEA-LETI/CEA-LITEN* research project aiming at 30% III-V//Si cell efficiency for low concentration photovoltaics applications. Different architectures of tandem and single junction solar cells with multiple configurations and optimizations were processed during this project. A brief explanation of the fabrication process and the materials characteristics are discussed hereunder.

II.2.1. Silicon cells

As reported by [1], [2], among different types of silicon solar cells, the monocrystalline are the most efficient in power conversion. Monocrystalline materials are made by two main processes Float Zone *FZ* and Czochralski *CZ* [3]–[5]. *CZ* material contains high oxygen concentration that can degrade Begin-Of-Life (*BOL*) performances of the solar cells by forming stable dopant-oxygen defect (i.e. B-O for p-type boron doped) [6], [7]. On the other hand, less impurities concentration is found in *FZ* material. It is thus more suitable to use *FZ* materials for high efficiency solar cells, even if the wafer price is higher compared to CZ; it remains roughly two orders of magnitude below GaAs wafers price [8], [9].

For this reason, we have been working with a 4-inch *FZ* material (single-side polished) in this study. The Si wafers were boron doped with a resistivity of 1 - 5 Ω.cm which corresponds to 1.5 x 10^{16} cm^{-3} - 2.8 x 10^{15} at./cm^{-3} at 300 K, with a total thickness of 525 µm. Such substrate thickness surpass the standard 180 - 200 µm thickness used in PV applications, however it was chosen for a better compatibility and yield during the wafer bonding process.

The homojunction silicon solar cells were manufactured at *CEA-INES* by the creation of full area n^+ emitter and p^+ Back Surface Field *(BSF)* on the front and rear surface respectively. On the one hand, the emitter n^+ was formed by phosphorus ($POCl_3$) diffusion at 850 °C with a maximum total doping level at the surface of 2.10^{20} cm^{-3} and a junction depth of 400 nm. On the other hand, boron diffusion (BBr_3) at 950 °C was performed for the formation of the *BSF* region with a doping level of 10^{20} cm^{-3} and thickness of 400 nm [10]. Either a single thermal activation step for both diffused boron and phosphorous was made at 950 °C - 1000 °C or two sequential annealing steps: boron diffusion with an annealing temperature at high temperature > 1000 °C, then a phosphorus diffusion with annealing temperature of 820 °C - 870 °C [11]. More details on the optimization of silicon material and fabrication process can be found in [10], [12].

II.2.2. III-V cells

The III-V top cells were grown lattice matched on a 4-inch GaAs substrate with inverted configuration (see Fig. II-2) by Metal-Organic Vapor Phase Epitaxy *(MOVPE)* at *Fraunhofer-ISE*[19] in the case of 3J GaInP/AlGaAs//Si [13]–[15] and by *IQE*[20] and *III-V* Lab[21] in the case of

[19] Fraunhofer-ISE website, www.ise.fraunhofer.de/
[20] IQE website, www.iqep.com/
[21] III-VLab website,www.3-5lab.fr/

2J AlGaAs//Si. The III-V layer stack includes appropriate tunnel junctions for series connection of III-V sub-cells and with Si bottom cell.

The choice of III-V material compositions is an important parameter for optimum conversion of the desired light spectrum. As seen in section I.2, the bandgap and lattice constant change with the chemical composition and stoichiometry of the semiconductor.

For instance, in the case of $Al_xGa_{1-x}As$, the lattice constant increases with increasing the aluminium fraction; it also impacts the material defect density as reported for DX-center by Heckelmann et al. [16]. The increasing Al fraction is correlated with an increasing bandgap for this ternary semiconductor, from 1.42 eV (874 nm) at x = 0 (GaAs) up to 2.17 eV (572 nm) at x = 1 (AlAs) [17]–[21]. A similar trend is observed with $Ga_xIn_{1-x}P$ semiconductor: the higher the Gallium fraction, the higher the bandgap and the lattice constant [22]–[24].

Tab. II-1 *Ternary III-V top and top/middle sub-cells composition and corresponding lattice parameters.*

Sub-cells	**Double Junction $Al_xGa_{1-x}As$//Si**			**Triple Junction $Ga_xIn_{1-x}P/Al_xGa_{1-x}As$//Si**		
	x	Bandgap (eV) / (nm)	Lattice constant (Å)	x	Bandgap (eV) / (nm)	Lattice constant (Å)
Top	0.22	1.7 / 730	5.66	0.52	1.9 / 653	5.65
Middle	-	-	-	0.03	1.46 / 850	5.65

The major efforts in III-V top cells architectures optimization are therefore to grow high quality AlGaAs on GaInP materials one hand, and to achieve a balance of current (by thickness adjustments) between the two/three sub-cells under a reference spectrum on the other hand. The stoichiometry of different III-V materials used in this study and their corresponding bandgaps & lattice constants are presented in Tab. II-1. As explained above, these cells were optimized for concentrator terrestrial application, hence current matching was optimized under AM1.5D reference spectrum (thus not under space AM0 spectrum). For the sake of simplicity, we will not mention the detailed fraction of different composition of these semiconductor materials afterwards, but rather refer to their composition as GaInP/AlGaAs//Si and AlGaAs//Si, for 3J and 2J solar cells respectively.

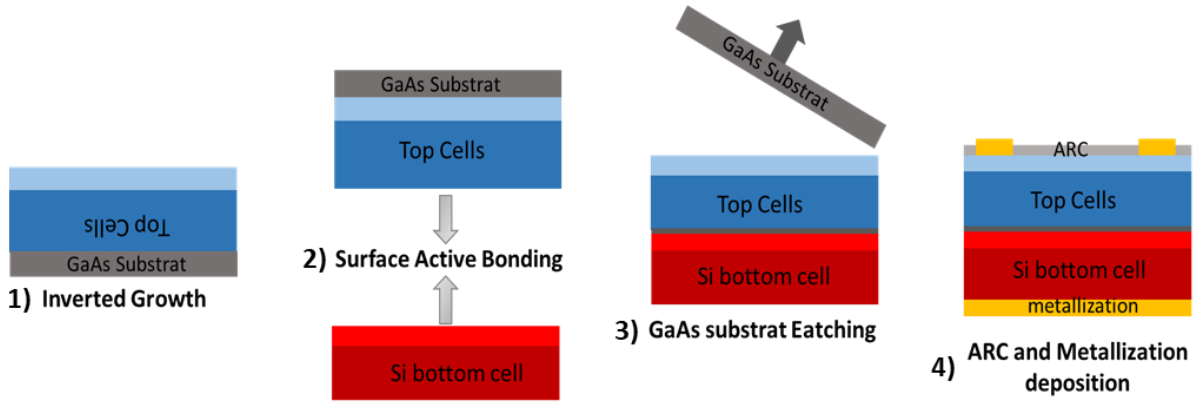

Fig. II-2 *Schematic of the four main steps for the fabrication of tandem III-V//Si solar cells: 1) Inverted growth of III-V sub-cells and the fabrication of Si cells separately, 2) Bonding of III-V on Si with the surface active wafer bonding process, 3) Etching of GaAs substrate used for growth and 4) Deposition of antireflective coating and metallization.*

II.2.3. Bonding and metallization process

As explained in section I.2, the direct growth process of III-V on Si materials results in a high defect density and thus a high recombination rate at III-V/Si interface and in the III-V bulk. Wafer bonding is thus a preferable solution for high efficiency III-V/Si solar cells, since sub-cells are prepared independently and lattice mismatch has no consequences. The principle of wafer bonding can be summarized as follow: creation of binding link (Van der Waals, hydrogen-bridges or covalent bonds) at the interface of two clean and mirror-polished surfaces brought together. In order to obtain strong covalent bonds, an annealing can be required. Different bonding process were tested prior this PhD thesis for the integration of III-V//Si solar cells at CEA: hydrophilic GaAs//Si, hydrophilic GaAs//GaAs by growing epitaxial GaAs layer on Si and Surface Activated Bonding (*SAB*) process for GaAs//Si [10], [25], [26]. Interface characterization by Scanning Acoustic microscopy *(SAM)* has revealed a higher defects and voids density for hydrophilic GaAs//Si bonding process, which could be caused mainly by particle contamination and trapped water. However less interface defects and voids were obtained for GaAs//GaAs/Si hydrophilic and *SAB* process. Further characterization on electrical properties resulted in a distorted current voltage curve for hydrophilic GaAs//Si interface, with an S-like shape most likely related to interface oxides and/or hydrogen platelets; hence this approach, resulting in sub-optimum conduction at III-V//Si interface [27], [28] was not selected. The best performances were obtained with the *SAB* process.

The integration of III-V top cells on silicon bottom cells, for this PhD work, was achieved with the *SAB* process [29]. First, the III-V and Si surfaces were cleaned and planarized with Chemical Mechanical Polishing (*CMP)*, then the wafers are loaded into *EVG580 ComBond*

ultra-high vacuum chamber. The formed surface oxide is removed with 200 eV argon beam bombardment, thus leaving dangling bonds at the surface [25], [26], [30], [31]. When the two wafers are brought together covalent bonds are formed at room temperature (see Fig. II-2). The specificity and attractiveness of this technique is the lack of annealing step to reinforce the bond interface. Hence, no degradation of III-V or cracks are originated from this bonding technique (despite the thermal expansion coefficient mismatch). However, a few nanometers (2 - 3 nm) of amorphous material are formed at the bonding interface due to the Ar bombardment, which can have a some minor impact (parasitic absorption) on interface/cells performances [32]–[34]. Afterwards, the GaAs substrate used for III-V inverted growth is removed by wet chemical etching (see Fig. II-2).

As a final step, the front grid and the full rear surface metallization were deposited by evaporation, with mesa etching down to 2 µm to define individual solar cells. One layer antireflective coating layer (Si_3N_4) and two layers (Si_3N_4/SiO_2) stack were deposited for single and tandem solar cells by plasma-enhanced chemical vapor deposition (*PECVD)* respectively. More details on this processing route are presented in reference [10].

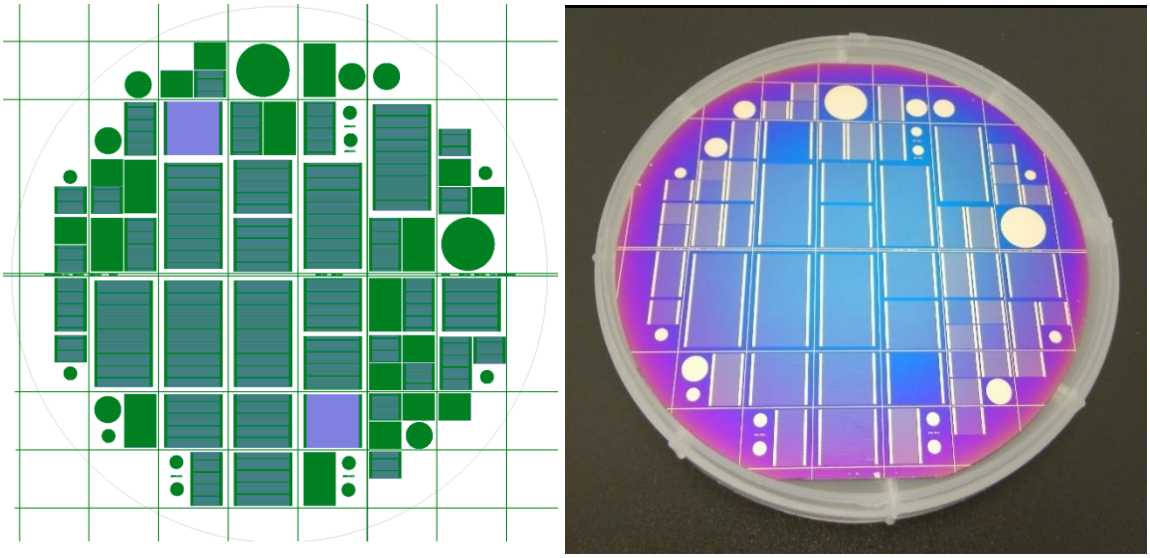

Fig. II-3 *Left: Schematic of the 4-inch solar cells mask, right: photographic view of the wafer including solar cells at the final step.*

During this III-V//Si manufacturing sequence, a lithography mask was used with several tens of cells on each 4-inch wafer. Fig. II-3 illustrates a schematic presentation and a photographic view of the solar cells on the wafer (cells sizes from 0.5 x 0.5 cm^2 up to 1 x 2 cm^2). Consequently, in order to avoid the time-consuming full characterization of multiple multi-junction solar cells (*MJSC*), we have used a fast and reliable method to identify the

statistical distribution of open circuit voltages in the batches: the quasi-steady-state open-circuit voltage *($QssV_{OC}$)*. The QssVoc technique, also known as Suns-Voc, consists in measuring the open circuit voltage of solar cells as a function of slowly varying illumination. Valuable information such as the effective lifetime and pseudo *I-V* characteristics can be extracted using this technique [35], [36]. While this technique is mainly used for 1J Si cells characterization, we found that it was a relevant approach for the Voc evalutation of Si-based tandem.

Fig. II-4 represents the statistical distribution of the implied open-circuit voltage measured at one sun illumination for 1J, 2J and 3J, c-Si (blue), AlGaAs//Si (red) and GaInP/AlGaAs//Si (grey), respectively. The lines help to identify for 1J, 2J and 3J, the three peaks of the distribution: they are mainly positioned at 583 mV, 1722 mV and 2842 mV. However, the high implied open-circuit voltage is a necessary but not sufficient condition to identify a performant solar cell; indeed at open circuit voltage, no current flows through the solar cell: therefore, the effect of series resistances and current matching are not taken into account. For this reason, the solar cells identified as promising after this first step must be characterized under a solar simulator in order to determine their actual performances.

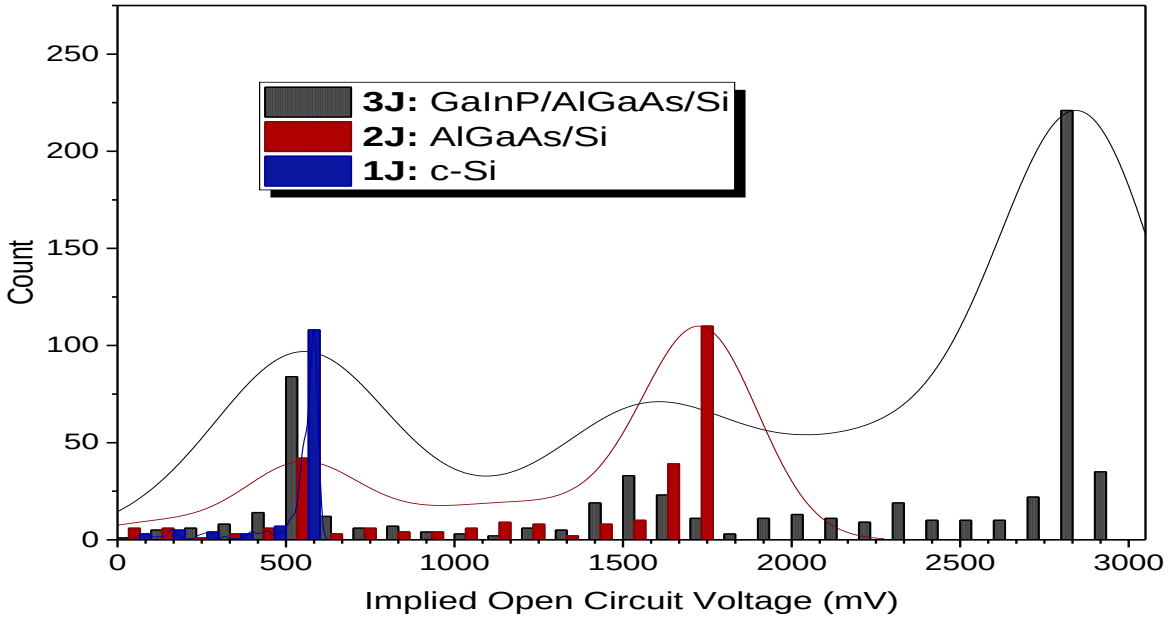

Fig. II-4 *Statistical results of implied open circuit voltage measured with Suns-Voc equipment for 1314 solar cells including 1J (c-Si) 2J (AlGaAs//Si) and 3J (GaInP/AlGaAs//Si) solar cells.*

In this set of measurement, we present 1314 manufactured solar cells including n-type, p-type, *FZ* and *CZ* materials for c-Si and bottom cell in the case of 2J and 3J. By contrast, we can see that not all the samples are well optimized and some present low open circuit voltage at begin of life due to imperfections during processing. Beside of that, as seen in section I.4,

n-type silicon and *CZ* materials are not suitable for space applications due to their low radiation hardness [37]–[39]. Thus, a limited number of solar cells were selected to use in this work for space applications. Fig. II-5 shows the statistical distribution of implied open circuit voltage for the most promising cells (~300 devices), in begin-of-life state. Of course, further characterizations will be performed to exclude the poorly performing solar cells, due for instance to low short-circuit current (e.g. defects in the front surface) and/or low fill factor (e.g. shunt resistance issue).

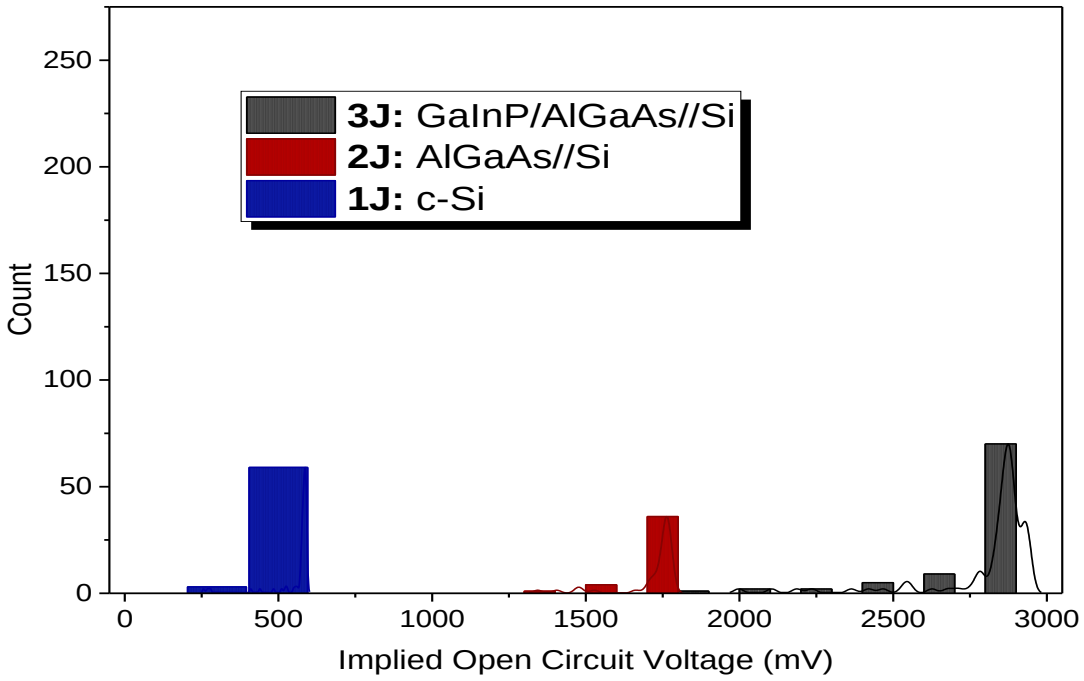

Fig. II-5 *Statistical results of implied open circuit voltage measured with Suns-Voc equipment for 300 solar cells including 1J (c-Si) 2J (AlGaAs//Si) and 3J (GaInP/AlGaAs//Si) solar cells used in this PhD thesis; for the sake of comparison, we have used the same y scale as in the previous figure.*

II.3 Characterizations sequences

As presented in section I.3, depending on the type, duration and target of the space mission, the satellite hence solar cells on its body are exposed to various harsh environments. In this thesis, we study environmental constraints representative of near earth and deep space conditions for III-V//Si solar cells. Fig. II-6 presents the test sequences of the two experiments representing those space environments.

For near earth conditions (terrestrial orbits), electrons and protons irradiations were performed at room temperature. Characterizations before and after irradiations were performed at 300 K under 1 AM0 spectrum (i.e. 1361.1 $W.m^{-2}$ [40], [41]) for light *I-V* measurements and at 300 K for quantum efficiency measurements.

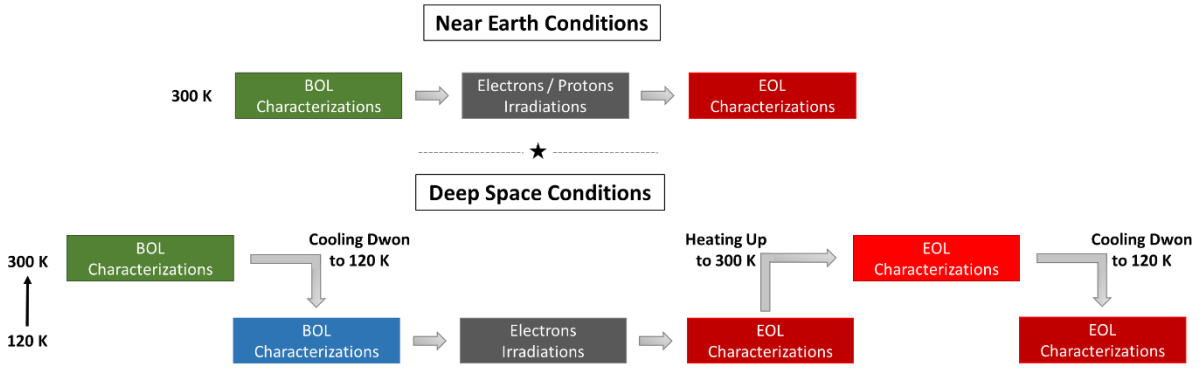

Fig. II-6 *Irradiation and characterization sequences for the two mission environments: (Top) Near Earth conditions and (Bottom) Deep space conditions.*

However, for deep space conditions, where solar cells operate at low temperature and low irradiance, only electron irradiations could be performed at 120 K. *BOL* light *I-V* characterizations were performed at 300 K under 1 AM0 and 0.038 AM0 spectrum, and after cooling down to 120 K in-situ characterizations were carried out under 0.038 AM0 spectrum as well. Once solar cells were irradiated, the same characterizations were made at End-Of-Life (*EOL*), namely, at 120 K under 0.038 AM0 and after heating up to 300 K under 0.038 and 1 AM0 spectrum. To quantify the effect of annealing step at 300 K the solar cells were characterized after a re-cooling down step down to 120 K. In-situ quantum efficiency measurements were planned at 120 K before and after electrons irradiation; however, due to some equipment issues, those in-situ & low temperature *EQE* measurement could not be performed during this thesis.

Now that the experimental test sequences of the two main studies were presented, we are going to introduce hereunder the different characterizations set-ups: the in-situ and ex-situ *I-V* measurements and the quantum efficiency principle. Then, we will detail how to accurately measure the III-V//Si tandem cells with such equipment. Finally, we will introduce the electrons and protons irradiations facilities as well as the range of parameters used in this study.

II.4 Quantum efficiency characterization

The quantum efficiency (*QE*) is one of the key characteristics of solar cells in general, and particularly for tandem solar cells. For conventional single-junction solar cells, *QE* helps to diagnose a possible dysfunction of different region of the cell, for instance poor charge carriers collection in the emitter or the base, recombination in the front and the rear surface (passivation quality) and even the quality of antireflective coating (*ARC*) [42]. In *MJSC*, *QE* can quantify the optical and electrical performances for each sub-cell that constitutes the device.

We distinguish two main quantities: external and internal quantum efficiencies. The internal quantum efficiency *IQE* is defined as the ratio between the number of collected photo-generated electrons divided by the number of absorbed photons (incident minus reflection and transmission). The external quantum efficiency, *EQE*, does not take into account the reflected (and eventually transmitted) photons; *EQE* is defined as the ratio of collected photo-generated electrons divided by incident photons [43]. The two quantities are related through the reflectivity R(λ) and transmission T(λ) according to the Eq. II-1 below:

$$IQE(\lambda) = {EQE(\lambda)}\Big/{[1 - R(\lambda) - T(\lambda)]} \qquad \text{II-1}$$

In the case of the cells used in this study, where the Si has a 525 µm thickness and a full wafer back contact metallization (see Fig. II-1). We assume that all photons that enter the solar cells are absorbed either by the bulk or by the rear metallization (negligible values); therefore, the transmission can be set to zero.

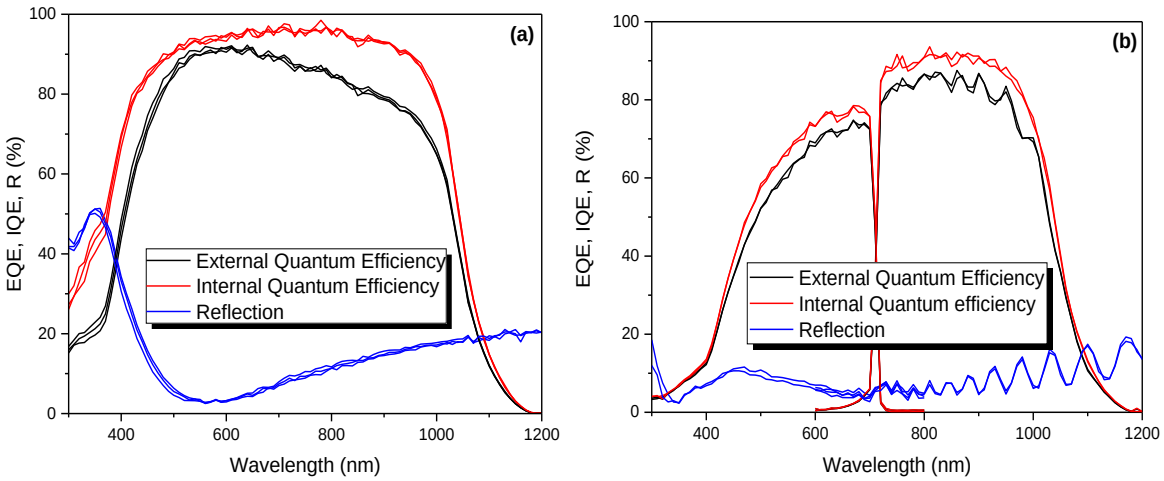

Fig. II-7 *Comparison between External and Internal Quantum Efficiency for (a) 1J c-Si and (b) 2J AlGaAs//Si.*

Fig. II-7 illustrates the differences between *IQE* and *EQE* in the case of a 1J c-Si and a 2J AlGaAs//Si. As one can see in those experimental curves, the *IQE* for the 1J c-Si is slightly higher than the *EQE*, especially at low and high wavelength (lower than 500 nm and higher than 700 nm) due to the high reflection in those regions. Therefore, in those wavelength ranges, less photons are entering the active region of the cells and thus less electron-hole pairs are generated. In the case of the 2J AlGaAs//Si presented in Fig. II-7, the magnitude difference between *IQE* and *EQE* is less pronounced than the one in the c-Si cells. This can be explained by a lower reflection thanks to a dual-layer *ARC*, compared to the 1J c-Si, which has only a single layer *ARC* (see Fig. II-1).

II.4.1. Experimental set-up

The *Oriel IQE 200* equipment was used in this study. A schematic representation of the set-up is presented in Fig. II-8. Concerning the working principle of the *QE* measurements, two main systems can be distinguished: i) hardware: the first part is composed of a light generation and its path until the cells under test, the light path will be described hereinafter; ii) software; the second part consists of the conversion of photo-generated current into *QE* magnitude.

The light is generated with a 200 W Xenon lamp, with a spectral range between 300 nm and 1800 nm (compared 380 - 1800 nm for Halogen lamp), that is sufficient since our tandem cells absorption band reaches only 1200 nm in the infrared region (silicon bandgap). This light is then filtered with a set of four optical filters (0 - 560 nm, 560 - 1040 nm, 1040 - 1850 nm and 1850 - inf. nm) and chopped at 30 Hz frequency. Then its passes through a monochromator that works with two diffracting gratings (0 - 720 nm and 720 - inf. nm) that separates the spectral component of the white light at its entrance into a monochromatic beam with predefined step controlled by the software. We chose a scanning step of 10 nm in the absorption band of the solar cells, as a good compromise between measurement speed (large wavelength steps) and precisions (small wavelength steps). The monochromatic beam is then splitted into two parts, one half is transmitted to the reference detector to measure the incident photons power and the second half is directed to the cells surface with a spot of 3 mm long and 1 mm wide. The spot surface is for our cell design large enough to cover an area with a numbers of current collection fingers (e.g. perpendicular to fingers) representative of the grid shading induced by front side metal contacts (excl. busbars).

With the monochromatic light beam excitation, the solar cell under test generates a photocurrent. A trans-impedance amplifier is used to amplify the photo-generated current and convert it to a voltage signal. Due to low monochromatic power source, a low voltage signal is measured and therefore a second amplification of the modulated light (with chopper wheel) is needed with a lock-in amplifier to reduce the signal to noise ratio. In the end, using the amplified signal measured from the excited cell and the power of incident photons (measured with the reference detector), the spectral response *SR* can be calculated. The *SR* represents the current generated by unit of power for the incident monochromatic beam ($A.W^{-1}$), and is linked to the *QE* by Eq. II-2, where q is the electric charge, h is Planck's constant, λ is the wavelength and c is the speed of light [44].

$$SR(\lambda) = \frac{q\lambda}{hc} QE(\lambda) \qquad \text{II-2}$$

As a side equipment to this *QE* set-up, the following features are available for the chuck: a vacuum pump to hold the cell on the chuck, a thermal regulation system (from 0 °C to 60 °C) and an angularly adjustable orientation system; however, those features were not essential in this study. The solar cells in this study were placed at an angle of 90° with respect to the *QE* light beam, with variation less than +/- 0.3°, and with a temperature of measurements of 25 °C.

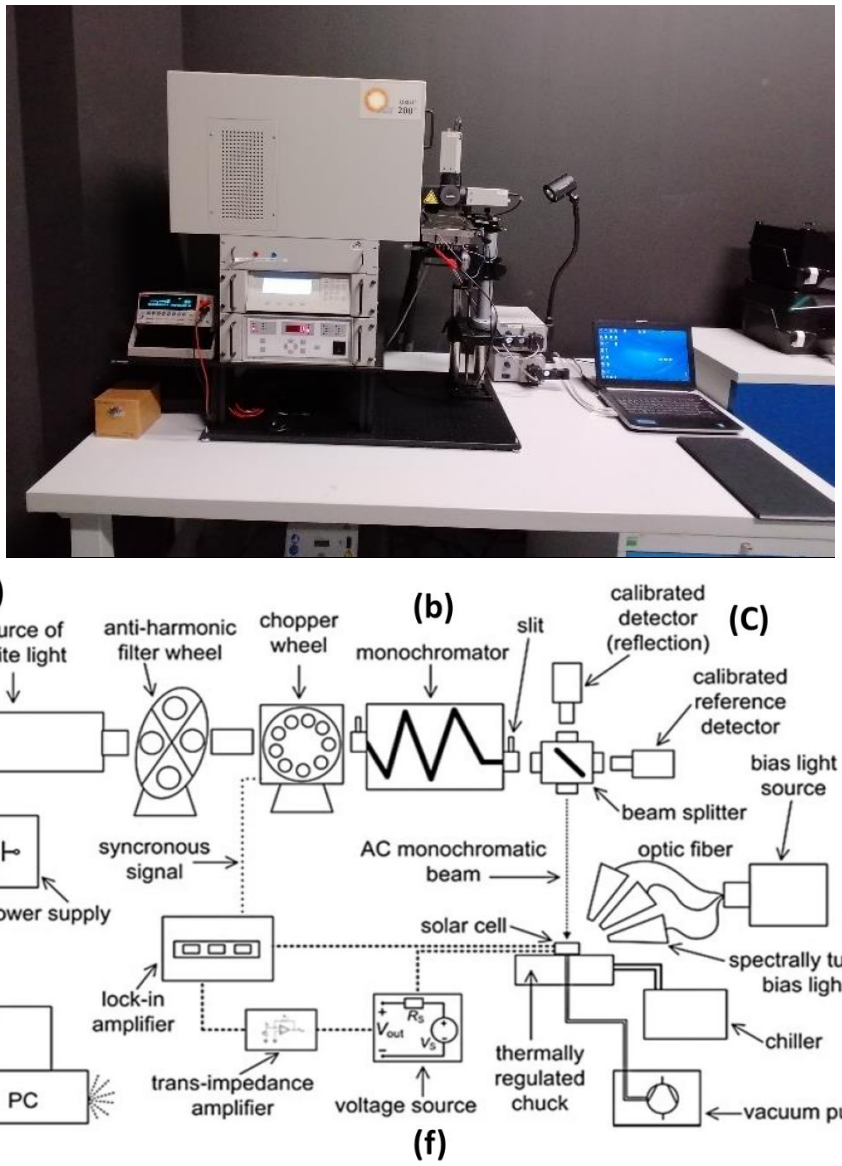

Fig. II-8 *Top: picture of the Oriel 200 IQE set-up, Bottom: schematic representation of the quantum efficiency measurements set-up with drawings of all necessary elements [43].*

II.4.2. Application to multi-junction solar cells

The measurement process described above is valid for single-junction solar cells. However, for tandem solar cells, with 2 sub-cells or more, the *QE* characterization is more complex. As

seen in section II.2 the tandem cells used in this study are series connected with in standard two terminal configuration. In this case, the total current of multi-junction solar cells is limited by the sub-cell that generates the lowest current. In order to illustrate this concept, let us take a 3J GaInP/AlGaAs//Si solar cell as an example. To measure one sub-cell (e.g. the top one), we need to be sure that this junction limits the current of the 3J. To fulfill this condition the two other sub-cells not being measured (e.g. middle & bottom) need to be illuminated and saturated (by other light sources). In this way, the photo-generated current with the monochromatic beam absorbed in the top cell is lower than the one photo-generated by the additional illumination of the two other sub-cells: the top cell current is limiting the device current. For the mid- and bottom-cells, the excess photocurrent will lead to radiative and non-radiative carrier recombination. We have used in this study two-halogen lamp as a source of white light equipped with a set optical long and short pass filters (*LPF* and *SPF*), directed with an optical fiber towards the solar cell under test. The light bias used for the case of the triple-junction is presented in Tab. II-2.

Tab. II-2 *Light bias spectrum ranges and external voltage bias applied on the triple-junction solar cells to measure the quantum efficiency of the top, middle and bottom sub-cells at room temperature.*

Sub-cells under test	Light Bias	Voltage Bias
Top : GaInP	LPF 630 nm (saturate mid + bot)	1.4 V
Middle : AlGaAs	LPF 1000 nm (saturate bot) SPF 650 nm (saturate top)	1.7 V
Bottom : Si	SPF 850 nm saturate (top + mid)	2.1 V

In principle, *QE* measurements must be performed at short-circuit current conditions, that is to say the bias of the sub-cell under test should be zero volt. However, the difficulty with this is that for two terminal tandem cells configuration, there are no individual sub-cell contacts. The external voltage of tandem cell (V_{ext}) is equal to the sum of individual sub-cell voltage as expressed in Eq. II-3 where V_{top}, V_{middle} and V_{bottom} are the voltage of the top, middle and bottom sub-cells respectively:

$$V_{ext} = V_{top} + V_{middle} + V_{bottom} \qquad \textit{II-3}$$

With no external bias voltage applied (i.e., V_{ext}=0 V), we can see from Eq. II-3 that the sub-cell under test (e.g. top) bias is equals in absolute value to the sum of the two other sub-cells open circuit voltage not under test (e.g. - (V_{middle}+V_{bottom})). Therefore, we need to apply

an external bias voltage at the terminal of the tandem solar cells in order to be in short-circuit conditions for the device under test (i.e., $V_{top} = 0$ V). More details about this method are presented below. We would like to point out that the estimation of the applied bias voltage depends on the number of sub-cells in a multi-junction, the bias light irradiance spectrum and the bandgaps of the different materials (see details below).

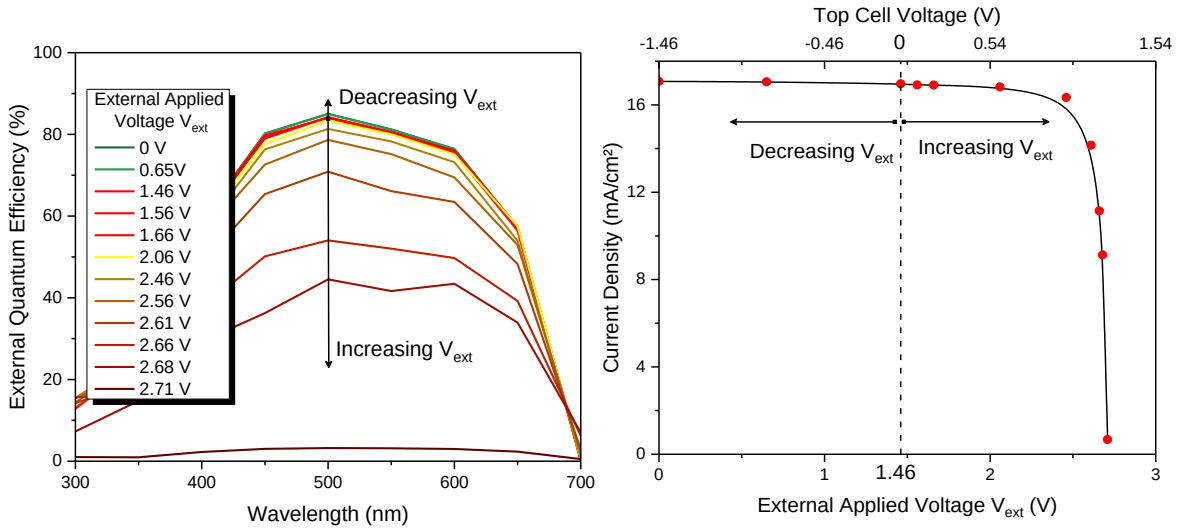

Fig. II-9 *Left: EQE characterization of GaInP/AlGaAs//Si top cell under different external applied voltage, right: short circuit current calculated form each QE characterization by convolution to AM0 spectrum.*

As presented in [45], beside the need to know the open circuit voltage for the junction under test, the maximum power point voltage V_{MPP} is also needed to estimate the bias voltage of sub-cell under test according to Eq. II-4. In contrast, V_{MPP} value is not easily known for the specific bias light irradiance spectrum and for sub-cells that are not being measured.

$$V_{ext} = 1/2 \sum_i (V_{OC} + V_{MPP})_i \qquad \text{II-4}$$

C. Dominguez et al., [43] propose another approximation relatively more easy to apply and which was used in this study to estimate the applied external voltage V_{ext}. In this approximation, an assumption of linearity between bandgaps (E_G), and open circuit voltage (V_{OC}) is used. This is in principle valid for direct bandgap; however, it was also applied for Si (indirect bandgap) bottom cell for the simple reason that the current is stable and almost equal to J_{SC} on large range of applied voltage; and this method is also used largely on Ge (indirect bandgap) of III-V/Ge solar cells. For a specific sub-cell under test (e.g. top), we make the ratio of the sum of sub-cells bandgaps not to be measured divided by the sum of all bandgaps that constitute the tandem solar cell (e.g. $(E_{G_{Mid}} + E_{G_{bot}})/E_{G_{total}}$). The corresponding *MJSC* open circuit voltage Voc at the specific bias light spectrum (e.g. LPF 630 nm) is then measured. The external bias voltage

(V_{ext}) to apply at the terminal of the tandem cell for the measurement of a specific sub-cell is calculated as presented in Eq. II-5.

$$V_{ext} = \frac{\sum E_G(not\ being\ measured)}{\sum E_G} V_{OC} \qquad \text{II-5}$$

Tab. II-2 shows the calculated external voltage bias applied for measuring the top, middle and bottom sub-cells with the corresponding bias light spectrum for 3J GaInP/AlGaAs//Si.

Fig. II-9 presents an external quantum efficiency characterization of top cell of 3J architecture under different external applied voltage (left) and the corresponding calculated short-circuit current (right). The top cell external quantum efficiency characterization in short-circuit condition (red line) was performed by applying an external bias of 1.46 V on the terminal of tandem solar cells, with our light bias spectrum. A decrease in QE magnitude is observed while increasing V_{ext} until reaches ~2.7 V: it corresponds to open circuit voltage conditions (for the top cell). At the opposite when decreasing V_{ext}, a slight increase is observed in *QE* that can be due to low shunt resistance of the top sub-cell.

The short-circuit condition is obtained for a zero volts bias at the top cell level, however, for solar cells with a high shunt resistance, the current is stable and almost equal to J_{SC} on a large range of applied voltage (see Fig. II-9 right). In this case, a variation in external applied voltage value (e.g. 0.6 - 1.66 V) does not have much impact on the *QE* characteristics (e.g. 0.4% variation on J_{SC} in this top cell). However, for solar cells with low shunt resistance, the variation in *QE* characteristic is more pronounced with variations of external voltage bias.

The short-circuit current density expressed in $mA.cm^{-2}$ can be calculated from convolution of the spectral response *SR(λ)* to the AM0 reference spectrum *Ø(λ)* according to the Eq. II-6.

$$J_{SC} = \int SR(\lambda)\, Ø(\lambda)\, d\lambda \qquad \text{II-6}$$

Due to large number of measurements and data used in the case of this study, an Excel macro was developed to assist with this data treatment. The program is divided into three major parts, as a first step, the users introduce the files for treatment, then the data are rearranged (extracting only essential data and changing format) and generation of graphs (*EQE*, *IQE* and R). The third part consist in short-circuit current density calculations. The numerical integral was calculated using the quadratic function known as Simpson's rule expressed below Eq. II-7. To reduce the calculation error, a reduction of measurements step (Δλ) from 10 nm to 1 nm were performed with a spline function.

$$\int_a^b f(\lambda)d\lambda = \frac{\Delta\lambda}{3}[f(\lambda_0) + 4f(\lambda_1) + 2f(\lambda) + 4f(\lambda_{n-1}) + \cdots + f(\lambda_n)] \quad \text{II-7}$$

Where $\Delta\lambda = \frac{b-a}{n}$ and $\lambda_i = a + i\Delta\lambda$ with a and b are the lower and upper limit of the absorption band, the function here is the product of the spectral response and the power density at each wavelength (λ).

Measurement repeatability was tested with our set-up and the calculation procedure: with 10 sequential quantum efficiency measurements on the same 1J c-Si solar cell, a 0.3% deviation on short-circuit current density was found.

II.5 Current-Voltage Characterization

As we have seen in section II.5, an accurate current-voltage characterization under illumination is needed to quantify the electrical performances of tandem solar cells.

There are many types of solar simulator in the market: flash simulator, steady state simulator (continuous illumination), one lamp source, multi-source, etc. Each one has its particularities, advantages and drawbacks [46]. In this study, two types of solar simulator were used, a flash and steady state simulator. The principle and the procedure used for characterizing solar cells, especially for multi-junction, is presented in this section.

II.5.1. Flash solar simulator

The solar simulator *Helios cells 3030* from SAV was used in this PhD work for *I-V* characterizations, both in *BOL* and *EOL*. The flash integrated in this equipment has a short discharge duration typically 9 ms; therefore, it does not offer a steady state illumination. During the discharge of the power supply capacity, the voltage (lamp bias) decreases and the illumination intensity as well. The solar spectrum varies also during the discharge, at the beginning of the flash the spectrum is blue rich due to high voltage and then with decreasing the voltage (i.e. at the end of the flash), the spectrum is richer in the red region [46]. It is then possible to choose the correct spectral distribution by choosing a specific moment for the measurement during the flash decay [47], [48].

The solar simulator is equipped with a Xenon lamp connected with the capacity power supply. The lamp is positioned on motorized rails with height-adjustable configuration (see Fig. II-10) to adjust the irradiance intensity at the test surface placed below. The test surface is equipped with fast *I-V* acquisition system placed on a temperature-regulated plate. The irradiance received on the test surface is adjustable in intensity by moving the lamp

(i.e. closer is the lamp higher is the intensity), and by adding neutral optical filters to attenuate the intensity. A set of lining are placed on the path of the light generated by the lamp to avoid and minimize the parasitic reflection.

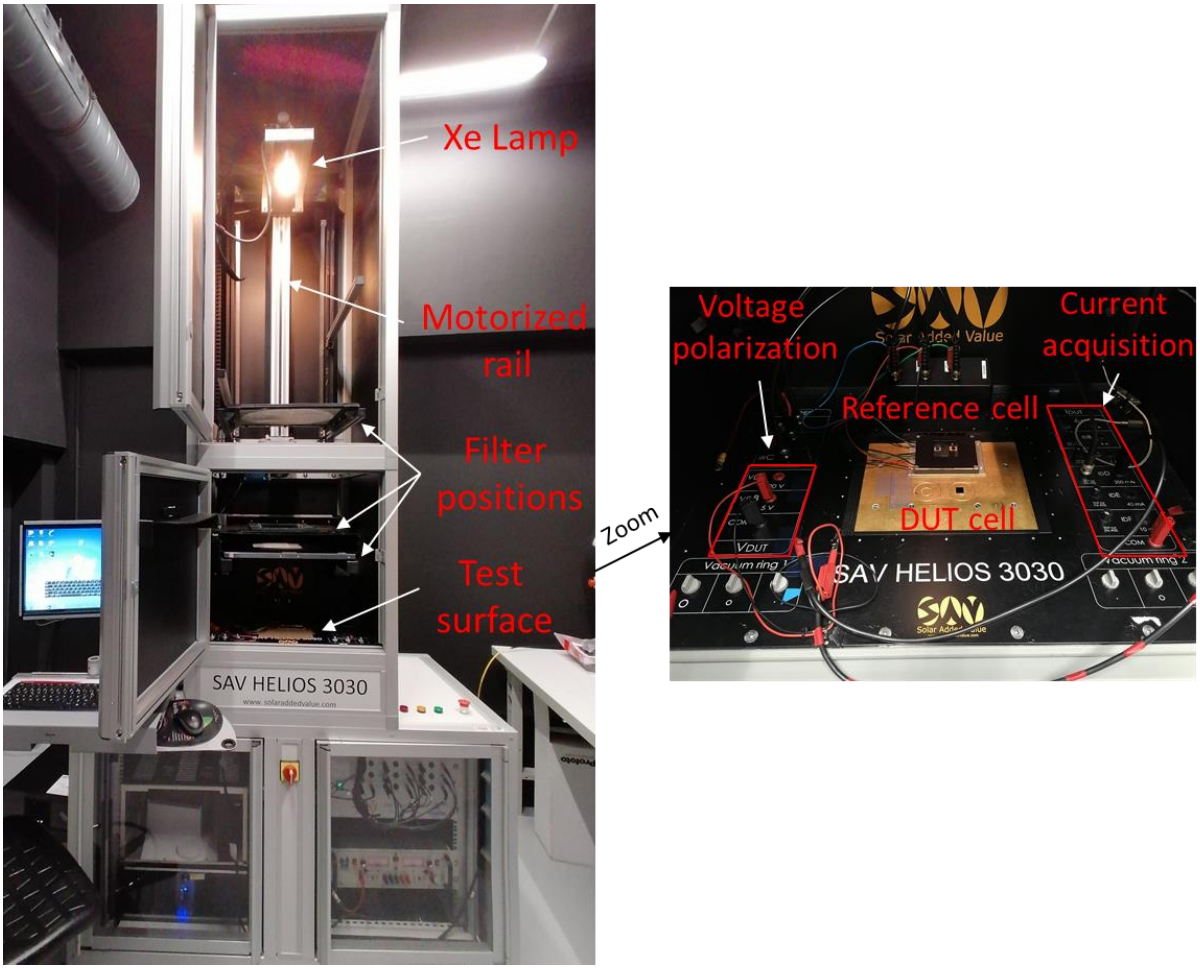

Fig. II-10 *Helios cells H3030 set-up for light current-voltage characterization: (left) vertical view with different elements, (right) zoom on the test surface including reference cells and Device Under Test DUT solar cells to be measured.*

II.5.1.1 Spectral irradiance and intensity adjustment

In the case of a flash simulator, it is necessary to use a reference cell that has the same absorption band as the cell under test. This is relatively easy to find for single-junction devices: a calibrated sister cell from the same batch of cells can be used for instance. In this case, the irradiance intensity factor *(X)* can be calculated during the discharge of the flash according to the Eq. II-8, where $J_{SC,\,Ref}$ is the photo-generated short-circuit current density calculated by the convolution of the reference cell external quantum efficiency to a specific solar spectrum under an equivalent 1 sun intensity (i.e. 1361.1 $W.m^{-2}$ for AM0 spectrum), and $J_{SC,\,measured}$ is the short circuit current density measured during the discharge of the flash for the device under test.

$$X\ (Suns) = {J_{SC,measured}}/{J_{SC,Ref}} \qquad \text{II-8}$$

However, this simple characterization is not sufficient for tandem cells, especially for two terminal configuration. In this case, the sub-cells are series connected, thus, the electrical properties cannot be measured for each sub-cell separately. Besides, each sub-cell absorb a specific portion of solar spectrum and the total short-circuit current density is limited by the sub-cell that deliver the smallest current (as seen in section I.2.5). Consequently, the tandem cells are much more sensitive to spectral variation that may have a non-negligible impact on the solar cells short circuit current, hence efficiency.

In the case of tandem cells measurement, isotypes cells allow a good control of simulator spectrum distribution on each sub-cell in order to obtain a good photocurrent balance between sub-cells (under the needed spectrum and irradiance intensity) [49]. Fig. II-11 shows a scheme of a 2J bottom cell isotype and its external quantum efficiency.

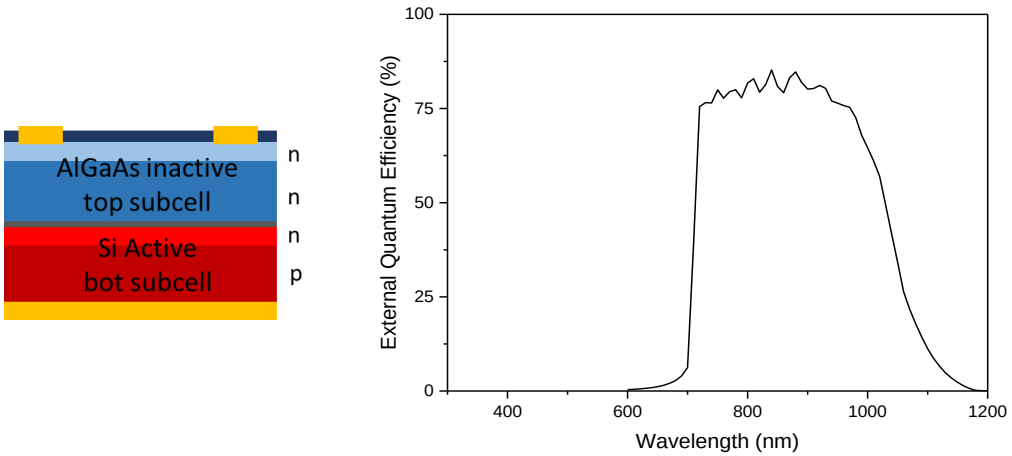

Fig. II-11 *(Left) schematic representation of bottom isotype of AlGaAs//Si (right) external quantum efficiency of AlGaAs//Si bottom isotype solar cells.*

The irradiance intensity factor $X_{sub,i}$ for each isotype cell is defined in Eq. II-9 as the ratio of the photocurrent measured with the simulator $J_{sub,i}^{sim}$, and the photocurrent calculated from quantum efficiency under 1 sun $J_{sub,i}^{EQE}$, *i* being the index of the sub-cell: bottom and top for 2J solar cell and top, middle and bottom for 3J.

$$X_{sub,i} = \frac{J_{sub,i}^{sim}}{J_{sub,i}^{EQE}} \qquad \text{II-9}$$

Fig. II-12 shows the irradiance intensity factor of the double-junction isotype during the discharge of the flash. In this case, we are looking to position the intersection of irradiance

intensity of all sub-cell at the irradiance intensity on which the measurements should be carried on [50]; 1 sun is chosen here. However, it is not always obvious to position the point where all the isotypes, hence all sub-cell of tandem cells, see the same irradiance intensity. In this case, the important point is to be sure that the two limiting sub-cell see the same irradiance intensity at the same time.

$$SMR_{i/j} = \frac{X_{sub,i}}{X_{sub,j}} = \frac{J_{sub,i}^{sim}/J_{sub,i}^{EQE}}{J_{sub,j}^{sim}/J_{sub,j}^{EQE}} \qquad \text{II-10}$$

The ratio between the irradiance intensity factor $X_{sub,i}$ is reported as the spectral matching ratio *SMR* (see Eq. II-10) [51]. When $SMR_{i/j} = 1$, the irradiance intensity is respected in both isotypes cells, so the solar simulator spectrum produce the same sub-cells photocurrent as under the reference spectrum. In contrast, when $SMR_{top/bot}$ is different from 1, the spectral balance is not respected. Hence, the irradiance intensity is not the same on the limiting sub-cells. The spectrum is blue rich if $SMR_{top/bot} > 1$, therefore, the top cell operates under higher irradiance intensity than the bottom cell. Conversely, at $SMR_{top/bot} < 1$ the spectrum is red rich so the bottom cell operate under higher irradiance intensity than top cells.

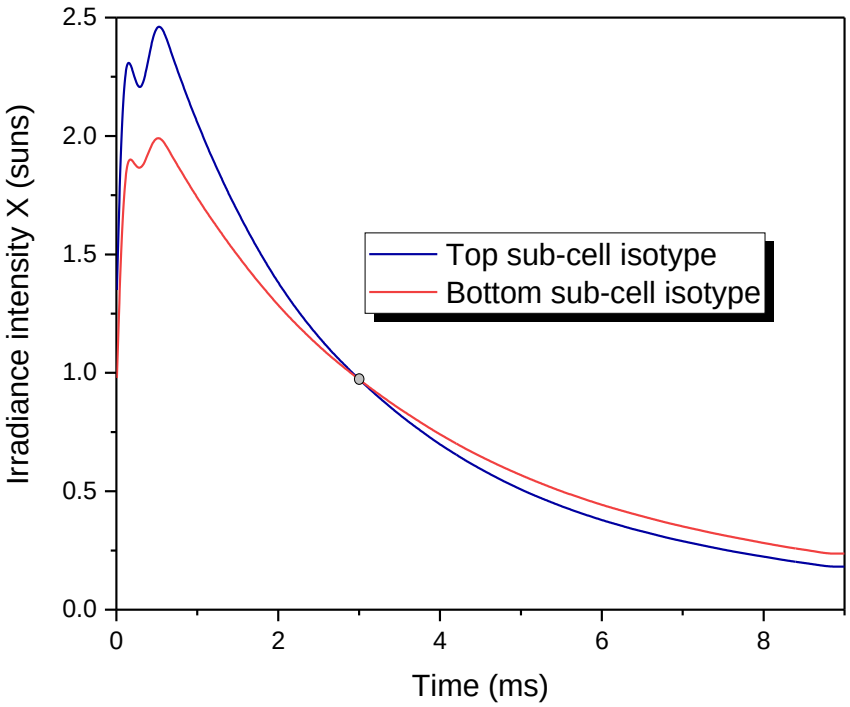

Fig. II-12 *Irradiance intensity X measured on each sub-cells isotype of 2J AlGaAs//Si during the discharge of the flash.*

Once isotypes cells are chosen, software configuration set and *SMR* = 1 is respected at the irradiance intensity of interest, one of the isotypes (middle or bottom) is chosen as a reference

for acquisition time measurements. In other words, during the flash discharge, at the moment when the chosen isotype reaches the desired irradiance intensity, a fast *I-V* acquisition is carried out. Since it is a fast discharge as explained above, one point only of the *I-V* measurement is acquired during a single flash discharge. To construct the entire *I-V* characteristic (e.g 0 V - V_{OC}), multiple flash discharges and *I-V* acquisitions are executed.

II.5.1.2 Solar simulator quality characterization

Solar simulators are classified according to three major specifications: temporal stability of irradiance intensity, homogeneity of irradiance intensity on the test surface and spectral matching to a reference spectrum [52]. Each specification can be ranked A, B or C, A being the lowest deviation from the target (see Tab. II-3)

- **The temporal stability** of irradiance intensity and spectral distribution is important for measurements, especially for tandem solar cells characterized under a multi-flash simulator; where limiting sub-cell can shift and change the behavior of the cells. Since the multi-flash mode is used in our simulator, artifact measurements can be the result of a high temporal deviation. For class A simulator, the temporal stability should be less than 2%, as calculated with Eq. II-11.

$$Non - uniformity\ (\%) = \left[\frac{X_{max} - X_{min}}{X_{max} + X_{min}}\right] \times 100\% \qquad \textit{II-11}$$

- **The spatial homogeneity** of the irradiance intensity on the test surface is required to reduce the uncertainty on the electrical parameters extracted from *I-V* curve, especially short-circuit current density, which depends linearly on the irradiance intensity. This expresses the deviation in the irradiance intensity between the reference cells and the solar cells to be measured; it is calculated through Eq. II-11. The international standard IEC 60904-9 reports that class A is achieved with non-uniformity less than 2% (over the test surface). Logically, reference cells shall be located as close as possible to the device under test to minimize the irradiance intensity deviation.
- **The spectral compatibility** with the reference spectrum is the most important criteria for the characterization of solar cells. In the case of single-junction solar cells, the specification for class A is that a ratio of 0.75 - 1.25 must be respected for each 100 nm wavelength range. However, for MJSC this is not sufficient for accurate measurements. An *SMR* = 1 is necessary as explained in section II.5.1.1 for a proper *I-V* measurements [53], [54].

The characteristics of the *Helios 3030* were investigated by means irradiance intensity measured from short-circuit current density evolution with a silicon single-junction solar cells. The results are shown in Tab. II-3.

For temporal stability evaluation, the c-Si solar cell is placed at the center of the test surface where the measured and reference solar cells are usually placed. Variations of less than 1% is calculated for 20 measurements performed every 10 seconds (see Fig. II-13 left). Since *I-V* curve is constructed with multiples flash delayed by 10 seconds, these measurements parameters respect the parameters used for the construction of the entire *I-V* curve. Therefore, no discontinuity on the *I-V* characteristics will be observed due to the temporal change of irradiance intensity.

Tab. II-3 *Solar simulator classification for their temporal stability, spatial homogeneity and spectral compatibility according to IEC 60904-9 standard requirements.*

Class	Temporal stability	Spatial homogeneity	Spectral compatibility
A	2%	2%	0.75 - 1.25 (±25%)
B	5%	5%	0.6 - 1.4 (±40%)
C	10%	10%	0.4 - 2.0
Helios 3030	0.8%	1.6%	400 - 1000 nm: Class A 1000 - 1100 nm: Class B
Quesma	1% 2 x 2 cm²	1%	400 - 500 nm: Class C 500 - 1100 nm: Class A

As for spatial homogeneity measurements, silicon single-junction solar cell was used on 5 x 11 positions to scan the irradiance intensity on the entire test surface (17 cm x 24 cm). A spatial non-homogeneity of 3% was calculated, which is high compared to class A. However, to estimate the impact of the non-homogeneity, we can use the effective surface that regroups the reference and measured solar cells represented by the red rectangle (typically 7 x 8 cm^2 for our cells) in Fig. II-13 (right). In this case, 1.6% non-homogeneity is obtained, hence the difference in irradiance intensity between the reference cells and the measured one is less than 2% that is recommended for class A solar simulator.

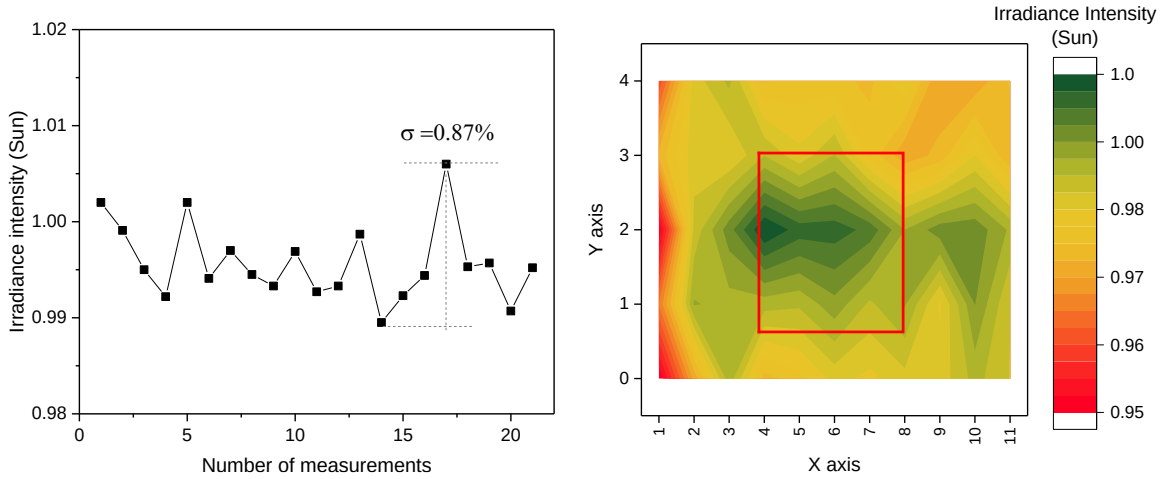

Fig. II-13 *Helios 3030 solar simulator characterizations, left: Temporal stability of irradiance intensity of 0.9% was calculated by Eq. II-11, right: spatially homogeneity measured by means of 1J solar cells on 17* x *24 cm² test surface.*

In order to analyze the variation of the spectrum during the flash discharge two spectrometers were used, a CMOS sensor so its response is limited around 1100 nm and an InGaAs detector which detection band reach 1700 nm. This analysis allows in one hand the classification of the solar simulator according to IEC 60904-9 standard. On the other hand, it helps to quantify the impact of the spectrum variation on the characterization of multi-junction solar cells. In this way, we can identify the moment of the flash decay where the SMR = 1 and thus an equivalent irradiance intensity is seen by each sub-cell.

As explained above during the fast flash discharge (10 ms) the incident light varies in intensity and in spectral distribution. Therefore, challenge of the proposed measurement is on the one hand to measure a complete spectrum over a short integration time but also to position the spectra in time. The used spectrometers offer a very short integration time that can reach 100 µs, which is very small compare to the overall flash duration hence the spectrum distribution and irradiance intensity can be considered as constant over this period. Only one measurement is carried out during a flash discharge. Spectra recorded with different flash are comparable since good reproducibility of measurements is achieved (non-homogeneity less than 1%).

Since the solar simulator and the set-up for spectra measurements are separate and not connected, a sensor is needed to detect the instant of the start of the flash T_0. Two series-connected solar cells with a voltage higher than 5 V under illumination were used as analogic signal 0 - 5 V to identify the beginning of the flash. Spectrum is then recorded at different time

$T = T_0 + \Delta T$ of the flash decay. Since optical fibers have a high curvature radius, it was not possible to perform measurements directly at the usual test surface as observed in Fig. II-14.

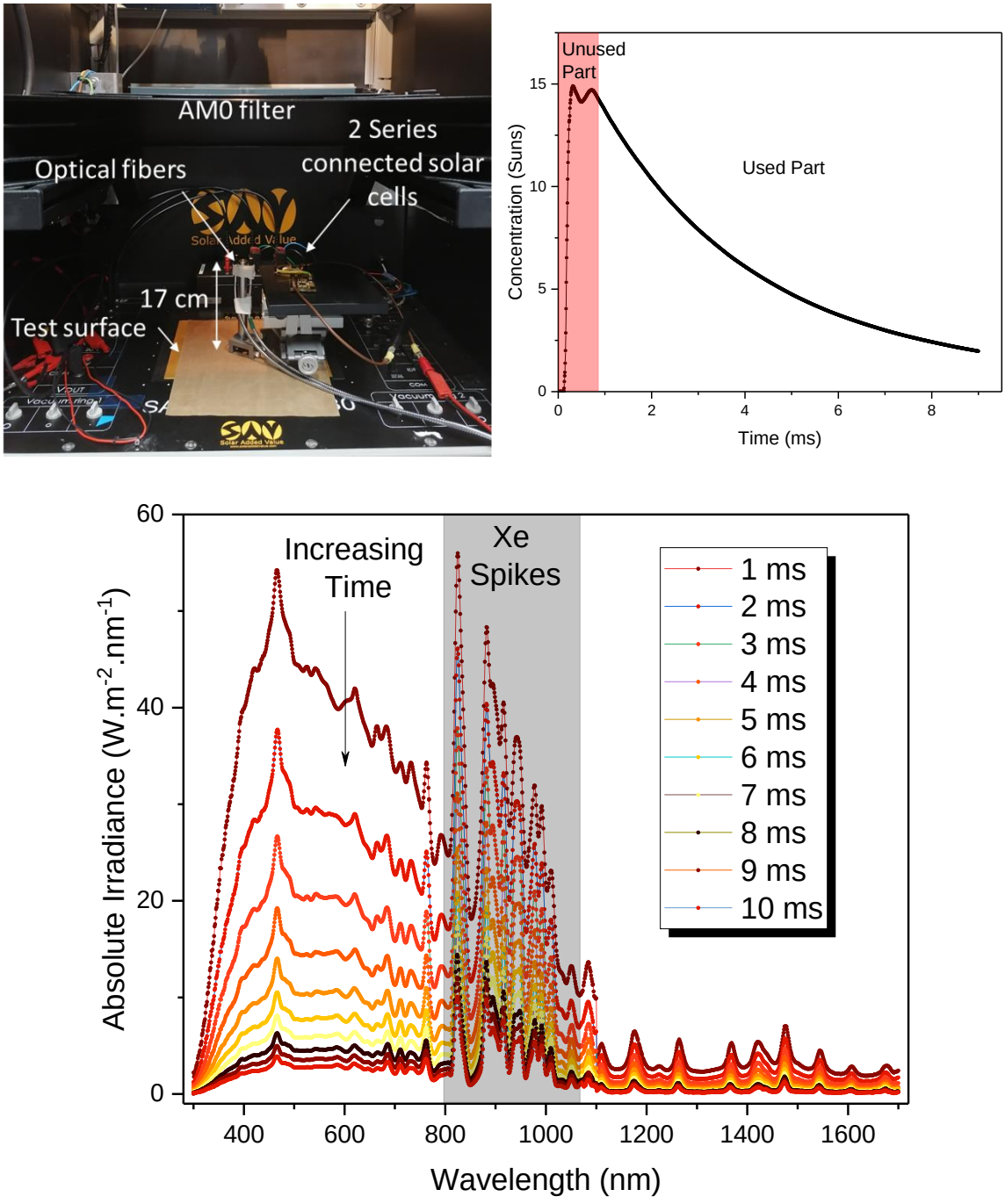

Fig. II-14 *Helios 3030 flash solar simulator characterization, top-left: picture of set-up used for spectrum measurements, top-right: typical irradiance intensity variation as a function of time of flash for a single junction or sub-cell, bottom: simulator spectrums recorded with a spectrometer at different time of the flash (w/o AM0 filter).*

In Fig. II-14 (top-right), the irradiance intensity received on the measurements surface is presented as a function of time of flash discharge. In the first millisecond the power of flash increases rapidly, this part is unusable because of a large and chaotic variation of spectrum

(different from target spectrum). In normal test conditions, measurements are made in the decreasing portion of the flash, i.e. T > 0.7 ms.

The *Helios 3030* spectra recorded at different time of flash discharge are presented in Fig. II-14 (bottom). At 1 ms, the spectrum is at its higher energy with blue rich part. With increasing time, the flash light intensity decreases and especially in the blue part of the spectrum, at the end of the flash the spectrum is red rich. As expected, Xenon emission bands in the range 850 - 1000 nm cause an over-illumination (without optical filter) of the Si bottom cell. In this illumination condition, the silicon photo-generates higher current, which inverse the limiting sub-cell of 3J from Si (bottom cell) to AlGaAs (middle cell). Short-circuit current density of each sub-cell is presented in Tab. II-4, it was calculated by convolution of the quantum efficiency of each sub-cell to the spectrum: i) AM0 reference, ii) *Helios 3030* without AM0 filter at 2 ms (as an example) of flash discharge.

Tab. II-4 *Short-circuit current density calculated for each sub-cell of 3J GaInP/AlGaAs//Si by convolution to the AM0 reference spectrum, Helios 3030 with and without AM0 filter at 2 ms (as an example) of flash discharge, the spectrum were scaled to the intensity of the spectrum at 2 ms with AM0 filter for a reliable comparison.*

Triple-junction	Jsc ($mA.cm^{-2}$) 11xAM0 spectrum	Jsc ($mA.cm^{-2}$) *Helios 3030* without AM0 filter @ 2ms	Jsc ($mA.cm^{-2}$) *Helios 3030* with AM0 filter @ 2 ms
GaInP	177.65	173	184
AlGaAs	133.1	159	141
Si	111.1	193.63	90

An optical filter that we call *AM0 filter* was used to attenuate the Xenon emission bands. Its optical transmission measured with CMOS and InGaAs detector is presented in Fig. II-15 comparing to *Helios 3030* spectrum without AM0 filter. In the wavelength band 300 - 760 nm the AM0 filter transmission is in the range 70 - 75%, from 760 - 1150 nm a transmission drop is observed with a minimum value of 29% is recorded around 900 nm, beyond 1150 nm the transmission slowly increases from 80% to 90%. The two spectra measured on *Helios 3030* with and without AM0 filter are presented in Fig. II-15 (right) in order to illustrate the purpose of using this filter. The spectrum is blue rich with low Xe emission rays intensity, which correspond to the spectral distribution of the AM0 reference spectrum. In normal test conditions, two neutral filters are added in the light path to reduce irradiance intensity to 1 sun. When normalizing its spectrum to the one measured with only AM0 filter, the spectra are superposed, thus no variation is induced with this configuration (AM0 + 2 Neutral filters) in

the spectrum distribution. In the next calculations, comparisons and solar simulator qualification, only AM0 filter was used in order to increase irradiance intensity thus reduce noise in the recoded spectrum.

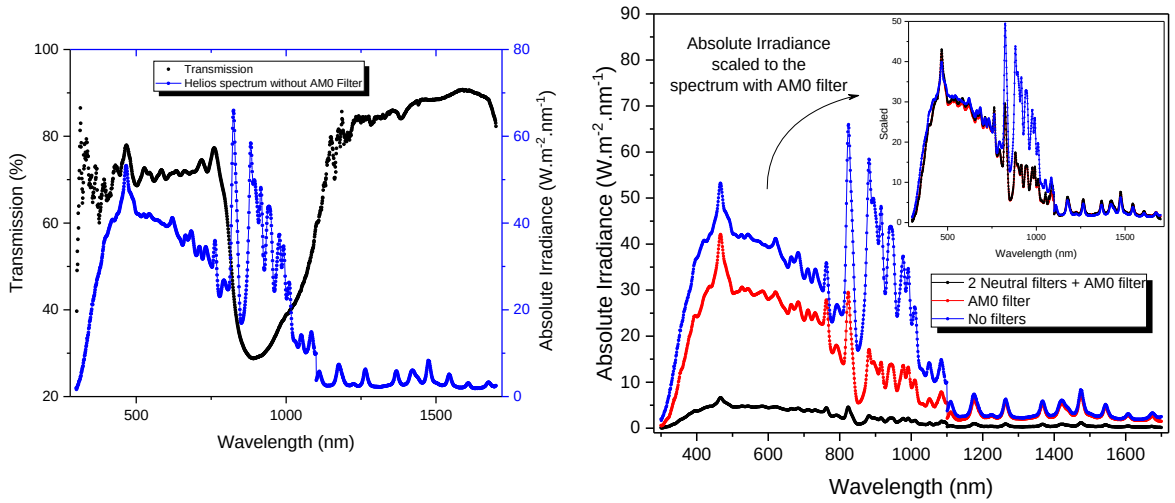

Fig. II-15 *Left: Transmission of the AM0 optical filter measured by CMOS and InGaAs detector, right: spectra recorded with a spectrometer at different time of the flash w/o AM0 filter, with AM0 filter and with AM0 + two neutral filters.*

The calculated short-circuit current by convolution of quantum efficiency to the *Helios 3030* with AM0 filter spectrum (as an example at 2 ms) is presented in Tab. II-4. Under these measurement conditions, the Si bottom cell limits the current of the 3J, which corresponds to normal operating conditions under AM0 reference spectrum.

The measured spectra at different times of the flash decay have been scaled to the spectrum measured at 2 ms and are compared in Fig. II-16. It is observed that the normalized spectra are superposed with a maximum deviation of 10 $W.m^{-2}.nm^{-1}$ around 900 nm. A better visualization of this deviation is observed in the graph of Fig. II-16. This graph represents the power ratio of the spectra measured throughout the flash divided by the spectrum at 2 ms. It shows a more or less constant ratio over the entire wavelength range.

The same trend is observed by comparing Helios spectra with the AM0 reference spectrum (dark line) with some variations: i) $\lambda < 400$ nm: higher absolute irradiance intensity for AM0 reference ii) 400 nm $< \lambda <$ 600 nm: a good correspondence between the reference and the *Helios 3030* spectra, iii) 600 nm $< \lambda <$ 1000 nm: higher absolute irradiance intensity of *Helios 3030* spectra than AM0; this is due to the presence of several spikes, iv) $\lambda >$ 1000 nm: AM0 spectrum has an overall irradiance higher than the one of *Helios 3030*.

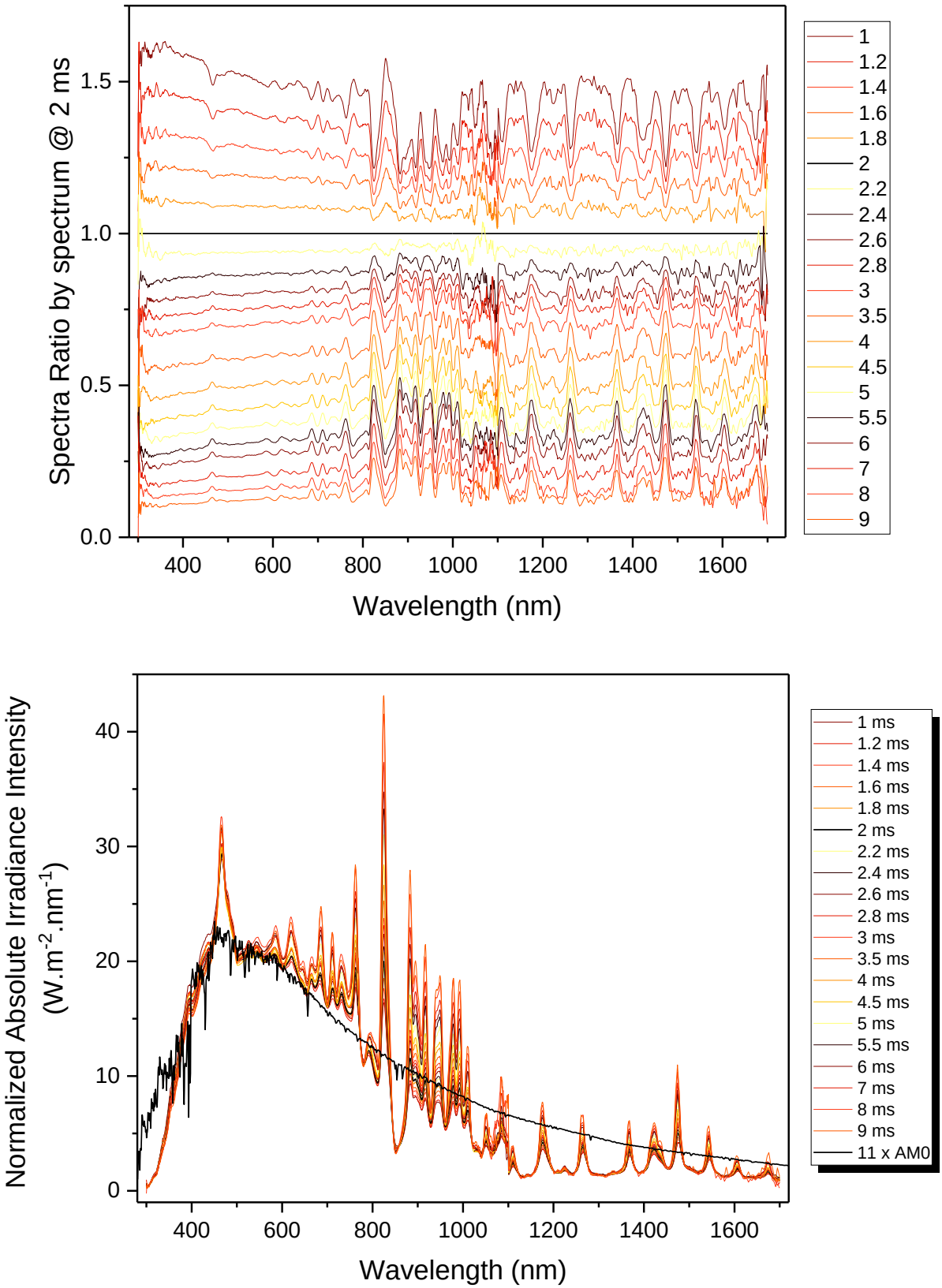

Fig. II-16 *Comparison of Helios 3030 spectra during flash discharge (scaled to the spectrum at 2 ms) with the AM0 reference spectrum. The graph in top, represent the ratio of spectrum measured at different times of flash discharge comparing to the one at 2 ms.*

In order to classify the spectral compatibility into the three defined classes (A, B and C), the ratio between the reference spectra and measured one were calculated using Eq. II-11 for each 100 nm wavelength range. The results of representative spectra during the flash discharge (1 - 8 ms) are shown in Fig. II-17. As explained above, in the standard there is no requirement for the wavelength range 300 - 400 nm and 1100 - 1200 nm. For the wavelength ranges in the center of interest (400 - 1100 nm), 6 out of the 7 intervals (400 - 1000 nm) are classified as class A, and the last one (1000 - 1100 nm) is classified as class B (red area). Thus, from these measurements, one can classify *Helios 3030* as class B solar simulator.

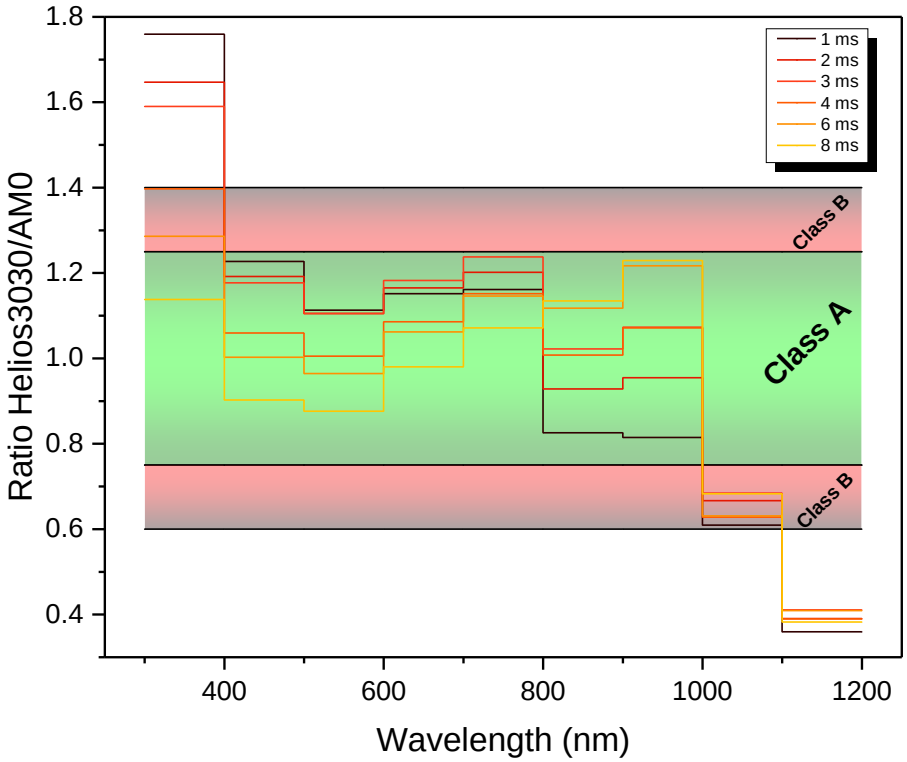

Fig. II-17 *Helios 3030 spectrum compatibility with AM0 reference spectrum for representative spectra during flash discharge.*

When isotype reference cells are available, the *I-V* characterization with the flash simulator is relatively simple, as explained above. However, when isotypes are not available, as it is the case for the multi-junction used in this thesis, the *I-V* characterization becomes more complex. The correspondence of the solar simulator spectrum to the AM0 reference was confirmed during all the flash discharges. The short-circuit current density was calculated for each sub-cell in the case of 2J and 3J by convolution of *EQE* to the measured (experimentally on *Helios 3030*) spectra during flash discharge. The results are presented in Fig. II-18. In the case of 2J, the top cell limits the overall current and the Si limits that of 3J under AM0 reference spectrum. Therefore, we ensured that the multi-junction cell in the solar simulator is limited by

the sub-cells, which limits the multi-junction under the reference AM0, i.e. there is no inversion of limiting sub-cell.

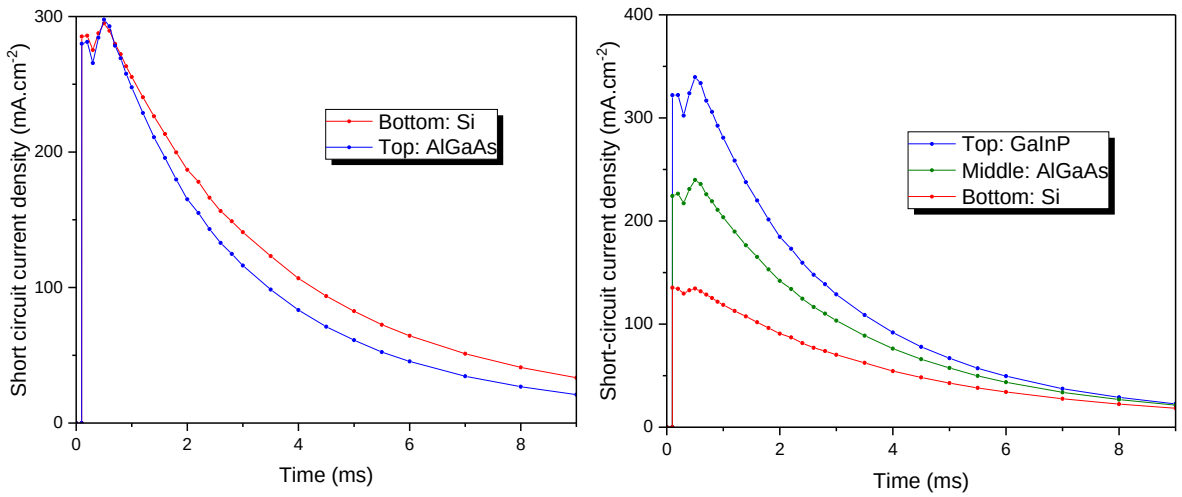

Fig. II-18 *Short circuit current density calculated by convolution of EQE to the measured spectra during flash discharge for each sub-cell of (left) 2J: AlGaAs//Si and (right) 3J: GaInP/AlGaAs//Si.*

For each sub-cell, the corresponding irradiance intensity (in suns) was calculated through Eq. II-9 and plotted as a function time of flash in Fig. II-19 in order to estimate the operating irradiance intensity (concentration) of each sub-cell. During flash discharge a sister multi-junction solar cells was used as reference cells, i.e. 2J and 3J from the same run was used as reference for 2J and 3J respectively. Therefore, the measured irradiance intensity by each tandem cells is plotted as a function of flash discharge in the same graph (black line).

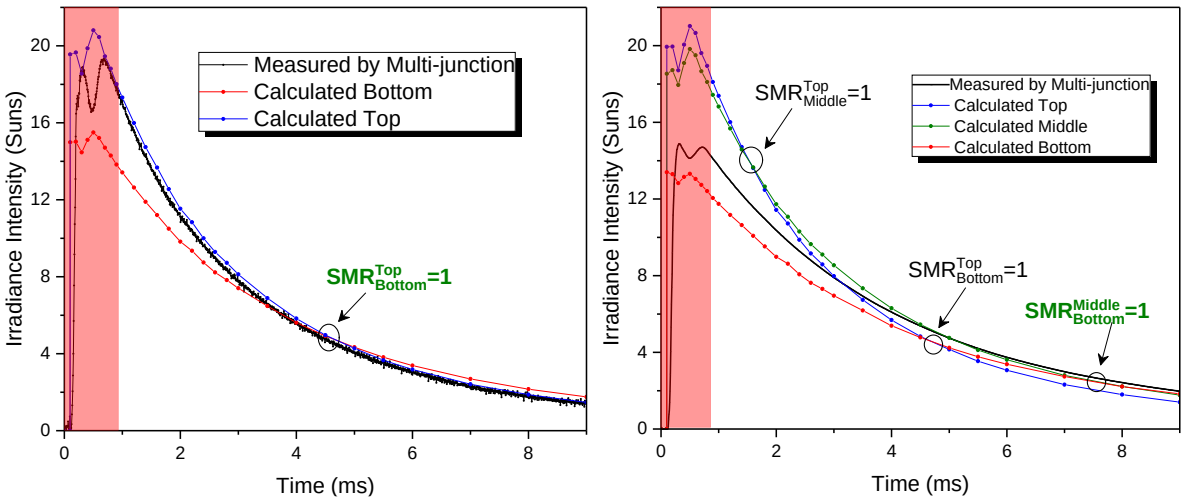

Fig. II-19 *Irradiance intensity in suns calculated by Eq. II-9 for each sub-cell in the case of (left) 2J: AlGaAs//Si and (right) 3J: GaInP/AlGaAs//Si. Time at where measurements were performed is placed at 4.5 ms and 7.5 ms for 2J and 3J respectively.*

An SMR = 1, that corresponds to an equivalence of operating concentration between the two sub-cells that are limiting the multi-junction is reached in both cases (2J and 3J).

The normalized Short-circuit current density by each sub-cell concentration was calculated and plotted as a function of *SMR* in Fig. II-20. As explained above, at *SMR* = 1 the two sub-cells operate at the same concentration, this is the most important criteria for a reliable *I-V* measurements. In case of 2J (resp. 3J), the top (resp. bottom) is limiting the current of multi-junction solar cells. This is translated in Fig. II-20 as a constant variation of normalized J_{SC} with respect to the *SMR* at a current equivalent to the one calculated by convolution of *EQE* to the AM0 reference spectrum.

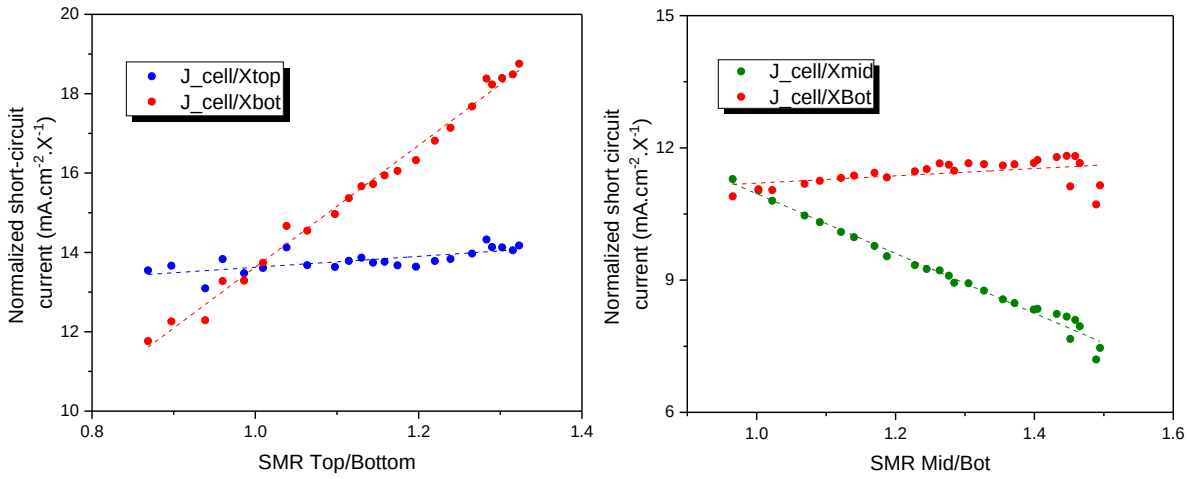

Fig. II-20 *Limiting sub-cell diagram in the case of (left) 2J: top/bottom limiting and (right) 3J: Mid/bottom limiting sub-cell.*

For single-junction c-Si all these calculations are not necessary since, there is no issues related to spectrum splitting on different sub-cell. In addition, measurements and calculations shown above on the spectrum quality reveal a class B of solar spectrum on all the range of usable flash discharge.

To summarize, a multi-junction solar cells *I-V* characterization protocol adopted in this study is:

- *EQE* measurements of the cell to be measured and a sister one (same batch, same wafer and same optimization)
- Acquisition of flash spectra during decay (0 - 10 ms) using a spectrophotometer, this is only done once since a good repeatability is recorded for flash discharge
- J_{SC} calculation for each sub-cell, by convolution of *EQE* to the solar simulator spectrum as a function of decay time
- Calculating of each sub-cell concentration compared of the one calculated by convolution of *EQE* to the AM0 reference spectrum $J_{SC} = J_{SC}^{Helios}/J_{SC}^{AM0}$

- Reading the crossing point time at which the two sub-cells (for 2J) or two limiting sub-cell (for 3J) where they receive the same concentration (irradiance intensity)
- Calculating the J_{SC} (Ref) of the sister multi-junction solar cell (convolution of *EQE* to AM0 spectrum)
- Plot the concentration variation of the sister solar cells **measured** by the solar simulator with the **calculated** concentration of each sub-cell and defines the ratio between the calculated cross point and the measured one for the sister cell at the crossing point time
- Set-up adjustment (lamp position ad filter insertion) in order to obtain the concentration at which measurements will be done (e.g. X = 1 sun) at a time decay of 4.6 ms and 7.5 ms for 2J and 3J respectively
- Since the spectrum composition and intensity is stable from one flash to another (repeatability), these measurements are not necessary for each *I-V* measurement.

To validate the above-explained methodology for tandem solar cells current-voltage characterizations, we have used a 4 cm² triple-junction GaInP/AlGaAs//Si. The solar cell was characterized using the same procedure, i.e. using a triple-junction that have the same spectral response as a reference cell to identify the time of flash where the solar cell is under 1 AM0 spectrum.

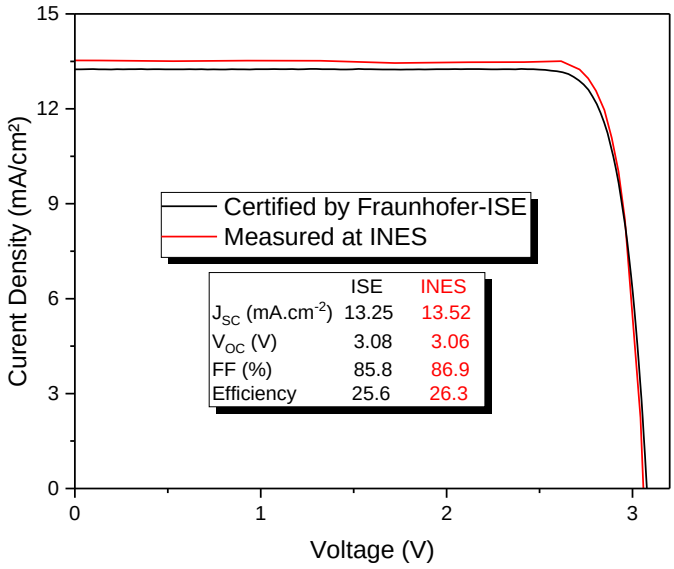

Fig. II-21 *Comparison of GaInP/AlGaAs//Si 3J solar cells current-voltage characterizations carried out at INES and Certified by Fraunhofer-ISE at 25°C under 1 AM0 spectrum.*

Current-voltage characterizations results performed under 1 AM0 and 25 °C, at INES and the *I-V* certified by Fraunhofer-ISE are presented in Fig. II-21. The two measurements are in good agreement. The calculated deviation for J_{SC}, V_{OC}, FF and efficiency are 1%, 0.3%, 0.64% and 1.3%, respectively. The deviation is acceptable considering the 2% tolerance defined by IEC 60904-9. Therefore, the methodology presented can be used for tandem solar cells characterization under flash solar simulator in absence of isotype solar cells.

Another characterization method that can be very interesting (especially when isotypes are not available) is the use of multi-junction cells as a reference cell [55]. To illustrate this method, we can take the example of 3 triple-junction sister cells (e.g. same batch, same wafer, same architecture, etc.). Two of those cells can be used as reference cells by saturating the desired sub-cells, using light and voltage bias as for *EQE* measurements (see section II.4). In that way one cell can operate at J_{SC} of one sub-cell, and the other at the J_{SC} of another sub-cell, therefore both cells can be used to calculate the received concentration factor and thus define the SMR = 1 condition.

II.5.2. Steady-state solar simulator (*LED*)

The *Quesma* (*LED*) solar simulator was used for in-situ current-voltage *BOL* and *EOL* characterizations (i.e. coupled with electron beam facility SIRIUS). Two modes are available for this solar simulator: a flash and continuous illumination. In contrast to the *Helios 3030* presented above, the flash mode does not mean a variation in solar spectrum distribution, but only refers to a reduced *LED* illumination duration during the experiment (to enhance their lifetime); indeed, for tandem cells the scanning voltage range is relatively high, thus it requires a relatively long measurement time. The compactness of this solar simulator makes it compatible and easy to integrate on an electron beam line such as SIRIUS beam lines facility.

The solar simulator is equipped with 43 *LEDs* to reproduce the AM0 spectrum. The maximum irradiance intensity achievable with this equipment is 20% AM0 spectrum (i.e. 272 $W.m^{-2}$). As seen in section I.3, the low irradiance levels are relevant for solar cells evaluation in deep space conditions; for instance, the irradiance around Jupiter is ~3.7% of AM0 spectrum that corresponds to 50 $W.m^{-2}$.

The batch of *LED*s is divided into 5 groups where the applied voltage can be varied to adjust the irradiance intensity. However, by varying the applied voltage, the spectral distribution can change, which may impact tandem cells response. For this reason, multiple measurements and experimental set-up adjustments were performed to reach a 3% AM0

intensity while respecting the AM0 spectral distribution in all sub-cells. As a first step, the voltage of the five groups of *LED* have been varied in order to reach a low intensity level. The irradiance intensity is measured by the ratio of short circuit current of 1J, 2J and 3J (cells to be under test) measured with the *LED* solar simulator and the short circuit current measured with quantum efficiency. As a second step, the simulated spectrum is recorded as a function of wavelength using two spectrophotometers (CMOS and InGaAs detector). Then, the deviation observed with AM0 reference spectrum is calculated and reduced by varying the potentiometers of each *LED*.

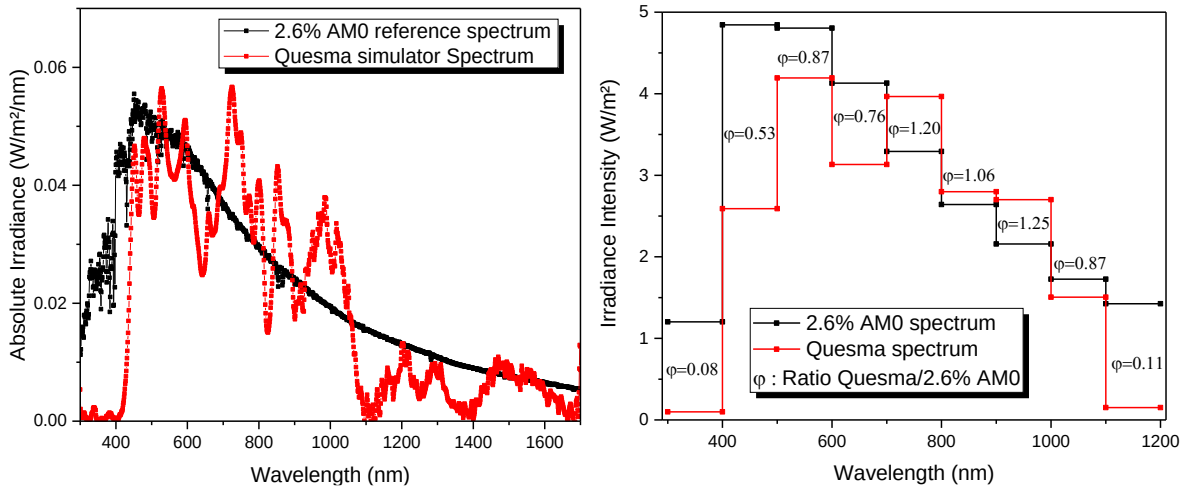

Fig. II-22 *Left: comparison of Quesma LED solar simulator spectrum with the 2.6% AM0 reference spectrum, right: comparison of incident power density between the Quesma and 2.6% AM0 reference spectrum for each 100 nm portion and the relative deviation.*

Despite this iterative process, it is not an easy task to reconstruct a perfect AM0 spectrum with a limited number of *LEDs* having a narrow light emissivity. Fig. II-22 (left) presents the AM0 spectrum obtained after several optimizations iterations in order to achieve the best spectral balance between sub-cells at 2.6% AM0 intensity. The intensity peaks are intentionally introduced by adjusting the potentiometers of some *LED* groups, to compensate for the nearby intensity dips.

Fig. II-22 (right) presents the integral of irradiance intensity for each 100 nm intervals, with the corresponding irradiance ratio $\varphi = Quesma/AM0$ in order to compare *Quesma* spectrum to the 2.6% AM0 reference spectrum ($\varphi = 1$ meaning perfect spectrum matching). For short and high wavelength ($\lambda < 400$ nm and $\lambda > 1100$ nm), the simulator delivers less power density than the reference spectrum with a low ratio reaching 0.08 - 0.11. However, in this wavelength range the standard does not mention any requirement. This large deviation is due to the unavailability of *LED* emitting at 1100 nm, and to the failure of the 375 nm *LED* in our set-up,

resulting in a dip around this wavelength. This results in a class C spectrum in the 400 - 500 nm band. In contrast, for wavelengths comprise between 500 nm and 1100 nm, the solar simulator emits a power density closer to that of the AM0 reference spectrum, with a ratio ranging from 0.76 to 1.25. In this portion of wavelength, the simulator spectrum is graded class A. Nevertheless, the impact of spectral deviation as calculated above will differ strongly depending on each sub-cell absorption bands as introduced in section II.2.

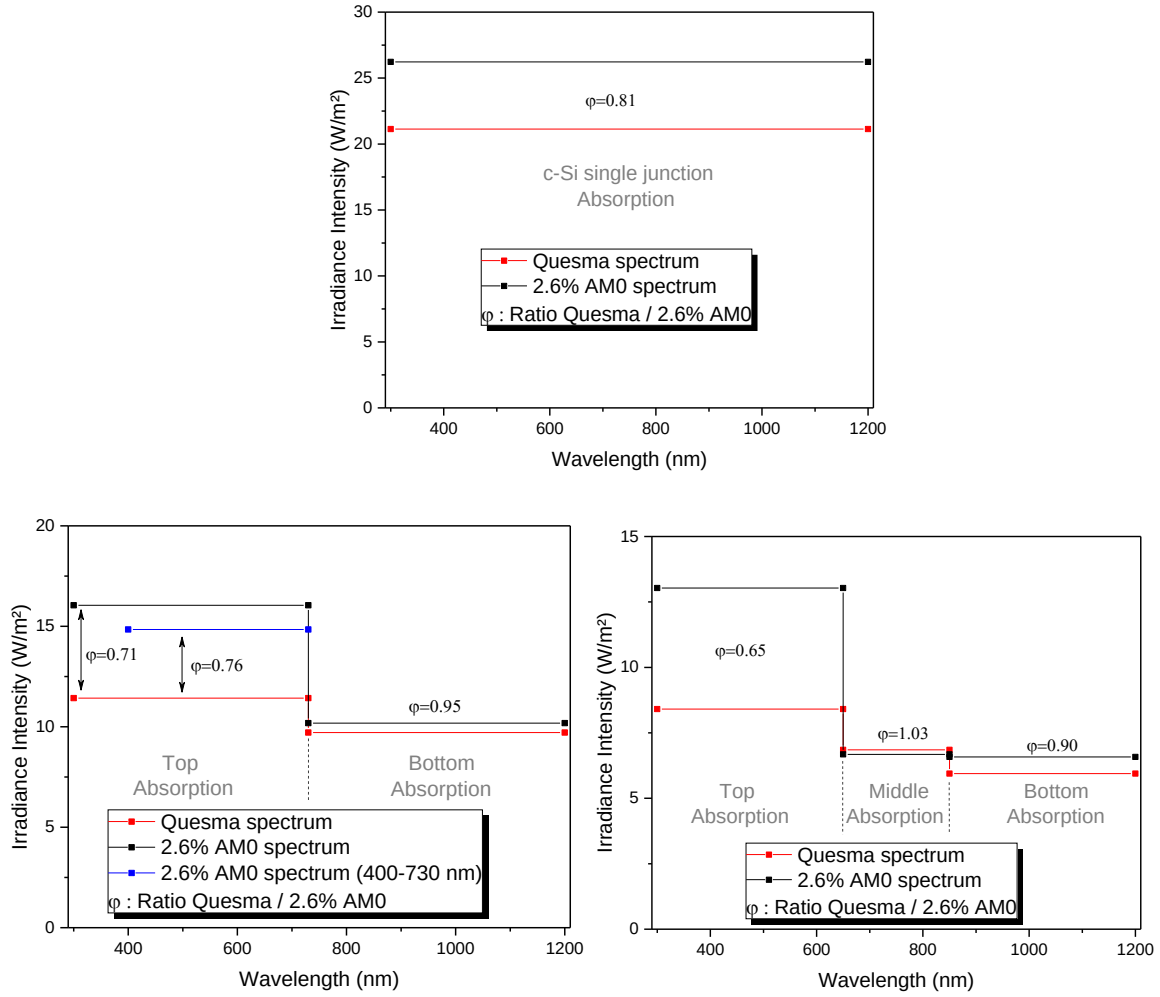

Fig. II-23 *Comparison of the incident power density between Quesma and 2.5% AM0 spectrum calculated for each three architecture designs, top: 1J c-Si, bottom-left: 2J AlGaAs//Si, bottom-right: 3J GaInP/AlGaAs//Si.*

The power density was calculated for each sub-cell of each of the three architectures depending on their absorption band, i.e. 300 - 1200 nm was taken for 1J c-Si, 2J: 300 - 730 nm and 730 - 1200 nm for top and bottom sub-cells, 3J: 300 - 650 nm, 650 - 850 nm and 850 - 1200 nm was taken for top middle and bottom sub-cells respectively. The results are shown in Fig. II-23.

For 1J c-Si (see Fig. II-23 top) where the absorption band extends from 300 to 1200 nm, the calculated power density of simulator spectrum is less than the reference 2.6% AM0 with a ratio of 0.81; this was the closest we could get to the targeted spectrum with this set-up.

For 2J AlGaAs//Si (see Fig. II-23 bottom-left) where the bottom absorption band range from 730 - 1200 nm, the power density ratio calculated of the solar simulator was around 0.95 compared to the 2.6% AM0 reference spectrum; thus this is an almost perfect match to the target spectrum. Regarding top cells the power density ratio between the simulator and the reference 2.6% AM0 is 0.71 in the absorption band 300 - 730 nm that class it as class B. However, low quantum efficiency is measured for short wavelength ($\lambda < 400$ nm) for the 2J cells used in this PhD work (see Fig. II-7 right). In consequence, this portion of spectrum has a limited impact on the behavior of the top cell since the photo-generated current below 400 nm by convolution with AM0 spectrum is 0.2 $mA.cm^{-2}$; it corresponds to less than 1.5% of the total current. A ratio of 0.76 was calculated for wavelength range 400 - 750 nm, which was considered as acceptable. It is important to note that this assumption is only valid for the used 2J solar cells where the top cells have low *QE*.

In the case of 3J GaInP/AlGaAs//Si (see Fig. II-23 bottom-right), the calculated power density ratio is 0.65, 1.03 and 0.9 for top (300 - 650 nm), middle (650 - 850 nm) and bottom (850 - 1200 nm) sub-cells, respectively. For top cell absorption band the *Quesma* delivers low irradiance intensity, compared to AM0 spectrum, which may have considerable effects since in normal conditions, the top cell does not limit the current of the 3J. In the case of our devices, by changing the voltage of the group of 300 - 600 nm *LED*, the current remains stable, which indicates that the top cell does not limit the tandem cells under the recorded spectrum. Therefore, the solar cell operates under the good conditions since the middle and bottom sub-cells limit the total current of multi-junction. So the spectrum is considered as acceptable for 3J since a low deviation is calculated in the absorption band of middle and bottom, which are the limiting sub-cells.

Spatial and temporal homogeneities were calculated through the variation of short circuit current density, which is very sensitive to irradiance intensity in comparison to other electrical parameters. A 1J c-Si solar cells of 1 x 1 cm^2 was used in 4 x 8 positions (that cover a surface of 4 x 8 cm^2) to investigate the variation of spatially homogeneity. A deviation of 35% was calculated at the beginning due to non-homogeneous distribution of irradiance intensity on Y-axis. After a correction, by removing a diffuser and *LED* repositioning, the deviation was

reduced to ~4%, which corresponds to class B simulator, a mapping graph of the short circuit current (so the irradiance intensity) measured on the test surface is presented in Fig. II-24 (left).

However, this deviation does not fully reflect the uncertainty of our measurements, since, on the one hand, 1 x 1 cm² and 2 x 1 cm² solar cells were mainly used in our study, which reduces the test surface, and on the other hand, the solar cells are placed at the same position for characterizations during each experiments. By taking into account these two criteria, non-homogeneity of 1% is calculated for a 2 x 2 cm² test surface; this fits into class A criteria.

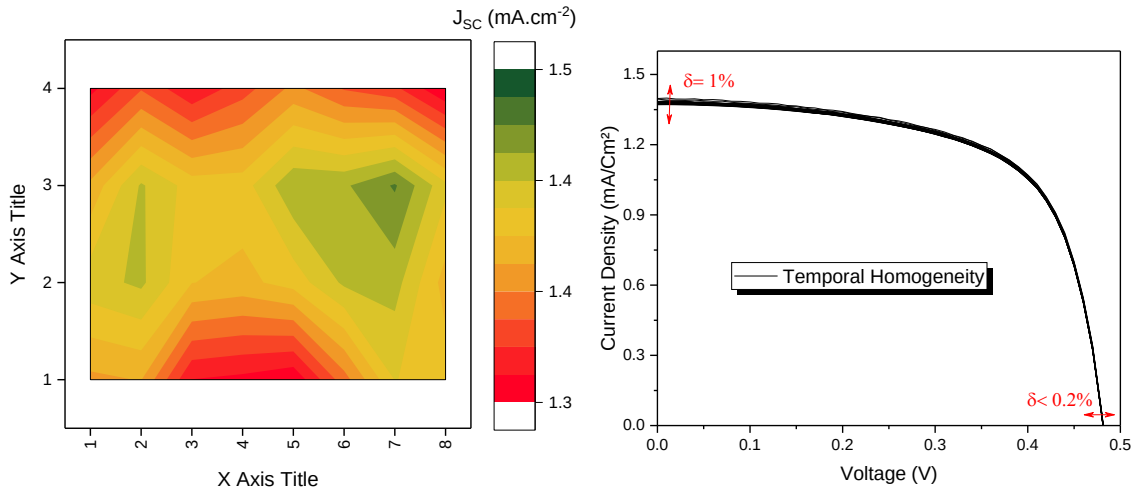

Fig. II-24 *Characterization of the Quesma solar simulator homogeneity with 1J c-Si solar cells, left: mapping of the short circuit current density homogeneity on the test surface (2.6% AM0), right: Temporal stability investigation through 20 I-V measurements delayed by 30 seconds.*

The same 1J c-Si was used to investigate the temporal stability of the solar simulator. Fig. II-24 (right) present the *I-V* characteristics over 20 measurements delayed by 30 seconds, as seen a deviation of 1% is calculated for temporal instability on short circuit current and hence irradiance intensity what qualifies it as a class A.

II.6 Irradiation facilities

As seen in section I.3, solar cells used for space application face charged and energetic ionizing particles flux, mainly electrons and protons. For ground test, particle accelerators are used to reproduce space environment and to characterize the behavior of solar cells in these conditions. In the framework of this PhD thesis, the SIRIUS facility hosted at *LSI* was used for electrons irradiation at both room and low temperature conditions. For protons implantation, the JANNUS platform at *CSNSM* was used.

II.6.1. JANNUS ORSAY (protons facility)

The platform of JANNUS Orsay[22] was used for protons implantation at room temperature, a schematic representation of the facility is presented in Fig. II-25 [64]. It is composed of 190 kV ion implanter *IRMA* that energy range from 10 keV to 570 keV and a 2 MV accelerator *ARAMIS* which particle energy range from 500 keV to 11 MeV [65]–[68]. The ARAMIS accelerator works on two modes, tandem and Van de Graaff. In tandem mode, a negative ions source with Cesium sputtering can provide up to 40 different elements that will be injected in a second step into the accelerator containing nitrogen gas that change the ion sign and multiplies it. Depending on the charge state of the ions, they can be accelerated up to 15 MeV. When operating as a Van de Graaff mode, a penning source is located in the accelerator that produce a positive charge state of gaseous elements as H, He and noble gases with energy from 150 keV up to 3 MeV.

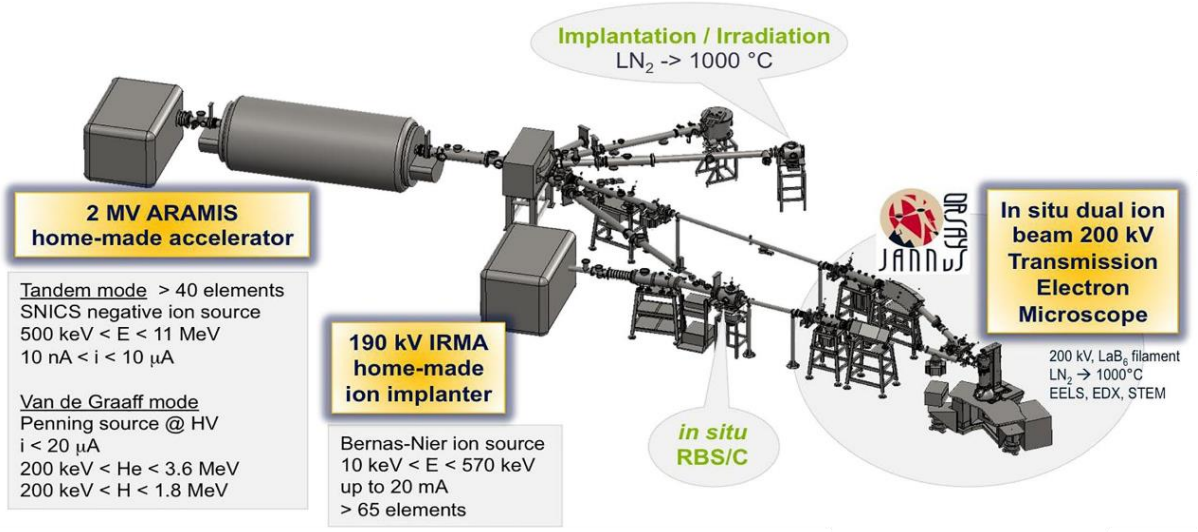

Fig. II-25 *schematics of JANNUS Orsay ion accelerator platform composed of 2 MV tandem/Van de Graff and a 190 kV IRMA accelerators [64].*

The accelerated ion beam is directed by switching magnets to the dedicated Cryostat that is directly connected into the beamline. A high vacuum is needed in the cryostat for implantation, typically 10^{-5} Torr. Once the required vacuum is achieved, the beamline gate is open so that the accelerated protons arrive directly on the solar cells placed onto the sample holder.

The protons fluence is measured by the current density of protons that hit the conductive metal piece placed between the beamline and the cryostat chamber. This metal piece has a

[22] JANNUS Orsay website, www.jannus.in2p3.fr/

circular frame with 8 cm radius to let pass the protons. The protons implantation parameters are listed in Tab. II-5: the solar cells were irradiated at room temperature at three different fluence with 1 MeV proton beam energy.

Tab. II-5 *Solar cells protons implantation parameters.*

Protons Energy	Flux ($p.cm^{-2}.s^{-1}$)	Total Fluence ($p.cm^{-2}$)		
1-MeV	5.10^{10}	1.10^{11}	3.10^{11}	1.10^{12}

II.6.2. SIRIUS (electrons)

SIRIUS facility is equipped with a pelletron (see Fig. II-26 left) accelerator that delivers a monoenergetic electrons beam between 200 KeV and 2.5 MeV and a current range between 15 nA to 50 µA. Pelletron accelerator was developed by the National Electrostatics Corporation (*NEC)* [69], it has the same principle as the Van de Graff accelerator [70].

The metallic pellet chain is charged by an induction scheme. The inductor push the electrons from the pellet connected with the roller. At its exit, the pellet transport the positive charge mechanically to the terminal where transferred charges are built up. In order to achieve higher voltage, the pelletron is enclosed in a high pressure (5.5 bar) of dry and purified sulfur hexafluoride (SF_6) to reduce the breakdown voltage. The electrons are accelerated between the high terminal voltage and the ground level.

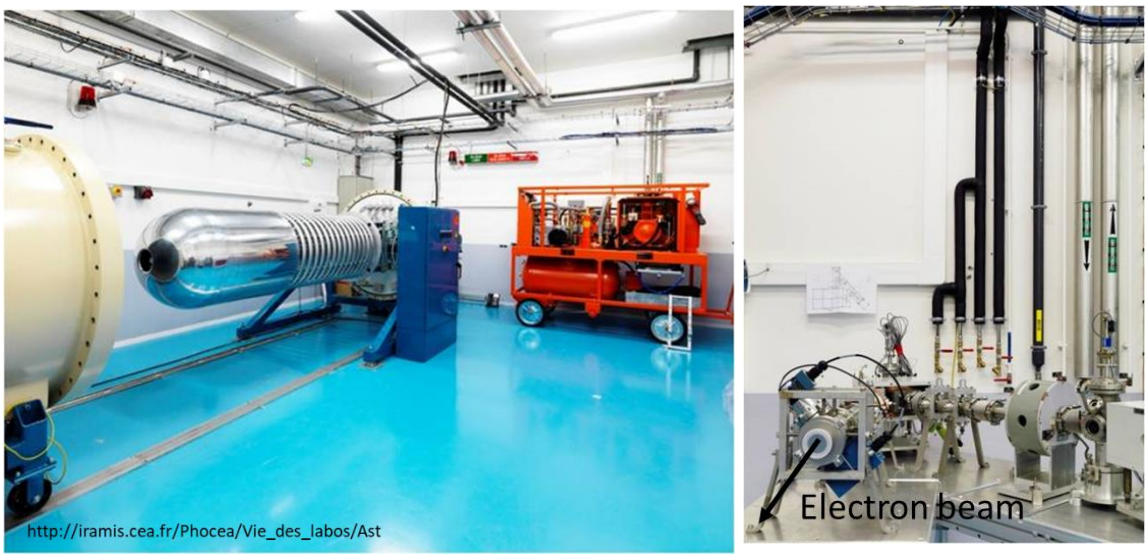

Fig. II-26 *View of SIRIUS platform facility, left: accelerator tank, right: irradiation beamline.*

At the exit of the accelerator, the high-energy electrons are directed to the irradiation cryostat for low temperature irradiation or vacuum chamber for room temperature irradiation

by mean of magnetic field. High vacuum is needed in the accelerator beam lines for stable electrons beam, typically lower than 10^{-7} Torr. Electron beamlines are presented in Fig. II-26. To isolate the beamline from the irradiation cryostat, a 25 µm stainless steel window is placed between. In this way, high vacuum is preserved in the beamline while the cryostat is pumped out with another rotary pump for removing and placing samples.

II.6.2.1 Room temperature irradiations cryostat

Since no in-situ characterizations are needed for solar cells irradiated at room temperature (no annealing is expected for these solar cells at room temperature), a small cryostat chamber was used for irradiation thanks to its simplicity and less time consuming for setting up. The samples were placed with kapton on a sample holder of 2 cm² total irradiated surface into a cryostat pressurized at 0.6 bar of helium. The samples were irradiated with 1 MeV electrons energy (Standard testing energy ECSS-E-ST-20-08C Rev.1 [71]) under an electron flux of 5.10^{11} $e.cm^{-2}.s^{-1}$. The solar cells were subjected to three different total fluences presented in Tab. II-6.

Tab. II-6 *Electron irradiation parameters at room and low temperature.*

Electrons energy	Flux ($e.cm^{-2}.s^{-1}$)	Total Fluence ($e.cm^{-2}$)		
1-MeV	5.10^{11}	1.10^{14}	3.10^{14}	1.10^{15}

II.6.2.2 Low temperature irradiation cryostat

As seen in sections I.3, the performance of solar cells can change drastically depending on their working environments like irradiance intensity and temperature. In addition, in-situ measurements are necessary to quantify the degradation of electrical performances after irradiation at low temperature since annealing can be present when heating up to room temperature and hence recovery of electrical performances. For these reasons, the large surface irradiated-cell [72] was used for low temperature irradiation that allows 4-wire electrical and optical parameters monitoring at such conditions, as presented in Fig. II-27.

The samples are mounted on a copper sample holder (see Fig. II-28) that is placed vertically inside the cryostat, which is equipped with two servomotors to control precisely the position of the irradiated surface, or characterized solar cells. The upper part of the large surface irradiated-cell is equipped with radiation-resistant window made of quartz glass that allows electrical and optical in-situ characterizations. Due to low temperature and vibration issue of the sample

holder during the irradiations and characterizations, some springs are used to maintain the solar cells in vertical position and to ensure proper the electrical contacts.

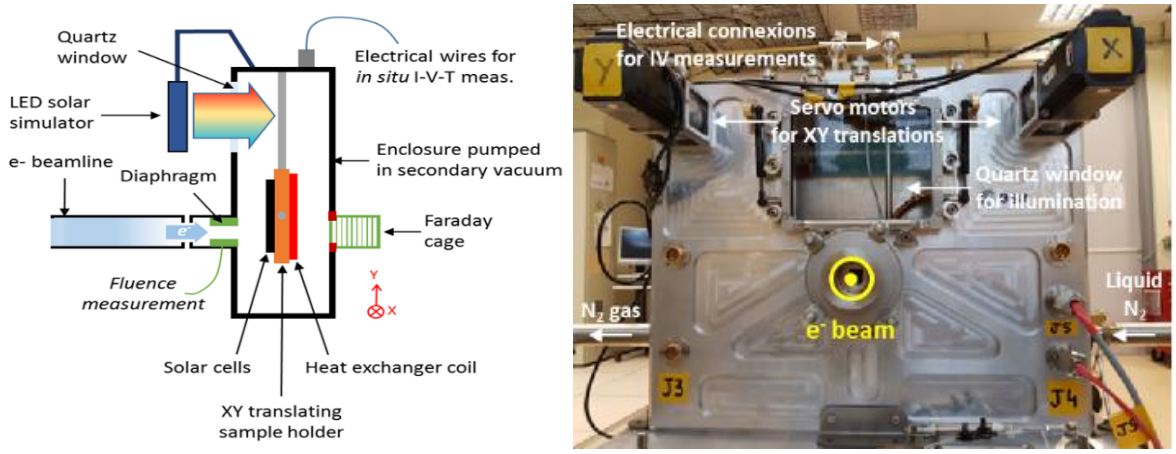

Fig. II-27 *Left: schematic representation of the large surface irradiated-chamber, right: real picture of the large surface irradiated-chamber.*

After characterizing the solar cells at low irradiance and room temperature conditions, solar cells are cooled down to 120 K by flowing liquid nitrogen in a coil welded at the back surface of the copper sample holder with integrated heating elements. Temperature is monitored on different part of the cryostat by means of four thermocouples. Three Cernox sensors measure temperatures at the entrance/middle/exhaust of liquid nitrogen to/in/from the cryostat. A Pt100 sensor is screwed at the middle of the sample holder to get the temperature of solar cells during experiments. Once temperature is stabilized at 120 K ± 3 K, the same characterizations as at low intensity and room temperature *LIRT* conditions are performed but in low intensity and low temperature *LILT* conditions.

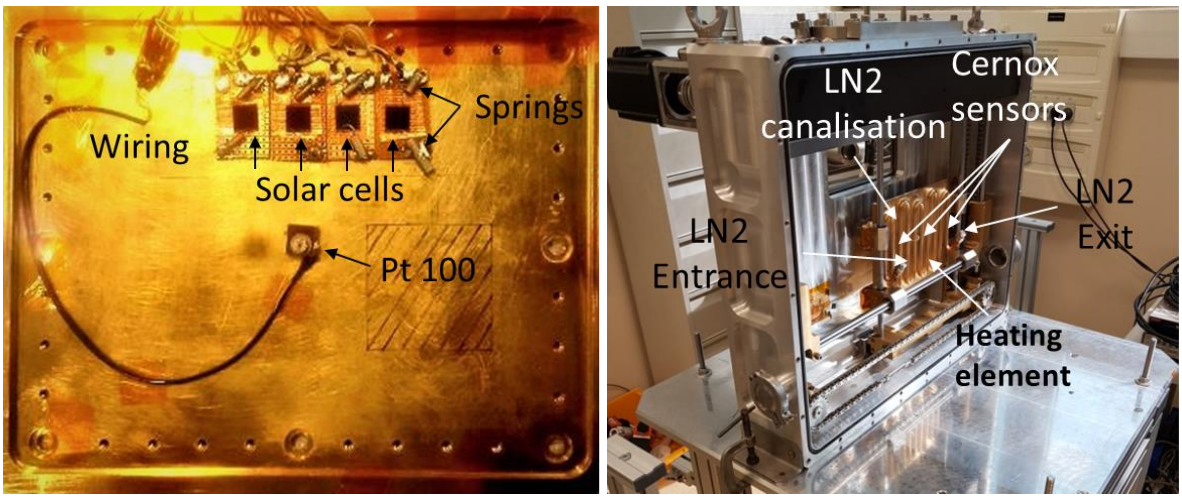

Fig. II-28 *Left: Picture of the copper sample holder with use of springs as electrical contact on solar cells, right: Inside view of the large surface irradiation chamber.*

The sample holder is moved to the lower part of the cryostat in such way the solar cells are placed in front of the beamline for the irradiation (see Fig. II-27). The large surface irradiation, typically 14 x 2.5 cm², is achieved by a translation of the sample holder in X- and Y-axis. The same irradiation parameters (i.e. flux and fluence) are used for low temperature irradiation and room temperature (see Tab. II-6).

As explained in section I.3, each space mission results in a specific operating environment for the solar cells. For telecommunication missions, the irradiation with a total fluence of 1.10^{15} $e.cm^{-2}$ corresponds to approximatively to the total fluence received at the solar cell level for 10 years in geostationary orbit (GEO). However, for deep space missions, e.g. JUICE mission, cells are exposed to larger fluences: a total around $1\text{-}3.10^{15}$ $e.cm^{-2}$ over the mission duration.

II.7 Conclusions

- III-V//Si tandem cells manufacturing process used in this study involves several steps: i) fabrication of the Si bottom cell, ii) growth of III-V top cells layers, iii) wafer bonding followed by III-V substrate removal and iv) deposition of metallization and anti-reflective coatings. This process involves many tools/facilities and expertise, thus the fabrication can take ~ 8 to 12 months (laboratory lead-time).
- III-V//Si tandem solar cells were developed prior to this PhD thesis for low concentration terrestrial application. Given the complexity of their fabrication process, and since this PhD research work was focusing on degradation mechanism, we have been using those non-space optimized III-V//Si cells with minor adaptations, to build comprehension and guide the design of future III-V//Si space cells.
- Within the set of available III-V//Si, a first screening of cells performances based on implied open circuit-voltage was carried out, to sort and select devices with best begin-of-life performances. In addition, the III-V//Si cells were also selected based on their Si wafer doping type (p-type are more radiation hard than n-type) and the wafer purity (FZ is more radiation hard than CZ). Thus, the set of cells used in this PhD thesis was defined according to their design and performances.
- The characterization of two-terminal multi-junction is complex; therefore, a detailed understanding of the characterization set-up and its limitations is necessary for a reliable measurement. This is crucial when comparative measurements made before and after irradiations.
- Two different solar simulators were used for current-voltage characterizations: i) *Helios 3030*, with a Xe flash, and ii) *Quesma*, with *LED* continuous illumination. For the first one, the spectrum and the intensity varies over time (flash discharge), therefore the use of calibrated reference solar cells and a spectrophotometer measurements are needed to identify the moment when the sub-cells reach the same irradiance intensity (reference and simulator spectrum match). For the second simulator, the continuous illumination offers a stable intensity and spectrum. However, a very labor intensive optimization was needed to get as close as possible to the AM0 reference spectrum; this simulator was used for in-situ (irradiation set-up) measurements.
- The accurate quantum efficiency measurement of one sub-cell requires the use of bias light and bias voltage to saturate the other sub-cells and bring the sub-cell under test in short-circuit condition.

- Two platforms were used to simulate the space radiation environment. Electron and proton irradiations were performed at SIRIUS and JANNUS Orsay facilities respectively with omnidirectional beam.
- In contrast to room temperature irradiation, solar cells irradiated at low temperature (e.g. 120 K) undergo a strong annealing effect when coming back to room temperature. Therefore, in-situ characterizations are necessary to monitor precisely the behavior of III-V//Si technology for typical deep space conditions.

II.8 References

[1] M. A. Green, E. D. Dunlop, D. H. Levi, J. Hohl-Ebinger, M. Yoshita, and A. W. Y. Ho-Baillie, "Solar cell efficiency tables (version 54)," *Prog. Photovolt. Res. Appl.*, vol. 27, no. 7, pp. 565–575, 2019, doi: 10.1002/pip.3171.

[2] M. A. Green, E. D. Dunlop, J. Hohl-Ebinger, M. Yoshita, N. Kopidakis, and A. W. Y. Ho-Baillie, "Solar cell efficiency tables (Version 55)," *Prog. Photovolt. Res. Appl.*, vol. 28, no. 1, pp. 3–15, 2020, doi: 10.1002/pip.3228.

[3] W. G. Pfann, "Temperature Gradient Zone Melting," *JOM*, vol. 7, no. 9, pp. 961–964, Sep. 1955, doi: 10.1007/BF03377594.

[4] J. Czochralski, "Ein neues Verfahren zur Messung der Kristallisationsgeschwindigkeit der Metalle," *Z. Für Phys. Chem.*, vol. 92U, no. 1, pp. 219–221, 1918, doi: 10.1515/zpch-1918-9212.

[5] K. Kakimoto, M. Eguchi, H. Watanabe, and T. Hibiya, "Direct observation by X-ray radiography of convection of molten silicon in the Czochralski growth method," *J. Cryst. Growth*, vol. 88, no. 3, pp. 365–370, May 1988, doi: 10.1016/0022-0248(88)90009-7.

[6] S. W. Glunz, S. Rein, W. Warta, J. Knobloch, and W. Wettling, "Degradation of carrier lifetime in Cz silicon solar cells," *Sol. Energy Mater. Sol. Cells*, vol. 65, no. 1, pp. 219–229, Jan. 2001, doi: 10.1016/S0927-0248(00)00098-2.

[7] L. Chen *et al.*, "Effect of oxygen precipitation on the performance of Czochralski silicon solar cells," *Sol. Energy Mater. Sol. Cells*, vol. 95, no. 11, pp. 3148–3151, Nov. 2011, doi: 10.1016/j.solmat.2011.06.044.

[8] D. C. Bobela, L. Gedvilas, M. Woodhouse, K. A. W. Horowitz, and P. A. Basore, "Economic competitiveness of III–V on silicon tandem one-sun photovoltaic solar modules in favorable future scenarios," *Prog. Photovolt. Res. Appl.*, vol. 25, no. 1, pp. 41–48, Jan. 2017, doi: 10.1002/pip.2808.

[9] M. Woodhouse and A. Goodrich, "Manufacturing cost analysis relevant to single-and dual-junction photovoltaic cells fabricated with III-Vs and III-Vs grown on Czochralski silicon (presentation)," National Renewable Energy Lab.(NREL), Golden, CO (United States), 2014.

[10] E. V. Vidal, "Fabrication, characterization and simulation of III-V on Si multi-junction solar cells," PhD thesis, Université Grenoble Alpes, 2018.

[11] A. Lanterne *et al.*, "Understanding of the annealing temperature impact on ion implanted bifacial n-type solar cells to reach 20.3% efficiency," *Prog. Photovolt. Res. Appl.*, vol. 23, no. 11, pp. 1458–1465, Nov. 2015, doi: 10.1002/pip.2574.

[12] L. Vauche *et al.*, "Silicon bottom subcell optimization for wafer-bonded III-V on Si multijunction solar cells," in *2018 IEEE 7th World Conference on Photovoltaic Energy Conversion (WCPEC) (A Joint Conference of 45th IEEE PVSC, 28th PVSEC 34th EU PVSEC)*, Jun. 2018, pp. 261–263, doi: 10.1109/PVSC.2018.8547745.

[13] R. Cariou *et al.*, "Monolithic Two-Terminal III–V//Si Triple-Junction Solar Cells With 30.2% Efficiency Under 1-Sun AM1.5g," *IEEE J. Photovolt.*, vol. 7, no. 1, pp. 367–373, Jan. 2017, doi: 10.1109/JPHOTOV.2016.2629840.

[14] A. Dobrich *et al.*, "New Efficiency Frontiers with Wafer-Bonded Multi-Junction Solar Cells.," *29th Eur. Photovolt. Sol. Energy Conf. Exhib.*, pp. 1975–1978, Nov. 2014, doi: 10.4229/EUPVSEC20142014-4CP.2.1.

[15] F. Dimroth *et al.*, "Wafer bonded four-junction GaInP/GaAs//GaInAsP/GaInAs concentrator solar cells with 44.7% efficiency," *Prog. Photovolt. Res. Appl.*, vol. 22, no. 3, pp. 277–282, 2014, doi: 10.1002/pip.2475.

[16] S. Heckelmann, D. Lackner, C. Karcher, F. Dimroth, and A. W. Bett, "Investigations on AlxGa1-xAs Solar Cells Grown by MOVPE," *IEEE J. Photovolt.*, vol. 5, no. 1, pp. 446–453, Jan. 2015, doi: 10.1109/JPHOTOV.2014.2367869.

[17] H. Ariza-Calderon, L. Tirado-Mejia, J. G. Mendoza-Alvarez, and G. Torres-Delgado, "Direct band gap determination in AlxGa1-xAs epitaxial layers in the indirect gap region 0.4 < x < 0.9," *Appl. Surf. Sci.*, vol. 123–124, pp. 513–516, Jan. 1998, doi: 10.1016/S0169-4332(97)00445-5.
[18] J. C. M. Henning, J. P. M. Amsems, and P. J. Roksnoer, "A photoluminescence study of the donor structure in AlxGa1-xAs," *Semicond. Sci. Technol.*, vol. 3, no. 4, pp. 361–364, Apr. 1988, doi: 10.1088/0268-1242/3/4/013.
[19] G. Oelgart, R. Schwabe, M. Heider, and B. Jacobs, "Photoluminescence of AlxGa1-xAs near the Γ-X crossover," *Semicond. Sci. Technol.*, vol. 2, no. 7, pp. 468–474, Jul. 1987, doi: 10.1088/0268-1242/2/7/015.
[20] N. Bouarissa, "Energy gaps and refractive indices of AlxGa1−xAs," *Mater. Chem. Phys.*, vol. 72, no. 3, pp. 387–394, Dec. 2001, doi: 10.1016/S0254-0584(01)00304-2.
[21] A. Baldereschi, K. Maschke, E. Hess, H. Neumann, K.-R. Schulze, and K. Unger, "Energy band structure of AlxGa1-xAs," *J. Phys. C Solid State Phys.*, vol. 10, no. 23, pp. 4709–4717, Dec. 1977, doi: 10.1088/0022-3719/10/23/007.
[22] K. Alberi, B. Fluegel, M. A. Steiner, R. France, W. Olavarria, and A. Mascarenhas, "Direct-indirect crossover in GaxIn1-xP alloys," *J. Appl. Phys.*, vol. 110, no. 11, p. 113701, Dec. 2011, doi: 10.1063/1.3663439.
[23] C. P. Kuo, S. K. Vong, R. M. Cohen, and G. B. Stringfellow, "Effect of mismatch strain on band gap in III-V semiconductors," *J. Appl. Phys.*, vol. 57, no. 12, pp. 5428–5432, Jun. 1985, doi: 10.1063/1.334817.
[24] A. Laugier and J. Chevallier, "About the band structure of GaxIn1−xP alloys," *Solid State Commun.*, vol. 10, no. 4, pp. 353–356, Feb. 1972, doi: 10.1016/0038-1098(72)90440-1.
[25] L. Vauche *et al.*, "Development-of-III-V-on-Si-Multijunction-Photovoltaics-by-Wafer-Bonding.pdf," *33rd Eur. Photovolt. Sol. Energy Conf. Exhib.*, pp. 1228–1231, 2017.
[26] L. Vauche *et al.*, "Wafer bonding approaches for III-V on Si multi-junction solar cells," in *2017 IEEE 44th Photovoltaic Specialist Conference (PVSC)*, Jun. 2017, pp. 2492–2497, doi: 10.1109/PVSC.2017.8366093.
[27] F. Shi, K.-L. Chang, J. Epple, C.-F. Xu, K. Y. Cheng, and K. C. Hsieh, "Characterization of GaAs-based n-n and p-n interface junctions prepared by direct wafer bonding," *J. Appl. Phys.*, vol. 92, no. 12, pp. 7544–7549, Nov. 2002, doi: 10.1063/1.1522484.
[28] Y. C. Zhou, Z. H. Zhu, D. Crouse, and Y. H. Lo, "Electrical properties of wafer-bonded GaAs/Si heterojunctions," *Appl. Phys. Lett.*, vol. 73, no. 16, pp. 2337–2339, Oct. 1998, doi: 10.1063/1.122454.
[29] M. M. R. Howlader, T. Watanabe, and T. Suga, "Investigation of the bonding strength and interface current of p-Si/n-GaAs wafers bonded by surface activated bonding at room temperature," *J. Vac. Sci. Technol. B Microelectron. Nanometer Struct. Process. Meas. Phenom.*, vol. 19, no. 6, pp. 2114–2118, Nov. 2001, doi: 10.1116/1.1414115.
[30] E. Veinberg-Vidal *et al.*, "Wafer-Bonded AlGaAs//Si Dual-Junction Solar Cells," in *2017 IEEE 44th Photovoltaic Specialist Conference (PVSC)*, Jun. 2017, pp. 2562–2565, doi: 10.1109/PVSC.2017.8366116.
[31] S. Essig and F. Dimroth, "Fast Atom Beam Activated Wafer Bonds between n-Si and n-GaAs with Low Resistance," *ECS J. Solid State Sci. Technol.*, vol. 2, no. 9, p. Q178, Jul. 2013, doi: 10.1149/2.031309jss.
[32] T. Yu, M. R. Howlader, F. Zhang, and M. Bakr, "Nanobonding for Multi-Junction Solar Cells at Room Temperature," *ECS Trans.*, vol. 35, no. 2, p. 3, Apr. 2011, doi: 10.1149/1.3568842.
[33] T. R. Chung, L. Yang, N. Hosoda, and T. Suga, "Room temperature GaAs-Si and InP-Si wafer direct bonding by the surface activated bonding method," *Nucl. Instrum. Methods*

Phys. Res. Sect. B Beam Interact. Mater. At., vol. 121, no. 1–4, pp. 203–206, 1997, doi: 10.1016/S0168-583X(96)00546-0.
[34] H. Takagi, K. Kikuchi, R. Maeda, T. R. Chung, and T. Suga, "Surface activated bonding of silicon wafers at room temperature," *Appl. Phys. Lett.*, vol. 68, no. 16, pp. 2222–2224, Apr. 1996, doi: 10.1063/1.115865.
[35] M. J. Kerr, A. Cuevas, and R. A. Sinton, "Generalized analysis of quasi-steady-state and transient decay open circuit voltage measurements," *J. Appl. Phys.*, vol. 91, no. 1, pp. 399–404, Dec. 2001, doi: 10.1063/1.1416134.
[36] R. A. Sinton and A. Cuevas, "A quasi-steady-state open-circuit voltage method for solar cell characterization," 2000.
[37] H. Matsuura *et al.*, "Si Substrate Suitable for Radiation-Resistant Space Solar Cells," *Jpn. J. Appl. Phys.*, vol. 45, no. 4R, p. 2648, Apr. 2006, doi: 10.1143/JJAP.45.2648.
[38] M. Yamaguchi *et al.*, "Deep level analysis of radiation-induced defects in Si crystals and solar cells," *J. Appl. Phys.*, vol. 86, no. 1, pp. 217–223, Jun. 1999, doi: 10.1063/1.370698.
[39] D. J. Curtin and R. L. Statler, "Review of Radiation Damage to Silicon Solar Cells," *IEEE Trans. Aerosp. Electron. Syst.*, vol. AES-11, no. 4, pp. 499–513, Jul. 1975, doi: 10.1109/TAES.1975.308112.
[40] C. A. Gueymard, "Revised composite extraterrestrial spectrum based on recent solar irradiance observations," *Sol. Energy*, vol. 169, pp. 434–440, Jul. 2018, doi: 10.1016/j.solener.2018.04.067.
[41] C. Baur, I. Kröger, S. Winter, F. Witt, V. Pichetto, and E. Rapp, "Comparison of primary high altitude and synthetic calibration methods of solar cells for space applications in view of an updated AM0 spectrum," in *2018 IEEE 7th World Conference on Photovoltaic Energy Conversion (WCPEC)(A Joint Conference of 45th IEEE PVSC, 28th PVSEC & 34th EU PVSEC)*, 2018, pp. 1570–1575.
[42] P. García-Linares, C. Domínguez, P. Voarino, P. Besson, and M. Baudrit, "Effect of the encapsulant temperature on the angular and spectral response of multi-junction solar cells," in *2014 IEEE 40th Photovoltaic Specialist Conference (PVSC)*, Jun. 2014, pp. 3298–3303, doi: 10.1109/PVSC.2014.6925640.
[43] C. Domínguez and P. García-Linares, "Characterization of Multijunction Concentrator Solar Cells," in *High Concentrator Photovoltaics*, P. Pérez-Higueras and E. F. Fernández, Eds. Cham: Springer International Publishing, 2015, pp. 39–84.
[44] E. F. Fernández, A. J. García-Loureiro, and G. P. Smestad, "Multijunction Concentrator Solar Cells: Analysis and Fundamentals," in *High Concentrator Photovoltaics*, P. Pérez-Higueras and E. F. Fernández, Eds. Cham: Springer International Publishing, 2015, pp. 9–37.
[45] M. Meusel, C. Baur, G. Létay, A. W. Bett, W. Warta, and E. Fernandez, "Spectral response measurements of monolithic GaInP/Ga(In)As/Ge triple-junction solar cells: Measurement artifacts and their explanation," *Prog. Photovolt. Res. Appl.*, vol. 11, no. 8, pp. 499–514, 2003, doi: 10.1002/pip.514.
[46] C. Domínguez, R. Herrero, and I. Antón, "Characterization of CPV Modules and Receivers," in *Handbook of Concentrator Photovoltaic Technology*, John Wiley & Sons, Ltd, 2016, pp. 639–684.
[47] C. Domínguez, I. Antón, and G. Sala, "Solar simulator for concentrator photovoltaic systems," *Opt. Express*, vol. 16, no. 19, pp. 14894–14901, Sep. 2008, doi: 10.1364/oe.16.014894.
[48] P. Besson, "Compréhension des comportements électrique et optique des modules photovoltaïques à haute concentration, et développement d'outils de caractérisations adaptés," PhD Thesis, Université de Lyon, 2016.
[49] A. W. Bett, G. Siefer, S. P. Philipps, T. Missbach, and J. Jaus, "Spectral measurements using component cells: Examinations on measurement precision," in *Proceedings of the 26th*

European Photovoltaic Solar Energy Conference and Exhibition, 2011, pp. 176–181, doi: 10.4229/26thEUPVSEC2011-1BO.12.5.
[50] E44 Committee, "Test Methods for Measurement of Electrical Performance and Spectral Response of Nonconcentrator Multijunction Photovoltaic Cells and Modules," ASTM International. doi: 10.1520/E2236-10R19.
[51] C. Domínguez, I. Antón, G. Sala, and S. Askins, "Current-matching estimation for multijunction cells within a CPV module by means of component cells," *Prog. Photovolt. Res. Appl.*, vol. 21, no. 7, pp. 1478–1488, 2013, doi: 10.1002/pip.2227.
[52] E44 Committee, "Specification for Solar Simulation for Photovoltaic Testing," ASTM International. doi: 10.1520/E0927-10.
[53] M. Pravettoni, A. Virtuani, K. Keller, M. Apolloni, and H. Müllejans, "Spectral mismatch effect to the open-circuit voltage in the indoor characterization of multi-junction thin-film photovoltaic modules," in *2013 IEEE 39th Photovoltaic Specialists Conference (PVSC)*, Jun. 2013, pp. 0706–0711, doi: 10.1109/PVSC.2013.6744249.
[54] K. Emery, D. Myers, and S. Rummel, "Solar simulation-problems and solutions," in *Conference Record of the Twentieth IEEE Photovoltaic Specialists Conference*, 1988, pp. 1087–1091 vol.2, doi: 10.1109/PVSC.1988.105873.
[55] N. Jost *et al.*, "From component to multi-junction solar cells for spectral monitoring," *AIP Conf. Proc.*, vol. 2012, no. 1, p. 100002, Sep. 2018, doi: 10.1063/1.5053546.
[56] F. J. Vorster and E. E. van Dyk, "High saturation solar light beam induced current scanning of solar cells," *Rev. Sci. Instrum.*, vol. 78, no. 1, p. 013904, Jan. 2007, doi: 10.1063/1.2432408.
[57] G. E. Bunea, K. E. Wilson, Y. Meydbray, M. P. Campbell, and D. M. D. Ceuster, "Low Light Performance of Mono-Crystalline Silicon Solar Cells," in *2006 IEEE 4th World Conference on Photovoltaic Energy Conference*, May 2006, vol. 2, pp. 1312–1314, doi: 10.1109/WCPEC.2006.279655.
[58] N. H. Reich *et al.*, "Crystalline silicon cell performance at low light intensities," *Sol. Energy Mater. Sol. Cells*, vol. 93, no. 9, pp. 1471–1481, Sep. 2009, doi: 10.1016/j.solmat.2009.03.018.
[59] R. W. Lof, "Weak Light Performance and Spectral Response of Different Solar Cell Types," in *20. European Photovoltaic Solar Energy Conference and Exhibition*, 2005, pp. 2120–2123.
[60] A. Halm, P. Hering, C. Comparotto, L. J. Koduvelikulathu, and R. Kopecek, "Low light intensity performance of n-and p-type silicon solar cells with different architectures," presented at the EU-PVSEC, 2011.
[61] K. Rühle, M. K. Juhl, M. D. Abbott, and M. Kasemann, "Evaluating Crystalline Silicon Solar Cells at Low Light Intensities Using Intensity-Dependent Analysis of I-V Parameters," *IEEE J. Photovolt.*, vol. 5, no. 3, pp. 926–931, May 2015, doi: 10.1109/JPHOTOV.2015.2395145.
[62] F. Oviedo, Z. Liu, Z. Ren, M. Thway, T. Buonassisi, and I. M. Peters, "Ohmic shunts in two-terminal dual-junction solar cells with current mismatch," *Jpn. J. Appl. Phys.*, vol. 56, no. 8S2, p. 08MA05, Jul. 2017, doi: 10.7567/JJAP.56.08MA05.
[63] C. Domínguez, I. Antón, and G. Sala, "Multijunction solar cell model for translating I–V characteristics as a function of irradiance, spectrum, and cell temperature," *Prog. Photovolt. Res. Appl.*, vol. 18, no. 4, pp. 272–284, 2010, doi: 10.1002/pip.965.
[64] A. Gentils and C. Cabet, "Investigating radiation damage in nuclear energy materials using JANNuS multiple ion beams," *Nucl. Instrum. Methods Phys. Res. Sect. B Beam Interact. Mater. At.*, vol. 447, pp. 107–112, May 2019, doi: 10.1016/j.nimb.2019.03.039.

[65] C.-O. Bacri *et al.*, “SCALP, a platform dedicated to material modifications and characterization under ion beam,” *Nucl. Instrum. Methods Phys. Res. Sect. B Beam Interact. Mater. At.*, vol. 406, pp. 48–52, Sep. 2017, doi: 10.1016/j.nimb.2017.03.036.
[66] N. Chauvin *et al.*, “Optics calculations and beam line design for the JANNuS facility in Orsay,” *Nucl. Instrum. Methods Phys. Res. Sect. B Beam Interact. Mater. At.*, vol. 261, no. 1, pp. 34–39, Aug. 2007, doi: 10.1016/j.nimb.2007.04.295.
[67] P. Trocellier *et al.*, “Application of multi-irradiation facilities,” *Nucl. Instrum. Methods Phys. Res. Sect. B Beam Interact. Mater. At.*, vol. 266, no. 12, pp. 3178–3181, Jun. 2008, doi: 10.1016/j.nimb.2008.03.224.
[68] Y. Serruys *et al.*, “JANNUS: experimental validation at the scale of atomic modelling,” *Comptes Rendus Phys.*, vol. 9, no. 3, pp. 437–444, Apr. 2008, doi: 10.1016/j.crhy.2007.10.015.
[69] R. G. Herb, “Pelletron accelerators for very high voltage,” *Nucl. Instrum. Methods*, vol. 122, pp. 267–276, Nov. 1974, doi: 10.1016/0029-554X(74)90487-X.
[70] R. J. Van de Graaff, K. T. Compton, and L. C. Van Atta, “The Electrostatic Production of High Voltage for Nuclear Investigations,” *Phys. Rev.*, vol. 43, no. 3, pp. 149–157, Feb. 1933, doi: 10.1103/PhysRev.43.149.
[71] *DIN EN 16603-10-12 - Space engineering - Method for the calculation of radiation received and its effects, and a policy for design margins; English version EN 16603-10-12:2014 | Engineering360*. .
[72] J. Lefèvre, P. L. Houedec, J. Losco, O. Cavani, and B. Boizot, “Dedicated Tool for Irradiation and Electrical Measurement of Large Surface Samples on the Beamline of a 2.5 Mev Pelletron Electron Accelerator: Application to Solar Cells,” *E3S Web Conf.*, vol. 16, p. 16003, 2017, doi: 10.1051/e3sconf/20171616003.

CHAPTER III Investigation of III-V//Si radiation hardness in near Earth conditions

III.1 Introduction

We have seen in section I.3 the characteristics of the space environment in which solar cells operate on board of satellites. We have also discussed the classical degradation mechanisms of solar cells in relation to radiation. In this chapter, we focus on near-earth environmental conditions (namely the LEO, MEO and GEO orbits). The charged particles spectrum (flux and energy) and thermal cycling profile can be very different in those orbits. However, the solar cells at operating condition, i.e. facing the sun, in these orbits are facing 1 AM0 spectrum and temperature reaching 60 °C.

To study the behavior of III-V//Si exposed to 1 MeV electrons irradiations, we have performed three main characterizations: current-voltage, quantum efficiency and electroluminescence. The global behavior as well as the study of the evolution of the electrical parameters of solar cells whether single junction or in tandem configuration, has been studied by the current-voltage characteristic curves. With these measurements, it is possible to track which solar cell parameters are driving the performances degradation. In a second step, solar cells spectral response was used to study the behavior of each sub-cell separately and gain more detailed information. This measurement allowed us to identify bulk degradation in each sub-cell, related to minority carriers life-time degradation. By coupling physical models and such experimental measurements of the internal quantum efficiency, we were able to calculate the evolution of the lifetime of the Si cell/sub-cell in the three architectures and compare these values with the literature. In a third step, electroluminescence measurements were carried out for the reconstruction of the current-voltage characteristic curves of each sub-cell constituting the tandem cells (2J and 3J) by means of the optoelectronic reciprocity [1]. These measurements provided access to the voltage of each sub-cell separately and thus allow to quantify the contribution of each sub-cell to the total degradation of the tandem solar cells. Finally, irradiations with 1 MeV protons were performed on the three solar cells architectures. Since the penetration depth of ions is much smaller than that of electrons, SRIM simulations were carried out on the three architectures to identify the stopping depths as well as the energies deposited in each sub-cell. The behavior of these solar cells was monitored as a function of the irradiation fluence with current-voltage and quantum efficiency measurements. By monitoring the degradation as a function of the deposited energy (function of the Non Ionizing Energy Loss *NIEL*), it is possible to compare the degradation of the solar cells electrical parameters as a function of particle type (electrons and protons). This approach is called the Displacement Damage Dose (*DDD*) and was proposed by the Naval Research Laboratory (NRL) [2].

III.2 Electron Irradiations

III.2.1. Interaction of electron flux with solar cells

As explained in section I.4, as the electrons pass through the solar cell, they give up their energy mainly by ionization and by atomic displacement until they stop into the material layer or they exit by the other side. The penetration profile of 1 MeV electrons was simulated using Penelope2014 software [3] in the case of 1J, 2J and 3J, results are shown in Fig. III-1. Due to the electrons low mass (2000 time lighter than protons) they deflect when colliding with the electrons of the target material, even at an energy of 1 MeV. Thus, the path of an electron in the material consists of a large number of changes of direction, this is clearly visible in thick materials as this is the case for the Si substrates used here (525 µm).

In order to estimate the penetration depth as well as the energy absorbed by each layer of the solar cell, calculations were performed using the stopping power and range tables from the Stopping Powers and Ranges for Electrons (*ESTAR)* database[23]. This database contains the stopping powers and ranges of electrons in all the elements of the periodic table. However, for alloys, such as III-V materials used for top and top/middle sub-cell, first, the threshold energy and mean excitation energy are calculated on the base of weight fraction and density of the target material; then stopping power and electrons range are calculated for the specific material properties. It is important to note that doping does not change the threshold energies and thus the deposited energy, given the low dopant atoms concentration (~ 10^{16} – 10^{19} at./cm^3) relative to the semiconductor matrix elements (~ 10^{22} at./cm^3). The range of electron defined as the average value of depth traveled by electrons down to rest is very important, ~ 2 mm for 1 MeV electrons in c-Si, compared to the thicknesses of solar cells in general and those considered in this study (525 - 530 µm). Significant amount of energy is transmitted through the solar cell device, with roughly 0.812 MeV, 0.810 MeV and 0.810 MeV for the 1J, 2J and 3J respectively (see Fig. III-1). The deposited energy is distributed homogeneously in the depth of the solar cell according to the physical properties of each layer, i.e. threshold energy. The deposited energy in the III-V top cells layers represent 0.14% and 0.23% for 2J and 3J respectively. The difference in absorbed energy by the 2J top sub-cell ($Al_{0.22}GaAs$) and the 3J middle sub-cell ($Al_{0.03}GaAs$) lies mainly in the thickness and density of the two sub-cells. The higher thickness and higher density in the case of 3J induce a greater deposited energy. Whereas on the other hand, the deposited energy for Si cells/sub-cell in all architectures represents ~ 18.8% of the

[23] ESTAR : https://dx.doi.org/10.18434/T4NC7P

total energy, in relation with its important thickness. Consequently, the electrons introduced defect rate is logically higher in Si than in the III-V materials constituting the upper sub-cells.

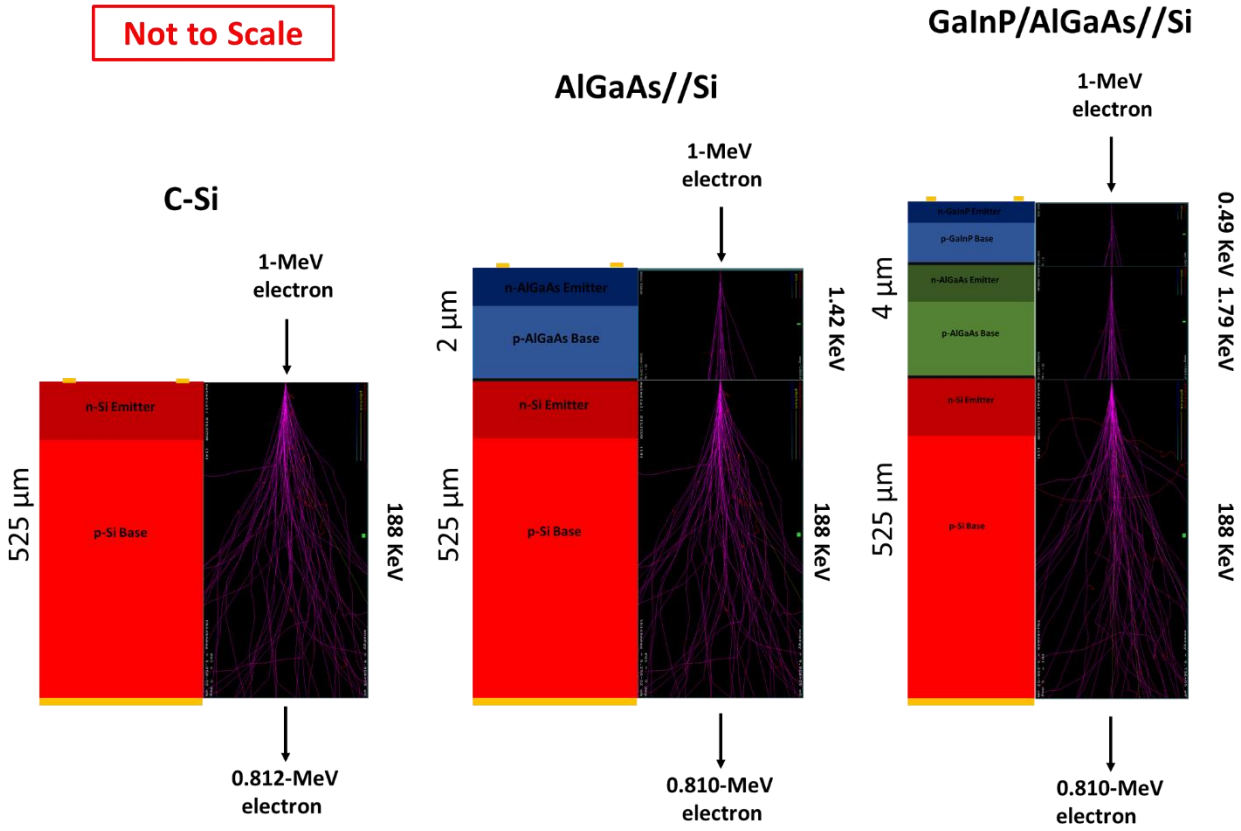

Fig. III-1 *Calculation of deposited energies for 1 MeV electron beam in the layers of different solar cell architectures, using ESTAR database. (left) 1J c-Si (Middle) 2J AlGaAs//Si and (right) 3J GaInP/AlGaAs//Si; the electrons penetration profiles in solar cells were simulated by Penelope2014.*

III.2.2. Spatial electroluminescence

In a first approach, an investigation of spatial ElectroLuminescence, (*EL*), was carried out on the solar cells before and after irradiation. The objective of this characterization was on one hand the identification of the most efficient solar cells: no/little shunt defects, cracks or broken fingers; and on the other hand, the spatial resolution of *EL* was also useful to check the absence of punctual defects due to electrons irradiation.

The principle of electroluminescence is simple, and somewhat opposite of the photovoltaic effect: by injecting a current at the contacting points of the solar cell, the electrons recombine with the holes in the p-n junction. Among the various recombination mechanisms possible, the direct transition from the conduction band to the valence band (radiative recombination), which emits a radiation of an energy equal to the bandgap energy, is the one responsible for the *EL* signal. With a high-resolution camera placed above the sample, it is possible to map the

intensity of this *EL* signal over the cell area and thus evaluate the quality of the cell. Indeed, the more defective semiconductor area will appear less bright or even black (no radiative recombination), and at the opposite, shunts will translate into very bright spots.

Results on spatial *EL* of the triple-junction GaInP/AlGaAs//Si and dual-junction AlGaAs//Si before and after 1-MeV 10^{15} e.cm^{-2} irradiation are presented in Fig. III-2. The two cells dimension are 1 x 1 cm², with an injected current equal to the short circuit current at *BOL*, i.e. 14 mA.cm^{-2} and 10 mA.cm^{-2} for 2J and 3J, respectively. Measurements with optical filters (long- and low-pass) were performed to analyze the *EL* signal of each sub-cell independently [4]. It should be noted that silicon with its indirect bandgap has a low radiative recombination and therefore a low *EL* signal close to its bandgap. However, for our set of cells, no additional valuable information was obtained compared to an unfiltered image, therefore only *EL* image with unfiltered light are presented. The emitting light correspond to mainly AlGaAs top cells and the combination of GaInP and AlGaAs for the 2J and 3J respectively.

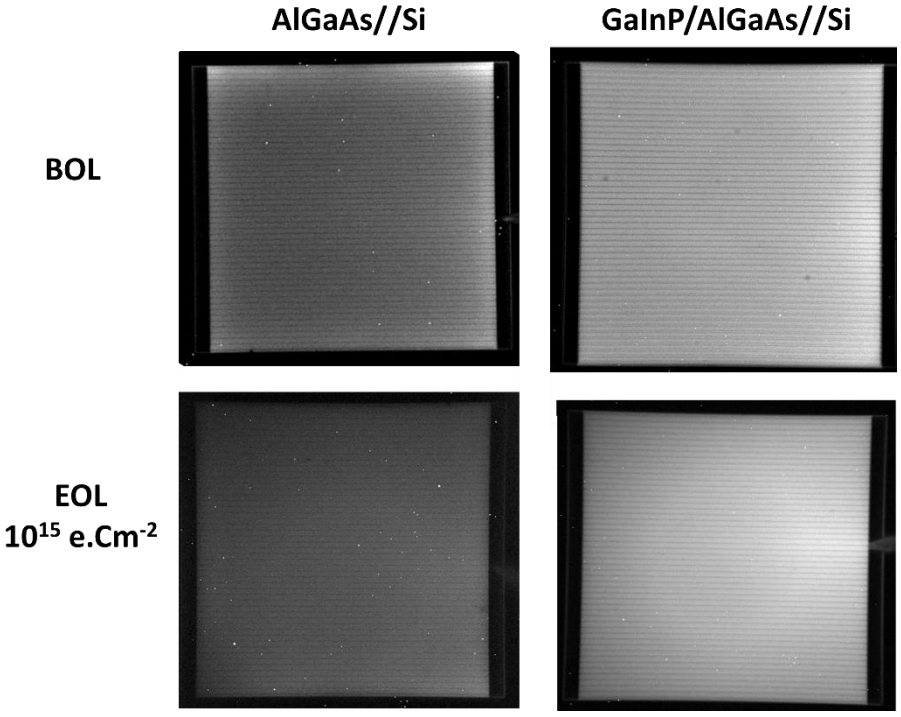

Fig. III-2 *Spatial electroluminescence characterizations of 1 x 1 cm² 2J AlGaAs//Si and 3J GaInP/AlGaAs//Si before and after irradiation at a fluence of 10^{15} e.cm^{-2}.*

In both cases, at *BOL* the solar cells do not have any manufacturing defects such as micro cracks in fingers or in the cell (see Fig. III-2 top). However, in the case of the 3J some black spots near the fingers are noticed which may be the result of surface defects. After irradiation, the luminescence is homogeneous over the entire surface of the irradiated cells and therefore

one can conclude that the degradation is uniform over the entire surface. A second technique that consists in measuring the spectral composition of the solar cell emission. This technique requires the use of a spectrophotometer and allows to follow the evolution of the illumination intensity as a function of the irradiation. The advantage of this technique is to be able to separate the behavior of each sub-cell; more details will be discussed later in section III.2.6.

III.2.3. Current-voltage characterization

The current-voltage characterization allows the determination of the global behavior of a solar cell. Two types of *I-V* characterizations have been carried out: under illumination and in dark conditions. In a first instance, the monitoring of electrical parameters at their operating conditions (light *I-V*) is done as a function of electron irradiation; and in a second step, the diode characteristics evolution is analyzed by comparing the dark *I-V* curves.

III.2.3.1 Light *I-V*

The solar cells were characterized before and after irradiation at an AM0 spectrum with a total irradiance intensity of 1367 $W.m^{-2}$ and at a temperature of 300 K. As explained before (see section I.2), the current-voltage curves reveal the overall behavior of a solar cell, thus giving access to the key electrical parameters of a solar cell, namely the short-circuit current density J_{SC}, the open circuit voltage V_{OC} and the fill factor FF and efficiency.

In section II.5.1, the results of the characterization of the *Helios 3030* solar simulator were discussed. A low spatial inhomogeneity (< 2%) was calculated for the irradiance intensity at the test surface, with also a good repeatability over time (> 98%). The same measurement parameters, conditions and configuration were used for all measurements in order to reduce the experimental-related errors. For instance, the calculated error for the J_{SC} (most sensitive to the illumination intensity) is less than 2% due to spatial and temporal inhomogeneities.

The current-voltage and power-voltage characterization results for the six c-Si solar cells are shown in Fig. III-3, see section II.2 for more details on solar cells architectures. Two different cell sizes were used, 2 x 1 cm^2 (dashed lines) and 1 x 1 cm^2 (solid lines). It should be noted that the color code is generally respected throughout this chapter; **Black** at *BOL*, **Red**, **Blue** and **Green** for fluence of 10^{14} $e.cm^{-2}$, 3.10^{14} $e.cm^{-2}$ and 10^{15} $e.cm^{-2}$. However, when comparing the different architectures (1J, 2J and 3J) in the same plot the color code is **Blue**, **Red** and **Black** for 1J, 2J and 3J.

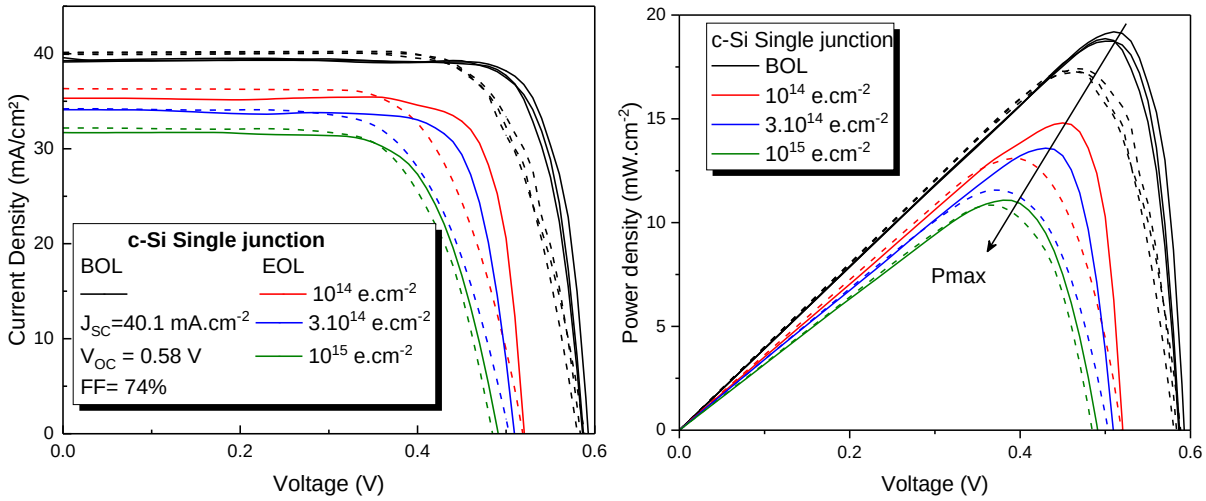

Fig. III-3 *Characterization of six solar c-Si cells with two different sizes, 2 x 1 cm² (black dashed lines) and 1 x 1 cm² (black solid lines), at BOL and EOL (solid and dashed colored lines) under 1367 W.m^{-2} AM0 spectrum and 300 K. Left: current voltage characteristics, right: Power-voltage characteristics.*

Before Irradiation (black curves), some differences are observed between the two groups (size) of solar cells. The largest solar cells have a J_{SC} around 40.1 mA.cm^{-2} while the smaller cells have a J_{SC} of 39.4 mA.cm^{-2}. This is a small difference (~ 1.8%), but this is systematically and clearly noticeable for the larger cells compared to the smaller one. In addition, it is clear that the large cells have a higher series resistance compared to the smaller one, which affects and reduces their FF. In the case of 2 x 1 cm² and 1 x 1 cm² cells, the FF is 74% and 82% respectively. These two differences result in difference in the output maximum power (see Fig. III-3). This deviation is at the origin of difference of fingers density on both solar cells, i.e. higher density is presents on 1 x 1 cm² compare to 2 x 1 cm^2. On the one hand the high density induces a decrease of the J_{SC} and on the other hand reduces the series resistance and thus increases the FF. However, a small deviation of J_{SC}, V_{OC} and FF is calculated within each group of solar cells and is less than 1%. The electrical parameters at beginning of life of the two solar cells sizes are shown in Tab. III-1. A comparison to the Azur Space silicon solar cells S32[24] is given in Tab. III-1. The cell base material is a 130 µm p-Type CZ <100> with TiO_x/Al_2O_3 *ARC*. This cell presents a higher efficiency compare to the cells used in this study. This difference is due to higher J_{SC} (by ~5 mA.cm^{-2}) and V_{OC} (45 mV) due to better doping profile and efficient *ARC* and a passivated surfaces.

The cells were divided into three groups, each group corresponding to a given irradiation fluence (10^{14}, 3.10^{14} and 10^{15} e.cm^{-2}). Due to the difference in the electrical parameters

[24] http://www.azurspace.com/index.php/en/products/products-space/space-solar-cells

especially the fill factor between large and small solar cells, each irradiation group contained one large and one small solar cell.

Tab. III-1 *Average electrical parameters for three 2x1 cm² solar cells and three 1x1 cm² solar cells at BOL, as characterized under AM0 spectrum and 300 K.*

c-Si solar cells	J_{SC} (mA.cm^{-2})	V_{OC} (V)	FF (%)	Efficiency (%)
2 x 1 cm²	40.1 ± 0.3%	0.583 ± 0.8%	73.8 ± 0.9%	12.7 ± 0.4%
1 x 1 cm²	39.4 ± 0.4%	0.587 ± 0.8%	81.8 ± 0.3%	13.9 ± 1%
AzurSpace Silicon S32	45.8 ± 1.5%	0.628 ± 1.5%	79.7 ± 1.5%	16.9± 1.5%

After irradiation, the current-voltage characterizations were performed according to the same experimental protocol, i.e. same parameters, conditions, solar cells emplacement at the test surface in order to reduce experimental errors due to spatial inhomogeneity. The *I-V* results are presented in Fig. III-3 (solid and dashed colored lines). A typical behavior is observed after irradiation, i.e. no anomaly in the post-irradiation response of solar cells such as a high series resistance or a low shunt resistance are detected; for the moderate dose, 10^{14} e.cm^{-2}, the FF remains stable in the two group of cells. A moderate degradation is observed in the electrical properties after irradiation with a shift of the maximal power point coordinates towards lower voltage and current (see Fig. III-3 right).

Tab. III-2 *Electrical parameters of c-Si after 1-MeV electrons irradiation at three different fluences.*

1-MeV electron fluence (e.cm^{-2})	**c-Si solar cells**	**J_{SC} (mA.cm^{-2})**	**V_{OC} (V)**	**FF (%)**	**Efficiency (%)**
10^{14}	2 x 1 cm²	36.4	0.519	68	9.4
	1 x 1 cm²	35.1	0.519	80.8	10.9
3.10^{14}	2 x 1 cm²	34	0.503	67	8.4
	1 x 1 cm²	34.1	0.509	78	9.9
10^{15}	2 x 1 cm²	32.2	0.483	70	7.9
	1 x 1 cm²	31.8	0.490	70	8
Reported by Azur Space @ 10^{15}	23.6 cm²	38.9	0.559	79	12.5

This degradation is correlated to the irradiation fluence, in relation with the increased defect density. Because of differences observed between the 1 x 1 cm² and 2 x 1 cm² cells at *BOL*, it results in differences at *EOL* between the two group of cell. The electrical parameters (J_{SC}, V_{OC}, FF and efficiency) after irradiation are summarized in Tab. III-2, with comparison to Azur Space Si solar cell after 1-MeV irradiation at 10^{15} e.cm^{-2}. As expected Azur Space cells have higher electrical performances than the cells irradiated in this study. It should be noted that this cell are commercial product and well optimized as opposed to the cell used in this study, which are under development.

Similar to the single-junction c-Si cells, the 2J tandem solar cells AlGaAs//Si were characterized under AM0 with an intensity of 1367 W/m² and at 300 K. Fig. III-4 illustrates the behavior (current- and power-voltage) of six 1x1 cm² solar cells at *BOL* (black lines). Identical behavior and performances are measured for the six samples with J_{SC} of 14.8 mA.cm^{-2} and V_{OC} of 1.78 V. The calculated deviation is less than 1% for all electrical parameters (low statistical dispersion). The averages of the electrical parameters are presented in Tab. III-3. A low shunt resistance is observed in the behavior of the 2J at *BOL* responsible of a slope in the voltage range 0 - 1.5 V. This leads to relatively low FF values and therefore to relatively low efficiencies.

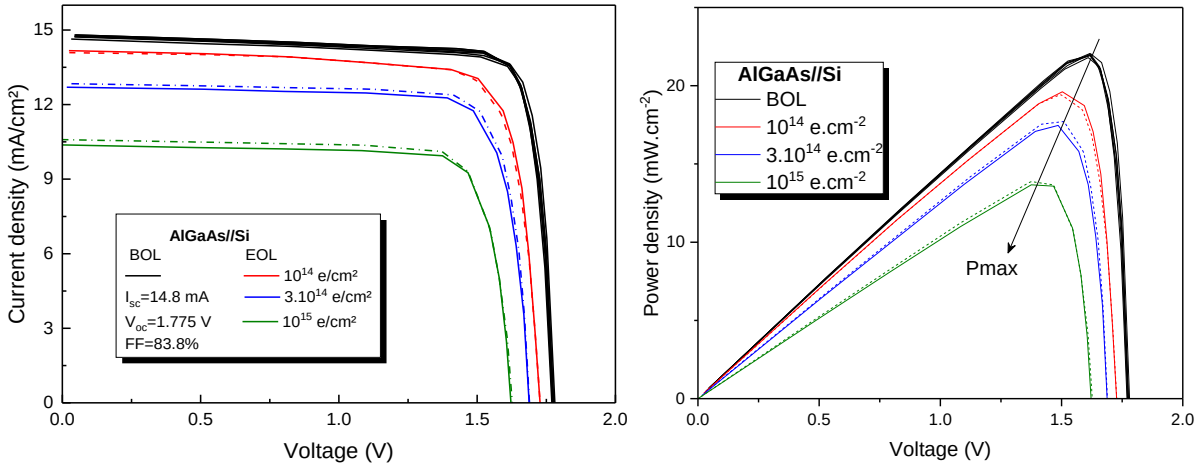

Fig. III-4 *Characterization of six 2J: AlGaAs//Si solar cells at BOL (solid black lines) and EOL under 1367 W.m^{-2} AM0 spectrum and 300 K (solid and dash colored lines). Left: current-voltage, right: power-voltage.*

The same experimental protocol was used: following *BOL* characterizations, measurements were performed after irradiation with 1-MeV electrons at three different fluences. The results are shown in Fig. III-4 (solid and dashed colored lines). A moderate (8.4%) degradation is observed for the V_{OC}, which is reduced from 1.78 V to 1.63 V at the

highest fluence (10^{15} e.cm^{-2}). Whereas in the case of the J_{SC}, a more pronounced degradation is observed: it drops to 10.5 mA.cm^{-2} at 10^{15} e.cm^{-2} and the effect of the low shunt resistance is less pronounced in the case of cells irradiated at a fluence higher than 3.10^{14} e.cm^{-2}. The same behavior is observed for each two solar cells irradiated at the same fluence (low statistical dispersion). The electrical parameters after irradiation are presented in the Tab. III-3.

Tab. III-3 *Average electrical parameters of six 2J: AlGaAs//Si solar cells of 1 x 1 cm² sizes at BOL and EOL characterized under AM0 spectrum and 300 K.*

Solar cells AlGaAs//Si	**J_{SC} (mA.cm^{-2})**	**V_{OC} (V)**	**FF (%)**	**Efficiency (%)**
BOL	14.8 ± 0.6%	1.78 ± 0.2%	83.7 ± 0.4%	16.1 ± 0.7%
***EOL* 10^{14} e.cm^{-2}**	14.1 ± 0.3%	1.74 ± 0.1%	80 ± 0.3%	14.3 ± 0.3%
***EOL* 3.10^{14} e.cm^{-2}**	12.8 ± 0.5%	1.69 ± 0.05%	82 ± 0.2%	12.9 ± 0.6%
***EOL* 10^{15} e.cm^{-2}**	10.5 ± 1%	1.63 ± 0.2%	81 ± 0.5%	10.1 ± 0.8%

Six 1 x 1 cm² 3J GaInP/AlGaAs//Si solar cells were used to study the evolution of the electrical parameters as a function of the irradiation fluence. Current- and power-voltage characterizations were performed at Normal Irradiance and Room Temperature (*NIRT*) conditions, results are shown Fig. III-5. Before irradiation (black lines), all six solar cells have the same electrical performances of 10.2 mA.cm^{-2} and 2.88 V for J_{SC} and V_{OC} respectively with 0.5% deviation on J_{SC}. Average electrical parameters are presented in Tab. III-4.

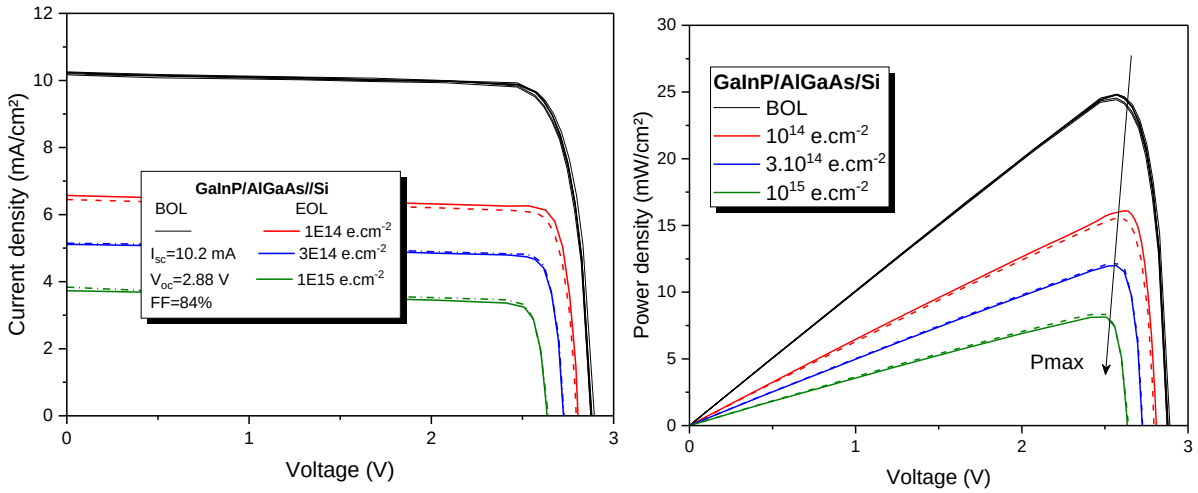

Fig. III-5 *Characterizations of six 3J: GaInP/AlGaAs//Si solar cells at BOL (solid black lines) and EOL (solid and dashed colored lines) under 1367 W.m^{-2} AM0 spectrum and 300 K (left) current voltage (right) Power-voltage.*

The solar cells were subdivided into three groups corresponding to the three fluences. After irradiation with 1-MeV electrons energy, the solar cells were characterized under the same conditions as before irradiation. The results are shown in Fig. III-5 (colored solid and dashed lines). Low dispersion on the electrical performances is observed for each two solar cells irradiated at the same fluence (see Tab. III-4). Contrary to the dual-junction cells, the degradation of the J_{SC} is significant from the lowest fluence and is proportional to the received one. The measured J_{SC} and V_{OC} reach 3.8 mA.cm^{-2} and 2.64 V respectively for the highest fluence.

Tab. III-4 *Average electrical parameters of six 3J: GaInP/AlGaAs//Si solar cells of 1 x 1 cm² sizes at BOL and EOL characterized under AM0 spectrum and 300 K.*

Solar cells GaInP/AlGaAs//Si	**J_{SC} (mA.cm^{-2})**	**V_{OC} (V)**	**FF (%)**	**Efficiency (%)**
BOL	10.2 ± 0.5%	2.88 ± 0.3%	84 ± 0.6%	18.1 ± 1%
***EOL* 10^{14} e.cm^{-2}**	6.5 ± 0.9%	2.80 ± 0.2%	87 ± 0.6%	11.6 ± 1.6%
***EOL* 3.10^{14} e.cm^{-2}**	5.1 ± 0.3%	2.73 ± 0.05%	86 ± 0.3%	8.9 ± 0.8%
***EOL* 10^{15} e.cm^{-2}**	3.8 ± 1%	2.64 ± 0.1%	82 ± 0.1%	6.0 ± 1.2%

With this first comparison between the three solar cell architectures, it is observed that the relative degradation of the open circuit voltage is lower when the number of junctions increases. Whereas for the short-circuit current the degradation is greater by increasing the number of junctions in the device. In all three cases, no significant degradation of fill factor compare to the J_{SC} was observed, thus no significant changes in series resistances or shunt resistances.

In order to better evaluate the degradation of the cells performance after irradiation, the remaining factors RF (*EOL/BOL* ratios) for fill factor, the short-circuit current density, the open circuit voltage and the efficiency were calculated for all architectures at the three fluences. One should keep in mind though that the remaining factor does not reflect the *EOL* performances but only the rate of degradation induced by irradiation, i.e. two cells with identical RF may have different *EOL* absolute electrical performances. Results of RF calculations for the three architectures are presented in Fig. III-6.

By using the standard empirical equation (III-1) linking the evolution of the electrical parameters to the fluence, it is possible to plot the behavior of each electrical parameter of each solar cell architecture on a wide range of fluence.

$$E_{p,EOL} = E_{p,BOL} - C_x \, Ln\left(1 + \frac{\emptyset}{\emptyset_x}\right) \qquad \textit{III-1}$$

Where $E_{p,\,BOL}$ and $E_{p,\,EOL}$ are the electrical parameters values before and after irradiation, Ø is the fluence, C_x and $Ø_x$ represent fit parameters. By modifying the Eq. III-1, the fit of the remaining factor is performed according to the Eq. III-2 presented below :

$$RF(E_p) = 1 - A_x \, Ln\left(1 + \frac{\emptyset}{\emptyset_x}\right) \qquad \textit{III-2}$$

And

$$A_x = {C_x}/{E_{p,BOL}} \qquad \textit{III-3}$$

The parameters A_x, and $Ø_x$ used for the fit of Eq. III-2 to the measured remaining factor are summarized in Tab. III-5 for the three solar cells architectures.

Tab. III-5 *Fitting parameters (A_x and $Ø_x$) for the remaining factors of 1J, 2J and 3J according to Eq. III-2.*

Architectures / Parameters		**RF(J_{SC})**	**RF (V_{OC})**	**RF(FF)**	**RF(Eff.)**
c-Si	A_x	0.038	0.022		0.096
	$Ø_x$(e.cm^{-2})	6.86 x 10^{12}	5.24 x 10^{11}		1.27 x 10^{13}
AlGaAs//Si	A_x	0.226	0.031	Does not fit	0.163
	$Ø_x$(e.cm^{-2})	3.79 x 10^{14}	6.43 x 10^{13}	to Eq. III-2	1.15 x 10^{14}
GaInP/AlGaAs//Si	A_x	0.117	0.030		0.138
	$Ø_x$(e.cm^{-2})	4.48 x 10^{12}	5.99 x 10^{13}		7.97 x 10^{12}

Short-circuit current density - J_{SC}: The relative degradation of J_{SC} is higher for GaInP/AlGaAs//Si compared to AlGaAs//Si and c-Si starting from the lowest fluence of 10^{14} e.cm^{-2} (see Fig. III-6 top-left). Below 3.10^{14} e.cm^{-2}, the relative degradation of J_{SC} is less pronounced for the dual-junction compared to the single-junction; above this fluence, the opposite trend is observed with a greater degradation for the dual-junction. The J_{SC} remaining factor of solar cells irradiated at 10^{15} e.cm^{-2} decreases with increasing the number of junctions on the top of Si. The J_{SC} degradation at this highest fluence is 20%, 30% and 63% for c-Si, AlGaAs//Si and GaInP/AlGaAs//Si, respectively. The difference in degradation observed

between the three architectures is related to the difference in architecture (series-connected sub-cells). More details will be discussed from the quantum efficiency measurements.

The Equation III-2 fits very well to the measured J_{SC} remaining factor for all three architectures, with a corresponding root mean square error (*RMSE)* of 5.10^{-3}. It is observed from the fit (see line in Fig. III-6) that J_{SC} degradation starts at 10^{10} e.cm^{-2}, 10^{11} e.cm^{-2} and 10^{12} e.cm^{-2} for 3J, 1J and 2J respectively. Even if the degradation of 2J starts one order of fluence magnitude higher than Si, a higher degradation rate of 2J leads to a crossover point where 1J degrades less than 2J. Taking into account the architecture of the 2J, this effect can be related to a change of limiting sub-cell, this will be detailed in section III.2.4.

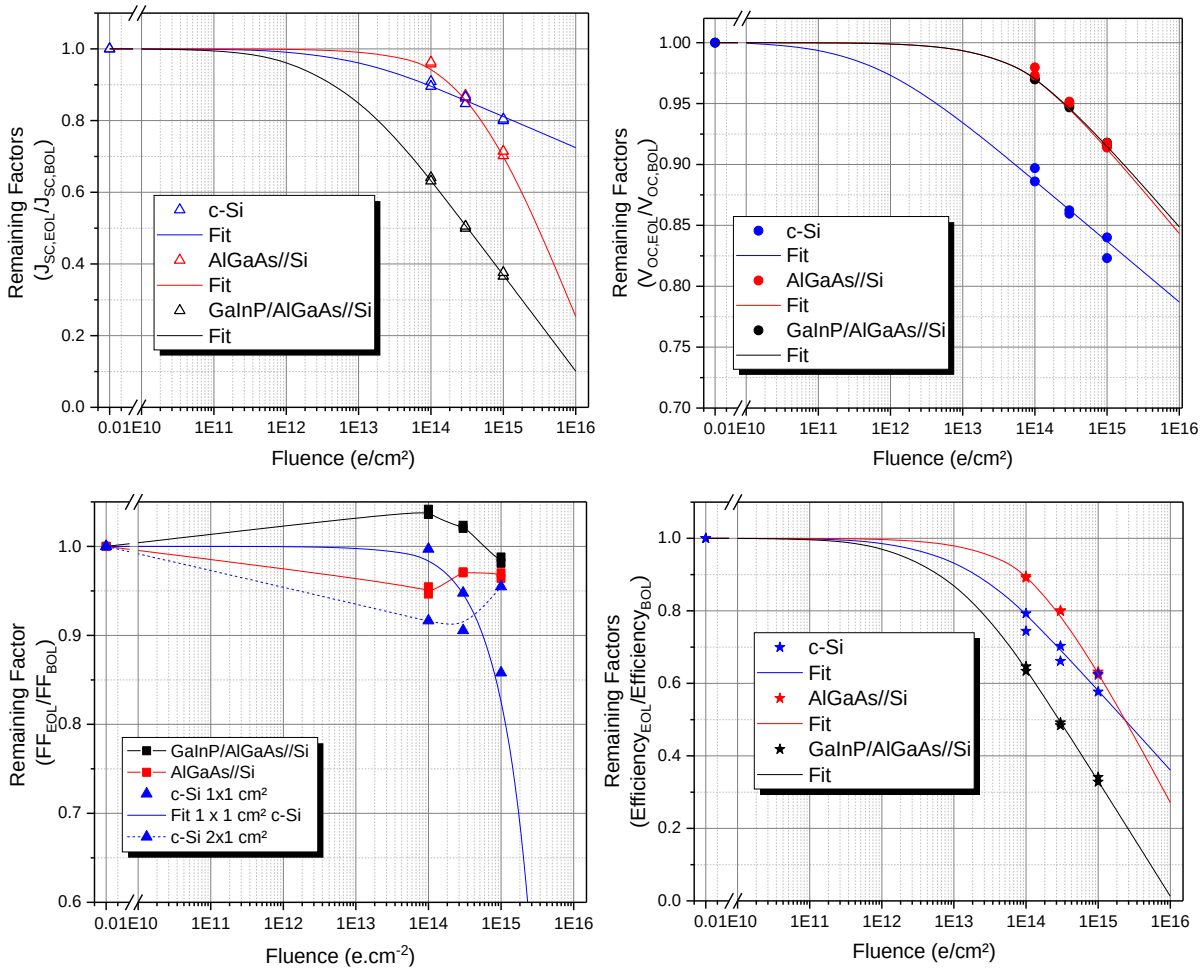

Fig. III-6 *Remaining factors calculations for the three solar cells architectures (1J, 2J and 3J). Top-left: short-circuit current density. Top-right: open circuit voltage. Bottom-left: fill factor. Bottom-right: efficiency. The measured electrical parameters are presented by symbols while the linear curve represents the fit using Eq. III-2. In the case of the fill factor, the lines are only plotted as guide to the eyes. Note: the Y-scale differs for all graphs in order to better display the variations of each electrical parameters as a function of 1-MeV electrons irradiation fluence.*

Open circuit voltage - Voc: the V_{OC} degradation is lower than J_{SC} degradation in both 2J and 3J solar cells, however for 1J solar cells V_{OC} and J_{SC} degradation magnitude are almost

equal as presented in Fig. III-6 (top-right). A 10% degradation is calculated for the single-junction at the lowest fluence (10^{14} e.cm^{-2}) while in the case of tandem cells, very low degradation of 2.5% is calculated at the same fluence. Contrary to the J_{SC}, the degradation of the V_{OC} is lower by increasing the number of junctions. An identical degradation is observed in the case of 2J and 3J. By increasing the fluence up to 10^{15} e.cm^{-2}, the degradation rate reaches 18% and 9% for the single- and both tandem solar cells respectively.

In the case of tandem cells, the degradation is expected to be lower in the case of 3J due to the contribution of GaInP that has a good radiation hardness. However, the difference in the composition of AlGaAs in 2J and 3J could be at the origin of this difference. This will be investigated through absolute V_{OC} calculation from electroluminescence measurements.

The measured data of the V_{OC} remaining factor collapse with the Eq. III-2 with an *RMSE* of 7.10^{-4}. In the case of 1J the degradation takes place from a fluence of 10^{10} e.cm^{-2} while for both 2J and 3J tandem solar cells the degradation is identical and starts from 10^{12} e.cm^{-2}.

Fill Factor - FF: In the case of AlGaAs//Si higher degradation is observed at 1.10^{14} e.cm^{-2} than at 1.10^{15} e.cm^{-2}. For 3J GaInP/AlGaAs//Si a higher FF than *BOL* values is observed at 10^{14} e.cm^{-2} by 5%. Then it decreases and reaches a degradation less than 5% at the highest fluence (see Fig. III-6 bottom-left). The non-linear variation are due most likely to variation in sub-cells current matching after irradiations. However, for the single-junction a degradation is observed from the lowest fluence and increases with fluence for 1 x 1 cm².

Due to current matching issues after irradiation in the case of tandem solar cells, the measured FF values do not fit to the Eq. III-2. In the case of 1J, the fit was applied only to the 1 x 1 cm² solar cells, however on the 2 x 1 cm² does not fit to the Eq. III-2 due to non-continuous degradation, i.e. low degradation of the cell irradiated at the highest fluence. This can be due to measurements uncertainty or non-homogenous irradiation of this cell. Due to the small number of available cells we could not have a large statistical distribution to explain this effect.

Efficiency - Eff.: The influence of J_{SC} drop in efficiency degradation becomes dominant with increasing number of junction on Si; whereas for the single junction, the degradation of efficiency is governed by the degradation of both short-circuit current and the open circuit voltage. The degradations calculated for the single, double and triple junction are 40%, 37% and 68% respectively for the highest fluence tested here (10^{15} e.cm^{-2}).

Given the small variation in FF compared to J_{SC} and V_{OC} in all the solar cells architectures, its impact (non-linear variation) does not propagate to the efficiency variation, therefore a good fit to Eq. III-2 is obtained with corresponding *RMSE* of 10^{-3}.

III.2.3.2 Dark *I-V*

Dark current-voltage measurements are carried out before and after irradiation on the same six 2J and six 3J solar cells. Unfortunately measurements on 1J c-Si solar cells were not performed. The measurement consists of applying a voltage bias and measuring the current generated in the dark. The results of the characterization of the 2J and 3J at *BOL* are presented in Fig. III-7 (solid lines). In the case of 2J AlGaAs//Si, 5 solar cells show a low statistical dispersion however one cell shows considerable dispersion especially at low voltage. This can be at the origin of shunt resistance and higher recombination in the Space Charge Region (*SCR*). However, no shunt effect nor lower performance was detected for *I-V* characterization under 1 AM0 (see Fig. III-4). The recombination at low Voltage (V < 0.9 V) is driven by that of *SRH* defect in the *SCR*. However, for higher voltage values, the *I-V* behavior is driven by the recombination at the emitter and the base region, which is in good agreement with the 2-diodes model [5].

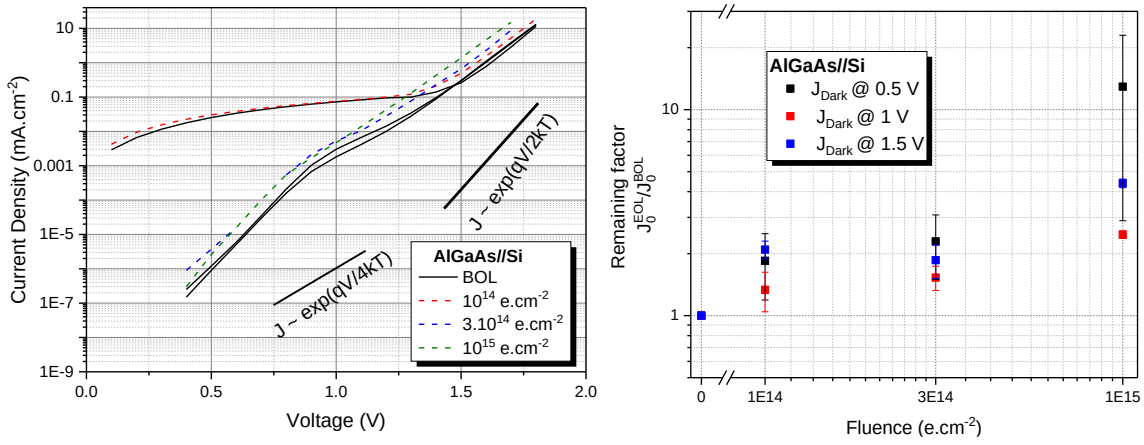

Fig. III-7 *(Left) Dark current-voltage characterization of six 2J solar cells before and after irradiation (right) Remaining factor of dark current as a function of fluence and applied voltage.*

After irradiation (colored curves), the same behavior is observed for all solar cells with an increase of dark current. The remaining factor of dark current at different voltage as a function of fluence is presented in Fig. III-7. An increase of the dark current is observed after irradiation (roughly by a factor of 2) at a low fluence of 10^{14} e.cm^{-2}. This increase is more pronounced with the fluence and reaches ~ 10 times the *BOL* value for a fluence of 10^{15} e.cm^{-2}. The increase of dark current is more pronounced at low voltage region than that at high voltage at the origin of higher recombination defects at *SCR* than at the emitter and the base region.

In the case of 3J (see Fig. III-8), before irradiation (dark curves) the dark *I-V* characteristic curves of the six solar cells show a large dispersion at low voltage, V < 2.4 V (*SRH* recombination domain in the *SCR* [6]). However, at high voltage, all the cells behave in the same way. After irradiation (colored curves), the same behavior is observed with differences in the dark current. The remaining factor of dark current at different voltage is expressed as a function of fluence in Fig. III-8. At low voltage (< 2.4 V) the dark current is lower than the one measured before irradiation with no clear trend with increasing electrons fluence. However, for higher voltages the dark current increases with increasing the fluence and is more pronounced for higher voltage. This is due to the induction of recombination defect at the emitter and the base region [6].

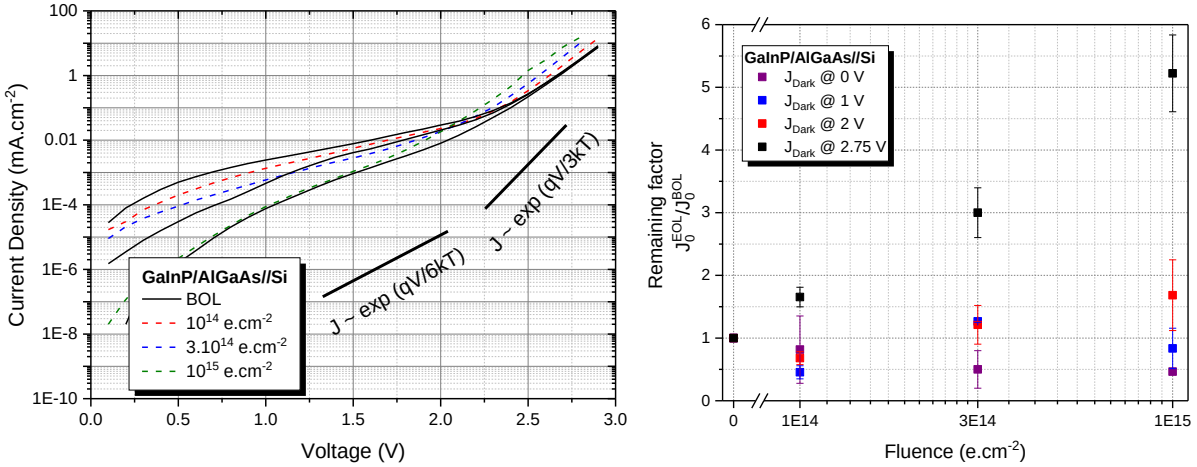

Fig. III-8 *Left: dark current-voltage characterization of six 3J solar cells before (dark lines) and after irradiation (colored lines). Right: remaining factor of dark current as a function of fluence for various voltage bias.*

III.2.4. Quantum Efficiency Characterization

Since current-voltage characterization under both dark and light illumination reflects the general behavior of the solar cells. In the case of tandem solar cells, the *I-V* characteristics are the contribution of 2 or 3 (or more) sub-cells with different architectures, different thicknesses and especially different response to electrons irradiations. For these reasons, Quantum Efficiency (*QE*) characterizations were performed on all solar cell architectures to investigate the spectral response of each sub-cell. As explained in the previously (see section II.4 for further details), the solar cell is photo-excited with a monochromatic beam spanning different wavelengths. The ratio of collected electrons to the incident photons then represents the quantum efficiency. The specificity of this measurement technique is that photons of different energies are absorbed at different depths of the cell (depending on the absorption coefficient of the material), i.e. high energy photons are absorbed at the top of the cell while low energy

photons are absorbed deeper in the cells. Therefore, this characterization allows an investigation of solar cells quality according to its depth.

III.2.4.1 External Quantum efficiency

The external quantum efficiency *EQE,* takes into account all incident photons even those reflected by the front surface (metallization and antireflective coating). Results of 1J c-Si characterization are presented in Fig. III-9 (left). Before irradiation (black curves), we distinguish three main regions according to the wavelength range. Low *EQE* magnitude (20%) at 300 nm due to high doping profile of the emitter and high recombination rate at the front surface due to non-passivated surface. Then the *EQE* gradually increases until it reaches 90% as a result of the progressive decrease of the emitter doping rate and the contribution of the *SCR* where electric fields rapidly separate the charged carrier.

Beyond 500 nm the contribution of *SCR* and emitter to that of bulk is negligible and therefore it is assumed that the *EQE* beyond this wavelength is primarily due to bulk. From 500 nm to 1000 nm the magnification of the *EQE* decreases from 90% to 70%. The observed decrease is due to high reflection at this wavelength range (see Fig. III-15). Between 1000 nm and 1200 nm the *EQE* drops rapidly due to backside recombination and weak absorption close to Si bandgap (~1110 nm).

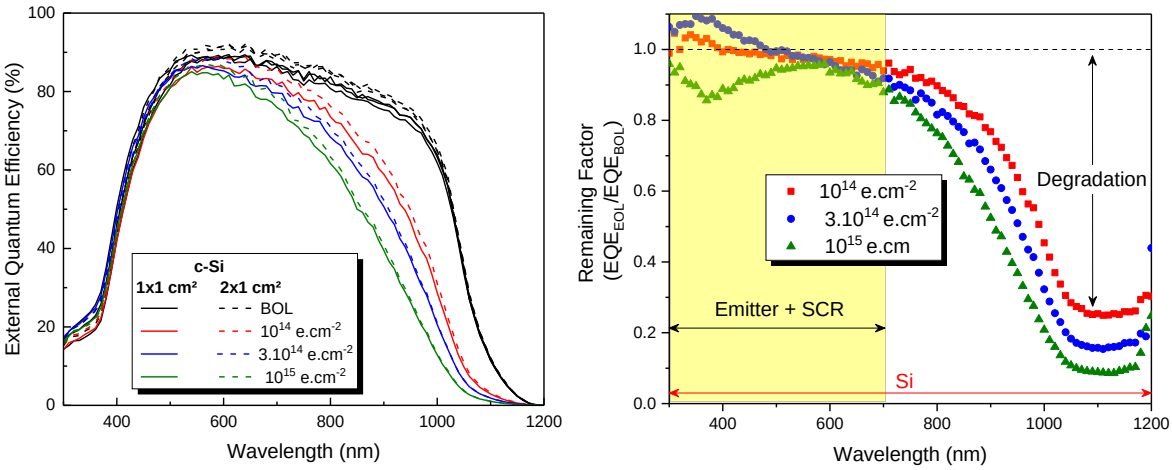

Fig. III-9 *Left: EQE characterization of six 1J solar cells (1x1 cm² and 2x1 cm²) at BOL (dark solid and dashed curves) and EOL (colored solid and dashed curves) with 1 MeV electrons irradiation. Right: the remaining factor of EQE as a function of wavelength.*

A higher *EQE* magnitude is observed for 2 x 1 cm² (dashed line) cells compared to 1 x 1 cm² cells (solid lines) as explained due to low fingers density on larger cells. The calculated J_{SC} by convolution of *EQE* to the reference spectrum AM0 gives values of 39.8 mA.cm^{-2} and 38.7 mA.cm^{-2} for 2 x 1 cm² and 1 x 1cm² respectively. The calculated

deviation for each group of cells is less than 0.5%. The J_{SC} calculated by *EQE* and measured by *I-V* characterizations, 40.1 mA.cm^{-2} and 39.4 mA.cm^{-2} for large and small cells respectively (see Tab. III-1) are in good agreement; the large cells have a higher J_{SC} than the small cells and calculated deviation less than 2% between the two characterizations methods.

After irradiation with 1 MeV electrons energy (colored curves), we distinguish three behaviors on the silicon absorption band according to the level of degradation. No or low degradation is detectable on the 300 - 500 nm absorption band region, from 500 - 700 nm a moderate degradation of the quantum efficiency is detected, and from 700 - 1200 nm the drop becomes more pronounced. To have a better view on the *EQE* degradation, the remaining factor is calculated by the ratio (EQE_{EOL}/EQE_{BOL}) as a function of wavelength, results are presented in Fig. III-9 (right). Around 400 nm, which corresponds mainly to the emitter contribution, the *EQE* increase is proportional to the irradiation for fluence lower than 3.10^{14} e.cm^{-2}, and then at 10^{15} e.cm^{-2} an opposite trend is observed with a dip by 15% degradation. The enhancement of the emitter response after irradiations (fluence < 3.10^{14} e.cm^{-2}) was observed for the large and small solar cells sizes and can be explained by the changes in doping level of the emitter. However, the degradation observed at 10^{15} e.cm^{-2} can be at the origin of high introduced defect density. In the absorption band 470 - 700 nm, where the overall *EQE* is governed by *SCR*, *EQE* degradation less than 10% is almost equal for the three fluences. At this region of the cells, the *SCR* electric fields for charge separation is not/low affected by the irradiation. Beyond 700 nm, global *EQE* is driven by the base response, the degradation more significant by increasing the wavelength (deeper in the cell) until reaching a steady state around 1100 nm where the degradation reaches its maximum, 91% at the highest fluence of this study. This is due to the introduction of defects in the base that act as recombination defects; therefore this degradation leads to minority carriers lifetime & diffusion length decrease. As a result, photo-generated electrons-hole pairs deeper in the cells have a lower collection probability (lots of them recombine before reaching the *SCR).*

Quantum efficiency characterization of tandem solar cells is more complicated than for single junction; the use of light and voltage bias are required for measuring each sub-cells independently in short-circuit conditions (for more details see section II.4). For dual-junction AlGaAs//Si, halogen lamp with Long Pass filter (*LPF)* 650 nm and Short Pass Filter (*SPF)* 800 nm were used to saturate the bottom and top sub-cells respectively (and thus put the sub-cell under test in current limiting conditions). The voltage bias applied to measure the top and

bottom on short-circuit condition is in the range of 0.8 V and 1.2 V respectively. The followed procedure for these values definition is presented in II.4 [7].

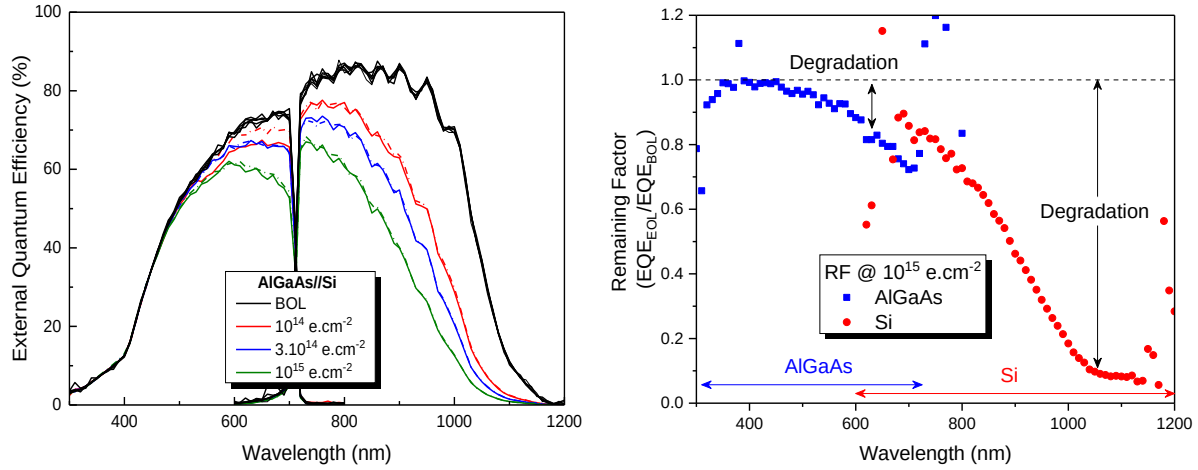

Fig. III-10 *Left: EQE characterization of each sub-cell of the six 2J AlGaAs//Si solar cells at BOL (dark curves) and EOL (colored curves) with 1 MeV electrons irradiation. Right: the remaining factor of EQE as a function of wavelength for each sub-cell.*

Fig. III-10 (left) presents the results of *EQE* characterization in *BOL* (dark curves) and *EOL* (colored curves). The top cells in AlGaAs has a bandgap energy of 1.71 eV so absorption takes place for wavelengths below 725 nm. The absorption of Si bottom cells, is limited on one hand by its bandgap energy 1.12 eV (~1110 nm, however is extended to 1200 nm due to its indirect transition), on the other hand by the absorption of the AlGaAs top cell. The *EQE* of the six solar cells studied are identical, the maximum deviation on the calculated J_{SC} for AlGaAs and Si is 0.75% and 0.5% respectively. After irradiation with electrons of 1 MeV energy, there is an overall decrease in the *EQE* signal with increasing fluence for both sub-cells.

As for 1J c-Si, the *EQE* remaining factor for both sub-cells at the highest fluence (10^{15} e.cm^{-2}) is presented in Fig. III-10 (right). It is clear that the *EQE* spectrum drop for both sub-cells is pronounced in the long wavelengths region of their absorption band (AlGaAs: 600 - 700 nm, Si: 800 - 1100 nm). In addition, the degradation as a function of fluence is more important for the Si bottom sub-cell where it reaches 91% close to the bandgap, as compared to 30% for AlGaAs at 10^{15} e.cm^{-2}. Indeed, the photons at this range of wavelength are absorbed deeply into the sub-cell bulk material, and thus the corresponding photo-generated minority carriers require long diffusion length to reach the *SCR* at the front.

As for dual-junction, different combination of optical filter (*SPF* and *LPF*) with the corresponding applied voltage were used to characterize each sub-cell of the triple-junction GaInP/AlGaAs//Si separately. Results of *EQE* characterization are presented in

Fig. III-11 (left). The absorption of each sub-cell is defined by its bandgap energy (GaInP: 1.9 eV, AlGaAs: 1.46 and Si: 1.12 eV) and the transmitted spectrum of the upper sub-cells. Three absorption bands can be distinguished here; GaInP: 300 - 650 nm, AlGaAs: 500 - 850 nm and Si: 700 - 1200 nm. The dips in the middle sub-cells *EQE* is related to *ARC* layer interferences. The six samples present similar *EQE* performances with a deviation less than 0.8% on the calculated J_{SC} for all sub-cells.

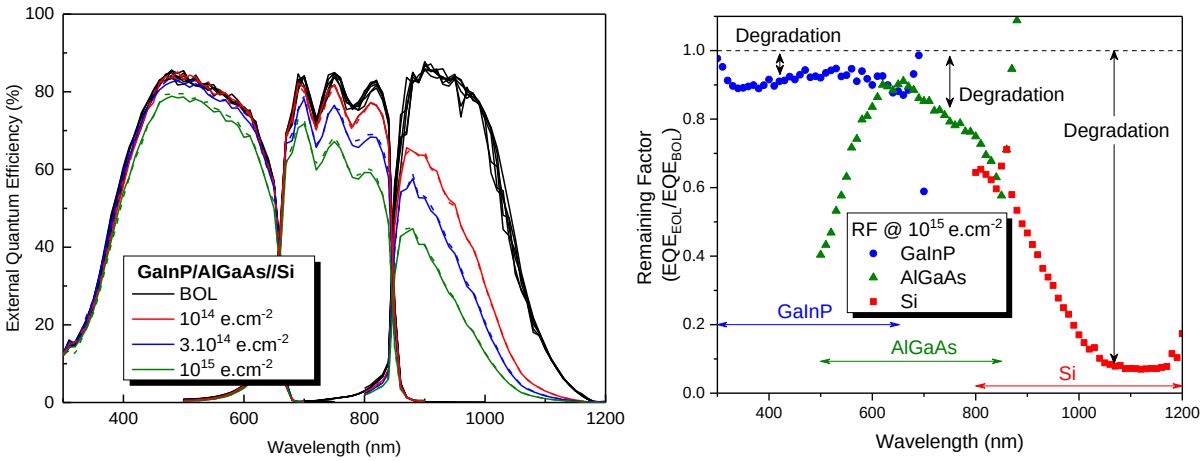

Fig. III-11 *Left: EQE characterization of each sub-cell of the six 3J GaInP/AlGaAs//Si solar cells at BOL (dark curves) and EOL (colored curves) with 1 MeV electrons irradiation. Right: the EQE remaining factor as a function of wavelength for each sub-cell.*

As with dual-junction, the decrease in *EQE* after irradiation is present over the entire absorption band and is greater as the fluence is higher. By looking at each sub-cell separately, we notice that the top cell degradation is only visible at a fluence higher than 3.10^{14} e.cm^{-2}, while for the other two junctions the decrease in *EQE* magnitude is visible starting from the lowest fluence (10^{14} e.cm^{-2}). We plot the *EQE* remaining factor at a fluence of 10^{15} e.cm^{-2} of each sub-cells as a function of wavelength in Fig. III-11 (right). For GaInP, homogenous *EQE* degradation is observed over the entire absorption band with a maximum value of 10%. This is due to the high radiation resistant GaInP materials as discussed in literature review [8]. In the case of AlGaAs middle sub-cell, the degradation is more present at high wavelengths (λ > 700 nm). However, in the case of Si bottom sub-cell high degradation (> 30%) is observed on the entire absorption range (λ > 800 nm) and is more pronounced at high wavelength where it reach 91% at 1100 nm (similar to single junction case).

Hereunder, the Si cells/sub-cells are compared before and after irradiation in Fig. III-12. Before irradiation, higher *EQE* magnitude is observed for tandem solar cells compared to 1J c-Si in the range 800 - 100 nm. This difference is due to a reduced reflection on the tandem solar

cells thanks to bi-layer *ARC* (SiN_x/SiO_2) compare to c-Si where only one layer of *ARC* (SiO_2) is used. After irradiation, it can be seen that the *EQE* magnitude is identical when comparing the common absorption band [850 - 1200 nm] in all three architecture. This is explained by the depth of electron penetration of about 2 mm at an energy of 1 MeV in Si (see section III.2). Thus, an equivalent recombination defect density is introduced in the 525µm Si case of all three architectures.

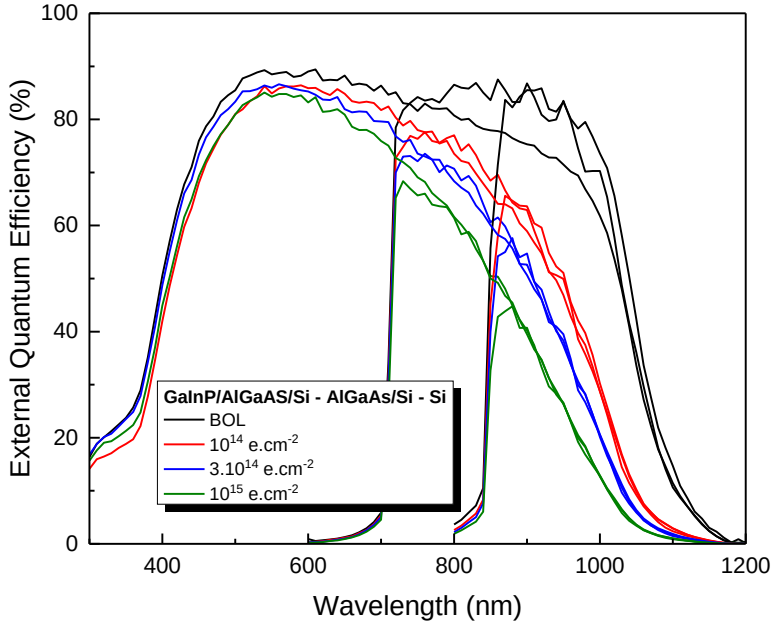

Fig. III-12 *Comparison of the Si EQE before and after irradiation in the case of the three solar cells architectures (1J, 2J and 3J) used in this study.*

As explained above, the high degradation observed at high wavelength is a result of the solar cells bulk (p-type) degradation. The recombination defects created due to atomic displacement are at the origin of the degradation of the minority carrier's diffusion length in the cell. Thus, the further away (from the *SCR*) the electrons-holes pairs are created, the lower is the probability to reach the junction for separation and collection.

Indirect bandgap Si (low absorption coefficient) requires a large thickness and therefore a high diffusion length to obtain a good efficiency and therefore the Si sub-cell is particularly sensitive to irradiation defects. Since the sub-cells are connected in series and the degradation of Si is the most pronounced due to its lower radiation resistance [9] and its substantial thickness (525 µm). However, in the case of top sub-cells (III-V materials), their intrinsic properties (direct bandgap with a high absorption coefficient) leads to thin junctions. Thin III-V layers are sufficient to collect large portion of spectrum (GaInP: 850 nm and AlGaAs (2J and 3J): 2500 nm); therefore the consequences of reducing minority carrier diffusion length is less

pronounced in these junctions [10]. In addition, the higher bandgap materials are reported to be more radiation hard than lower bandgap where the degradation of J_{SC} is less important at high bandgap [11]–[13].

Effect on short-circuit current density J_{SC}

The short-circuit current density calculated by convolution of *EQE* to the AM0 spectrum is plotted as a function of fluence for each sub-cells of each architectures in Fig. III-13. The lines represent the fit of the measured J_{SC} to the fluence according to Eq. III-1.

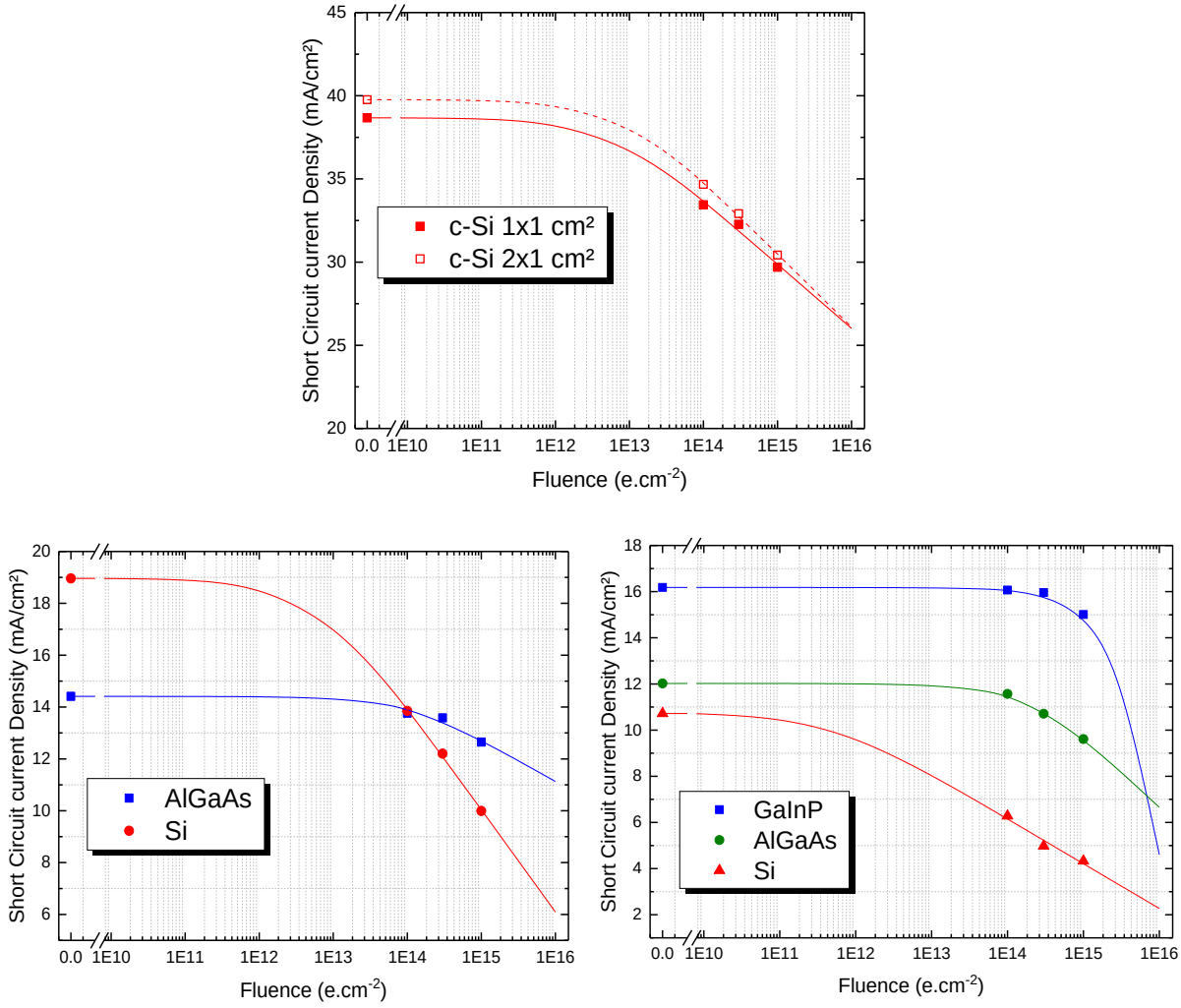

Fig. III-13 *Evolution of short circuit current density of each sub-cell measured by convolution of EQE to the AM0 reference spectrum as a function of fluence (top) c-Si (bottom-left) 2J AlGaAs//Si (bottom-right) 3J GaInP/AlGaAs//Si. The symbols represent the measured data, whereas the lines represent the fit with Eq. III-1.*

In the case of c-Si, the J_{SC} are 39.8 mA.cm^{-2} and 38.7 mA.cm^{-2} for large and small cells respectively at *BOL* (see Fig. III-13 top). After irradiation, the J_{SC} decreases in the same way for both cell sizes, the difference in performance at *EOL* is due to that at *BOL*. According to the fit, the J_{SC} starts to be visible from a fluence of 10^{12} e.cm^{-2}. At the highest fluence studied,

the J_{SC} reaches 30 mA.cm^{-2}, which is in good agreement to the measured one with *I-V* characterizations.

In the case of 2J, the AlGaAs and Si photo-generate a J_{SC} of 14.4 mA.cm^{-2} and 19 mA.cm^{-2} respectively at *BOL* (see Fig. III-13 bottom-left). The large difference between the J_{SC} of the two sub-cells underlines that they are not optimized for AM0 spectrum. Thus, the top sub-cells limits the overall current of the 2J device at 14.4 mA.cm^{-2} (in good agreement with the measured J_{SC} by *I-V* measurements) due to series connection of the sub-cells.

After irradiation, there are two behaviors depending on the fluence below and above 10^{14} e.cm^{-2}. For fluence lower than 10^{14} e.cm^{-2}, a low degradation is observed for AlGaAs which still limits the current of the overall device. For Si bottom sub-cell the degradation becomes visible around 10^{11} e.cm^{-2} and it is higher than that for AlGaAs sub-cell. However, the J_{SC} photo-generated remains higher than that for AlGaAs sub-cell. Therefore, the degradation of the dual-junction J_{SC} is driven by that of AlGaAs. At 10^{14} e.cm^{-2}, a crossover point is reached between the J_{SC} of both sub-cells; they operate at current match conditions around 13.8 mA.cm^{-2}.

Due to a higher degradation of Si compared to AlGaAs an inversion of limiting sub-cells occurs at a fluence of 10^{14} e.cm^{-2}. At higher fluence the Si bottom sub-cell limits the overall current of the 2J, therefore the J_{SC} degradation of the overall device. Because of the low radiation hardness of Si and the limited spectral range transmitted through the top cell, the J_{SC} drops to 10 mA.cm^{-2}. While for AlGaAs, J_{SC} remains at 12.7 mA.cm^{-2}.

This explains the behavior of the double junction by *I-V* characterizations (see Fig. III-4), where a low degradation is observed at 10^{14} e.cm^{-2} while a faster degradation is observed for the upper fluence. On the other hand the low relative degradation observed for the overall 2J, is the result of the ratio of EOL_{Si}/BOL_{AlGaAs} since it is the Si that limit the current at fluence higher than 3.10^{14} e.cm^{-2}.

In the case of 3J, the photo-generated current density before irradiation is 16.2 mA.cm^{-2}, 12 mA.cm^{-2} and 10.7 mA.cm^{-2} for GaInP, AlGaAs and Si, respectively (see Fig. III-13 bottom-right). So the Si bottom sub-cells is limiting the overall current of the 3J 10.7 mA.cm^{-2} that is in good agreement to the J_{SC} measured by *I-V* characterizations (10.2 mA.cm^{-2}). After irradiation, the current density decreases slightly for GaInP and reaches 15 mA.cm^{-2}, moderately for AlGaAs (9.6 mA.cm^{-2}) and strongly for Si with a J_{SC} value after irradiation of

3.6 mA.cm^{-2} at a fluence of 10^{15} e.cm^{-2}. Unlike the dual junction, the Si, which was already limiting in *BOL*, remains logically the limiting cell in terms of J_{SC}.

As seen in the *EQE* response of each sub-cell of each architecture, the degradation is more important at the high wavelength of each sub-cell, which means a strong degradation of the minority carriers diffusion length. This degradation is due to the formation of complex recombination defects due to atoms displacement. From the comparison of the Si *EQE* in each architecture, it is deduced that the same degradation occurs independently of the solar cell architecture. On the other hand, due to the low absorption band (limited to high wavelength) of the Si in the case of 3J and 2J and compared to 1J, the degradation of the J_{SC} is more important in tandems architectures. Therefore, at high fluence the tandem solar cells J_{SC} is driven by the variation of the Si bottom sub-cell and is more present when increasing the number of junction on the top of Si bottom sub-cells. From these results, one can conclude that an optimized tandem cell must have an appropriate current mismatch at *BOL* (higher J_{SC} for Si sub-cell) to end up after irradiation in current matching condition. For instance, the 2J cell is optimized for a fluence of 10^{14} e.cm^{-2}.

III.2.5. Internal Quantum efficiency

The principle and the characterization protocol of solar cells in Internal Quantum Efficiency *IQE* is the same than *EQE*. Nevertheless, in the case of *IQE* the front side reflected photons are taken into account as detailed in Eq. III-4. Since the reflection R(λ) is always superior (or equal to) zero, the magnitude of the *IQE* is logically (most of the time) higher than that of the *EQE* [7].

$$IQE(\lambda) = \frac{EQE(\lambda)}{1 - R(\lambda)} \qquad \textit{III-4}$$

By using this characterization, it is possible on the one hand to remove the influence of possible reflectivity variation with irradiation (*ARC* degradation). On the other hand, it allows to quantify by physical models and analyses the behavior of the minority carriers diffusion length. The characterization results of the three solar cell architectures in *IQE* and reflection are presented in Fig. III-14.

In the set-up used to measure the *IQE*, we do not have an integrating sphere to collect all the reflected photons; the measurement captures only specular reflection. Thus, we were not sure about the accuracy of our *IQE* measurements. To solve this issue, measurements were also

performed with the spectrophotometer UV-Vis-NIR PERKINELMER Lambda 950 with an integrating sphere, in order to measure both specular and diffuse reflections.

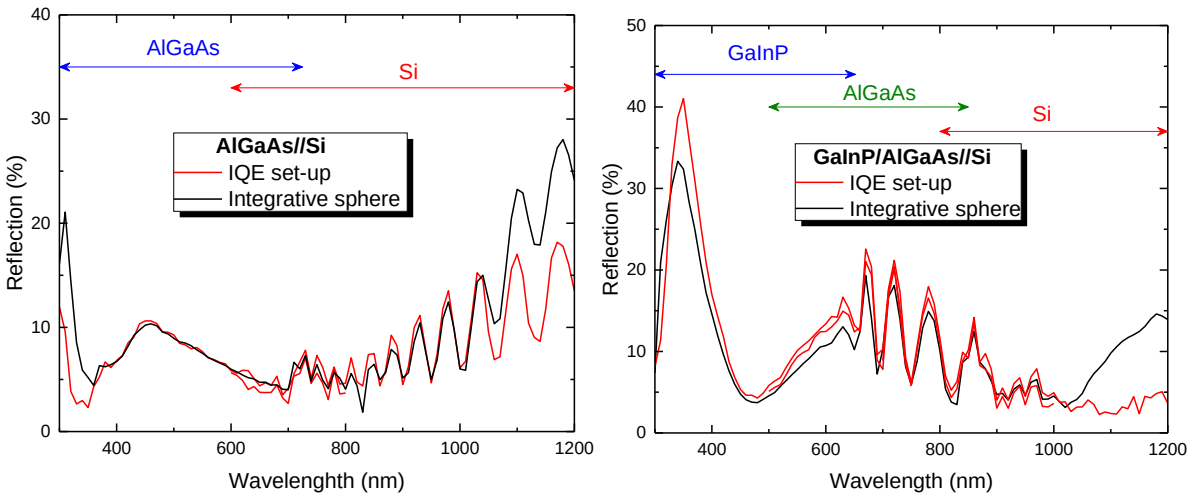

Fig. III-14 *Characterization of reflection as a function of wavelength for (left) 2J AlGaAs//Si and (right) 3J GaInP/AlGaAs//Si using our standard Quantum efficiency set-up (specular reflection only) and a spectrophotometer with an integrative sphere.*

Results on 2J (left) and 3J (right) reflection characterization by the two set-up are shown in Fig. III-14. Measurements were performed on multiple samples with the same fingers density on the surface in order to maintain the same metal reflection over the entire samples and gives the same results. However only one sample is shown for each architecture to simplify the plots.

As a first comparison between the two architectures, on one hand higher reflection is observed for 3J compare to 2J at low wavelength with values of 33% and 20% respectively. On the other hand, at high wavelength reflection is higher in 2J than 3J with values of 25% and 15% respectively. This difference is due mainly to the difference in the *ARC* layers (SiN/SiO_2) thicknesses of 85/85 nm for 3J and 50/70 nm for 2J. This optimization was implemented to enhance the J_{SC} of the Si bottom sub-cells in the 3J since it is the limiting sub-cell.

Now by comparing the two setups (black VS red curves), it is observed in both architectures a reflection gap between the two measurements at low ($\lambda < 350$ nm) and long wavelengths ($\lambda > 1040$ nm) with 10% (absolute value) maximum deviation. Despite this, in the wavelength range 350 - 1040 nm, the two measurements agree very well with average deviation less than 1.5% in absolute value.

In the case of the used solar cells, the *EQE* is low at both long and short wavelengths and is less than 40%. If we take an average deviation on reflection of 5% in absolute values, the resulting *IQE* deviation is below 3% in absolute values. On the other hand, in the medium

wavelength range where the *EQE* approaching 90%, the resulting *IQE* deviation of 2% (abs. values) is calculated for 1.5% deviation of reflection. The calculated reflection effect is small and can be neglected. In addition, the wavelength range of interest for the calculation of the minority carrier diffusion length is narrowed down to the middle wavelength range (se details in the section III.2.5.1). Therefore, the *IQE* measurements can be carried out with a reasonable accuracy in the set-up without the addition of the integrating sphere (see Fig. III-15).

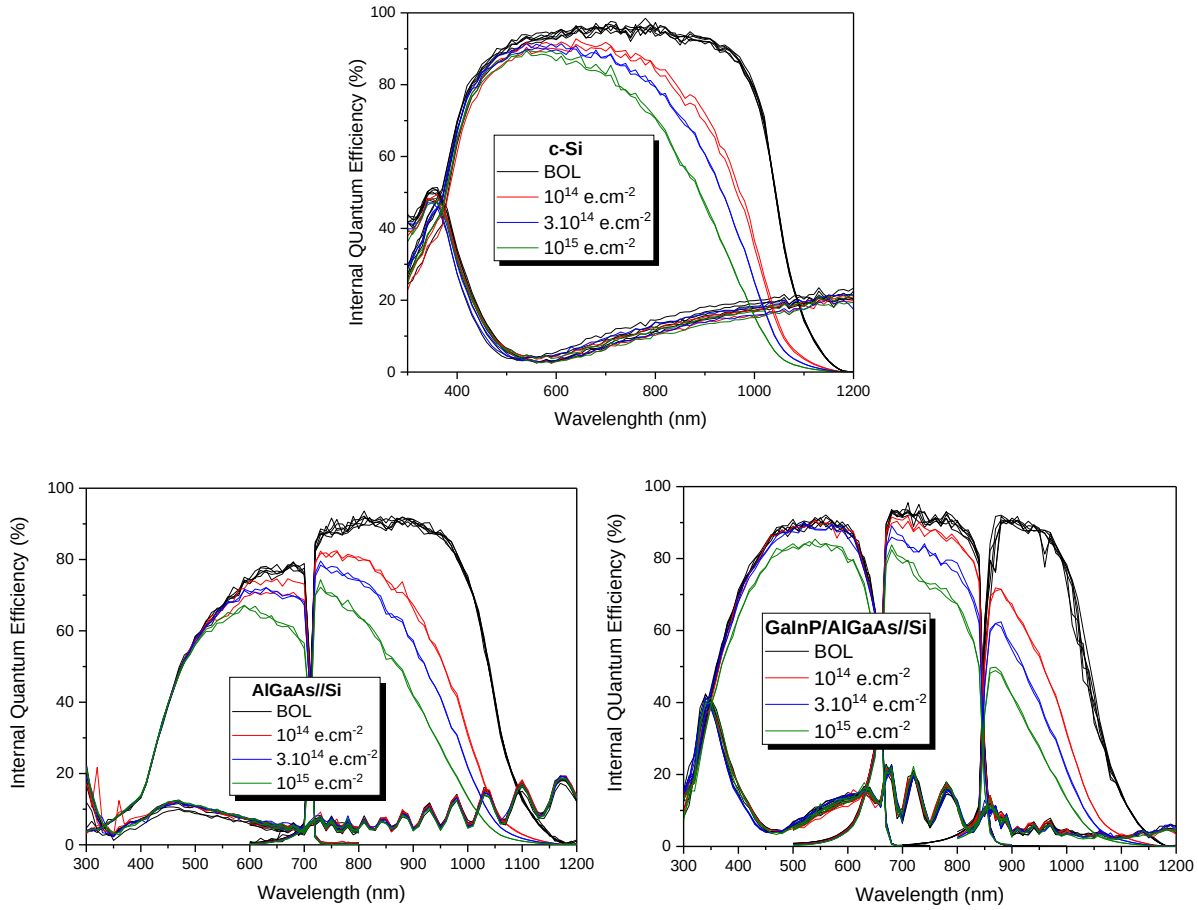

Fig. III-15 *IQE and reflection characterization before and after irradiation (top) 1J c-Si (bottom-left) 2J AlGaAs//Si and (bottom-right) 3J GaInP/AlGaAs//Si.*

In the case of the single-junction c-Si (see Fig. III-15 top), it can be seen that at *BOL* (dark curves) both large and small cells have the same *IQE* behavior unlike to *EQE* one. This is due to the higher finger density in the large cells compared to the small ones, introduced to minimize the effect of high series resistance (high current). The magnitude of the *IQE* is higher than the *EQE* globally and especially at long wavelengths where the reflection is higher due to one *ARC* layer. As indicated above the appearing dips on the *EQE* of 3J have disappeared in the *IQE* measurements with the corresponding wavelength coordinates that coincide perfectly with the reflection peaks. After irradiation, the same behavior is observed as for *EQE*: some degradation

is detected on all the absorption range, however the effect is more pronounced at long wavelengths for all the solar cells architectures. The obtained results for 2J and 3J are presented in Fig. III-15 left and Fig. III-15 right respectively.

In the following, we analyze the measured reflection for the three architectures as a function of irradiation fluence to answer the question whether irradiation has an effect on the reflection; this point is important to discriminate minority carrier degradation from *ARC* optical losses. Fig. III-16 presents the measured reflection of the three architectures before (solid curves) and after 1 MeV electrons irradiation with a fluence of 10^{15} e.cm^{-2} (dashed curves).

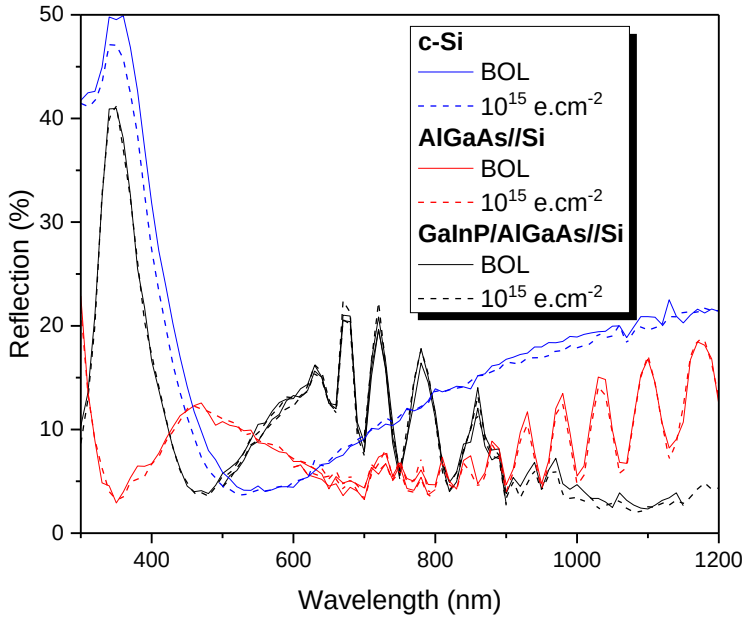

Fig. III-16 *Comparison of reflection before and after irradiation with a fluence of 10^{15} e.cm^{-2} for the three solar cells architectures for a fluence of 10^{15} e.cm^{-2}.*

In the case of c-Si, the reflection measured at *EOL* is slightly lower than that measured at *BOL*, the maximum calculated deviation is very small (~5% in absolute value) and may be related to measurement and handling uncertainties. However, in the case of tandem cells for both 2J and 3J, an almost perfect match is observed for the reflection measured in *EOL* to *BOL*, which indicates that the irradiations have quasi-no effect on the quality of the *ARC* layers used in this study. Thus, after validating that electron irradiation has no/minor effect on *ARC* layers and front reflectivity, we decided to quantify the impact on minority carrier's diffusion length using a model based on the *IQE* measurements.

III.2.5.1 Determination of effective diffusion length

The long wavelength *EQE* degradation observed suggests a degradation of minority carrier diffusion length in the Si cell/sub-cell, thus we have extracted this parameter from the experimental quantum efficiency curves. In the *IQE* model proposed by Fisher et al. [14], a part from the emitter region is modeled as a dead layer where collection is set to zero. We would like to point that this dead layer does not correspond to the one often described in other studies related to the highly doped front side region with low *IQE* [15]. The model describes the experimental *IQE* data on a wide wavelength range according to Eq. III-5.

$$IQE(\lambda) = \frac{1}{k}\exp\left(-\frac{X_d}{L_\lambda}\right).\frac{1}{1+\frac{L_\lambda}{L_{eff}}} \qquad \textit{III-5}$$

With L_λ the absorption length (Si absorption coefficient data were taken from [16]), L_{eff} the bulk minority carrier diffusion length, X_d the width of front side equivalent dead layer and k a scaling factor [14], [17]–[20]. The scaling factor is introduced as a method of *IQE* correction, independent of the wavelength; B. Fischer has reported values in the range of 0.01 ± 0.0002 if all the *IQE* is properly measured taking into account shading and reflectance due to metallization [21]. The dead layer corresponds to a front side zone of thickness X_d with no carriers collection [22].

In order to extract X_d, k and L_{eff}, the experimental *IQE* curves were fitted with Eq. III-5 in the regions where Eq. III-5 is in applicable :

i) When the absorption length has to be long enough so that the contributions of the *SCR* and the emitter thicknesses (W_{SCR} and W_e, respectively) can be neglected: $L_\lambda > W_e + W_{SCR} \sim$ 0.58 µm (equivalent to $\lambda > 470$ nm).

(ii)When the light penetration is small compared to the base thickness: $L_\lambda < \frac{W_b}{4}$, thus ~ 130 µm this work (525 µm Si), which corresponds to $\lambda < 990$ nm.

The solution of the three involved parameters is obtained from linear regression of two equations. As a first step, X_d and k are obtained from linear regression of Eq. III-6 with an initial arbitrary value of L_{eff}. Where the interception and the slope of the plot gives k and X_d.

$$Ln\left(IQE_{meas}.\left(1+\frac{L_\lambda}{L_{eff}}\right)\right) = f(L_\lambda^{-1}) \qquad \textit{III-6}$$

The second step refines L_{eff} and k by linear regression of Eq. III-7 where k is the interception and L_{eff} is the ratio k on the slope. After few iterations, the model converges to the optimal solution. We precise that this second plot is an extension of the method proposed by Basore [23] for the determination of L_{eff}. However, in the dead layer method a correction of the inverse of *IQE* is added (emitter losses) to extend the method to wider wavelength range.

$$IQE^{-1}.\exp(-X_d/L_\lambda) = f(L_\lambda) = k + \frac{k}{L_{eff}} L_\lambda \qquad \textit{III-7}$$

In Fig. III-17 we present as an example the resolution of the model according to the Eq. III-6 (see Fig. III-17 left) and the Eq. III-7 (see Fig. III-17 right) in the case of a 1J c-Si cell before irradiation.

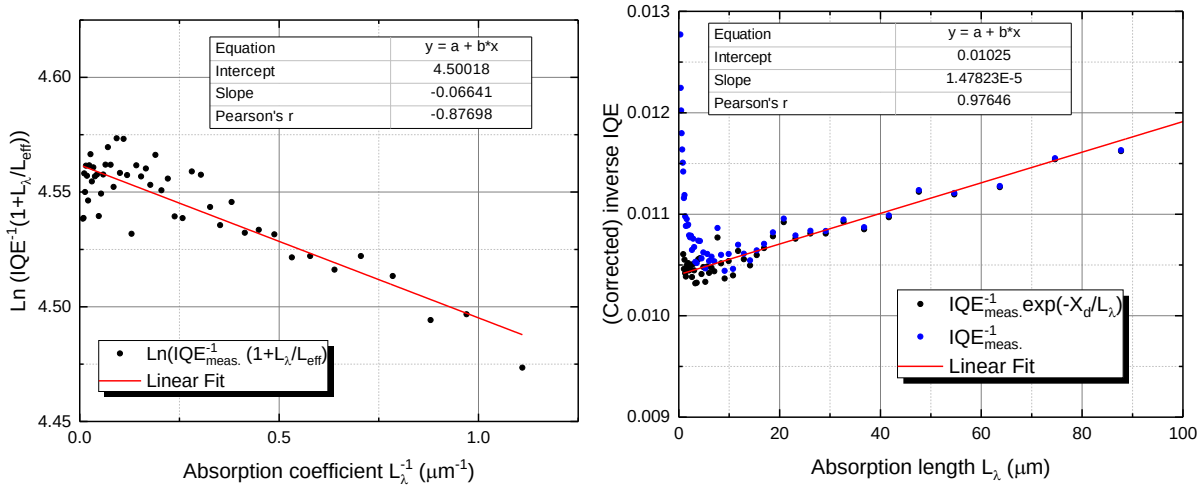

Fig. III-17 *IQE fit results with III-5, for the determination of W_d, k and L_{eff} for 1J c-Si at BOL (left) Determination of W_d and k by linear interpolation of Eq. III-6, (right) determination of L_{eff} and refinement of k value by linear interpolation of Eq. III-7.*

In this case, we have used an initial diffusion length of 800 µm, which seems compatible with the thickness of the c-Si cell of 525 µm. In a first step, we have plotted the Eq. III-6 as a function of the absorption coefficient (L_λ^{-1}) using experimental *IQE* data and initial diffusion length guess. Then, a linear fit of those data points gave us a first estimate of k and X_d (from the interception with Y-axis and the slope) with values of 0.0104 and 67 nm respectively. By inserting the X_d value in Eq. III-7, a second linear fit was used to refine the value of k and L_{eff}; the new values obtained were 0.0104 and 689 µm respectively. After few iterations (~6), the model converges towards an optimal solution with 79 nm, 0.0103 and 657.8 µm corresponding to X_d, k and L_{eff} respectively, for our c-Si solar cell in *BOL*.

The model was applied on the six solar cells of each architectures in *BOL* and *EOL*. Since the Si bottom sub-cells is the most degraded and is the limiting sub-cell the overall tandem solar

cells J_{SC}, the model was applied only to estimate the Si bottom sub-cells diffusion length. The results on *IQE* calculation using Eq. III-5 (solid curves) as a comparison to measured data (symbols) are shown in Fig. III-18.

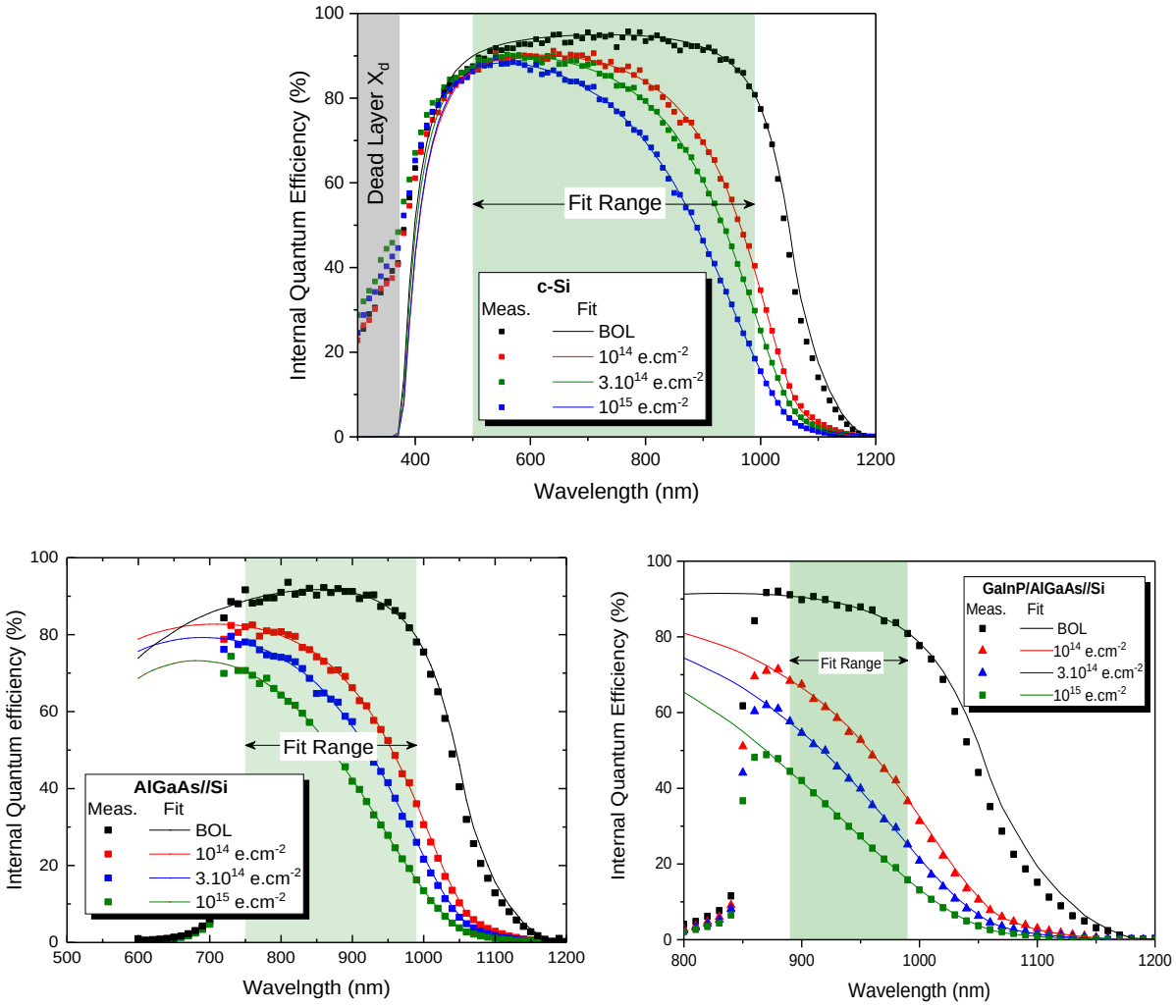

Fig. III-18 *Comparison of measured (symbols) and calculated (solid lines) IQE using III-5, with the L_{eff} deduced from the fitting procedure. For BOL and EOL in the case of Si (top) 1J c-Si (bottom-left) 2J AlGaAs//Si and (bottom-right) 3J GaInP/AlGaAs//Si. The green area represents the wavelength region used for the fit using Eq. III-5.*

The applied model matches very well with the experimental measurements on the three architectures. In the case of 1J c-Si, the fit range covers 500 nm up to 990 nm where the *RMSE* is between 0.6 - 1 for all cells in *BOL* and *EOL*. Moreover, beyond 990 nm the model fit very well with experimental measurements. Below 500 nm as explained before, one can clearly distinguish the dead layer which corresponding thickness is around 70 nm where the *IQE* is set to zero. In the case of tandem solar cells, the fit region is narrowed toward higher wavelength range. Since the upper limit of the fit region is limited by the thickness of the solar cell, it remains unchanged for all three architectures (same thickness). In contrast, for tandem cells the

lower limit is defined by both the emitter/*SCR* thickness and the absorption of the top sub-cells. Therefore, the fit range become 750 - 990 nm and 890 - 990 nm for 2J (see Fig. III-18 bottom-left) and 3J (see Fig. III-18 bottom-right) respectively.

Even by narrowing the fit region, a very good fit with the model is obtained to the experimental measurements with an *RMSE* generally lower than 1 in the fit region. However, some cells show a value of 2 due to small fluctuation observed experimentally during the measurements. Beyond 990 nm, the model is slightly higher than the experimental measurements in *BOL* while in *EOL* the model fits very well at these wavelengths. Below the respective fit region for each architecture, the dead layer is not apparent because the model does not take into account the top sub-cells absorption. Even if this parameter has no physical representation in the case of 2J and 3J, it is kept only for the fit and the determination of k and L_{eff}.

The L_{eff} values for all architectures at *BOL* and *EOL* are summarized in Fig. III-19. For the scaling factor k, almost all values are in the range 0.01 ± 0.0002, which is in good agreement with literature. However, in some cases (not related to irradiation) k can reach 0.0104 that can be due to the fact that the absorption by metallization is not taken into account in *IQE* measurements, however this slight variation does not induces much degradation on L_{eff} calculation.

In the case of c-Si cells before irradiation the calculated diffusion length is 676 µm, comparing to the thickness of the solar cell this means that the electron-hole pairs photo-generated deep in the cell (525 µm) have a reasonable probability to reach the p-n junction and therefore participate in the current photo-generated by the cell. However, after irradiation, a significant degradation of L_{eff} is observed even at the lowest fluence 10^{14} e.cm^{-2} with L_{eff} equal to 92 µm while at the highest fluence (10^{15} e.cm^{-2}) it reaches 29 µm. In this case the electron-hole pairs created at a depth beyond 29 µm that correspond to a wavelength higher than 890 nm have a low probability to reach the p-n junction to be separated and collected, therefore they recombines in the bulk. In the case of tandem cells, the L_{eff} calculated before irradiation is around 550 µm, which is lower compared to the calculated values for 1J. This effect could be related to the additional bonding process that induces some recombinant defects in the bottom cell or at the interfaces. After irradiation, the same behavior is observed for both tandem cells with a strong degradation from the lowest fluence. Diffusion length values around 80 µm and 25 µm are calculated after irradiation with a fluence of 10^{14} e.cm^{-2} and 10^{15} e.cm^{-2} respectively.

As in the case of 1J cells, the photo-generated e-h pairs deep within the cell have a lower probability of reaching the p-n junction. In addition to this effect, the impact is more pronounced in the case of tandem cells; where the large part of the bottom J_{SC} is the result of the separation and collection of charge carriers created deep within the cell. These calculations explain the high degradation of the quantum efficiency at high wavelength in addition to the high degradation of J_{SC} observed by *I-V* measurements.

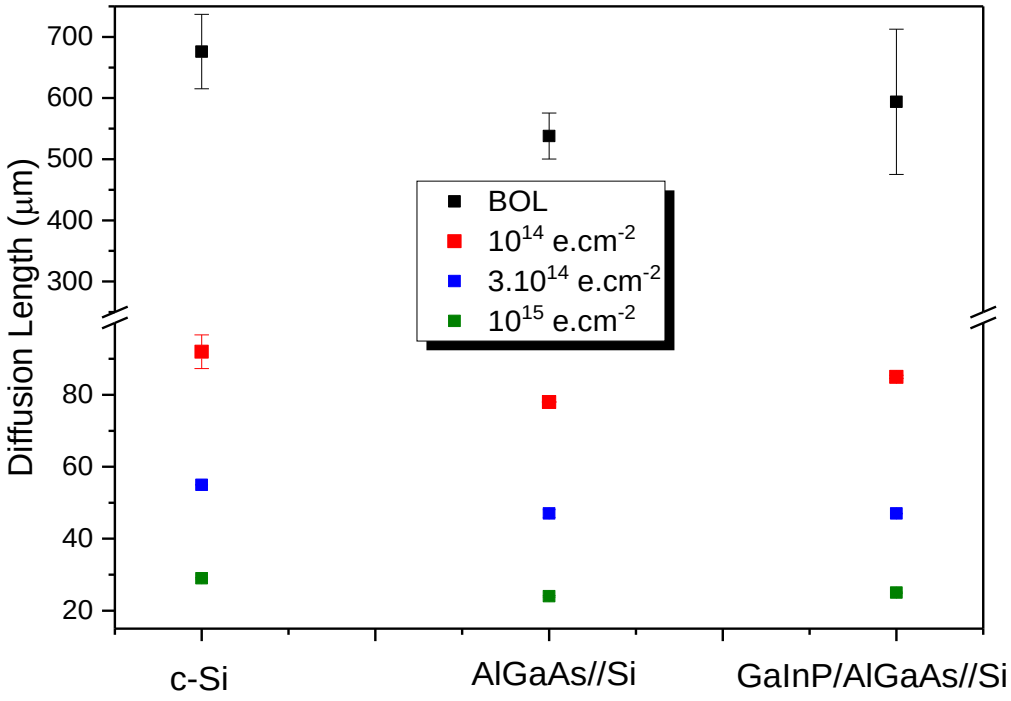

Fluence	**L_{eff} (µm)**		
e.cm^{-2}	1J	2J	3J
BOL	676 ± 9%	538 ± 7%	594 ± 20%
10^{14}	92 ± 5%	78 ± 0.1%	85 ± 0.5%
3.10^{14}	55 ± 0.1%	47 ± 2.3%	47 ± 0.2%
10^{15}	29 ± 0.7%	24 ± 0.9%	25 ± 0.7%

Fig. III-19 *Calculated L_{eff} at BOL and EOL for all three solar cells architectures (1J, 2J and 3J).*

One of the most used analytical equation in the field of solar cells degradation in space application is expressed in Eq. III-8, where the diffusion length L_{eff} is linked to the damage coefficient (K_L, dimensionless) [24].

$$\frac{1}{L_{eff}^2} = \frac{1}{L_0^2} + \sum \frac{\sigma_i \nu_{ti} I_{ti}}{D} \emptyset = \frac{1}{L_0^2} + K_L \emptyset \qquad \textit{III-8}$$

Where L_0 is the pre-irradiated value of L_{eff}, I_{ti} is the introduction rate of the i^{th} recombination center, σ_i is the capture cross section of the i^{th} recombination center, ν_{ti} is the thermal velocity of the minority carriers, D is the diffusion coefficient and Ø is the fluence. As seen in the Eq. III-8 all the parameters related to the defects are gathered in the damage coefficient constant K_L.

The damage coefficient was calculated based on the diffusion length obtained by the *IQE* model and Eq. III-8 for all three architectures and are:

For c-Si $\quad K_L = 1.18x10^{-10}$

For Si in 2J $\quad K_L = 1.74x10^{-10}$

For Si in 3J $\quad K_L = 1.60x10^{-10}$

The resulting Si damage coefficients in the single, dual and triple junction are shown in Fig. III-20. Looking at the slope in this graph, some dispersion is visible between the different cells architecture. However, as Yamaguchi et al. have reported in [25], the evolution of K_L in Si with doping concentration can be expressed as follow:

$$K_L = 4x10^{-20} p^{0.596} \qquad \textit{III-9}$$

Where p is the base doping concentration in cm^{-3}

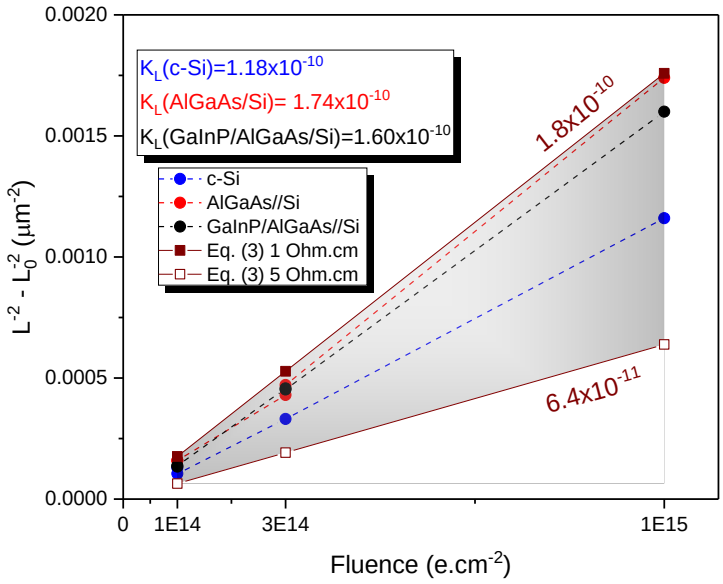

Fig. III-20 *Calculated damage coefficient of L_{eff} of the Si in the three solar cells architectures (blue, red and black curves), compared to the empirical equation (see Eq. III-9) proposed in literature.*

Thus, using this equation and the resistivity range given for this type of Si wafers (1 - 5 Ohm.cm); we obtain the area shown in grey in Fig. III-20. As one can see, the K_L for all architectures fall within this interval and thus are fully consistent with the formula of Eq. III-9.

III.2.6. Electroluminescence

As explained at the beginning, Spectral ElectroLuminescence (*EL-S*) measurements were performed to analyze each sub-cell of the multi-junction separately. The principle of this technique is based on the fact that the solar cell operates as an emitting diode (*LED*) by injecting a current at these terminals. The photons emitted are the result of the radiative recombination of the current injected mainly close to the bandgap of each sub-cell [26]. Since in multi-junction the bandgap energy of sub-cells is decreasing from the top to the bottom, the emitted photons will not be absorbed on its way out of the cell (by the front) by the upper sub-cells. Additional absorbance due to defects and interfaces has low impact on the electroluminescence for high quality crystal with an *EQE* higher than 90% [27].

In the case of the measurements performed in this study, a CMOS detector was used to collect the emitted photons as a function of their energy with the detector limit at 1100 nm. At the end of the optical fiber, a correcting cosine is used to maximize the collection of photons in the whole plane of the fiber.

Due to the indirect bandgap of Si, it is more complex to measure the emitted photons with the used spectrophotometer because the recombinations are mainly not radiative. In addition, the 1J c-Si cell allows to follow the evolution of the Si sub-cell in the case of the two tandem solar cell architectures, since the same Si bottom cell is used for all solar cells and due to the fact that the 1-MeV electron energy penetrates the full depth of all the device (thus creating an equivalent number of defects). For these reasons, the *EL-S* measurements were focused on the characterization of the III-V sub-cells (GaInP and AlGaAs in the 3J) and (AlGaAs in the 2J) before and after irradiation. In order to maximize the signal intensity and to reduce the signal to noise ratio, the integration time used for *EL-S* spectra acquisition was set to 15 seconds with an averaging on 5 measurements.

The *EL-S* spectra of the 2J cells are shown in Fig. III-21 (left) in *BOL* and *EOL* for an injected current of 14 mA ($J_{inj} = J_{SC}$) as an example. The observed signal represents the emission of the AlGaAs sub-cell with a signal peak positioned at 706 nm, which corresponds to 1.75 eV close to the bandgap of the AlGaAs sub-cell (1.71 eV). The *EL-S* spectra were measured for each cell as a function of the injection level. The results of peak intensity are plotted as a

function of injected current (1 - 15 mA) for all cells in Fig. III-21 (right) at *BOL* and *EOL*. The sensibility of the detector limits the measured signal at low injected current. The curves show that for a given fluence, the intensity of the *EL-S* is correlated to the injected current according to $Ln(ElS) \propto Ln(J_{inj})$, and it degrades with increasing electron fluence at a given injection level according to Eq. III-1.

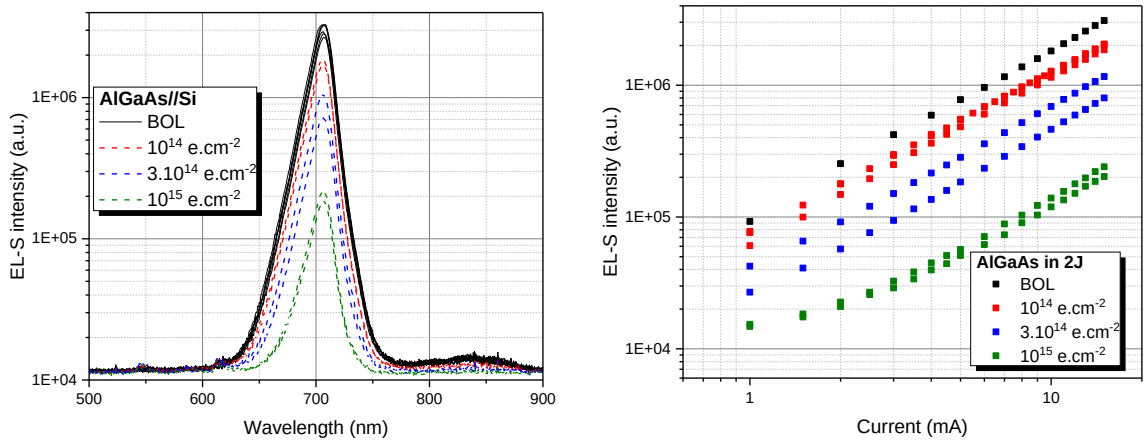

Fig. III-21 *EL-S characterizations of 2J AlGaAs//Si before and after irradiation (left) EL-S emission as a function of wavelength at an injected current of 14 mA, (right) Peak EL-S emission intensity for AlGaAs as a function of injected current I_{inj}. Two cells are considered per condition.*

Before irradiation (black curves), low statistical dispersion is observed between the measured cells. A peak with Full Width at Half Maximum (*FWHM*) of 20 nm is measured (wavelength band where the *EL-S* intensity is higher than 50%). A strong degradation is observed for the *EL-S* signal peak after irradiation with a drop of 43%, 70% and 94% for a fluence of 10^{14} e.cm^{-2}, 3.10^{14} e.cm^{-2} and 10^{15} e.cm^{-2} respectively. The *FWHM* values remain unchanged for all three fluences at a value of 20 nm; this is also seen on quantum efficiency characterization by by the slight effect of irradiation on the *EQE* slope near the bandgap of III-V materials. The created defects by irradiation behave as non-radiative recombination centers (*SRH*), resulting in degradation of charge carrier lifetime. The defects centers capture the electrons and combine with them in a non-radiative manner, resulting in degradation of *EL-S* intensity [28]. Furthermore, *EL-S* intensity is directly related to the concentration of non-radiative recombination defects, such that a degradation of the *EL-S* is noticeable once the non-radiative defect density introduced by irradiation *N* is higher than the number N_0 initially present in the crystal [29]. The *EL-S* signal at 14 mA as a function of fluence was fitted using Eq. III-1 (see Fig. III-22). It is clear that *EL-S* signal degradation is only noticeable from a fluence of 10^{11} e.cm^{-2}. Defect induced by irradiation into GaAs material were extensively studied back in the old days [30];the main defects for this material are localized at an energy of E_C - 0.96 eV

(labelled E5) and E_V + 0.41 eV (labeled H2) corresponding to electrons and holes traps with an introduction rate in the range of k = 0.1 cm^{-1} [31], [32]. Their initial concentration in the cell is of the order of 10^{10} cm^{-3} and it becomes more important beyond a fluence of 10^{11} $e.cm^{-2}$; it reaches 10^{14} cm^{-3} at a fluence of 10^{15} $e.cm^{-2}$, i.e. four order of magnitude higher compared to *BOL*.

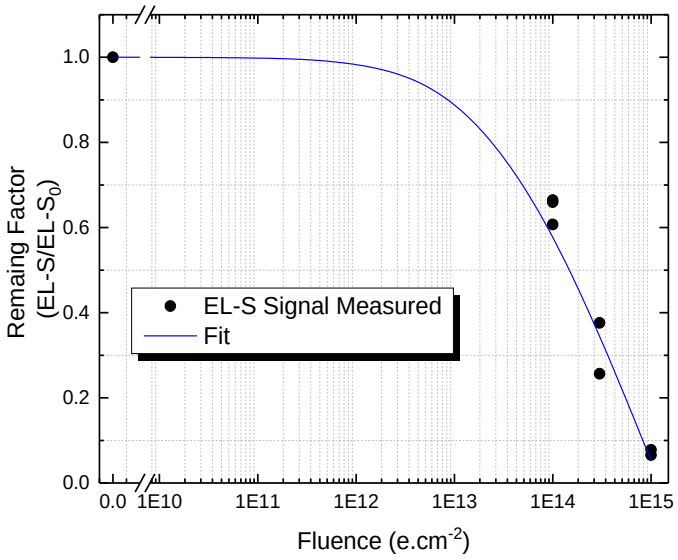

Fig. III-22 *EL-S peak intensity remaining factor of AlGaAs in the case of 2J at a current injected of 14 mA as a function of fluence. Symbols represent the measured data, whereas solid line represent the fit to the Eq. III-1.*

The same characterization was performed for the 3J cells. The results of the *EL-S* spectra are shown in Fig. III-23 for an injected current of 10 mA. The first peak of the signal is positioned at a wavelength of 657 nm that is equivalent to 1.89 eV which is close to the GaInP sub-cell bandgap energy (1.9 eV). The second peak is positioned at a wavelength of 843 nm, which corresponds to a photon energy of 1.47 eV and thus represent the response of the AlGaAs sub-cell (1.46 eV). It appears that the emitted *EL-S* intensity of GaInP is ~3 times higher than AlGaAs. At *BOL*, the *FWHM* value is around 20 nm for both sub-cells and remains unchanged after irradiation. After irradiation, the degradation of the maximum *EL-S* intensity is 39% (resp. 69%) 76% (resp. 94%) and 93% for GaInP (resp. AlGaAs) for fluences of 10^{14} $e.cm^{-2}$, 3.10^{14} $e.cm^{-2}$ and 10^{15} $e.cm^{-2}$, respectively. A higher degradation is observed for AlGaAs compared to that of the GaInP sub-cell, which coincides with the fact that GaInP is more resistant to a radiative environment than AlGaAs [12], [33], [34].

Measurement of the *EL-S* were performed as a function of injected current (2 - 18 mA) for each cells in *BOL* and *EOL*. At a fluence of 10^{15} $e.cm^{-2}$, the AlGaAs signal is too weak and therefore injected current was increased until 50 mA in order to measure a distinguishable signal

(see Fig. III-23). As for dual-junction, the *EL-S* peak intensity is proportional to the injected current for both sub-cells. The degradation at a specific injected current is more pronounced at high fluence and for AlGaAs material.

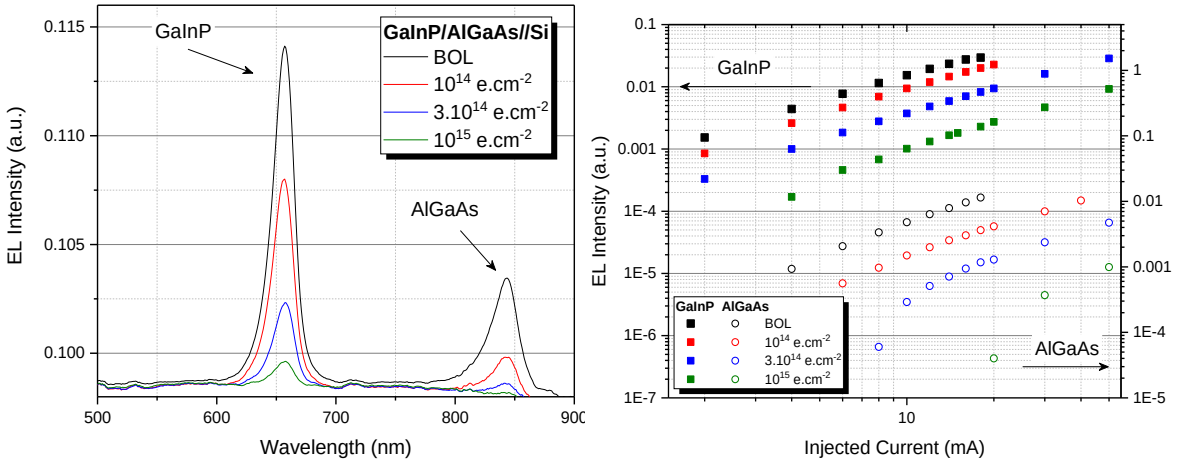

Fig. III-23 *EL-S characterization of 3J GaInP/AlGaAs//Si before and after irradiation (left) EL-S emission as a function of wavelength at an injected current of 10 mA as an example (right) Peak EL-S emission of GaInP and AlGaAs as a function of injected current I_{inj} (base line subtracted).*

The measured remaining factor of the *EL-S* maximum was performed using Eq. III-1. Results are shown in Fig. III-24 for both sub-cells. At low fluence, below 10^{13} e.cm^{-2}, the degradation is higher for AlGaAs than for GaInP. However by increasing the fluence beyond 10^{13} e.cm^{-2}, the two degradation rates tend to slowly converge and reach values greater than 90% for both sub-cells (however the degradation of GaInP remains lower even at 10^{15} e.cm^{-2}). Previous studies have shown that the main recombination center in GaInP cells is identified as H2 ($E_V + 0.55$ eV) with a introduced of recombination defect rate in the order of $k = 9.3 \times 10^{-2}$ cm^{-1} [35]–[39]. It is observed from Fig. III-24 that the degradation of GaInP and AlGaAs *EL-S* is noticeable only after a fluence of 10^{11} e.cm^{-2} and 10^{9} e.cm^{-2} respectively. Based on this statement and the non-radiative recombination center rate (the defect concentration is equal to the product of the fluence and the introduced defect rate), the initial concentration of non-radiative recombination defects before irradiation is in the range of 9.10^{9} cm^{-3} and 10^{8} cm^{-3} for GaInP and AlGaAs respectively which is in good agreement with research in [39]. Beyond each sub-cell respective critical fluence, the introduced defects become more important ~ 9.10^{14} cm^{-3} and ~ 10^{14} cm^{-3} for GaInP and AlGaAs respectively at a fluence of 10^{15} e.cm^{-2}, i.e. 5 order of magnitude higher than at *BOL*.

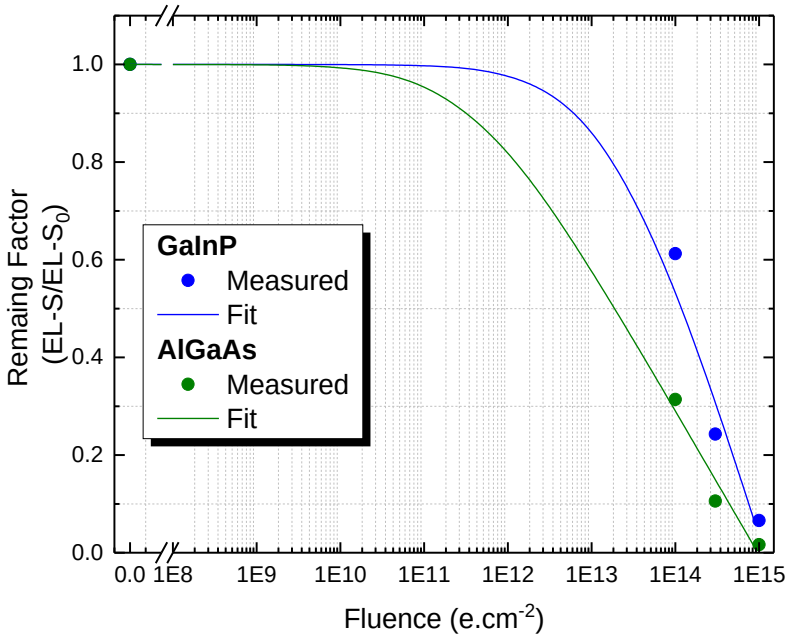

Fig. III-24 *Variation of EL-S peak remaining factor of GaInP and AlGaAs in the case of 3J at a current injected of 10 mA as a function of fluence. Circles represent the measured data, whereas solid line represent the fit to the Eq. III-1.*

Optoelectronic reciprocity

In the case of two-terminal tandem cells, it is impossible to characterize each sub-cell separately in *I-V* measurements. However, for a better understanding of the behavior of each sub-cell, generally isotype cells are used, i.e. same architecture as an *MJSC* but only one sub-cell is electrically active. On the other hand, it is still not always simple to have the corresponding isotype cells due to additional cost, time consuming and to the possible difference between the isotypes and the *MJSC* sub-cells resulting in a difference in *I-V* behavior.

In order to solve this issue, the reciprocity relation between the *EL-S* emission (φ_{ELS}), the *EQE* and the spectral photon density of a black body (φ_{BB}) via Eq. III-10 was used [1], [40], [41].

$$\varphi_{ELS}(E,V) = EQE(E).\varphi_{BB}(E).\left[\exp\left(\frac{qV}{kT}\right) - 1\right] \qquad \textit{III-10}$$

With

$$\varphi_{BB}(T,E) = \frac{2\pi E^2}{h^3c^2}.\frac{1}{[exp\,(E/kT) - 1]} \approx \frac{2\pi E^2}{h^3c^2}.\exp\left(\frac{-E}{kT}\right) \qquad \textit{III-11}$$

Where kT/q is the thermal voltage (25.86 mV at 300 K), E the photons energy, h is Planck constant and c is the vacuum speed of light. Here V is the internal voltage defined as the splitting of quasi Fermi levels near the *SCR* [42].

By rearranging Equation Eq. III-10, it is then possible to express the voltage of each sub-cell as a function of its *EL-S* and *EQE* near the bandgap according to Eq. III-12 [43], [44].

$$V_i = \frac{kT}{q}.Ln\left(\varphi_{ELS,i}\right) + \frac{E}{q} - \frac{2kT}{q}.Ln(E) - \frac{kT}{q}Ln(EQE_i) - \frac{kT}{q}.Ln(C) \qquad \textit{III-12}$$

Where (i) refers to each sub-cell of the solar cells. The constant C is introduced to account the fact that *EL-S* is measured in arbitrary units. The terms $\delta V_C = kT/q.Ln(C)$ is the same for all sub-cells and is independent of the energy. Thus, it can be derived by comparing the V_{OC} of the multi-junction measured by *I-V* characterization and the sum of the V_{OC} calculated according to Eq. III-13. However, this is only possible if all sub-cells are characterized in *EL-S* that is not the case for the measurements made in this study since the Si bottom sub-cell was not characterized due to its very low *EL-S* intensity.

$$\delta V_C = \frac{kT}{q}.\ln(C) = \frac{1}{i}\left[V_{OC,MJSC} - \sum V_i\left(I_{inj,i} = I_{SC,i}\right)\right] \qquad \textit{III-13}$$

It is then possible to reconstruct the dark *I-V* of each sub-cell by solving Eq. III-12 at wide range of injected current. The applied procedure for the calculation is outlined below.

Procedure

- Measure the *EQE* of each sub-cell at 300 K.
- Measure the *EL-S* at different injected currents, especially for $I_{inj} < I_{SC}$ values.
- Resolve the Eq. III-12 with an arbitrary value of the constant C, using the maximum value of the *EL-S* and its corresponding *EQE* in energy.
- Plot the injected current as a function of the calculated voltage $I_{inj} = f(V_i)$.
- Calibration using constant C, since the Si sub-cell *EL-S* was not measured due to its low emission we used isotype V_{OC}, measured by Suns-V_{OC} (labeled #1 in Fig. III-25):
    - Case 2J: the Values of constant C is changed in a way that the measured voltage (V_i) at $I_{inj} = I_{SC} = 14$ mA is equal to the measured $V_{OC} = 1.21$ V with Suns-Voc (translated to AM0 spectrum);
    - Case 3J: a triple junction solar cells GaInP/AlGaAs//Si(inactive) where only the top cells are electrically actives was used as reference cells with $V_{OC} = 2.320$ V. The value C is changed in a way that the sum of the measured voltage ($\sum V_i$) at each sub-cells I_{SC} (16 mA and 12 mA for GaInP and AlGaAs respectively) is equal to the measured one $V_{OC} = 2.320$ V with Suns-Voc (translated to AM0 spectrum);

- It is important to note that the constant C will induce translation on the X-axis, therefore when the same value is used at *BOL* and *EOL* comparative study can be made;

- The same procedure is used for *BOL* and *EOL* solar cells, while keeping the same constant C at both conditions.
- Once the dark curves are plotted and calibrated for each sub-cell, it is then possible to plot the *I-V* behavior under a specific spectrum of each sub-cell.

The results of the application of the above procedure are presented for the dual-junction at *BOL* and *EOL* in Fig. III-25 (left), where the data are expressed in terms of I_{inj} vs. V_i for the AlGaAs sub-cell. It is important to note that the injected current is equivalent to the diode dark current, and therefore the graph represents the dark *I-V* characteristics of the AlGaAs sub-cell.

By comparing the behavior of the AlGaAs sub-cell with the two components of the two-diode equation; exp(qV/2kT) and exp(qV/kT), it is clear that recombination in the emitter and base region takes place following the second component of 2-diode equation at the high-current [44], i.e. n = 1. After irradiation, the same trend is observed for all sub-cell irradiated at the three fluences where an increase of dark current is observed at high-injected current region due to the introduction of defects in the emitter and the base region. This translation results in the degradation of the open circuit voltage of the AlGaAs sub-cell.

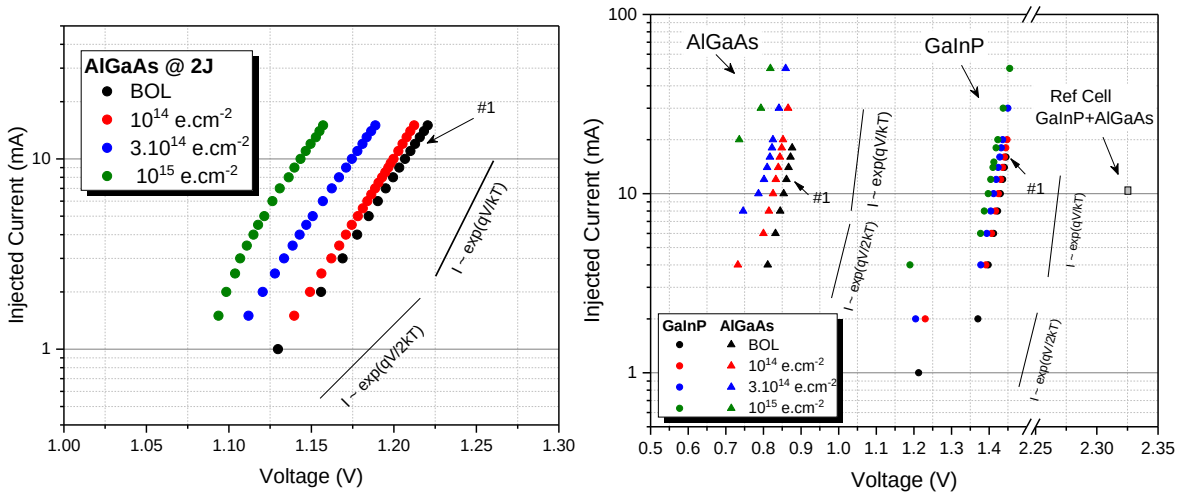

Fig. III-25 *Dark I-V calculated using the optoelectronic reciprocity between the EL-S , EQE and V at BOL and EOL for (left) AlGaAs sub-cell in the 2J and (right) GaInP and AlGaAs in 3J.*

As explained above it was not possible to measure the *EL-S* signal at low injection current due to the low sensitivity of the detector. However, in the literature [43]–[45] they report that in the case of GaAs, it is the *SRH* recombination in *SCR* that is dominant at *BOL* and at low

injection level. Whereas at *EOL* the recombination in *SCR* is negligible compared to that of the emitter and the base, thus the sub-cell behavior follows the second component of the 2-diodes equation (n = 1) even at low injection level.

The same procedure was used to calculate the dark *I-V* from the *EL-S* measurements for the two sub-cell GaInP and AlGaAs in the case of 3J (see Fig. III-25 right). In a first view, it is observed a higher increase of dark current of the AlGaAs sub-cell compared to the GaInP one. This is due to the relatively low radiation hardness of AlGaAs. A comparison of the sub-cell behavior to the simplified 2-diode model components is made. In the case of the AlGaAs sub-cell, before irradiation at high injection current (J_{inj} > 10 mA) the recombination in the base and emitter region is dominant, whereas at low injection level (J_{inj} < 10 mA) it is the *SRH* recombination in the *SCR* that takes the advantages that is in accordance with the 2-diode model. After irradiation, the same behavior is observed as in *BOL* with an increase of the dark current of the two components of the 2-diodes equation. However, a larger increase is recorded for *SRH* recombination in *SCR*.

In the case of the GaInP sub-cell, the same behavior is observed with a current of 4 mA where both recombinations are equal, i.e. recombinations at base and emitter drive the behavior of the sub-cell for I_{inj} > 4 mA and the *SCR* that takes the advantages for I_{inj} <4 mA. After irradiation, it is observed a small increase in the dark current of the recombination in the emitter and the base region compare to the one observed at low injection level for *SRH* recombinations in the *SCR*. It is also observed at low injection level for both sub-cells an important effect of the shunt resistance, which appears even before irradiation and increases with increasing the electrons fluence.

Subsequently, the *I-V* characteristic curves could be constructed under AM0 spectrum for each sub-cell whose dark *I-V* was measured using *EL-S* data, i.e. AlGaAs for 2J and GaInP and AlGaAs for 3J. The results are shown in Fig. III-26 where the *I-V* data calculated by the *EL-S* (symbols) were fitted using the 2-diode equation (solid line) at *BOL* and *EOL*.

We recall that these measurements do not take into account the series resistance R_S, and therefore the fill factor calculated can be different from the real one. Since the short-circuit current density is already known and its evolution has been discussed above (see III.2.4), we are in this case mainly interested in the degradation of the open circuit voltage V_{OC} of each sub-cell. Concerning the sub-cell measured by the *EL-S,* the degradation is directly calculated from the respective calculated *I-V* curves whereas for the Si bottom sub-cell the degradation is

deduced from the degradation of the multi-junction cell measured by *I-V* characterization (see III.2.3).

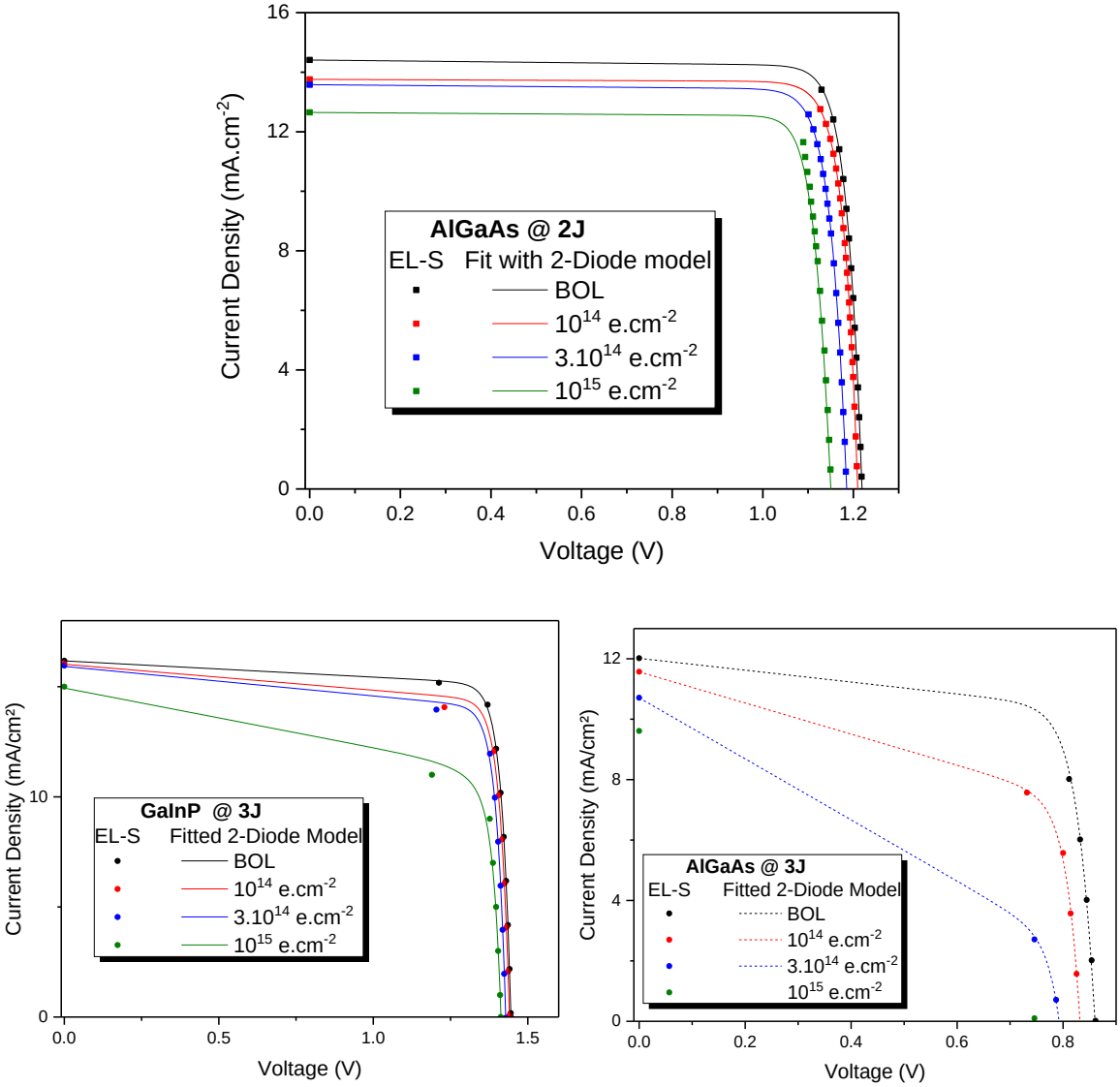

Fig. III-26 *Calculated light I-V under AM0 spectrum for (top) AlGaAs in the case of 2J, (bottom-left) GaInP in the case of 3J and (bottom-right) AlGaAs in the case of 3J.*

In the case of the AlGaAs sub-cell of the double junction, the data calculated by the *EL-S* fit very well with the 2-diode equation. In *BOL*, the AlGaAs V_{OC} is 1.219 V and the one calculated ($V_{OC,2J}$ - $V_{OC,AlGaAs}$) for the Si is 0.556 V. As shown above, after irradiation the increase in dark current induces V_{OC} degradation of 10 mV, 34 mV and 67 mV for fluence of 10^{14} e.cm^{-2}, 10^{14} e.cm^{-2} and 10^{15} e.cm^{-2} respectively. Thus, the deduced degradation for Si is 30 mV, 52 mV and 84 mV for fluence up to 10^{15} e.cm^{-2}. Results of V_{OC} are summarized in Tab. III-6.

Tab. III-6 *Absolute Open circuit voltage V_{OC} values for AlGaAs and Si in the case of 2J with the corresponding absolute degradation. The Si bottom sub-cell absolute values where deduced from 2J I-V measurements and compared to 1J c-Si sister cell.*

Fluence e.cm^{-2}	**Top : AlGaAs**		**2J : AlGaAs//Si**	**Bottom : Si**		**1J c-Si**	
	Voc (V)	Δ Voc (mV)	Voc (V)	Voc (V)	Δ Voc (mV)	Voc (V)	Δ Voc (mV)
BOL	1.219	0	1.775	0.556	0	0.587	0
10^{14}	1.209	10	1.735	0.526	30	0.519	68
3.10^{14}	1.185	34	1.689	0.504	52	0.509	78
10^{15}	1.151	67	1.624	0.472	84	0.490	97

By comparing the degradation of both AlGaAs and the Si sub-cell of the 2J, we observe a slightly higher degradation in the case of the Si. However, it is the relative degradation that reflects the radiation resistance between the two sub-cells where AlGaAs loses 4% of its initial V_{OC} while the Si loses 15% at a fluence of 10^{15} e.cm^{-2}. The difference in *BOL* V_{OC} (30 mV) between the Si bottom sub-cell and 1J c-Si can be due to the difference in illumination. In the case of 1J the Si is illuminated by all the spectrum. However, in the case of 2J, the Si bottom sub-cell is illuminated only with half the spectrum (23 - 46 mV decrease is calculated theoretically). The difference between the V_{OC} absolute degradation of Si bottom sub-cell and 1J c-Si may be due to the fact that cells with lower *BOL* performances are less sensitive to irradiation induced defects and therefore presents less V_{OC} degradation.

The same procedure was applied in the case of 3J for the reconstruction of *I-V* under AM0 spectrum for GaInP (see Fig. III-26 bottom-left) and AlGaAs (see Fig. III-26 bottom-right) sub-cells. In the both cases at *BOL* and *EOL* for the two sub-cells, the data fit very well with the 2-diode equation. In the case of AlGaAs irradiated at 10^{15} e.cm^{-2}, not sufficient data were obtained at low injection current (sensibility issues); therefore, the fit was not performed.

A low shunt resistance R_{SH} is observed for both sub-cells, and is more present for the middle AlGaAs sub-cell. The effect of the R_{SH} is more pronounced with increasing fluence that can be at the origin of radiation-induced defects that degrade the fill factor of each sub-cell *I-V* characteristics in one case. Alternatively, in another case, this *pseudo* shunt effect may be related to the low intensity of the *EL-S* at the low injection level (low voltage) and therefore

data are not reliable in this range. Further measurements are required in order to conclude whether the sub-cell have low R_{SH} or low sensitivity issues. However, since we are only interested in the variation of the V_{OC} (high injection level) and not in the FF, these measurements are sufficient for absolute values and comparison of V_{OC} at *BOL* and *EOL* (see Tab. III-7).

Tab. III-7 *Open circuit voltage V_{OC} values for GaInP and AlGaAs and Si in the case of 3J with the corresponding absolute degradation. The Si bottom sub-cell absolute values where deduced from 3J I-V measurements and compared to 1J c-Si variation.*

Fluence e.cm^{-2}	GaInP		AlGaAs		3J		Bottom Si	
	Voc (V)	Δ Voc (mV)	Voc (V)	Δ Voc (mV)	Voc (V)	Δ Voc (mV)	Voc (V)	Δ Voc (mV)
BOL	1.445	0	0.861	0	2.88	0	0.574	0
10^{14}	1.44	5	0.831	30	2.8	80	0.529	45
3.10^{14}	1.428	17	0.794	67	2.73	150	0.508	66
10^{15}	1.412	33	0.737	124	2.64	240	0.491	83

At *BOL*, the absolute values of V_{OC} are 1.445 V, 0.861 V and 0.574 V for GaInP, AlGaAs and Si bottom sub-cells respectively. As explained for Si bottom sub-cell in 2J, the Si bottom sub-cell in 3J is illuminated by ~1/3 of AM0 spectrum, which induces lower V_{OC} compared to the one in 1J solar cells (decrease by 37 - 74 mV). At *EOL*, the calculated absolute degradations for GaInP are 5 mV, 17 mV and 33 mV for a fluence of 10^{14} e.cm^{-2}, 3.10^{14} e.cm^{-2} and 10^{15} e.cm^{-2} respectively. Expectedly the degradation of AlGaAs is more pronounced with values of 30 mV, 67 mV and 124 mV at the three fluences due to the relatively lower radiation hardness than GaInP. The degradation of Si bottom sub-cell in the case of 3J is in good agreement with that calculated for 2J and 1J.

In the literature, different degradation values are reported for GaInP. Our calculations are in good agreement with those presented by Hoheisel et al. [44], where the V_{OC} degradation of GaInP sub-cell is 18 mV at a fluence of 4.10^{14} e.cm^{-2}. Whereas in other references the degradation of GaInP is higher and around twice as much degradation [28], [46]. When comparing the degradation values reported to those calculated in the case of the 3J cells used in

this study, non-logical results are obtained where Si degradation is zero. This is due to the architecture differences (doping profile, cell thickness, etc.).

III.3 Proton Irradiations

In this section, we present the evolution and behavior of solar cells as a function of proton irradiation. The irradiations were performed with 1 MeV protons beam at three different fluences, 10^{11} p.cm^{-2}, 3.10^{11} p.cm^{-2} and 10^{12} p.cm^{-2}. The energy of 1 MeV is within the range of energies proposed by the irradiation platform and is widely used in the context of conventional III-V/Ge cells. In terms of studied fluences, they are equivalent to the electrons one since a proton deposits an energy in the range of thousand times that of one electron. This allows comparing both irradiations by unidirectional electrons and protons beam. The same solar cells samples were used as for the electrons irradiation (thickness, doping level, *ARC* and passivation layer) except for the triple junction solar cells where the emitter of Si bottom sub-cell were obtained by ion implantation instead of diffusion for the previous cells.

First, simulations using the Monte Carlo ion transport code SRIM developed by J.F. Ziegler [47] have been performed to define the energy deposited in each cell layer as well as the proton penetration depth. *I-V* characterization under illumination are performed under AM0 and 300 K to follow the electrical parameters as a function of the irradiation fluence.

Experimental characterizations were carried out before and after the irradiation to follow the evolution of the behavior of the solar cell in general by *I-V* measurements and by *QE* characterizations to follow the evolution of each sub-cell as a function of the irradiation. The *IQE* model was applied to calculate the diffusion length as a function of the irradiation and thus the damage coefficient.

III.3.1. SRIM simulation

In this section, we present the interaction of protons which enter the solar cells, for the 1J, 2J & 3J devices used in this PhD work. The energy loss of protons in samples is dependent on the materials physical properties of the medium, i.e. atomic displacement threshold, composition and density. Depending on the initial energy of the protons and the thickness of the solar cell, the particles can pass through the cell or settle in at different depths. One of the key parameters for Non Ionizing Energy Loss (*NIEL*) calculation is the atomic displacement energy E_d, where different values are reported in the literature (see Tab. III-8). In the case of Si values of 11 and 12.9 eV have been reported [14]. However a value of 21 eV has also been proposed in literature [48] [49]. Similarly, for Ga and As, values of 10 eV have been published

[41], [42] as well as 21 - 24 eV [52]. In the case of Ga, In and P values of 10 eV, 7 eV and 9 eV can be found [50]–[53] as well as 24 eV, 7 eV and 3.5 [49], [53], [54].

The atomic displacement values used in the simulation are summarized in the Tab. III-8, labelled with a star sign. Among all the literature values, the choice was guided by the best fit of electrical parameters evolution according to the displacement damage dose (will be detailed later).

Tab. III-8 *Displacement Energy Ed for each sub-cell constituting atoms. (*) denotes the E_d used for SRIM simulations [48],[49], [53], [54].*

Composition Atoms	**Ga**	**In**	**P**	**Al**	**As**	**Si**
Displacement energy E_d	10 eV 21 eV 24 eV*	6.7 eV 7 eV*	9 eV 8.7 eV 3.5 eV*	20 eV*	10 eV 21 eV 24 eV*	10 eV 12.9 eV 21 eV*

The interaction result of 10^5 p.cm^{-2} with an energy of 1 MeV during their trajectory in a 3J GaInP/AlGaAs//Si cell is presented in Fig. III-27 (plotting depth 0 - 20 μm). In the case of unidirectional protons beam, no variation (deposited energy per ion, penetration depth or the number of induced displacements) is observed as a function of the fluence. This is why a low fluence 10^5 p.cm^{-2} has been studied in order to reduce the simulation time. Due to the high mass in comparison with electrons, the protons have low penetration depth into the material where it reaches 14.7 μm (from the top of the cell) in the 3J. Therefore, an implantation of proton will happen into the Si sub-cell, when bare III-V/Si cells are exposed to this type of proton beam. By taking into account the top and middle sub-cell, the protons stop at a depth of 11.2 μm into the Si bottom sub-cell far from the top of the Si sub-cell.

In the case of top and middle sub-cells, the energy transmitted by the protons is relatively constant as a function of their depth (see Fig. III-27 right). The average energy loss is about 5 eV.Å^{-1} and 7 eV.Å^{-1} in the GaInP and AlGaAs sub-cells, respectively. However, non-homogenous energy loss is observed in the case of Si bottom sub-cell due to its high thickness. At the beginning of Si sub-cell (~ 3.5 μm from the top of the solar cells); the energy loss is about 4.8 eV.Å^{-1} and its increase where it reach 6.4 eV.Å^{-1} at 10 μm. By going deeper into the cell the deposited energy increase rapidly and reach its maximum 11.2 eV.Å^{-1} where the protons come to rest (Bragg peak).

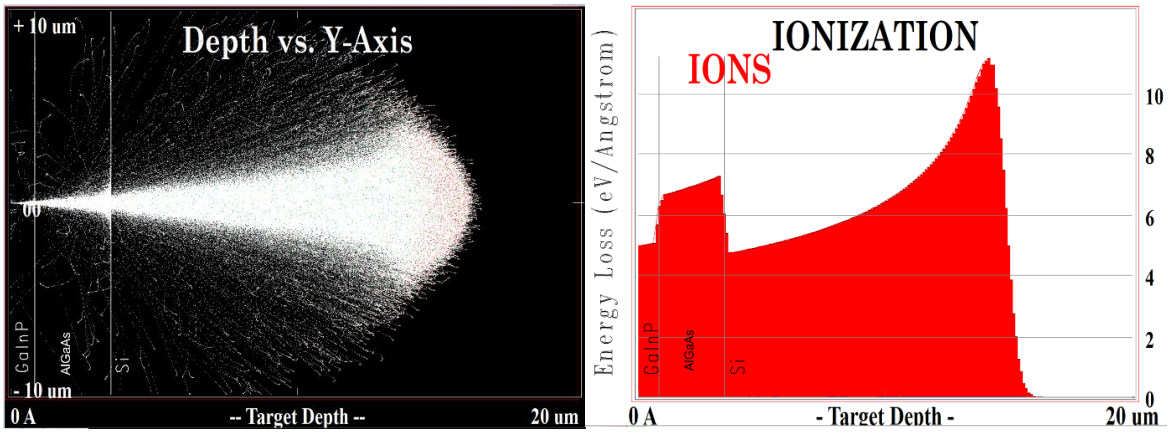

Fig. III-27 *(Left) Trajectory of 10^5 p.cm^{-2} with 1-MeV unidirectional proton beam into 3J GaInP/AlGaAs//Si (right) deposited energy by ionization into each sub-cell of the 3J simulated using Monte Carlo ion transport code SRIM.*

The same simulations were conducted on both 1J and 2J solar cells in order to quantify the deposited energy and the protons range. In the case of 1J, near the surface the proton energy loss is about 4 eV.Å^{-1} and reach 11.3 eV.Å^{-1} at a depth of 16.5 µm where the protons come to rest. For 2J solar cells, the energy losses in the AlGaAs top sub-cell are relatively homogenous with an average energy of 6.5 eV.Å^{-1}. However for Si bottom sub-cell the same behavior is observed as for 3J and 1J where the energy losses near the interface AlGaAs//Si is about 4.5 eV.Å^{-1} and reach 11.3 eV.Å^{-1} at Bragg peak (15.3 µm). The simulated parameters (energy losses, range into the cell and into the Si sub-cell) are summarized in Tab. III-9 for the three solar cells architectures.

Tab. III-9 *Protons energy losses into 1J and each sub-cells of the 2J and 3J with the corresponding penetration depth of protons into the solar cells.*

Sub-cells	**1J**	**2J**		**3J**		
	Si	AlGaAs	Si	GaInP	AlGaAs	Si
Energy losses (eV.Å^{-1})	4 - 11.3	6.5	4.5 - 11.3	5	7	4.8 - 11.3
Range (µm)						
Solar cells	16.5	15.3		14.7		
Si cells/sub-cell		13.1		11.2		

The difference in energy losses in the top sub-cell of the 2J ($Al_{0.22}GaAs$) and the middle sub-cell of the 3J ($Al_{0.03}GaAs$) is mainly due to the difference in material density, i.e. higher density in the case of the 3J due to the low concentration of Al, therefore higher energy losses.

In the case of electron irradiation, the deposited energy does not vary within the depth of each junction. This is not the case of 1 MeV protons irradiation where in the case of the Si in all three architectures, the energy lost at the beginning of the path is higher in the case of 3J than in 2J and 1J. This is because in the case of 3J, top/middle slow down more the protons as they pass through than in the case of top sub-cells in 2J and low energy protons deposit more energy than energetic one [55].

From simulation results, it is observed that the protons penetration depth decrease by increasing the number of junction (see Tab. III-9) because of additional layers. Due to the relatively small thickness of top and top/middle sub-cells in the case of 2J and 3J (~ 2 - 4 μm), the deposited energy over their entire depth is relatively constant, therefore a homogenous degradation is expected on all the junctions depth. However, in the case of Si it is observed that energy losses is not homogenous and it is more important close to the implantation depth. Therefore we distinguish three main regions in the Si bottom cell: i) the first part, a few micrometers (~ 10 μm) where the degradation is relatively homogenous, ii) the second part is highly degraded due to high energy deposited near the Bragg peak (protons end of track); the depth depends on solar cells architectures (16.5 μm for 1J, 13.1μm and 11.2 μm for 2J and 3J respectively), and finally iii) the third region where the Si is not irradiated, beyond the Bragg peak. These three main regions are responsible for a very different minority carrier diffusion length according to the cell depth, i.e. qualitatively a low L_{eff} in the first region, a very low L_{eff} in the second region and a high (un-affected) L_{eff} in the third region.

III.3.2. Current-Voltage Characterization

The investigation of the behavior of each solar cell with respect to 1 MeV protons irradiation was performed by means of *I-V* measurements on nine solar cells for each architecture before and after irradiation (three samples per fluence). The same condition and characterization protocol were followed as for electron irradiation, i.e. AM0 spectrum at an intensity of 1367 $W.m^{-2}$ and at 300 K using *Helios 3030* solar simulator.

In the case of 1J (see Fig. III-28 top), 1x1 cm^2 samples were used, at *BOL* (black curves), their *I-V* characteristic curves show low statistical dispersion with average values of J_{SC}, V_{OC} and FF of 39.1 $mA.cm^{-2}$, 0.559 V and 82% respectively. After irradiation (colored curves), a strong decrease in the J_{SC} is observed compared to the V_{OC} and it is more pronounced with increasing fluence. However, no irregularities or uncommon degradations influencing the fill

factor were observed. The absolute electrical parameters are summarized in the Tab. III-10 with a low analyzed dispersion (< 3%) for each cells group at a given fluence.

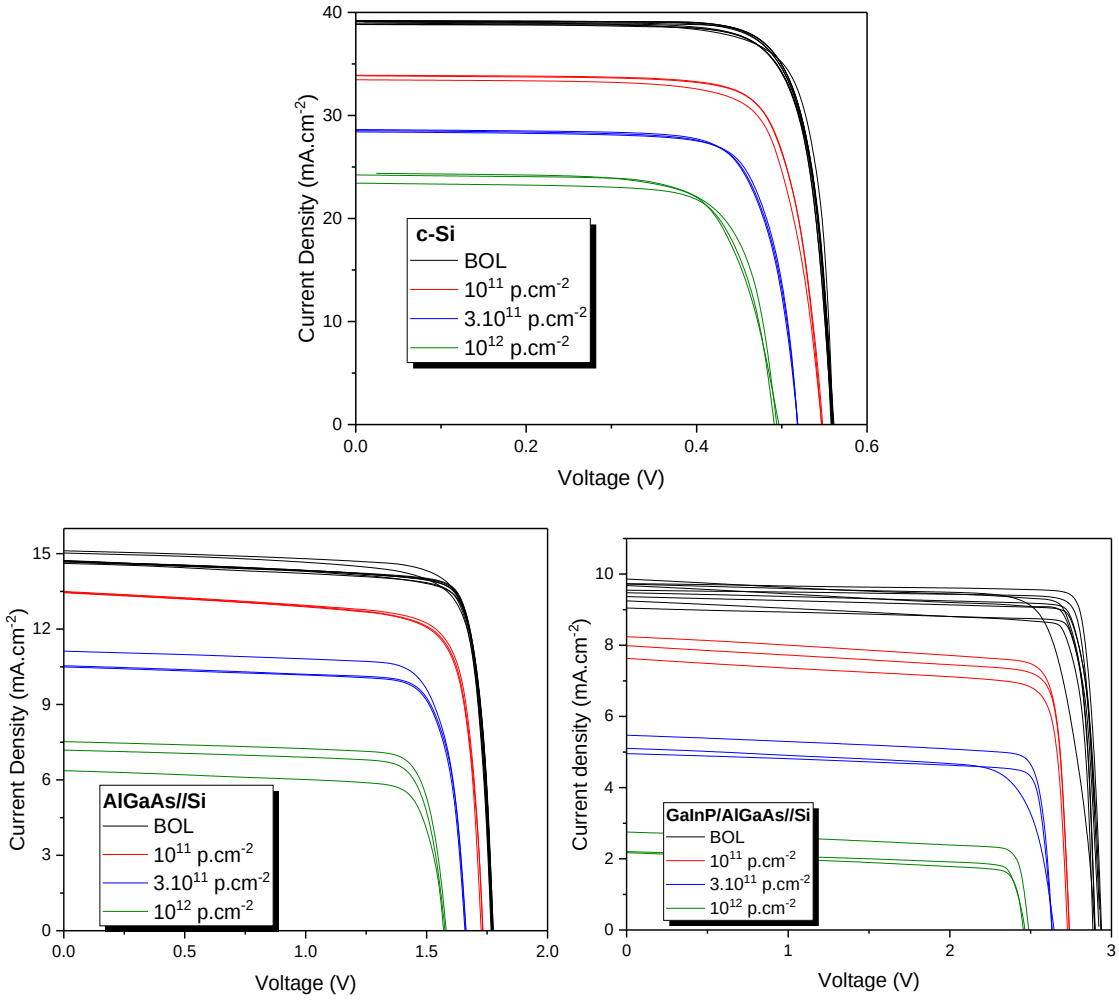

Fig. III-28 *Current Voltage characterization of the three solar cells architectures at BOL and EOL under AM0 spectrum and 300 K (top) 1J c-Si 1 x 1 cm² (bottom-left) 2J AlGaAs//Si 1 x 1 cm² and 2 x 1 cm² (bottom-right) 3J GaInP/AlGaAs//Si 0.5 x 1 cm², 1 x 1 cm² and 2 x 1 cm². High statistical dispersion for 3J solar cells is due to the difference in solar cells sizes.*

Tab. III-10 *Average electrical parameters on nine solar of 1x1 cm² sizes characterized at AM0 spectrum and 300 K at BOL and EOL.*

1J c-Si	**BOL**	**10^{11} p.cm^{-2}**	**3.10^{11} p.cm^{-2}**	**10^{12} p.cm^{-2}**
J_{SC} (mA.cm^{-2})	39.1 ± 0.5%	33.7 ± 0.7%	28.5 ± 0.4%	24 ± 2.1%
V_{OC} (V)	0.559 ± 0.3%	0.547 ± 0.1%	0.519 ± 0.04%	0.494 ± 0.5%
FF (%)	82 ± 0.5%	79 ± 1.1%	79 ± 1%	76 ± 2.8%

Efficiency (%)	13.2 ± 1.1%	10.7 ± 1.7%	8.5 ± 0.4%	6.6 ± 2.5%

In the case of 2J AlGaAs//Si (see Fig. III-28 bottom-left), two large cells (2 x 1 cm^2 size) have a higher J_{SC} at *BOL* compared to the 1 x 1 cm^2 ones, which have a low data dispersion (< 2.3%). After irradiation, a low degradation on J_{SC} is observed at the lowest fluence 10^{11} $p.cm^{-2}$, however by increasing the fluence, a higher degradation is measured. This is due to the fact that the AlGaAs is limiting the total current of the 2J at a fluence lower than 10^{11} $p.cm^{-2}$ thus a moderate degradation is observed. However, by increasing the fluence above 10^{11} $p.cm^{-2}$ an inversion of limiting sub-cell occurs from AlGaAs to the Si one, which is less radiation hard, so a higher J_{SC} degradation is observed, this trend will be investigated in more details later in this manuscript by using *EQE* measurements. Due to differences of electrical performances between the two cells sizes at *BOL* leads to differences after irradiation, i.e. the cell with higher J_{SC} remains higher after irradiation. The absolute electrical performances at *BOL* and *EOL* are resumed in Tab. III-11.

Tab. III-11 *Average electrical parameters on nine 2J solar of 2x1 cm² and 1x1 cm² sizes characterized at AM0 spectrum and 300 K at BOL and EOL.*

2J AlGaAs//Si	**BOL**	**10^{11} p.cm^{-2}**	**3.10^{11} p.cm^{-2}**	**10^{12} p.cm^{-2}**
J_{SC} (mA.cm^{-2})	14.8 ± 1.7%	13.5 ± 0.2%	10.7 ± 3%	7 ± 8.3%
V_{OC} (V)	1.773 ± 0.3%	1.731 ± 0.2%	1.661 ± 0.2%	1.577 ± 0.3%
FF (%)	84 ± 1.1%	80 ± 0.5%	81 ± 0.7%	81 ± 1.8%
Efficiency (%)	16.1 ± 2.3%	13.7 ± 0.5%	10.6 ± 2.8%	6.6 ± 10.4%

Considering the 3J GaInP/AlGaAs//Si (see Fig. III-28 bottom-right), high statistical dispersion reaching 6% on efficiency is observed for the *I-V* characteristics curves of the selected solar cells at *BOL*. This is due to the different samples sizes used (2 x 1 cm^2, 1 x 1cm^2 and 0.5 x 1 cm^2). After irradiation, a low degradation is observed at the lowest fluence 10^{11} $p.cm^{-2}$ contrary to expectation because it the Si bottom sub-cell that limits the current of the 3J even at *BOL*, this behavior will be investigated by *EQE* of the sub-cells. However, by increasing the fluence, a high J_{SC} degradation is observed due to the Si degradation (low radiation hardness). The degradation of electrical properties is correlated to the irradiation

fluence with also higher statistical dispersion reaching 16% at EOL. Tab. III-12 presents the absolute electrical parameters at *BOL* and *EOL* for 3J solar cells.

Tab. III-12 *Average electrical parameters on nine 3J solar of 2x1 cm², 1x1 cm² and 0.5x1 cm² sizes characterized at AM0 spectrum and 300 K at BOL and EOL.*

3J GaInP/AlGaAs//Si	BOL	10^{11} p.cm^{-2}	3.10^{11} p.cm^{-2}	10^{12} p.cm^{-2}
J_{SC} (mA.cm^{-2})	9.5 ± 4.3%	8 ± 4%	5.2 ± 5%	2.4 ± 12%
V_{OC} (V)	2.919 ± 1%	2.738 ± 0.2%	2.639 ± 0.3%	2.472 ± 0.6%
FF (%)	87 ± 5%	84 ± 0.5%	82 ± 3%	76 ± 3%
Efficiency (%)	17.8 ± 6%	13.4 ± 4%	8.3 ± 6%	3.3 ± 16%

In order to compare the evolution of the electrical parameters between each solar cell architecture (1J, 2J and 3J) it is preferable to follow the evolution of the remaining factor as a function of the fluence, especially in the case where a strong dispersion is analyzed at *BOL*. The calculated remaining factor values are plotted against 1 MeV protons fluence (symbols) in Fig. III-29 for J_{SC}, V_{OC} FF and efficiency. Measured data were fitted using Eq. I-2 to investigate the behavior of each electrical parameters on a wide range of protons fluence (solid lines). The fit curves coincide very well with the evolution of all the measured electrical parameters as reported in literature [24], [50], [56] with an *RMSE* of 7.10^{-3} except in the case of the 2J fill factor which did not fit with Eq. I-2 due to limiting sub-cell variation. The fit parameters found when using Eq. III-2 are presented in Tab. III-13.

Tab. III-13 *The used fit Parameters (A_x and $Ø_x$) of electrical parameters remaining factor for 1J, 2J and 3J according to Eq. III-2 after protons irradiation.*

Architectures / Parameters		RF(J_{SC})	RF (V_{OC})	RF(FF)	RF(Eff.)
c-Si	A_x	0.121	0.058	0.024	0.15
	$Ø_x$(p.cm^{-2})	4.17 x 10^{10}	1.49 x 10^{11}	4.14 x 10^{10}	3.8 x 10^{10}
AlGaAs//Si	A_x	0.355	0.0526	Des not Fit	0.279
	$Ø_x$(e.cm^{-2})	2.87 x 10^{11}	1.41 x 10^{11}		1.33 x 10^{11}
GaInP/AlGaAs//Si	A_x	0.341	0.0533	0.193	0.309
	$Ø_x$(e.cm^{-2})	1.21 x 10^{11}	5.56 x 10^{10}	9.13 x 10^{11}	7.34 x 10^{10}

In the case of the **J_{SC}** (see Fig. III-29 top-left), a low degradation less than 20% is calculated for the three architectures at the lowest fluence 10^{11} p.cm^{-2}. By increasing the protons irradiation fluence the defect density increases, thus higher degradation is measured where it reaches 40%,

53% and 75% for the 1J, 2J and 3J respectively at the highest fluence 10^{12} p.cm^{-2}. The degradation becomes visible from a fluence of 10^{9} p.cm^{-2} where it is identical for 1J and 3J and is lower than 2J. Beyond a fluence of 10^{10} p.cm^{-2} the degradation of 3J is more important in comparison with the two other cell architectures due to the limited absorption range of Si to the high wavelength where the irradiation effect is more important because of low diffusion length of minority carrier (electrons in p-type). Considering 1J and 2J, a crossover point is observed at a fluence of 3.10^{11} p.cm^{-2} where the degradation under irradiation of 1J solar cell is higher below and lower above that fluence. This behavior can be explained by the fact that the top sub-cell (AlGaAs) with a better radiation hardness limits the total current of the 2J at a fluence lower than 3.10^{11} p.cm^{-2}, while beyond this fluence it is the Si sub-cell with its lower radiation hardness that takes over the limitation of the 2J current. For a better understanding of the solar cells J_{SC} evolution according to the irradiation fluence, further characterization on each sub-cells by *EQE* will be discussed.

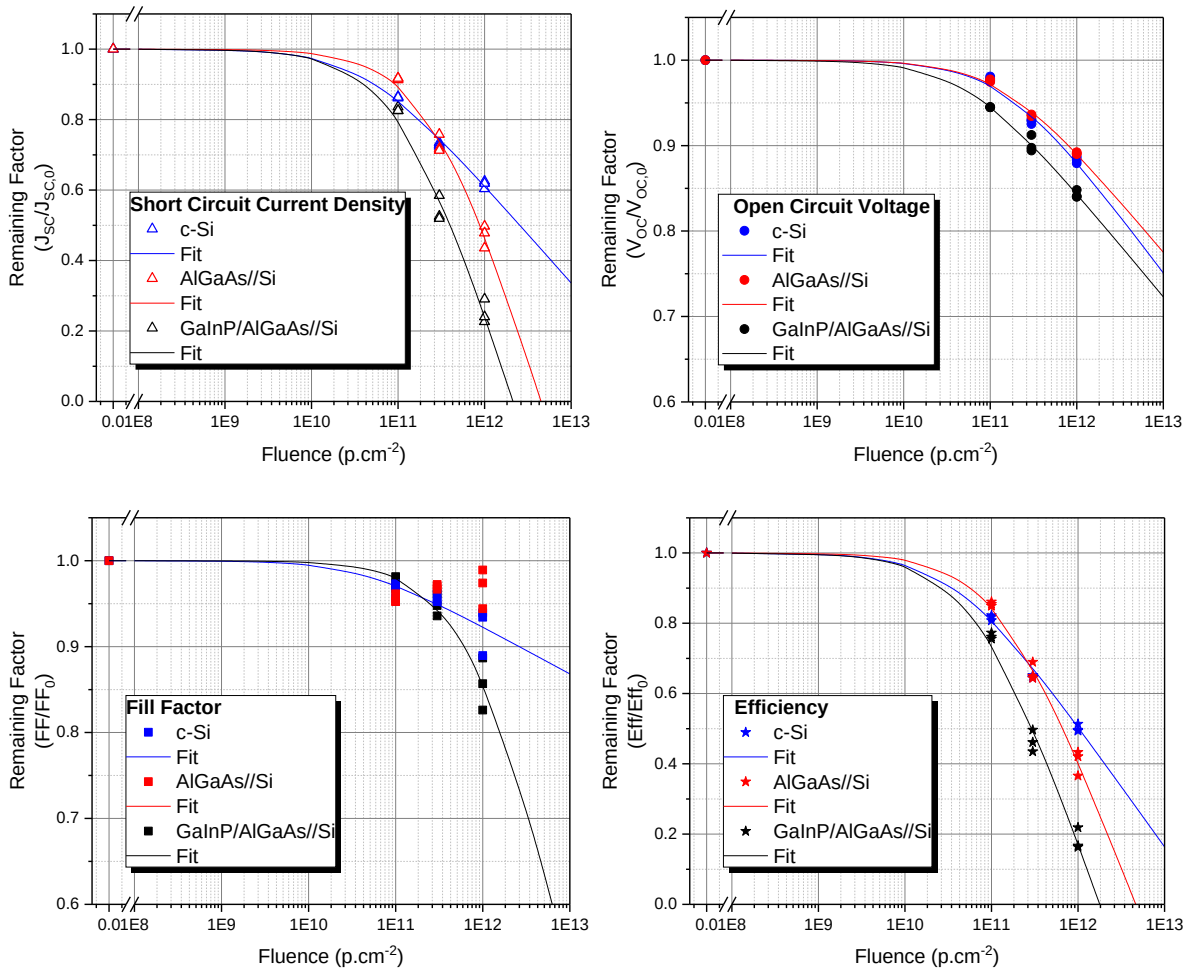

Fig. III-29 *Remaining factor calculations of the three architectures solar cells (1J, 2J and 3J) after 1 MeV protons irradiation on the (top-left) Short-circuit current density (top-right) Open circuit voltage (bottom-left) Fill Factor (bottom-right) Efficiency. The measured electrical parameters are presented by symbols while the linear curve*

represents the fit using Eq. III-2. Note: the Y-scale is not the same for all graphs in order to show clearly the variation of each electrical parameters as a function of 1-MeV electrons fluence.

The degradation of the **V_{OC}** (see Fig. III-29 top-right) of the three architectures is visible from a fluence of 10^{10} p.cm^{-2} however low values are calculated of 11 % for both 1J and 2J and 15% for 3J at 10^{12} p.cm^{-2} . By comparing the degradation of the three architectures as a function of fluence, it is observed that the degradation is more important for the 3J over the whole irradiation range whereas for the 1J and 2J almost the same degradation is calculated. This trend is in contrary to our expectations given that the 3J is composed from three sub-cells with the top and the middle that have a better resistance to radiation. This effect can be due to the high energy deposited in the top GaInP and middle AlGaAs sub-cell compare to the case of electrons, and to the homogenous degradation in the top cells compare to the Si where defects are localized in the first ~15 μm of the sub-cell.

A low degradation is calculated for the **FF** on all three architectures and is less than 20% at the highest fluence considered in this work 10^{12} p.cm^{-2} (see Fig. III-29 bottom-left). In the case of 1J and 3J, the FF evolves as a function of protons fluence according to Eq. III-2. However, in the case of 2J, a low degradation (5%) is observed at a fluence of 10^{11} p.cm^{-2} and then a recovery is observed at high fluence (degradation less than 5%). As in the case of electrons irradiated 2J, this effect is explained by an inversion of limiting sub-cell at a fluence of 10^{11} p.cm^{-2}. This phenomenon does not appear in the case of the 3J because there is no limiting sub-cell inversion.

Due to the high degradation of J_{SC} compared to the V_{OC} and FF, the **efficiency** variation follows the behavior of the J_{SC}. Higher degradation is observed for 3J compared to 1J and 2J with values reaching 80% at a fluence of 10^{12} p.cm^{-2}. In the case of 1J and 2J, a crossover point at a fluence of 10^{11} p.cm^{-2} is observed where the degradation of 2J efficiency is higher than the 1J at low fluence and higher at high fluence. We would like to remind to the reader that the remaining factor does not reflect the absolute values for each architectures but only the relative degradation compare to the *BOL* ones.

III.3.3. Quantum efficiency characterization

Quantum efficiency measurements were performed on the three 300 K solar cell architectures before and after proton irradiation. As previously explained, this technique allows the analysis of the behavior of each sub-cell separately and to investigate the quality of each sub-cell as a function of its depth. Fig. III-30 (top) shows the results of the *EQE* measurements carried out on the 1J at *BOL* (black curves) and *EOL* (colored curves).

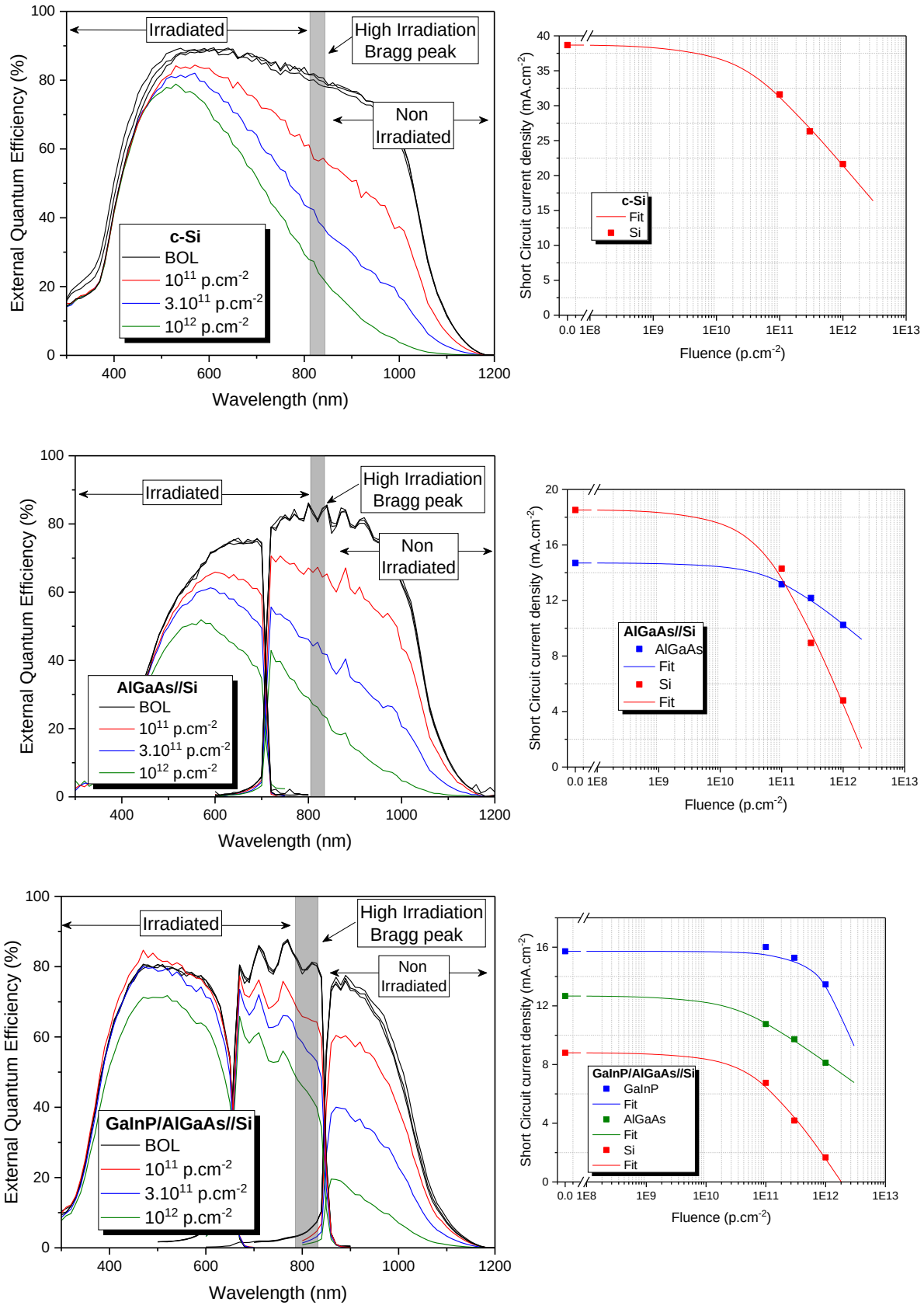

Fig. III-30 *Quantum efficiency characterization of each sub-cell of the three solar cells architectures at BOL and EOL with respect to their J_{SC} evolution as a function of fluence for (top) 1J c-Si, (middle) and 2J AlGaAs//Si (bottom) 3J GaInP/AlGaAs//Si. The grey rectangle represent the region where the energy transferred to recoils is more than 10%.*

After irradiation, degradation is observed over a large absorption range of Si. Contrary to the behavior observed after electron irradiation, a slight degradation is observed even at the short wavelengths (~500 nm) which corresponds to the response of the emitter and the *SCR*. This can be explained by the fact that protons during their way through the cells deposit a greater amount of energy in these two layers and therefore a higher defect density. Beyond a wavelength of 500 nm, a higher degradation is observed and is more pronounced at high wavelength (deeper in the cell) due to decrease in the minority carrier diffusion length.

It has been shown by *SRIM* simulations that 1 MeV protons come to rest in the Si cell at a depth of 16.5 μm, where the density of deposited energy is very high resulting in high defect density. The grey rectangle in the *EQE* graph represents the region where the energy transferred to recoils (that cause the most damage on solar cells properties) is more than 10% (inhomogeneous degradation) resulting in a region that extend from 12.4 μm to 16.2 μm. For a fluence of 10^{11} p.cm^{-2} and 3.10^{11} p.cm^{-2}, a different behavior (*EQE* slope) is observed before and after the area of high defect density. A greater slope is observed in the irradiated area and a smaller slope where the cell has not been irradiated. A longer diffusion length after this region compared to that in the irradiated area explains this result. However, at higher fluence we consider that high density of defects is introduced in the cells, therefore the degradation of the minority carrier diffusion length is too important, which hides the effect of non-irradiated part since e-h pairs created at this region has to cross all the irradiated region to reach the junction. For this reason, the difference in *EQE* behavior is not observed at a fluence of 10^{12} p.cm^{-2}.

In the case of 2J (see Fig. III-30 middle), degradation is present on both sub-cells (AlGaAs and Si) and is pronounced at the strong absorption wavelengths of each sub-cells. The grey rectangle represents the part where the degradation is more important due to protons stopping at this region. It extends from 12.3 to 16.1 μm, which corresponds according to the absorption coefficient of Si, to a wavelength range of 805 - 835 nm. By analyzing the *EQE* of the 2J this wavelength portion is part of the absorption of Si. As for 1J, a two different behaviors of the Si sub-cell are observed: i) the degradation is more severe in the region before the Bragg peak where the cell has been irradiated, and ii) the collection probability is better after the Bragg peak because this region has not seen irradiation related recombination defects. At a fluence of 10^{11} p.cm^{-2} and 3.10^{11} p.cm^{-2}, this effect is more visible than the one at a fluence of 10^{12} p.cm^{-2} due to the relatively high introduced defects and thus very low minority carrier diffusion length for this fluence.

By analyzing the behavior of each sub-cell of the 3J (see Fig. III-30 bottom) it can be observed that the degradation is more important in the case of AlGaAs and Si compared to that of GaInP due to its high radiation hardness [57]–[60]. Note that in the case of GaInP, the higher *EQE* observed at low wavelength (400 - 500 nm) after irradiation at the lowest fluence (red curve) is due set-up calibration issues, and thus has no physical meaning. Due to the strong decrease of the minority carrier diffusion length, the *EQE* drop is more pronounced at longer wavelengths. In Fig. III-31 the collision events (displacement and vacancies) are presented as a function of Si cell depth using SRIM simulation, since the displaced atoms and the vacancies are at the origin of the formation of stable complex defect that degrades the diffusion length. It has been identified that a defect density higher than 10% is introduced into the Si sub-cell at a depth range between 10.2 µm and 15.8 µm that correspond to absorption in the wavelength range 786 – 833 nm. In the 3J architecture, this region is non-effective in terms of Si absorption and is positioned in the AlGaAs absorption band. However, this region does not affect the behavior of the AlGaAs sub-cell. Therefore, the observed *EQE* of Si represents the non-irradiated part of the sub-cell with a low degradation at 10^{11} p.cm^{-2} and 3.10^{11} p.cm^{-2} and a higher degradation at 10^{12} p.cm^{-2}.

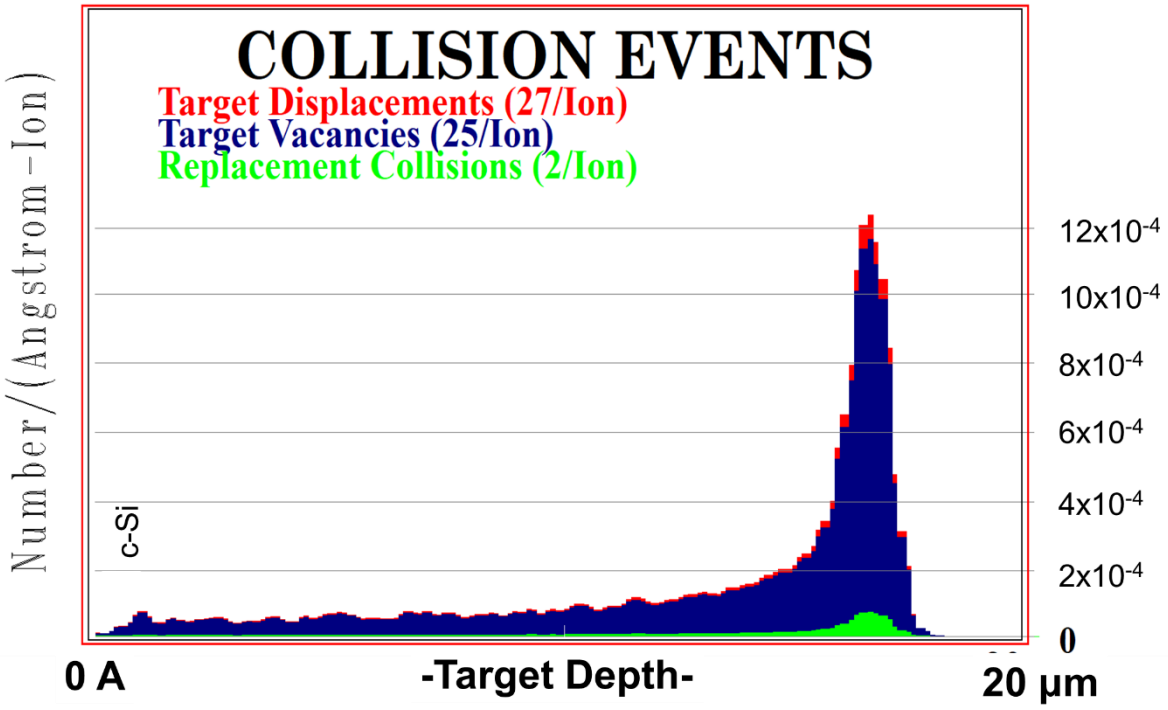

Fig. III-31 *simulation of the induced displacement, vacancies and replacement atoms of Si solar cells irradiated by 1 MeV protons beam.*

The calculated J_{SC} (convolution of *EQE* to the AM0 spectrum) for each sub-cell in all architectures is plotted against 1 MeV protons fluence in Fig. III-30 (right). For 1J cells, the J_{SC}

degradation under protons irradiation can be detected from a fluence of 10^9 p.cm^{-2}. The J_{SC} values decrease from 38.7 mA.cm^{-2} at *BOL* down to 21.6 mA.cm^{-2} at an *EOL* fluence of 10^{12} p.cm^{-2}. The symbols represent the measured data and the solid lines represent the fit to Eq. III-1.

In the case of 2J, the AlGaAs and Si sub-cells photo-generate a J_{SC} of 14.7 mA.cm^{-2} and 18.5 mA.cm^{-2}, respectively. Thus, the AlGaAs is the current limiting sub-cell. The degradation of AlGaAs becomes visible at a fluence 10 times higher than for Si sub-cell. Due to high degradation of Si in comparison to AlGaAs cells, at a fluence of 10^{11} p.cm^{-2}, both sub-cells reach almost the same photo-generated current of ~ 14 mA.cm^{-2}. After this critical fluence, the photo-generated J_{SC} for Si bottom sub-cell is less than the AlGaAs top cells, therefore limits the total current of the 2J where values of 10.2 mA.cm^{-2} and 4.8 mA.cm^{-2} are calculated for AlGaAs and Si sub-cells respectively at a fluence of 10^{12} p.cm^{-2}. For these reasons, fluctuation of FF is observed for 2J, where after the FF value reaches its minimum at a fluence of 10^{11} p.cm^{-2} due to current matching between sub-cells. However for fluence higher than 10^{11} p.cm^{-2}, the two sub-cell deviate from the current matching condition again, thus the FF increases so it remaining factor (see Fig. III-29 bottom-left).

For 3J cells, the fluence at which the J_{SC} degradation of the three sub-cells becomes visible is shifted by a factor of 10 between each sub-cell, i.e. 10^{11} p.cm^{-2}, 10^{10} p.cm^{-2} and 10^9 p.cm^{-2} for GaInP, AlGaAs and Si respectively due to the difference in material radiation hardness differences. At *BOL*, the Si bottom sub-cell limits the overall current of the 3J at 8.8 mA.cm^{-2} while the AlGaAs and GaInP photo-generate a current of 12.7 mA.cm^{-2} and 15.7 mA.cm^{-2} respectively. After irradiation at a fluence of 10^{11} p.cm^{-2}, a slight degradation of the Si sub-cell is observed that reaches a value of 1.7 mA.cm^{-2} at a fluence of 10^{12} p.cm^{-2}. In the case of the tops cells AlGaAs and GaInP a lower degradation is observed. The low J_{SC} degradation observed by current-voltage characterizations of 3J at low fluence is due to the fact that the Si bottom sub-cell (limiting sub-cells) *EQE* represents only the non-irradiated region. However, at higher fluence more defects are introduced inducing higher degradations on the overall bottom sub-cell.

Effective diffusion length calculation

In order to calculate the minority carriers diffusion length, we use the model proposed by B. Fischer [14] described by III-5. The resolution and explanation of the model have been given earlier (see section III.2.5).

Within the fit region 500 - 990 nm, the model fits well with experimental results at *BOL* (see Fig. III-32 left) with *RMSE* values of 0.75. However, after irradiation, by using the same wavelength region the model does not fit to the experimental data (*RMSE* of 6.02). This large deviation is due to the fact that in EOL, the protons irradiations has created an inhomogeous defect densities within the wafer depth. This is responsible for the shape of the EOL EQE curve, and can be modeled by a variation of minority carrier's apparent diffusion length (defined has diffusion length of minority carriers photo-generated by a given photons wavelength range). In the 500 - 830 nm wavelength range, a smaller apparent diffusion length is expected compared to the 830 - 990 nm range due to the pristine region as shown by SRIM simulation. Considering these two wavelength portions, i.e. applying the model to each region separately, the model fits very well to the experimental results with an RMSE value in the order of ~ 1 (see Fig. III-32 right). The Tab. III-14 summarized the calculated diffusion lengths. Before irradiation, a value of 658 µm is calculated. After 1 MeV protons irradiation, the calculated apparent diffusion length values for the 500 - 830 nm region (resp. 830 - 990 nm) are 31.8 µm (resp. 240 µm) 11.2 µm (resp. 96 µm) and 4.6 µm (resp. 4.6 µm) for a fluence of 10^{11} p.cm^{-2}, 3.10^{11} and 10^{12} p.cm^{-2} respectively.

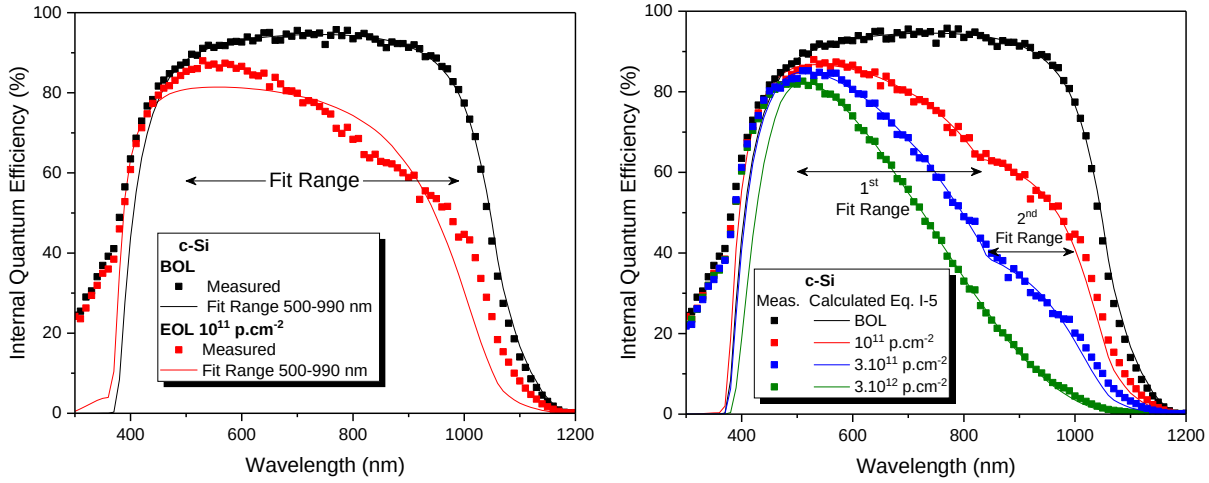

Fig. III-32 *Dead layer IQE model application on 1J c-Si solar cell to defines the minority carrier lifetime: (left) using a single wavelength band 500-990 nm including the irradiated and non-irradiated part of the cell and (right) using two wavelength band separating the irradiated and non-irradiated region of the cell.*

As expected, high degradation of apparent L_{eff} is observed at the region 500 - 830 nm compared to the region 830-990 nm. It is important to note that the effective L_{eff} of the non-irradiated part does not change and remains at its initial value (~600 µm) since it is not irradiated. However, the calculated values by the model represent the apparent effective diffusion length of the e-h pairs photo-generated at this part and crossing all the irradiated one to reach the junction. However, at the highest fluence (10^{12} p.cm^{-2}) it was not necessary to

divide the fit region into two parts because the same diffusion length value is obtained over the whole range 500 – 990 nm. The large rate of introduced defects causes too much degradation and therefore affects the apparent lifetime in the non-irradiated part where it reaches the same as the irradiated one.

The same calculations were performed on the Si sub-cell of the 2J where the two fit regions are 750 - 840 nm and 840 - 990 nm for the irradiated and non-irradiated portion, respectively. The Tab. III-14 presents the calculated minority carrier diffusion lengths. The same pattern is observed as for the 1J cell, with a strong degradation of L_{eff} in the irradiated region relative to the second while the same degradation is observed at the higher fluence 10^{12} p.cm^{-2}. It was shown that the *EQE* of the Si in the 3J represents only the non-irradiated part due to the absorption of the top sub-cells. Therefore, the fit was carried out over the entire absorption band of the Si 890 - 990 nm. Before irradiation, a low apparent L_{eff} value of 225 µm is calculated due to low quality of Si bottom sub-cell. After irradiation, a small degradation is calculated where apparent L_{eff} value reaches 51 µm at a fluence of 10^{12} p.cm^{-2}. This is due on one hand the Si sub-cell is located in pristine undamaged regions of the 3J and on the other hand to the low quality of the Si bottom cell with smaller L_{eff} value at *BOL*.

Tab. III-14 *Minority carrier diffusion length (& apparent diffusion length) calculated from IQE measurements in all architectures on BOL and EOL (irradiated & non-irradiated region) of the Si cell/sub-cell.*

Diffusion Length L_{eff}	**1J c-Si**		**Si @ 2J**		**Si @ 3J**
	1st region	2nd region	1st region	2nd region	2nd region
BOL	658 µm		509 µm		225 µm
10^{11} p.cm^{-2}	32 µm	241 µm	181 µm	388 µm	203 µm
3.10^{11} p.cm^{-2}	11 µm	96 µm	29 µm	134 µm	157 µm
10^{12} p.cm^{-2}	4.6 µm		9.9 µm		51 µm

In order to validate these results, *IQE* simulations were performed using PC1D software on the 1J solar cell architecture. The obtained results are presented in Fig. III-33. A first simulation was performed with one effective minority carriers diffusion length (L_{eff} = 32 µm) for the whole thickness of the Si cell. By comparing the simulated IQE (blue dash line) to experimental results (black symbols), it is observed a relative shape similarity at lower wavelength (λ < 800 nm). However, for higher wavelength (λ > 800 nm) the simulation does

not reproduce the trend observed in the measured data. For the second simulation, three zones were defined where a first zone is homogeneously degraded (L_{eff} = 32 µm), the second zone strongly degraded due to ion implantation bragg peak (L_{eff} = 7 µm) and the third zone not degraded with (L_{eff} = 658 µm). By comparing the simulation using three zones (red line) to experimental data, a satisfying correspondence was observed on the whole absorption range. These measurements confirm our hypothesis established above with a difference in diffusion length depending on the depth of ion penetration.

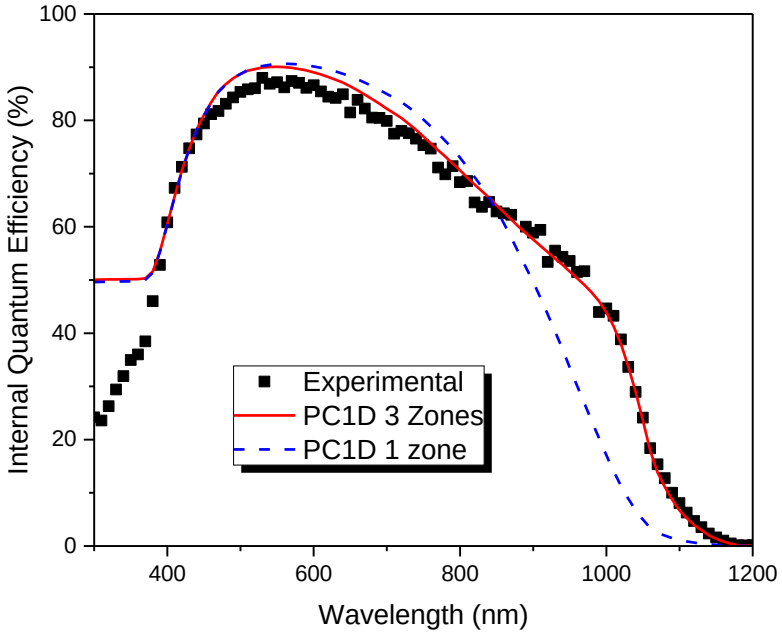

Fig. III-33 *IQE simulation using PC1D on 1J solar cells architecture after 1 MeV protons irradiation with a fluence of 10^{11} p.cm^{-2}. Black symbols represent experimental results while lines represent simulation (blue) using one L_{eff} for the whole Si cell and (red) using three L_{eff} depending on local degradation.*

From the apparent diffusion length calculated by the *IQE* model on the experimental measurements and Eq. III-8, which expresses the evolution of L_{eff} as a function of fluence, we have calculated the proton damage coefficient K_L. However, due to the non-homogeneous irradiation and thus the introduced defect as a function of the thickness of the Si cell/sub-cell, the damage coefficient has been calculated for both regions; 1st region: irradiated and 2nd region: non-irradiated. It is important to note that the K_L on the 2nd region represent an apparent effective values of the e-h pairs that are generated in the non-irradiated region and travel all along the irradiated region. Results of calculation are shown in Tab. III-15.

In the case of 1J and 2J cells, it was possible to calculate the diffusion length in the irradiated part of the cell unlike the case of 3J where the thickness of the irradiated cell does

not participate in the creation of e-h pairs (light filtering by the tops cells). Therefore, the calculation of the damage coefficient of the irradiated part that is representative of the effect of proton irradiation on the diffusion length is calculated only for 1J and 2J. Values of 5.3 x 10^{-6} and 1.2 x 10^{-6} are obtained for the Si in the case of 1J and 2J respectively.

Tab. III-15 *Damage coefficients calculated for the Si diffusion length in the irradiated and non-irradiated region as a function of fluence range. The second region represent the e-h pair that are generated in the non irradiated part but cross all the 1st region (irradiated) to reach the junction.*

L_{eff} Damage coefficient	**1st region fit irradiated portion**	**2nd region fit non irradiated portion**	
Fluence range (p.cm^{-2})	10^{11} - 10^{12}	10^{11} - 3.10^{11}	3.10^{11} - 10^{12}
c-Si	5.3 x 10^{-6}	4.6 x 10^{-8}	6.7 x 10^{-6}
AlGaAs//**Si**	1.2 x 10^{-6}	2.4 x 10^{-8}	1.5 x 10^{-6}
GaInP/AlGaAs//**Si**	Not applicable	8.1 x 10^{-9}	4.9 x 10^{-8}

Considering the case of the 2nd region, the apparent minority carriers diffusion length is affected by the defects created in the few micrometers at the top of the Si cell/sub-cell (10 - 16 μm) thus it does not reflect properly the effect of protons induced-defects degradation. As explained above, two regimes are distinguished at this region; a low degradation is observed at fluence below 3.10^{11} p.cm^{-2} compared to higher fluence up to 10^{12} p.cm^{-2}. For this reason, damage coefficients are calculated for these two fluence ranges (see Tab. III-15). At low fluence (< 3. 0^{11} p.cm^{-2}) low effect of introduced defects on minority carrier diffusion length is observed for all architectures. For both 1J and 2J, values in the order of 10^{-8} is calculated, however in the case of 3J, the K_L value reach 10^{-9}. That means that the degradation of L_{eff} in the non-irradiated region is two order of magnitude lower than the one observed at the irradiated one at low fluence. By increasing the fluence higher than 3.10^{11} p.cm^{-2}, the damage coefficient values for 1J and 2J decrease and reach similar values as for the 1st region (irradiated) in the order of 10^{-6}. Pointing that the same degradation of L_{eff} at non-irradiated region is observed as for the irradiated one at high fluence.

In the literature, research groups [61], [62] have reported empirical equations for the evolution of the damage coefficient of the scattering length as a function of proton energy. Eq. III-14 and Eq. III-15 present the approximate value of K_L as a function of proton energy for Si with a doping level of 1 Ω.cm and 10 Ω.cm respectively.

$$K_L(E_p) = 1.5\text{x}10^{-5}.E_p^{-1} \qquad \textit{III-14}$$

$$K_L = 1.56 \text{ x } 10^{-6}.E_p^{-0.933} \quad \textit{III-15}$$

The values calculated for the 1J and 2J (5.3 - 1.2 x 10^{-6}) are in satisfactory agreement with those calculated by the two equations above-mentioned of 0.15 - 1.56 x 10^{-6} and with respect to other values obtained experimentally in other references [63]–[68].

III.4 General discussion

Simulations of the interaction of electrons and protons respectively with *PENELOPE2014* and *SRIM* revealed that a homogeneous degradation as a function of cell depth is obtained for 1 MeV electrons as opposed to 1 MeV protons. During the trajectory of the particles, the low mass electrons give up a small amount of energy compared to the (heavy) proton. In results, the electrons exceed the whole thickness of the cell (~ 525 μm) by yielding a uniform quantity of energy during their way through (in the same material). On the other hand, the protons are stopped in the active part of the solar cell (12 - 16 μm) where a significant quantity of energy is deposited at the Bragg peak (stopping depth). This induces a non-uniform irradiation of the Si cell/sub-cell: before this depth, the irradiation damage are important, and beyond this depth, the material is non-irradiated. An energy higher than 9 MeV would be necessary in order to obtain a uniform protons irradiation in the solar cells used in this study; this was not possible to achieve in the JANNUS Orsay platform. This non-uniform irradiation is not observed at 1 MeV for thinner cells such as GaAs (~1 μm of active region), where proton energy lower than few keV (~100 keV) are needed to stop within the active region of the cell [69]. When charged energetic particles pass through the semiconductor, they slow down by giving up part of their energy to the material; it creates atoms displacements and vacancies [24], [50].

The resulting Frenkel pairs (interstitials-vacancies) can interact with themselves or with impurities in the material and thus generate complex and stable defects such as recombination defects [70], [71]. Several researches have been carried out by deep-level transient spectroscopy (*DLTS*) in order to identify the deep level defects in irradiated Si [72]–[80]. Di-vacancy (V - V) in FZ materials with low energy levels (E_C - 0.23 eV and E_C - 0.39 eV) have been identified and also K - centers with an energy of E_V + 0.36 eV [75], [81]–[83]. These defects act as traps for photo-generated electron-hole pairs and hence degrade the minority carriers diffusion length. This is translated as a degradation at wavelengths close to the bandgap for each sub-cell in *EQE* measurements. Since photons in those energy ranges are absorbed deeply into the cells, this degradation is the consequence of minority carriers diffusion length drop in the p-type base.

The quantification of the minority carrier diffusion length changes as a function of nature of the particle and fluence was based on the *IQE* results of the Si cell/sub-cell. In the case of electron irradiation, homogeneous degradation is observed over the entire solar cell, resulting in a single L_{eff} value for the entire absorption band that drop from ~ 600 μm to 30 μm after irradiation with 1 MeV electrons at fluence of 10^{15} e.cm^{-2} for the three architectures. However, in the case of proton irradiation, two L_{eff} values were calculated for the two regions (irradiated and non-irradiated) for fluence lower than 3.10^{11} p.cm^{-2}. In contrast, at the highest fluence 10^{12} p.cm^{-2} the same L_{eff} was observed for all the absorption range due to the high-introduced defect density, which significantly degrades the diffusion length at the irradiated part. Thus the e-h pairs generated at the non-irradiated part are mostly affected by this region when they cross it to reach the junction. The calculated values at this fluence reach 6 μm, 10 μm and 51 μm for 1J, 2J and 3J respectively. Low L_{eff} values of 3J at *BOL* induces low degradation compared to high *BOL* L_{eff} of the 1J and 2J. The damage coefficient were calculated for Si in all three architectures and found to be in very good agreement with those reported in literature. The low L_{eff} value result in a very low probability that the electron-hole pairs photo-generated beyond a depth equivalent to L_{eff} reach the junction to participate in the total cell current. Thus, a low J_{SC} value after irradiation is observed in the *I-V* measurements where degradation of 20% (resp. 39%), 30% (resp. 53%) and 63% (resp. 75%) are observed at the highest fluence 10^{15} e.cm^{-2} (resp. 10^{12} p.cm^{-2}) for electron (resp. protons) irradiation of 1J, 2J and 3J respectively.

At highest fluence, the degradation of J_{SC} is proportional to the number of junctions in the case of III-V//Si cells. This is due to the solar cell architecture in which the Si absorption band (the limiting sub-cell with the lowest radiation hardness) is thinned and restricted to the longer wavelengths where the effect of diffusion length degradation is the most important. The total J_{SC} of the 1J c-Si cell is the contribution of the entire cell thickness (0 - 525 μm). Whereas in the case of the 2J and 3J tandems, the total J_{SC} of the Si is the product of the photo-generated e-h pairs at a depth higher than 5 μm and 19 μm of the Si sub-cell, respectively. As explained above, the proton fluences studied are in the range of equivalence to the electrons irradiation fluence. Thus, the deposited energies between the two irradiation (particles type, energy and fluence) are equivalent.

The absorption length of photons in silicon is presented as a function of wavelength in Fig. III-34 (left). By superimposing this curve with respect to the 1J c-Si architecture taking into account the Bragg peak of protons in the cell (10.2 - 15.8 μm) represented by a gray

rectangle, we observe that this thickness of the cell corresponds to an absorption of photons of wavelength in the range 800 - 830 nm. In other words, the photons of wavelength less than 800 nm are absorbed in the irradiated part of the cell and the photons beyond 830 nm are absorbed in both the irradiated and non-irradiated part of the cell.

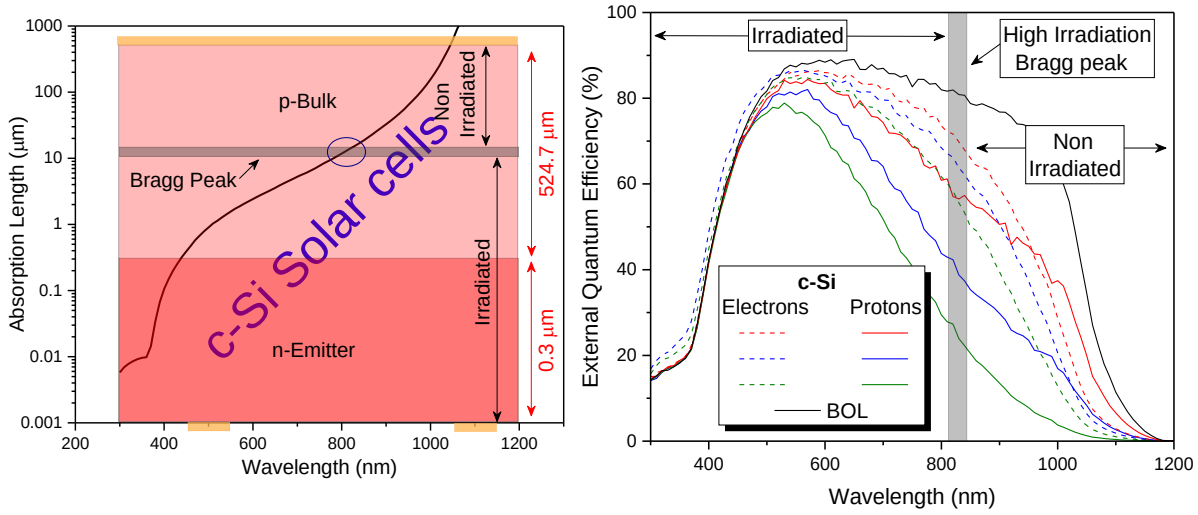

Fig. III-34 *(left) Absorption length of photons in silicon as a function wavelength overlayed on c-Si solar cells architecture (right) EQE comparison of 1J solar cells irradiated with 1 MeV electron at a fluence of 10^{14}, 3.10^{14} and 10^{15} e.cm^{-2} and 1 MeV protons at a fluence of 10^{11}, 3.10^{11} and 10^{12} p.cm^{-2}.*

Fig. III-34 (right) shows a comparison of the 1J solar cells irradiated with 1 MeV electrons (dashed curves) and those irradiated with 1 MeV protons (solid curves). In the damaged region, a slight degradation of the cells irradiated with electrons compared to those irradiated with protons is observed. To correctly compare the behavior of solar cells under electron and proton irradiation it is more meaningful to compare them as a function of the displacement damage dose by each particle and not as a function of the fluence (more details will be given latter). This result could be correlated to the fact that for the solar cell architecture studied in this work, the Bragg peak of 1 MeV protons is located inside the solar cells. By contrary, Bragg peak is usually located far from the bottom cell junction for typical III-V/Ge solar cells [84]. We have therefore in this work a higher amount of energy in the first micrometers and therefore a higher defect density during proton irradiations. As a comparison the protons irradiated with the lowest fluence 10^{11} p.cm^{-2} (solid red curve) have the same behavior as the cell irradiated with the highest electrons fluence 10^{15} e.cm^{-2} (dashed green curve). Beyond the irradiated part (thickness > 16 µm) the behavior of the cell changes due to a higher diffusion length (non-irradiated part of the absorber). In the light absorption range higher than 1000 nm, the degradation is less pronounced in the case of cells irradiated in protons. This is only true for fluence lower than 3.10^{11} p.cm^{-2}, due to the presence of a non-irradiated absorber region

compared to cells irradiated in electrons. However, at a high fluence 10^{12} p.cm^{-2}, the degradation is more pronounced due to the significant degradation of the diffusion length. The same behavior is observed in the case of Si in 2J and 3J solar cells architectures (not shown here).

Irradiation defects degrade also the open circuit voltage (see Fig. III-35) by generating electron-hole pairs thus increasing the dark saturation current J_0 (see Fig. III-7, Fig. III-8 and Fig. III-25) [85]. This effect is more pronounced in silicon material compared to III-V materials [58], and thus as observed here the V_{oc} remaining factor is lower in the case of Si single junction compared to III-V//Si tandem [8], [50], [60] in the case of electrons irradiation.

The spectral electroluminescence measurements allowed the reconstruction of the *I-V* characteristic curves (under dark and illumination) of each sub-cell by resolving the optoelectronic reciprocity between the *ELS*, the *EQE* and the internal voltage of each sub-cell. The *I-V* curves under illumination of the tandem cell characterized by a solar simulator as well as the *I-V* characteristic curves of the III-V sub-cells (AlGaAs in 2J, and GaInP and AlGaAs in 3J) are shown in Fig. III-35. Since Si has a low radiative recombination efficiency (thus weak *EL-S* signal), its characteristic curve have been deduced from the I-V measurements of the tandem and the III-V junctions.

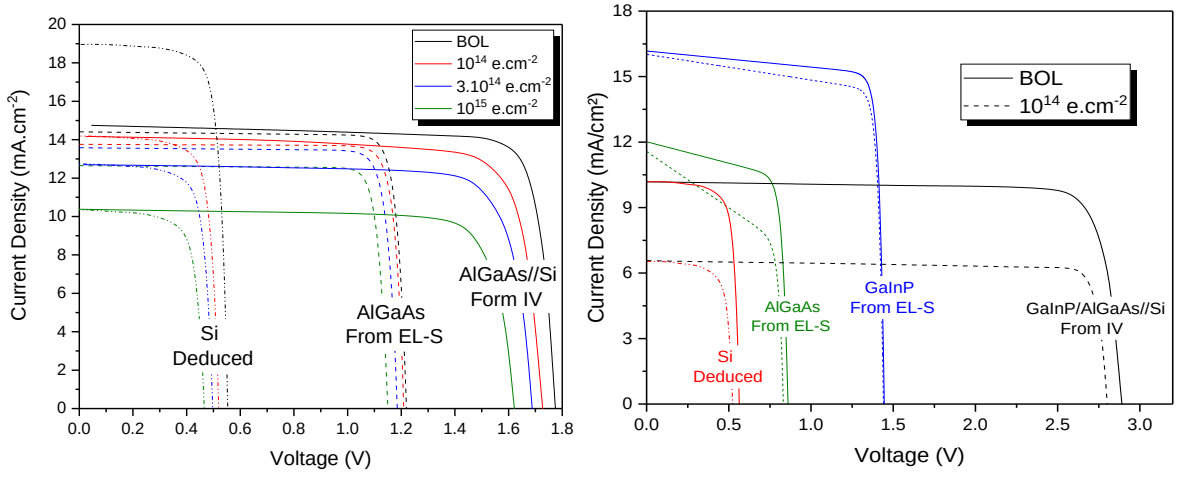

Fig. III-35 *Reconstruction of each sub-cell I-V characteristic curves at BOL and EOL (electrons) from ELS and EQE measurements for (left) 2J AlGaAs//Si (right) GaInP/AlGaAs//Si.*

The current of each sub-cell was characterized by *EQE* measurements, with the total current of tandem cells being limited and driven by that of Si sub-cell at high fluence; in addition the *ELS* measurements were not sensitive enough to measure the signal at very low injection level (for reconstructing the Pmax point). However, reliable measurements are obtained at high

injection level (in the range of V_{OC}). Thus, we were interested by these measurements in the quantification and evolution of the open circuit voltage as a function of the electron irradiation fluence (see Fig. III-36).

The degradation of the V_{OC} of the tandem cells is the sum of the degradation of the V_{OC} of each sub-cell given their series connection. In the case of 2J, the absolute degradation of the V_{OC} of the Si bottom sub-cell is almost equivalent to that of the AlGaAs top sub-cell. On the other hand, when compared to the V_{OC} of each sub-cell, the degradation is 3 times greater in Si than in AlGaAs due to its low resistance to radiation as reported in the literature [11], [57], [86]. In the case of 3J, a very low degradation of the V_{OC} is calculated for GaInP compared to that of AlGaAs and Si; this due to its high resistance to radiation. The relative degradation to each sub-cell V_{OC} is 0.1%, 7.8% and 11.5% respectively at a fluence of 3.10^{14} e.cm^{-2}. The higher degradation of $Al_{0.03}Ga_{0.97}As$ in the case of 3J compare to the one $Al_{0.22}Ga_{0.78}As$ in 2J solar cells is due to the higher density (less Al content) and thickness, which results in a higher deposited energy in the 3J architectures in both cases of electrons and protons irradiation.

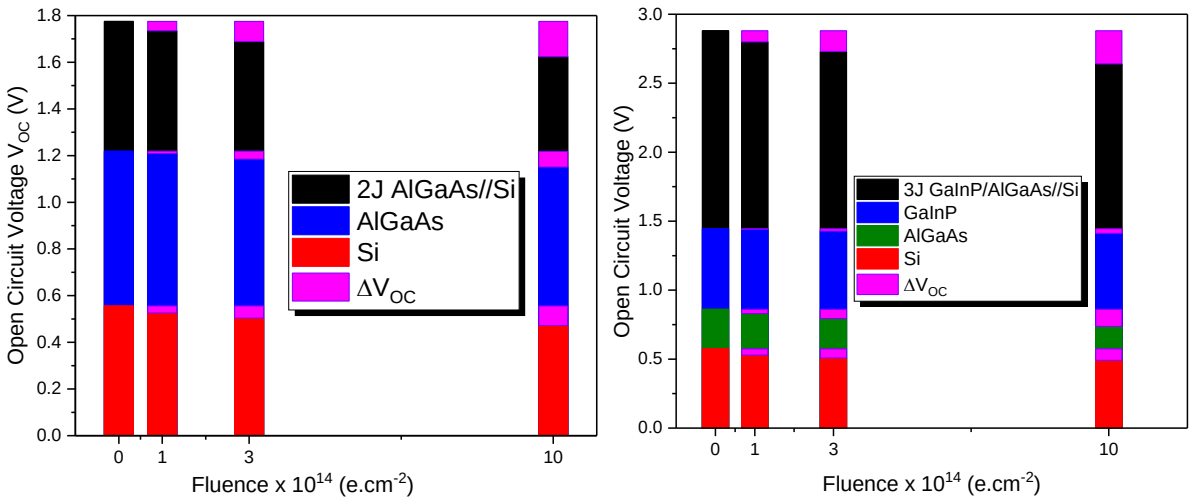

Fig. III-36 *Open circuit voltage degradation of each sub-cell according to electrons irradiation fluence for (left) 2J AlGaAs//Si and (right) 3J GaInP/AlGaAs//Si.*

Concerning the FF, in case of 2J and 3J, the variations are influenced by current matching changes in the different sub-cells; FF reaches a minimum at sub-cells current matching point ($J_{Top} - J_{Bot} = 0$ and $J_{Mid} - J_{Bot} = 0$ in the case of 2J and 3J respectively) as presented in Fig. III-37 (top) [87]–[89]. In the case of 3J, a pronounced current mismatch (bottom-middle) after electrons irradiation can thus lead to increased FF (see Fig. III-37 right) which led to a remaining factor higher than 1 at a fluence lower than 3.10^{14} e.cm^{-2}. By increasing the fluence, RF(FF) degrades and reach values lower than 1 due to high introduced defect density. In

contrast, in the case of proton irradiation this effect has not been observed where the RF(FF) < 1 (see Fig. III-37 right) from the lowest fluence. This may be due on the one hand to the greater degradation of the top sub-cells compared to that observed with electron irradiation and therefore a smaller current deviation. On the other hand, it can be due to the higher defect density in the case of proton irradiation in the case of energy and fluence used in this thesis.

In the case of 2J irradiated by both electrons and protons particles, a low RF(FF) value is observed at the lowest fluence (10^{14} e.cm^{-2} and 10^{11} p.cm^{-2}) and then it increases indicating that a low degradation is observed at high fluence (see Fig. III-37 left). This is explained by the fact that at low fluence both sub-cells of the 2J reach the current matching condition so that the shape factor is at this lower value and therefore a low RF(FF). By increasing the fluence, an inversion of limiting sub-cell occur (from AlGaAs to Si) where the current difference increases with the fluence which induces an increase in the FF and thus a higher RF(FF). At higher fluence of 10^{15} e.cm^{-2} and 10^{12} p.cm^{-2} a decrease is observed for FF due to the high density of defects introduced.

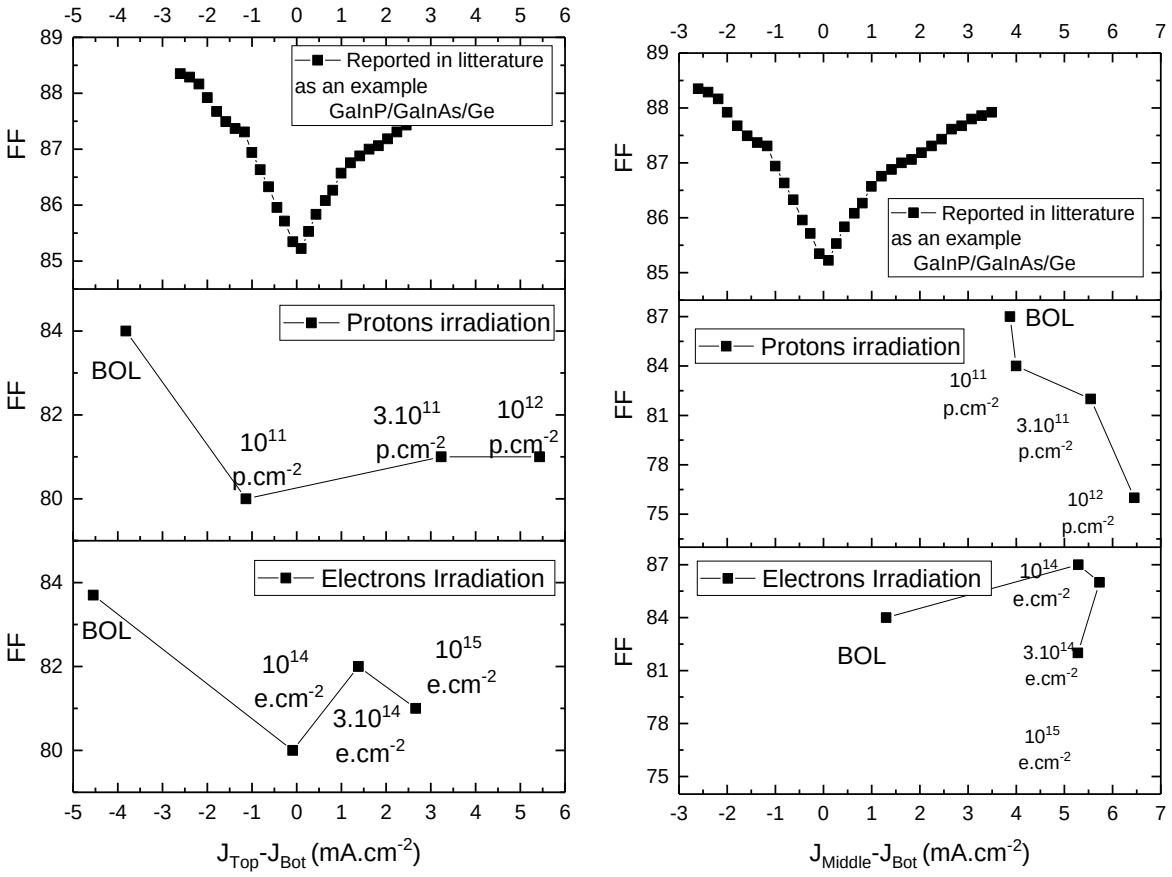

Fig. III-37 *Fill factor variation according to current matching conditions (irradiation fluence) for (left) 2J AlGaAs//Si and (right) 3J GaInP/AlGaAs//Si. Top represents a reported variation of Fill factor for 3J GaInP/GaInAs/Ge according to SMR or CM conditions [87]–[89].*

Electrons and protons correlation

Currently there are two approaches for modelling the degradation of efficiency (and other electrical parameters) as a function of irradiation. The first method was developed by Jet Propulsion Laboratory JPL more than 40 years ago [24], [56]. This method is based on the calculation of the Relative Damage Coefficients *RDCs* as a function of irradiation according to Eq. III-16 and Eq. III-17 for electrons and protons respectively.

$$RDCs(E_p, e, E) = \frac{\emptyset_{crit}(E_p, e, 1\ MeV)}{\emptyset_{crit}(E_p, e, E)} \quad \textit{III-16}$$

$$RDCs(E_p, p, E) = \frac{\emptyset_{crit}(E_p, p, 10\ MeV)}{\emptyset_{crit}(E_p, e, E)} \quad \textit{III-17}$$

The *RDCs* is defined as the ratio of the critical fluence, $\emptyset_{crit}$, for which the degradation of one of the electrical parameters, E_p, is 25% at 1 MeV for electrons and 25% at 10 MeV for protons with respect to the critical fluence at a given energy, E. Four electron energies and eight proton energies with eight fluence for each energy are required to have sufficient data to plot the *RDCs* as a function of particle energy.

The second method was developed by the US Naval Research Laboratory (NRL) [2], [90], [91] and is applied for the correlation between electrons and protons degradation of the cells used in this study. This approach is based on the calculation of the energy dependence of the damage coefficient and the electron and protons incident spectra on bare solar cells. Since only few experimental data are required (one electrons and one protons energy), it is easier to apply this method on new solar cells technologies. In this approach, the evolution of electrical parameters or their degradation is plotted as a function of the dose received and not as a function of fluence. In this way, all the degradation curves as a function of energy collapse into a single curve for electrons and protons which surpass the thickness of the solar cell and therefore for which the *NIEL* is homogeneous as a function of thickness. The displacement damage dose D_d can be calculated by the product of the *NIEL* and fluence according to Eq. III-18.

$$D_d = NIEL_p(E).\emptyset_p \quad \textit{III-18}$$

In the case of electron irradiation, the variation of damage is not linear for all the cells type (e.g. p-type Si). Therefore in order to reduce all the degradation curves, the concept of effective damage dose, $D_{d,eff}$, is introduced (see Eq. III-19).

$$D_{d,eff}\,(1MeV) = NIEL_e(E).\emptyset_e.\left[\frac{NIEL_e(E)}{NIEL_e(1\ MeV)}\right]^{n-1} \qquad \textit{III-19}$$

In the case of cells irradiated with 1 MeV electrons, the *NIEL* value is constant over the entire depth of the solar cell. Therefore, the effective displacement damage dose is calculated by using Eq. III-19 and a *NIEL* value of 2.8 x 10^{-5} MeV.cm^2.g^{-1} Calculated with the so-called SR-NIEL calculator. In this program, the input parameters are the target material composition, element fraction and to the threshold displacement energy.

Due to the small thickness of conventional III-V and III-V/Ge cells, 1 MeV protons beams stopping depth is located beyond the active part of the Ge bottom cell, and therefore the *NIEL* is constant throughout the irradiated part [92]. However in the case of the cells used in this thesis, the protons stop in the active part of the Si cell/sub-cell. Therefore, the assumption that the *NIEL* is constant is no longer valid and it varies significantly with the decrease of its energy where it reaches its maximum towards the penetration depth. S. Messenger et. al. [69] have reported a method for the application of displacement damage dose approach on the cell where protons stops within the active region of the cell. This method is based on the calculation of an adjusted *NIEL* over the entire cell thickness. The *NIEL* value can be calculated from the results of the *SRIM* simulation, more details can be found elsewhere [93]. The NIEL value derived from *SRIM* is then divided by the thickness of the cell/sub-cell Si (525 µm). The adjusted *NIEL* calculated from this procedure is equal to 0.0151 MeV.cm^2.g^{-1} (non-adjusted *NIEL* 0.0634 MeV.cm^2.g^{-1}) that is used further for the calculation of displacement damage dose according to Eq. III-18.

Once the degradation curve is plotted as a function of the displacement damage dose, it is then possible to reduce (normalization) the degradation curve to 10 MeV proton fluences according to Eq. III-20 where 10 MeV protons *NIEL* values is 9.4 x 10^{-3} MeV.cm^2.g^{-1}. Normalization to 10 MeV protons energy is commonly used in space solar cell irradiation community since the degradation is approximately equivalent to the 1 MeV electrons irradiation [94], [95].

$$\emptyset_{\boldsymbol{p}}(10\ MeV) = \frac{NIEL_p(1\ MeV).\emptyset_p(1\ MeV)}{NIEL_p(10\ MeV)} \qquad \textit{III-20}$$

The degradation results of the efficiency (RF(Eff.) =RF(Pmax)) remaining factor are presented in Fig. III-38 (left) in terms of the irradiation fluence of 1 MeV electrons (black) and

10 MeV protons (red) energy for the three architectures. It is observed that the two degradation curves (electron-protons) are parallel for 1J and 2J and not in the case of 3J due to cell architectures differences.

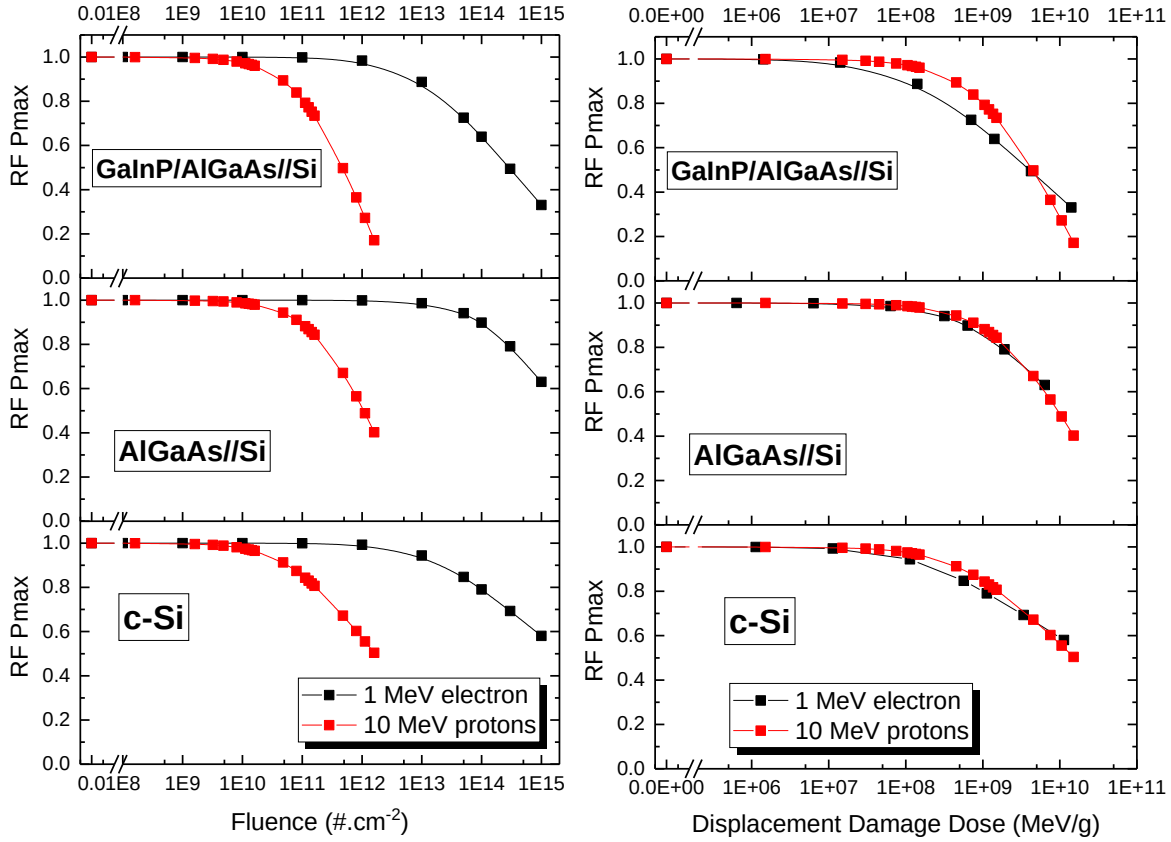

Fig. III-38 *Correlating electrons and protons efficiency degradation of the three solar cells architectures (left) Evolution of RF(efficiency) according to the fluence of 1 MeV electrons and 10 MeV protons irradiation (right) Efficiency degradation curves as a function of displacement damage dose.*

In order to correlate the degradation of cells irradiated with electrons with those irradiated with protons, a fluence ratio R_{ep} should be determined. In the case of n-type semiconductors the ratio is calculated by the ratio of the respective *NIEL* values. However, for the case of p-type semiconductors it is not as simple; it is defined experimentally as the fluence ratio that produces the same degradation by 1 MeV electrons as that by 10 MeV protons. A value of 3500 was determined for p-type Si of 80 µm [91]. In the case of experimental results found in this thesis the calculated R_{ep} are 830, 1478 and 665 for 1J, 2J and 3J solar cells respectively. The difference between the reported values in literature and the one found in this study can be due mainly to the solar cells architectures variations.

Once all the quantities are calculated (adjusted *NIEL* and R_{ep}) it is then possible to report the degradation of the efficiency of the three architectures as a function of the displacement damage dose according to Eq. III-18 and Eq. III-21.

$$D_d = \frac{D_{d,eff}\,(1MeV)}{R_{ep}.\frac{NIEL_e(1\ MeV)}{NIEL_p(10\ MeV)}} \qquad \textit{III-21}$$

The results of this procedure are shown in Fig. III-38 (right). In the case of 3J the two degradation curves does not fit perfectly with a degradation which is initiated at a lower *DDD* in the case of electron irradiation compared to the proton one. Whereas at higher doses the degradation is more pronounced in the case of proton irradiation. The type of irradiating particles may not be the cause of the difference in degradation but rather the difference in architecture between the Si sub-cell in the case of cells irradiated with electrons and protons due to different fabrication process (emitter obtained by diffusion and implantation) and quite different *BOL* diffusion length. For the two cell architectures 1J and 2J, the two degradation curves as a function of *DDD* collapse into a single degradation curve. From these curves, it is then possible to determine the degradation of each solar cell architecture for a given fluence and a given energy beyond the experimentally tested parameters. As an example, 30% efficiency degradation of 1J Si solar cells is caused by 10 MeV electrons with 2.10^{13} e.cm^{-2} or by 100 MeV protons with 2.10^{12} p.cm^{-2}. These calculations are based on the *NIEL* value, i.e. divide the *NIEL* values of specific particle energy, which gives the necessary fluence to obtain this degradation.

Comparison to GaInP/GaAs/Ge

In this part, the degradation of the new III-V//Si solar cell technology is compared to that of the III-V/Ge cells conventionally used for space applications; one should keep in mind though that III-V/Ge cells have been extensively studied and optimized for operating in a radiative environment, with a broad absorption of the AM0 reference solar spectrum.

The Azur space triple junction GaInP/GaAs/Ge (3G28) data were taken from the datasheet of the constructor with irradiation at 300 K with 1 MeV electrons energy at three different fluences $2.5.10^{14}$ e.cm^{-2}, 5.10^{14} e.cm^{-2} and 10^{15} e.cm^{-2}. Current-voltage characterization were performed under 28 °C and 1367 W.m^{-2}. Fig. III-39 presents the remaining factor of the main electrical parameters as a function of the irradiation fluence of 3G28 (purple) cells compared to the data from the silicon-based cells studied in this work.

The behavior of conventional space optimized GaInP/GaAs/Ge cells differs from that of our III-V//Si. Before irradiation, the top cell limits the total current (by design) and the Ge bottom cell has a large excess current due to its wide absorption band, which extends up to 1880 nm. After irradiation at room temperature, a low degradation is observed for the GaInP sub-cell in contrast to the GaAs middle cell which in best case is current matched with GaInP or limits the overall current of multijunction [96]–[98]. This behavior explains the low J_{SC} degradation, i.e. 4% at 10^{15} e.cm^{-2}, due to the high radiation hardness of III-V material. In some structures, the integration of a Bragg mirror under GaAs sub-cell reduces the current losses [99]. However, a similar degradation is observed for the FF (2% at 10^{15} e.cm^{-2}) and V_{OC} (8% at 10^{15} e.cm^{-2}) than the Si based tandem solar cells used in this study. This is explained by the fact that same type of III-V sub-cells are used in both technologies, thus they have similar radiation hardness.

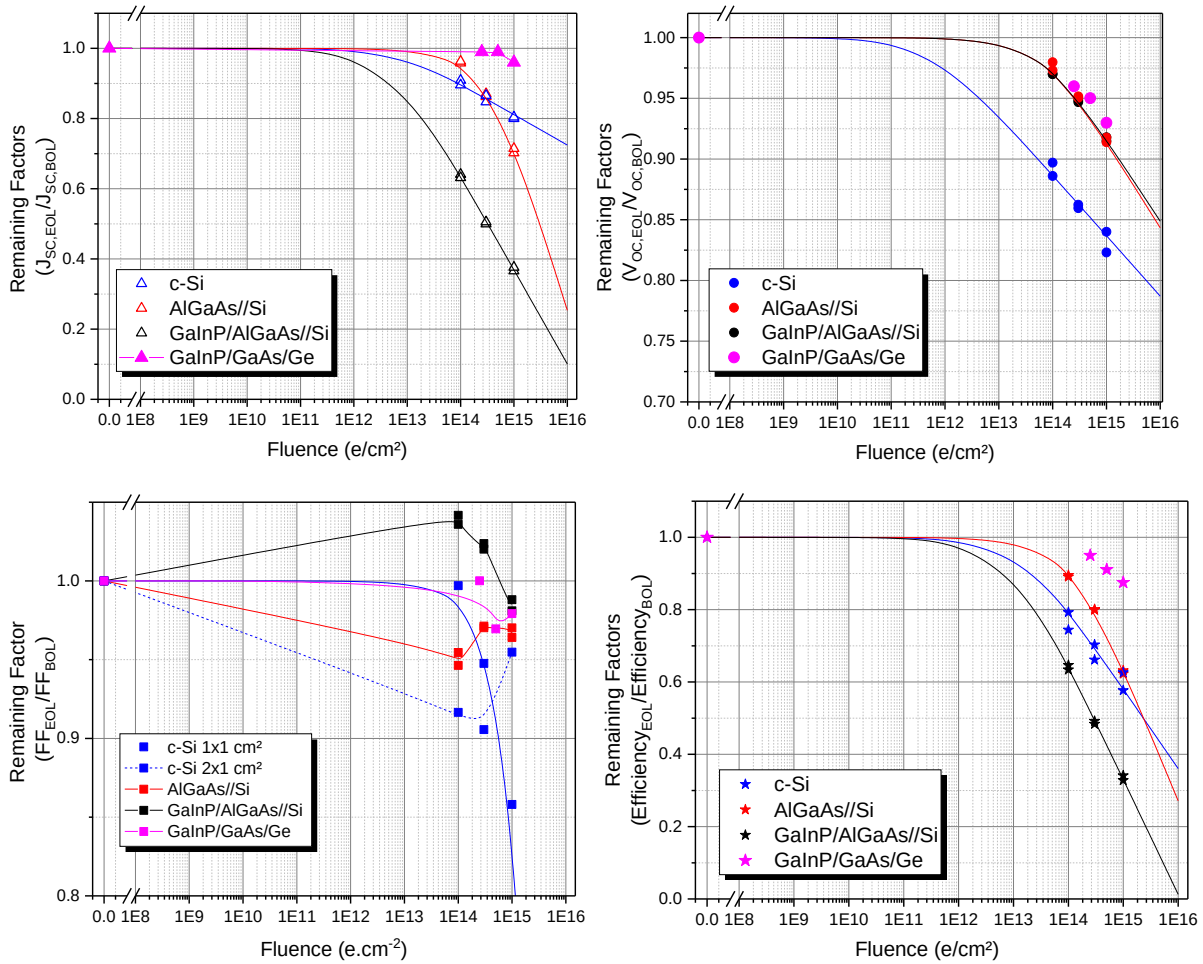

Fig. III-39 *Electrical parameters remaining factors comparison between the conventional AzurSpace 3G28 GaInP/GaAs/Ge solar cells used in space application to the Si based solar cells used in this thesis as a function fluence after 1 MeV electrons irradiation at 300 K.*

In our case, the Si bottom cell has a weaker radiation hardness compared to AlGaAs middle cell; thus, Si ends up as the limiting *EOL* sub-cell in 2- and 3-junctions configuration. It explains the large discrepancy when comparing the efficiency degradation of the 1J, 2J and 3J (40%, 37%, 68% respectively at 10^{15} e.cm^{-2}) of this work, to the triple junction 3G28 (13% at 10^{15} e.cm^{-2}). Besides that, these commercial cells technologies are fully optimized for space applications unlike the laboratory scale & low technology readiness level (*TRL*) III-V//Si cells used in this study.

While the limitations of III-V//Si tandem solar cells appears clearly in this study, two interesting perspectives remain: a) Using this III-V//Si technology for short term or low irradiation missions (e.g. Low Earth Orbit - *LEO*), once the fabrication process is up-scaled and cost effective (e.g. by direct growth of III-V on Si). b) Designing a specific radiation hard device architecure, by focusing on Si bottom cell *EOL* performance optimization. For instance researches [25], [70], [100], [101] have identified the role of base thickness and doping level on the radiation hardness of Si. A higher Si wafer resistvity (14-140 Ω.cm) is for instance the optimum for *EOL* performance at low fluence range (< 10^{15} e.cm^{-2}). The effect of an optimum doping level on Jsc remaining factor has been simulated with PC1D [102] for c-Si simple junction cell (L_{eff} was estimated by using Eq. 2 and Eq. 3). In Table 4, we report the simulated short circuit current density remaining factor (the most sensitiv parameters), at 10^{15} e.cm^{-2}, in comparison with the one measured in this study. When increasing only the resistivity from 1 - 5 Ω.cm to 10 - 20 Ω.cm, the J_{SC} remaining factor increase from 76% to 82 %.

Tab. III-16 *A comparison of the short circuit current remaining factor of c-Si simple junction cells from this work to PC1D simulated cells with various doping levels and thicknesses.*

Cells	Thickness (µm)	Doping Level (Ω.cm)	RF J_{SC} 1J
This Work	525 µm	1-5 Ω.cm	76%
PC1D simulation	300 µm	1-5 Ω.cm	77%
	100 µm	1-5 Ω.cm	81%
	525 µm	10-20 Ω.cm	82%
	300 µm	10-20 Ω.cm	83%
	100 µm	10-20 Ω.cm	88%

Furthermore, as seen above with large decrease of minority carriers diffusion length, it is also clear that thin Si wafers results in a significant increase of the charge carrier collection probability (see Tab. 4). An increase of the Jsc remaining factor from 76% to 81% is predicted for a 100 µm thick bottom cell (instead of 525 µm). By combining those relatively simple doping and thickness changes (without light trapping), we estimate that 88% short circuit current remaining factor can be reached after 10^{15} e.cm^{-2}. Ultimately, ultra-thin silicon cells (<50 µm) with appropriate light trapping features (e.g. photonic mirror) should boost even further Si radiation hardness. These bottom cell *EOL* current improvement will directly translate into performance gain for the III-V//Si 2 & 3J.

In addition to optimizations of the Si bottom cells, higher bandgap or semi-transparent top cells would be a preferable *EOL* design, by allowing more photons to reach the Si radiation weak cell. This could be done for instance by using Al in top an middle cell for widening the bandgap combined with controlled absorber thickness reduction.

III.5 Conclusion

- Simulations of the particles interaction with the three solar cells architectures have been performed. The main statements are:
  - 1 MeV Electrons yield a uniform amount of energy as they pass through the solar cell. Therefore, a homogeneous defects creation is expected over the entire thickness of each sub-cell/cell.
  - 1 MeV protons irradiation induces uniform degradation on the top and top/middle sub-cells of the 2J and 3J due to low variation of protons energy through their thickness (2 - 4 μm).
  - In the case of Si cell/sub-cell, the proton energy varies considerably according to the penetration depth and therefore the deposited energy, which induces non-uniform degradation. Three regions have been distinguished; a first region where the Si is homogeneously irradiated (~10 μm), a second region where the Si is strongly irradiated (Bragg peak) and a third region where the Si is not irradiated (> 16 μm).
- Quantum efficiency measurements at 300 K before and after irradiation both electrons and protons irradiation of the three solar cells architectures resulted in the following findings:
  - High degradation is observed at higher wavelength of each sub-cell absorption range. This is a consequence of minority carrier diffusion length degradation in the p-type due to the introduction of complex defect that act as recombination center.
  - Higher degradation is observed in the case of Si compared to the AlGaAs and GaInP due to its low radiation hardness.
  - J_{SC} degradation of Si sub-cell is more important when increasing the number of junctions of the device. This is due to the thinning of the Si absorption band toward long wavelength (the region most affected by irradiation).
  - In the case of our 2J a limiting sub-cell inversion (from Al to Si) is observed after irradiation at a fluence of 3.10^{14} $e.cm^{-2}$ and 3.10^{11} $p.cm^{-2}$.
  - Non-homogenous degradation is observed on the *EQE* of Si sub-cell after 1 MeV protons irradiation on 1J and 2J, which is translated by slope change at the Bragg peak. In the case of 3J, the Bragg peak occurs at a depth below the region that is responsible of e-h pairs generation thus the slope changes are not visible.

  - A diffusion length calculation model based on experimental *IQE* results has been applied on the Si of the three solar cell architectures:
    - Case of electrons irradiation: a degradation from ~600 µm to ~30 µm is observed at a fluence of 10^{15} e.cm^{-2} for Si in all architectures. The respective damage coefficient of 1.2-1.7 x 10^{-10} are in good agreement with values reported in literature.
    - Case of protons irradiation: the model was applied on the two region (irradiated and non-irradiated) of Si cells/sub-cell where values can drop from 650 µm to 5 µm in the case of 1J after 10^{12} p.cm^{-2}. The calculated damage coefficient for diffusion length of K_L = 1-5 x 10^{-6} is in good agreement with the values reported in literature.
- The statement made from current-voltage measurements under AM0 spectrum and 300 K are:
  - Higher degradation of J_{SC} is observed after irradiation compare to the V_{OC} and FF for all three architectures.
  - The non-standard evolution of FF according to the fluence is related to current matching condition between sub-cells of tandem devices.
  - The efficiency decrease is driven by the decrease of J_{SC} in all architectures.
- The NRL method based on the displacement damage dose was applied to correlate the degradation of the three sub-cells when irradiated with 1 MeV electrons and 1 MeV protons particles. This method allows defining the degradation of each solar cells architectures under a large range of electrons and protons irradiation spectrum (different energy with different fluence).
- The following statements are set by comparing the behavior of III-V//Si to III-V/Ge face to electrons irradiation:
  - Low J_{SC} degradation due to the high radiation hardness of the limiting sub-cells (GaInP & GaAs). Comparable FF and V_{OC} degradation was observed due to the similarity of III-V used materials in both technologies.
  - Lower efficiency degradation observed in III-V/Ge compared to III-V//Si. However, due to the low cost and low mass that offers the Si-based solar cells, their use can be promising for low fluence mission.

III.6 References

[1] U. Rau, “Reciprocity relation between photovoltaic quantum efficiency and electroluminescent emission of solar cells,” *Phys. Rev. B*, vol. 76, no. 8, p. 085303, Aug. 2007, doi: 10.1103/PhysRevB.76.085303.

[2] G. P. Summers, E. A. Burke, and M. A. Xapsos, “Displacement damage analogs to ionizing radiation effects,” *Radiat. Meas.*, vol. 24, no. 1, pp. 1–8, Jan. 1995, doi: 10.1016/1350-4487(94)00093-G.

[3] F. Salvat, J. M. Fernández-Varea, and J. Sempau, “PENELOPE-2006: A code system for Monte Carlo simulation of electron and photon transport,” in *Workshop proceedings*, 2006, vol. 4, p. 7.

[4] H. Nesswetter, W. Dyck, P. Lugli, A. W. Bett, and C. G. Zimmermann, “Luminescence based series resistance mapping of III-V multijunction solar cells,” *J. Appl. Phys.*, vol. 114, no. 19, p. 194510, Nov. 2013, doi: 10.1063/1.4831749.

[5] S. Suckow, T. M. Pletzer, and H. Kurz, “Fast and reliable calculation of the two-diode model without simplifications: Fast and reliable calculation of the two-diode model without simplifications,” *Prog. Photovolt. Res. Appl.*, vol. 22, no. 4, pp. 494–501, Apr. 2014, doi: 10.1002/pip.2301.

[6] R. Hoheisel, F. Dimroth, A. W. Bett, S. R. Messenger, P. P. Jenkins, and R. J. Walters, “Electroluminescence analysis of irradiated GaInP/GaInAs/Ge space solar cells,” *Sol. Energy Mater. Sol. Cells*, vol. 108, pp. 235–240, Jan. 2013, doi: 10.1016/j.solmat.2012.06.015.

[7] C. Domínguez and P. García-Linares, “Characterization of Multijunction Concentrator Solar Cells,” in *High Concentrator Photovoltaics*, P. Pérez-Higueras and E. F. Fernández, Eds. Cham: Springer International Publishing, 2015, pp. 39–84.

[8] M. Yamaguchi, C. Uemura, A. Yamamoto, and A. Shibukawa, “Electron Irradiation Damage in Radiation-Resistant InP Solar Cells,” *Jpn. J. Appl. Phys.*, vol. 23, no. 3R, p. 302, Mar. 1984, doi: 10.1143/JJAP.23.302.

[9] A. ur Rehman, S. H. Lee, and S. H. Lee, “Silicon space solar cells: progression and radiation-resistance analysis,” *J. Korean Phys. Soc.*, vol. 68, no. 4, pp. 593–598, Feb. 2016, doi: 10.3938/jkps.68.593.

[10] R. Lang, J. Schön, J. Lefèvre, B. Boizot, F. Dimroth, and D. Lackner, “Radiation hardness and post irradiation regeneration behavior of GaInAsP solar cells,” *Sol. Energy Mater. Sol. Cells*, vol. 211, p. 110551, 2020.

[11] M. Yamaguchi, “Radiation-resistant solar cells for space use,” *Sol. Energy Mater. Sol. Cells*, vol. 68, no. 1, pp. 31–53, 2001.

[12] M. Yamaguchi, “Radiation resistance of compound semiconductor solar cells,” *J. Appl. Phys.*, vol. 78, no. 3, pp. 1476–1480, Aug. 1995, doi: 10.1063/1.360236.

[13] M. Yamaguchi, A. Khan, and N. Dharmarasu, “Analysis for superior radiation resistance of InP-based solar cells,” *Sol. Energy Mater. Sol. Cells*, vol. 75, no. 1, pp. 285–291, Jan. 2003, doi: 10.1016/S0927-0248(02)00171-X.

[14] B. Fischer, M. Keil, P. Fath, and E. Bucher, “Scanning IQE-measurement for accurate current determination on very large area solar cells,” in *Conference Record of the Twenty-Ninth IEEE Photovoltaic Specialists Conference, 2002.*, May 2002, pp. 454–457, doi: 10.1109/PVSC.2002.1190557.

[15] D. Nobili, A. Armigliato, M. Finnetti, and S. Solmi, “Precipitation as the phenomenon responsible for the electrically inactive phosphorus in silicon,” *J. Appl. Phys.*, vol. 53, no. 3, pp. 1484–1491, Mar. 1982, doi: 10.1063/1.330646.

[16] M. A. Green and M. J. Keevers, “Optical properties of intrinsic silicon at 300 K,” *Prog. Photovolt. Res. Appl.*, vol. 3, no. 3, pp. 189–192, Jan. 1995, doi: 10.1002/pip.4670030303.

[17] E. J. Schneller, K. Öğütman, S. Guo, W. V. Schoenfeld, and K. O. Davis, “Crystalline Silicon Device Loss Analysis Through Spatially Resolved Quantum Efficiency Measurements,” *IEEE J. Photovolt.*, vol. 7, no. 4, pp. 957–965, Jul. 2017, doi: 10.1109/JPHOTOV.2017.2689160.
[18] M. Hirsch, U. Rau, and J. H. Werner, “Analysis of internal quantum efficiency and a new graphical evaluation scheme,” *Solid-State Electron.*, vol. 38, no. 5, pp. 1009–1015, May 1995, doi: 10.1016/0038-1101(95)98669-T.
[19] P. K. Basu and S. N. Singh, “On the determination of minority carrier diffusion length in the base region of n+-p-p+ silicon solar cells using photoresponse methods,” *Sol. Energy Mater. Sol. Cells*, vol. 33, no. 3, pp. 317–329, Jul. 1994, doi: 10.1016/0927-0248(94)90234-8.
[20] T. Luka, S. Eiternick, and M. Turek, “Rapid Testing of External Quantum Efficiency using LED Solar Simulators,” *Energy Procedia*, vol. 77, pp. 113–118, Aug. 2015, doi: 10.1016/j.egypro.2015.07.018.
[21] B. Fischer, *Loss analysis of crystalline silicon solar cells using photoconductance and quantum efficiency measurements*. Cuvillier Göttingen, 2003.
[22] M. Spiegel, B. Fischer, S. Keller, and E. Bucher, “Separation of bulk diffusion length and back surface recombination velocity by improved IQE-analysis,” in *Conference Record of the Twenty-Eighth IEEE Photovoltaic Specialists Conference - 2000 (Cat. No.00CH37036)*, Sep. 2000, pp. 311–314, doi: 10.1109/PVSC.2000.915823.
[23] P. A. Basore, “Extended spectral analysis of internal quantum efficiency,” in *Conference Record of the Twenty Third IEEE Photovoltaic Specialists Conference - 1993 (Cat. No.93CH3283-9)*, May 1993, pp. 147–152, doi: 10.1109/PVSC.1993.347063.
[24] B. E. Anspaugh, R. G. Dowing, H. Y. Tada, and J. R. Carter Jr, *Solar Cell Radiation Handbook*, Third Edition. National Aeronautics and Space Administration, 1982.
[25] M. Yamaguchi, A. Khan, S. J. Taylor, M. Imaizumi, T. Hisamatsu, and S. Matsuda, “A detailed model to improve the radiation-resistance of Si space solar cells,” *IEEE Trans. Electron Devices*, vol. 46, no. 10, pp. 2133–2138, Oct. 1999, doi: 10.1109/16.792008.
[26] C. Karcher, H. Helmers, M. Schachtner, F. Dimroth, and A. W. Bett, “Temperature-dependent electroluminescence and voltages of multi-junction solar cells,” *Prog. Photovolt. Res. Appl.*, vol. 22, no. 7, pp. 757–763, 2014, doi: 10.1002/pip.2431.
[27] H. Helmers, M. Schachtner, and A. W. Bett, “Influence of temperature and irradiance on triple-junction solar subcells,” *Sol. Energy Mater. Sol. Cells*, vol. 116, pp. 144–152, Sep. 2013, doi: 10.1016/j.solmat.2013.03.039.
[28] G. Yan, J. Wang, J. Liu, Y. Liu, R. Wu, and R. Wang, “Electroluminescence analysis of VOC degradation of individual subcell in GaInP/GaAs/Ge space solar cells irradiated by 1.0 MeV electrons,” *J. Lumin.*, vol. 219, p. 116905, Mar. 2020, doi: 10.1016/j.jlumin.2019.116905.
[29] M. Zazoui and J. C. Bourgoin, “Space degradation of multijunction solar cells: An electroluminescence study,” *Appl. Phys. Lett.*, vol. 80, no. 23, pp. 4455–4457, May 2002, doi: 10.1063/1.1485134.
[30] D. Pons and J. C. Bourgoin, “Irradiation-induced defects in GaAs,” *J. Phys. C Solid State Phys.*, vol. 18, no. 20, pp. 3839–3871, Jul. 1985, doi: 10.1088/0022-3719/18/20/012.
[31] N. Dharmarasu *et al.*, “Majority- and minority-carrier deep level traps in proton-irradiated n+/p-InGaP space solar cells,” *Appl. Phys. Lett.*, vol. 81, no. 1, p. 64, Jun. 2002, doi: 10.1063/1.1491005.
[32] J. C. Bourgoin and M. Zazoui, “Irradiation-induced degradation in solar cell: characterization of recombination centres,” *Semicond. Sci. Technol.*, vol. 17, no. 5, pp. 453–460, Apr. 2002, doi: 10.1088/0268-1242/17/5/308.

[33] N. Dharmarasu *et al.*, "High-radiation-resistant InGaP, InGaAsP, and InGaAs solar cells for multijuction solar cells," *Appl. Phys. Lett.*, vol. 79, no. 15, pp. 2399–2401, Oct. 2001, doi: 10.1063/1.1409270.
[34] M. Yamaguchi, T. Okuda, S. J. Taylor, T. Takamoto, E. Ikeda, and H. Kurita, "Superior radiation-resistant properties of InGaP/GaAs tandem solar cells," *Appl. Phys. Lett.*, vol. 70, no. 12, pp. 1566–1568, Mar. 1997, doi: 10.1063/1.118618.
[35] A. Khan, M. Yamaguchi, J. C. Bourgoin, N. de Angelis, and T. Takamoto, "Room-temperature minority-carrier injection-enhanced recovery of radiation-induced defects in p-InGaP and solar cells," *Appl. Phys. Lett.*, vol. 76, no. 18, pp. 2559–2561, Apr. 2000, doi: 10.1063/1.126407.
[36] A. Khan, M. Yamaguchi, J. C. Bourgoin, and T. Takamoto, "Thermal annealing study of 1 MeV electron-irradiation-induced defects in n+p InGaP diodes and solar cells," *J. Appl. Phys.*, vol. 91, no. 4, pp. 2391–2397, Feb. 2002, doi: 10.1063/1.1433936.
[37] H. S. Lee *et al.*, "Recovery of Electron/Proton Radiation-Induced Defects in n+ p AlInGaP Solar Cell by Minority-Carrier Injection Annealing," 2007.
[38] J. Wang, R. Wu, G. Yan, and R. Wang, "Temperature-dependent photoluminescence processes of GaInP top cell irradiated with 11.5 MeV and 1.0 MeV electrons," *Nucl. Instrum. Methods Phys. Res. Sect. B Beam Interact. Mater. At.*, vol. 450, pp. 66–68, Jul. 2019, doi: 10.1016/j.nimb.2018.08.017.
[39] A. Khan, M. Yamaguchi, J. C. Bourgoin, K. Ando, and T. Takamoto, "Recombination enhanced defect reactions in 1 MeV electron irradiated *p* InGaP," *J. Appl. Phys.*, vol. 89, no. 8, pp. 4263–4268, Apr. 2001, doi: 10.1063/1.1353806.
[40] T. Kirchartz, A. Helbig, W. Reetz, M. Reuter, J. H. Werner, and U. Rau, "Reciprocity between electroluminescence and quantum efficiency used for the characterization of silicon solar cells," *Prog. Photovolt. Res. Appl.*, vol. 17, no. 6, pp. 394–402, 2009, doi: 10.1002/pip.895.
[41] T. Kirchartz, J. Nelson, and U. Rau, "Reciprocity between Charge Injection and Extraction and Its Influence on the Interpretation of Electroluminescence Spectra in Organic Solar Cells," *Phys. Rev. Appl.*, vol. 5, no. 5, p. 054003, May 2016, doi: 10.1103/PhysRevApplied.5.054003.
[42] W. Gong *et al.*, "Influence of energetic disorder on electroluminescence emission in polymer:fullerene solar cells," *Phys. Rev. B*, vol. 86, no. 2, p. 024201, Jul. 2012, doi: 10.1103/PhysRevB.86.024201.
[43] R. Hoheisel, D. Scheiman, S. Messenger, P. Jenkins, and R. Walters, "Detailed Characterization of the Radiation Response of Multijunction Solar Cells Using Electroluminescence Measurements," *IEEE Trans. Nucl. Sci.*, vol. 62, no. 6, pp. 2894–2898, Dec. 2015, doi: 10.1109/TNS.2015.2498838.
[44] R. Hoheisel, F. Dimroth, A. W. Bett, S. R. Messenger, P. P. Jenkins, and R. J. Walters, "Electroluminescence analysis of irradiated GaInP/GaInAs/Ge space solar cells," *Sol. Energy Mater. Sol. Cells*, vol. 108, pp. 235–240, Jan. 2013, doi: 10.1016/j.solmat.2012.06.015.
[45] N. Gruginskie *et al.*, "Electron radiation–induced degradation of GaAs solar cells with different architectures," *Prog. Photovolt. Res. Appl.*, vol. n/a, no. n/a, doi: 10.1002/pip.3224.
[46] W. Rong, L. Yunhong, and S. Xufang, "Effects of 0.28–2.80MeV proton irradiation on GaInP/GaAs/Ge triple-junction solar cells for space use," *Nucl. Instrum. Methods Phys. Res. Sect. B Beam Interact. Mater. At.*, vol. 266, no. 5, pp. 745–749, Mar. 2008, doi: 10.1016/j.nimb.2007.12.076.
[47] J. F. Ziegler, M. D. Ziegler, and J. P. Biersack, "SRIM – The stopping and range of ions in matter (2010)," *Nucl. Instrum. Methods Phys. Res. Sect. B Beam Interact. Mater. At.*, vol. 268, no. 11, pp. 1818–1823, Jun. 2010, doi: 10.1016/j.nimb.2010.02.091.

[48] Insoo Jun *et al.*, "Proton nonionizing energy loss (NIEL) for device applications," *IEEE Trans. Nucl. Sci.*, vol. 50, no. 6, pp. 1924–1928, Dec. 2003, doi: 10.1109/TNS.2003.820760.
[49] G. P. Summers, E. A. Burke, P. Shapiro, S. R. Messenger, and R. J. Walters, "Damage correlations in semiconductors exposed to gamma, electron and proton radiations," *IEEE Trans. Nucl. Sci.*, vol. 40, no. 6, pp. 1372–1379, Dec. 1993, doi: 10.1109/23.273529.
[50] B. E. Anspaugh, "GaAs solar cell radiation handbook," 1996.
[51] L. Yun-Hong, W. Rong, C. Xin-Yu, and W. Yong-Xia, "Correlation between Displacement Damage Dose and Proton Irradiation Effects on GaInP/GaAs/Ge Space Solar Cells," *Chin. Phys. Lett.*, vol. 26, no. 2, p. 026102, Feb. 2009, doi: 10.1088/0256-307X/26/2/026102.
[52] C. Baur *et al.*, "Displacement Damage dose and DLTS Analyses on Triple and Single Junction solar cells irradiated with electrons and protons," Apr. 2017, Available: https://arxiv.org/abs/1704.06495v1.
[53] Y. Okuno, N. Ishikawa, M. Akiyoshi, H. Ando, M. Harumoto, and M. Imaizumi, "Degradation prediction using displacement damage dose method for AlInGaP solar cells by changing displacement threshold energy under irradiation with low-energy electrons," *Jpn. J. Appl. Phys.*, vol. 59, no. 7, p. 074001, Jun. 2020, doi: 10.35848/1347-4065/ab9713.
[54] Y. Okuno *et al.*, "Radiation degradation prediction for InGaP solar cells by using appropriate estimation method for displacement threshold energy," *J. Appl. Phys.*, vol. 122, no. 11, p. 114901, Sep. 2017, doi: 10.1063/1.4989891.
[55] T. Ohshima *et al.*, "Mechanism of anomalous degradation of silicon solar cells subjected to high-fluence irradiation," *IEEE Trans. Nucl. Sci.*, vol. 43, no. 6, pp. 2990–2997, Dec. 1996, doi: 10.1109/23.556896.
[56] B. E. D. Anspaugh, "Radiation effects in silicon and gallium arsenide solar cells using isotropic and normally incident radiation," Sep. 1984. Available: https://ntrs.nasa.gov/search.jsp?R=19840026722.
[57] G. Augustine, A. Rohatgi, and N. M. Jokerst, "Base doping optimization for radiation-hard Si, GaAs, and InP solar cells," *IEEE Trans. Electron Devices*, vol. 39, no. 10, pp. 2395–2400, Oct. 1992, doi: 10.1109/16.158814.
[58] M. Yamaguchi and K. Ando, "Mechanism for radiation resistance of InP solar cells," *J. Appl. Phys.*, vol. 63, no. 11, pp. 5555–5562, Jun. 1988, doi: 10.1063/1.340332.
[59] R. J. Walters *et al.*, "Radiation response of heteroepitaxial n+p InP/Si solar cells," *J. Appl. Phys.*, vol. 82, no. 5, pp. 2164–2175, Sep. 1997, doi: 10.1063/1.366024.
[60] I. Weinberg and D. J. Brinker, "Indium phosphide solar cells: status and prospects for use in space," 1986.
[61] W. C. Cooley and R. J. Janda, "Handbook of space-radiation effects on solar-cell power systems," National Aeronautics and Space Administration Washington DC, 1963.
[62] M. Yamaguchi, S. J. Taylor, M.-J. Yang, S. Matsuda, O. Kawasaki, and T. Hisamatsu, "High-energy and high-fluence proton irradiation effects in silicon solar cells," *J. Appl. Phys.*, vol. 80, no. 9, p. 4916, Aug. 1998, doi: 10.1063/1.363534.
[63] M. J. Barrett and R. H. Stroud, "Proton-induced damage to silicon solar cell assemblies - A state-of-the-art survey Quarterly report," 1968.
[64] T. Markvart and L. Castañer, "Semiconductor Materials and Modeling," in *McEvoy's Handbook of Photovoltaics*, Elsevier, 2018, pp. 29–57.
[65] D. L. Crowther, E. A. Lodi, J. DePangher, and A. Andrew, "An Analysis of Non-Uniform Proton Irradiation Damage in Silicon Solar Cells," *IEEE Trans. Nucl. Sci.*, vol. 13, no. 5, pp. 37–46, Oct. 1966, doi: 10.1109/TNS.1966.4324326.
[66] W. Rosenzweig, F. M. Smits, and W. L. Brown, "Energy Dependence of Proton Irradiation Damage in Silicon," *J. Appl. Phys.*, vol. 35, no. 9, pp. 2707–2711, Sep. 1964, doi: 10.1063/1.1713827.

[67] E. A. Burke, “Energy Dependence of Proton-Induced Displacement Damage in Silicon,” *IEEE Trans. Nucl. Sci.*, vol. 33, no. 6, pp. 1276–1281, Dec. 1986, doi: 10.1109/TNS.1986.4334592.
[68] J. R. Srour, S. Othmer, and K. Y. Chiu, “Electron and Proton Damage Coefficients in Low-Resistivity Silicon,” *IEEE Trans. Nucl. Sci.*, vol. 22, no. 6, pp. 2656–2662, Dec. 1975, doi: 10.1109/TNS.1975.4328185.
[69] S. R. Messenger, E. A. Burke, G. P. Summers, and R. J. Walters, “Application of displacement damage dose analysis to low-energy protons on silicon devices,” *IEEE Trans. Nucl. Sci.*, vol. 49, no. 6, pp. 2690–2694, Dec. 2002, doi: 10.1109/TNS.2002.805359.
[70] M. Alurralde, “Experimental and theoretical radiation damage studies on crystalline silicon solar cells,” *Sol. Energy Mater. Sol. Cells*, Mar. 2004, doi: 10.1016/j.solmat.2003.11.029.
[71] M. Imaizumi, M. Yamaguchi, S. J. Taylor, S. Matsuda, O. Kawasaki, and T. Hisamatsu, “Mechanism for the anomalous degradation of Si solar cells induced by high-energy proton irradiation,” *Sol. Energy Mater. Sol. Cells*, vol. 50, no. 1–4, pp. 339–344, 1998.
[72] G. D. Watkins and J. W. Corbett, “Defects in Irradiated Silicon: Electron Paramagnetic Resonance and Electron-Nuclear Double Resonance of the Si-E Center,” *Phys. Rev.*, vol. 134, no. 5A, pp. A1359–A1377, Jun. 1964, doi: 10.1103/PhysRev.134.A1359.
[73] G. D. Watkins and J. W. Corbett, “Defects in Irradiated Silicon: Electron Paramagnetic Resonance of the Divacancy,” *Phys. Rev.*, vol. 138, no. 2A, pp. A543–A555, Apr. 1965, doi: 10.1103/PhysRev.138.A543.
[74] J. W. Corbett and G. D. Watkins, “Production of Divacancies and Vacancies by Electron Irradiation of Silicon,” *Phys. Rev.*, vol. 138, no. 2A, pp. A555–A560, Apr. 1965, doi: 10.1103/PhysRev.138.A555.
[75] M. Yamaguchi *et al.*, “Deep level analysis of radiation-induced defects in Si crystals and solar cells,” *J. Appl. Phys.*, vol. 86, no. 1, pp. 217–223, Jun. 1999, doi: 10.1063/1.370698.
[76] N. R. Zangenberg and A. Nylandsted Larsen, “On-line DLTS investigations of vacancy related defects in low-temperature electron irradiated, boron-doped Si,” *Appl. Phys. A*, vol. 80, no. 5, pp. 1081–1086, Feb. 2005, doi: 10.1007/s00339-003-2358-3.
[77] A. Rohatgi, J. P. Schaffer, G. Augustine, and M. S. Ramanachalam, “A review of selected techniques for characterizing radiation-induced defects in solar cells,” *Sol. Cells*, vol. 31, no. 4, pp. 379–394, Sep. 1991, doi: 10.1016/0379-6787(91)90106-Y.
[78] M. Tajima, M. Warashina, T. Hisamatsu, O. Anzawa, and S. Matsuda, “Dominant Radiation-Induced Defects in Space Solar Cell Silicon Manifested by Photoluminescence Spectroscopy,” *ESASP*, vol. 502, p. 741, May 2002.
[79] H. S. Reehal, M. P. Lesniak, and A. E. Hughes, “Application of DLTS to silicon solar cell processing,” *J. Phys. Appl. Phys.*, vol. 29, no. 3, p. 934, 1996.
[80] M. Kuhnke, E. Fretwurst, and G. Lindstroem, “Defect generation in crystalline silicon irradiated with high energy particles,” *Nucl. Instrum. Methods Phys. Res. Sect. B Beam Interact. Mater. At.*, vol. 186, no. 1, pp. 144–151, Jan. 2002, doi: 10.1016/S0168-583X(01)00886-2.
[81] J. C. Bourgoin and N. de Angelis, “Radiation-induced defects in solar cell materials,” *Sol. Energy Mater. Sol. Cells*, vol. 66, no. 1, pp. 467–477, Feb. 2001, doi: 10.1016/S0927-0248(00)00208-7.
[82] S. Z. Karazhanov, “Effect of radiation-induced defects on silicon solar cells,” *J. Appl. Phys.*, vol. 88, no. 7, p. 3941, 2000, doi: 10.1063/1.1290453.
[83] A. Hamache, N. Sengouga, A. Meftah, and M. Henini, “Modeling the effect of 1MeV electron irradiation on the performance of n+–p–p+ silicon space solar cells,” *Radiat. Phys. Chem.*, vol. 123, pp. 103–108, Jun. 2016, doi: 10.1016/j.radphyschem.2016.02.025.
[84] S. Park, “Irradiation effect in triple junction solar cells for spatial applications,” Theses, Université Paris-Saclay, 2018.

[85] R. Walters, “Materials, Cell Structures, and Radiation Effects,” *Photovolt. Sol. Energy Fundam. Appl.*, p. 433, 2017.
[86] T. V. Torchynska, “III-V material solar cells for space application,” 2002.
[87] E. F. Fernández, A. J. García-Loureiro, and G. P. Smestad, “Multijunction Concentrator Solar Cells: Analysis and Fundamentals,” in *High Concentrator Photovoltaics*, P. Pérez-Higueras and E. F. Fernández, Eds. Cham: Springer International Publishing, 2015, pp. 9–37.
[88] M. Boccard and C. Ballif, “Influence of the Subcell Properties on the Fill Factor of Two-Terminal Perovskite–Silicon Tandem Solar Cells,” *ACS Energy Lett.*, vol. 5, no. 4, pp. 1077–1082, Apr. 2020, doi: 10.1021/acsenergylett.0c00156.
[89] M. Bonnet-Eymard, M. Boccard, G. Bugnon, F. Sculati-Meillaud, M. Despeisse, and C. Ballif, “Optimized short-circuit current mismatch in multi-junction solar cells,” *Sol. Energy Mater. Sol. Cells*, vol. 117, pp. 120–125, Oct. 2013, doi: 10.1016/j.solmat.2013.05.046.
[90] S. R. Messenger, M. A. Xapsos, E. A. Burke, R. J. Walters, and G. P. Summers, “Proton displacement damage and ionizing dose for shielded devices in space,” *IEEE Trans. Nucl. Sci.*, vol. 44, no. 6, pp. 2169–2173, Dec. 1997, doi: 10.1109/23.659032.
[91] G. P. Summers *et al.*, “A new approach to damage prediction for solar cells exposed to different radiations,” in *Proceedings of 1994 IEEE 1st World Conference on Photovoltaic Energy Conversion - WCPEC (A Joint Conference of PVSC, PVSEC and PSEC)*, Dec. 1994, vol. 2, pp. 2068–2075 vol.2, doi: 10.1109/WCPEC.1994.521828.
[92] S. R. Messenger, G. P. Summers, E. A. Burke, R. J. Walters, and M. A. Xapsos, “Modeling solar cell degradation in space: A comparison of the NRL displacement damage dose and the JPL equivalent fluence approaches,” *Prog. Photovolt. Res. Appl.*, vol. 9, no. 2, pp. 103–121, 2001.
[93] S. R. Messenger *et al.*, “Nonionizing energy loss (NIEL) for heavy ions,” *IEEE Trans. Nucl. Sci.*, vol. 46, no. 6, pp. 1595–1602, 1999.
[94] S. J. Taylor *et al.*, “Comparison of the effects of electron and proton irradiation on n+–p–p+ silicon diodes,” *J. Appl. Phys.*, vol. 83, no. 9, pp. 4620–4627, May 1998, doi: 10.1063/1.367246.
[95] S. J. Taylor, M. Yamaguchi, M. Imaizumi, and T. Ito, “Improved model of radiation damage to silicon solar cells,” *J. Appl. Phys.*, vol. 82, no. 7, pp. 3627–3629, Oct. 1997, doi: 10.1063/1.365685.
[96] M. Imaizumi *et al.*, “Study of radiation response on single-junction component sub-cells in triple-junction solar cells,” in *Proceedings of 3rd World Conference onPhotovoltaic Energy Conversion, 2003*, May 2003, vol. 1, p. 599–602 Vol.1.
[97] M. Imaizumi, T. Takamoto, and T. Ohshima, “Analysis on degradation characteristics of component subcells in IMM triple-junction solar cells,” in *2016 IEEE 43rd Photovoltaic Specialists Conference (PVSC)*, Jun. 2016, pp. 3396–3400, doi: 10.1109/PVSC.2016.7750297.
[98] M. Imaizumi, T. Nakamura, T. Takamoto, T. Ohshima, and M. Tajima, “Radiation degradation characteristics of component subcells in inverted metamorphic triple-junction solar cells irradiated with electrons and protons,” *Prog. Photovolt. Res. Appl.*, vol. 25, no. 2, pp. 161–174, 2017, doi: 10.1002/pip.2840.
[99] M. Z. Shvarts, O. I. Chosta, I. V. Kochnev, V. M. Lantratov, and V. M. Andreev, “Radiation resistant AlGaAs/GaAs concentrator solar cells with internal Bragg reflector,” *Sol. Energy Mater. Sol. Cells*, vol. 68, no. 1, pp. 105–122, Apr. 2001, doi: 10.1016/S0927-0248(00)00349-4.
[100] D. J. Curtin and R. L. Statler, “Review of Radiation Damage to Silicon Solar Cells,” *IEEE Trans. Aerosp. Electron. Syst.*, vol. AES-11, no. 4, pp. 499–513, Jul. 1975, doi: 10.1109/TAES.1975.308112.
[101] M. Cappelletti, G. Casas, A. Cedola, and E. Peltzer, *Theoretical study of the maximum power point of n-type and p-type crystalline silicon space solar cells*, vol. 28. 2013.
[102] D. A. Clugston and P. A. Basore, “PC1D version 5: 32-bit solar cell modeling on personal computers,” in *Conference Record of the Twenty Sixth IEEE Photovoltaic Specialists Conference - 1997*, Sep. 1997, pp. 207–210, doi: 10.1109/PVSC.1997.654065.

CHAPTER IV Investigation of III-V//Si radiation hardness under low temperature and low intensity conditions

IV.1 Introduction

The different operating environments for solar cells onboard spacecraft have been described in section I.3. In terms of fluences, it can be quite different from one mission to another. However, the distance from the sun is not the main parameter driving the fluence seen by solar arrays: it depends on the magnetosphere of the subject planet, the mission duration, its trajectory (and others parameters). The main differences resulting from the sun distance lie in the temperature and illumination intensity for the operation of the solar cells. In this chapter, we have studied the operation of solar cells in deep space conditions, i.e. for missions to Mars or Jupiter for instance, which are the subject of multiple studies and future exploration plans. In those specific environments, the solar cells operate under the combined constraints of Low Intensity and Low Temperature, commonly called *LILT* conditions. When irradiation happens at low temperatures, the induced irradiation primary defects have a lower mobility and therefore can induce more performance degradation at solar cells level.

In order to study the behavior of Si-based tandem solar cells for deep space mission, an electron irradiation of 1 MeV energy at low temperature 120 K was performed at three different fluence 10^{14}, 3.10^{14} and 10^{15} $e.cm^{-2}$. The highest fluence is close to the equivalent fluence received on the future Jupiter exploration mission called *JUICE*, which reaches $1.5 - 3.10^{15}$ $e.cm^{-2}$ [1]. This fluence values also corresponds to that considered in the context of irradiation at 300 K in this study, where the solar cells operate under Normal Irradiance and Room temperature, *NIRT*, conditions. It gives us opportunities for comparisons between the two irradiations conditions, 120 K and 300 K.

Current-voltage, quantum efficiency and spectral electroluminescence characterizations were performed throughout the process before and after irradiation. First, the effect of illumination intensity was investigated by comparing the measurements made at 300 K under a 100% AM0 and ~3% AM0 spectrum. Then the influence of thermal cycling on the mechanical resistance of the solar cells (metallization, *ARC*, and bonding) as well as on the evolution of the electrical parameters was studied. Once proven the good solar cells resistance to thermal cycling, they were cooled down to 120 K in the electron beam cryostat. According to state-of-the-art reviews, anomalies can be observed in the *LILT* conditions that are not observable at ambient temperature even at low intensity such as flat spot effect and S-like shape [2]. Therefore, in-situ measurements were compared to measurements in *LIRT* conditions where the well known anomalies such as “broken knee” and the “S-like shape” were observed. The effect

of irradiation at 120 K on key electrical properties as well as on *EQE* and *ELS* was investigated and quantified for the three solar cell architectures as a function of fluence. Finally, the cells were heated up back to room temperature to quantify and analyze the effect of annealing on the behavior of the solar cells. In the end, a comparison between the Si-based solar cells and the conventional AzurSpace 3G28 cells used for space is presented, and the advantages and limitations of each technology are discussed.

IV.2 Effect of Low intensity

IV.2.1. Solar simulator comparison

To investigate solar cells behavior at low intensities level, *I-V* characterizations were performed with the *Helios 3030* equipment (see section II.5.1). A 1 x 1 cm² 2J AlGaAs//Si was characterized under different irradiance intensities ranging from 1 sun to 0.05 sun. To reach such low intensities, several neutral optical filters (metallic mesh) are used between light source (Xe lamp) and the test surface; the current-voltage results are presented in Fig. IV-1 (top).

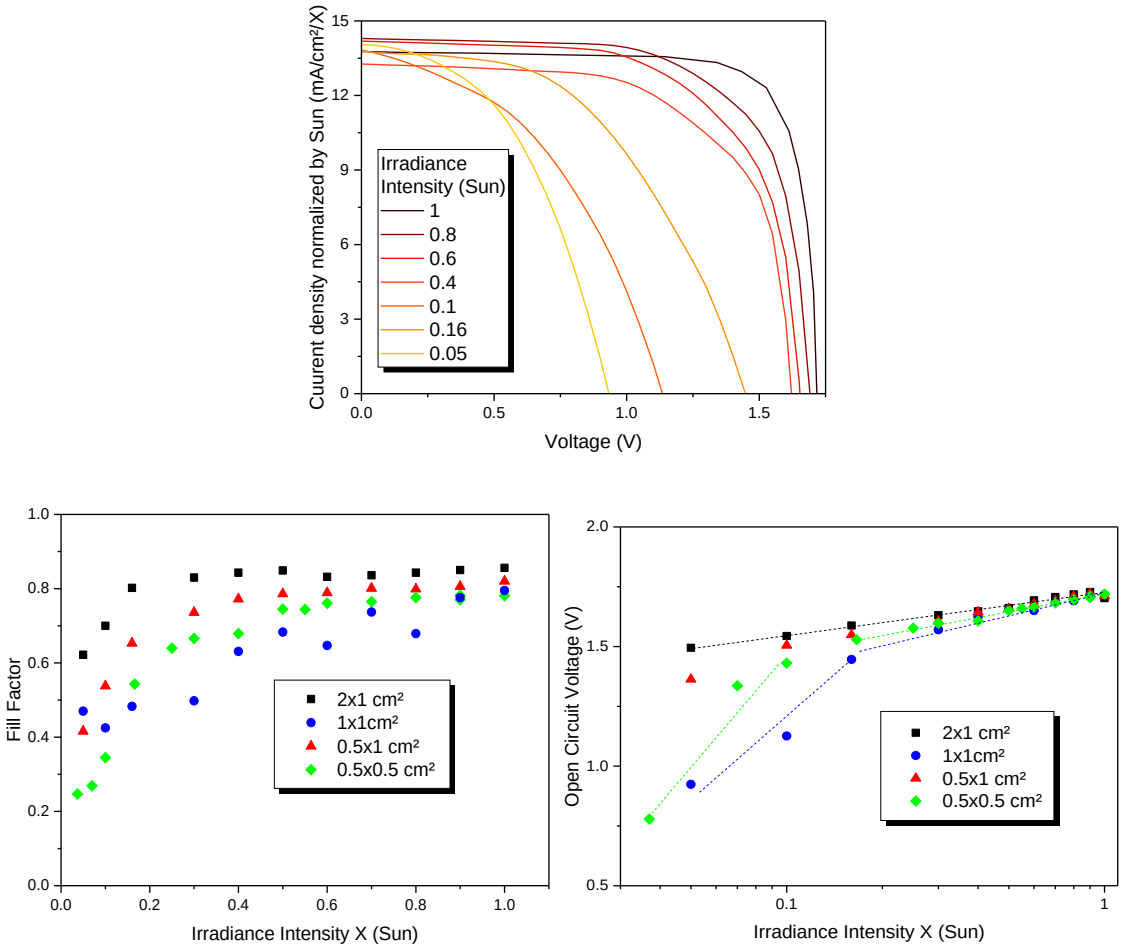

Fig. IV-1 *Current-voltage characterizations of 2J AlGaAs//Si under different irradiance levels ranging from 1 sun down to 3% of 1 sun, top: I-V characteristics, bottom-left: Fill Factor evolution with concentration, bottom-right: open circuit voltage evolution with irradiance intensity.*

With decreasing the irradiance intensity, the short circuit current density (normalized by sun numbers) remains relatively stable around 13 mA.cm^{-2} with a deviation of ± 2.5%; this is theoretically expected (linear variation with intensity). However, an anomalous decrease of open circuit voltage (non-logarithmic variation) and fill factor are observed with decreasing irradiance intensity. Multiple dual-junction solar cells sizes (0.5 x 0.5 cm², 1 x 0.5 cm² and

2 x 1 cm²) were tested under the same conditions; the evolution of fill factor and the open circuit voltage with irradiance intensity are presented in Fig. IV-1 (bottom).

By decreasing the irradiance intensity from 1 to 0.4 sun, the fill factor remains relatively stable within the range of 60 - 85% depending on the cells size (& perimeter/area ratio). Below 0.4 sun, a strong decrease is observed for the four cells sizes: the smaller are the cells, the lower is the FF (down to 25% for 0.5 x 0.5 cm² solar cells) except in the case of 1 x 1 cm² cells. The differences between the cells fill factor can be related to the parasitic recombination at the edge of solar cells, in other words when the perimeter/area ratio is high, the photo-generated electrons have more probability to recombine at the edge of solar cells; and this effect becomes more pronounced at low light intensity.

In contrast to FF, open-circuit voltage varies theoretically as a simple logarithmic function of the irradiance intensity (see section I.3), it is thus represented in logarithmic scale (see Fig. IV-1). Surprisingly, two types of behaviors are observed for open circuit voltage: a logarithmic decrease until 0.16 sun then a slope change with a stronger decrease until 0.03 sun. A lower shunt resistance may be at the origin of such FF and V_{OC} behaviors. Under low irradiance intensity, less e-h pairs are photo-generated, hence the effect of defects can be more pronounced [3]. The solar cells with low parallel resistance will have a maximum power point in this shunted part of *I-V* characteristics, and consequently it will affect strongly the electrical performances [4]–[8]. Therefore, this batch of 2J solar cells appeared as not suitable for use at low intensities.

A second experiment was carried out under the same conditions, i.e. *Helios 3030* equipment under different irradiance intensity, using 1J c-Si solar cells which dimensions are 0.5 x 0.5 cm², 1 x 0.5 cm² and 2 x 1 cm². The 1 x 2 cm² current-voltage characteristics under different irradiation levels are presented in Fig. IV-2 (top). The short circuit current density normalized by irradiance intensity remains stable around 39.7 $mA.cm^{-2}$ (with 2% deviation).

Unlike the trend observed with the 2J solar cells (see Fig. IV-1), no anomalous degradations were detected on FF or open circuit voltage (see Fig. IV-2 bottom). The fill factor is stable around 75% on a large low irradiance intensity levels (ranging from 1 sun to 0.1 sun). For concentration below 0.1 sun, a similar trend is observed as found in literature [9] with a small decrease on the FF: it reaches 60% for the smallest solar cell. The open circuit voltage values fit very well to the logarithmic theoretical equation (see Fig. IV-2 bottom-right) on all the irradiance levels, with a logarithmic function of the concentration.

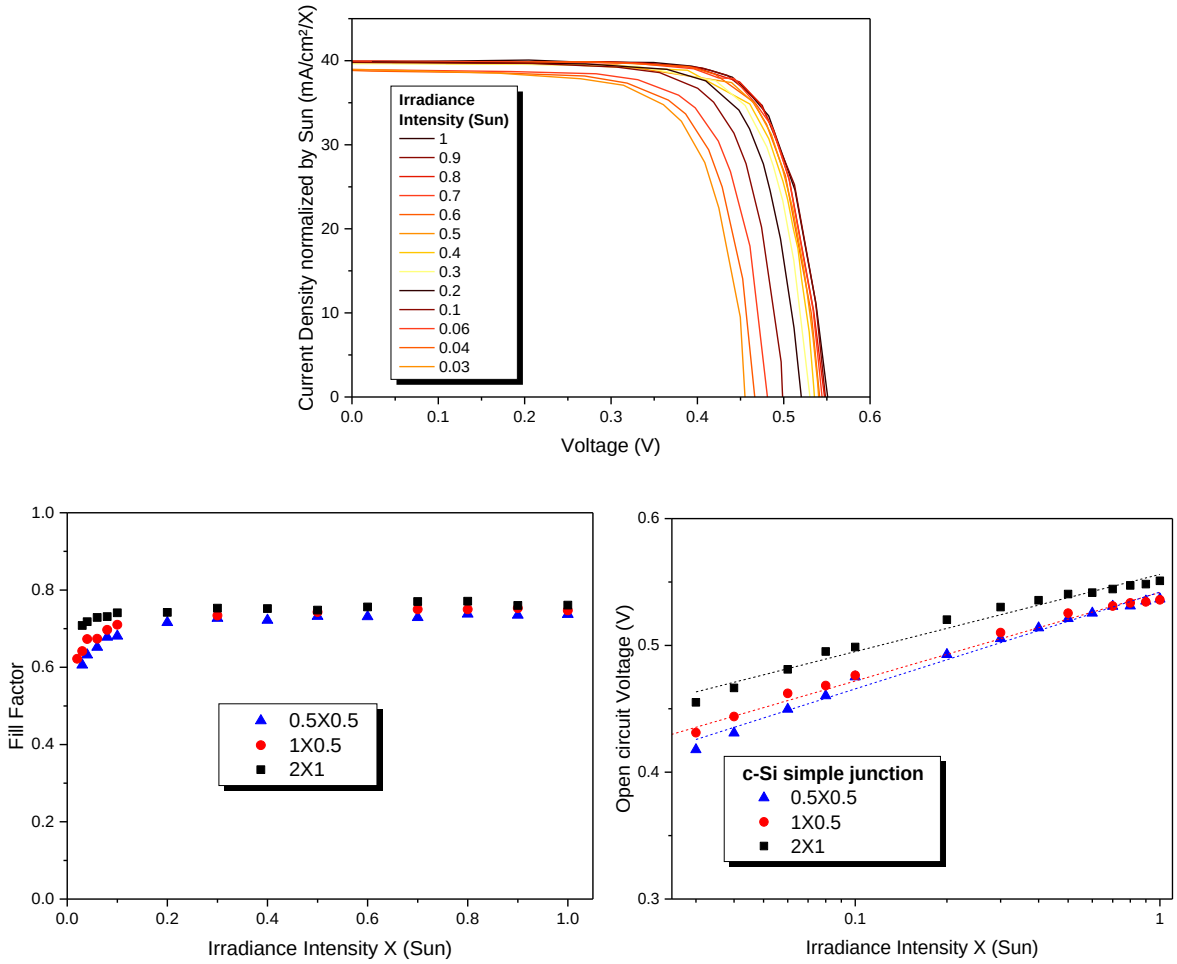

Fig. IV-2 *Current-Voltage characterization of 1J c-Si solar cells as a function of irradiance level ranging from 1 sun down to ~3% AM0, top: I-V characteristics, bottom-left: variation of fill factor with concentration, Bottom-right: open circuit-voltage evolution with irradiance level.*

Based on these two experiments, we can make the assumption at this stage that the low shunt resistance issue (at low irradiance) comes from the top sub-cell or from the surface activated wafer bonding process (*SAB* – see section II.2), since the Si cell is identical in both architectures (Fig. IV-1 and Fig. IV-2). Another possible explanation is that the solar simulator *Helios 3030* is not optimized and suitable for 2J solar cells characterizations at low irradiance intensity (X < 0.2 sun).

To investigate this point in more details, both c-Si and AlGaAs//Si solar cells (exact same samples) were characterized with the *Quesma* (*LED*) solar simulator (see section II.5.2), suitable for low irradiance level. The *I-V* characteristics measured at room temperature under 3.7% AM0 are presented in Fig. IV-3.

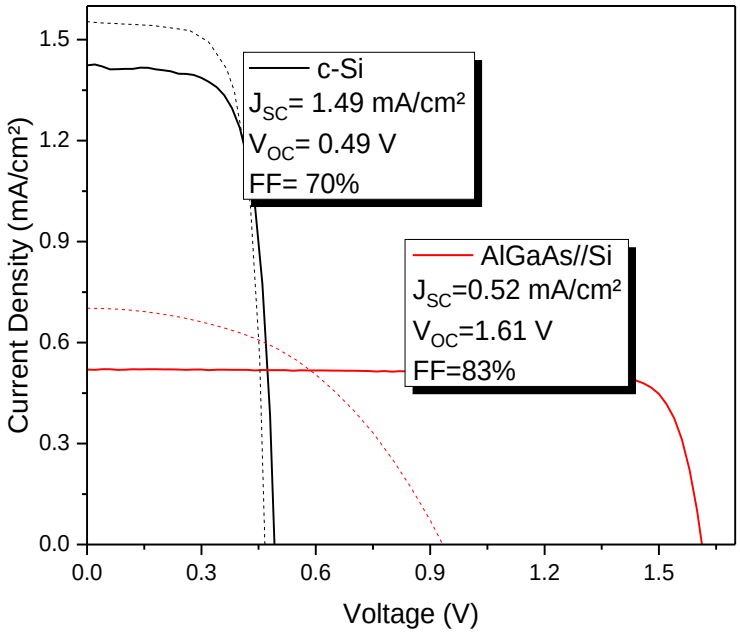

Fig. IV-3 *characterization of 1J c-Si and 2J AlGaAs//Si under 3.7% sun intensity with Quesma (solid lines) compared to Helios (dashed lines) solar simulator.*

A "normal" behavior is observed for the two types of solar cells: no degradation occurs, neither for the fill factor nor for the open circuit voltage. A value of 1.61 V and 83% is measured for the 2J with *Quesma* for V_{OC} and FF respectively while 0.78 V and 25% were previously measured with *Helios 3030* (see Tab. IV-1) at 0.05 Sun. One can conclude that the degradations observed above, are equipment-related issues rather than intrinsic problems with the 2J architecture. This AlGaAs//Si wafer bonded dual-junction does not show any anomalous behavior at low intensities, as confirmed by *Quesma* measurements. The *Helios 3030* solar simulator was initially conceived and optimized for high concentrations concentrator cells ($X \geq 1$ sun). In order to use it for low intensities, the flash lamp was positioned at the maximum height in the solar simulator (far from the cell); in addition, 7 optical filters, supposed to be "neutral", are placed in the light path to attenuate the irradiance intensity and reach the very low irradiance intensities below 0.1 sun. This configuration most likely distorts the simulator spectrum spectrally and increases the spatial inhomogeneity, hence non-reliable measurements were observed only on 2J that is more sensitive to spectral balance than c-Si. As reported in [10], the severity of current mismatch, MM between the two sub-cell determines the severity of the shunting effect on V_{OC} and FF, this lead to a decrease of the total V_{OC} to approach the non-shunted sub-cell one (Si in the case of 2J). Since the *Helios 3030* appeared not adapted for low irradiance measurements, *I-V* characterizations at ~ 3% AM0 were performed only with *Quesma* solar simulator for the rest of this study.

Tab. IV-1 *Electrical parameters comparison of both 2J AlGaAs//Si and 1J: c-Si characterized with Helios 3030 and Quesma solar simulators at low intensity.*

Electrical parameters	**2J: AlGaAs//Si**		**1J: c-Si**	
	Helios 3030 (X = 0.05)	*Quesma* (X = 0.037)	*Helios 3030* (X = 0.04)	*Quesma* (X = 0.037)
J_{SC} (mA.cm^{-2})	0.68	0.52	1.56	1.49
J_{SC}/X (mA.cm^{-2}.X^{-1})	13.6	14.1	39	40.3
V_{OC} (V)	0.92	1.61	0.47	0.49
FF (%)	47	83	72	70
Eff (%)	4.3	13.7	9.7	10.1

A comparison of *I-V* characteristics measured with the *Helios 3030* at 1 sun but extrapolated to low intensity and with *Quesma* solar simulator directly measured at low intensity for the three solar cells architecture is presented in Fig. IV-4. The lumped model proposed by C. Dominguez et al. [11] was used for extrapolating *Helios 3030* measurements to low intensities. The corresponding equations that describe the current-voltage characteristics on the input and output of the model are presented hereunder. Since measurements were performed at room temperature, no variations are expected in short-circuit current or voltage of the solar cells due to temperature. It is assumed a linear variation of short-circuit current with irradiance intensity according to Eq. IV-1. The output solar cells voltage can be expressed according to Eq. IV-2.

$$I_{out} = I_{in} . \mathrm{X} \qquad \textit{IV-1}$$

$$V_{out} = V_{in} + \Delta V(X) \qquad \textit{IV-2}$$

where I_{in} and V_{in} are the measured current and voltage of the solar cells at one sun intensity, I_{out} and V_{out} are the calculated current and the voltage of the solar cells at an irradiance intensity X and $\Delta V(X)$ is the voltage variation due to irradiance intensity.

The voltage of tandem solar cells is the sum of the sub-cells voltage that can be expressed as a function of solar cell current (see section I.2.3), so it is expressed as Eq. IV-3.

$$V = \sum V_i - IR_s \qquad \textit{IV-3}$$

If we consider a 2J solar cell, the ΔV(X) is expressed as a function of the sum of the top and bottom sub-cell voltage extracted from one diode model (see Eq. IV-4 and Eq. IV-5). We introduce a new constant $K_i = X_i/X$, which corresponds to the variation of the irradiance level on each sub-cell as a consequence to the spectrum variation.

$$\Delta V(X_{top}, X_{bot}) = V_{out} - V_{in} \qquad \textit{IV-4}$$

$$\begin{aligned} = \frac{kT}{q}\Bigg[& \left(n_{top} + n_{bot}\right)\ln(X) \\ & + \ln\left(\left(\frac{K_{top}I_{ph,top,in} - I_{in}}{I_{ph,top,in} - I_{in}}\right)^{n_{top}}\left(\frac{K_{bot}I_{ph,bot,in} - I_{in}}{I_{ph,bot,in} - I_{in}}\right)^{n_{bot}}\right)\Bigg] \\ & - I_{in}(X-1)R_s \end{aligned} \qquad \textit{IV-5}$$

where $I_{ph,top,in}$ and $I_{ph,bot,in}$ are the top and bottom sub-cell measured photo-generated current using isotypes reference cells, k is the Boltzmann constant, q is electrons charge and T is the temperature.

Considering that no spectrum variation is observed (i.e. $K_i = 1$) the produced voltage variation is equal to the one calculated with 1J. Therefore, the variation in voltage is simplified to the Eq. IV-6 below, where n_{top} and n_{bot} are the ideality factor of the top and bottom cells that are considered as fitting parameters.

$$\Delta V(X) = \frac{kT}{q}\left(n_{top} + n_{bot}\right)\ln(X) - I_{in}(X-1)R_s \qquad \textit{IV-6}$$

In order to compare the two solar simulators, the lumped model was applied to translate current voltage measurements carried out under 1 AM0 with H*elios 3030* to current voltage characteristics at 3.7 % AM0 at room temperature.

The results of the model application on 1J c-Si, 2J AlGaAs//Si and 3J GaInP/AlGaAs//Si solar cells are presented in Fig. IV-4. The solid lines represent the measured *I-V* characteristics; the dashed lines represent the calculated *I-V* characteristic using the lumped model with input measurements taken at 1 sun AM0 spectrum. As one can see, the three calculated behavior agree very well to the *I-V* characteristics measured at ~ 3% AM0 spectrum using *Quesma* solar simulator. Silicon single-junction has however a more pronounced series resistance when measured at low intensity compared to its projected values. Overall, with this procedure, the

measurements can be compared between the solar cells measured with the *Quesma* and *Helios 3030* solar simulator thanks to this lumped model.

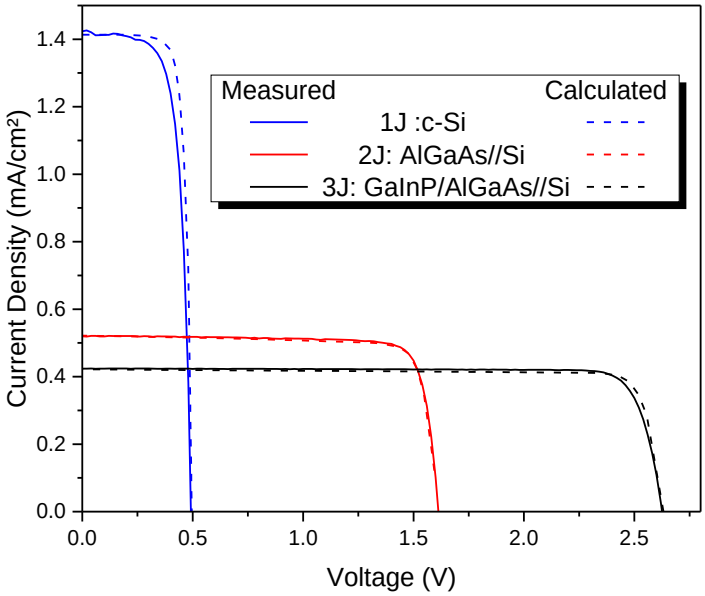

Fig. IV-4 *Comparison of 1J c-Si, 2J AlGaAs//Si and 3J GaInP/AlGaAs//Si solar cells I-V characteristics measured at ~3% AM0 with Quesma and calculated for the same intensity with the lumped model using Helios 3030 I-V measurements at 1 sun .*

IV.2.2. Current Voltage characterizations

The *I-V* characterization results of the three solar cell architectures at ~3% AM0 and 300 K called *LIRT* (Low Intensity and Room Temperature) in comparison to those performed at 1 sun AM0 and 300 K called *NIRT* (Normal Intensity and Room Temperature) are presented in Fig. IV-5.

In this first section where the effects of irradiance intensity is investigated, the characterization at *NIRT* conditions has been carried out with the *Helios 3030* solar simulator. However, in the rest of this chapter, the *I-V* characterizations were carried out using the *Quesma* solar simulator that is optimized for low intensity measurements. Six solar cells samples are used for the three architectures along this chapter.

In the case of c-Si 1J (see Fig. IV-5 top), the six 1 x 1 cm^2 solar cells at *NIRT* conditions (dark curves) have almost the same *I-V* behavior. The measured values of J_{SC} and V_{OC} are respectively 38.6 $mA.cm^{-2}$ and 0.56 V with low deviation less than 0.8%. However, the main differences remains in the FF, where values of 78% are calculated with a deviation of 5% that induces high deviation (6%) on the efficiency. By decreasing the intensity to ~3% AM0, high decrease of J_{SC} is observed compared to the V_{OC} where they reach 1.38 $mA.cm^{-2}$ and 0.50 V. The 3% variation observed on J_{SC} can be explained by set-up temporal homogeneities since the

J_{SC} is very sensitive to illumination intensity. In addition, at low intensity, the defects can have pronounced effects on solar cells behavior [3]. However, in the case of V_{OC} (low sensitivity to illumination) a deviation of 2.2% is calculated. This can be explained to the different solar cell quality, further details will be discussed later by comparing the variation of V_{OC} to the theoretical expectation. The calculated FF is 74% with high deviation of 6% already present at *NIRT* conditions.

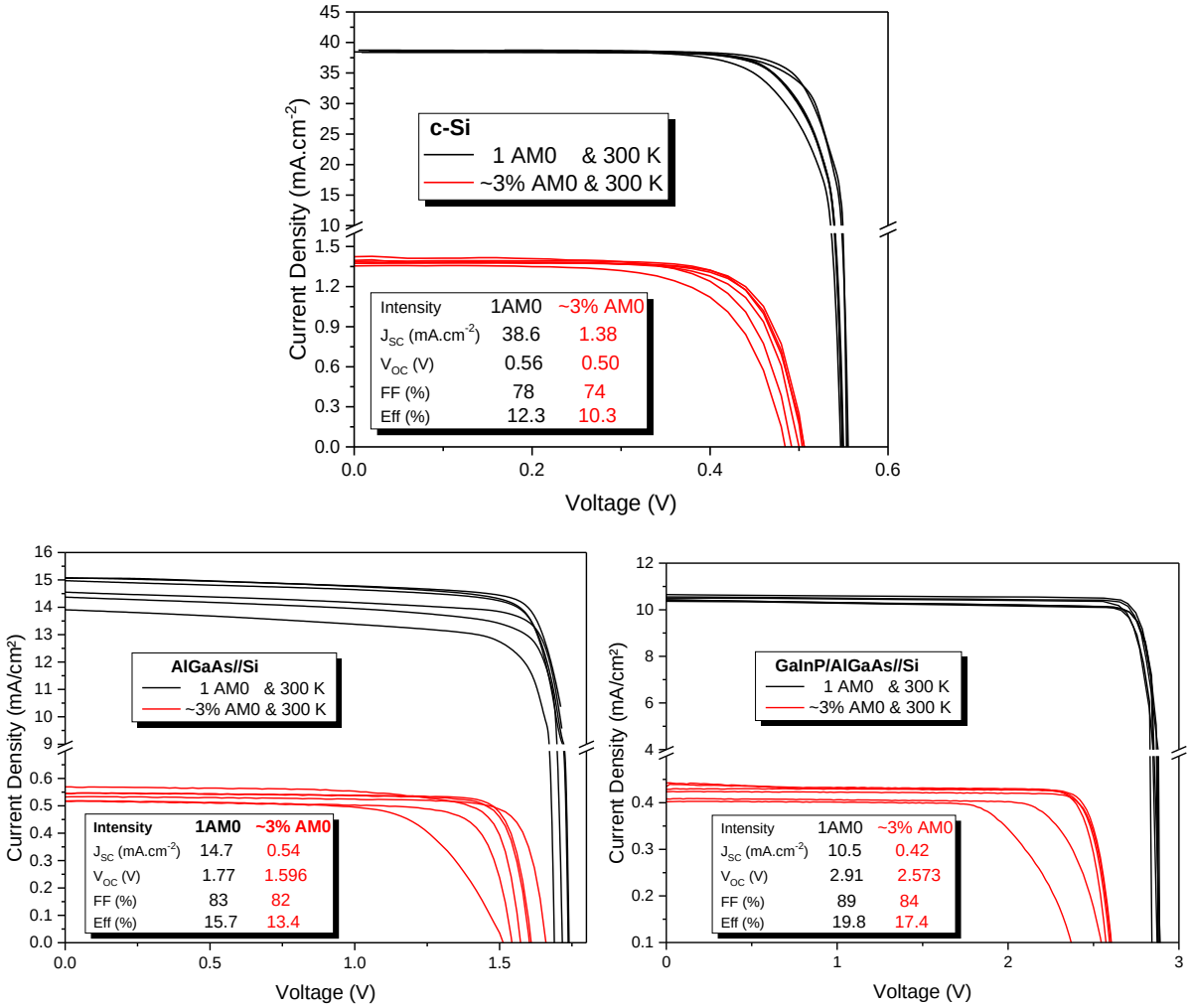

Fig. IV-5 *Characterization of six solar cells at NIRT (1 AM0 & 300 K) and LIRT (~3% AM0 & 300 K) conditions (top) 1J c-Si (bottom-left) 2J AlGaAs//Si (bottom-right) 3J GaInP/AlGaAs//Si. The absolute electrical parameters are averaged on the six solar cells for each architectures at both conditions.*

In the case of 2J (see Fig. IV-5 bottom-left), two solar cells sizes (3 samples for each size) were used 1 x 1 cm^2 and 2 x 1 cm^2 (for solar cells visualization see Fig. II-1). The six solar cells *I-V* measured at *NIRT* behavior show a strong deviation due to difference in solar cells quality and in shading factor: large solar cells have less finger shading (thus higher J_{SC}) than the smaller solar cells that have a denser finger pattern. The absolute values (resp. deviation) of J_{SC}, V_{OC} and FF are 14.7 $mA.cm^{-2}$ (resp. 4%), 1.77 V (resp. 1.8%) and 83% (resp. 2.4%). The deviation

on electrical parameters among sub-group of cells is 0.5% for 1 x 2 cm^2 and less than 2.3% for 1 x 1 cm^2. When the solar cells are measured at *LIRT* conditions, they show the same trend as at *NIRT* condition with averaged values of J_{SC}, V_{OC} and FF of 0.54 $mA.cm^{-2}$, 1.596 V and 82% and similar deviations as for *NIRT* are calculated, with the exception of the V_{OC} (deviation of 3.3% observed).

Considering the six (2 x 1 cm^2 and 1 x 1 cm^2) *I-V* behaviors of the 3J cells (see Fig. IV-5 bottom-right), they present a low deviation (<2%) for all electrical parameters at *NIRT* conditions with averaged values of J_{SC}, V_{OC} and FF of 10.5 $mA.cm^{-2}$, 2.91 V and 89%. At *LIRT* conditions the averaged measured values of J_{SC}, V_{OC} and FF are 0.42 $mA.cm^{-2}$, 2.573 V and 84% with a higher deviation (maximum of 8%) on J_{SC} and FF and 4% on V_{OC}.

In summary from the measurements under *LIRT* conditions compared to *NIRT* conditions, it is observed that the deviation increases at low intensities especially for the V_{OC}. Subsequently we will present the evolution of the J_{SC} and V_{OC} as a function of illumination intensity and compare it to theoretical behavior.

As presented in section I.3, the variation of the short-circuit current density has theoretically a linear variation with the illumination intensity (see Eq. IV-7), such as solar cell at 3% AM0 would have 3% of its J_{SC} at 1 AM0.

$$J_{SC}(X) = X.J_{SC}(1\ Sun) \qquad \textit{IV-7}$$

In Fig. IV-6 (left), the measured J_{SC} by *I-V* characterizations (symbols) is plotted as a function of the irradiance intensity, while the solid line curve represents the Eq. IV-7. In the three Fig. cases (1J, 2J and 3J), the variation of the J_{SC} is in agreement with the theoretical variation with the corresponding deviation due to the difference between solar cells shading factor and solar simulator inhomogeneities.

In the case of open circuit voltage, the variation with irradiance intensity is logarithmic according to Eq. IV-8.

$$V_{OC}(X) = V_{OC}(1\ sun) + \frac{nkT}{q}.Ln(X) \qquad \textit{IV-8}$$

Where V_{OC}(1 sun) is the measured at X = 1 sun and n is the ideality factor. In the case of 1J the ideality factor is comprised between n = 1 and n = 2. However, in the case of tandem cell the ideality factor is multiplied by the number of junction, i.e. for 2J and 3J the n is comprise between 2 - 4 and 3 - 6 [11], [12]. As for the J_{SC}, the measured V_{OC} values by *I-V*

characterization are presented in Fig. IV-6 (right) as a function of irradiance intensity by symbols whereas the theoretical variation is presented by the region between the two solid lines (gray region) calculated by the two ideality factor for each solar cell architecture.

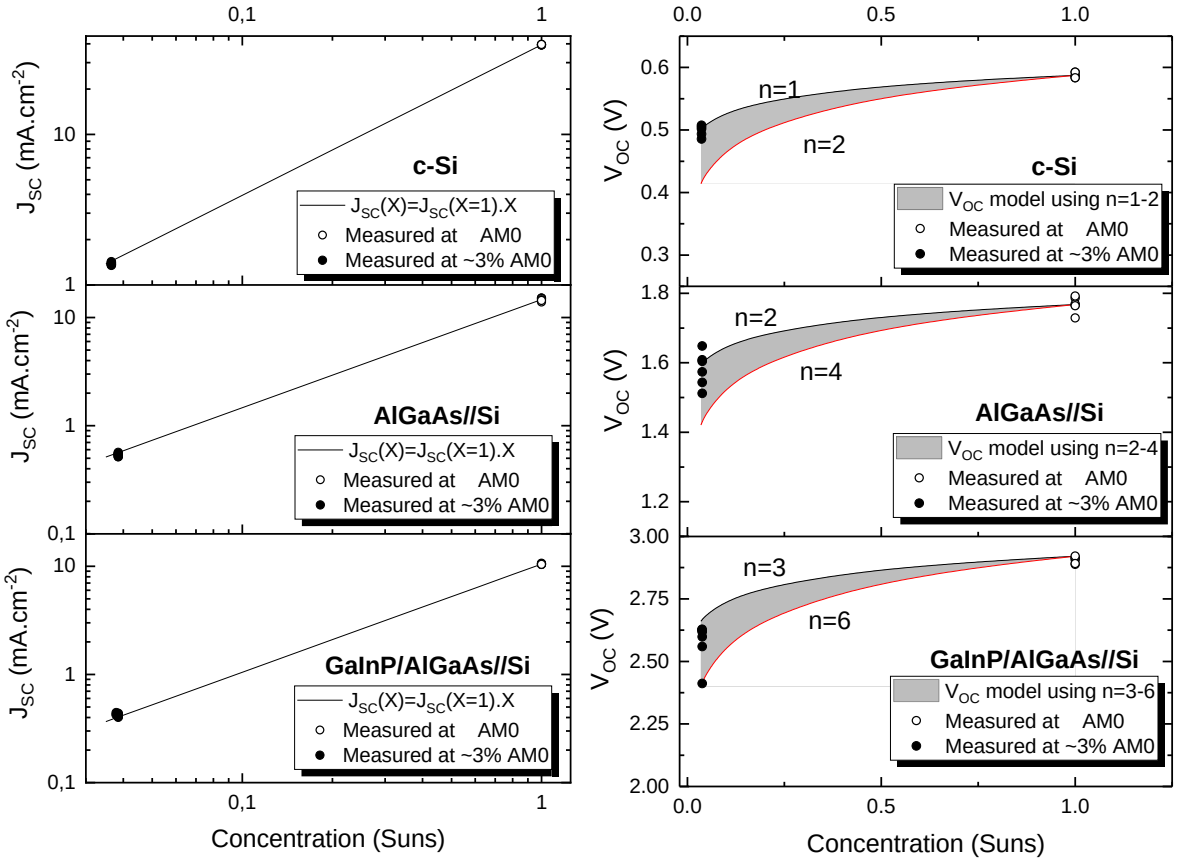

Fig. IV-6 *Evolution of measured electrical data as a function of irradiance intensity for 1J, 2J and 3J with comparison to theoretical evolution variation of (left) J_{SC}, and (right)V_{OC}.*

From Fig. IV-6 (right), it is observed that the V_{OC} deviation between the two ideality factors values is higher when decreasing the irradiance intensity. The absolute deviations for 1J, 2J and 3J are 0.1 V, 0.17 V and 0.26 V at an intensity of ~3% AM0.

Comparing the measured data to the theoretical curves, it is noticed that for all three architectures, the V_{OC} values fit well into the theoretical region with values of n close to the lower limit (1, 2 and 3 for 1J, 2J and 3J) in the majority of cases. In the case of a few cells 2J and 3J, the value of n is much closer to the upper limit (4 and 6 for 2J and 3J). This can be explained either by the lower quality of the solar cell in question or by the degradation of the cell during its positioning in the sample holder using springs (introduction of surface recombination center).

In conclusion, the low intensity measurements are in rather good agreement with the behavior reported in the literature. As explained before, the observed deviation of the electrical parameters is short-circuited due to the relative comparison, i.e. the evolution of the electrical parameters is tracked as a function of temperature, illumination and irradiation for each cell separately.

IV.3 Effect of Low Intensity and Low Temperature

IV.3.1. Thermal cycling experiments

As a first step, the mechanical resistance of the III-V//Si bonding interface as well as the metallization fingers/busbar against thermal cycles is investigated, and then the cells electrical performances are characterized under 4% AM0 and 300 K before and after cycling. The thermal cycling sequence is shown in Fig. IV-7. From room temperature, the samples are tempered for 90 s in liquid nitrogen in a Dewar, which temperature is approximately 77 K under 1 atm., then heated up to 300 K (RT) for 2 min and 400 K for 2 min as well. Finally, the solar cells are brought back to RT for 2 min before starting a new cycle. The 3J GaInP/AlGaAs//Si and 1J c-Si were used for this experiment. The 3J was submitted to 10 thermal cycling whereas 1J was submitted to 20 thermal cycling. Even if in real operating conditions the solar cells actually face a higher number of cycles, i.e. 16 per day for LEO and 1 per day for GEO [13], it provides us with information about the behavior of solar cells during the first cycles (monitoring of early defects).

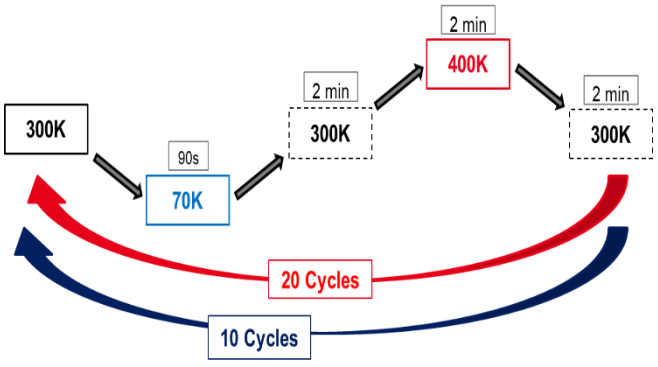

Fig. IV-7 *Thermal cycling plan.*

The integrity of the cells was examined after cycling using optical microscope observations (x100 magnification): no delamination, cracks or micro-cracks were detected. Measurements before and after thermal cycling, performed under 1sun AM0 and at 300 K, show almost no degradation of the electrical performances for both 1J and 3J (graph not shown here).

The results of the *I-V* characterizations under ~ 4% AM0 using at 300 K *Quesma* solar simulator of the 3J solar cell before and after 10 thermal cycles (80 - 400 K) are presented in Fig. IV-8 (left). In terms of electrical performance, no degradation is observed on the J_{SC} and FF. However, for the open circuit voltage, a slight degradation of 20 mV is observed for the triple junction. Fig. IV-8 (right) shows the *I-V* characteristics of the 1J before and after thermal cycling. A slight increase of J_{SC} of 0.8% is observed after thermal cycling, this deviation is within the limit of the sun simulator homogeneity thus can be neglected. On the other hand, no degradation is observed on the open circuit voltage.

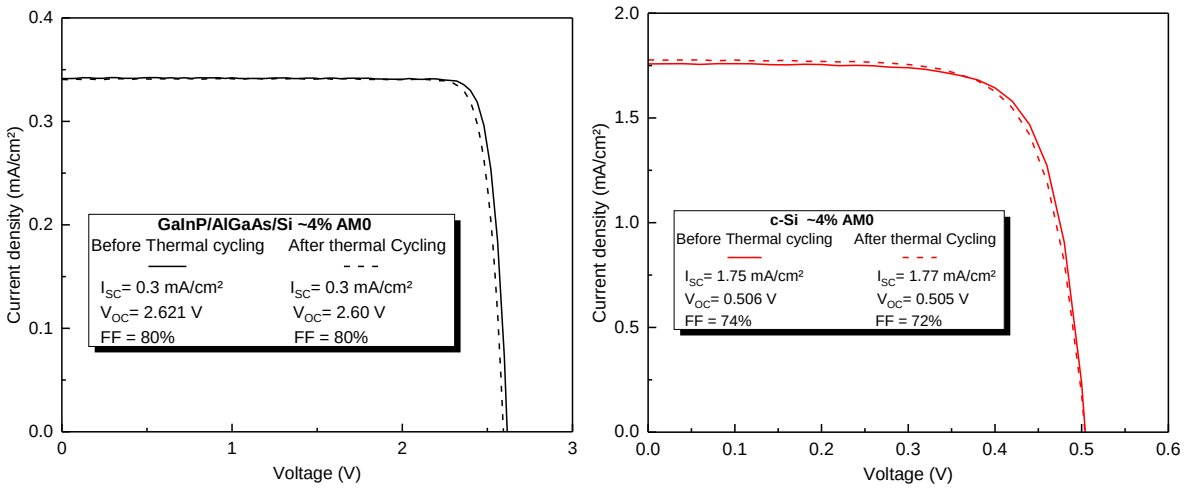

Fig. IV-8 *I-V characterization before and after thermal cycling performed at 300 K under ~4% AM0 (left) 3J GaInP/AlGaAs//Si → 10 thermal cycling (right) 1J c-Si → 20 thermal cycling.*

At low irradiance, the defects present in the different layers may have a greater effect on the electrical parameters than at high intensity [4],[8],[14]. This is why the slight degradation of the open circuit voltage is visible only at ~ 4% AM0. By exposing the 1J to twice as many thermal cycles as the 3J, there is no noticeable degradation, which may suggests that the bonding interface degradation could be responsible for the open circuit voltage decrease if we assume the absence of degradation in the III-V layers. However to confirm this hypothesis more statistical measurements are needed. Nevertheless, in the framework of our study, the solar cells are subject to only one thermal cycling and the degradation observed in 3J is very low compared to that expected after irradiation, so the effect can be considered negligible. Thus, measurements can be performed at low temperature (120 K).

IV.3.2. Current voltage characterizations

For the investigation of the global behavior of the three solar cells architectures at Low Intensity and Low temperature (*LILT*) conditions, *I-V* characterizations were performed also

with the *Quesma* solar simulator. The *I-V* behavior measured at ~ 3% AM0 and 120 K are presented in Fig. IV-9 (blue lines) with comparison to the one measured at ~ 3% AM0 and 300 K (red lines). The irradiation and characterization protocol adopted in this chapter is presented in section II.3.

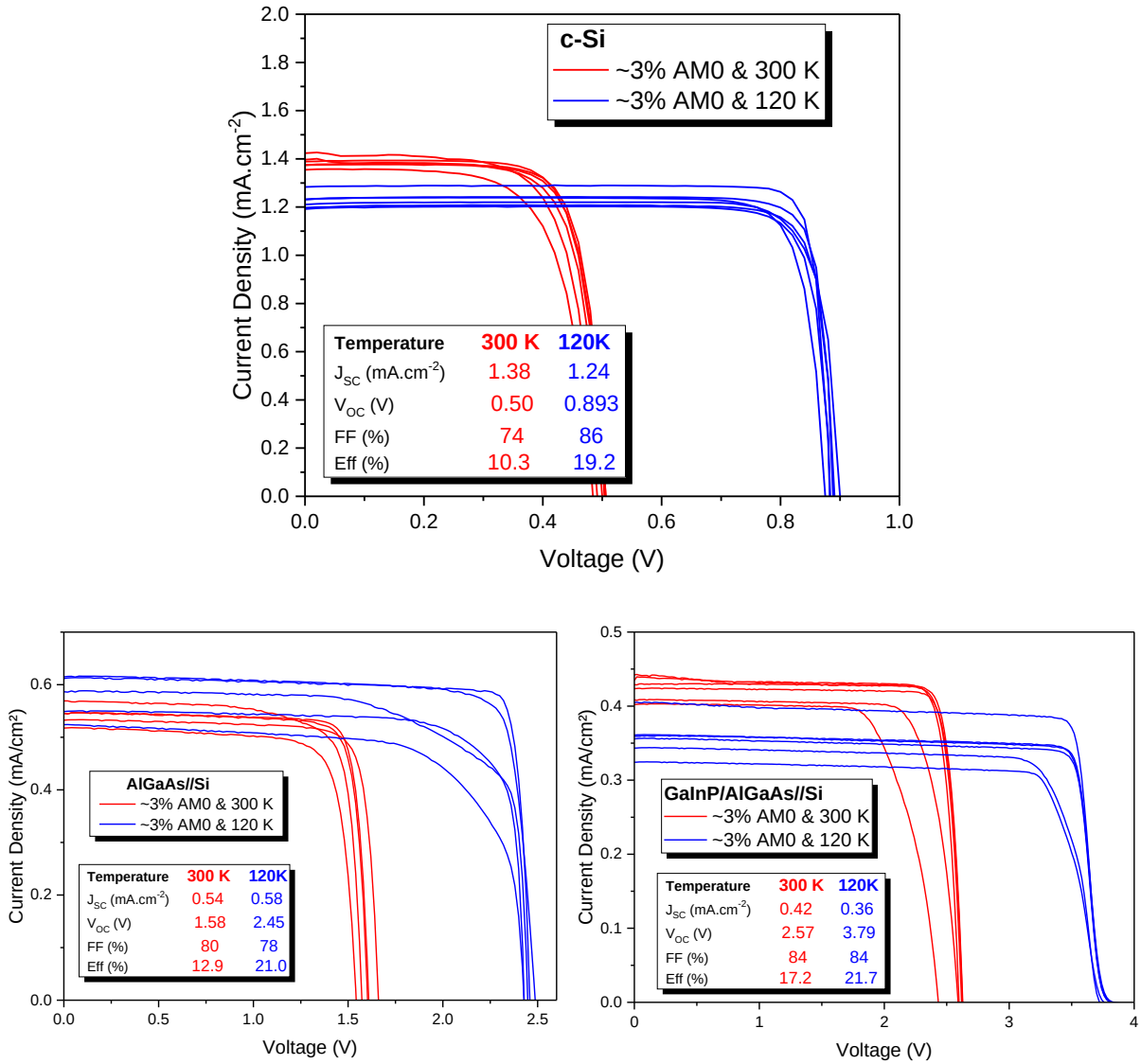

Fig. IV-9 *Current-voltage characterization under ~3% AM0 at 300 K in red and 120 K in blue (top) 1J c-Si (bottom-left) 2J AlGaAs//Si (bottom-right) 3J GaInP/AlGaAs//Si. values on the legend are the average of the six solar cells for each architectures.*

After cooling down the 1J solar cells (see Fig. IV-9 top), it is observed a slight decrease of J_{SC} with average value of 1.24 mA.cm^{-2} compare to 1.38 mA.cm^{-2} at *LIRT* conditions, with a corresponding deviation of 2.7 % for the six solar cells (equivalent to the one measured at *LIRT* conditions). On the other hand, a pronounced increase of the open circuit voltage is observed with values reaching 0.893 V compared to 0.500 V at *LIRT* condition, with 0.8% deviation among the six tested solar cells. The FF also increases from 74% at *LIRT* conditions to reach

86% at *LILT* conditions with 2.7% deviation. The efficiency is reaching 19.2% compared to 10.3% at *LIRT* condition with 4.6% deviation among this set of six solar cells. This increase is mainly due to the V_{OC} boost at *LILT*, almost two times the *LIRT* values.

In the case of 2J solar cells (see Fig. IV-9), it is observed that the J_{SC} values slightly increase at *LILT* conditions compared to the one at *LIRT* with average value of 0.54 $mA.cm^{-2}$ and 0.58 $mA.cm^{-2}$ at 300 K and 120 K, respectively. The same trend was observed in [15] where measurements as a function of temperature were performed on isotype solar cells. For the V_{OC}, a pronounced increase is observed, with average value reaching 2.45 V; its x1.5 higher than the V_{OC} measured at 300 K. The FF on its side decreases slightly and reaches values of 78% (2% in abs. less than that observed at 300 K). As observed in Fig. IV-9, the maximum statistical deviation of 12% is calculated. In addition, one of the 2J cells shows a phenomenon known for solar cells under *LILT* conditions which translates as a flat spot (or broken knee) near the point of maximum power. This is explained in [2], [14], [16]–[18] by a particular type of defect due to an alteration of the p-n junction and the formation of a localized *MSL* - metal-semiconductor interface - underneath the front grid metallization. The *MSL* occurs after thermal activation during the manufacturing steps, i.e. localized reaction of Si with the adjacent metallization that lead to a formation of highly conductive region between the metal and the base of the solar cells. This region is modeled by a diode and a resistor in parallel to the p-n junction. The series resistance difference between both *MSL* interface and the p-n junction is at the origin of the double knee, where at low voltage the *I-V* behavior is controlled by the *MSL* interface and by increasing the voltage near V_{OC}, the *I-V* follows the p-n junction. This effect is present on only one of the cell among six studied. Certainly, this effect reduces the performance of the cell but relative comparisons are made before and after irradiation in this thesis, i.e. each cell is monitored separately.

This effect is not identifiable with measurements at room temperature, either at normal or low intensity [2], [19]–[23]. Furthermore, the effect can vary quite strongly from cell to cell, which for a given solar cell design is likely to cause the flatness effect to appear, resulting in very unpredictable *LILT* performances. Therefore, a screening selection is performed on all cells at *LILT* conditions before arrays integration phase. However, in our case this is not possible with the small number of samples available contrary to conventional and commercial III-V/Ge solar cells.

Tab. IV-2 *Average electrical parameters for the three solar cells architectures (1J, 2J and 3J) characterized at Low Intensity and Low Temperature condition ~3% AM0 and 120 K.*

Solar cells	*LILT* conditions			
	J_{SC} mA.cm^{-2}	V_{OC} (V)	FF (%)	Eff (%)
1J	1.24 ± 2.7%	0.893 ± 0.8%	86 ± 2.7%	19.2 ± 4.6%
2J	0.58 ± 8.3%	2.45 ± 1.2%	78 ± 12%	21 ± 20%
3J	0.36 ± 11%	3.79 ± 1.3%	84 ± 3.4%	21.7 ± 14.3%

Considering the case of 3J (see Fig. IV-9 bottom-right), the performances at *LILT* conditions show a decrease of J_{SC} compared to *LIRT* where it reach an average values of 0.36 mA.cm^{-2}. As for both 1J and 2J architectures high increase of V_{OC} is observed for 3J architecture at *LILT* conditions with average value around 3.79 V (1.5 times *LIRT* average value). At low temperature, the FF average value does not change and remains at 84%. This is due to the appearance of a behavior known as S-Like Shape at 120 K near V_{OC}. This behavior is probably due to a majority charge carrier barrier (*MCB*) that occurs at the metal-semiconductor hetero-interfaces, at the backside passivation surface [2], [18]. It is important to note that this behavior does not affect the V_{OC} but only the FF therefore the efficiency.

After cooling down to 120 K, the bandgap energy increases (e.g. silicon will increase from 1.12 eV at 300 K to 1.16 eV at 120 K). From Eq. IV-9 that relates the V_{OC} to the bandgap energy Eg, the dark saturation current I_0 and short-circuit current density J_{SC}, it is clear that V_{OC} values increase with the increase of the bandgap [24]. In the case of tandem solar cells, the boost of V_{OC} is the combination of the increase of each junction V_{OC} depending on their respective temperature coefficient.

$$V_{OC}(T) = \frac{E_g(T)}{q} - \frac{nkT}{q}.Ln\left(\frac{I_0(T)}{I_{SC}(T)}\right) \qquad \textit{IV-9}$$

In the case of the 1J and 3J cells (Si limiting sub-cell), a decrease of the J_{SC} is observed at low temperature. This is explained by the fact that the absorption band decreases leading to a decrease of photo-generated current. In addition, a low thermal excitation of electrons leads to low photo-generated current. However, in the case of 2J the AlGaAs sub-cell limits the current of the multi-junction at 300 K. Studies have shown that the quantum efficiency of the GaInAs sub-cell is shifted towards the short wavelength at low temperature [25], [26]. This leads us to believe that an increase in the quantum efficiency of AlGaAs in the blue portion of the solar spectrum, which is more energetic, leads to an increase in the photo-generated current of the

AlGaAs sub-cell and consequently that of the double junction. Measurements of the in-situ quantum efficiency at low temperatures are needed to monitor the evolution of the quantum efficiency of each sub-cell and to confirm this hypothesis. However, these measurements could not be performed due to set-up issues for the quantum efficiency measuring at 120 K.

In order to monitor the electrical parameters in details with temperature, *I-V* measurements have been carried out in the temperature range 300 - 120 K under a constant irradiance intensity of ~3% AM0 spectrum. The characteristic curves for both 1J and 3J are presented in Fig. IV-10. In both cases, a small decrease is observed for the J_{SC} compared to the V_{OC} increases.

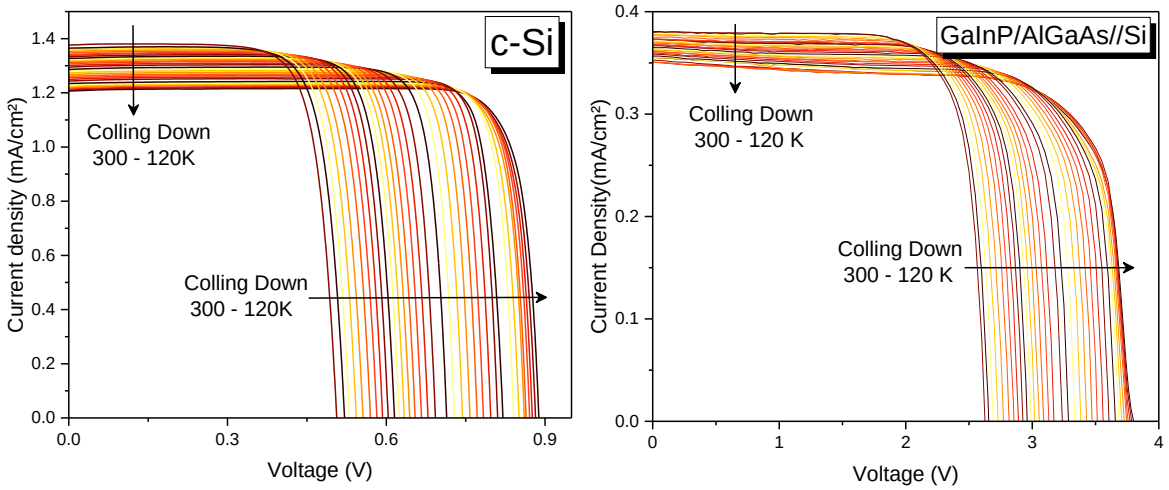

Fig. IV-10 *Current-voltage characterization under ~3% AM0 as a function of temperature from 300 K down to 120 K for (left) 1J c-Si (right) 3J GaInP/AlGaAs//Si.*

The electrical parameters J_{SC}, V_{OC}, FF and efficiency are presented in Fig. IV-11 as a function of temperature. In the case of J_{SC}, a linear decrease is observed for both 1J and 3J with the corresponding temperature coefficient of 0.8 $\mu A.cm^{-2}.K^{-1}$ and 0.3 $\mu A.cm^{-2}.K^{-1}$. As explained, this decrease is due mainly to the narrowing of the absorption band due to the increase of the bandgap energy. It is observed that the temperature coefficient of 3J is seven times lower than that of 1J; i.e. higher decrease of J_{SC} is observed for 1J compared to 3J. This can be explained by the fact that in 3J, the bandgap of Si increases which decreases its absorption band at the long wavelength, however the bandgap of the middle sub-cell also shifts to shorter wavelength, therefore increasing the photons transmission at shorter wavelength. Thus, the current limiting Si sub-cell receives less long wavelength photons (~1100 - 1200nm) but more shorter wavelength photons (~800 - 900nm). In contrast, in the case of 1J the absorption band is not extended to lower wavelength. A linear current variation is also assumed for the 2J architectures which was only measured at RT and 120 K. However, it J_{SC} values

increase with decreasing temperature (-0.2 $\mu A.cm^{-2}.K^{-1}$) which can be related to the enhancement of the absorption at lower wavelength.

For the V_{OC}, a linear behavior is also observed for 1J and 3J while assumed for 2J in the temperature range considered in this study. The calculated variation with temperature are -2.2 $mV.K^{-1}$, -4.8 $mV.K^{-1}$ and -6.8 $mV.K^{-1}$ for the 1J, 2J and 3J respectively. It is observed that by increasing the number of sub-cells in a solar cell architecture, the temperature coefficient increases due to the contribution of each sub-cell.

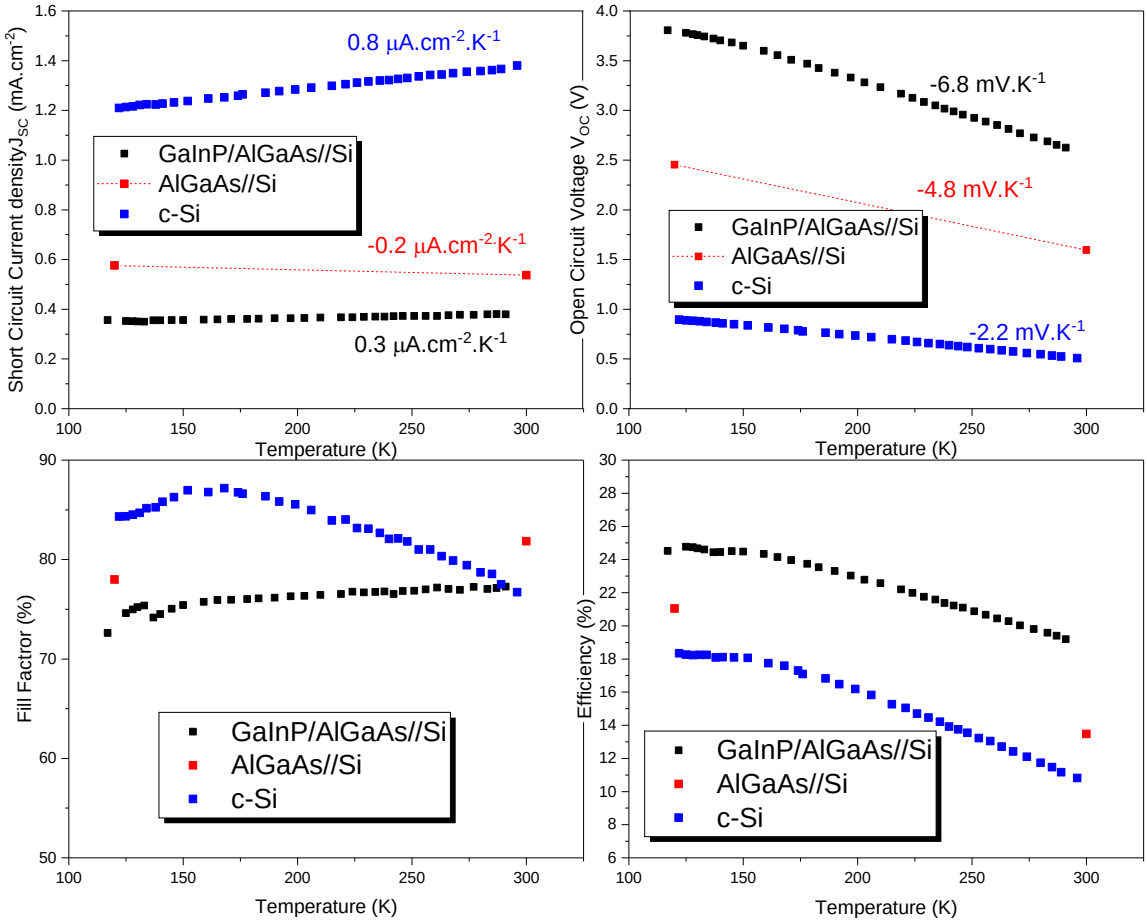

Fig. IV-11 *Electrical parameters variation as a function of temperature for the three cells architectures (top-left) short-circuit current density J_{SC} (top-right) open circuit voltage V_{OC} (bottom-left) fill factor FF (bottom-right) efficiency. In the case of 2J solar cells, measurement were made only at 300 and 120 K, thus the dashed lines represent only guide to the eyes.*

In the case of 1J, we observe that the FF increases and reaches its maximum around 150 K at a value of 87% due to the fact that the dark current decrease at low temperature, thus the *I-V* curve tend to be more rectangular. After that it decreases due to the non-negligible effect of the tunneling current at low temperature that become at the same order of magnitude than the recombination and dark saturation current [19], [27]. In contrast, in the case of tandem cells it

is observed that the FF continuously decreases in the temperature range studied here where it reach values of 78% and 72% in the case of 2J (hypothesis) and 3J respectively. This effect can be related to the variation of photo-generated current between the sub-cells as the temperature decrease (blue shift) and the appearance of S-like shape at low temperature for the 3J and the broken knee in the case of 2J.

Based on the measurements made on both 1J and 3J architecture, it is observed that the efficiency increases linearly in the temperature range 300 - 150 K with a temperature coefficient of -4.9 %.K^{-1} and -2.5 %.K^{-1} for 1J and 3J respectively. The strong increase in V_{OC} and the small decrease in J_{SC} are the main reasons for the significant increase of efficiency. However, in the temperature range 150 - 120 K, it is observed that the efficiency is saturated due to the FF decrease as explained above. Taking these two cases, we assume the same hypothesis in the case of 2J, where a linear increase is assumed in the range 300 - 150 K with a temperature coefficient of -3.8 %.K^{-1} and a stabilization of the efficiency around 21% in the range 120 - 150 K. The linear variation of JSC and VOC with temperature in addition with the saturation of efficiency due to FF limitation at very low temperature are in very good agreement with reported behavior of tandem solar cells at this temperature range [17], [19], [28]–[31].

Dark *I-V* measurements were performed as a function of temperature for all the three solar cells architectures. Fig. IV-12 presents a comparison between the dark *I-V* characteristics carried out at 300 K (red) and at 120 K (blue). In all three cases, a shift of the *I-V* curve towards high voltages is observed. This is due to the increased bandgap energy as observed in the case of *I-V* measurements under illumination. A second point to be emphasized is the decrease of the dark current at low temperature. The dark current is proportional to the density of the occupied state in the conduction band. At low temperature, the lower occupied state density for electrons (the higher bandgap energy and lower thermal energy) results in dark current reduction. A current density of the order of 10^{-8} - 10^{-9} A is measured for low voltage for all three architectures. The noisy signal measured at low voltage is due to the low sensitivity of the measuring equipment to such low current values.

It is also observed a relatively high statistical dispersion (5 order of magnitude in the dark current) even with the used cells coming from the same batch. However, given the low dark current compared to the photo-generated current under illumination, it induces a low dispersion on light *I-V* (see Fig. IV-9).

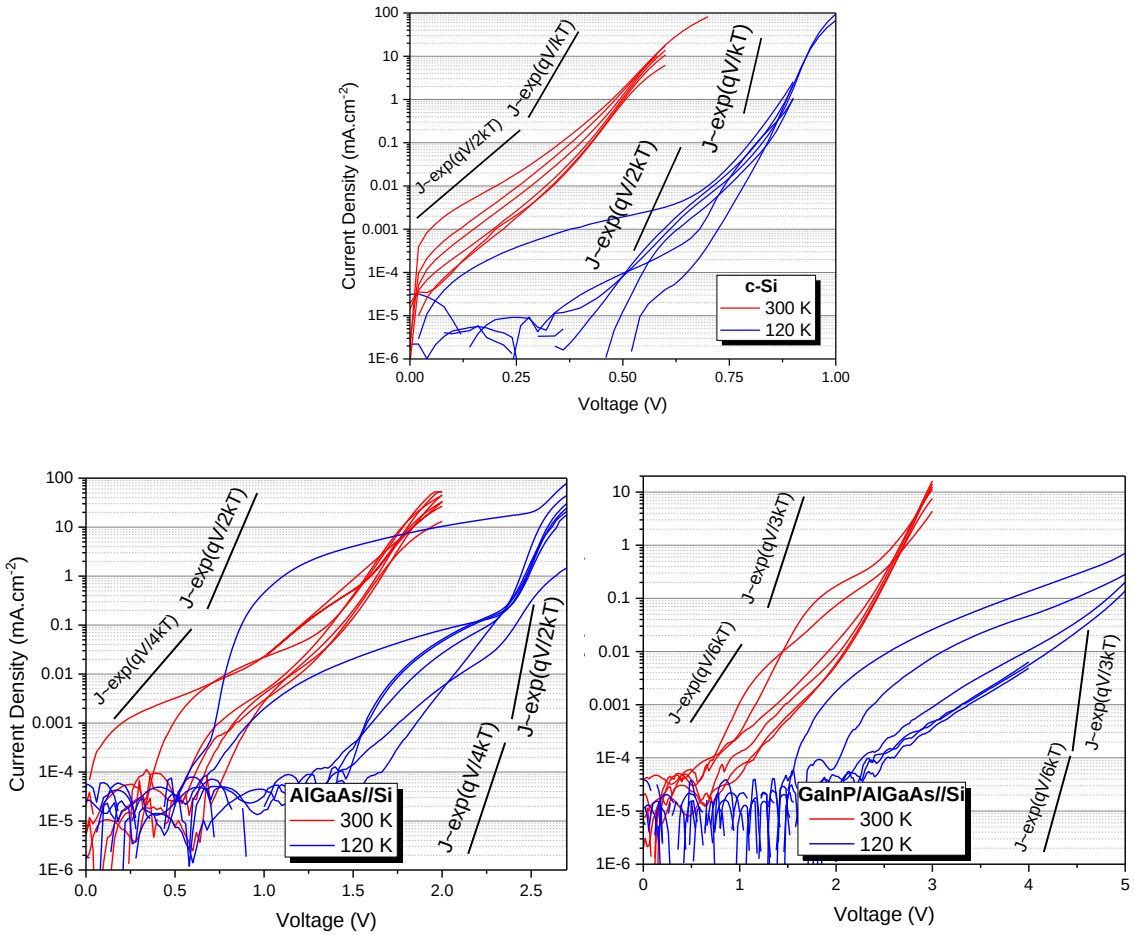

Fig. IV-12 *Dark I-V characterization at 300 K (red) and 120 K (blue) in the case of (top) 1J c-Si (bottom-left) 2J AlGaAs//Si (bottom-right) 3J GaInP/AlGaAs//Si.*

IV.3.3. Quantum Efficiency measurements

As explained above, *EQE* in-situ measurements could not be performed due to issues with the measuring equipment especially for tandem solar cells were light bias was needed to measure each sub-cell separately. However, an alternative solution was found to measure the *EQE* manually (with no access to the equipment software) on 1J c-Si using the *Quesma* solar simulator (*LED*) by following the steps below reported in ASTM E1021 - 15(2019) [32]:

- Measure the spectral response of a c-Si cell in calibrated equipment SR_{Ref}.
- Calculating the power (P_{LED}) of each *LED* lamp by dividing the measured current I_{Ref} when turning on the *LED* by the reference spectral response according to Eq. IV-10.

$$P_{LED}(\lambda) = \frac{I_{Ref}(\lambda)}{SR_{Ref}(\lambda)} \qquad \textit{IV-10}$$

Repeat the procedure for all the *LED* lamp (37) from 375 nm to 1300 nm.

- Measure the photo-generated current of the solar cells under test when photo-excited by each *LED* lamp separately.
- Calculate the spectral response of the device under test SR_{DUT} according to Eq. IV-11

$$SR_{DUT}(\lambda) = \frac{I_{DUT}(\lambda)}{P_{LED}(\lambda)} \qquad \textit{IV-11}$$

- Calculate the *EQE* of the device under test according to Eq. IV-12.

$$EQE(\lambda) = \frac{hc}{q\lambda}.SR_{DUT}(\lambda) \qquad \textit{IV-12}$$

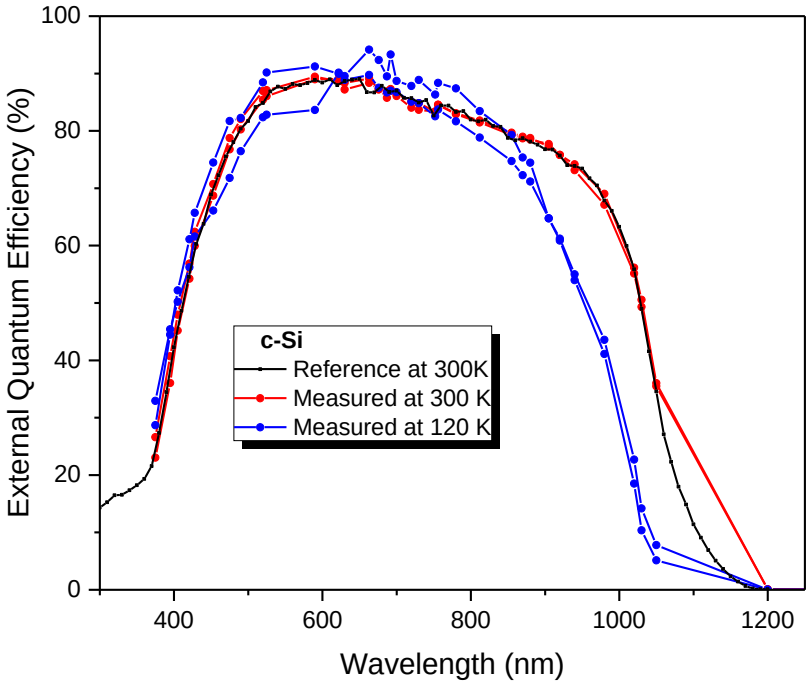

Fig. IV-13 *EQE characterizations of 1J c-Si solar cells at 300 K (red line) comparing to the reference one measured at a reliable set-up (black line) and at 120 K (blue lines).*

Fig. IV-13 present the results of the application of this procedure on two 1J c-Si solar cells at 300 K (red lines) and 120 K (blue lines). Comparing the measurements made at 300 K in a calibrated equipment (dark lines) with the measurements made manually, very good agreement is observed in the absorption band 375 - 1050 nm. However, beyond 1050 nm, the measurements do not agree due to the lack of *LED* lamp in this range to accurately reproduce the evolution of the *EQE*. Nevertheless these measurements show the effect of temperature on the variation of the bandgap energy thus on the absorption band of c-Si. By cooling down the temperature to 120 K, the measurements on both cells shows the decrease of absorption band to lower wavelength (higher energy). The slight enhancement of *EQE* magnitude at low

wavelength (λ < 430 nm) is due to a lower front surface recombination and can be due to the enhancement of the front passivation. A small deviation is calculated (less than 1% in terms of J_{SC}) for the two measurements made on two different solar cells, showing the reliability of the measurement.

In order to calculate the evolution of the bandgap as a function of temperature, we use the method proposed by H. Helmers et al. in [33] for the extraction of E_g from *EQE* measurements. Fig. IV-14 shows the *EQE* plots in semi-logarithmic scale as a function of photons energy at 300 K and 120 K. By plotting an exponential function in the form of exp(a+b.E), where a and b are fitting parameters, near the band edge and at saturation part, the bandgap is therefore extracted by the intersection of the two Fit functions. The Si bandgap values extracted from *EQE* measurements at 300 K and 120 K respectively are 1.118 eV and 1.158 eV.

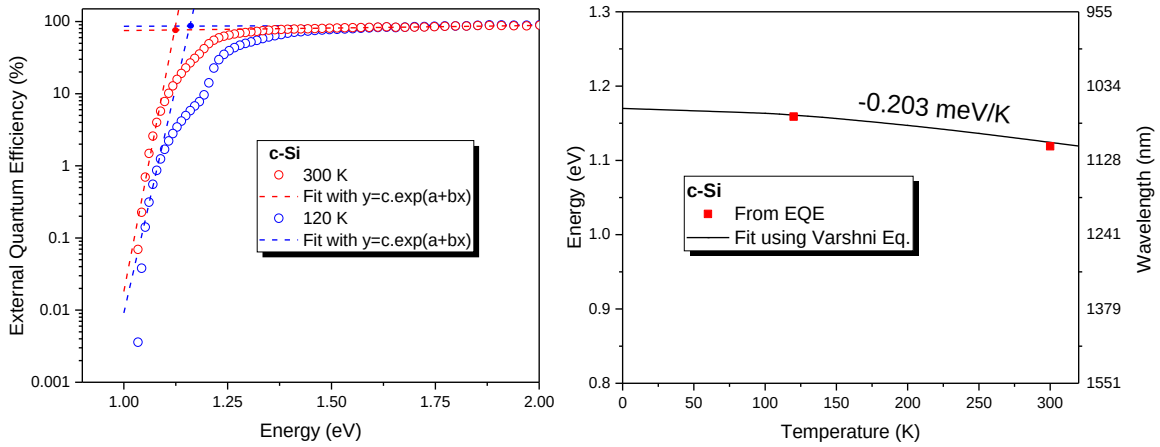

Fig. IV-14 *(Left) Extraction of the Si bandgap energy from EQE at 300 K and 120 K. the E_g is defined as the intersection of the two exponential fit near the bandgap edge and the saturation of EQE. (Right) the symbols represent the calculated E_g evolution as a function of temperature while the line represent the fit of these data according to the Varshni Equation IV-13.*

According to Varshni [34] empirical equation (see Eq. IV-13), the bandgap as a function of temperature, T, can be expressed as:

$$E_g(T) = E_g(0) + \frac{\alpha . T^2}{\beta + T} \qquad \textit{IV-13}$$

Where $E_g(T)$ is the bandgap at a given temperature, $E_g(0)$ is the bandgap at 0 K, α and β are fitting parameters. In the case of Si semiconductor a reported value of 1.17 eV, 4.73 x 10^{-4} eV.K^{-1} and 636 K respectively for $E_g(0)$, α and β are used. A comparison of the results obtained from *EQE* measurements and the one calculated by Eq. IV-13 is presented in Fig. IV-14 (right) where good agreement is observed. The bandgap temperature coefficient

dE_g/dT for Si semiconductor is found to be -0.203 meV.K^{-1} if when assume a linear variation in the temperature range considered in this study.

Since the Si architecture is identical in the three solar cells architectures (1J, 2J and 3J), it is then possible to deduce the *EQE* of the Si bottom sub-cell in the case of 2J and 3J based on measurements made at low temperature. The difference between the tandem cell and the 1J lies in the *ARC*: dual layers SiN_x/SiO_2 are deposited on top for 2J and 3J while for the 1J cells, only one SiO_2 layer is deposited; however, this *ARC* difference shall not be influence the *IQE*. The procedure to calculate the hypothetical Si *EQE* in the case of 2J and 3J is detailed below:

- First, we make the assumption that the refractive index does not change as a function of temperature as presented in [35], [36] and therefore the reflection at 120 K is equal to that at 300 K (see Eq. IV-14).

$$R(\lambda)_{300K} = R(\lambda)_{120K} \qquad \textit{IV-14}$$

- The *IQE* of the 1J at 120 K is calculated from the *EQE* measurements at 120 K according to Eq. IV-15.

$$IQE(\lambda)^{1J}{}_{120K} = \frac{EQE(\lambda)^{1J}{}_{120K}}{1 - R(\lambda)^{1J}{}_{300K}} \qquad \textit{IV-15}$$

- The *EQE* of the 2J is calculated from the *EQE* of the 1J at 120 K using the reflection of the 2J at 300 K (see Eq. IV-16). Similarly for the 3J using the reflection of the 3J at 300 K (see Eq. IV-17).

$$EQE(\lambda)^{2J}{}_{120K} = \frac{IQE(\lambda)^{1J}{}_{120K}}{1 - R(\lambda)^{2J}{}_{300K}} \qquad \textit{IV-16}$$

$$EQE(\lambda)^{3J}{}_{120K} = \frac{IQE(\lambda)^{1J}{}_{120K}}{1 - R(\lambda)^{3J}{}_{300K}} \qquad \textit{IV-17}$$

- The limitation of the absorption band are identified for both 2J and 3J through:
  - Upper wavelength limit is already taken into account by 1J measurement at 120 K
  - The lower wavelength limits depend on the bandgap energy of the upper sub-cell, where for higher energy the Si absorption is set to zero. The bandgap of the AlGaAs is defined through *EL-S* (explained thereafter) measurements for both top in the 2J and middle in the case of 3J.

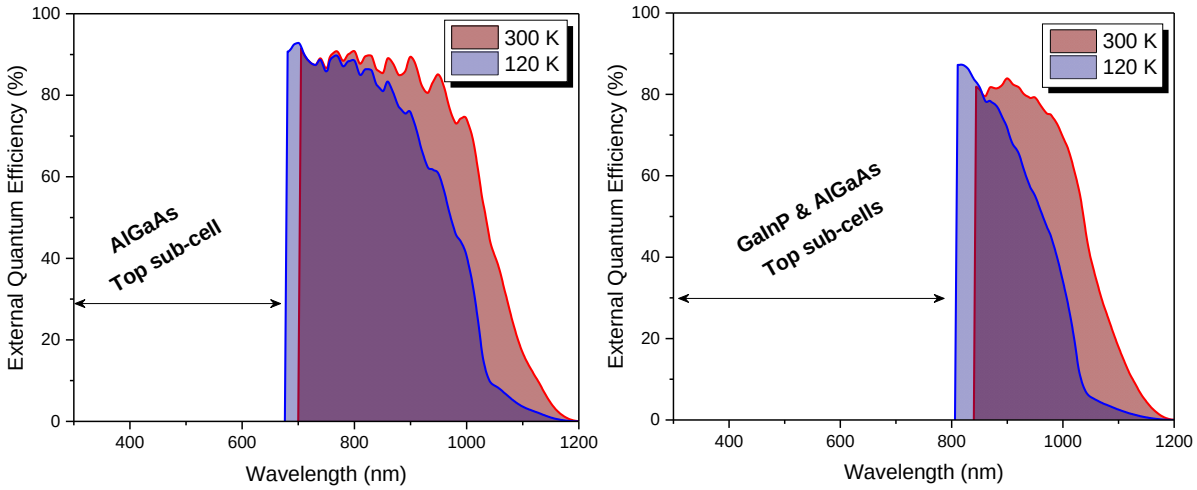

Fig. IV-15 *Calculated EQE of the Si bottom sub-cell at 300 K and 120 K from the EQE of 1J cell in the case of (left) AlGaAs//Si (right) GaInP/AlGaAs//Si.*

The results of these calculations are shown in Fig. IV-15. In both cases, the Si bottom sub-cell loses a portion of the absorbed spectrum at long wavelengths due to the increase in bandgap energy. However, it benefits from additional absorption band at lower wavelength (10 - 30 nm) a portion absorbed at short wavelengths due to the increase in top sub-cells bandgap energy. This is also seen in the decrease of J_{SC} calculated from *EQE* (see Tab. IV-3) where higher absolute loss is observed in the case of 1J (0.11 mA.cm^{-2}) compared to 2J and 3J (0.05 mA.cm^{-2}).

Tab. IV-3 *The calculated J_{SC} for the Si cell/sub-cell at 300 K and 120 K by convolution of its measured EQE in the case of 1J and calculated in the case of 2J and 3J.*

Solar cells	**J_{SC} of Si (mA.cm^{-2}) under ~3% AM0**	
	300 K	120 K
1J: c-Si	1.41	1.30
2J: AlGaAs//Si	0.79	0.74
3J: GaInP/AlGaAs//Si	0.42	0.36

IV.3.4. Spectral electroluminescence measurements

Spectral electroluminescence measurements (*EL-S)* were carried out on the two tandem solar cell architectures, i.e. 2J and 3J. The characterization results are presented in Fig. IV-16. As explained earlier, besides the low sensitivity of the used detectors, the nature of the non-radiative recombination that take the leads in the case of Si semiconductor it was not possible to measure its behavior by *EL-S*.

In the case of 2J solar cells (see Fig. IV-16 left), the injected current density is equal to four times that of the J_{SC} (60 mA.cm^{-2}). At 300 K, the observed signal as a result of radiative recombination is located at 707 nm equivalent to an energy of 1.76 eV that corresponds to the optical bandgap of the top AlGaAs sub-cell. After cooling down to 120 K (blue curves), as expected the maximal signal coordinate shift to lower wavelength and higher intensity [37]. The peak signal wavelength is located at 681 nm, which correspond to a bandgap energy of 1.82 eV. This leads to an increase of the signal peak at 120 K where it reach 14 times the ones measured at 300 K.

In the case of 3J (see Fig. IV-16 right), two signals are observed with maximums at 300 K located at 657 nm and 844 nm. The first signal corresponds to the radiative response of the GaInP top sub-cell with an energy gap of 1.89 eV. The second signal corresponds to the response of the AlGaAs sub-cell with a bandgap of 1.47 eV. By cooling down to 120 K, it is observed that in the case of both sub-cell the bandgap energy shift to high values of 1.94 eV and 1.53 eV which is in good agreement to theoretical behavior. However, two different behavior are observed in terms of maximum signal intensity. In the case of middle sub-cell AlGaAs, the signal increase by decreasing the temperature. Which is not the case of the top GaInP sub-cell, where the signal intensity decreases with temperature that goes against our expectations. This effect has already been observed in GaInP top cells and can possibly be linked to the ordering of the GaInP material [22], [38], [39].

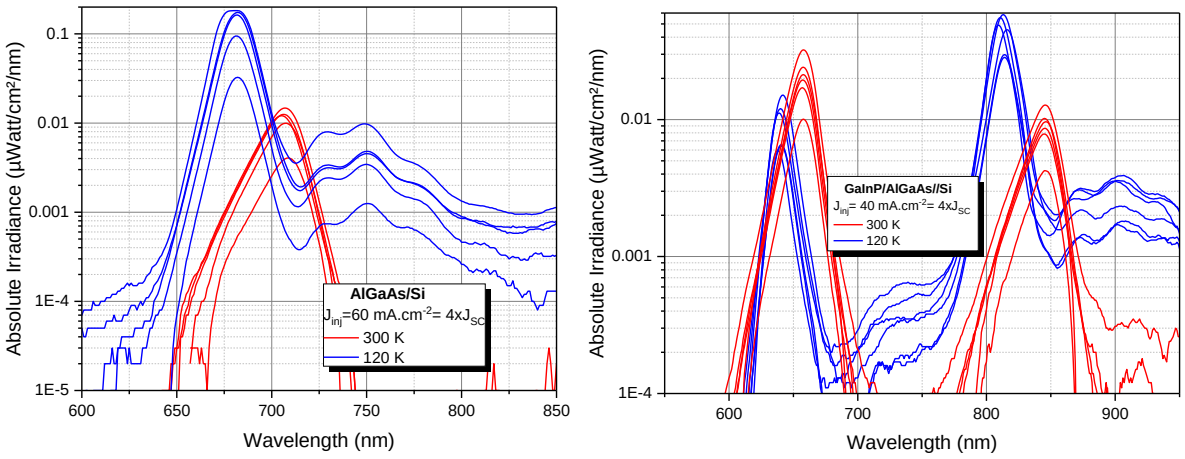

Fig. IV-16 *EL-S characterization at 300 K (red lines) and 120 K (blue lines) at an injected current four times the J_{SC} one (left) AlGaAs//Si (right) GaInP/AlGaAs//Si.*

Another interesting point is the appearance of a signal due to radiative recombination in the wavelength range 725 - 780 nm in the case of 2J and 700 - 750 nm and 850 - 950 nm in the case of 3J. In the case of 2J, this part of the absorption band is located deeper than the sub-cells.

Moreover, in the case of 3J, the first signal is located between the two top sub-cell and the second is located deeper in the cell after the middle sub-cell. However, this does not correspond to the wavelengths of the recombination of the Si, neither for its direct (~ 350 nm) nor for its indirect (~1070 nm) bandgap. In addition, this cannot be due to the created amorphous GaAs by bonding process, since there is no p-n junction for this interface (n-GaAs/n-Si). One possible explanation is that this radiative recombination is the response of the tunnel junctions. In the case of both 2J and 3J, the signal at ~750 nm and ~900 nm looks like a signal of an indirect bandgap semiconductor. Alternatively, the signal is distorted due to the interference oscillation due to overlapping reflection in the device [37].

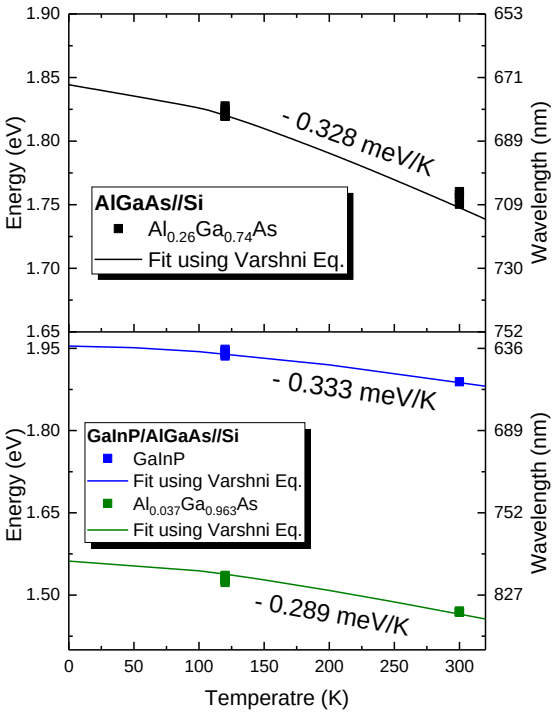

Fig. IV-17 *Representation of the III-V top cells bandgap energy as a function of temperature in the case of (top) AlGaAs in 2J (bottom) GaInP and AlGaAs in the 3J. Measured data by EL-S are presented by symbols while lines represent the fit to the Varshni equation IV-13.*

As for Si, a comparison between the Varshni equation and the values of E_g obtained from the spectral electroluminescence measurements is shown in Fig. IV-17. In the case of $Al_xGa_{1-x}As$ semiconductor, the used parameters α and β are 5.41 x 10^{-4} $eV.K^{-1}$ and 204 K [40]. However, the $E_g(0)$ depends on the sub-cell composition of Al (x) and is calculated according to Eq. IV-18 for the wave vector Γ with x = 0.26 for top sub-cell in 2J and x = 0.037 for middle sub-cell in 3J architecture.

$$E_g(0,x) = 1.519 + 1.155\,x + 0.37\,x^2(eV) \qquad \textit{IV-18}$$

In the case of GaInP top sub-cell in the 3J architecture, the parameters $E_g(0)$, α and β were used as fit parameters of the Eq. IV-13 to the measured E_g by *EL-S* and found values of 1.95 eV, 5.289 x 10^{-4} eV.K^{-1} and 420 K. In both tandem solar cells cases, the bandgap energy calculated from *EL-S* measurements as a function of temperature fit very well to the values reported in literature and to Varshni equation.

IV.4 Effect of Irradiation

Once the solar cells have been characterized at low temperature, the sample holder is moved by positioning it facing the electron beam to initiate the irradiation. Similarly to the room temperature irradiation, three fluences were considered, i.e. 10^{14}, 3.10^{14} and 10^{15} e.cm^{-2}. The choice of these fluences is based on the fact that the 10^{15} e.cm^{-2} fluence close to that received by the solar cells in the case of the *JUICE* mission (1.5 - 3.10^{15} e.cm^{-2}). On the other hand, this choice was also guided by the interest of comparing the results of irradiation carried out at 120 K with those performed at 300 K (same electrons fluences).

IV.4.1. Current-Voltage characterizations

In-situ measurements were carried out after irradiation at low temperature and under a ~3% AM0 spectrum. The results of the *I-V* characterization in *EOL* (colored lines) compared to *BOL* one (dark lines) are presented in Fig. IV-18 for the three architectures.

For all three architectures, the same behavior as for *NIRT* conditions is observed: a slight degradation of the open circuit voltage compared to the short circuit current. This effect is more pronounced at higher fluences. Average absolute values of electrical parameters for the three solar cells architectures irradiated at a fluence of 10^{15} e.cm^{-2} are given in Tab. IV-4 as an example. No anomalies on the *I-V* behavior is detected in post-irradiation at low temperature.

In the case of 1J, the J_{SC} drops from 1.24 mA.cm^{-2} at *BOL* to a value of 0.7 mA.cm^{-2} at an irradiation fluence of 10^{15} e.cm^{-2}. On the other hand, a slight degradation is observed for the V_{OC} where it drops from 0.893 V to 0.854 V at the highest fluence of this work.

Considering the case of 2J, low V_{OC} degradation is observed where a drop from 2.45 V to 2.230 V at a fluence of 10^{15} e.cm^{-2}. When evaluating the J_{SC} evolution, a weak degradation is observed at the lowest fluence 10^{14} e.cm^{-2} where the J_{SC} drops from 0.58 mA.cm^{-2} to 0.46 mA.cm^{-2}. By increasing the fluence the degradation is much more important: it reaches a value of 0.23 mA.cm^{-2} at a 10^{15} e.cm^{-2} fluence. This effect is probably due to the inversion of limiting sub-cells as explained in *NIRT* conditions. At low fluence (less than 10^{14} e.cm^{-2}), the

J_{SC} evolution of the 2J is governed by the evolution of the J_{SC} of the top sub-cell in AlGaAs, which has a good radiation hardness and therefore a low degradation is observed. On the other hand, by increasing the fluence above 10^{14} e.cm^{-2}, the defects induced in the Si sub-cell are much larger than those induced at the top sub-cell thus the Si sub-cell becomes the limiting one. Given the low radiation resistance of the Si to radiation, a higher degradation is observed in the 10^{14} - 10^{15} e.cm^{-2} fluence range.

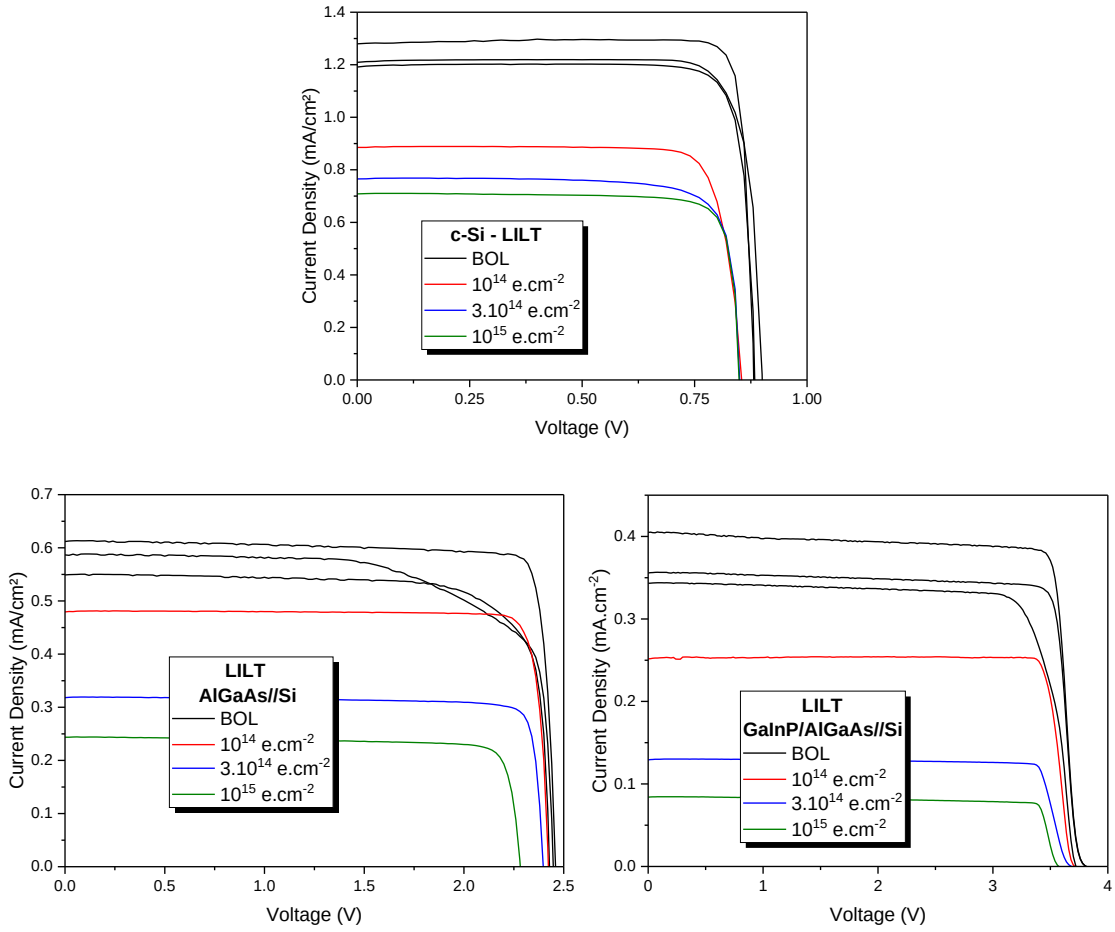

Fig. IV-18 *Current voltage characterization at LILT conditions before (black lines) and after irradiation at 120 K (colored lines) for (top) 1J c-Si (bottom-left) 2J AlGaAs//Si (bottom-right) 3J GaInP/AlGaAs//Si.*

Tab. IV-4 *Average of absolute electrical parameters on two solar cells for the three architectures after irradiation with 10^{15} e.cm^{-2} measured at LILT conditions.*

Architectures	**J_{SC} mA.cm^{-2}**	**V_{OC} (V)**	**FF (%)**	**Efficiency (%)**
c-Si	0.7 ± 0.8%	0.854 ± 0.3%	85 ± 0.8%	10.2 ± 0.8%
AlGaAs//Si	0.23 ± 6.6%	2.230 ± 0.7%	85 ± 0.6%	8.5 ± 5.3%
GaInP/AlGaAs//Si	0.08 ± 5%	3.596 ± 0.5%	84 ± 1%	4.6 ± 5.6%

An important point to highlight in the behavior of the 2J cells is the disappearance of the observed broken knee observed at *BOL* when they have been irradiated (green curves). This can be due to the high defect density introduced after irradiation especially at a fluence of 10^{15} e.cm^{-2}, thus the effect of *MSL* may become weaker than the one induced by irradiation defects.

In the case of 3J, the J_{SC} drops from 0.36 mA.cm^{-2} in *BOL* to a value of 0.25 mA.cm^{-2} at a fluence of 10^{14} e.cm^{-2}. By increasing the fluence to 10^{15} e.cm^{-2}, the degradation is greater where average J_{SC} values reach 0.08 mA.cm^{-2}. In the case of this architecture, it is the Si sub-cell, which limits the total current of the device before irradiation. Since the radiation hardness of Si is lower than that of AlGaAs and GaInP sub-cells, the degradation is more pronounced for the bottom sub-cell. Therefore, the behavior of the whole device is governed by that of the Si sub-cell in all the fluence range by contrary to the 2J devices. As for 1J and 2J, low degradation is observed for the V_{OC} where values drops from 3.79 V to 3.596 V at a fluence of 10^{15} e.cm^{-2}. The same behavior is observed at *EOL* as at *BOL* near V_{OC} conditions where the solar cells present an S-like shape due to the majority carrier barrier for all the fluence range. In terms of statistical dispersion on the two cells irradiated at the same fluence, low values of less than 1% are calculated for all 1J electrical parameters (J_{SC}, V_{OC}, FF and efficiency) for the three fluences studied. In the case of tandem cells (2J and 3J), values of less than 1% are calculated for both the V_{OC} and the FF. In contrast, higher dispersions are observed for the J_{SC} and thus efficiency in the range of 5 - 6.6% for both architectures. These values are relatively large, however even at *BOL*, large deviations have been calculated which were explained by the difference in solar cells quality (& manufacturing process).

To compare the evolution of the electrical parameters of the three architectures, the remaining factor RF(E_p) were calculated as a function of the irradiation fluence Ø. The results are presented in Fig. IV-19 where the symbols represent the experimental measurements and the solid curves represent the fit using the semi-empirical equation (Eq. IV-19).

$$RF(E_p) = 1 - A_x \, Ln\left(1 + \frac{Ø}{Ø_x}\right) \qquad \textit{IV-19}$$

The parameters A_x and $Ø_x$ used for the fit of J_{SC} and efficiency for the three architectures are summarized in Tab. IV-5. The obtained fit is in good agreement to the measured data with an *RMSE* of less than 0.1 for both J_{SC} and efficiency in all three architectures.

Tab. IV-5 *Fitting parameters (A_x and $Ø_x$) for the remaining factors of 1J, 2J and 3J according to Eq. IV-19 with the respective RMSE for each fitting curve to the measured data.*

Architectures / Parameters		RF(J_{SC})	RF(Eff.)
c-Si	A_x	0.08	0.08
	$Ø_x$(e.cm^{-2})	3.27 x 10^{12}	2.8 x 10^{12}
	RMSE	0.03	0.03
AlGaAs//Si	A_x	0.15	0.17
	$Ø_x$(e.cm^{-2})	1.82 x 10^{13}	3.18 x 10^{13}
	RMSE	0.06	0.1
GaInP/AlGaAs//Si	A_x	0.23	0.27
	$Ø_x$(e.cm^{-2})	2.96 x 10^{14}	4.9 x 10^{13}
	RMSE	0.08	0.09

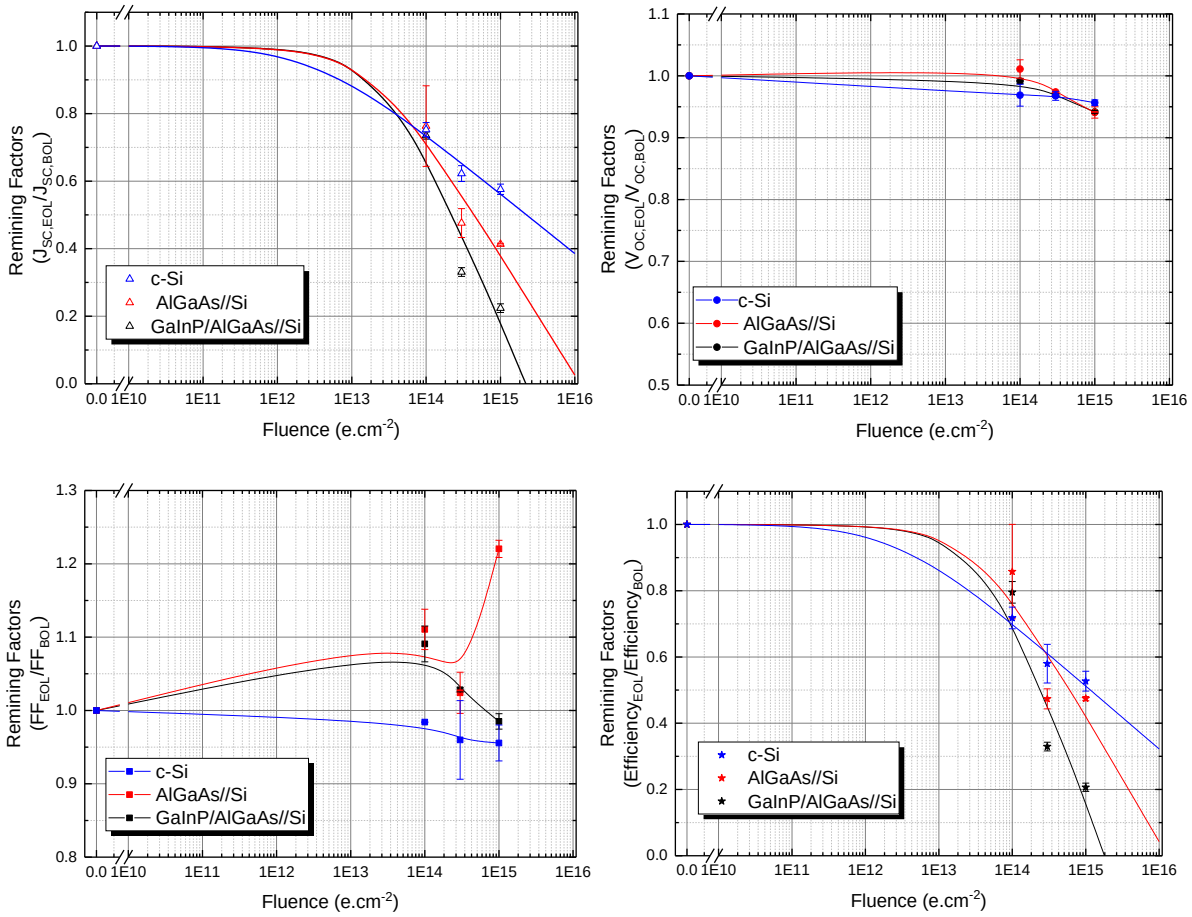

Fig. IV-19 *Remaining factors calculations at LILT conditions for the three solar cells architectures (1J, 2J and 3J) with average value of 2 cells per fluence. Top-left: short-circuit current density. Top-right: open circuit voltage. Bottom-left: fill factor. Bottom-right: efficiency. The measured electrical parameters are presented by symbols while the linear curve represents the fit using Eq. IV-19. In the case of the FF and V_{OC}, the lines are only plotted as guide to the eyes. Note: the Y-scale differs in the FF and V_{OC} graphs in order to highlight their variations.*

Short-circuit current density - J_{SC}: At a fluence of about 10^{14} e.cm^{-2}, the J_{SC} relative degradation is equal for the three solar cells architectures with a calculated degradation value of 25% (see Fig. IV-19 top-left).

According to the fit, below 10^{14} e.cm^{-2} the degradation is almost identical for the two tandem cells (2J and 3J). This is at odds with our expectations, since in this fluence range the Si sub-cell limits the behavior of the 3J whereas in the 2J it is the AlGaAs that limits the 2J. Therefore, a higher degradation is expected in the case of the 3J compared to the 2J (radiation hardness difference). It is also observed that the degradation of the 1J is lower compared to tandem cells behavior under irradiation. Comparing to 2J, it is understandable that this degradation is lower because the AlGaAs top sub-cell (higher radiation hardness than Si) is the limiting one in this fluence range. However, in comparison with 3J where the Si limits all the device, its absorption band is only limited to the higher wavelengths where the effect of irradiation is more important (see section III.2.4), this trend is not expected. This leads us to believe that another phenomenon occurs at low temperatures or that the measurement at 10^{14} e.cm^{-2} is overestimated in the case of 3J (not enough irradiation point at a fluence lower than 10^{14} e.cm^{-2}).

Beyond a fluence of 10^{14} e.cm^{-2}, the relative degradation is less important for 1J compared to 2J and 3J. At this fluence range, the relative degradation is more important by increasing the number of junction on the top of Si bottom sub-cell. This is explained by the fact that in tandem architectures the Si absorption band is restricted for higher wavelength at which the effect of reducing minority carrier diffusion length is the most important. A degradation values of 42%, 59% and 78% are calculated for the J_{SC} of 1J, 2J and 3J respectively at a fluence of 10^{15} e.cm^{-2}.

Open circuit voltage - V_{OC}: The V_{OC} degradation is much lower compared to that of the J_{SC}. Values of less than 6% are calculated for the three architectures at the highest fluence of this study 10^{15} e.cm^{-2}. At a fluence lower than 3.10^{14} e.cm^{-2}, higher degradation is observed for 1J compared to tandem cells. This is explained by the contribution of the top sub-cells to the total multijunction V_{OC} with a better radiation resistance as opposed to the 1J where only the V_{OC} of Si which is accounted.

On the other hand, at a fluence of 10^{15} e.cm^{-2}, the degradation of 1J is slightly lower than that of the tandem cells. In reality, this difference can be due to the temperature effect and not to the irradiation fluence. As shown in section IV.3.2, the V_{OC} is the most sensitive parameter to the temperature. One possible explanation can be the slight deviation on measurements

temperature at *BOL* and *EOL* that induces differences on RF(V_{OC}). However, they might be others effects contributing to this low degradation. Additional measurements are needed for a better understanding.

The fit using Eq. IV-19 was not applied on the case of V_{OC}, since degradation is very low and measurements are not sufficient for the tendency.

Fill factor - FF: In all three cases, the degradation of the FF is non-existent (recovery) or very low depending on the irradiation fluence (see Fig. IV-19 bottom-left). In the case of 1J, the degradation is present from the lowest fluence studied. The degradation of the FF increases with fluence and reaches a value of 5% at a fluence of 10^{15} e.cm^{-2}. In the case of tandem cells, an opposite behavior is observed. At 10^{14} e.cm^{-2}, the FF of 2J and 3J increases from its *BOL* value by ~10%. By increasing the fluence at 3.10^{14} e.cm^{-2}, degradation of the FF is observed relatively to that observed at 10^{14} e.cm^{-2} but remains slightly higher than the calculated *BOL* value by 2.5%. In the case of 3J, the FF continues to degrade by increasing the fluence where it reaches a degradation of 2% compared to the *BOL* values. However, in the case of 2J, by increasing the fluence to 10^{15} e.cm^{-2} it is observed that the FF remaining factor increases and reaches a value of 1.2, i.e. the *EOL* value is 20% higher than the *BOL* value.

The evolution of the FF in the case of tandem cells is more complex than in single junction cells because of its dependence on the current-photo-generated by each sub-cell and by the defects created by irradiation. At low fluence, the increase of current mismatch conditions lead to an increase of FF for the 3J. However, in the case of 2J the increase of FF at 10^{14} e.cm^{-2} is due to the disappearance of the flat spot effect (less pronounced than others cells) observed at BOL. By increasing the fluence higher than 10^{14} e.cm^{-2} the created defects take over and limits the increase of FF. The observed high increase of 2J at 10^{15} e.cm^{-2} is due to the disappearance of the broken knee observed at *BOL* (decrease FF) after irradiation at 10^{15} e.cm^{-2} thus increase the FF.

Efficiency - Eff.: Since the efficiency is the combination of all the electrical parameters mentioned above, its degradation is the combination of that of J_{SC}, V_{OC} and FF (see Fig. IV-19 bottom-right). As shown above, the degradation of both V_{OC} and FF is very low (less than 6%) in all three architectures, their effects on efficiency are minimal compared to that of J_{SC}. The efficiency degradation with values of 48%, 52% and 80% is calculated for 1J, 2J and 3J at a fluence of 10^{15} e.cm^{-2}. This degradation is mainly due to the degradation of the J_{SC} in the whole fluence range considered in this study. As explained above, this degradation is due to the J_{SC}

degradation of the Si due to the strong decrease in the lifetime of the minority carriers and the absorption band limited by the top cells.

The Equation IV-19 is in very good agreement with experimental efficiency measurements where the calculated RMSE is less than 0.1 in all three architectures. According to the Fit, a crossing point of the degradation of 1J and 3J is observed at 10^{14} e.cm^{-2} where the relative degradation of 1J is higher at low fluence and less pronounced at higher fluence. A similar behavior is observed comparing 1J and 2J where the crossing point is located at a fluence of 3.10^{14} e.cm^{-2}.

Fig. IV-20 presents the results of dark *I-V* characterization carried out on the three solar cells architectures before (solid lines) and after irradiation at 120 K (dashed lines). At low applied voltage, the measured current is very noisy due to the sensitivity of the equipment for low current values, which is in the order of few nA. The dark *I-V* curves of the three architectures are compared to the slopes of the two components of the ideal *I-V* curve, i.e. depending on the ideality factor. The observed difference between measured curves and the ideal slope is due to the presence of defects in the devices.

In the case of 1J, it is observed that the dark current increases after irradiation by a factor ranging from 2 to 4 in the considered fluence range. However, irradiation at 3.10^{14} e.cm^{-2} induces a higher dark current increase that can reach 20 times the one at *BOL*. Even this higher current, no aberrant degradation or high shunt effect is observed on the FF characterized by light *I-V* measurements.

In the case of 2J, there is a slight decrease in current in the dark in the voltage range 0.5 - 2 V. Above 2V, a higher current is observed in *EOL* than in *BOL* where it reaches the maximum increase at an applied voltage in the range 2.25 - 2.75 V (near the V_{OC}). The increase of dark current at this applied voltage is due to the introduction of defects in the bulk of the cells that leads to a decrease of V_{OC}. In the case of 3J, a slight decrease in current is observed for a fluence lower than 3.10^{14} e.cm^{-2}. However, by increasing the fluence up to 10^{15} e.cm^{-2} the dark current increases and reach 2 times the ones at *BOL*. In the case of all three architectures, the same behavior is observed before and after irradiation. The observed increase of the dark current is due to the irradiation induced generation defect; this type of defects degrades the open circuit voltage.

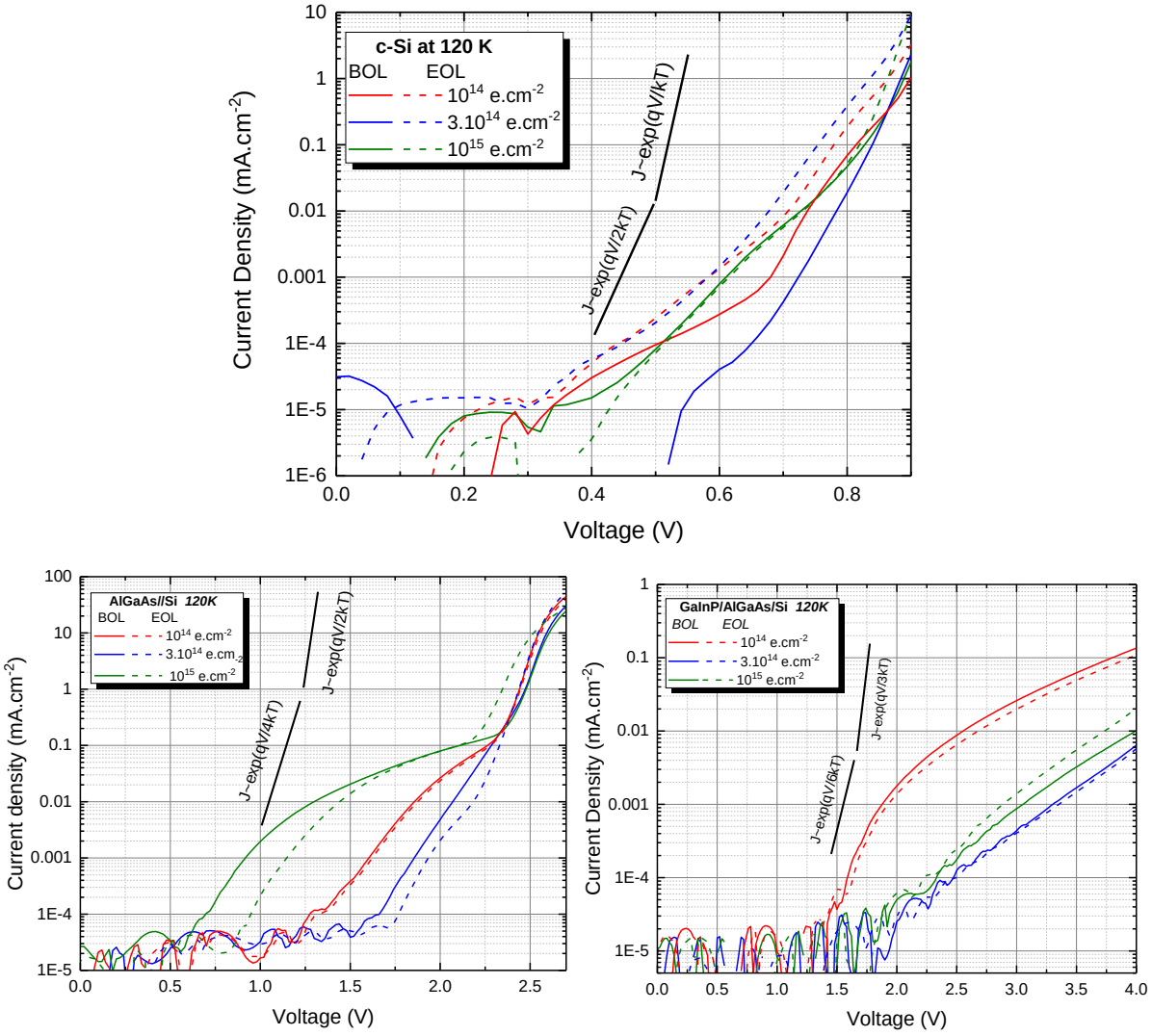

Fig. IV-20 *Dark current voltage characterization at 120 K at BOL (solid lines) and EOL (dashed lines) in the case of (top) 1J c-Si (bottom-left) 2J AlGaAs//Si (bottom-right) 3J GaInP/AlGaAs//Si.*

IV.4.2. Quantum efficiency

The measurements of the *EQE* after irradiation at a fluence of 3.10^{14} e.cm^{-2} and 10^{15} e.cm^{-2} were performed on only the 1J c-Si due to the complexity of measuring tandem cells (bias light and bias voltage) with the available equipment. The same experimental protocol used at *BOL* has been used at *EOL*, i.e. calculating the *EQE* from the photo-generated current of the cell for each *LED* lamp in the range 375 - 1200 nm. The comparison of *BOL* and *EOL* experimental results at 120 K are presented in Fig. IV-21.

We distinguish for 1J cells three different behavior zones where the *EQE* degradation is different. In the first zone 375 - 450 nm, no degradation is detectable. In this region (emitter response) the high doping induce more important defects compared to those induced by

irradiation. In the absorption band 450 - 700 nm, moderate *EQE* degradation is observed where it is in the range of 4 - 25% at 3.10^{14} e.cm^{-2} and 5 - 52% at 10^{15} e.cm^{-2} such that the degradation is more important at longer wavelengths. This region mainly represents the response of the photons absorbed in the space charge region therefore reflect its quality. In the 700 - 1200 nm region, which represents the bulk response of the cell, high degradation is observed and increases with wavelength where it reaches a maximum of 85% and 92% in the 1000-1200 nm range at an irradiation fluence of 3.10^{14} e.cm^{-2} and 5 - 52% at 10^{15} e.cm^{-2}.

The *EQE* characteristics of the Si sub-cell of the 2J and 3J were calculated in *EOL* in the same way as in *BOL*, i.e. the reflection is considered as constant in the temperature range studied 300 - 120 K, according to Eq. IV-20.

$$EQE_{Tandem}(\lambda) = EQE_{Si}(\lambda).\left(\frac{1 - R_{tandem}(\lambda)}{1 - R_{Si}(\lambda)}\right) \qquad \textit{IV-20}$$

In section III.2, we have shown that electrons of 1 MeV energy have a very high penetration depth (2 ~ 3 mm) with respect to the thickness of the three solar cell architectures considered in this study (~ 525 μm). Moreover, by simulation we have shown that the same amount of energy is deposited in the Si of the 1J, 2J and 3J therefore the same defect rate. In the same chapter, we have shown that the *IQE* of the Si of the three architectures is identical after irradiation at the same fluence. In this chapter where the cells were irradiated at low temperature, we made the same hypothesis: constant reflection with temperature, identical degradation on 1J, 2J and 3J. Results of these calculations are shown in Fig. IV-21.

In the case of 2J, the absorption of Si is limited by the absorption of the AlGaAs top sub-cell and by the Si band gap to the range 681 - 1070 nm. In this region, the absorption of photons occurs mostly in the bulk of the solar cell away from the p-n junction. The calculated degradation for the cell irradiated at 10^{15} e.cm^{-2} is in the range 40 - 94% with more pronounced degradation at longer wavelength.

In the case of 3J, the absorption of Si is more restricted due to the absorption of the two top/middle sub-cells at 805 - 1070 nm. In this region the photons are absorbed deep in the solar cell and therefore have a greater distance to travel before reaching the junction to be separated and collected. A degradation rate of 64 - 93% is calculated as a function of wavelength for the cell irradiated at a fluence of 10^{15} e.cm^{-2}.

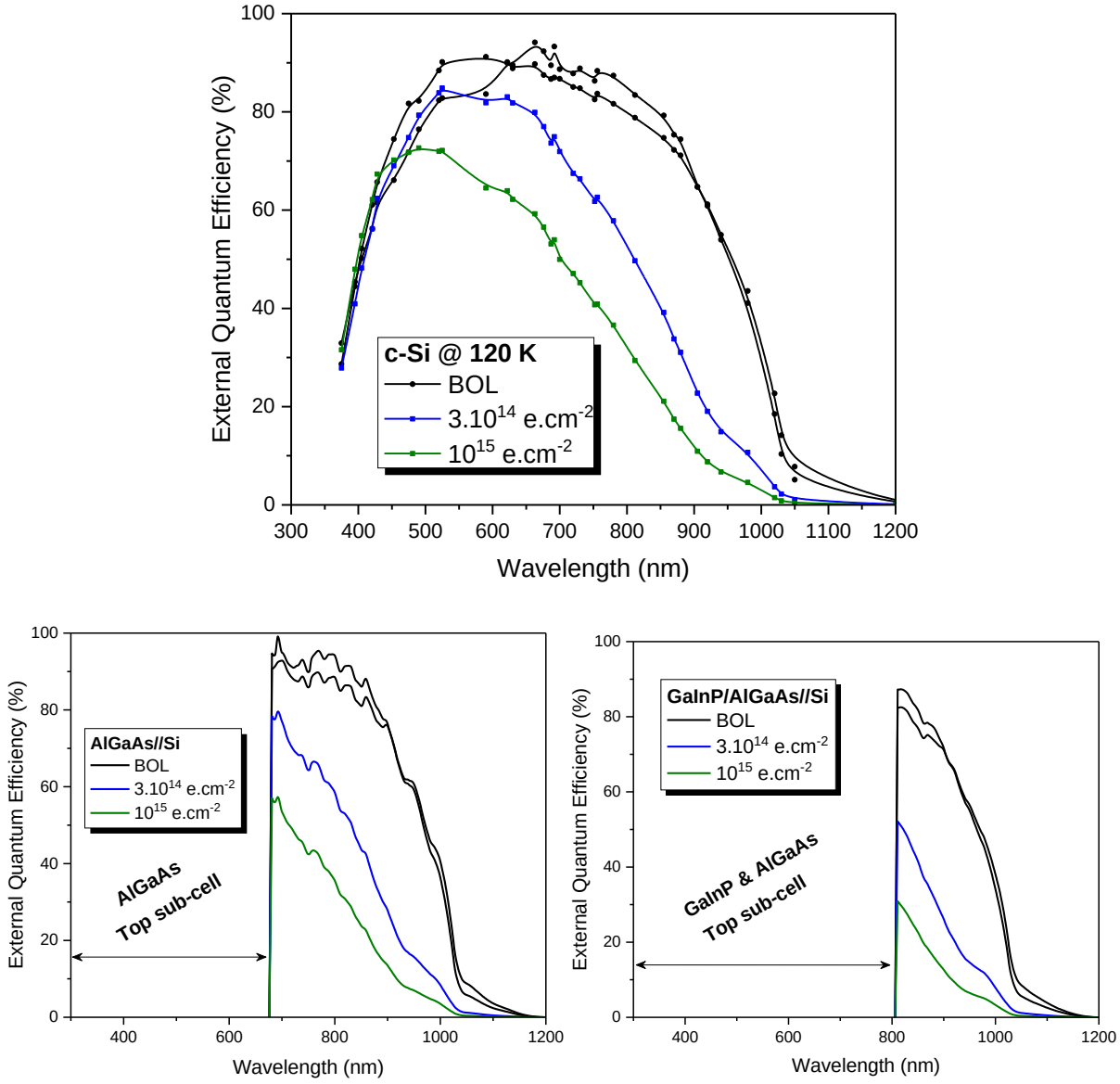

Fig. IV-21 *EQE characterization before (black lines) and after irradiation at 120 K (colored lines), (top) measured 1J c-Si (bottom-left) calculated EQE in the case of 2J (bottom-right) calculated EQE in the case of 3J.*

The degradation of the Si *EQE* in all three solar cell architectures is due to the strong decrease of the diffusion length of the photo-generated minority carriers mainly in the bulk, due to the introduction of recombination defects. Thus, charge carriers created at a large depth (higher than the diffusion length) have a low probability of reaching the junction. The difference between the three solar cell architectures lies in the extent of the absorption band of the Si (the sub-cell of low radiation resistance). In the 1J, the degradation is less pronounced due to the contribution of the emitter and the *SCR* (low wavelength) to the total J_{SC} where the degradation is relatively lower than at long wavelength. However, in the case of tandem cell this contribution is zero. The calculated J_{SC} of the Si cell/sub-cell by convolution of *EQE* to ~3% AM0 spectrum before and after irradiation at 120 K are reported in Tab. IV-6.

Tab. IV-6 *The calculated J_{SC} by convolution of EQE at BOL and EOL characterized at 120 K for the Si cells/sub-cell in the case of 1J, 2J and 3J.*

Solar cells	J_{SC} of Si (mA.cm-2) at 120 K & ~3% AM0		
	BOL	3.10^{14} e.cm^{-2}	10^{15} e.cm^{-2}
1J: c-Si	1.30	0.99	0.76
2J: AlGaAs//Si	0.74	0.41	0.25
3J: GaInP/AlGaAs//Si	0.36	0.14	0.07

IV.4.3. Electroluminescence

EL-S measurements were performed after irradiation at 120 K for both tandem architectures. Results at *EOL* are shown in Fig. IV-22 in comparison to *BOL* measurements for an injected current four times the J_{SC}, i.e. 60 mA.cm^{-2} for 2J and 40 mA.cm^{-2} for 3J.

In the case of 2J, the signal observed at 681 nm represents the response of the AlGaAs sub-cell (direct bandgap). At BOL, a peak of 0.17 µW.cm^{-2}.nm^{-1} intensity with Full Width at Half Maximum (*FWHM*) of 14 - 17 nm is measured (wavelength band where the *EL-S* intensity is higher than 50%). A strong degradation is observed for the *EL-S* signal peak after irradiation with a drop of 41%, 83% and 99% for a fluence of 10^{14} e.cm^{-2}, 3.10^{14} e.cm^{-2} and 10^{15} e.cm^{-2} respectively.

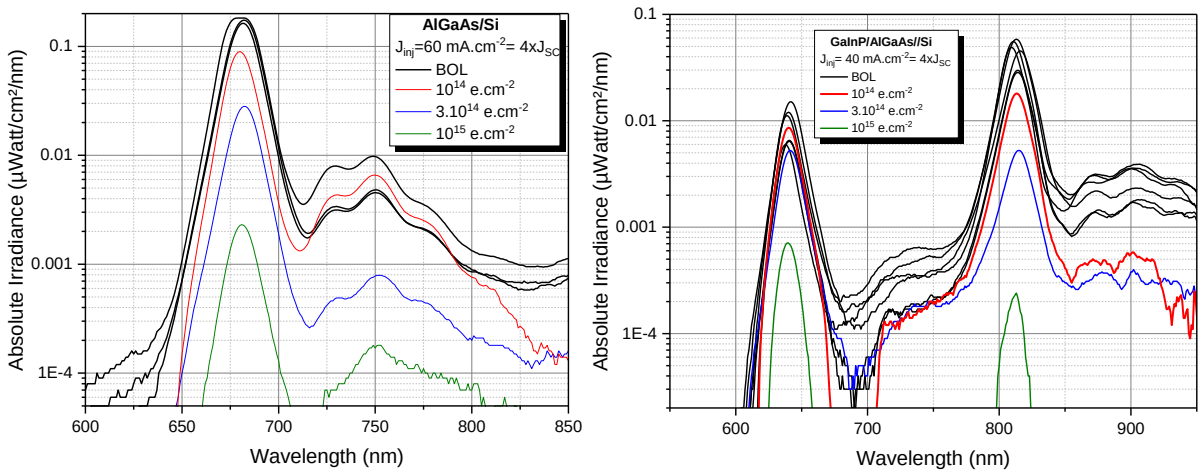

Fig. IV-22 *EL-S characterization at 120 K before (black) and after irradiation at 120 K (colored lines) at an injected current four times the J_{SC} one (left) AlGaAs//Si (right) GaInP/AlGaAs//Si.*

In the case of 3J, the two signals presented at 640 nm and 811 nm represent the response of the GaInP and AlGaAs sub-cells respectively. At *BOL*, the maximum intensity (resp. *FWHM*) is 0.013 µW.cm^{-2}.nm^{-1} (resp. 15 nm) and 0.16 µW.cm^{-2}.nm^{-1} (resp. 20 nm) of the GaInP

and AlGaAs respectively. After irradiation, a higher degradation is observed for AlGaAs compared to GaInP with a rate of 28% and 69% respectively at a fluence of 10^{15} e.cm^{-2}. In the case of AlGaAs in 2J and the GaInP and AlGaAs in 3J, the *FWHM* remains unchanged after irradiation in the fluence range of this study. The higher observed degradation of AlGaAs compared to the GaInP sub-cell is due to the higher radiation hardness of the GaInP as reported in [41]–[43].

The defects created by irradiation behave as non-radiative recombination centers (*SRH*), resulting in a degradation of the charge carriers lifetime. These defects capture electrons and combine with them in a non-radiative way, which leads to a degradation of the *EL-S* intensity [44], [45].

In the case of both architectures, the signals identified probably as a tunnel junction response (at 750 nm for the 2J and at 725 and 900 nm for the 3J) degrade in the same way as the tandem sub-cells. The degradation of the signal peak increases with the irradiation fluence.

The remaining factors of *EL-S* as a function of fluence are reported in Fig. IV-23 where the lines represent the fit of experimental data (symbols) to the semi-empirical equation (Eq. IV-19). In the case of 2J, the AlGaAs *EL-S* degradation increases with the fluence. It is clear that the degradation is only visible from a fluence of 10^{11} e.cm^{-2}. In the case of 3J, the effect of irradiation thus the induced defects is only visible from a fluence of 10^{10} e.cm^{-2} and 10^{12} e.cm^{-2} for AlGaAs and GaInP sub-cell respectively with higher degradation of AlGaAs than GaInP as explained above.

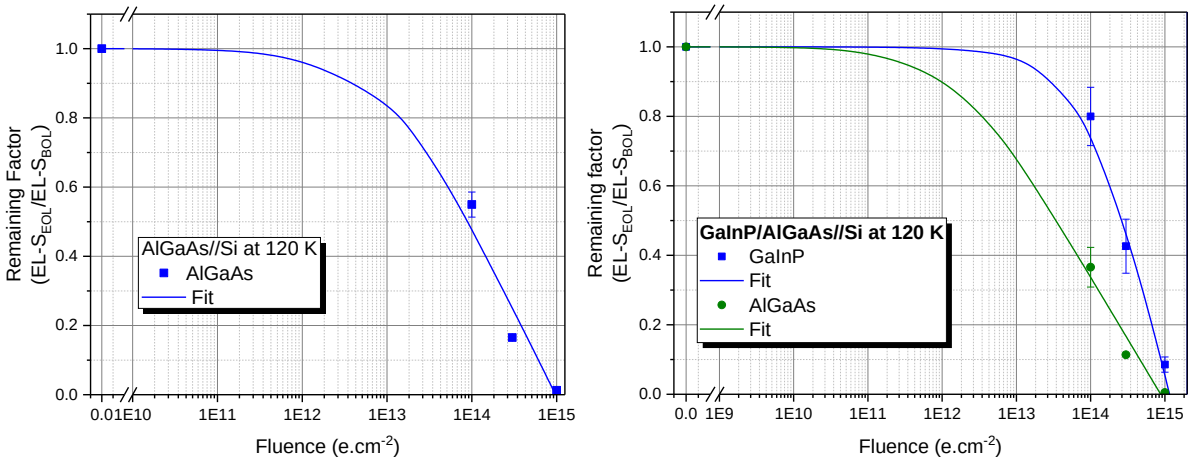

Fig. IV-23 *Remaining factor evolution of EL-S peak signal according to the fluence for (left) 2J AlGaAs//Si (right) 3J GaInP/AlGaAs//Si.*

When comparing the two AlGaAs sub-cells in the 2J and 3J, it is observed that a higher degradation of *EL-S* is observed for the 3J. In the case of 2J, degradation is only visible at a fluence of 10^{11} e.cm^{-2}; however, in the 3J it is visible from a fluence of 10^{10} e.cm^{-2}, one order of magnitude lower. This effect may be due to two characteristic parameters: thickness and stoichiometry. The low composition of Al in the case of 3J (x = 0.037) compare to 2J (x = 0.26) leads to higher density and thus a higher energy and defect density. In addition, the higher thickness in the case of 3J (2.6 µm) compare to 2J (2.2 µm) leading to higher deposited energy and thus higher defects density with irradiation.

IV.5 Effect of annealing at room temperature

After irradiation and characterization at low temperature, the samples are heated up to 300 K. Once the solar cells reach room temperature, the *EQE*, *I-V* at ~3% AM0 and *EL-S* characterizations are performed on the three solar cell architectures. The objective of these measurements is to compare the *BOL* - *EOL* behavior under *LIRT* conditions. In a second investigation, the annealing effect of the electrical parameters will be studied by comparing the temperature coefficients when cooling down the solar cells at *BOL* compared to their heating up after irradiation.

IV.5.1. Electroluminescence

EL-S measurements were performed after irradiation at 300 K. The results obtained for the two tandem cells are presented in Fig. IV-24 by comparing *EOL* measurements at 120 K (blue line) and those measured in *EOL* at 300 K (red line).

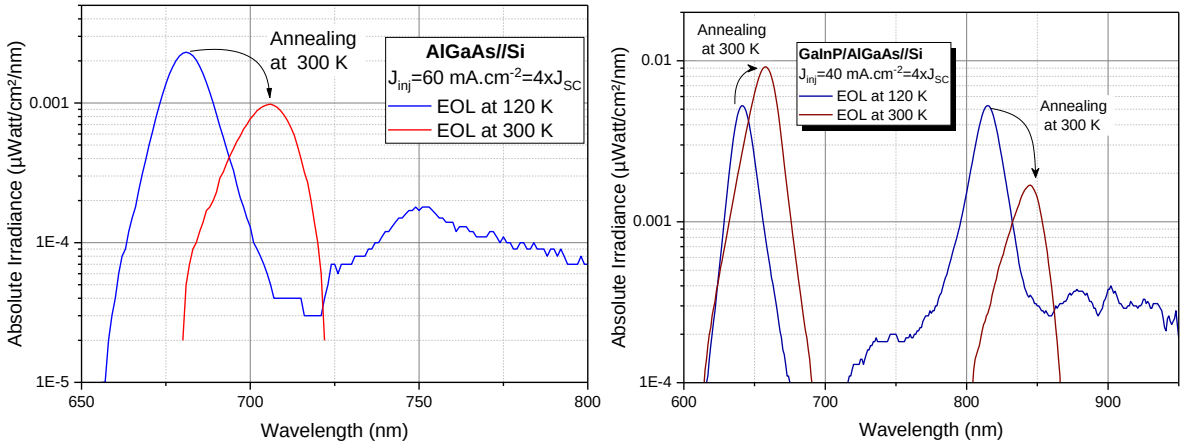

Fig. IV-24 *EL-S characterization at 120 K (blue line) and after annealing at 300 K (red line) of (left) AlGaAs//Si irradiated with 10^{15} e.cm^{-2}(right) GaInP/AlGaAs//Si irradiated with 3.10^{14} e.cm^{-2}.*

As explained before, in the case of 2J (see Fig. IV-24 left) the observed signal corresponds to the AlGaAs top sub-cell. By bringing the cell to room temperature after irradiation at

10^{15} e.cm^{-2} we observe that the signal peak red shift (681 nm to 705 nm) with a decrease of signal intensity. This difference is due to the narrowing of the bandgap energy from 1.82 eV to 1.76 eV.

In the case of 3J (see Fig. IV-24 right), the two signals represent the response of the GaInP and the AlGaAs sub-cells. The curves shown in the graph represent the cell irradiated at 3.10^{14} e.cm^{-2}, because at higher fluence the AlGaAs signal at 300 K is very weak comparing to the detector sensibility. After annealing at 300 K, a shift of signal peak energy to higher wavelength due to the narrowing of the sub-cell bandgap energy from 1.93 eV to 1.9 eV and from 1.52 eV to 1.47 eV for the GaInP and AlGaAs respectively. As at *BOL* different behavior are observed between the GaInP and the AlGaAs; *EL-S* of the AlGaAs decrease with the temperature as theoretically expected however the GaInP intensity increases that was possibly due to ordered/disordered layer [37], [38]. For both architecture, the signals identified as a possible tunnel junction response disappears with temperature.

IV.5.2. Quantum efficiency

After irradiation, *EQE* measurements were performed at 300 K. The results of these characterizations on the Si cell/sub-cell of all three architectures are presented in Fig. IV-25 by comparison to *BOL* results at both 300 K and 120 K. The results presented shows the *EQE* behavior in *EOL* at 120 K (blue dashed line) and at 300 K (red dashed line). For the sake of simplicity, only the solar cells irradiated at 10^{15} e.cm^{-2} are presented.

In the case of 1J (see Fig. IV-25 top), after irradiation at 120 K (blue dashed line), a significant drop of the minority carrier lifetime induces an important degradation of the *EQE* magnitude at long wavelengths. After annealing at room temperature (blue to red dashed line), a shift of the absorption band is observed to higher wavelength due to the narrowing of the bandgap energy from 1.16 eV to 1.12 eV. In addition, a clear increase of the *EQE* is observed on the 450-1200 nm absorption band. In this wavelength range, the calculated maximum increase of *EQE* is 40% in absolute value at 850 nm.

The *EQE* of the tandem cells was characterized ex-situ by an equipment adapted to the characterization of each sub-cell of the multijunction (see section II.4). The behavior of the top sub-cells of the 2J and 3J are not presented in this comparison on annealing effect since they were not measured at low temperature. However, a comparison will be made with the irradiations carried out at room temperature at the end of this chapter.

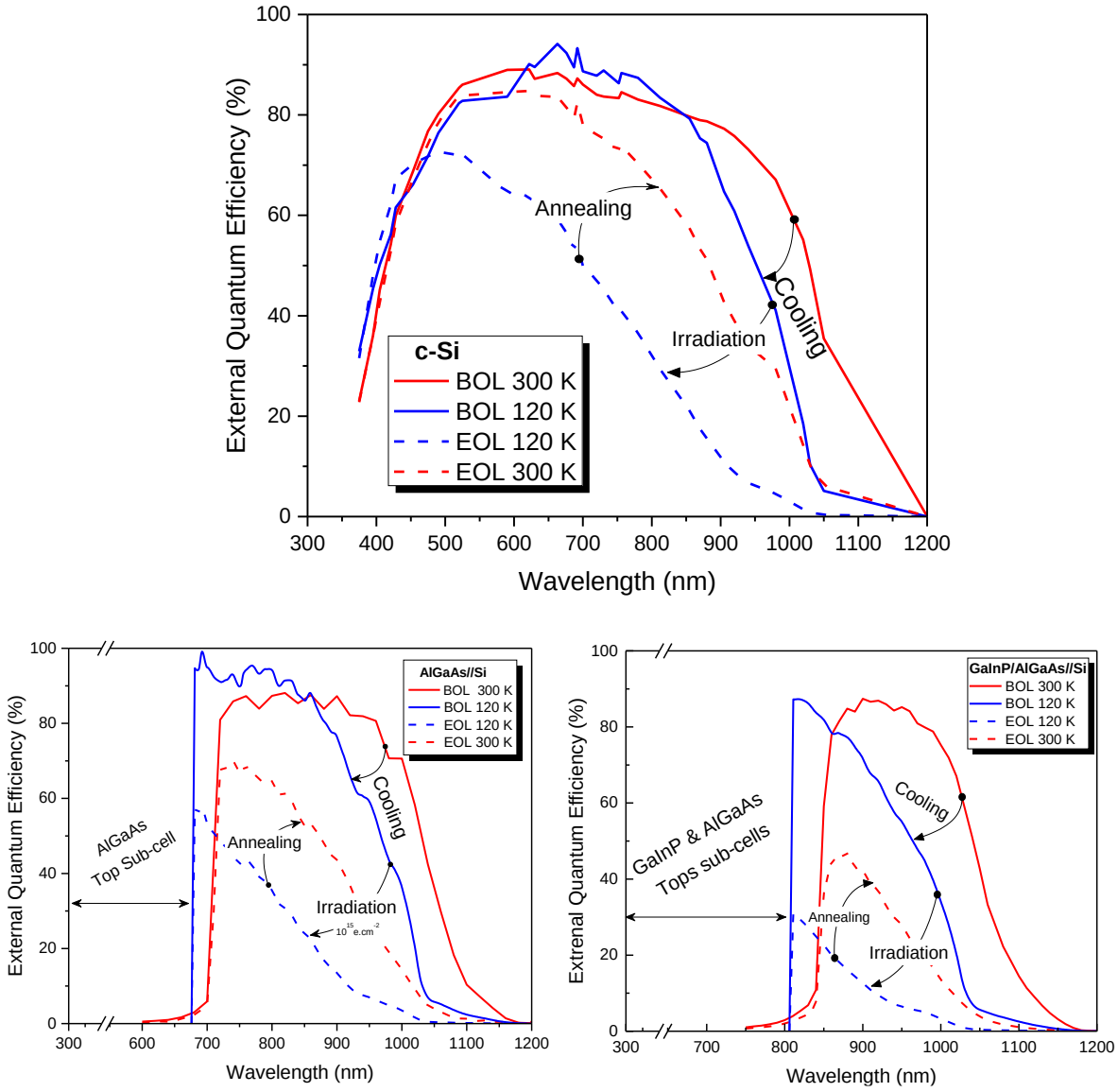

Fig. IV-25 *EQE Characterization at BOL (solid lines) and EOL (dashed lines) after irradiation with 10^{15} e.cm^{-2} at 120 K (blue) and after annealing at 300 K (red) in the case of (top) 1J c-Si (bottom-left) 2J AlGaAs//Si (bottom-right) 3J GaInP/AlGaAs//Si.*

After irradiation at 120 K, very high degradation is observed for the Si in both 2J and 3J cells (calculated from the measures Si *EQE*) due to drop in minority carrier diffusion length in addition to the limited absorption band to only high wavelength. When the cells are heated up to 300 K, the absorption band shifts to the longer wavelengths due to the decrease of the Si bandgap energy from and that of the AlGaAs sub-cell from 1.82 eV to 1.76 eV. Similarly to 1J cells, a clear improvement in the Si bottom sub-cell *EQE* magnitude is observed on its entire absorption band with a maximum absolute value of 30% around 850 nm. One may wonder why the annealing rate in the tandem cells is different from that of the 1J cell even considering that the electron degradation is assumed to be uniform in the Si in all three architectures. Indeed the degradation is uniform but the difference lies in the difference on the reflection between the 1J

and the tandem cells and is 15% and 8%, respectively, i.e. the *IQE* annealing rate is the same for all the three architectures.

The increase of the *EQE* after annealing at 300 K results in the recovery of the Si cell/sub-cell J_{SC} and thus of the J_{SC} of overall tandem cell. The calculated J_{SC} by convolution of the *EQE* characteristics presented in Fig. IV-25 to the spectrum ~3% AM0 are summarized in Tab. IV-7 for the three solar cells architectures.

Tab. IV-7 *Calculated J_{SC} by convolution of EQE characterized at EOL (10^{15} e.cm^{-2}) at 120 K and 300 K of the Si cells/sub-cell in the case of 1J, 2J and 3J.*

Solar cells	**J_{SC} of Si (mA.cm^{-2}) under ~3%AM0**	
	10^{15} e.cm^{-2} 120 K	10^{15} e.cm^{-2} Annealing 300 K
1J: c-Si	0.76	1.12
2J: AlGaAs//Si	0.25	0.41
3J: GaInP/AlGaAs//Si	0.07	0.15

The relative decrease of J_{SC} at *BOL* when cooling down from 300 K to 120 K is 8%, 3% and 15% for the Si in the 1J, 2J and 3J respectively (see section IV.3). However, after irradiation the calculated relative increase of J_{SC} from 120 K to 300 K is 48%, 61% and 105% for Si in 1J, 2J and 3J. By comparing the evolution of the J_{SC} with temperature at both *BOL* and *EOL*, the relative degradation of J_{SC} is 6 - 20 times higher at *EOL* than at *BOL*. This gap shows that the improvement of the *EQE* is not only due to the shift of the absorption band due to the decrease of the bandgap energy but also to annealing of the created defects at low temperature by heating the cell in the temperature range 120 - 300 K.

IV.5.3. Current Voltage

After the characterization campaign carried out at *EOL* under *LILT* conditions, the solar cells were heated up to room temperature in order to carry out a battery of *I-V* measurements under *LIRT* conditions.

The characterization results performed on the three solar cell architectures are presented in Fig. IV-26 comparing to *BOL* results at both 300 K and 120 K. A comparison of *I-V* characteristics at *EOL* under *LIRT* conditions are compared to *EOL* at *LILT* conditions for all the architectures. For simplicity, only the cell irradiated at a fluence of 10^{15} e.cm^{-2} are shown.

After irradiation at 120 K, we observe a strong degradation of the J_{SC} compared to the V_{OC} for all architectures. This degradation is due to the degradation of the minority carrier diffusion length as observed by the *EQE* characterizations.

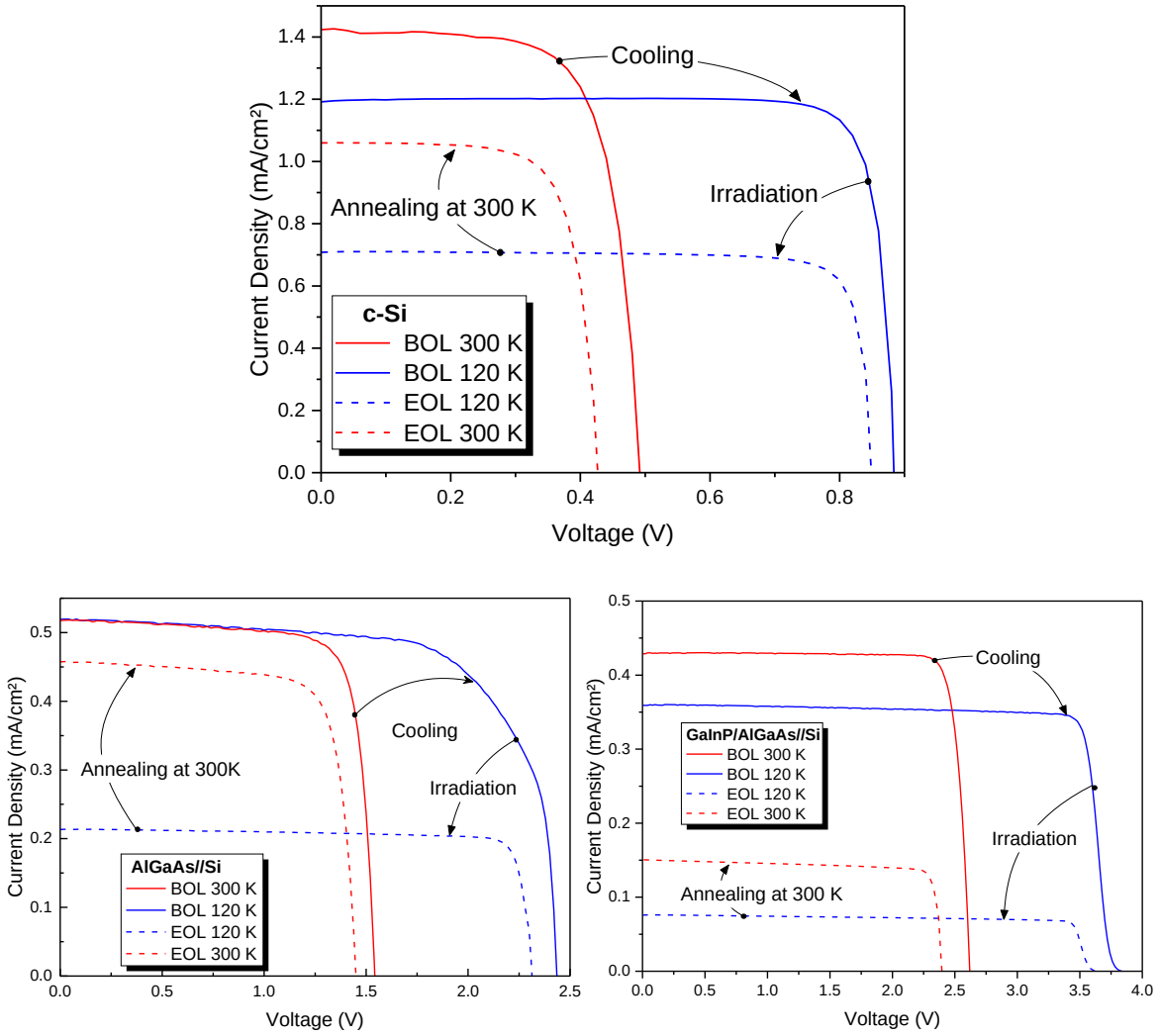

Fig. IV-26 *Comparison of current-voltage characterization at both BOL (solid lines) and EOL (dashed lines) at 120 K (blue) and after annealing at 300 K (red) in the case of irradaition with 10.15 e.cm-2 (top) 1J c-Si (bottom-left) 2J AlGaAs//Si (bottom-right) 3J GaInP/AlGaAs//Si. All I-V measurements were performed using Quesma equipement except the 3J at LIRT conditions where I-V curves were translated from NIRT to LIRT measurements using Helios 3030 with the lumped model.*

After heating up the solar cells at 300 K, characterization were performed at *LIRT* conditions (red dashed line). In the case of 1J (see Fig. IV-26 top), the V_{OC} decreases from 0.854 V to 0.429 V and the J_{SC} increases from 0.7 mA.cm^{-2} to 1.05 mA.cm^{-2}. Similarly, for 2J (see Fig. IV-26 bottom-left) a decrease in V_{OC} is observed from 2.3 V to 1.44 V and an increase of J_{SC} from 0.23 mA.cm^{-2} to 0.47 mA.cm^{-2}. The measured J_{SC} values under *LIRT* conditions are in good agreement with the calculated one by convolution of the *EQE* to the AM0 spectrum with deviation of 7 - 11% for the 10^{15} e.cm^{-2} fluence considered here. This deviation is mainly

due to low *EQE* accuracy due to a low number of *LED* covering the whole absorption band especially in the 950 - 1200 nm range. In addition, the J_{SC} calculated from *EQE* and the one measured by *I-V* are obtained for a slightly different AM0 spectrum, i.e. set-up compared to reference one (see section II.5.2).

In the case of 3J, the *I-V* measurements under *LIRT* conditions (not shown here) show a very high J_{SC} (~ 0.33 mA.cm^{-2}). In the first analysis, we thought that this effect is due to the annealing effect where it is higher than the one observed in the case of 1J and 2J. However, when comparing the J_{SC} measured under *LIRT* conditions with the one calculated from *EQE*, a large deviation (83%) was observed. In addition measurements made under *NIRT* conditions (100% AM0 spectrum and 300 K) were in good agreement with the *EQE* J_{SC}. We believe that this discrepancy is due to a calibration/measurement issue in the case of the 3J cells measured at *EOL* in the *LIRT* conditions. As a consequence, the measurements performed at *NIRT* conditions (100% AM0 and 300 K) are translated to *LIRT* conditions by using the lumped model [11] (see section IV.2) for this comparison.

The results on the 3J characterization and calculations are presented in Fig. IV-26 (bottom-right). In this case, the Voc decreases from 3.6 V to 2.389 V and the J_{SC} increases from 0.08 mA.cm^{-2} to 0.15 mA.cm^{-2}. The measured J_{SC} is in good agreement with the calculated one by *EQE* with 6% deviation. The electrical parameters for the three architectures characterized at *EOL* under *LILT* and *LIRT* conditions are summarized in Tab. IV-8.

Tab. IV-8 *Electrical parameters for the three solar cells architectures (1J, 2J and 3J) characterized at LILT conditions and LIRT (annealing) conditions after irradiation at a fluence of 10^{15} e.cm^{-2}. The 3J data at LIRT conditions were extrapolated from NIRT conditions using the lumped model.*

	***LILT* Conditions**			
	J_{SC} (mA.cm^{-2})	V_{OC} (V)	FF (%)	Eff. (%)
1J: c-Si	0.7 ± 0.8%	0.854 ± 0.3%	85 ± 0.8%	10.2 ± 0.8%
2J: AlGaAs//Si	0.23 ± 6.6%	2.230 ± 0.7%	85 ± 0.6%	8.5 ± 5.3%
3J: GaInP/AlGaAs//Si	0.08 ± 5%	3.596 ± 0.5%	84 ± 1%	4.6 ± 5.6%
	***LIRT* Conditions**			
	J_{SC} (mA.cm^{-2})	V_{OC} (V)	FF (%)	Eff. (%)
1J: c-Si	1.05 ± 0.4%	0.429 ± 0.3%	74 ± 1.3%	6.7 ± 1.1%
2J: AlGaAs//Si	0.47 ± 3%	1.442 ± 0.6%	76 ± 2%	9.8 ± 0.5%
3J: GaInP/AlGaAs//Si	0.15 ± 0.9%	2.389 ± 0.3%	86 ± 1%	5.9 ± 2%

The V_{OC} decrease is due to the narrowing of the bandgap energy at 300 K, in return leads to an increase of the sub-cells respective absorption bands and finally their J_{SC} values. Due to the series connection of the sub-cells, the variation of the J_{SC} is governed by the variation of the absorption band of only the limiting sub-cell, which is the Si in all the architectures at a fluence of 10^{15} e.cm^{-2}. In the other hand, the series connection leads to higher V_{OC} absolute values decrease due to the contribution of more sub-cell to the decrease of the overall V_{OC}, i.e. the degradation of the V_{OC} of 3J corresponds to the decay of the 3 sub-cells whereas in the case of 1J the decay is due only to Si cell.

The remaining factor of J_{SC} and efficiency are calculated as a function fluence for all the architecture and are shown in Fig. IV-27. We present also a comparison of the RF at the *LIRT* conditions (solid symbols and dashed lines) to the one calculated under the *LILT* conditions (empty symbols and solid lines).

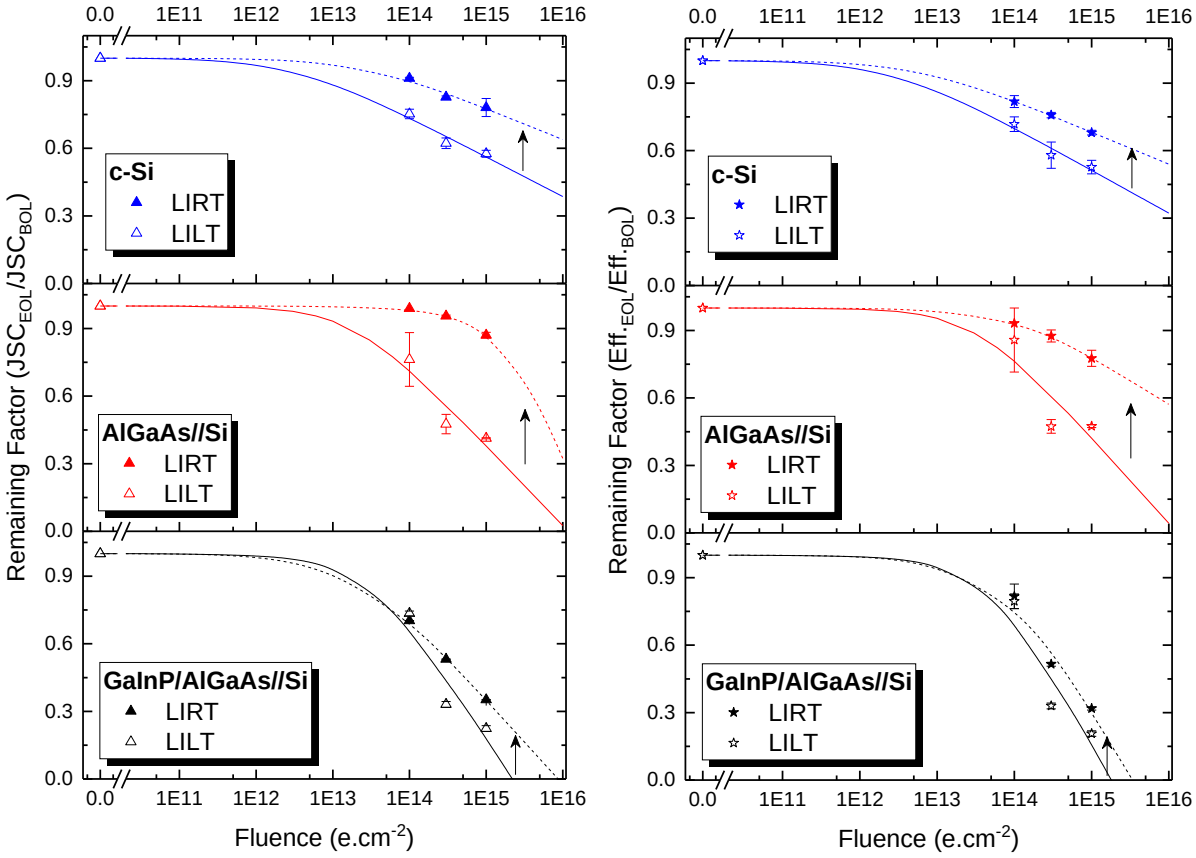

Fig. IV-27 *A comparison of (left) J_{SC} (right) Efficiency remaining factor in the case of 1J, 2J and 3J characterized at LILT (~3% AM0 & 120 K) and LIRT (~3% AM0 & 300 K) conditions.*

A small degradation of the V_{OC} less than 6% was observed under *LILT* conditions over the whole fluence range considered in this work. However, under *LIRT* conditions, the calculated

degradation is higher and is 9% for tandem cells and 14% for 1J cells at a fluence of 10^{15} e.cm^{-2}. This effect was observed by Imaizumi et. al.[20] and can be due to the effect of temperature on V_{OC}, i.e. higher V_{OC} values at low temperature. Therefore the ratio of *EOL/BOL* V_{OC} value is lower at 300 K than at 120 K. In the case of FF, the degradation remains very low and is less than 4% for the three architectures at a fluence of 10^{15} e.cm^{-2}.

In the case of the J_{SC} (see Fig. IV-27 left), a strong increase in RF thus a lower degradation is observed for all three architectures especially for 1J and 2J cells. The calculated absolute gain on J_{SC} degradation is 20%, 45% and 13% for 1J, 2J and 3J respectively at a fluence of 10^{15} e.cm^{-2}. By comparing the three architectures, it is observed that the degradation of the 3J is invariably the most important. However, the recovery of the 2J places it above the 1J with a lower degradation rate after annealing at 300 K. This high increase of RF(J_{SC}) is due to the limiting sub-cell inversion therefore the RF(J_{SC}) in the case of 2J is calculated through J_{SC}(Si)/J_{SC}(AlGaAs). In addition, from *EQE* characterization we have shown that the recovery is at its maximum around 850 nm that lies in the Si(2J) absorption wavelength band.

The same effect is observed for the efficiency (see Fig. IV-27 right) of the three architectures where the absolute gains after degradation of the 1J, 2J, and 3J are 15% 30% and 11% respectively at a fluence of 10^{15} e.cm^{-2}. These values are lower than those reported for the J_{SC} due to the contribution of the V_{OC} with it higher degradation at *LIRT* conditions as explained above. The same behavior observed on both J_{SC} and V_{OC} was observed in irradiation of a triple junction GaInP/GaAs/Ge at *LILT* conditions and *LIRT* conditions: The amplitude of J_{SC} improvement with annealing is higher than the efficiency improvement because of the V_{OC} decreases with this annealing steps [20].

IV.6 General discussion

IV.6.1. LILT conditions

We have shown, using computer simulations of electron interaction with solar cells materials [46] in section III.2, that 1 MeV electrons have a penetration depth much greater than the thickness of the solar cells used in this study (~2 mm in Si versus 0.525 mm wafer). The amount of energy deposited in the Si in all architectures is thus equal. Consequently, the density of defects created is identical and induces the same degradation on the Si cell/sub-cell in the single, dual and triple junctions studied.

The mechanism of primary defect creation is independent of temperature. The electrons hits the nuclei of the target atom, if the transferred energy is higher than the threshold displacement energy, it moves from its crystalline site. Therefore, the primary created defect are an interstitial and its associated vacancy, called Frenkel Pair. The main difference in low temperature irradiation is the freeze in of the created primary defect [47]. In addition, during irradiation at low temperature the semiconductor can be amorphized (due to lower defects mobility) depending on the irradiation fluence [48], [49]. The induce irradiation defects behave as recombination centers for minority carriers or as generation centers of majority charge carriers which increases the saturation current.

I-V characterization has been performed in order to follow the evolution of the electrical parameters of the solar cells according to the operating conditions, i.e. effect of illumination intensity and temperature as well as irradiation at 120 K. A representation of the key global electrical parameters of the three solar cells architectures (1J, 2J and 3J) are presented in Fig. IV-28 as a function of all the *BOL* and *EOL* characterization sequence for only the highest fluence considered in this thesis 10^{15} e.cm^{-2}. Thereafter we will only comment on the evolution of the 1J key parameters as a function of irradiance intensity, temperature, irradiation and annealing.

By decreasing the intensity from 100% to ~3% of the AM0 reference spectrum, a decrease of the J_{SC}, V_{OC} and FF is observed as theoretically expected. The variation of the J_{SC} of the three architectures follows the linear evolution with respect to the irradiance intensity. In the case of tandem cells, the tandem variation follows the one of the limiting sub-cell. On the other hand, the Voc is less sensitive to the illumination intensity where it varies as a logarithmic function. The V_{OC} variation as a function of illumination intensity is in very good agreement with theoretical equation.

When solar cells are cooled down, the bandgap energy of the semiconductors changes as described by Varshni equation (see Eq. IV-13). It shows that the bandgap increases as the temperature decreases. This evolution is divided in two groups: a first range where linear evolution with temperature is expected, in the second region a plateau is reached at very low temperature. The temperature that separate the linear variation and the saturated one is dependent on semiconductor properties.

In the case of the semiconductors studied in this thesis, the evolution of the bandgap is in the quasi-linear regime in the 300 - 120 K range. By comparing the results obtained by *EL-S* for direct III-V bandgap materials and by *EQE* measurements for Si, a very good agreement is obtained. The Si bandgap energy increases from 1.12 eV to 1.16 eV when cooling down from 300 K to 120 K. In the case of 2J, the $Al_{0.26}Ga_{0.76}As$ sub-cell bandgap increases from 1.76 eV to 1.82 eV. Considering 3J cells, the bandgap of GaInP and $Al_{0.037}Ga_{0.963}As$ increases from 1.89 eV to 1.94 eV and 1.47 eV to 1.53 eV respectively. As presented in section I.2, for this variation is the increase of interatomic spacing due to low thermal excitation (decrease of atomic vibration) at low temperature, which in turn reduces the size of the energy bandgap [50]. In a similar way, the modulation of interatomic distance, such as by applying compressive (tensile) stress, also causes an increase (decrease) of the bandgap.

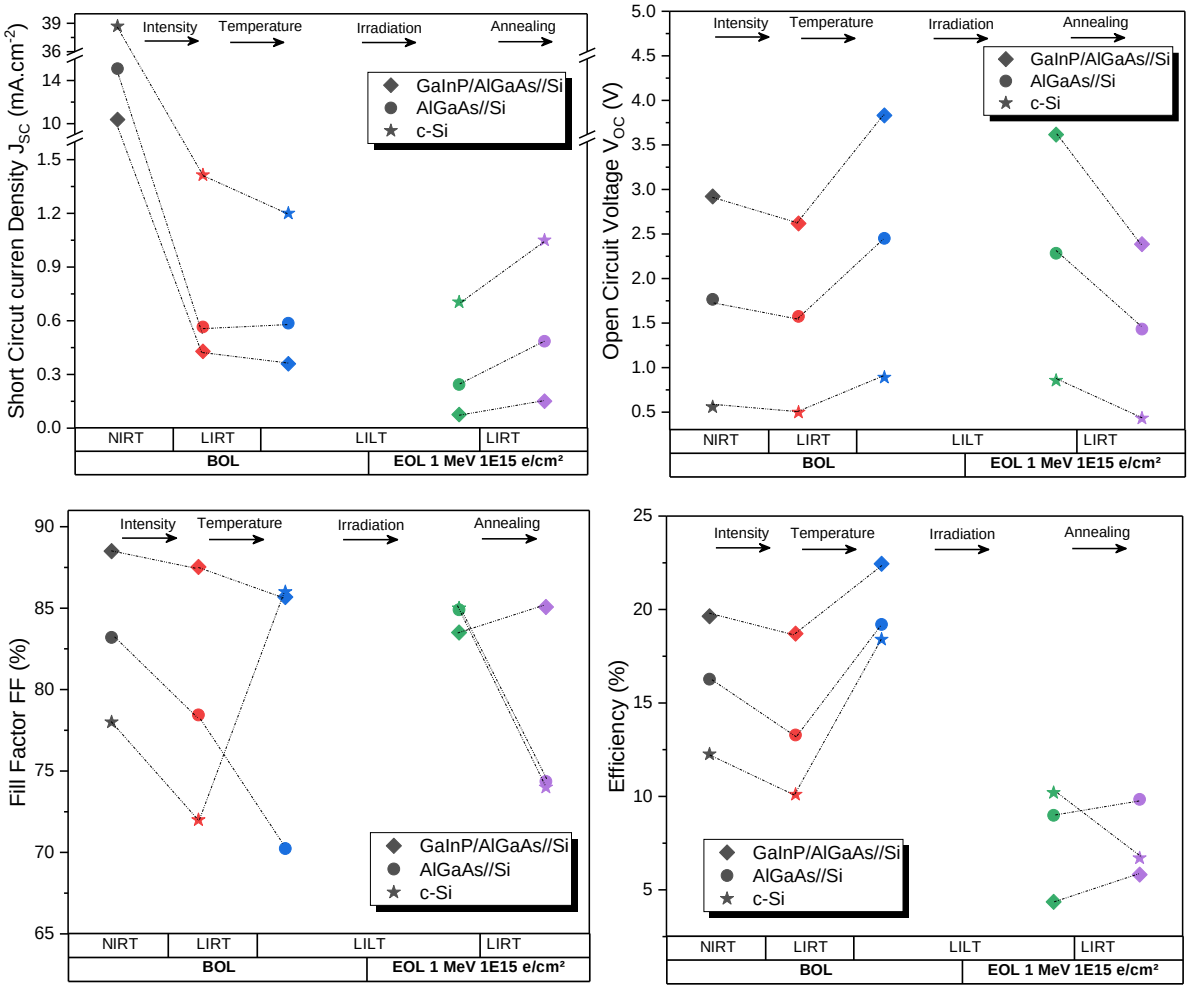

Fig. IV-28 *Evolution of absolute electrical parameters according to the whole characterization and irradiation sequence in the case of 1J c-Si irradiated at 10^{15} e.cm^{-2}.*

By increasing the atomic spacing at low temperature, the potential seen by the electrons in the material increases, allowing higher splitting of quasi-fermi levels and thus higher open circuit voltage. This explains the large increase in the open circuit voltage by a value of 389 mV, 870 mV and 1220 mV for the 1J, 2J and 3J respectively. By increasing the number of junctions in the device, the V_{OC} rise is increased due to the contribution of each sub-cell increase to the total V_{OC} value.

In counterpart, the increase in the bandgap energy induces a shift and a decrease in the absorption band of each sub-cell towards high energies (short wavelength). This decrease leads to a smaller portion of the solar spectrum being absorbed and converted and thus a weaker J_{SC} photo-generated [51]. In the case of 1J and 3J where the Si limits the device, before irradiation a decrease in J_{SC} by 0.15 $mA.cm^{-2}$ and 0.06 $mA.cm^{-2}$ is observed at 120 K compared to 300 K. However, in the case of the 2J cells where the AlGaAs limits the overall J_{SC}, an increase of J_{SC} by 0.04 $mA.cm^{-2}$ is observed at 120 K. This mismatch to the behavior of the others sub-cell and to our expectations can be explained by the fact that at low temperatures an improvement of the *EQE* can be observed which increases the J_{SC}. A similar trend was observed in [15] where a study was performed using isotype of the GaInP/GaAs/Ge solar cells as a function of temperature and found that the J_{SC} of the middle sub-cell (GaAs) increases by decreasing the temperature. This J_{SC} improvement has been explained in [25] by a decrease of the recombination rate in the window layer that increases the *EQE* at low wavelength thus increases the J_{SC}. Unfortunately, low temperature *EQE* measurements could not be performed on the tandem cells to validate this hypothesis.

The FF has non-direct physical explanation, it reflects the effect of shunt and series resistance on the *I-V* curves under illumination of solar cells. The magnitude of J_{SC} and V_{OC} values can affect also the FF. The FF has a negative temperature coefficient according to semi-empirical equation expressed in [52], [53]. Therefore, it explains the increase of FF in the case of 1J at low temperature. However, in the case of tandem solar cells, the FF is related to the variation of current mismatch; lower values are observed at Current Matching *(CM)* condition and it increase when deviating from this point.

In the case of 2J, a continuous and remarkable decrease is observed where the FF decreases from 79% to 70%. This decrease may be due to the convergence towards *CM* conditions; a more important degradation of the Si sub-cell J_{SC} in counterpart of the increase of the AlGaAs J_{SC}, in addition to the appearance of the effect of a broken knee for some samples at low

temperature. In the case of 3J, a very low degradation is observed from 87% to 86%, which may be due this time to the appearance of S-like shape at low temperature.

The efficiency is proportional to the product $J_{SC}.V_{OC}.FF$ and, therefore, the temperature coefficient of efficiency is determined by the sensitivity of J_{SC}, V_{OC}, and FF to temperature. The efficiency temperature coefficient is expressed as the sum of all parameters temperature coefficient normalized to their absolute values. In the case of the three architectures, a linear increase of efficiency is observed in the temperature range 300 - 150 K. This increase tends to flatten in the range 150 - 120 K due to the effect of J_{SC} and FF decrease.

After irradiation at 120 K, we observe a strong degradation of the J_{SC} compared to the V_{OC} and FF for all architectures. The degradation of the V_{OC} is due to an increase in dark saturation current. This increase is due to the introduction defects that acts as generation centers, such as tri-vacancy (V_3) labeled E4 and E5 with a trapping level at E_C - 0.36 eV and E_C - 0.46 eV respectively [54]. Another defect identified as a possible V_2O or carbon related centers with a trap energy level at E_C - 0.545 eV could be at the origin of dark current increases [55]. Spectral *EL* measurements also show the degradation of the V_{OC} for the top sub-cells given the direct relationship between the *EL-S* and the internal sub-cell voltage. However, it was not possible to reconstruct the individual *I-V* characteristics curves due to lack of *EQE* data for these sub-cells at low temperature. By comparing the degradation of all electrical parameters, it is obvious that the degradation of efficiency is driven by that of the J_{SC} (see Fig. IV-19). This degradation is due to the degradation of the minority carrier diffusion length as observed by the *EQE* characterization (explained hereunder).

The *EQE* characterization allows assessing the degradation of the J_{SC} of the Si cell/sub-cell, which is mainly due to the degradation of the minority carrier diffusion length. Fig. IV-29 present the results of *EQE* characterization on 1J solar cells throughout the entire process. The labeled arrows detail the *EQE* evolution as a function of temperature and irradiation; in addition only one cell irradiated at the highest fluence 10^{15} e.cm^{-2} is shown.

The effect of temperature on bandgap energy thus the absorption wavelength band is presented in Fig. IV-29 where the *EQE* (red to blue solid lines) of the cell shift to lower wavelength as explained above. After irradiation at 120 K (blue solid lines to blue dashed lines), a significant drop of *EQE* magnitude is observed in almost all the absorption band and is more important at higher wavelength. This is due to the high degradation of minority carrier diffusion length. The e-h photo-generated deeper in the cells encounter recombining defects that reduce

their probabilities to reach the junction [56], [57]. After annealing at room temperature (blue to red dashed lines), a clear increase of the *EQE* is observed on the 450 - 1200 nm absorption band. In this wavelength range, the maximum increase on the *EQE* is 40% in absolute value and it happens at 850 nm.

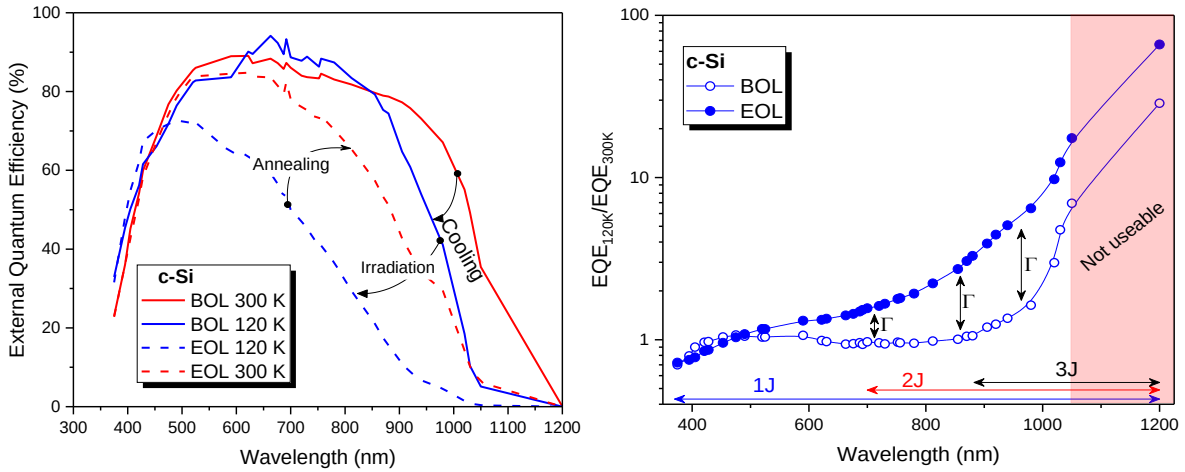

Fig. IV-29 *(Left) evolution of EQE characterization with temperature and irradiation at 10^{15} e.cm^{-2} for 1J solar cells, (right) EQE ratio 300 K/120 K at BOL and EOL as a function of wavelength.*

After annealing, the opposite behavior is observed with respect to that observed when cooling the samples; an increase in J_{SC} with a decrease in both V_{OC} and FF (see Fig. IV-28). However, this behavior may be due to the effect of the decrease in bandgap energy or linked to other effects such as annealing of created defect (primary or stable defects) when heating up the solar cells. To answer this question two comparisons are performed. The first one is the analysis of the *EQE* evolution as a function of annealing (see Fig. IV-29). The second one is the comparison of the two slopes (temperature coefficient) at *BOL* and *EOL* for the three architectures in Fig. IV-30.

In order to better analyze the evolution of the *EQE* as a function of annealing, the ratio (Γ) of the *EQE* at 120 K to that at 300 K is calculated as a function of wavelength before and after irradiation (see Fig. IV-29 right). In the region 375 - 500 nm, the same ratio is calculated for both conditions (*BOL* and *EOL*). At long wavelengths ($\lambda > 1050$ nm), the data are not usable because of the low *EQE* value in this region, i.e. a small deviation induces very high ratios. However the region where the effect of irradiation is the most important and the data are reliable (500 - 1050 nm), it is observed that at *EOL* the max ratio is four times higher than at *BOL*. This is a first hint that the recombining defects are annealed when heating up from 120 K to 300 K.

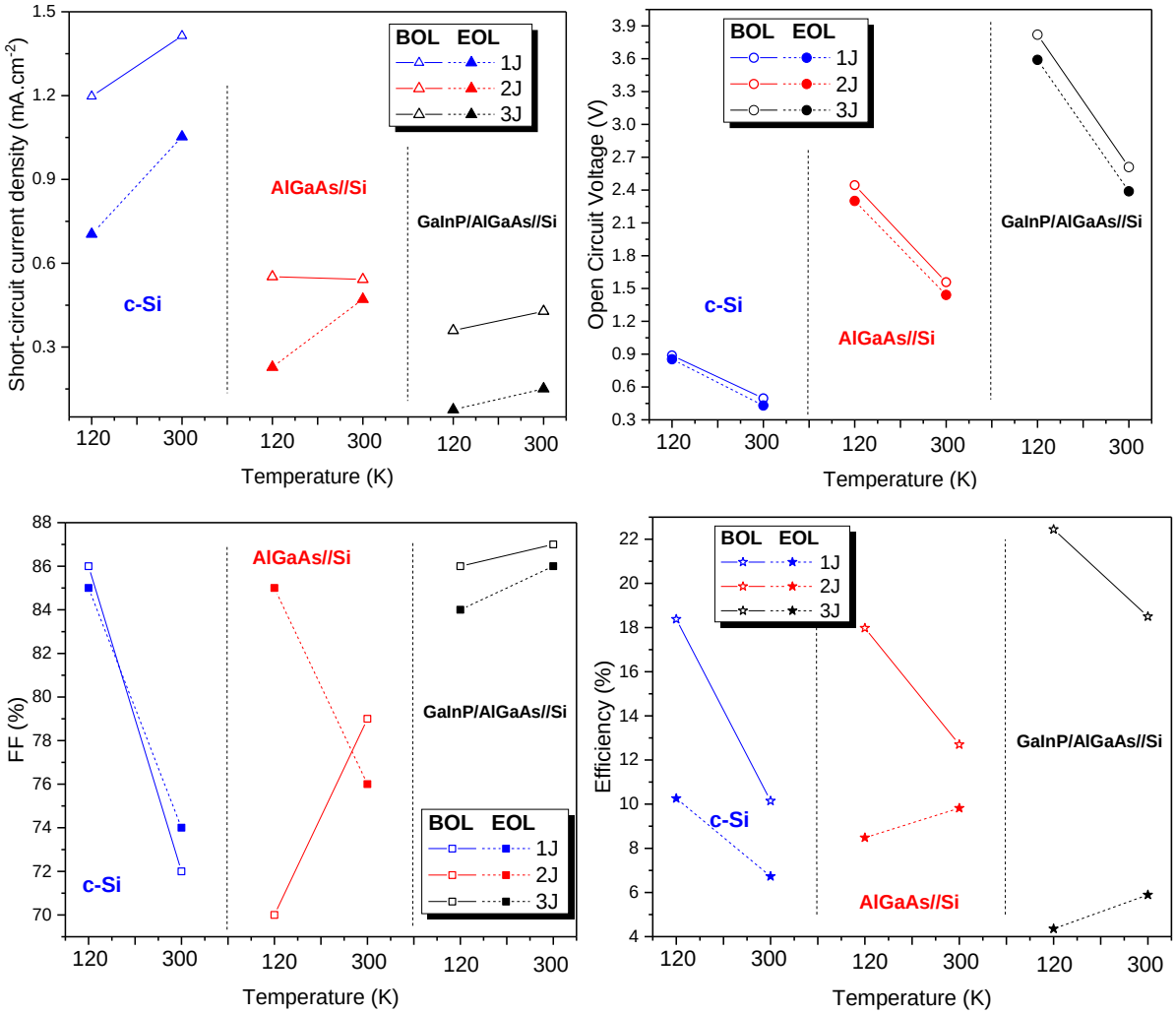

Fig. IV-30 *Electrical parameters variation as a function of temperature at BOL and EOL after irradiation with 10^{15} e.cm^{-2} for the three solar cells architectures (1J, 2J and 3J). Top-left: short-circuit current density. Top-right: open circuit voltage. Bottom-left: fill factor. Bottom-right: efficiency. The temperature coefficient is calculated and compared between BOL and EOL.*

The results presented in Fig. IV-30, shows the absolute value of the electrical parameters (J_{SC}, V_{OC}, FF and eff.) before and after irradiation under 3% AM0 at 300 K and 120 K for the three architectures. The evolution of these parameters has already been discussed above. However, in this section, we are interested in the evolution of the electrical parameters temperature coefficient in the two conditions *BOL* (solid lines) and *EOL* (dashed line), the values are summarized in Tab. IV-9.

The J_{SC} temperature coefficient calculated for 1J, 2J and 3J respectively at *BOL* is 1.2, -3.5x10^{-3} and 0.39 µA.cm^{-2}.K^{-1}. After irradiation, in the case of 1J and 3J the J_{SC} follows the same evolution with a higher dJ_{SC}/dT with values of 1.94 and 0.42 µA.cm^{-2}.K^{-1}. In the case of 2J, the evolution with temperature at *EOL* is opposite to that at *BOL* with a dJ_{SC}/dT of 1.36 µA.cm^{-2}.K^{-1}, i.e. the J_{SC} increases with temperature. This can be explained by the fact that

after irradiation it is the Si bottom sub-cell that limits the 2J, thus the J_{SC} temperature coefficient follows that of the Si (see Fig. IV-30). The change in dJ_{SC}/dT under both *BOL* and *EOL* conditions suggests that the variation in J_{SC} is not only due to the variation of the absorption band with temperature. An annealing of irradiation induced recombination defects that degrade the J_{SC} at *EOL* occurs when heating up the cell to 300 K where the dJ_{SC}/dT in *EOL* is 1.1 - 1.35 times higher than in *BOL* for 1J and 3J, and is 380 times higher in the case of 2J (changing in the limiting sub-cell).

Tab. IV-9 *Electrical parameters temperature coefficients at BOL and EOL of one solar cell after irradiation with 10^{15} e.cm^{-2} for the 1J, 2J and 3J. Values are compared to AzurSpace c-Si (S32) and GaInP/GaAs/Ge (3G28).*

Architectures		**dJ_{SC}/dT $\mu A.cm^{-2}.K^{-1}$**	**dV_{OC}/dT $mV.K^{-1}$**	**dFF/dT $\%.K^{-1}$**	**dEff./dT $\%.K^{-1}$**
1J	*BOL*	1.2	-2.2	-0.078	-0.046
	EOL	1.94	-2.4	-0.06	-0.02
2J	*BOL*	$3.5x10^{-3}$	-4.96	0.05	-0.027
	EOL	1.36	-4.8	-0.05	0.009
3J	*BOL*	0.39	-6.7	0.01	-0.021
	EOL	0.42	-6.8	0.01	0.009
S32	*BOL*	1.1	-2.02	N/A	
	EOL	2.0	-2.17		
3G28	*BOL*	0.41	-6	N/A	
25 - 80 °C	*EOL*	0.5	-6.4		

The temperature coefficients reported for the c-Si (S32) and GaInP/GaAs/Ge (3G28) Azur space cells are compared with the values obtained in this work. In the case of the single junction Si, very comparable values are presented with a slight difference due to the difference of the cell architecture. However in the case of the 3J, the difference is due to the difference of the limiting sub-cell of the two architectures, i.e. GaAs & GaInP in the 3G28 and the Si in this study.

The annealing of irradiation induced defects in Si has been extensively studied in the past [58]–[63]. In these studies, the temperature and the annealing mechanisms of the defects are reported. In the annealing temperature range considered in this study 120 - 300 K it is observed that the annealing takes place mainly for primary defects such as V, I^-, B and some complex defects,

i.e. interstitial + impurity or vacancy + impurity, such VB, PV^- or V_2I. In the case of complex defects as V_2, I_2^+ and VO_i are annealed at temperatures above 400 K and does not occurs in the annealing range considered in this study. Temperature annealing range are summarized in Tab. IV-10.

Tab. IV-10 *Annealing temperature of primary and complex induced irradiation defects [64]–[68].*

Radiation induced defects	Annealing temperature range
V^0	150 - 180 K
$V^= \rightarrow V^*$	90 - 120 K
I^-	140 - 180 K
B_i	250 - 300 K
VB	250 - 280 K
V_2I	225 - 250 K
PV^-	130 - 170 K
$V_2/V_2I/I_2^+/VO_i/C_iO_i$	400 - 723 K

In the case of the V_{OC}, the same behavior is observed for the three architectures at *BOL* and *EOL*. The calculated dV_{OC}/dT for 1J, 2J and 3J respectively are -2.2, -4.9 and -6.7 $mV.K^{-1}$ at both conditions. The stability of dV_{OC}/dT in *BOL*/*EOL* points out that the variation of the V_{OC} as a function of temperature is mainly due to the variation of the band gap energy (and not influenced by irradiation). This behavior can be explained by the fact that the introduced generation defects responsible for the V_{OC} degradation are not annealed when solar cells are heated to room temperature.

Considering the evolution of the FF, the opposite behavior is observed for 1J and 3J in both conditions; for 1J, the FF decreases with temperature and for 3J, the FF increases with temperature. In the case of 3J, this behavior is due to the appearance of S-like shape at 120 K. The calculated dFF/dT is -0.07 and 0.01 $\%.K^{-1}$ for 1J and 3J respectively at both *BOL* and *EOL*.

In the case of 2J, the calculated dFF/dT at *BOL* is 0.05 $\%.K^{-1}$. After irradiation, an inverse behavior is observed with a negative dFF/dT of -0.05 $\%.K^{-1}$. This behavior is due to the disappearance of the broken knee after irradiation at 120 K.

The efficiency temperature coefficient is expressed as the sum of the temperature coefficient normalized by their absolute values of the three electrical parameters J_{SC}, V_{OC} and

FF. Since dV_{OC}/dT is quasi-constant for all three architectures at both *BOL* and *EOL*, therefore its effect on the variation of dEff./dT is zero. In the case of 1J, the dEff./dT is negative at both conditions and is lower for *EOL*, i.e. lower decrease of efficiency with is observed at *EOL*. However in the case of tandem solar cells, the calculated dEff./dT change its sign after irradiation (from negative to positive). Thus, the efficiency increase when heating up the cell up to 300 K. for all architectures considered in this study, the efficiency temperature coefficient increases at *EOL* compare to *BOL*. The enhancement or lower efficiency decrease with temperature is due to the high recovery observed on J_{SC} and FF at *EOL*.

Tab. IV-11 *Evolution of absolute efficiency of 1J 2J and 3J at EOL characterized under LILT and LIRT conditions as a function of fluence.*

Architectures		Efficiency (%)		
		10^{14} e.cm^{-2}	**3.10^{14} e.cm^{-2}**	**10^{15} e.cm^{-2}**
1J	*LILT*	12.7	10.6	10.1
	LIRT	8.5	7.9	6.7
2J	*LILT*	19.9	12.8	9
	LIRT	13	12.8	9.8
3J	*LILT*	14.4	7.7	4.4
	LIRT	11.9	9.4	5.8

When comparing the absolute conversion efficiencies of the three architectures (see Tab. IV-11), we conclude that, for our set of samples, the 2J cell is the best performing cell under *LILT* conditions for mission where 1 MeV electrons irradiation fluence is lower than 3.10^{14} e.cm^{-2}. The calculated efficiency at this fluence is 12.8% compare to 10.6% for 1J and 7.7% for 3J. However when increasing the fluence higher than 3.10^{14} e.cm^{-2}, the 1J c-Si solar cells appears more suitable to use with an efficiency of 10.1% at 10^{15} e.cm^{-2} comparing to 9% and 4.4% for 2J and 3J respectively. However, if the solar cells can be heated up to room temperature during mission, the 2J and 3J are more suitable for use due to their high efficiency recovery. A second cooling down step (after annealing at 300 K) is needed to see if the induced irradiation defects are totally annealed or can be reactivated at low temperature. It is important to note that these statements are only true for the used solar cells in this thesis, i.e. thickness, doping profile, type, etc. As a more general statement, Si-based double junction cells (top limiting sub-cell at *BOL*) are more relevant for use at *LILT* conditions compared to 1J and 3J cells for low fluence. However, at higher fluence the 1J is more preferred. The low/high fluence

separation point is defined as the fluence at which an inversion of limiting sub-cell takes place for the 2J.

IV.6.2. Comparison to electrons irradiation at 300 K

In this part, a comparison between the behavior of the three architectures irradiated at 300 K and 120 K is carried out. In a first place, *EQE* characterizations performed at 300 K for the cell irradiated at both 300 K and 120 K are presented in Fig. IV-31. For both irradiation temperature, it is observed that the degradation of the AlGaAs and Si sub-cells is more important for high wavelength. However, in the case of GaInP sub-cell the degradation is present on its whole absorption band with lower degradation compare to the AlGaAs and the Si sub-cells. Nevertheless, an important point to emphasize is the higher *EQE* magnitude observed for the cell irradiated at 120 K (solid lines) comparing to the one irradiated at 300 K (dashed lines). This is only true in the case of AlGaAs and Si sub-cells, whereas in the case of the GaInP sub-cell an inverse behavior is observed.

In the case of the two AlGaAs and Si sub-cells, it is observed that at a low fluence (10^{14} e.cm^{-2}) the difference between the *EQE* is large. By increasing the fluence the observed gap is reduced such that at the highest fluence of this work (10^{15} e.cm^{-2}), the *EQE* of each sub-cell irradiated at 300 K and 120 K are almost identical.

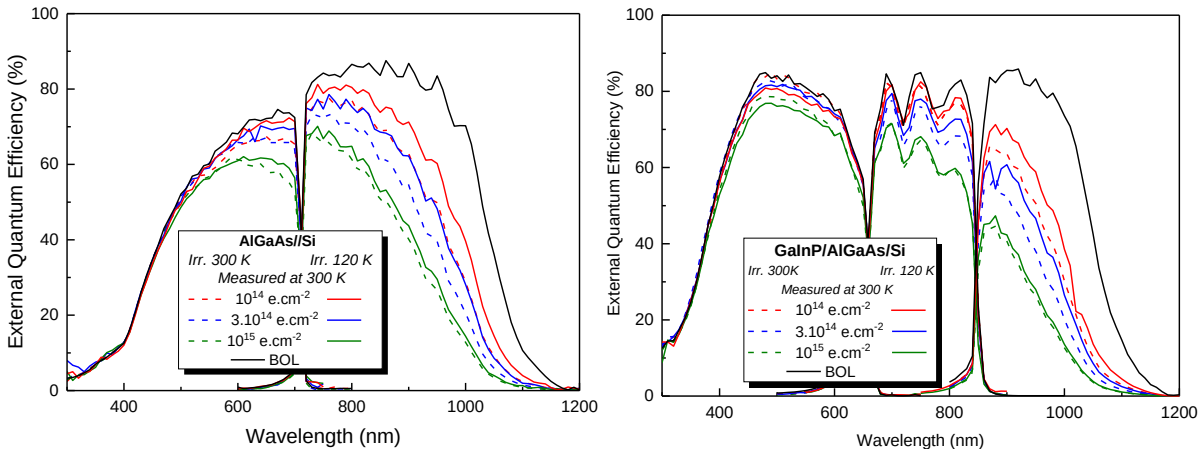

Fig. IV-31 *EQE comparison between the cells irradiated at 300 K and 120 K and both characterization were performed at 300 K in the case of (left) 2J AlGaAs//Si (right) 3J GaInP/AlGaAs//Si.*

In Fig. IV-32 the remaining factor calculated for the three architectures is presented as a function of the irradiation fluence. Solar cells irradiated at 120 K and characterized under *LILT*

conditions are presented by solid lines while cells irradiated at 300 K and characterized under *NIRT* conditions are presented by dashed lines.

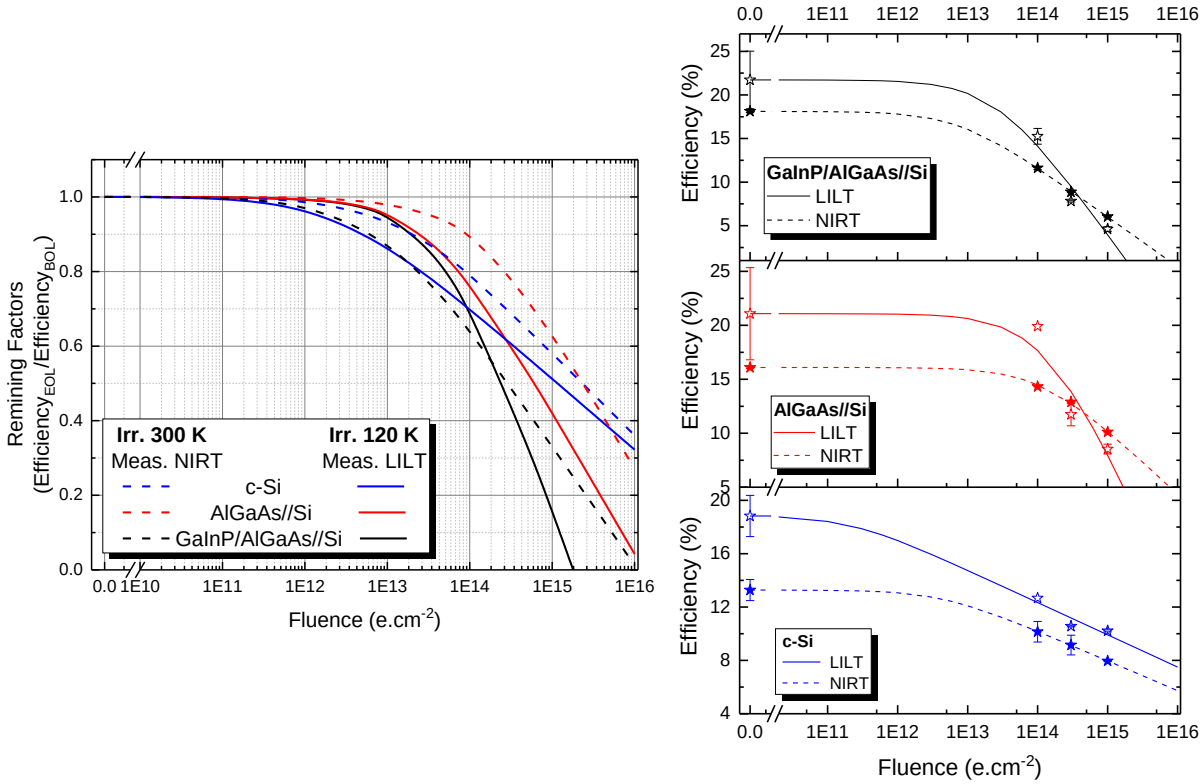

Fig. IV-32 *Evolution of efficiency as a function of fluence in the case of cell irradiated at 300 K and operate at NIRT conditions (Dashed lines) compared to the one irradiated at 120 K and operate at LILT conditions (left) Remaining factor; (right) absolute efficiency values.*

In the case of 1J and 2J, the degradation rate are 5 % and 20% lower for cells operating under *NIRT* conditions compared to *LILT* conditions at an irradiation fluence of 10^{15} e.cm^{-2}. The calculated gap is smaller in the case of 1J compared to 2J. In the case of 3J, we observe that for a fluence lower than 2.10^{14} e.cm^{-2} the degradation is less pronounced in the case of cells operating under *LILT* conditions. Beyond this fluence the degradation is stronger compared to *NIRT* conditions.

As explained previously, the remaining factor shows the degradation rate and not the end-of-life efficiency. In Fig. IV-32 (right), the absolute conversion efficiency values are presented as a function of fluence, cell architecture and operating conditions. Although the 1J degrades more under *LILT* conditions, its efficiency is still higher compared to *NIRT* conditions. The behavior of the 1J cell over the entire irradiation fluence range (fitted by the semi-empirical equation) the 1J c-Si cell is more suitable for use under *LILT* than *NIRT* conditions.

In the case of the two tandem solar cells, a crossover point is observed at a fluence of 3.10^{14} e.cm^{-2}. At a lower fluence, the absolute efficiency of the two tandem cells operating under *LILT* conditions is higher than the one operating under *NIRT* conditions. By increasing the irradiation fluence higher than 3.10^{14} e.cm^{-2}, the higher degradation rate lead to a lower efficiency at *LILT* comparing to *NIRT* conditions.

IV.6.3. Comparison to conventional AzurSpace 3G28 cell

In this part, the degradation of the new III-V//Si solar cell technology is compared to that of the III-V/Ge cells conventionally used for space applications; one should keep in mind though that III-V/Ge cells have been extensively studied and optimized for operating in a radiative environment, with a broad absorption of the AM0 reference solar spectrum. While in the case of the laboratory cells used in this study, AM0 was not the originally intended operating conditions, but rather concentrated terrestrial spectrum (AM1.5D is red rich compared to AM0). Therefore, the cells in this study were designed with higher finger density to avoid series resistance effect at high injection, and high thickness due to manufacturing set-up process limitation. It is important to note that the absolute efficiencies between these two technologies of solar cells are note comparable.

The comparison data were taken for the AzurSpace 3G28 triple junction GaInP/GaAs/Ge originates from a research work performed in the same laboratory and irradiation facilities *SIRIUS* [15]. However, the in-situ *I-V* characterizations were performed with a different solar simulator based on Xe and halogen lamps instead of *LED* solar simulator (*Quesma*).

Fig. IV-33 presents the key electrical parameters remaining factors as a function of 1 MeV electrons irradiation fluence. The GaInP/GaAs/Ge were irradiated at three different fluence 7.10^{14}, $1.5.10^{15}$ and 3.10^{15} e.cm^{-2} at 123 K. in-situ *I-V* characterization at *BOL* and *EOL* were performed at *LILT* conditions (~3.7% AM0 and 123 K).

In the case of J_{SC}, a very low degradation (less than 2%) is observed for a fluence lower than $1.5x10^{15}$ e.cm^{-2} by increasing the fluence to 3.10^{15} e.cm^{-2} the degradation becomes more important and reach 6%. This notable difference in the degradation rate is due to the fact that at low fluence the GaInP sub-cell limits the III-V/Ge current while at higher fluence the GaAs sub-cell becomes the limiting cell. Thus, the difference is due to the difference between the sub-cells radiation hardness. For the Ge bottom sub-cell, even with its relatively low radiation hardness it does not limit the total current given the low bandgap - thus its wide absorption band. However, the degradation is still much lower compared to Si-based cell degradation. This

is explained by the fact that the III-V top cells limits the overall current of the III-V/Ge with higher radiation hardness compared to the III-V//Si where the Si bottom sub-cell is the limiting one in our case with low radiation hardness.

Considering the degradation of the V_{OC}, it is clear from Fig. IV-33 (top-right) that the degradation is slightly lower in the case of III-V/Ge (lower than 6%) but remains in the same order of magnitude than the III-V//Si. This is explained by the fact that the V_{OC} is the sum of the sub-cells respective V_{OC}, and since the top sub-cells are composed of same type of III-V alloys (relatively same radiation hardness) as III-V//Si, their degradation is follow similar trends.

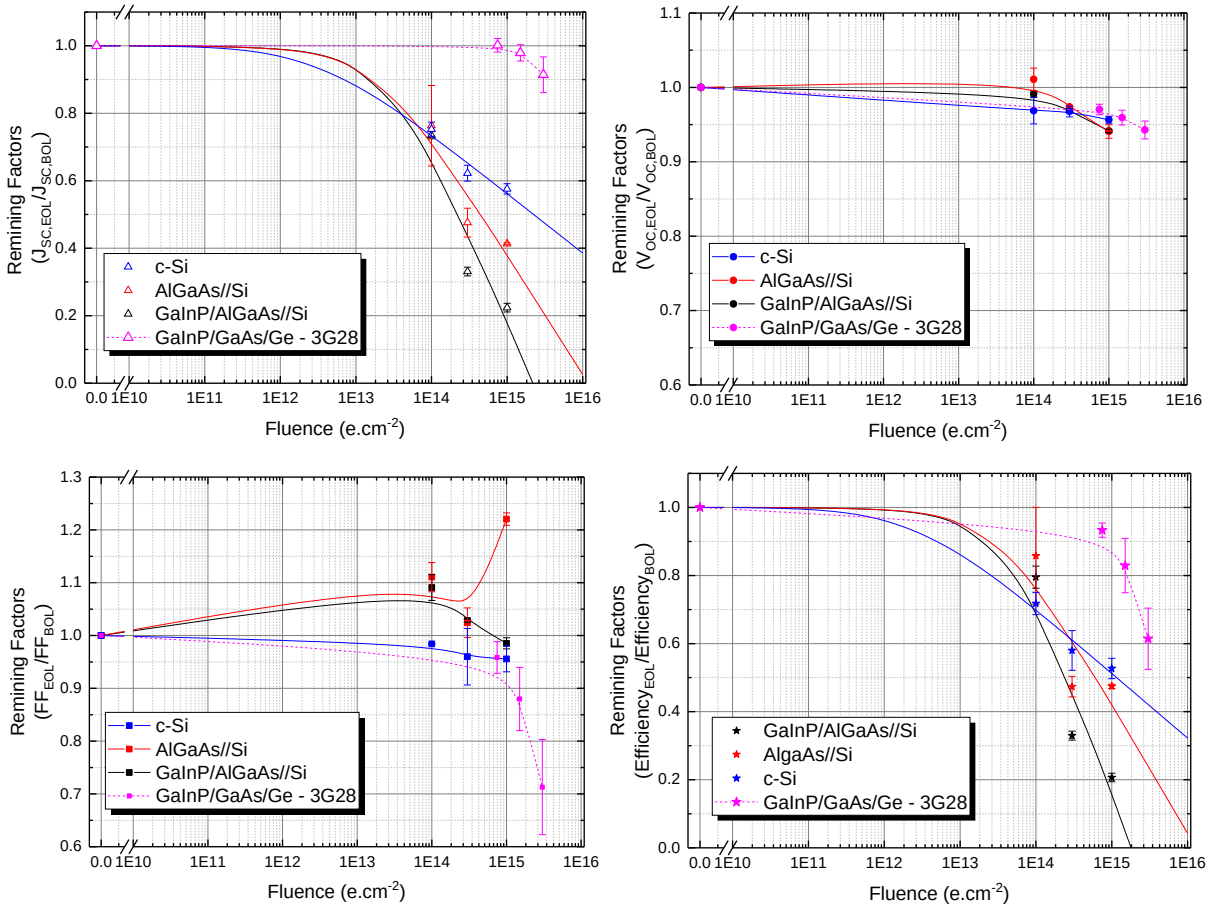

Fig. IV-33 *Electrical parameters remaining factors comparison between the conventional AzurSpace 3G28 GaInP/GaAs/Ge solar cells used in space application to the Si based solar cells used in this thesis.*

The second main difference lies in the FF variation as a function of fluence between the III-V/Ge and III-V//Si (see Fig. IV-33 bottom-left). No increase in FF was observed after irradiation in the case of III-V/Ge cells, since the two limiting sub-cells top and middle are almost in current match conditions at *BOL* and *EOL*. However, a strong degradation with high statistical distribution is observed in these cells compared to the low FF degradation in the case

of III-V//Si cells. In the case of III-V/Ge cells, this pronounced FF degradation has been explained in [15] by an increase of dark saturation current which is due to tunneling effect in the p-n junction of all the sub-cells. Due to the low J_{SC} photo-generated at low intensity, a low dark current can induce a large effect on the triple junction. The Ge bottom sub-cells was identified as the highest sensitive to the irradiation at low temperature. The tunneling effect is due to the introduction of defects in the space charge region that act as trap for majority carrier. In addition to this, the large statistical dispersion observed is due to the randomness of the occurrence and intensity of excess current. It is true that in the case of the cells studied in this thesis, a relatively low statistical dispersion is observed. However, in the case of the cells used in this study, this effect is most probably due to the difference in sample size as opposed to III-V/Ge cells used with of equivalent size.

In the case of efficiency (see Fig. IV-33 bottom-right), its evolution is governed by the unpredictable variation of the FF in the case of III-V/Ge, contrary to the case of III-V/Si cells where the degradation is governed by the degradation of the J_{SC}.

The biggest problem in the behavior of III-V/Ge cells is the prediction of their behavior under *LILT* conditions. Indeed, the rate of the tunnel current excess in addition to the strong statistical dispersion that increases with fluence makes the prediction of Pmax difficult at *LILT*. An example the efficiency degradation is 7% at a fluence of 7.10^{14} $e.cm^{-2}$ with an absolute deviation of 5%, by increasing the fluence up to 3.10^{15} $e.cm^{-2}$, the degradation reach 39% with an absolute deviation of 9%. However in the case of III-V//Si, low statistical dispersion is observed in addition to the fact that the degradation is predictable. In fact, the degradation of III-V//Si solar cells is due mainly to the degradation of the Si bottom sub-cells J_{SC} that is easily quantifiable and predictable. The challenging point is to enhance the Si bottom cell resistance to radiation.

IV.7 Conclusion

- Accurate multi-junction low irradiance characterizations is not straightforward with standard solar simulator set-ups. Operating results on the two solar simulators have shown that the flasher *Helios 3030* used for ex-situ characterization cannot be used for low intensity ~3% AM0 due to spectrum distortion. However, the *Quesma LED* steady state solar simulator shows good results by optimizing the spectrum at this illumination intensity. However, an interpolation to low intensities using the lumped model proposed by Dominguez et al. [11] can be used to compare the I-*V* characterization by the two solar simulators.
- The electrical parameters of the three architectures evolve with irradiance intensity according to our expectations and in very good agreement with the theoretical equations. The J_{SC} varies as a linear function with the illumination intensity. Moreover, the V_{OC} varies as a logarithmic function with different ideality factors from one cell to another of the same batch but remains within the theoretical limitations, i.e. n = 1 - 2 for 1J, n = 2 - 4 for 2J and n = 3 - 6 for 3J.
- After characterization under *LILT* conditions, the following statements are established:
    - No thermal cycling effects are observed either on the mechanical properties of the deposited layers or on the key electrical properties of the solar cells, which suggest a good mechanical integrity of the wafer bonded cells dipped at cryogenic temperature.
    - The variation of bandgap energy measured by *EL-S* and *EQE* with temperature is in good agreement with the Varshni equation [34] in the temperature range 120 - 300 K.
    - Linear variation of J_{SC} (decrease) and V_{OC} (high increase) as a function of temperature in the range 300 - 120 K.
    - The efficiency increases by cooling down the cells is a linear function until saturation at a temperature of 150 K.
    - Appearance of the anomalies known as broken knee in the case of some 2J solar cells and the S-like shapes in the case of 3J solar cells at 120 K. This effect reduce the solar cell FF.

- The efficiency degradation is driven mainly by the J_{SC} degradation after irradiation. The J_{SC} degradation is due to the high drop in minority carrier diffusion length as observed by *EQE* measurements for Si cell/sub-cell.
- A strong degradation of the maximum power is observed after irradiation in the case of 3J (80%) compared to 2J (52%) and 1J (47%) at a fluence of 10^{15} e.cm^{-2}. This effect is all the more important in the case of tandem cells given the low absorption band of Si below III-V top cells
- A non-negligible recovery is observed after annealing at 300 K. This effect is mainly due to the annealing of the primary defect that acts as a recombination center in all three architectures translated by a higher temperature coefficient at *EOL* compare to *BOL*. However, no V_{OC} annealing effect was observed post-irradiation when heating up the cells.
- The cells architecture with the highest *EOL* power depends on the irradiation fluence and potential annealing sequence. For example, in a mission where the equivalent 1 MeV irradiation fluence at *LILT* conditions (w/o annealing) is lower than 3.10^{14} e.cm^{-2}, the 2J offers a better absolute *EOL* efficiency. However, for higher fluence, the 1J offer a higher efficiency.
- By comparing the behavior of III-V//Si cells to the III-V/Ge cells, we can draw the following conclusions :
    - III-V/Ge: Very low degradation of J_{SC} is observed since it is limited by the tops sub-cells with high radiation hardness and therefore a low degradation on efficiency is calculated after irradiation. However, a high FF degradation is observed that drive the efficiency degradation. This degradation is due to the tunneling effect in the p-n junction, which is unpredictable with high statistical dispersion. Therefore, makes the efficiency of III-V/Ge under *LILT* conditions relatively unpredictable.
    - III-V//Si: A very high degradation is observed in the J_{SC} therefore the efficiency of the three solar cells architectures. This degradation is due to the low radiation hardness of Si solar cells that limits the current of the total solar cells. However, a relatively low statistical dispersion is observed on the efficiency degradation with a well-known degradation origin that can be subsequently improved. This made the prediction of the efficiency of the III-V//Si solar cells realistic at *LILT* conditions.

IV.8 References

[1] O. Grasset *et al.*, "JUpiter ICy moons Explorer (JUICE): An ESA mission to orbit Ganymede and to characterise the Jupiter system," *Planet. Space Sci.*, vol. 78, pp. 1–21, Apr. 2013, doi: 10.1016/j.pss.2012.12.002.

[2] R. Hoheisel, R. J. Walters, and A. W. Bett, "Low temperature effects in photovoltaic devices for deep space missions," in *2015 IEEE 42nd Photovoltaic Specialist Conference (PVSC)*, Jun. 2015, pp. 1–5, doi: 10.1109/PVSC.2015.7355666.

[3] F. J. Vorster and E. E. van Dyk, "High saturation solar light beam induced current scanning of solar cells," *Rev. Sci. Instrum.*, vol. 78, no. 1, p. 013904, Jan. 2007, doi: 10.1063/1.2432408.

[4] G. E. Bunea, K. E. Wilson, Y. Meydbray, M. P. Campbell, and D. M. D. Ceuster, "Low Light Performance of Mono-Crystalline Silicon Solar Cells," in *2006 IEEE 4th World Conference on Photovoltaic Energy Conference*, May 2006, vol. 2, pp. 1312–1314, doi: 10.1109/WCPEC.2006.279655.

[5] N. H. Reich *et al.*, "Crystalline silicon cell performance at low light intensities," *Sol. Energy Mater. Sol. Cells*, vol. 93, no. 9, pp. 1471–1481, Sep. 2009, doi: 10.1016/j.solmat.2009.03.018.

[6] R. W. Lof, "Weak Light Performance and Spectral Response of Different Solar Cell Types," in *20. European Photovoltaic Solar Energy Conference and Exhibition*, 2005, pp. 2120–2123.

[7] A. Halm, P. Hering, C. Comparotto, L. J. Koduvelikulathu, and R. Kopecek, "Low light intensity performance of n-and p-type silicon solar cells with different architectures," presented at the EU-PVSEC, 2011.

[8] K. Rühle, M. K. Juhl, M. D. Abbott, and M. Kasemann, "Evaluating Crystalline Silicon Solar Cells at Low Light Intensities Using Intensity-Dependent Analysis of I-V Parameters," *IEEE J. Photovolt.*, vol. 5, no. 3, pp. 926–931, May 2015, doi: 10.1109/JPHOTOV.2015.2395145.

[9] E. F. Fernández, A. J. García-Loureiro, and G. P. Smestad, "Multijunction Concentrator Solar Cells: Analysis and Fundamentals," in *High Concentrator Photovoltaics*, P. Pérez-Higueras and E. F. Fernández, Eds. Cham: Springer International Publishing, 2015, pp. 9–37.

[10] F. Oviedo, Z. Liu, Z. Ren, M. Thway, T. Buonassisi, and I. M. Peters, "Ohmic shunts in two-terminal dual-junction solar cells with current mismatch," *Jpn. J. Appl. Phys.*, vol. 56, no. 8S2, p. 08MA05, Jul. 2017, doi: 10.7567/JJAP.56.08MA05.

[11] C. Domínguez, I. Antón, and G. Sala, "Multijunction solar cell model for translating I–V characteristics as a function of irradiance, spectrum, and cell temperature," *Prog. Photovolt. Res. Appl.*, vol. 18, no. 4, pp. 272–284, 2010, doi: 10.1002/pip.965.

[12] G. S. Kinsey, P. Hebert, K. E. Barbour, D. D. Krut, H. L. Cotal, and R. A. Sherif, "Concentrator multijunction solar cell characteristics under variable intensity and temperature," *Prog. Photovolt. Res. Appl.*, vol. 16, no. 6, pp. 503–508, 2008, doi: https://doi.org/10.1002/pip.834.

[13] K. K. de Groh, B. A. Banks, S. K. R. Miller, and J. A. Dever, "Chapter 28 - Degradation of Spacecraft Materials," in *Handbook of Environmental Degradation of Materials (Third Edition)*, M. Kutz, Ed. William Andrew Publishing, 2018, pp. 601–645.

[14] V. G. Weizer and J. D. Broder, "On the cause of the flat-spot phenomenon observed in silicon solar cells at low temperatures and low intensities," *J. Appl. Phys.*, vol. 53, no. 8, pp. 5926–5930, Aug. 1982, doi: 10.1063/1.331435.

[15] S. Park, "Irradiation effect in triple junction solar cells for spatial applications," Theses, Université Paris-Saclay, 2018.

[16] C. J. Gelderloos, K. B. Miller, R. J. Walters, G. P. Summers, and S. R. Messenger, “Low intensity low temperature performance of advanced solar cells,” in *Photovoltaic Specialists Conference, 2002. Conference Record of the Twenty-Ninth IEEE*, 2002, pp. 804–807.
[17] D. A. Scheiman and D. B. Snyder, “Low intensity low temperature (*LILT*) measurements of state-of-the-art triple junction solar cells for space missions,” in *2008 33rd IEEE Photovoltaic Specialists Conference*, May 2008, pp. 1–6, doi: 10.1109/PVSC.2008.4922707.
[18] P. M. Stella, F. S. Pool, M. A. Nicolet, and P. A. Iles, “PV technology for low intensity, low temperature (*LILT*) applications,” in *Photovoltaic Energy Conversion, 1994., Conference Record of the Twenty Fourth. IEEE Photovoltaic Specialists Conference-1994, 1994 IEEE First World Conference on*, 1994, vol. 2, pp. 2082–2087.
[19] C. Baur *et al.*, “Development status of triple-junction solar cells optimized for low intensity low temperature applications,” in *Photovoltaic Specialists Conference (PVSC), 2013 IEEE 39th*, 2013, pp. 3237–3242.
[20] M. Imaizumi *et al.*, “Irradiation and measurement of solar cells at low intensity, low temperature (*LILT*) conditions,” in *Photovoltaic Specialists Conference, 2008. PVSC’08. 33rd IEEE*, 2008, pp. 1–5.
[21] D. A. Scheiman, P. P. Jenkins, D. J. Brinker, and J. Appelbaum, “Low-intensity low-temperature (*LILT*) measurements and coefficients on new photovoltaic structures,” *Prog. Photovolt. Res. Appl.*, vol. 4, no. 2, pp. 117–127, 1996.
[22] D. Walker, J. C. Nocerino, J. E. Baidoo, Y. Y. Lao, C. J. Mann, and S. H. Liu, “Low-temperature characterization of multijunction solar cells using a combined characterization approach,” in *2018 IEEE 7th World Conference on Photovoltaic Energy Conversion (WCPEC) (A Joint Conference of 45th IEEE PVSC, 28th PVSEC 34th EU PVSEC)*, Jun. 2018, pp. 2248–2251, doi: 10.1109/PVSC.2018.8548259.
[23] R. Nybakken, “The Juno mission to Jupiter — A pre-launch update,” in *2011 Aerospace Conference*, Mar. 2011, pp. 1–8, doi: 10.1109/AERO.2011.5747272.
[24] S. Chander, A. Purohit, A. Sharma, Arvind, S. P. Nehra, and M. S. Dhaka, “A study on photovoltaic parameters of mono-crystalline silicon solar cell with cell temperature,” *Energy Rep.*, vol. 1, pp. 104–109, Nov. 2015, doi: 10.1016/j.egyr.2015.03.004.
[25] G. Jungst, A. M. Gras, J. M. Aguilar, and C. Baur, “Spectral Response of a monolithic triple junction space solar cell at low and high temperatures,” Jun. 2009, pp. 001312–001315, doi: 10.1109/PVSC.2009.5411255.
[26] D. Aiken, M. Stan, C. Murray, P. Sharps, J. Hills, and B. Clevenger, “Temperature dependent spectral response measurements for III-V multi-junction solar cells,” in *Photovoltaic Specialists Conference, 2002. Conference Record of the Twenty-Ninth IEEE*, 2002, pp. 828–831.
[27] J. A. del Alamo and R. M. Swanson, “Forward-bias tunneling: A limitation to bipolar device scaling,” *IEEE Electron Device Lett.*, vol. 7, no. 11, pp. 629–631, Nov. 1986, doi: 10.1109/EDL.1986.26499.
[28] A. Boca, “Solar Cell Testing for the Jupiter Environment: Low Irradiance, Low Temperature and High Radiation,” in *2019 IEEE 46th Photovoltaic Specialists Conference (PVSC)*, Jun. 2019, pp. 2787–2791, doi: 10.1109/PVSC40753.2019.8981342.
[29] V. Khorenko *et al.*, “BOL and *EOL* Characterization of Azur 3G *LILT* Solar Cells for ESA Juice Mission,” 2017, doi: 10.1051/e3sconf/20171603011.
[30] S. Brambillasca, F. Topputo, A. Ercoli-Finzi, R. Campesato, and C. SpA, “*LILT* Measurement on Silicon Solar Cells of Rosetta Lander Philae,” in *XX AIDAA Congress, Milano, Italy, June*, 2009, vol. 29.
[31] D. DADAMO and M. PETRUZZIELLO, “Design of an experimental device to recreate *LILT* environment,” 2014.

[32] E44 Committee, “Test Method for Spectral Responsivity Measurements of Photovoltaic Devices,” ASTM International. doi: 10.1520/E1021-15R19.
[33] H. Helmers, C. Karcher, and A. W. Bett, “Bandgap determination based on electrical quantum efficiency,” *Appl. Phys. Lett.*, vol. 103, no. 3, p. 032108, Jul. 2013, doi: 10.1063/1.4816079.
[34] Y. P. Varshni, “Temperature dependence of the energy gap in semiconductors,” *Physica*, vol. 34, no. 1, pp. 149–154, Jan. 1967, doi: 10.1016/0031-8914(67)90062-6.
[35] D. B. Leviton and B. J. Frey, “Temperature-dependent absolute refractive index measurements of synthetic fused silica,” in *Optomechanical Technologies for Astronomy*, Jul. 2006, vol. 6273, p. 62732K, doi: 10.1117/12.672853.
[36] B. J. Frey, D. B. Leviton, and T. J. Madison, “Temperature-dependent refractive index of silicon and germanium,” in *Optomechanical Technologies for Astronomy*, Jul. 2006, vol. 6273, p. 62732J, doi: 10.1117/12.672850.
[37] C. Karcher, H. Helmers, M. Schachtner, F. Dimroth, and A. W. Bett, “Temperature-dependent electroluminescence and voltages of multi-junction solar cells,” *Prog. Photovolt. Res. Appl.*, vol. 22, no. 7, pp. 757–763, 2014, doi: 10.1002/pip.2431.
[38] Z. C. Su *et al.*, “Electroluminescence probe of internal processes of carriers in GaInP single junction solar cell,” *Sol. Energy Mater. Sol. Cells*, vol. 168, pp. 201–206, Aug. 2017, doi: 10.1016/j.solmat.2017.04.041.
[39] L. Bhusal, B. Fluegel, M. A. Steiner, and A. Mascarenhas, “Ordering induced direct-indirect transformation in unstrained GaxIn1−xP for 0.76≤x≤0.78,” *J. Appl. Phys.*, vol. 106, no. 11, p. 114909, Dec. 2009, doi: 10.1063/1.3266175.
[40] D. E. Aspnes, “GaAs lower conduction-band minima: Ordering and properties,” *Phys. Rev. B*, vol. 14, no. 12, pp. 5331–5343, Dec. 1976, doi: 10.1103/PhysRevB.14.5331.
[41] N. Dharmarasu *et al.*, “High-radiation-resistant InGaP, InGaAsP, and InGaAs solar cells for multijuction solar cells,” *Appl. Phys. Lett.*, vol. 79, no. 15, pp. 2399–2401, Oct. 2001, doi: 10.1063/1.1409270.
[42] M. Yamaguchi, “Radiation resistance of compound semiconductor solar cells,” *J. Appl. Phys.*, vol. 78, no. 3, pp. 1476–1480, Aug. 1995, doi: 10.1063/1.360236.
[43] M. Yamaguchi, T. Okuda, S. J. Taylor, T. Takamoto, E. Ikeda, and H. Kurita, “Superior radiation-resistant properties of InGaP/GaAs tandem solar cells,” *Appl. Phys. Lett.*, vol. 70, no. 12, pp. 1566–1568, Mar. 1997, doi: 10.1063/1.118618.
[44] G. Yan, J. Wang, J. Liu, Y. Liu, R. Wu, and R. Wang, “Electroluminescence analysis of VOC degradation of individual subcell in GaInP/GaAs/Ge space solar cells irradiated by 1.0 MeV electrons,” *J. Lumin.*, vol. 219, p. 116905, Mar. 2020, doi: 10.1016/j.jlumin.2019.116905.
[45] S. Makham, M. Zazoui, and J. C. Bourgoin, “Analysis of Multijunction solar cells: Electroluminescence study,” *M J Condens Matter*, vol. 5, Jan. 2004.
[46] F. Salvat, J. M. Fernández-Varea, and J. Sempau, “PENELOPE-2006: A code system for Monte Carlo simulation of electron and photon transport,” in *Workshop proceedings*, 2006, vol. 4, p. 7.
[47] S. Lazanu, I. Lazanu, A. Lepadatu, and I. Stavarache, “Defect production in silicon and germanium by low temperature irradiation,” in *2009 International Semiconductor Conference*, Oct. 2009, vol. 2, pp. 379–382, doi: 10.1109/SMICND.2009.5336700.
[48] R. D. Goldberg, R. G. Elliman, and J. S. Williams, “The kinetics of self ion amorphization of silicon,” *Nucl. Instrum. Methods Phys. Res. Sect. B Beam Interact. Mater. At.*, vol. 80–81, pp. 596–599, Jun. 1993, doi: 10.1016/0168-583X(93)96189-J.
[49] O. W. Holland, J. Narayan, and D. Fathy, “Ion beam processes in Si,” *Nucl. Instrum. Methods Phys. Res. Sect. B Beam Interact. Mater. At.*, vol. 7–8, pp. 243–250, Mar. 1985, doi: 10.1016/0168-583X(85)90561-0.

[50] W. D. C. Jr and D. G. Rethwisch, *Fundamentals of Materials Science and Engineering: An Integrated Approach*. John Wiley & Sons, 2012.
[51] C. Algora and I. Rey-Stolle, Eds., *Handbook of concentrator photovoltaic technology*. Chichester, West Sussex: Wiley, 2016.
[52] M. A. Green, "Solar cells: operating principles, technology, and system applications," 1982.
[53] D. T. Cotfas, P. A. Cotfas, and O. M. Machidon, "Study of Temperature Coefficients for Parameters of Photovoltaic Cells," *International Journal of Photoenergy*, Apr. 01, 2018. https://www.hindawi.com/journals/ijp/2018/5945602.
[54] R. M. Fleming, C. H. Seager, D. V. Lang, and J. M. Campbell, "Transformation kinetics of an intrinsic bistable defect in damaged silicon," *J. Appl. Phys.*, vol. 111, no. 2, p. 023715, Jan. 2012, doi: 10.1063/1.3678581.
[55] R. Radu, I. Pintilie, L. C. Nistor, E. Fretwurst, G. Lindstroem, and L. F. Makarenko, "Investigation of point and extended defects in electron irradiated silicon—Dependence on the particle energy," *J. Appl. Phys.*, vol. 117, no. 16, p. 164503, Apr. 2015, doi: 10.1063/1.4918924.
[56] J. R. Srour and J. M. McGarrity, "Radiation effects on microelectronics in space," *Proc. IEEE*, vol. 76, no. 11, pp. 1443–1469, Nov. 1988, doi: 10.1109/5.90114.
[57] R. J. Walters, S. Messenger, J. H. Warner, C. D. Cress, M. Gonzalez, and S. Maximenko, "Modeling of radiation induced defects in space solar cells," in *Physics and Simulation of Optoelectronic Devices XIX*, Feb. 2011, vol. 7933, p. 79330P, doi: 10.1117/12.873902.
[58] G. P. Gaidar, "Annealing of radiation-induced defects in silicon," *Surf. Eng. Appl. Electrochem.*, vol. 48, no. 1, pp. 78–89, Feb. 2012, doi: 10.3103/S1068375512010061.
[59] B. L. Gregory and H. H. Sander, "Transient annealing of defects in irradiated silicon devices," *Proc. IEEE*, vol. 58, no. 9, pp. 1328–1341, Sep. 1970, doi: 10.1109/PROC.1970.7925.
[60] M.-A. Trauwaert, J. Vanhellemont, H. E. Maes, A.-M. V. Bavel, and G. Langouche, "Low temperature anneal of electron irradiation induced defects in p type silicon," *Mater. Sci. Technol.*, vol. 14, no. 12, pp. 1295–1298, Dec. 1998, doi: 10.1179/mst.1998.14.12.1295.
[61] H. J. Stein and F. L. Vook, "Electrical Studies of Electron-Irradiated n-Type Si: Impurity and Irradiation-Temperature Dependence," *Phys. Rev.*, vol. 163, no. 3, pp. 790–800, Nov. 1967, doi: 10.1103/PhysRev.163.790.
[62] O. O. Awadelkarim, "Low temperature radiation damage in silicon: II. Production rates and annealing studies on p-type material," *Phys. B C*, vol. 145, no. 1, pp. 39–44, 1987.
[63] O. O. Awadelkarim, "Low-temperature radiation damage in silicon: I. Annealing studies on n-type material," *Phys. BC*, vol. 144, no. 3, pp. 341–350, Feb. 1987, doi: 10.1016/0378-4363(87)90015-5.
[64] G. D. Watkins, "EPR of a trapped vacancy in boron-doped silicon," *Phys. Rev. B*, vol. 13, no. 6, pp. 2511–2518, Mar. 1976, doi: 10.1103/PhysRevB.13.2511.
[65] L. C. KIMERLING, "Defects and Radiation Effect in Semiconductors 1980," *Inst Phys Conf Ser*, vol. 59, p. 217, 1981.
[66] Y.-H. Lee, N. N. Gerasimenko, and J. W. Corbett, "EPR study of neutron-irradiated silicon: A positive charge state of the $〈100〉$ split di-interstitial," *Phys. Rev. B*, vol. 14, no. 10, pp. 4506–4520, Nov. 1976, doi: 10.1103/PhysRevB.14.4506.
[67] G. D. Watkins, "Defects in irradiated silicon: EPR and electron-nuclear double resonance of interstitial boron," *Phys. Rev. B*, vol. 12, no. 12, pp. 5824–5839, Dec. 1975, doi: 10.1103/PhysRevB.12.5824.
[68] P. J. Dean, "Radiation Effects in Semiconductors," *Phys. Bull.*, vol. 23, no. 12, pp. 737–738, Dec. 1972, doi: 10.1088/0031-9112/23/12/03

General Conclusion

The objective of this thesis was to characterize & understand the degradation mechanisms of the emerging III-V//Si solar cells when exposed to irradiations under different temperature and illumination conditions representative of space operating environments; in other words, to analyze the potential of the Si-based tandem solar cells technology for space applications. For this purpose, we have been working with dual-junctions $Al_{0.22}Ga_{0.78}As$//Si and triple-junctions GaInP/$Al_{0.037}Ga_{0.963}As$//Si realized by surface activated wafer bonding to join the high bandgaps III-Vs with Si bottom cell. Single-junctions c-Si, with the same characteristics than the Si bottom cell, were also used as a third reference cell architecture.

In order to reach the above-mentioned objective, this work tackled the 4 main points: i) characterizations methodology, precision & reliability for these III-V//Si cells, ii) effects of irradiations on the behavior Si based tandem solar cells iii) Combined effects of the irradiations and operating environment (temperature & illumination intensity) on these cells performance iii) advantages and limitations of III-V//Si technology, and comparison with actual III-V/Ge space standards.

Main contributions of this thesis

The approach adopted was based on comparative experimental study, with different characterization methods (*I-V*, *QE* and *EL-S*), before and after irradiation. Accurate *I-V* characterizations for this new cell technology was challenging in the absence of reference isotype cells; we have thus performed intensive optimizations to get as close as possible to the reference AM0 spectrum (reduction of temporal and spectral variations) with the two set-ups of this study: a flash lamp (ex-situ) and *LED* (in-situ) sun simulators. Therefore, we adopted a new measurement protocol combining *IQE*, *EQE* and spectrophotometry. Operations and characterization processes performed on both solar simulator are comprehensively described in chapter II.

Current-voltage measurements conducted before and after irradiations revealed a monotonous degradation of the cells electrical parameters with increasing fluence for the three architectures, with the exception of the fill factor (FF), in some cases. Indeed, an improvement with fluence may happen when sub-cells current balance changes significantly as a result of their different radiation hardness. A common feature for III-V//Si cells is the strong degradation of the J_{SC} that drives the efficiency degradation. From a fundamental point of view, this degradation is the consequence of minority carriers diffusion length reduction following the creation of complex defects acting as recombination centers. *EQE* measurements thus reveal a

degradation in the long wavelength range, close to sub-cells bandgaps, more pronounced in the case of silicon. Due to sub-cells series connection & silicon weak radiation hardness, Si happens to be current limiting for all high fluences; though a change of limiting sub-cell (III-V→Si) may happen at intermediate fluences depending on *BOL* design (e.g. 2J cell in this thesis). The more junctions are added on top of Si, the greater is the multi-junction sensitivity to irradiations: indeed, an increasing number of junction restrict the absorption band of Si to the long wavelength range, spectral part with lower collection probability. The III-V sub-cells on their side only contribute to the degradation of the tandem V_{OC} (e.g. 44% for 2J and 65% for 3J at 10^{15} e.cm^{-2} in our case) since they are not current limiting.

Unlike electrons irradiation, the degradation is non-homogeneous as a function of cell depth after irradiation with 1 MeV protons energy. This results from the protons implantation in the active region of the Si cell at a depth of ~11 - 16 µm below top surface (depending on the presence and the thicknesses of the tops cells). Therefore, three main behavior were observed: i) a first region homogenously degraded (< 10 µm), ii) a second region strongly degraded (Bragg peak) and ii) a third region with no damage (> 16 µm). However, by using a modified calculation of the non-ionizing energy loss it was possible to correlate the degradation observed for electrons and protons irradiated at 300 K as a function of displacement damage dose. This approach allowed us to quantify and predict the degradation of this new III-V//Si cell technology for any space mission (fluence, energy, e-/H+).

In a second part, we have analyzed the effect of the operating environment, i.e. the influence of irradiance intensity and temperature: characterizations and irradiations were performed at 120K & 3% AM0 (*LILT*) and compared with *NIRT* results (300K, 100% AM0). As a first step, we could demonstrate the mechanical/electrical integrity of the wafer bonding interface with thermal cycling at cryogenic temperature; this is promising since wafer bonding enables several high efficiency multi-junction architectures. However, with the switch from *NIRT* to *LILT* conditions, specific anomalies were detected such as S-like IV shape on 3J cells and broken knee on 2J. These anomalies tend to impact the fill factor and consequently the efficiency. Nevertheless, the efficiency of all three solar cell architectures tested at *BOL* were found significantly higher in *LILT* compared to *NIRT* conditions (low temperature Voc boost). After irradiation at 120 K, similar behavior is observed at *LILT* as for *NIRT* conditions: a strong degradation of the J_{SC} compared to the other electrical parameters. In addition, the degradation

rate at *LILT* is higher than *NIRT* conditions (e.g. 20% absolute RF(Eff.) difference for 2J at 10^{15} e.cm^{-2}); this is linked to the lower defects mobility (and thus annealing) at low temperature. Overall, the higher *BOL* efficiencies combined with higher degradation rate results in a cross-over point: in this study, below ~ 3.10^{14} e.cm^{-2}. III-V//Si efficiencies are higher in *LILT* compared to *NIRT* (and opposite at lower fluences). In the case of single-junction silicon however, *LILT* conditions offers higher efficiencies at any fluences (see Fig. 1). The cells temperature coefficient analysis during cooling down in *BOL* and heating up in *EOL* has revealed a non-negligible annealing, leading to J_{SC} and thus efficiency recovery. Among the three cell architectures tested here, we found that the dual-junction architecture is the most performant option in both *NIRT* and *LILT* applications. Indeed, the 2J configuration appears as a compromise: on the one hand its benefits from the reduced thermalization losses (compared to 1J) inherent of multi-junction architectures and on the other hand by using only one top cell, the reduction of the absorption band of the Si, less radiation hard, is relatively limited. Thus, in the perspective of III-V//Si cells developments for space, the 2J architecture may be the wise option.

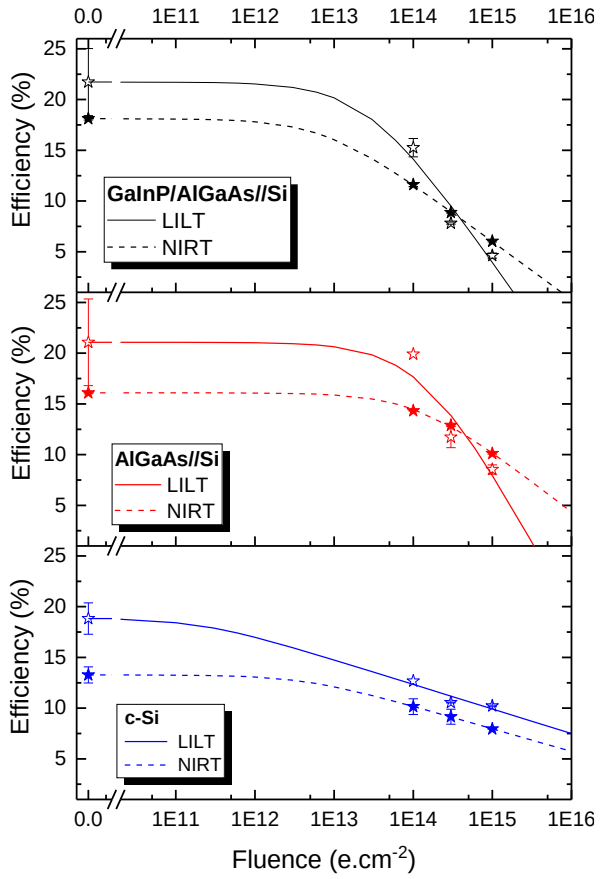

Fig. 1 *Efficiency as a function of electron fluence for 1J, 2J and 3J for both NIRT and LILT environment. Symbols are measured data and lines represent fit to semi-empirical equation.*

As expected and experimentally observed, III-V//Si technology radiation hardness is relatively weak in comparison to III-V/Ge standards. The *EOL* efficiency gap observed here disqualify the use of this new technology for high fluences environments (especially in *LILT* conditions). However, for low fluences (10^{13} - 10^{14} e.cm^{-2}) and *NIRT* conditions the difference is less pronounced even with our non-optimized cells batches (e.g. < 15% absolute RF(Eff.) difference for 2J). Though not tested here, these two conclusions may hold as well for champion (>30%) III-V//Si devices. Nevertheless, in the case of *LILT* conditions, we have observed a low statistical dispersion for the *EOL* performances within our III-V//Si dataset, contrary to the case of III-V/Ge (variable FF degradation) for which *EOL* prediction is complicated (variable FF &

efficiency dispersion). Overall, whether or not III-V//Si cells will become a viable solution for low/intermediate radiative space environments will depends on its capacity to reach full industrial maturity at lower cost than III-V/Ge counter parts; the challenging manufacturing path of direct growth of III-V on Si substrate might be the winning approach in that sense.

Perspectives

These results open several perspectives for the scientific and devices aspects of the III-V//Si tandem cells. For instance, it would be interesting to investigate whether the recovery observed after irradiation at 120 K and annealing at 300 K is persistent, or whether the defects are reactivated once cooled back down to 120 K. Indeed, in a *LILT* mission scenario, if we assume that annealing at 300 K is performed, the solar array would again operate at low temperature afterward. In addition, we have only here studied proton irradiations at 300 K; experimental plan with proton irradiations at low temperature would certainly bring interesting insights, in order to see whether the *DDD* method is still applicable at low temperature. Extensive work was carried out toward the end of this thesis to mount and adjust the in-situ, on the electron beam line, the quantum efficiency equipment; however, several issues could not be solved before until now. *EQE* measurements on all sub-cells may be of interest to analyze their behavior precisely as a function of temperature and irradiation conditions.

From the device performance point of view, several improvement paths are foreseen for a better *EOL* III-V//Si tandem cells performance. The first priority shall be made on the Si sub-cell, the less radiation hard material, with the following development axis:

i) Optimization of the Si bulk doping level and element (e.g. low doping for low fluence), to reduce the diffusion length damage coefficient (K_L). The use of Ga atoms as dopant for instance leads to a reduction of electrically active radiation-induced defects density.

ii) Reduction of the Si sub-cell thickness: with front side p-n junction, the collection probability of photo-generated charge carrier deep in the bulk

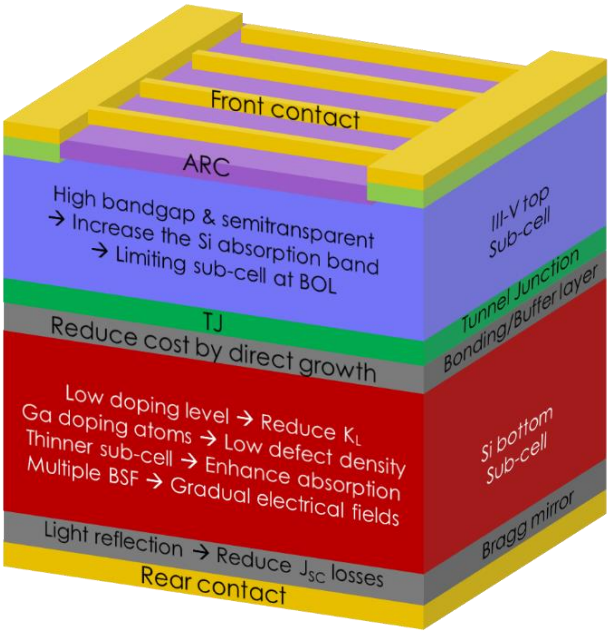

Fig. 2 *Improvement way for higher radiation hardness of III-V//Si solar cells*

decreases under irradiation, which translates into J_{SC} degradation. The key is thus to design a cell which decouple the absorption length and diffusion length. Very thin Si wafers (~50 µm), in combination with effective rear-side mirror, are very promising in that sense since they can maintain full absorption and require limited diffusion length for efficient collection. Alternatively, locally thinned wafers (e.g. waffle or holes structures) may be an interesting compromise with respect breakage risk.

As a second priority, the use of top sub-cells with adjusted higher bandgaps would result in a wider Si absorption band and thus attenuate its relative irradiation sensitivity. The use of thinner top sub-cells with some degree of transparency would also increase absorption in Si. Thus, at the cost of lower *BOL* efficiency, those optimizations would improve the radiation hardness of the III-V//Si technology by unlocking higher *EOL* performances. Ultimately, multi-junction cells design could be optimized for various missions to maximize *EOL* results in various environment. These development directions are schematically summarized in Fig. 2.

Résumé

Ce travail s'intéresse au comportement en environnement spatial d'une nouvelle technologie de cellules solaires photovoltaïques : les tandems III-V//Si (2- et 3-jonctions), obtenues par collage direct. Ces cellules ont été exposées à des irradiations électrons et protons et testées dans deux types d'environnement : a) irradiance normale, 1 soleil, et température ambiante 300K, condition *NIRT* (orbites terrestres) et b) basse irradiance, 0,03 soleil, et basse température 120K, condition *LILT* (espace lointain). Dans une étape préliminaire une étude comparative a été menée sur 2 simulateurs solaires, équipés respectivement d'une lampe flash et de lampes *LED*, afin d'assurer la fiabilité et la reproductibilité des mesures de ces multi-jonctions. Pour le simulateur flash, une méthode de caractérisation pour tandems *I-V* sous 1 soleil qui s'affranchit de l'utilisation de cellules de référence isotype a été adoptée, en se basant sur des mesures d'*EQE* et des mesures de spectre du flash. Pour le simulateur *LED*, monté in-situ sur le faisceau d'irradiation, une optimisation du spectre a été effectuée afin de se rapprocher de la référence à basse irradiance, soit ~3% AM0. Cette étude comparative a également permis d'établir la validité de l'extrapolation par le calcul de mesures *I-V* sous 1 soleil vers les basses irradiances.

Ensuite, la compatibilité de cette technologie tandem III-V//Si, avec d'une part le cyclage thermique et d'autre part les irradiations a été démontrée, l'interface de collage maintient son intégrité mécanique et électrique face à ces contraintes. L'impact des irradiations sur les performances cellules a révélé certaines similitudes à 300K et 120K : - une décroissance marquée du courant de court-circuit (liée à la diminution de la longueur de diffusion) - une diminution plus faible de la tension de circuit-ouvert (défauts de type génération). Du fait de la connexion en série des sous-cellules, la dégradation de la limitante Si (faible résistance intrinsèque aux irradiations) domine le comportement de la multi-jonction. Il a été démontré que l'ajout d'un nombre croissant de cellules sur le Si se traduit par une sensibilité accrue aux irradiations ; en effet, la configuration tandem restreint la bande d'absorption du Si au proche infrarouge, partie spectrale la plus affectée par la baisse de longueur de diffusion. L'utilisation d'un modèle basé sur l'*IQE* a permis de quantifier cette dégradation de longueur de diffusion dans le Si en tandem, ainsi que le coefficient de dommage. A la différence des électrons, les irradiations aux protons 1 MeV sont à l'origine d'une dégradation non-uniforme dans le Si ; par des mesures *EQE* couplées à de la simulation, nous avons corrélé cette dégradation non-homogène dans le Si avec la position du pic de Bragg correspondant.

Pour l'étude basse température, une augmentation linéaire de l'efficacité a été observée jusqu'à ~150K ; et en deçà, des anomalies de caractéristiques *I-V* ont été détectées ; de type « *S-like shape* » et « *flat spot* » ces défauts affectent le FF et donc le rendement. Documentés dans la littérature, ces effets sont caractéristiques des conditions *LILT*, et souvent liés à des modifications des interfaces métal/semi-conducteur. Bien qu'importante, la dégradation des performances électriques fin de vie *LILT* des III-V//Si s'avère être plus prédictible que celles des III-V/Ge *LILT* (dispersion statistique). Nous avons également démontré qu'un passage à 300K, après irradiation à 120K, entraine une guérison marquée du courant de court-circuit ; ceci souligne l'importance des caractérisations in-situ pour quantifier le vieillissement cellule en conditions de fonctionnement. L'approche *DDD* « *Displacement Damage Dose* » a été appliqué pour les électrons et protons 1 MeV afin de comparer le taux de dégradation induit. Cette approche permet de prédire la dégradation de ces cellules quelle que soient la fluence, les particules et l'énergie, pour une mission spatiale à 300K.

List of Figures

List of Tables

ECOLE DOCTORALE

Titre : Etude du comportement de la nouvelle technologie des cellules solaires III-V//Si sous irradiations pour les applications spatiales.

Mots Clés : Cellules solaires, Tandem sur silicium, III-V//Si, Irradiation électronique, Irradiation protonique, Conditions NIRT, Conditions LILT, Applications spatiales.

Résumé : Ce travail s'intéresse au comportement en environnement spatial d'une nouvelle technologie de cellules solaires photovoltaïques : les tandems III-V//Si (2- et 3-jonctions), obtenues par collage direct. Ces cellules ont été exposées à des irradiations électrons et protons et testées dans deux types d'environnement : a) irradiance normale, 1 soleil, et température ambiante 300K, condition *NIRT* (orbites terrestres) et b) basse irradiance, 0,03 soleil, et basse température 120K, condition *LILT* (espace lointain). Dans une étape préliminaire une étude comparative a été menée sur 2 simulateurs solaires, équipés respectivement d'une lampe flash et de lampes *LED*, afin d'assurer la fiabilité et la reproductibilité des mesures de ces multi-jonctions. Pour le simulateur flash, une méthode de caractérisation pour tandems *I-V* sous 1 soleil qui s'affranchit de l'utilisation de cellules de référence isotype a été adoptée, en se basant sur des mesures d'*EQE* et des mesures de spectre du flash. Pour le simulateur *LED*, monté in-situ sur le faisceau d'irradiation, une optimisation du spectre a été effectuée afin de se rapprocher de la référence à basse irradiance, soit ~3% AM0. Cette étude comparative a également permis d'établir la validité de l'extrapolation par le calcul de mesures *I-V* sous 1 soleil vers les basses irradiances.

Ensuite, la compatibilité de cette technologie tandem III-V//Si, avec d'une part le cyclage thermique et d'autre part les irradiations a été démontrée, l'interface de collage maintient son intégrité mécanique et électrique face à ces contraintes. L'impact des irradiations sur les performances cellules a révélé certaines similitudes à 300K et 120K : - une décroissance marquée du courant de court-circuit (liée à la diminution de la longueur de diffusion) - une diminution plus faible de la tension de circuit-ouvert (défauts de type génération). Du fait de la connexion en série des sous-cellules, la dégradation de la limitante Si (faible résistance intrinsèque aux irradiations) domine le comportement de la multi-jonction. Il a été démontré que l'ajout d'un nombre croissant de cellules sur le Si se traduit par une sensibilité accrue aux irradiations ; en effet, la configuration tandem restreint la bande d'absorption du Si au proche infrarouge, partie spectrale la plus affectée par la baisse de longueur de diffusion. L'utilisation d'un modèle basé sur l'*IQE* a permis de quantifier cette dégradation de longueur de diffusion dans le Si en tandem, ainsi que le coefficient de dommage. A la différence des électrons, les irradiations aux protons 1 MeV sont à l'origine d'une dégradation non-uniforme dans le Si ; par des mesures *EQE* couplées à de la simulation, nous avons corrélé cette dégradation non-homogène dans le Si avec la position du pic de Bragg correspondant.

Pour l'étude basse température, une augmentation linéaire de l'efficacité a été observée jusqu'à ~150K ; et en deçà, des anomalies de caractéristiques *I-V* ont été détectées ; de type « *S-like shape* » et « *flat spot* » ces défauts affectent le FF et donc le rendement. Documentés dans la littérature, ces effets sont caractéristiques des conditions *LILT*, et souvent liés à des modifications des interfaces métal/semi-conducteur. Bien qu'importante, la dégradation des performances électriques fin de vie *LILT* des III-V//Si s'avère être plus prédictible que celles des III-V/Ge *LILT* (dispersion statistique). Nous avons également démontré qu'un passage à 300K, après irradiation à 120K, entraine une guérison marquée du courant de court-circuit ; ceci souligne l'importance des caractérisations in-situ pour quantifier le vieillissement cellule en conditions de fonctionnement. L'approche *DDD* « *Displacement Damage Dose* » a été appliqué pour les électrons et protons 1 MeV afin de comparer le taux de dégradation induit. Cette approche permet de prédire la dégradation de ces cellules quelle que soient la fluence, les particules et l'énergie, pour une mission spatiale à 300K.

Title : Investigation of the emerging III-V//Si tandem solar cell behavior under irradiations for space applications.

Keywords : Solar cells, Tandem on silicon, III-V//Si, Electrons irradiation, Protons irradiation, NIRT conditions, LILT conditions, Space application.

Abstract : This work focuses on the behavior in space environment of a new photovoltaic solar cell technology : the III-V//Si tandems (2- and 3-junctions), obtained by direct bonding. These cells have been exposed to electrons and protons irradiations and tested in two types of environment: a) normal irradiance, 1 sun and room temperature, 300K - *NIRT* conditions (Earth orbits) and b) low irradiance, 0.03 sun, and low temperature, 120K - *LILT* conditions (deep space).

In a preliminary stage, a comparative study was conducted on 2 solar simulators, respectively equipped with a flash lamp and *LEDs*, in order to ensure the reliability and reproducibility of the measurements of these multi-junctions. For the flash simulator, a characterization method for 1-sun *I-V* measurements that does not require the use of isotypes reference cells has been adopted, based on *EQE* and flash spectrum measurements. For the *LED* simulator, mounted in-situ on the electron irradiation beam, a spectrum optimization was performed in order to approach the low irradiance reference, i.e. ~3% AM0. This comparative study also allowed us to assess the validity of the extrapolation by calculation of the 1-sun I-V measurements towards the low irradiances.

Then, the compatibility of this tandem III-V//Si technology with thermal cycling on the one hand and irradiations on the other hand has been demonstrated. The bonding interface maintains its mechanical and electrical integrity with these constraints. The impact of the irradiations on the cell performances has revealed certain similarities at 300K and 120K: - a pronounced decrease of the short-circuit current (linked to diffusion length drop) - a less pronounced open-circuit voltage decrease (generation defects). Due to the series connection of the sub-cells, the degradation of the limiting Si (low intrinsic resistance to irradiation) dominates the behavior of the multi-junction. We have shown that an increasing number of cells on Si results in an increased sensitivity to irradiations; indeed, the tandem configuration restricts the absorption band of the Si to the near infrared, the spectral part the most affected by the diffusion length decrease. The use of a model based on the *IQE* allowed the quantification of this Si diffusion length degradation in the tandem, as well as the damage coefficient. Unlike electrons, 1 MeV proton irradiations are responsible for a non-homogeneous degradation in Si; by *EQE* measurements coupled with simulation, we have correlated this non-homogeneous degradation in Si with the position of the corresponding Bragg peak.

For the low-temperature study, a linear increase in efficiency was observed up to ~150K; and below this, anomalies of *I-V* characteristics were detected; of "S-like shape" and "flat spot" type, these defects affect the FF and thus the efficiency. Reported in the literature, these effects are characteristic of *LILT* conditions, and are often related to changes in the metal/semiconductor interfaces. Although significant, the *LILT* end-of-life electrical performance degradation of III-V//Si happened to be more predictable than that of III-V/Ge *LILT* (less statistical dispersion). We have also shown that a 300K annealing after irradiation at 120K leads to a marked healing of the short-circuit current; this underlines the importance of in-situ characterizations to quantify cell ageing under operating conditions. The Displacement Damage Dose (*DDD*) approach was applied for 1 MeV electrons and protons in order to compare the rate of induced degradation. This approach allows to predict the degradation of these cells whatever the fluence, particles and energy, for a space mission at 300K.

Institut Polytechnique de Paris
91120 Palaiseau, France